Investigation of the Resonance-like $a_1(1420)$ Signal and First Partial-Wave Decomposition of the $\pi^- K_S^0 K_S^0$ Final State at COMPASS

Dissertation
zur
Erlangung des Doktorgrades (Dr. rer. nat.)
der
Mathematisch-Naturwissenschaftlichen Fakultät
der
Rheinischen Friedrich-Wilhelms-Universität Bonn

von
Mathias Wagner
aus
Engelskirchen

Bonn, November 2023

Angefertigt mit Genehmigung der Mathematisch-Naturwissenschaftlichen Fakultät der Rheinischen Friedrich-Wilhelms-Universität Bonn

1. Gutachter:	Prof. Dr. Bernhard Ketzer
2. Gutachter:	Prof. Dr. Hartmut Schmieden
Tag der Promotion:	22.03.2024
Erscheinungsjahr:	2024

Para mi roca en la tempestad, mi caja de quejas,
mi rayo de luz en tiempos de desesperanza,
la mejor asistente de investigación, la mejor compañera,
mi esposa.

Abstract

"Investigation of the Resonance-like $a_1(1420)$ Signal and First Partial-Wave Decomposition of the $\pi^- K_S^0 K_S^0$ Final State at COMPASS"

In 2014, a supernumerous light-meson state was found by the COMPASS collaboration. This discovery bore similarities to some of the XYZ states in the heavy-meson sector, discovered at e^+e^- colliders, that did not fit the expectations from the quark model and hence were called exotic states. The partial-wave decomposition of the COMPASS data for the $\pi^-\pi^+\pi^-$ final state, which is employing an isobar model, revealed a narrow signal with axial-vector quantum numbers in the $f_0(980)\pi$ P-wave. Since it was found at an energy of 1.4 GeV by a resonance-model fit with a relativistic Breit-Wigner model, it was called $a_1(1420)$. This thesis investigates the nature of the signal, following two avenues.

In the first part, it is shown how a rescattering of final-state particles can produce such a signal by explicitly performing a projection of a K^*K intermediate state to the $f_0(980)\pi$ final state. The resulting theoretical model is fitted to the COMPASS data and the quality is compared to a fit using a conventional relativistic Breit-Wigner model. Several systematic studies are performed. This includes a fit to each of the systematic studies of the underlying partial-wave decomposition, as well as a bootstrap analysis and modifications of the theoretical model. In all cases except one, the rescattering interpretation shows a better compatibility with the data.

In the second part, an event selection of the complementary $\pi^- K_S^0 K_S^0$ final state is performed, where the optimal vertex separation for the K_S^0 mesons is determined by means of a significance study to reduce background coming from a possible 5π final state. A total of $\sim$ 240 000 exclusive events are selected, superseding the statistics of previous experiments of diffractive $\pi^- K_S^0 K_S^0$ production by a factor of $\sim$ 240. Based on the selected data set, a first partial-wave decomposition is performed, revealing strong evidence for the $a_1(1420)$ signal in the $f_0(980)\pi$ P-wave of the $\pi^- K_S^0 K_S^0$ final state in form of an enhancement in the intensity and a phase motion in the relative phase to other waves, even for both resonance-spin projections $M = 0$ and $M = 1$. At the same time, no resonance-like signal is visible at $\sim$ 1.4 GeV in the $K^*(892)K_S^0$ S-wave, which agrees well with the interpretation of a rescattering effect. The spin-exotic $\pi_1(1600)$, a candidate for the lightest hybrid meson, manifests itself as a broad peak in the $K^*(892)K_S^0$ P-wave, however, no significant evidence for a relative phase motion with other partial waves is observed. Another hybrid candidate with ordinary quantum numbers, the pseudoscalar $\pi(1800)$, shows up as a clean narrow peak in the $f_0(980)\pi$ S-wave. It is accompanied by a narrow resonance-like signal at 1.4 GeV, i.e. an enhancement in the intensity together with phase motion in the relative phase to other partial waves. This could be the first observation of a "$\pi(1420)$" rescattering effect, similar to the $a_1(1420)$, but with pseudoscalar resonance quantum numbers.

Contents

CHAPTER 1

Introduction / Motivation

1.1 The Standard Model of Particle Physics

One of the biggest and most successful models in physics is the standard model of particle physics. It not only covers the unification of electromagnetic (em) and weak interaction into the electro-weak interaction, but it also incorporates our current understanding of the strong force. The latter one is responsible for the binding of protons and neutrons inside the nucleus – mostly pion-exchange-induced – as well as for the binding of the constituents inside of the nucleons themselves, where gluon-exchange is the relevant mechanism.

Force carriers, such as photons for the em interaction, gluons and even pions[1] for the strong interaction, as well as $W^{\pm}$ and Z^0 bosons for the weak interaction, all carry integer spin and, thus, they are bosons. On the other hand, the constituents of matter are fermions, i.e. half-integer-spin particles. Examples are electrons, protons and neutrons that make up all atoms on the periodic table, as well as quarks that are the constituents of the nuclei. Figure 1.1 shows nicely which force carriers interact with which fermions by encircling them accordingly. The fermions can be grouped into pairs, for example the up and down quark build a doublet $\begin{pmatrix} u \\ d \end{pmatrix}$ according to the electro-weak model[2] with their weak charge – also known as flavor charge – defined by their identity. Since they carry color charge (for each quark there exist three versions, a red (R), a green (G) and a blue one (B)), em charge ($+\frac{2}{3}$ for up-type quarks and $-\frac{1}{3}$ for down-type quarks) and flavor charge, they can interact with all previously mentioned elementary force carriers. The gluon, as the elementary force carrier of the strong interaction, also carries color charge, which enables self-interactions between the force carriers themselves making the strong force behave very differently compared to em interactions.

The leptonic doublet[3] $\begin{pmatrix} \nu_e \\ e \end{pmatrix}$ is the electron combined with the electron-neutrino, of which the latter was first introduced as the missing piece in the explanation of nuclear β decays. Carrying em charge and flavor charge, the electron does not interact with the gluon. Neutrinos, on the other hand, only

[1] While all others are considered to be elementary, the pion itself is made up of quarks and gluons.

[2] Things are a bit more complicated, because according to the electro-weak model we have a doublet of left-chiral quarks and two singlets of right-chiral quarks.

[3] Also here we have a left-chiral doublet and two right-chiral singlets of which the neutrino singlet would not interact with anything, therefore, making its existence questionable.

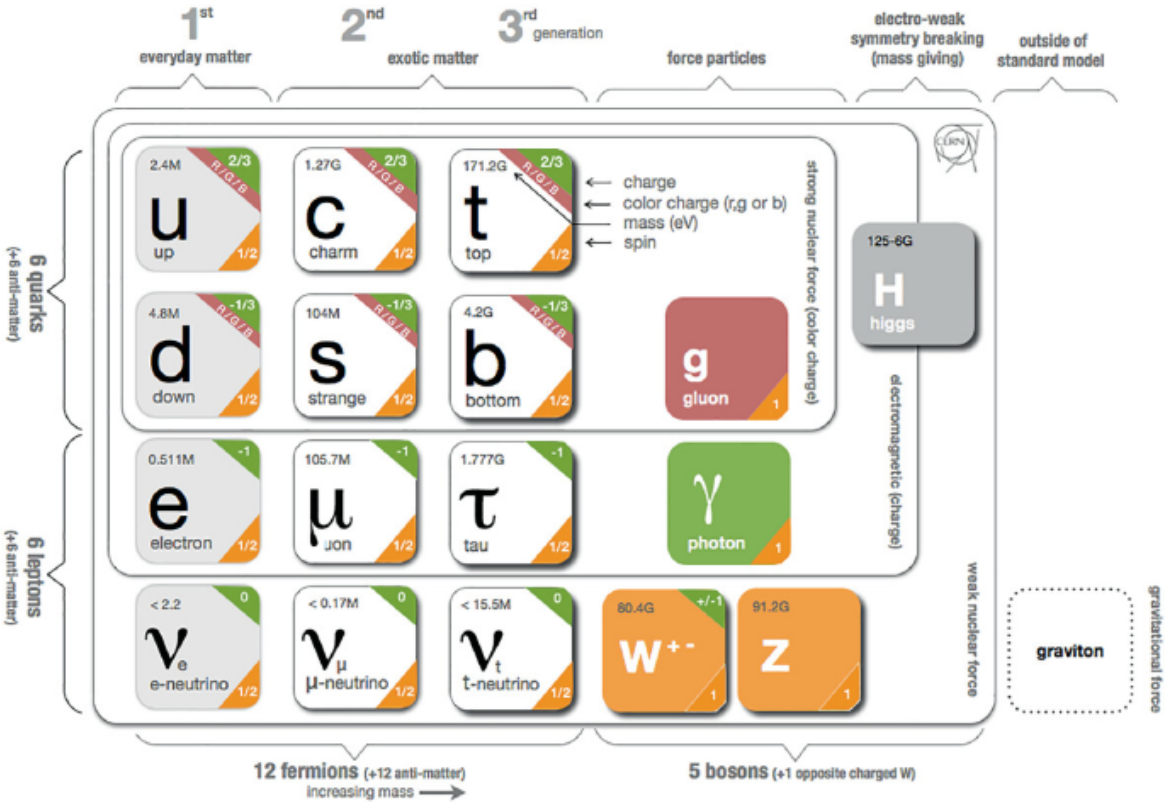

Figure 1.1: Depiction of the particles described by the Standard Model of Particle Physics (and the graviton), [1]

have flavor charge, enabling them to solely interact weakly via W and Z exchange.

All these pairs turn out to come in three copies, so-called particle generations, differentiated by their increase in mass. In addition to every of these fermions, there exists the corresponding antifermion[4] that has the same mass and opposite em/color/flavor charge.

The graviton, as so far hypothetical force carrier of gravitation, is not part of the standard model. This leads to the fact that the mass-interaction of (elementary) particles with each other is not described. It can also be safely neglected with respect to the other forces, because for example the em force between an electron and a positron at a distance of $r = 1\,\mathrm{m}$ is $F_{\mathrm{em}} = \frac{e^2}{4\pi\varepsilon_0 r^2} = 2.3 \times 10^{-28}\,\mathrm{N}$ while the gravitation between the two at the same distance amounts to $F_G = G\frac{m_e^2}{r^2} = 5.54 \times 10^{-71}\,\mathrm{N}$. This is 43 magnitudes smaller and, thus, safely negligible within all experimental uncertainties.

However, there is a particle in the standard model that has to do with mass, the Higgs boson. This particle gives mass to the elementary fermions[5] as well as the W and Z bosons by making particles heavier the stronger they interact with it.

[4] One exception could be the neutrino. There exists an extension for the standard model according to which the neutrino could be its own antiparticle $\bar{\nu}_e \equiv \nu_e$ and proof for this is searched for in neutrino-less double-β decays, where the two antineutrinos of each β decay could annihilate although they would have the same flavor charge.

[5] All fermions except the neutrinos obtain their mass through the Higgs mechanism. We know that neutrinos have mass due to the observation of neutrino oscillations, however, this mass has to be produced by a different mechanism. According to the standard model of particle physics neutrinos are massless.

1.2 The Quark Model and Exotic States

Although originally only intended to group found states and predict new ones, it later turned out that there is a lot of truth behind defining mesons as quark-antiquark pairs and baryons as 3-quark states. At the beginning, only the light up quark u, down quark d and strange quark s were known. Their masses were assumed to be of the order of 300 MeV for u and d quarks and 450 MeV for the s quark. Two u and one d quark produce a proton, and one u and two d quarks produce a neutron, both of approximately 900 MeV mass. Replacing one of the u quarks of the proton by an s quark, we obtain 1 050 MeV, which is close to the mass of the Λ baryon. Now, these masses are known as constituent-quark masses and are highly model-dependent. However, if one includes corrections due to spin interactions of the quarks, they work surprisingly well to estimate the masses of baryons. Also for mesons, constituent-quark models exist and work to predict the masses of most of the light pseudoscalar and vector mesons.

Nowadays, we know that quarks do not actually have their constituent-quark mass as stated above, but are a lot lighter. The biggest part of the meson and baryon mass is created through the strong interaction that is responsible for the binding by allowing for the creation of so-called sea quarks and gluons. The former are temporary fluctuations of internal gluons into a pair of a virtual quark and virtual antiquark of the same flavor and immediate annihilation of these ones. Thus, the Higgs mechanism only explains a small fraction of the mass of mesons and baryons, specifically the contribution from the bare "current"-quark mass.

The reason, why quarks were just considered a theoretical classification concept at first, is "confinement". This means that nature exclusively allows for "white" combinations, more precisely color singlets. We have (anti)quarks as color-(anti)triplet states, because they can have one of three different (anti)colors. Gluons, on the other hand, are color-octet states having a combination of a color and an anticolor. Therefore, neither quarks nor gluons can exist freely.

All physical states, like hadrons, have to be color-neutral and color-singlet states. This means that all colors are contributing to them equally. In the case of baryons, we also have to make sure that this combination is completely antisymmetric under exchange of any two spin-$\frac{1}{2}$ constituents in order to satisfy Fermi statistics. A wave function for a color singlet can be obtained by taking a color and the corresponding anticolor forming mesonic states with $\Psi_{\text{color}}^{\text{meson}} = \frac{1}{\sqrt{3}}\left(R\bar{R} + G\bar{G} + B\bar{B}\right)$. Another combination is three (anti)quarks having three different (anti)colors forming an (anti)baryon. The color wave function of a baryon $\Psi_{\text{color}}^{\text{baryon}} = \frac{1}{\sqrt{6}}\left(RGB - RBG + GBR - GRB + BRG - BGR\right)$ is antisymmetric under exchange of any two quarks. Confinement does not forbid combinations of more quarks, like tetraquarks with two quarks and two antiquarks, pentaquarks with four quarks and one antiquark, and so on. Also, some combination of quarks with additional "constituent gluons" could be possible, called hybrids, the simplest case of which could be expressed as a $q\bar{q}'g$ state. More precisely, it would rather be a state where the "color string" connecting the two quarks can be excited. Another possibility is a state entirely made up of constituent gluons, called glueball. Although in the past, it seemed as if only simple meson and baryon states were present in nature, now, more and more additional states appear that could not be explainable as one of these simple combinations.

The best way to search for these states is in places where one does not expect to find any simple mesons or baryons. For example in the case of mesons, this can be done with a combination of internal Quantum Numbers (QNs) that could not be created by a $q\bar{q}$ state. Such states are termed spin-exotic and they specifically are the combinations $J^{PC} \in \left\{0^{--}, \text{even}^{+-}, \text{odd}^{-+}\right\}$. However, also in

the "normal"-spin sector tetraquarks, pentaquarks, glueballs and hybrids are expected. But since they have the same QNs, they will mix and interfere with the ordinary mesons and baryons. To disentangle these states, one has to find different strategies that will have to be determined on a case-by-case basis. One way to predict where such states could be found, is lattice-QCD (ℓQCD). Here, one uses numerical calculations in order to calculate physics on a discretized space-time lattice using constraints from first principles.

The group of exotic states does not only incorporate objects built by combining different amounts of (anti)quarks and gluons. One can also think of meson and baryon molecules that are formed by constituent mesons and baryons. Their concept is not at all unknown, since all chemical elements – heavier than plain hydrogen – are nothing else than baryon molecules consisting of protons and neutrons. Instead of gluon exchange, the binding is created by meson exchange, resulting in objects with slightly larger volumes than tetraquarks and pentaquarks. In addition, kinematic effects, such as rescattering of the decay products of well-known mesons and baryons, can produce experimental signatures similar to the ones of ordinary states.

1.3 Motivation and Outline: Exotic Mesons at COMPASS

While theoretical explorations of exotic states already took place before, their experimental story started in 2002. A resonance was found by the Belle collaboration [2], which had QNs inconsistent with an interpretation as an ordinary meson according to the simplest quark model, the so-called $X(3872)$, now renamed as $\chi_{c1}(3872)$. Soon after, other states $Y(4260)$ ([3]) and $Z_c(3900)$ ([4, 5]) were found that also did not find a place in the expected meson spectrum obtained by combining a quark and an antiquark. These states together formed a new class of heavy mesons called XYZ states.

But not only in the heavy quark sector unexpected new discoveries were made. In 2014, the COMPASS experiment at CERN found a signal at 1.4 GeV in diffractive pion-proton scattering [6] that also did not meet the expectations of an ordinary meson. Its mass – determined by a fit with a conventional relativistic Breit-Wigner model – and its QNs gave it the name $a_1(1420)$, and while being nothing extraordinary at first sight, it was one state too much in the line of radially-excited axial-vector states, a so-called supernumerous state. Although being too close to the ground state and even narrower, the signal was very persistent throughout all systematic studies of the underlying partial-wave decomposition of the $\pi^-\pi^+\pi^-$ final state, therefore, it had to be there and it had to be something different.

Many of the heavy exotics are discussed as a molecular state of two meson or a tetraquark. For the supernumerous $a_1(1420)$ decaying into $f_0(980)\pi$, there exists a different possibility, a so-called triangle singularity. Such a mathematical logarithmic singularity can mimic the behavior of a pole, which corresponds to an ordinary resonance. However, it is a kinematic effect that occurs when the products of a decay interact again to perform a rescattering. In this case the ground state $a_1(1260)$ will decay to $K^*(892)\overline{K}$, first. Then, the $K^*(892)$ will decay to $K\pi$. Now, this K and the $\overline{K}$ from the initial decay meet to form the $f_0(980)$, which, finally, will decay into the investigated $\pi^-\pi^+\pi^-$ final state. Calculating the corresponding Feynman-like diagram, it turns out that such a singularity can also show up as a peak in the invariant mass of the final-state system. Additionally, it even creates a strong phase motion in the interference with other resonances. Both are usually signs for a resonance, for example described by a commonly used relativistic Breit-Wigner model.

To further strengthen this interpretation as a rescattering effect, one has to look at other reactions

and other final states where it can appear. One promising place is the decay of a τ lepton that can have a $\pi^-\pi^+\pi^-$ final-state subsystem. The advantage over the diffractive production, is that there is no background coming from the non-resonant Deck-like process, which provides a strong contribution to the COMPASS data. The Belle experiment is currently investigating in this direction [7], already seeing the $a_1(1420)$ signal in preliminary results of a partial-wave decomposition [8]. But also at COMPASS, we have other accessible final states that we can search in, one of which is the $\pi K\overline{K}$ final state. In the past, an event selection of the $\pi^- K^+ K^-$ final state was performed [9], however, the detector acceptance became finite only above 1.5 GeV, due to kinematic limitations of the RICH detector in the particle identification. This leads to the idea of looking at the $\pi^- K_S^0 K_S^0$ final state, since neutral K_S^0 can be detected via their decay into a $\pi^+\pi^-$ pair with a displaced vertex from the original interaction inside of the target.

In this thesis, we focus on the COMPASS Experiment to search for exotic mesons. Due to its wide variety of accessible final states – from both pion and kaon beams diffractively scattered off of a fixed hydrogen target – it allows for the investigation of states in different decay modes. The experimental setup is introduced in chapter 2 together with a description of the COMPASS analysis framework (section 2.2).

Chapter 3 introduces general concepts of scattering theory (section 3.1) and how to construct Breit-Wigner models (section 3.3), where their complex structures are investigated in detail. Furthermore, the concept of partial-wave decompositions is explained (section 3.4) and a method is presented that allows to calculate Dalitz plots from a theoretical model (section 3.5). Next, a more sophisticated way to calculate the amplitude of a rescattering process is discussed. It involves performing a projection of one partial wave onto another, which allows for the proper inclusion of spins and orbital angular momenta of the involved particles and decays (sections 3.6 and 4.3.3). In chapter 4, we apply this method to the case at COMPASS and we discuss the fit of this new model to the results of the partial-wave decomposition of the $\pi^-\pi^+\pi^-$ data from the COMPASS experiment. It is compared to a second fit with the previously mentioned Breit-Wigner model (section 4.4) and several systematic studies are performed (section 4.6).

Chapter 5 of this thesis deals with the event selection of the $\pi^- K_S^0 K_S^0$ final state (section 5.2), which enables the search for the $a_1(1420)$ in a second final state at COMPASS. In chapter 6, a first attempt at the subsequent partial-wave decomposition is performed that is needed to separate contributions of different QNs from each other (section 6.3). Not only gives this access to a possible sign of the $a_1(1420)$ in the $\pi^- K_S^0 K_S^0$ sector, but it also allows us to look for the same resonances as in the already analyzed $\pi^-\pi^+\pi^-$ final state at COMPASS. This includes the lightest spin-exotic candidate $\pi_1(1600)$, whose decay into $K^*\overline{K}$ is predicted by ℓQCD [10].

CHAPTER 2

The COMPASS Experiment

2.1 The Experimental Setup

The COmmon Muon Proton Apparatus for Structure and Spectroscopy (COMPASS), see Figure 2.1 and [11], is located in the North Area of the European Council for Nuclear Research (CERN). It obtains its proton beam from the Super Proton Synchrotron (SPS) at a beam energy of approximately 400 GeV. This primary proton beam is shot on a thin beryllium target inside the beam tunnel at the M2 beam line, producing all kinds of particles. With a system of magnets these particles can be focussed and selected according to their momentum and charge.

This thesis focusses on data collected with a negative hadron beam with a momentum of roughly 190 GeV, which consists to 96.8 % out of π^-, to 2.4 % out of K^- and to 0.8 % out of $\overline{p}$ (Table 2 of [11]). Two ChErenkov Detectors with Achromatic Ring focus (CEDARs), which allow for the identification of these hadronic beam particles, are located inside the beam tunnel. The beam trajectory[1] is precisely measured with the beam telescope consisting of several Silicon microstrip detectors (Silicons) and Scintillating Fibers (SciFis). The former are placed directly around the COMPASS target and are very important for vertex reconstruction.

The COMPASS target is located at the entrance to the experimental hall and can be changed depending on the physics of interest. For diffractive scattering, a lead target was used in 2004. To minimize multiple scattering, it was changed to a liquid-hydrogen target (ℓH2) for the data taking in 2008 and 2009.

In transversal direction to the beam axis, the target is surrounded by the Recoil-Proton Detector (RPD). It is a time-of-flight detector that consists out of two barrels of scintillating slabs (cf. Figure 5.1) and measures the velocity of particles that are hit out of the target at large angles. It is specifically calibrated to identify recoiling protons and – depending on which slab is hit – it provides a rough determination of their azimuthal angle. Since each slab is read out from both sides, it also allows for a measurement of the polar angle by determining the time difference between the arrival of the signals on both sides. However, this information is mostly used for calibration purposes.

A trigger system is put in place in order to select for different types of events. For this thesis, the so-called Diffractive Trigger (DT0) is of importance. It is a combination of the alternative Beam Trigger (aBT) and the previously mentioned RPD as well as a system of veto detectors, see section 5.2.2 for more details on them.

[1] The Beam Momentum Station (BMS) that can measure the momentum of the beam, is only used for muon beams.

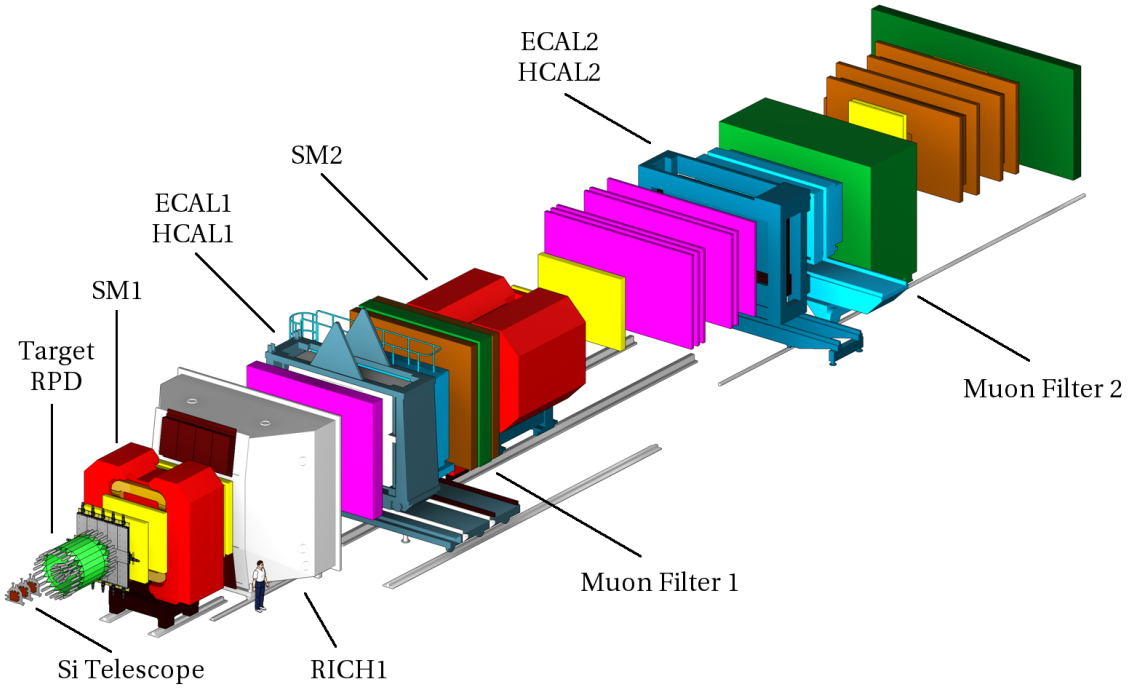

Figure 2.1: COMPASS Setup for the hadron runs in 2008 and 2009, from [11].

In order to identify particles that leave the target in longitudinal beam direction, a Ring-Imaging CHerenkov detector (RICH) is used. With its help, one can distinguish pions from kaons and (anti)protons. For this project, it is mainly used as veto detector due to its limitations in the identification power for large particle momenta.

The COMPASS spectrometer has two big dipole magnets – called Spectrometer Magnet 1 (SM1) and Spectrometer Magnet 2 (SM2) – that separate its setup into two areas. The area between SM1 and SM2 is called Large-Angle Spectrometer (LAS) since only particles with small momenta or large initial angles are detected here. Accordingly, the area behind SM2 is called Small-Angle Spectrometer (SAS) because the second magnet separates particles further, which are closer to the beam line and have higher momenta. Besides of this separation from the beam axis, the bending of the trajectory of charged particles by the magnets, together with the information of several (mostly gaseous) tracking detectors of various sizes and with different resolution depending on their location and purpose, enable a precise momentum measurement. Small-Area Trackers (SATs) like Silicons, Micro MEsh GAseous Structures (MicroMEGAS), Gas Electron Multipliers (GEMs) and Pixel Gas Electron Multipliers (PixelGEMs) are located around the beam trajectory and Large-Area Trackers (LATs) like Drift Chambers (DCs), Wire chambers (W45), Multi-Wire Proportional Chambers (MWPCs) and Straw Tube Trackers (Straws), including the so-called "RICH wall", cover the rest. Details on the individual detector types can be found in [11].

In both LAS and SAS, we have an Electromagnetic CALorimeter (ECAL) and a Hadronic CALorimeter (HCAL) to measure the energy of particles, especially neutrals. The calorimeters in the LAS – namely

ECAL1 and HCAL1 – have a huge hole in the center allowing neutrals at small angles to pass through and being detected in the calorimeters in the SAS, ECAL2 and HCAL2. Also every other detector has a hole in the center, because otherwise, due to the high beam rates, they would drown in signals from unscattered beam particles and would be blind for other particles. Only some special detectors, like Silicons and PixelGEMs[2], can handle these high data rates. Additionally, especially for the LATs, a separation of clusters would be very challenging in the center due to the high track density.

After each HCAL are Muon Walls (MWs), which are drift tube detectors surrounding thick absorber walls, also known as Muon Filters. Only muons can pass through these absorbers[3] and, therefore, a track that is followed by a signal in one of the MWs after the absorbers, can only be originating from a muon.

This two-staged spectrometer setup provides a good angular and kinematic acceptance with a precise momentum determination and particle tracking, making it very versatile. Hadron beams can be employed for the study of diffractive $\pi + p$ or $K + p$ scattering, the Drell-Yan process [12] and a measurement of the pion polarizability [13, 14] as well as of the chiral anomaly [15] via the Primakoff process. In addition, a muon beam is available that allows for the investigation of generalized-parton-distribution functions via deeply-virtual compton scattering [16, 17] and Semi-Inclusive Deep Inelastic Scattering [18].

Besides of other interesting physics programs, the Apparatus for Meson and Baryon Experimental Research (AMBER) [19] – the successor of COMPASS – has planned a diffractive scattering run with increased kaon or antiproton fractions in the beam. This would enable AMBER to do the same for kaon spectroscopy as what COMPASS did for pion spectroscopy: precisely measure the hadron spectrum and find "exotic" particles ($\pi_1(1600)$) and unexpected signals ($a_1(1420)$) that lead to exciting conclusions. But more on that in the chapters 4 and 6.

2.2 The Analysis Framework of COMPASS

The Data AcQuisition (DAQ) of the COMPASS experiment stores the raw detector information in files which are read and processed by the COmpass Reconstruction ALgorithm (CORAL) that itself stores the reconstructed events in so-called Data Storage Trees (DST). These files are ROOT trees containing the geometry[4] of the COMPASS detector as well as all information needed for further analyses.

The next step in the analysis chain is a preselection on the data for a specific final state or a set of possible final states, see section 5.2.1 for an example. Its main purpose is to reduce the combined file sizes and the run time of further selections such that the individual analysts can work on them without the need for large computer clusters. Here, one defines rough cuts on the data that reduce the background without removing desired events. Like this, one can drastically cut down the amount of data that has to be analyzed in the following steps and, therefore, these data files are called mini DSTs (mDST). The PHysics Analysis Software Tools (PHAST) can be used to perform the preselection

[2] For normal GEMs the centers are deactivated by turning off their high-voltage and, thus, disabling their electron multiplication feature. This is not needed for PixelGEM, since they have a pixelized readout for the central area allowing tracking also for high particle densities and high beam intensities.

[3] Also the absorber in the LAS has a large hole in the center to allow charged particles, which are close to the beam trajectory, to enter SAS and be detected there.

[4] The geometry is created with TGEANT and provided to CORAL.

and all further event selections. PHAST reads the data tree on an event-by-event basis and allows the user to write `UserEvents`, where one can fill histograms and specify cuts that events have to fullfil in order to be stored for further analyses. After the final event selection stage, the results can once more be stored in DSTs which are usually called micro DST (μDST), since they are even smaller.

Once an event selection for a specific final state of interest is performed (see section 5.2.3), usually, one wants to analyze the results with a "mass-independent" Partial-Wave Decomposition (PWD) (see section 3.4) and a subsequent "mass-dependent" resonance-model fit (see section 4.4) to search for peaks in the invariant-mass spectra of the final-state particles. But no experiment can provide full geometric and kinematic coverage. In addition no detector is doing its job perfectly. This is especially true if it is composed out of so many individual elements with their own efficiencies, as it is the case for the COMPASS setup. Therefore, another step is necessary before one can dive deep into the depths of the data: the Monte-Carlo (MC) simulation. The COMPASS collaboration created a program based on the C++ library GEometry ANd Tracking (GEANT). The previous version of this software was based on GEANT3 and was called COMGEANT, and its successor TGEANT uses GEANT4 as a base. This tool contains a detailed geometry description of all involved detectors together with their holding structures and is able to virtually track particles through the detector setup simulating detector hits and energy depositions on their way. Also particle decays, multiple scattering and any other physics process in matter are emulated.

The results of this simulation are fed through CORAL as well, where the actual detector response is simulated and the events are reconstructed in exactly the same way as Real Data (RD) events. Like this, one can directly relate every generated MC (gMC) event to its corresponding reconstructed MC (rMC) event. A stronger deviation between the two for a specific set of kinematic variables can hint towards a general detection inefficiency or can show the necessity of additional detectors to cover holes in the geometrical coverage of the complete COMPASS setup.

For one specific final state of interest, one can create gMC events with the four-vectors of the final-state particles distributed according to phase space, so-called "signal" MC. On these, one performs the event reconstruction, as just mentioned, to obtain the corresponding rMC events. Finally, one performs the same event selection as for RD to determine the accepted MC (aMC) events, i.e. the events that survive all selection criteria. From this, the detector acceptance for this specific final state is defined as the ratio aMC/gMC. And since we know exactly which aMC event corresponds to which gMC event, we can calculate such an acceptance not only for everything combined, but also as a function of a specific kinematic variable, such as the invariant mass of the final-state system or its subsystems.

Such an acceptance function can be used to rescale the RD in order to obtain acceptance-corrected spectra. A better way of performing such an acceptance correction, is to feed these aMC events into a PWD to perform the acceptance correction on an event-by-event basis, while at the same time separating the contributions from different intermediate-state QNs. An application of such a procedure for one specific final state can be found in chapter 6.

CHAPTER 3

(Re-)Scattering and Partial-Wave Decomposition

Scattering theory (or reaction theory) is a good tool to describe physical reactions of $M \to N$ body scattering. From an experimental view only decays ($M = 1$) and scattering between two particles ($M = 2$) make sense due to the nature of particle interaction and the difficulty in creating crossing beams of more than two particles at exactly the same point in space-time. For a final state, it is possible to consider any positive number, but the experiment becomes a lot more challenging with increasing N. Although, for example, $3 \to 3$ scattering might not be directly accessible via an experimental setup, it still plays a role in rescattering effects of final states with at least 3 particles. Also crossing symmetry would allow us to relate it to a $2 \to 4$ scattering. That is why we will not constrain us to any specific case, yet. For the next section, we loosely follow chapter 3 of [20], but most – if not all – of the discussed relations and formulas can be found in any text book about scattering theory as well, e.g. [21, 22].

3.1 Scattering Theory

The operator $\boldsymbol{S}$ represents all possible interactions. A priori, it contains all scattering information for all possible initial and final states, all particle resonances, kinematic thresholds, and all intermediate interactions. Applying it on an initial state $|i\rangle$ and looking for a specific final state $|f\rangle$ will result in one specific element S_{fi} of the $\boldsymbol{S}$-matrix:

$$\langle f|\, \boldsymbol{S}\, |i\rangle = S_{fi}, \qquad P_{i\to f} = \left|S_{fi}\right|^2, \tag{3.1}$$

where the second expression describes the probability of such a process to occur. By determining how the $\boldsymbol{S}$-operator acts on every possible pair of initial state and final state basis functions $|i\rangle$ and $|f\rangle$, respectively, we can calculate the full matrix representation of this operator for the given basis. Therefore, the concept of an operator and a matrix are strongly coupled and in the following, we will call it the $\boldsymbol{S}$-matrix operator or simply the $\boldsymbol{S}$-matrix with a specific element S_{fi} when evaluated on the states as in equation (3.1).

If we do not look for one specific final state $|f\rangle$, but add up the probability of $|i\rangle$ going to any final

state $|f'\rangle$, we should end up at a probability of 1, meaning

$$1 = \sum_{f'} \left|S_{f'i}\right|^2 = \sum_{f'} \left|\langle f'| \boldsymbol{S} |i\rangle\right|^2 = \sum_{f'} \langle i| \boldsymbol{S}^\dagger |f'\rangle \langle f'| \boldsymbol{S} |i\rangle = \langle i| \boldsymbol{S}^\dagger \sum_{f'} \Big(|f'\rangle \langle f'| \Big) \boldsymbol{S} |i\rangle = \langle i| \boldsymbol{S}^\dagger \boldsymbol{S} |i\rangle ,$$

where we use the fact that the sum over a full set of final states yields the unit-matrix operator, $\sum_{f'} |f'\rangle \langle f'| = \mathbf{1}$. Since this has to be true for any possible initial state $|i\rangle$, the $\boldsymbol{S}$-matrix has to be unitary as a direct consequence of probability conservation, giving us the unitarity relation:

$$\boldsymbol{S}^\dagger \boldsymbol{S} = \boldsymbol{S}\boldsymbol{S}^\dagger = \mathbf{1}. \tag{3.2}$$

$\boldsymbol{T}$-Matrix and $\boldsymbol{K}$-Matrix

Usually, we are just interested in events where something happens between the involved particles, therefore, we can split off the identity and define the $\boldsymbol{T}$-matrix operator via

$$\boldsymbol{S} =: \mathbf{1} + 2\mathrm{i}\, \boldsymbol{T}. \tag{3.3}$$

Inserting this into equation (3.2) yields the unitarity relation for the $\boldsymbol{T}$-matrix

$$\boldsymbol{T} - \boldsymbol{T}^\dagger = 2\mathrm{i}\, \boldsymbol{T}\boldsymbol{T}^\dagger. \tag{3.4}$$

By multiplying this equation with $\boldsymbol{T}^{-1}$ from the left and with $(\boldsymbol{T}^\dagger)^{-1}$ from the right, and afterwards rearranging things a bit, we obtain

$$(\boldsymbol{T}^\dagger)^{-1} - \boldsymbol{T}^{-1} = 2\mathrm{i}\, \mathbf{1} \qquad \Leftrightarrow \qquad (\boldsymbol{T}^{-1} + \mathrm{i}\, \mathbf{1})^\dagger = (\boldsymbol{T}^{-1} + \mathrm{i}\, \mathbf{1}),$$

which lets us define a hermitian matrix operator $\boldsymbol{K}^{-1} := \boldsymbol{T}^{-1} + \mathrm{i}\, \mathbf{1}$, allowing us to put the $\boldsymbol{T}$-matrix in a different form

$$\boldsymbol{T} = (\boldsymbol{K}^{-1} - \mathrm{i}\, \mathbf{1})^{-1} = \boldsymbol{K}(\mathbf{1} - \mathrm{i}\, \boldsymbol{K})^{-1}. \tag{3.5}$$

Like this, we can guarantee unitarity of the model by simply creating a hermitian operator $\boldsymbol{K}$, for example by making its corresponding matrix symmetric and real.

Cross Section

As for the $\boldsymbol{S}$-matrix, we can also evaluate the $\boldsymbol{T}$-matrix operator on an initial state $|i\rangle$ and a final state $|f\rangle$ to connect it to experimental observations. These states are M and N body states, respectively, where every particle is parametrized by its four-momentum p and spin s

$$|i\rangle = |p_1^{(i)}, s_1^{(i)}\rangle \otimes \ldots \otimes |p_M^{(i)}, s_M^{(i)}\rangle , \quad |f\rangle = |p_1^{(f)}, s_1^{(f)}\rangle \otimes \ldots \otimes |p_N^{(f)}, s_N^{(f)}\rangle ,$$

where the wave function of each state

$$|p, s\rangle := \frac{k(p, s)}{\sqrt{2E}} \exp(p \cdot x) \tag{3.6}$$

satisfies the Klein-Gordan equation $(\Box + m^2)\,|p,s\rangle = 0$. For scalar particles we have $k \equiv 1$, for spin-$\frac{1}{2}$ we have Dirac spinors $k = u_\alpha$ and for spin-1 we have the polarization vector $k = \epsilon_\mu$. With this, we can define elements of the $\boldsymbol{T}$-matrix in the same way as for the $\boldsymbol{S}$-matrix:

$$T_{fi} := \langle f|\,\boldsymbol{T}\,|i\rangle\,.$$

By taking out the $\frac{1}{\sqrt{2E}}$ factors from the particle wave functions in (3.6) and by explicitly enforcing four-momentum conservation between initial and final state, we arrive at the Lorentz-invariant matrix element $\mathcal{M}$

$$T_{fi} =: (2\pi)^4\delta^{(4)}\left[\sum_{j=1}^{M} p_j^{(i)} - \sum_{k=1}^{N} p_k^{(f)}\right] \cdot \prod_{j=1}^{M} \frac{1}{\sqrt{2E_j^{(i)}}} \prod_{k=1}^{N} \frac{1}{\sqrt{2E_k^{(f)}}} \cdot \mathcal{M}_{fi}. \tag{3.7}$$

Next, we want to take the squared magnitude of this expression, which will yield the square of a δ-distribution. For this, we can use equation (2.10) of [23]

$$\left[\delta^{(4)}(x)\right]^2 = \frac{Vt}{(2\pi)^4}\delta^{(4)}(x), \tag{3.8}$$

for a unit time t and a unit volume V. If we further compare equation (2.17) of [23], giving $N_n = \sqrt{2E_n V}^{-1}$ as the normalization of the wave functions, with the one we use here in equation (3.6), we see that – for the case at hand – it follows $V = 1$. So taking the squared magnitude of the $\boldsymbol{T}$-matrix element per unit time, we obtain

$$\frac{\left|T_{fi}\right|^2}{t} = (2\pi)^4\delta^{(4)}\left[\sum_{j=1}^{M} p_j^{(i)} - \sum_{k=1}^{N} p_k^{(f)}\right] \cdot \prod_{j=1}^{M} \frac{1}{2E_j^{(i)}} \prod_{k=1}^{N} \frac{1}{2E_k^{(f)}} \cdot \left|\mathcal{M}_{fi}\right|^2.$$

Now, we are constraining us to a $2 \to N$ scattering, however, we do not care about differentiating the probability for each and every momentum configuration of these N final state particles. Therefore, we sum over all possible momentum configurations, or rather integrate over them since the momentum is continuously distributed:

$$\sum_{p(N\text{-body})} \sim \int \prod_{k=1}^{N} \frac{\mathrm{d}^3\vec{p}_k^{(f)}}{(2\pi)^3} \quad \rightsquigarrow \quad \mathrm{d}\Gamma_{fi} := \sum_{p(N\text{-body})} \frac{\left|T_{fi}\right|^2}{t} = \frac{1}{4E_1^{(i)}E_2^{(i)}} \cdot \left|\mathcal{M}_{fi}\right|^2 \mathrm{d}\Phi_N^{(f)}, \tag{3.9}$$

with the definition of the Lorentz-invariant N-body phase space

$$\mathrm{d}\Phi_N^{(f)} = (2\pi)^4\delta^{(4)}\left[P - \sum_{k=1}^{N} p_k^{(f)}\right] \prod_{k=1}^{N} \frac{\mathrm{d}^3\vec{p}_k^{(f)}}{(2\pi)^3 2E_k^{(f)}} \qquad \text{with } P = \sum_{j=1}^{M} p_j^{(i)}, \tag{3.10}$$

where P is the full four-momentum of the reaction as given by the initial state. We will omit the superscript where the final state is unambiguous. For a two-body system, a calculation of $\mathrm{d}\Phi_2$ can be found in appendix A.1, equation (A.8). For any other case the phase-space-recursion formula of equation (A.9) can help.

Finally, the cross section is defined as the transition rate Γ_{fi} divided by the incident particle flux $\phi^{(i)} = v^{(i)} n^{(i)}$, so the relative velocity $v^{(i)}$ times the particle density $n^{(i)}$. This can be simplified for one particle per unit volume to $\phi^{(i)} = v^{(i)}/V = v^{(i)}$, resulting in

$$\mathrm{d}\sigma_{i\to N} = \frac{\mathrm{d}\Gamma_{fi}}{v^{(i)}} = \frac{1}{F} \left|\mathcal{M}_{fi}\right|^2 \mathrm{d}\Phi_N, \tag{3.11}$$

with the so-called flux factor F that contains all kinematics of the initial state (we drop the (i) superscript)

$$F = 4E_1 E_2 v = 4\sqrt{(p_1 \cdot p_2)^2 - m_1^2 m_2^2}. \tag{3.12}$$

The last equality can be shown by inserting $v = \left|\vec{p}_1\right|/E_1 + \left|\vec{p}_2\right|/E_2$ for the relative velocity of a collinear collision of two particles on the left-hand side and $p_1 \cdot p_2 = E_1 E_2 + \left|\vec{p}_1\right|\left|\vec{p}_2\right|$ as well as $m_i^2 = E_i^2 - \left|\vec{p}_1\right|^2$ on the right-hand side. The final expression is Lorentz-invariant, therefore, it holds for any frame of reference.

In general, we have to constrain N four-momenta of the final state, this gives $4N$ degrees of freedom. By assuming all final-state particles to be on mass shell, we get N constraints of the form $m^2 = E^2 - |\vec{p}|^2$, reducing the number of degrees of freedom to $3N$. Four-momentum conservation between initial and final state reduces this number additionally by 4. Therefore, in total we have

$$N_{\mathrm{dof}} = 3N - 4 \tag{3.13}$$

degrees of freedom in a reaction with fully known initial state and N final-state particles on mass shell. This can be seen as well in the differential phase space in equation (3.10), where we have $3N$ integrations from the three-momenta, of which four integrations are removed by the δ-distribution. Note that for every off-shell final-state particle, we get an additional degree of freedom, i.e. its invariant mass.

Unitarity Relation for $\mathcal{M}$ in $2 \to 2$ Scattering

Evaluating the unitarity relation for $\boldsymbol{T}$ in equation (3.4) on an initial state $|i\rangle$ and final state $|f\rangle$ yields

$$T_{fi} - T_{if}^* = 2\mathrm{i}\ \langle f|\boldsymbol{T} \underbrace{\left(\sum\nolimits_{f'} |f'\rangle \langle f'|\right)}_{\equiv \mathbf{1}} \boldsymbol{T}^\dagger |i\rangle = \sum_{f'} T_{ff'} T_{if'}^*,$$

by using $\langle f'|T^\dagger|i\rangle = T_{if'}^*$ and inserting a full set f' of intermediate states. For a $2 \to 2$ scattering, we can exploit time-reversal symmetry[1] of $\boldsymbol{T}$ on the second term of the left-hand side, i.e. $T_{if}^* = T_{fi}^*$. For the right-hand side, we split off the sum over all momentum configurations from $\sum_{f'}$ as of

[1] As stated by Olive [24], time-reversal symmetry – or rather PT-invariance in case of an arbitrary $2 \to 2$ scattering – is not necessary to show $T_{if}^* = T_{fi}^*$. He demonstrates that unitarity – or equivalently the CPT-theorem – are sufficient to make such a statement, independent of the number of particles involved in the scattering.

equation (3.9):

$$2\mathrm{i}\,\mathrm{Im}(T_{fi}) = T_{fi} - T_{fi}^* \quad = \quad 2\mathrm{i}\sum_{f'}\int\prod_{\ell=1}^{N_{f'}}\frac{\mathrm{d}^3\vec{p}_\ell^{\,(f')}}{(2\pi)^3}T_{ff'}T_{if'}^*. \tag{3.14}$$

Inserting the definition of $\mathcal{M}$ from equation (3.7) everywhere, we see that we can cancel the energy products of the external states $|i\rangle$ and $|f\rangle$ on both sides[2], while the energy product over the internal states $|f'\rangle$ appears twice, resulting in $\prod_\ell^{N_{f'}}\frac{1}{2E_\ell^{(f')}}$. Regarding the product of the δ-distributions, we can rewrite it as

$$\delta_{f'i}^{(4)}\cdot\delta_{f'f}^{(4)} = \delta_{fi}^{(4)}\cdot\delta_{f'f}^{(4)} = \delta_{fi}^{(4)}\cdot\delta_{f'i}^{(4)}, \qquad \text{with } \delta_{xy}^{(4)} = \delta^{(4)}\left[\sum_{j=1}^{N_x}p_j^{(x)} - \sum_{k=1}^{N_y}p_k^{(y)}\right],$$

of which we can omit $\delta_{fi}^{(4)}$ since it also appears on the left-hand side. This brings us to the unitarity condition for the matrix element:

$$\mathrm{Im}(\mathcal{M}_{fi}) = \sum_{f'}\int \mathrm{d}\Phi_{N_{f'}}^{(f')}\mathcal{M}_{ff'}\mathcal{M}_{if'}^*. \tag{3.15}$$

Here, we could combine all remaining terms into the differential phase space, equation (3.10).

One quick application of this unitarity relation is the optical theorem. One obtains it by evaluating this equation for equal initial and final states, i.e. elastic scattering. This yields

$$\mathrm{Im}(\mathcal{M}_{ii}) = \sum_f\int \mathrm{d}\Phi_{N_f}^{(f)}\left|\mathcal{M}_{if}\right|^2 = F\cdot\sum_f\sigma_{i\to f} = F\cdot\sigma_{i,\mathrm{tot}}, \tag{3.16}$$

which shows that the total cross section – as the sum over all cross sections from a specific initial state to any final state – is proportional to the imaginary part of the elastic scattering amplitude of the given initial state.

We will see another application of this unitarity relation in section 3.4 when discussing a simple example for a partial-wave decomposition.

From causality follows[3] one important property of the $\boldsymbol{S}$-matrix (section 2.1 of [21]), namely its (complex) analyticity in $s = P^2$, the full squared four-momentum of the intermediate reaction. For a complex-analytic function, its Taylor expansion converges in the close neighborhood of every point of its domain. This means that it fulfills the Schwarz Reflection Principle (see next section 3.2.1 equation (3.18)) and also makes it a holomorphic function, i.e. a complex-differentiable function and, thus, an infinitely often continuously-differential function. However, this property is constrained to the complex plane away from the real axis. From its definition in equation (3.3), we immediately see that $\boldsymbol{T}$ inherits this analyticity (as well as $\mathcal{M}$). On the real axis itself, we can still have poles and branch points, with the latter opening up gates to different Riemann sheets, where additional singularities can

[2] All prefactors of $\mathcal{M}$ in equation (3.7) are real, therefore, they can be pulled out of the Im-function.

[3] [22] states that analyticity is rather a postulate (section 4.1).

occur. All these complex structures are propagated from the $\boldsymbol{S}$-matrix to $\boldsymbol{T}$ and $\mathcal{M}$. To get a better understanding of what this implies, let us start with a look at these mathematical concepts in the next section.

3.2 Complex Analysis with Branch Points

In physics, we are very often dealing with complex numbers, however, their introduction usually only covers the very basics. Especially in scattering theory, we are dealing with branch cuts, discontinuities and Riemann sheets, therefore, we will review these topics here.

We know that we have two basic representations of an arbitrary complex number $z \in \mathbb{C}$ using two independent real numbers, the Cartesian one and the polar one, showing the direct connection of $\mathbb{C}$ with $\mathbb{R}^2$:

$$z = x + \mathrm{i}\, y, \quad \text{with } x, y \in \mathbb{R}, \qquad z = r\mathrm{e}^{\mathrm{i}\,\varphi}, \quad \text{with } r > 0, \varphi \in (-\pi, \pi].$$

We gave one possible choice for the range of the angle φ that is used by `Mathematica` ([25]), calling it the `Mathematica` convention. Another common possibility is $\varphi \in [0, 2\pi)$ which we will call the physics convention, however, throughout this section 3.2 we will use the former one in the formulas.

3.2.1 Discontinuity, Schwarz Reflection Principle and Dispersion Relations

For real valued functions, one can sometimes obtain a jump in the function, a point where the function is not continuous anymore. One simple example would be $\frac{1}{x}$ which jumps from $-\infty$ to $+\infty$ at $x = 0$. Although this is also some kind of "discontinuity", we usually mean something different if we speak of discontinuities for complex-valued functions. Normally, they appear if the corresponding real-valued function has a point at which it cannot be continued, like the square root or the logarithm for values $x < 0$. Such a point is called a branch point and it is the starting point for a (complex) discontinuity in the complex analogue of the function.

Mathematically, one can define the discontinuity of a function via

$$\mathrm{Disc}[f](z) = \lim_{\varepsilon \to 0} \Big(f(z + \mathrm{i}\,\varepsilon) - f(z - \mathrm{i}\,\varepsilon) \Big). \tag{3.17}$$

More general is the discontinuity defined as the value of a function on one side of a branch cut minus the value on the other side, not necessarily in direction of the imaginary axis ($\pm \mathrm{i}\,\varepsilon$) as in equation (3.17). Everywhere, where the function f itself is continuous, its discontinuity will simply vanish. But if there is a point or usually a line where – when crossed – we experience a jump in either the real part or the imaginary part of the function, the definition of a discontinuity makes sense. We will discuss the two previously mentioned examples in the following, the square root in section 3.2.2 and the logarithm in section 3.2.4.

Schwarz Reflection Principle

In case a function fulfills the "Schwarz Reflection Principle"

$$f(z^*) = \Big(f(z) \Big)^* \tag{3.18}$$

and the discontinuity is located on the real axis ($z = x$), we can express it through the imaginary part of the function in the following way

$$\begin{aligned} \text{Disc}[f](x) &= \lim_{\varepsilon\to 0}\Big(f(x+\mathrm{i}\,\varepsilon) - f\big((x+\mathrm{i}\,\varepsilon)^*\big)\Big) = \lim_{\varepsilon\to 0}\Big(f(x+\mathrm{i}\,\varepsilon) - \big(f(x+\mathrm{i}\,\varepsilon)\big)^*\Big) \\ &= \lim_{\varepsilon\to 0} 2\mathrm{i}\,\mathrm{Im}\Big(f(x+\mathrm{i}\,\varepsilon)\Big) = 2\mathrm{i}\,\mathrm{Im}\Big(f(x)\Big). \end{aligned} \tag{3.19}$$

Although this seems to be a very specific feature for a function, it is actually quite common since the complex conjugation can be distributed in a sum $(a+b)^* = a^* + b^*$ and in a product $(a\cdot b)^* = a^*\cdot b^*$. As a direct consequence, complex polynomials fulfill it since they are just a specific combination of multiplications and additions. The same is true for differences, fractions, and even chains of functions if each function separately fulfills the principle:

$$f\Big(g(z^*)\Big) = f\Big(\big(g(z)\big)^*\Big) = \Big(f\big(g(z)\big)\Big)^*.$$

For the exponential function we have to do a bit of work to see it:

$$\exp(z^*) = \exp(x - \mathrm{i}\,y) = \underbrace{\exp(x)}_{\in\mathbb{R}}\cdot\big(\cos(y) - \mathrm{i}\,\sin(y)\big) = \Big(\exp(x)\cdot\big(\cos(y) + \mathrm{i}\,\sin(y)\big)\Big)^* = \Big(\exp(z)\Big)^*.$$

Effectively, this principle says that the values that a function takes on the upper half of the complex plane ($f(x+\mathrm{i}\,y), y > 0$), completely determine its values on the lower half ($f(x-\mathrm{i}\,y) = f^*(x+\mathrm{i}\,y)$).

Any analytic function – as the ones discussed above – which satisfies equation (3.18), automatically has to take real values on the real axis, because for $z = x = z^*$ we will have $f(x) = f^*(x) \in \mathbb{R}$. If the discussed function is not real on the real axis, but fulfills equation (3.18), it must have a discontinuity on the real axis, what can also be seen immediately from equation (3.19). The complex square root and the complex logarithm are such functions, since they become purely imaginary on the negative real axis for the `Mathematica` convention, but more details on that later.

One prominent example in particle physics for a function fulfilling the Schwarz Reflection Principle, is the complex amplitude $\mathcal{M}$ describing a scattering process and since it is expected to be analytic in the complex plane, it can only have poles, branch points and discontinuities on the real axis [22]. That $\mathcal{M}$ has to have a discontinuity on the real axis, can directly be see in equation (3.15), since its imaginary part for real values of s does not vanish.

Dispersion Relations

Although these discontinuities do not seem to be very useful, they actually are. The reason is that one completely knows an analytic function if one knows its discontinuity on the real axis. Such a relation is called a "dispersion relation" and it is a direct consequence of the Cauchy Theorem:

$$f(s) = \frac{1}{2\pi\mathrm{i}}\oint_C \frac{f(s')}{s'-s}\mathrm{d}s', \tag{3.20}$$

which holds for all values s inside of the closed contour C if the function f is analytic inside of C. By

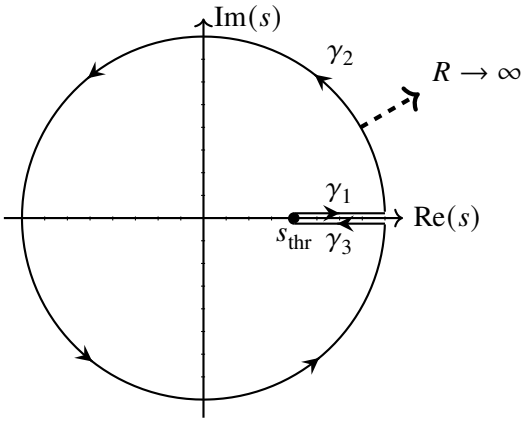

Figure 3.1: Integration contour used in equation (3.20) with $s_{\text{thr}} = 4$, modified from [26].

using the contour from Figure 3.1 we obtain the dispersion relation

$$f(s) = \frac{1}{2\pi \mathrm{i}} \int_{s_{\text{thr}}}^{\infty} \frac{\text{Disc}[f](s')}{s' - s} \mathrm{d}s', \tag{3.21}$$

where we require $f(s) \overset{|s|\to\infty}{\longrightarrow} 0$ such that the integral over the circular path γ_2 vanishes when extending it to infinity. The discontinuity is obtained from γ_1 and $-\gamma_3$ integrated from $s_{\text{thr}} \to \infty$.

If the function f does not drop fast enough for $|s| \to \infty$, we can introduce a temporary pole to the function by looking at $g(s) = f(s)/(s - s_0)$. If this function has the required behavior at complex infinity, we can perform the contour integral with a slightly adjusted contour to avoid the newly introduced pole. For this, we integrate from the outer circle γ_2 to the pole position at $s = s_0$, clock-wise around this pole resulting in minus the residual of $g(s')/(s' - s)$, i.e. $f(s_0)/(s - s_0)$, and back on the path from the pole to where we started on γ_2, exactly cancelling out the first additional path integral. The result is

$$\begin{aligned} f(s; s_0) &= f(s_0) + \frac{(s - s_0)}{2\pi \mathrm{i}} \int_{s_{\text{thr}}}^{\infty} \frac{\text{Disc}[f](s')}{(s' - s)(s' - s_0)} \mathrm{d}s' \\ f(s; 0) &= f(0) + \frac{s}{2\pi \mathrm{i}} \int_{s_{\text{thr}}}^{\infty} \frac{\text{Disc}[f](s')}{(s' - s)s'} \mathrm{d}s', \end{aligned} \tag{3.22}$$

which is known as a subtraction. This procedure can be repeated as often as needed, until the integrand has the required limiting behavior. The more subtractions one has to perform, the more so-called subtraction constants, as the $f(0)$ above, will appear. These subtraction constants are free parameters of the model and have to be fixed by the experiment.

By using equation (3.19), we can rewrite the dispersion relation as

$$f(s) = \frac{1}{\pi} \int_{s_{\text{thr}}}^{\infty} \frac{\text{Im}\Big(f(s')\Big)}{s' - s} \mathrm{d}s'. \tag{3.23}$$

3.2.2 Complex Square Root

Let us discuss a very important function for particle physics in more detail, the complex square-root function. Here, we can see the impact of the choice of the φ range mentioned in the introduction of this section 3.2, when having a look at the square root for complex arguments

$$\sqrt{z} = \sqrt{r}\mathrm{e}^{\mathrm{i}\frac{\varphi}{2}}, \qquad \mathrm{Disc}_{z<0}[\sqrt{z}] = 2\mathrm{i}\sqrt{r}, \qquad \texttt{sqrt}(z;\phi) = \mathrm{e}^{\mathrm{i}\frac{\phi}{2}}\sqrt{z\mathrm{e}^{-\mathrm{i}\phi}}. \tag{3.24}$$

For the chosen range $\varphi \in (-\pi, \pi]$, we will experience a jump – the discontinuity as introduced in the previous section 3.2.1 – when going from

$$\sqrt{r\mathrm{e}^{\mathrm{i}(\pi-\varepsilon)}} = \sqrt{r}\mathrm{e}^{\mathrm{i}(\pi-\varepsilon)/2} \approx \mathrm{i}\sqrt{r} \qquad \text{to} \qquad \sqrt{r\mathrm{e}^{\mathrm{i}(-\pi+\varepsilon)}} = \sqrt{r}\mathrm{e}^{\mathrm{i}(-\pi+\varepsilon)/2} \approx -\mathrm{i}\sqrt{r},$$

although the input arguments are both close to $-r$, i.e. slightly on opposite sides of the negative real axis. With the mathematical definition of a discontinuity in equation (3.17), this gives us the expression as stated in equation (3.24). The strength and the starting point $z = 0$ of this discontinuity – the so-called branch point – will not change no matter how we choose the φ-range, however, the path it takes can be different. In our case, we have a discontinuity only for negative real values as indicated by the subscript $\mathrm{Disc}_{z<0}$ in equation (3.24).

Since the direction of the branch cut is depended on the convention you are choosing, any statements or physics arguments have to be independent on its direction. Having said that, other derived statements might have to be reformulated if the convention is a different one. For example, the statement that there are no poles, singularities or branch cuts allowed on the first Riemann sheet of the scattering amplitude outside of the real axis, only holds for the physics convention. It is not true anymore if the direction of the square-root branch cut is chosen to follow $\mathrm{i}\,\mathbb{R}$ for whatever reason. And it can also be beneficial to rotate the branch cuts such that we can use easier integration paths like a straight line, instead of a circle around the branch point. Because if we carelessly cross a branch cut with an integration path, we will pick up the corresponding discontinuity and, as a consequence, we will obtain wrong and discontinuous integration results. Such a cut rotation can be obtained in `Mathematica` by modifying the default square-root function to `sqrt` as given in equation (3.24). We simply rotate the complex number z by an angle $-\phi$ before applying the square root, and afterwards we compensate this additional rotation by rotating half the angle in the opposite direction. Like this we effectively change the allowed range to $\varphi \in (-\pi + \phi, \pi + \phi]$. We can obtain the physics convention from the `Mathematica` convention by using $\texttt{sqrt}(z;\pi)$, or more precisely $\texttt{sqrt}(z;\pi-\varepsilon)$ since otherwise the range would be $\varphi \in (0, 2\pi]$ instead of $\varphi \in [0, 2\pi)$. However, this ε is only important if we are evaluating the function exactly on the positive real axis, therefore, for most of the following discussions an angle of $\phi = \pi$ is sufficient. For the formulas, the square-root symbol $\sqrt{\cdot}$ will still correspond to the `Mathematica` convention or equivalently to $\texttt{sqrt}(z;0)$.

The effect of such a rotation can be seen in Figure 3.2. We see that at the beginning, for $\phi = 0$, the imaginary part has a jump at the negative real axis as we calculated before, while the real part is continuous, but not smooth! If we rotate the cut more and more, the jump in the imaginary part gets smaller and the real part develops a discontinuity as well. In the center of Figure 3.2, we have the physics convention with $\phi = \pi$, and if we do the rotation until $\phi = 2\pi$, we obtain the plot in the bottom-right corner. This plot shows a completely different real and imaginary part, which brings us to the concept of Riemann sheets. If we would glue the orange plot (real part) of the bottom-right-corner

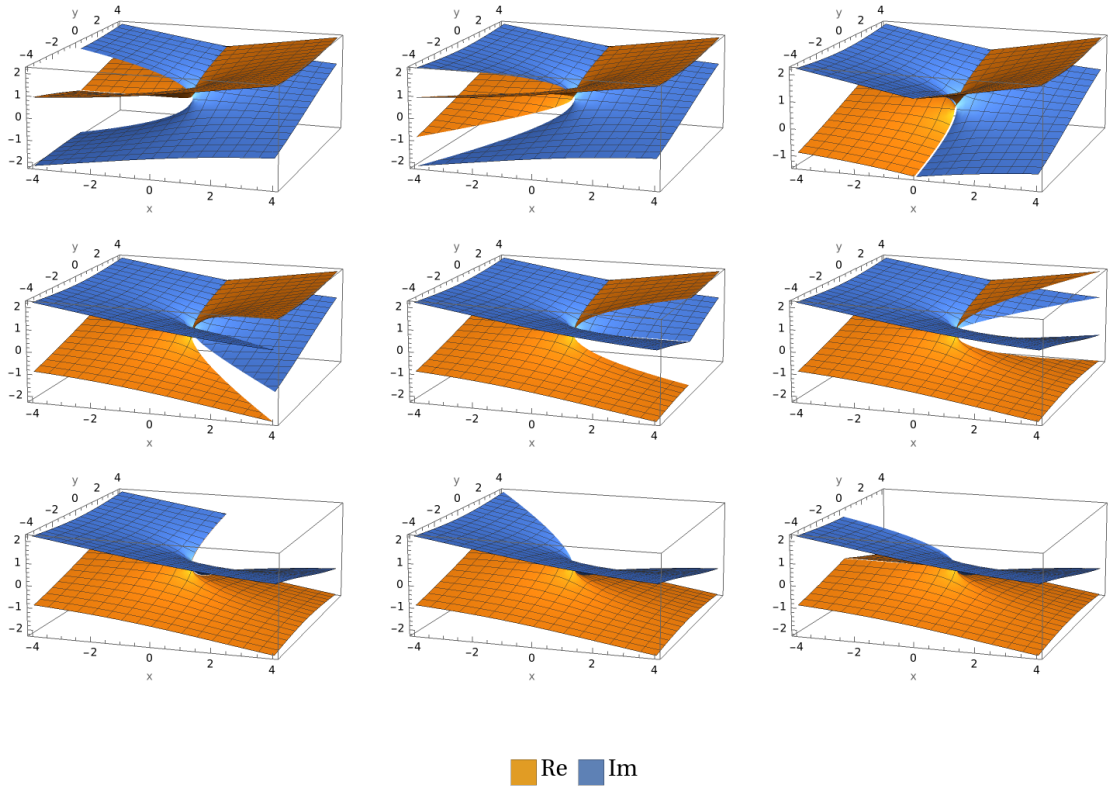

Figure 3.2: Square root "`sqrt`" of equation (3.24) as a function of a complex argument $z = x + \mathrm{i}\, y$ for different rotations $\phi \in \{0, \frac{\pi}{4}, ..., 2\pi\}$ (row-by-row from left to right). Plotted is the real part in yellow and the imaginary part in blue. The `Mathematica` convention is the top left plot and the physics convention is the central plot.

plot to the one of the top-left-corner plot, we would obtain a completely continuous transition both coming from above the negative real axis and coming from below. If we would walk smoothly along this newly constructed functional plane in a circle around the branch point at zero, we would have to run around it twice, before we end up at the same place. The same is true for the blue plot (imaginary part). Therefore, we say that the square-root function has two Riemann sheets, giving us effectively two different square-root functions $\sqrt{z} = \texttt{sqrt}(z; 0)$ and $\sqrt[\mathrm{II}]{z} = \texttt{sqrt}(z; 2\pi) = -\sqrt{z}$. Here, we directly see why we have exactly two Riemann sheets, since after two rotations $\phi = 4\pi$ we are back at $\texttt{sqrt}(z; 4\pi) = \sqrt{z}$. A similar depiction of the square-root function, now with both Riemann sheets plotted, can be found in Figure 3.3. We see that we always have a smooth transition from the first Riemann sheet (yellow to green, and blue to red) for all rotation angles ϕ.

As mentioned before, the complex square root fulfills the Schwarz Reflection Principle for the `Mathematica` convention, which we can immediately see from its definition in equation (3.24) and the fact that the exponential function fulfills the principle. However, if we change to the physics convention, this is not the case anymore since complex conjugation $\left(\sqrt{r}\mathrm{e}^{\mathrm{i}\,\phi}\right)^* = \sqrt{r}\mathrm{e}^{-\mathrm{i}\,\phi}$ will always leave the allowed range for $\phi \in [0, 2\pi)$. Another way to see this, is in the central plot of Figure 3.2, where the imaginary part (blue surface) does not vanish on the negative real axis, although this would be a direct requirement from equation (3.18) for a continuous function. By performing the complex

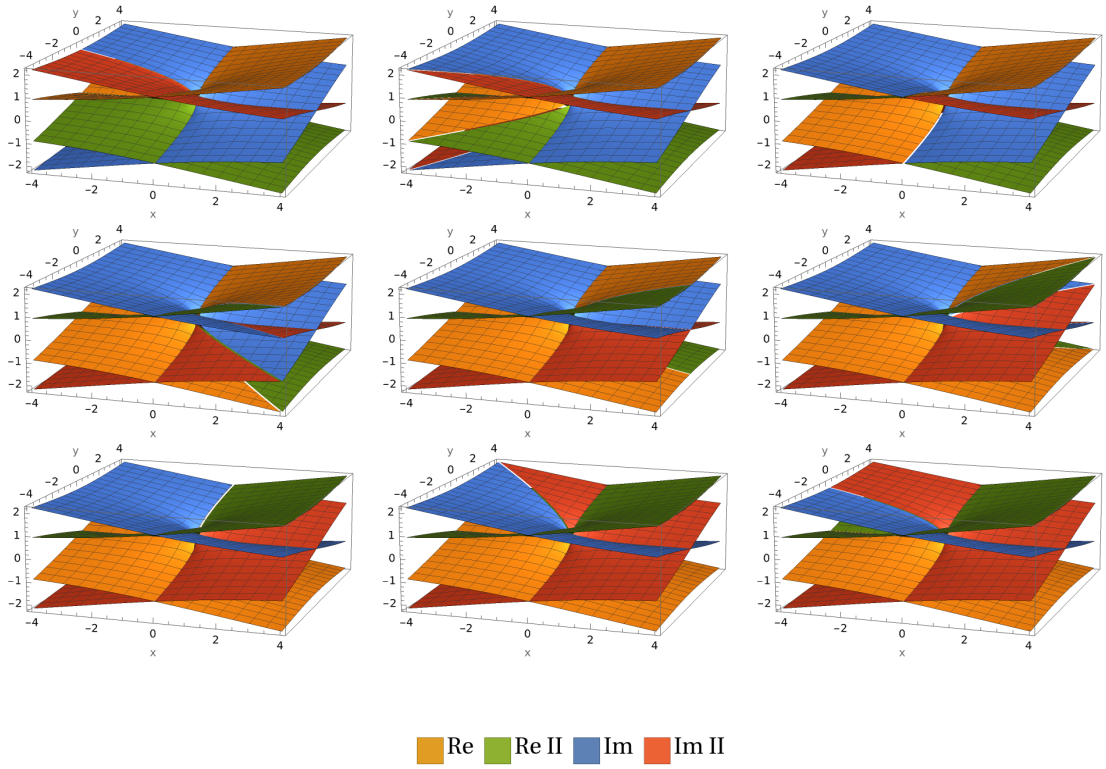

Figure 3.3: Square root `sqrt` of equation (3.24) as a function of a complex argument $z = x + \mathrm{i}\, y$ for different rotations $\phi \in \{0, \frac{\pi}{4}, \ldots, 2\pi\}$ (row-by-row from left to right). Plotted is the real part of the first Riemann sheet in yellow, the second Riemann sheet in green, and the imaginary part on the first Riemann sheet in blue, on the second Riemann sheet in red.

conjugation, we effectively jump on the second Riemann sheet, i.e. rotate the cut in the opposite direction when starting from the `Mathematica` convention:

$$\texttt{sqrt}(z^*;\pi) = \mathrm{e}^{\mathrm{i}\frac{\pi}{2}}\sqrt{z^*\mathrm{e}^{-\mathrm{i}\,\pi}} = \left(\mathrm{e}^{-\mathrm{i}\frac{\pi}{2}}\sqrt{z\mathrm{e}^{\mathrm{i}\,\pi}}\right)^* = \left(\texttt{sqrt}(z;-\pi)\right)^* = -\left(\texttt{sqrt}(z;\pi)\right)^*, \tag{3.25}$$

where we applied the Schwarz Reflection Principle on $\sqrt{\cdot}$ in the definition of $\texttt{sqrt}(z;\pi)$. Replacing π by an arbitrary rotation angle ϕ again, we see immediately that this generalizes to $\texttt{sqrt}(z^*;\phi) = \left(\texttt{sqrt}(z;-\phi)\right)^*$, which shows that the Schwarz Reflection Principle will only hold for $\phi = -\phi = 0$, the `Mathematica` convention. However still, there exists a simple relation between $F(z^*)$ and $\left(F(z)\right)^*$ which can lead to the generalization of the Schwarz Reflection Principle and the introduction of the Schwarz function that performs such a mapping of the reflection (complex conjugation) on a curve in complex plane (the branch cut of $F(z)$).

Putting that aside for now, let us come back to the physical application of the complex square root.

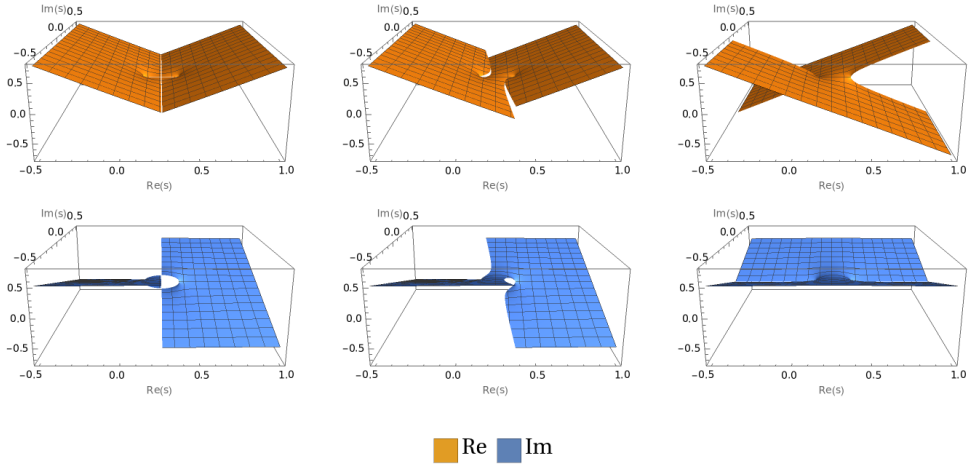

Figure 3.4: Real part (orange, top) and imaginary part (blue, bottom) of the numerator of the two-body phase space for $K^{*0}(892) \to K^+\pi^-$ with $\tilde{\Gamma}_{K^*} = 0.1\,\text{GeV}$ for complex argument s for the `Mathematica` convention (left) and the physics convention (right). The middle column is obtained by using $\phi = \pi/8$ for `sqrt` in equation (3.24).

3.2.3 Complex Phase Space

The first application of such a complex square-root function in physics comes, when we talk about the two-body phase space as of equation (A.8). If we simply plot it for complex arguments, we can see the result for the two conventions in Figure 3.5 for a neutral K^* with artificially increased decay width of $\tilde{\Gamma}_{K^*} = 0.1\,\text{GeV}$ decaying into K^+ and π^-. To fully understand what we are seeing, we write it in the following way

$$\Phi_2(s, m_1^2, m_2^2) = \frac{1}{8\pi}\frac{\sqrt{(s - s_{\text{thr}})(s - s_{\text{pth}})}}{s}, \qquad \text{with } s_{\text{thr}} = (m_1 + m_2)^2, \quad s_{\text{pth}} = (m_1 - m_2)^2,$$

defining the threshold s_{thr} and the pseudo-threshold s_{pth}. Next, we break it down into separate pieces by starting only with the numerator, which is plotted in Figure 3.4.

Here, we observe something strange for the `Mathematica` convention (left column): we have a branch cut connecting the two thresholds as expected, since the product under the square root is negative there. However, we also have a cut along $s_+ \pm \mathrm{i}\, y$ for $y \in \mathbb{R}$ where we defined $s_\pm = (s_{\text{thr}} \pm s_{\text{pth}})/2$. Although it is mathematically possible to define the square root[4] such that it only has the connecting branch cut on the real axis, we can still easily understand why `Mathematica` is doing what it is doing by inserting $s = s_+ + \mathrm{i}\, y \pm \varepsilon$ into the numerator of the phase space. These are values slightly on the left ($-\varepsilon$) and slightly on the right ($+\varepsilon$) of the suspicious branch cuts. If there is a branch cut, we expect to

[4] This is usually demonstrated with the function $\sqrt{z^2 - 1}$. If we substitute $s \to s + s_+$, resulting under the square root in $-(s - s_-)(s + s_-) = -s_-^2(z^2 - 1)$ with $z = s/s_-$, we obtain a similar complex structure.

see a jump from one side to the other. And indeed, the argument of the square-root function

$$\sqrt{(s-s_{\text{thr}})(s-s_{\text{pth}})}\Big|_{s=s_+ + \mathrm{i}\, y \pm \varepsilon} = \sqrt{\underbrace{-(y^2+s_-^2)}_{>0} \pm 2\varepsilon y \mathrm{i} \underbrace{+\varepsilon^2}_{\approx 0}}$$

is once slightly above $(+2\varepsilon y\mathrm{i})$ and once slightly below $(-2\varepsilon y\mathrm{i})$ the negative real axis, where the `Mathematica` convention defines the branch cut of the square root. As indicated by the middle column of Figure 3.4 where we replace the $\sqrt{\cdot}$ symbol by the `sqrt` function of equation (3.24) and rotate the cut a tiny bit by an angle $\phi = \pi/8$, the vertical branch cuts along the imaginary direction split at the real axis and rotate together with the respective half of the connecting branch cut in opposite directions, until we reach the physics convention with $\phi = \pi$ on the right column. One can easily convince oneself that, mathematically, such a rotation is equal to $\texttt{sqrt}(s - s_{\text{thr}}; \pi)\sqrt{s - s_{\text{pth}}}$, meaning that we rotate the cut, starting at the threshold, towards the right and keeping the cut at the pseudo threshold pointing towards the left.

This discussion shows the importance of correctly and consciously rotated cuts, because otherwise, it is very easy to cross such branch cuts when integrating in complex plane. The advantage of the physics convention over the `Mathematica` convention is that we have a fully connected complex plane, meaning that we can find a continuous path from every point of the complex plane to every other point without having to cross branch cuts. This can be achieved by first walking in a straight line to the middle point s_+ between the two thresholds on the real axis and, then again, in a straight line to the destination. Although this path is overly complicated for points on the same half plane, it is still valid and the integral along this path will be the same as for the direct connection, since the integrands are usually analytic function.

To arrive at the full complex phase space in Figure 3.5, we only have to include the $1/s$ factor, which introduces an unphysical pole at $s = 0$. But although this sounds problematic, we will see that this barely affects us in the end. As a side node, this pole only appears for unequal daughter masses $m_1 \neq m_2$. For equal masses, the pseudo threshold vanishes and, therefore, we obtain a $\sqrt{s}$ from the numerator that transforms the pole in a $1/\sqrt{s}$ branch point.

3.2.4 Complex Logarithm

Another important function, especially for this thesis, is the logarithm. Similar to the square root, also the real-valued logarithm creates problems when being evaluated on the negative real axis. This also leads to a branch cut if one extends its definition to the complex plane. Taking the logarithm of a complex number $z = r\exp(\mathrm{i}\,\varphi)$ results in $\log(z) = \log(r) + \log(\exp(\mathrm{i}\,\varphi)) = \log(r) + \mathrm{i}\,\varphi$ if we simply apply the logarithm rules that we know from real-valued mathematics. But here, we directly see the problem, again arising from the $2\pi\mathrm{i}$ -periodicity of the exponential function, since z will not change if we rotate the complex number by an angle of 2π in complex plane. However, the value on the right hand side will gain an extra $2\pi\mathrm{i}$ changing the imaginary part of the complex logarithm if we stick to the same rules as for real arguments. While for the square root, we saw that rotating by a total of 4π gave us back the original value, here, the imaginary part will keep increasing with every 2π rotation.

Similarly to before and starting from the `Mathematica` convention, we can manually rotate the

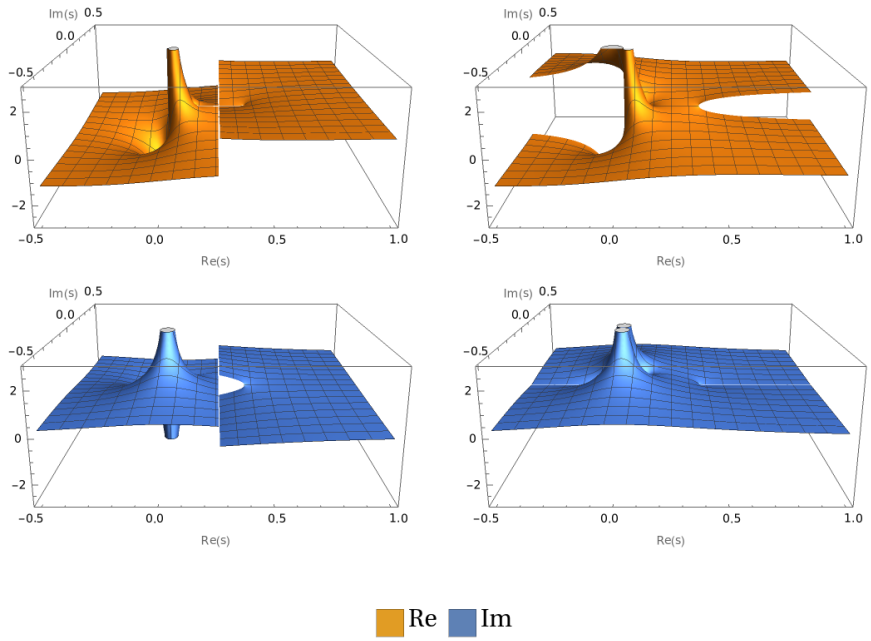

Figure 3.5: Real part (orange, top) and imaginary part (blue, bottom) of the two-body phase space for $K^{*0}(892) \to K^+\pi^-$ with $\tilde{\Gamma}_{K^*} = 0.1\,\text{GeV}$ for complex argument s for the `Mathematica` convention (left) and the physics convention (right).

branch cut of the logarithm to any other direction by using

$$\log(z) = \log(r) + \mathrm{i}\,\varphi, \qquad \mathrm{Disc}_{z<0}[\log](z) = 2\pi\mathrm{i}\,, \qquad \texttt{log}(z;\phi) = \log\left(z\mathrm{e}^{-\mathrm{i}\,\phi}\right) + \mathrm{i}\,\phi. \tag{3.26}$$

This can be seen in action in Figure 3.6. We see that the imaginary part spirals upwards for increasing ϕ, while the real part stays where it is, only its white line rotates, where `Mathematica` expects a possible branch cut. The diagonal shows three different Riemann sheets of the complex logarithm that – glued together – will result in a continuous upwards spiral around $z = 0$. Like this, we see immediately that we do not only have two Riemann sheets as a result, but an infinite amount of them, each separated by $2\pi\mathrm{i}\,n$ for any $n \in \mathbb{Z}$.

As for the square root, also the complex logarithm fulfills the Schwarz Reflection Principle for the `Mathematica` convention as one can directly see from its definition in equation (3.26): $\log(z^*) = \log(r) - \mathrm{i}\,\phi = \left(\log(r) + \mathrm{i}\,\phi\right)^*$.

In reaction theory, we define particles and resonances as poles in the complex energy plane below the real axis on the second Riemann sheet. On the real axis itself – where experiments are performed – the well-known Breit-Wigner (BW) shape corresponds to such a pole in the case of an isolated and narrow resonance. One has to analytically continue such a real-valued model to the complex s-plane and has to evaluate it slightly above the real axis, at $s + \mathrm{i}\,\varepsilon$, to avoid other poles and branch cuts

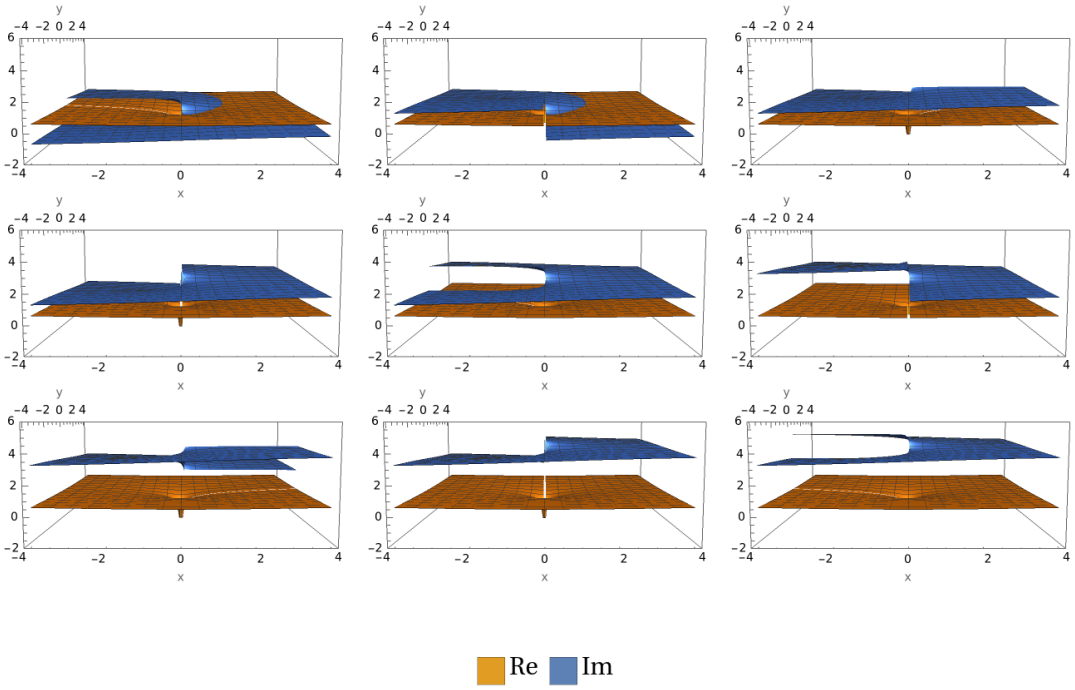

Figure 3.6: Real part (orange) and imaginary part (blue) of the "normalized" logarithm for complex arguments $z = x + \mathrm{i}\, y$. Row-by-row is plotted $\texttt{log}(z;\phi)/\pi$ for values $\phi \in \{0, \pi/2, ..., 4\pi\}$.

that might and will be located there. See the next section 3.3 for some details on building a more sophisticated Breit-Wigner Model (BWM).

3.3 Breit-Wigner Model

As just mentioned, a resonance is defined as a pole in the complex energy plane. However, an experiment can only measure values on the real axis, thus, what one can actually observe, is only the tail of that pole. Its maximum will appear at the mass of the resonance. The broader a signal is, the further the pole is away from the real axis. Therefore, the width of the measured peak is directly related to the imaginary part of the pole position.

One function that fulfills these conditions is the relativistic BW:

$$\texttt{BW}_{\text{const}}(s; m, \Gamma) = \frac{m\Gamma}{m^2 - s - \mathrm{i}\, m\Gamma}, \quad \text{with pole at } s_p = m^2 - \mathrm{i}\, m\Gamma. \tag{3.27}$$

The normalization in the numerator is chosen such that $\left|\texttt{BW}\left(s = m^2\right)\right|^2 = 1$, meaning that the height of the intensity is normalized to 1. When fitting to data, one needs an additional parameter A that scales the BW to match the strength of the data. With such a normalization, it makes it easier to guess the starting parameter and it decouples the signal strength from the mass and width parameters during a fit.

Usually, $\sqrt{s}$ is plotted on the x-axis and one defines the pole mass as real part and the pole width as

half of the imaginary part of the pole in $\sqrt{s}$, respectively:

$$\sqrt{s_p} =: m_p - \mathrm{i}\,\frac{\Gamma_p}{2}. \tag{3.28}$$

Squaring this expression and comparing it to equation (3.27) gives simple relations between the BW mass and width and the pole mass and width as follows:

$$m^2 = m_p^2 - \frac{\Gamma_p^2}{4},\ m = m_p\sqrt{1 - \frac{\Gamma_p^2}{4m_p^2}}, \qquad \Gamma = \frac{m_p\Gamma_p}{m} = \frac{\Gamma_p}{\sqrt{1 - \frac{\Gamma_p^2}{4m_p^2}}}. \tag{3.29}$$

The bigger m_p and the smaller Γ_p, the closer these two masses and widths are to each other, which means that the BW parameters are a good approximation for a narrow or heavy resonance.

The other direction is a bit more difficult to find if one wants to express the pole parameters in terms of the BW parameters. For this, one starts with the first equation in equation (3.29), multiplies it by m_p^2 and replaces $m_p^2\Gamma_p^2 = m^2\Gamma^2$, as can also be seen on the right in equation (3.29). This is a quadratic equation in m_p^2 and its solutions are $m_p = \frac{m}{\sqrt{2}}\sqrt{1 \pm \sqrt{1 + \frac{\Gamma^2}{m^2}}}$ of which only the one with the plus sign yields a real number. The expression for Γ_p can be obtained in a similar manner by multiplying Γ_p^2 to the first equation in (3.29) and again using $m_p^2\Gamma_p^2 = m^2\Gamma^2$, but this time to get rid of m_p^2. Now, we have a quadratic equation in Γ_p^2 with the two solutions $\Gamma_p = m\sqrt{2}\sqrt{-1 \mp \sqrt{1 + \frac{\Gamma^2}{m^2}}}$. Here, the sign inside the outer square root has to be positive as well, in order to give a real number for Γ_p, resulting in the final expressions:

$$m_p = \frac{m}{\sqrt{2}}\sqrt{1 + \sqrt{1 + \frac{\Gamma^2}{m^2}}}, \qquad \Gamma_p = m\sqrt{2}\sqrt{-1 + \sqrt{1 + \frac{\Gamma^2}{m^2}}}. \tag{3.30}$$

Once more, we get equal masses if we take the limit $\Gamma/m \to 0$, but for the width doing so simply results in 0. This means that we have to perform a Taylor expansion of the inner square root $\sqrt{1+x} = 1 + \frac{x}{2} - \mathcal{O}\left(x^2\right)$ with $x = \Gamma^2/m^2$ first, resulting in $\Gamma_p = \Gamma\sqrt{1 - \mathcal{O}\left(\frac{\Gamma^2}{m^2}\right)}$. Then, we also obtain equal widths as expected from the previous direction.

There are two ways, how such a complex function is usually visualized for real-valued arguments. Firstly, one can plot the squared magnitude and the complex argument also known as phase. And secondly, one can plot the imaginary part against the real part in a so-called Argand diagram. For such a BWM, the phase will rise from 0° up to 180° and it will cross 90° for $s = m^2$. On the Argand diagram, this corresponds to a full circle on the upper half of the complex plane. Some examples for the following more advanced BWM can be found in section 6.2.1.

If we plot the relativistic BW of equation (3.27) for complex arguments, we obtain Figure 3.7. Here – additionally to real (orange) and imaginary part (blue) – we plot the squared magnitude of the amplitude (green) as this would be what we observe e.g. for the cross section (cf. equation (3.11)). In the corresponding contour plots on the lower row one can see the position of the pole as expected at

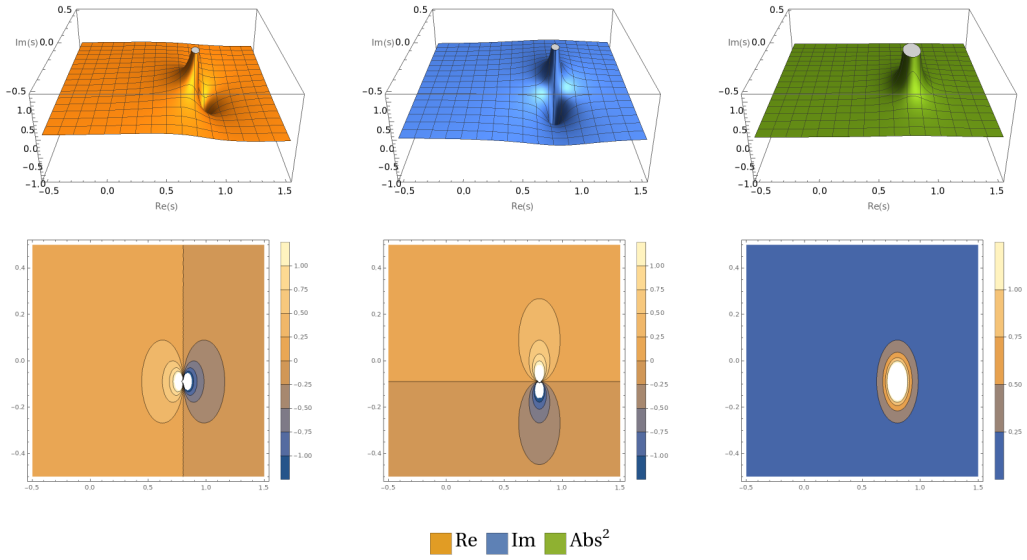

Figure 3.7: Relativistic BW of equation (3.27) for a $K^{*0}(892) \to K^+\pi^-$ with $\tilde{\Gamma}_{K^*} = 0.1\,\text{GeV}$. Plotted are the real part (left, orange), the imaginary part (middle, blue) and the squared magnitude (right, green) for complex values of s. The lower row shows contour plots where lines of equal height are plotted and the color indicates the average height of the corresponding function in between those lines.

$s_p = m_{K^*}^2 - \mathrm{i}\, m_{K^*}\tilde{\Gamma}_{K^*} \approx (0.8 - \mathrm{i}\,0.1)\,\text{GeV}^2$.

But as always, things are not that easy in reality. Interference with other resonances can disturb the shape of the peaks and shift the position of the peaks, or even make resonances appear as dips in the spectrum, as it is the case for the $f_0(980)$ in the $[\pi\pi]_S$ spectrum[5] for example. Adding BWMs with a complex phase between them can cope with this, however, this is not a good option, since it violates unitarity. But due to its simplicity over more sophisticated unitary models, like the K-matrix approach as presented in equation (3.5), it is still common practice. Also a BWM is very intuitive, since a good estimate for the mass and width of a resonance can easily be read off directly from the shape of the data, while for models using the previously introduced $\boldsymbol{K}$-matrix, its parameters only indirectly correlate with the pole mass and width of the resonance. One always has to analytically continue the model into the complex plane to find the actual pole on the second Riemann sheet of the $\boldsymbol{T}$-matrix.

Another possibility is the opening of additional decay thresholds within the close proximity of a resonance mass. This can create cusps or asymmetries where the resonance has a broader high-mass tail than low-mass tail.

And also from theory side, we have a problem with such a simple model, since from analyticity of the decay amplitude it follows that it cannot have poles in the complex plane away from the real axis – more precisely on the first Riemann sheet – which the simple BWM does have, as equation (3.30) clearly shows. This is, however, only an issue if one needs to do something with the model besides of

[5] Looking at low-energetic $\pi^+ + \pi^- \to \pi^+ + \pi^-$ scattering with involved orbital angular momentum $L = 0$, we have three resonances $f_0(500)$, $f_0(980)$ and $f_0(1500)$ appearing. The first one has a very broad width extending it over a large mass range and creating interference with especially the $f_0(980)$ (Fig. 13 of [27]).

evaluating it slightly above the real axis as during a simple fit to real data for example.

3.3.1 Breit-Wigner with Energy-Dependent Width

Before it gets too complicated, let us start with the concept of an energy-dependent width. This is a simple and common method (e.g. described in [28]) to directly incorporate some dependence on the decay channel into the parametrization of the resonance, and additionally as we will see, it also solves the problem with the pole on the first Riemann sheet. For a two-body decay of a resonance with mass M into two daughter particles with masses m_1 and m_2, we can calculate the decay width using Fermi's Golden Rule[6]:

$$\Gamma(s; M, m_1, m_2) = \frac{1}{2M} |\mathcal{M}|^2 \Phi_2(s, m_1^2, m_2^2), \tag{3.31}$$

with the two-body phase space Φ_2 calculated in appendix A.1 and given in equation (A.8). The simplest model for the matrix element $\mathcal{M}$ – in case of a spinless resonance decaying into two scalar particles – is a constant, the coupling g of the decay vertex. Since this coupling is in general not known or has to be taken from experiment or ℓQCD, one can normalize Γ with $\Gamma_0 := \Gamma(s = M^2)$ as given by the Particle Data Group [29] (PDG) and look at the ratio, resulting in:

$$\Gamma(s; M, \Gamma_0, m_1, m_2) = \Gamma_0 \frac{\Phi_2(s, m_1^2, m_2^2)}{\Phi_2(M^2, m_1^2, m_2^2)} = \Gamma_0 \frac{M}{\sqrt{s}} \frac{q}{q_0},$$

with the break-up momentum q as given in equation (A.2), and $q_0 = q(s = M^2)$.

In case the two-body resonance has spin (still decaying into two scalars), this spin appears as orbital angular momentum in the decay and a constant matrix element is not a good model anymore. One can show ([20]) that close to the threshold $s \gtrsim s_{\text{thr}}$ the expected behavior of the matrix element would rather be

$$\mathcal{M} \sim q^L, \qquad \text{for a decay with orbital angular momentum } L, \tag{3.32}$$

however, for large values it has to be damped again to not rise infinitely. Therefore, phenomenological barrier factors h_L are introduced that combine these requirements resulting in

$$\mathcal{M} \approx g \cdot h_L(q). \tag{3.33}$$

In this thesis, we use the parametrization derived by Blatt and Weisskopf [28, 30] in the version as it is defined in appendix D of [20]. The functional forms are given in appendix A.2 for direct reference.

Applying this adjustment to the energy-dependent width results in

$$\Gamma(s; M, \Gamma_0, m_1, m_2) = \Gamma_0 \frac{\Phi_2(s, m_1^2, m_2^2)}{\Phi_2(M^2, m_1^2, m_2^2)} \frac{h_L^2(q)}{h_L^2(q_0)} = \Gamma_0 \frac{M}{\sqrt{s}} \frac{q}{q_0} \frac{h_L^2(q)}{h_L^2(q_0)}. \tag{3.34}$$

Note that this width will only be used in the denominator of equation (3.27), while the numerator keeps Γ_0:

$$\mathtt{BW}(s; M, \Gamma_0, m_1, m_2) = \frac{M\Gamma_0}{M^2 - s - \mathrm{i}\, M\Gamma(s; M, \Gamma_0, m_1, m_2)} \tag{3.35}$$

[6] Compare this with equation (3.9) for a decay, i.e. a $1 \to N$ reaction. One obtains only $(2E_1^{(i)})^{-1}$ as a prefactor, which is evaluated in the rest frame of the decaying resonance to $(2M)^{-1}$ as in Fermi's Golden Rule.

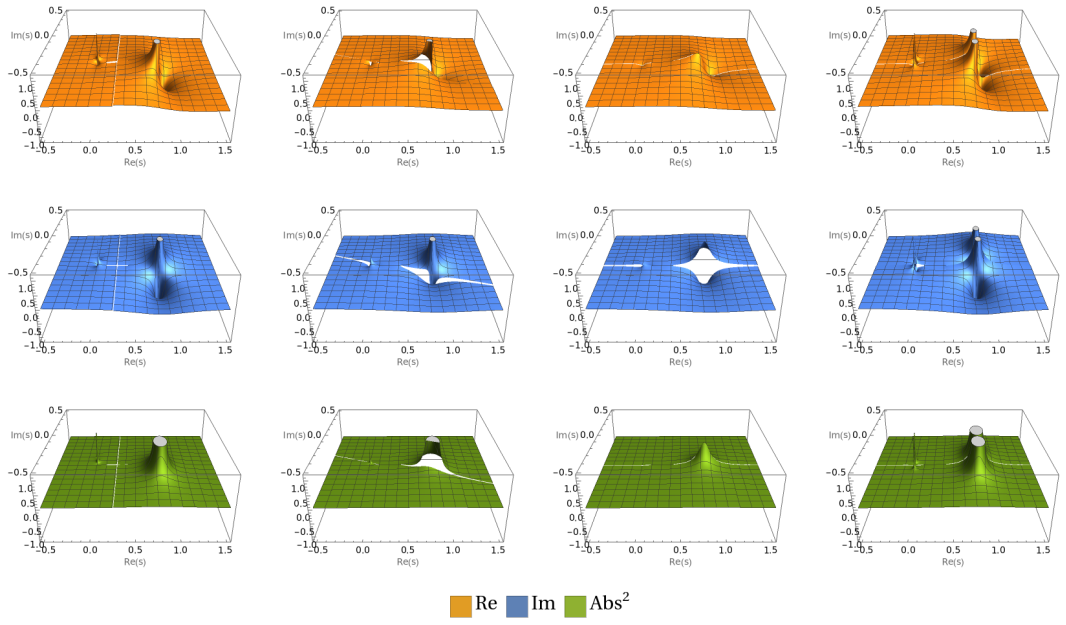

Figure 3.8: BW with energy-dependent width for complex argument s for the decay $K^{*0}(892) \to K^+\pi^-$ with $\tilde{\Gamma}_{K^*} = 0.1\,\text{GeV}$. Plotted are real part (orange, top row), imaginary part (blue, middle row) and squared magnitude (green, bottom row) for `Mathematica` convention (left), $\phi = 7\pi/8$ (middle left), physics convention (middle right), and the second Riemann sheet of the physics convention with $\phi = -\pi$ (right).

The normalization of the BW function will not be affected, because – by construction – the energy-dependent width becomes Γ_0 for $s = M^2$.

By introducing the phase space in the denominator of the BW, we are able to "hide" the pole on the second Riemann sheet created by the square-root function inside the phase space if we rotate the branch cut according to the physics convention. This is made visible in Figure 3.8. Note that it is very important to **only rotate the cut of the energy-dependent term** $\Phi_2(s, m_1^2, m_2^2)$, keeping the normal $\sqrt{\cdot}$ for the constant normalization $\Phi_2(M^2, m_1^2, m_2^2)$, which will always be a real number anyways. Otherwise a rotation by $\phi = \pi$ will result in the same complex structures as a rotation by $\phi = -\pi$ although they should not, since they uncover a different part of the other Riemann sheet.

We see that the pole starts to vanish for a rotation of $\phi = 7\pi/8$ (middle left) and is gone for the physics convention (middle right). However, looking at the second Riemann sheet of the physics convention (right) obtained by a rotation of $\phi = 3\pi$ or equivalently $\phi = -\pi$, we suddenly see two poles instead of only one. The second pole is created by the square-root function $\sqrt[\text{II}]{\cdot} = -\sqrt{\cdot}$ on the second Riemann sheet. If we use the `Mathematica` convention, we will have one pole on the first Riemann sheet from Φ_2 at approximately $m^2 - \mathrm{i}\, m\Gamma_0$, and on the second Riemann sheet from $\Phi_2^{\text{II}} = -\Phi_2$ at approximately $m^2 + \mathrm{i}\, m\Gamma_0$. Rotating the cut to the physics convention will still hide both poles, however, if the resonance appears very close to the threshold we can also feel the effect of this artificial second pole on the real axis. Additionally, the unphysical pole of the phase space that, now, is moved away from $s = 0$ into the complex plane, is hidden for the physics convention.

3.3.2 Flatté Parametrization of the Decay Width

If the resonance has two or more possible decay channels i, its decay width in the denominator of equation (3.35) is the sum of all partial widths $\Gamma_0 = \sum_i \Gamma_i$. We will focus on two possible channels, however, the discussed method can easily be adapted for more than two. If the coupling strengths g_i to each of these decays are known, one can employ equation (3.31) for each of the Γ_i and insert the respective coupling for the matrix element $\mathcal{M}_i = g_i h_L(q_i)$:

$$\begin{aligned}\Gamma_{\text{Flatté}}(s; M, g_i, m_{ij}) &= \frac{1}{2M}\left[g_1^2\Phi_2(s, m_{11}^2, m_{12}^2)h_L^2(q_1) + g_2^2\Phi_2(s, m_{21}^2, m_{22}^2)h_L^2(q_2)\right] \\ &= \frac{1}{M}\frac{g_1^2}{16\pi}\left(\frac{2q_1}{\sqrt{s}}h_L^2(q_1) + \frac{g_2^2}{g_1^2}\frac{2q_2}{\sqrt{s}}h_L^2(q_2)\right), \end{aligned} \tag{3.36}$$

where q_i denotes the break-up momentum of decay channel $i \in \{1, 2\}$ into two daughters $j \in \{1, 2\}$ with masses m_{ij}. This is called the Flatté parametrization and a less phenomenological derivation of it can be found in [20], where one deduces it from the $\boldsymbol{K}$-matrix and, thus, can proof that it satisfies unitarity.

In the case of unknown couplings, we can use the energy-dependent width of equation (3.34) for both partial widths Γ_i, as it is also presented in equations (2.6) and (2.7) of [28]. If we define the branching fraction $r = \frac{\Gamma_1}{\Gamma_0}$ and $(1 - r) = \frac{\Gamma_2}{\Gamma_0}$, we can pull Γ_0 out and obtain

$$\begin{aligned}\Gamma_{\text{Flatté}}(s; M, \Gamma_0, r, m_{ij}) &= \Gamma_0\left(r\frac{\Phi_2(s, m_{11}^2, m_{12}^2)}{\Phi_2(M^2, m_{11}^2, m_{12}^2)}\frac{h_L^2(q_1)}{h_L^2(q_{0,1})} + (1-r)\frac{\Phi_2(s, m_{21}^2, m_{22}^2)}{\Phi_2(M^2, m_{21}^2, m_{22}^2)}\frac{h_L^2(q_2)}{h_L^2(q_{0,2})}\right) \\ &= \Gamma_0\left(r\frac{M}{\sqrt{s}}\frac{q_1}{q_{0,1}}\frac{h_L^2(q_1)}{h_L^2(q_{0,1})} + (1-r)\frac{M}{\sqrt{s}}\frac{q_2}{q_{0,2}}\frac{h_L^2(q_2)}{h_L^2(q_{0,2})}\right), \end{aligned} \tag{3.37}$$

where we use the same nomenclature as above, with the addition of $q_{0,i} = q_i(s = M^2)$. Without loss of generality, we can assume a higher mass threshold for decay 2, meaning $m_{\text{thr},2} = m_{21} + m_{22} > m_{11} + m_{12} = m_{\text{thr},1}$. Below the threshold of the second decay, we can simply drop the second term. This will give us only a fraction of the full width, $\Gamma_0 \cdot r = \Gamma_1$. But this is also expected, since below the threshold of the second decay, the partial width of the first decay should correspond to the total width of the resonance. And the width will increase, once the other channel starts to open up, creating some asymmetry in the process.

Another way to deal with thresholds, is to make the break-up momentum imaginary below threshold[7], i.e. $q(s < s_{\text{thr}}) = \mathrm{i}\,|q|$. This effectively increases the mass of the isobar, as one can see by inserting this imaginary phase space into equation (3.34). One example where this finds its application is the Flatté parametrization of the $f_0(980)$ used at COMPASS [31] and described in section 6.2.1, Figure 6.7(a), since a better agreement with the data could be achieved that way.

In the end both threshold handlings are equally correct and wrong, since they are both just ways to give more freedom to the shape of the BW. What effectively happens is that the pole is moved around as a function of s, basically contradicting the idea of a resonance being a static pole in the complex plane.

[7] This is the result if one takes the complex square root in equation (A.2), meaning $\sqrt{-x} = \mathrm{i}\sqrt{x}$.

3.3.3 Chew-Mandelstam Decay Width

If one is concerned about the complex structure of the BWM, for example if it appears inside of an integrand, one can express the energy-dependent width with the Chew-Mandelstam function `CM`. It is obtained by calculating the amplitude for a loop diagram of the resonance decaying to the two daughter particles, which rejoin to form the original resonance again, [32]. The following parametrization from equation (2.30) of [33] is used in this thesis

$$\begin{aligned}
\texttt{CM}(s, m_1^2, m_2^2) &= \frac{1}{16\pi^2}\Bigg(\overbrace{\frac{\lambda^{1/2}(s, m_1^2, m_2^2)}{s}}^{A(s)=} \log\Bigg[\overbrace{\frac{m_1^2 + m_2^2 - s + \lambda^{1/2}(s, m_1^2, m_2^2)}{2m_1 m_2}}^{B(s)=}\Bigg] \\
&\quad - \underbrace{\frac{m_1^2 - m_2^2}{s}\log\left[\frac{m_1}{m_2}\right]}_{=C(s)} + \underbrace{\frac{m_1^2 + m_2^2}{m_1^2 - m_2^2}\log\left[\frac{m_1}{m_2}\right] - 1}_{=D}\Bigg) \qquad (3.38) \\
&= \frac{1}{16\pi^2}\Big(A(s)\log\big[B(s)\big] - C(s) + D\Big).
\end{aligned}$$

Plotting this as well in the complex plane for different values of ϕ, reveals that its complex structure is independent on which convention we choose for the square root (see Figure B.1). We see the effect of the rotation of the square-root cut by the white lines that `Mathematica` draws, where it expects a possible jump simply due to the appearance of the square-root function. However only on the real axis, starting at the threshold, we see a jump in the imaginary part, while the Chew-Mandelstam BW is smooth everywhere else. The reason for this, is the logarithmic term which introduces another branch cut that is hiding the pole on the second Riemann sheet, this time not the second sheet of the square-root function, but of the logarithm.

Now, let us apply the knowledge gained on the complex logarithm in section 3.2.4 to understand the complex structure of the Chew-Mandelstam function by breaking it into separate parts A, B, C and D as introduced in equation (3.38).

Although D seems to diverge in the limit $m_1 \to m_2$ at first glance, its first product will actually converge to 1, resulting in $D \to 0$. In this limit, also $C(s)$ will vanish, leaving us only with the first row. For the further steps, we will only consider the case of unequal masses, since this is also the case that we actually encounter for its application in this thesis, specifically as before, the decay of $K^{*0}(892) \to K^+ + \pi^-$.

Let us address the shortcomings of the two-body phase space and how they are cured here. $A(s)$ is – apart from its normalization – the two-body phase space and, as previously discussed, it has a pole at $s = 0$ for unequal daughter masses. This pole, however, gets exactly cancelled by $C(s)$, which expressed mathematically means $A(s)\log[B(s)] - C(s) \overset{s\to 0}{\to} 0$. To show this, one can simply insert $s = 0$ into the numerators of A and B, and use $\lambda^{1/2}(0, m_1^2, m_2^2) = m_1^2 - m_2^2$ and $B(0) = m_1/m_2$ for $m_1 > m_2$. If $m_2 > m_1$, we obtain $\lambda^{1/2} = m_2^2 - m_1^2$, but also the fraction in $B(0)$ will be flipped giving us another minus sign, which means that the limit for $s \to 0$ still vanishes.

We want to see how the Chew-Mandelstam function behaves in the physical region, meaning for $s > s_{\text{thr}}$. There, the terms $C(s)$ and D are always real, and exactly at threshold we can see that

$B(s = s_{\text{thr}}) = -1 < 0$. Expressing B in terms of $x := s - s_{\text{thr}} \geq 0$ we can transform it into

$$B(x) = \frac{m_1^2 + m_2^2 - s_{\text{thr}} - x + \sqrt{x(x + s_{\text{thr}} - s_{\text{pth}})}}{2m_1 m_2} = -1 + \frac{x}{2m_1 m_2}\overbrace{\left(-1 + \underbrace{\sqrt{1 + \frac{4m_1 m_2}{x}}}_{>1}\right)}^{>0}. \quad (3.39)$$

This is a monotonously rising function, which approaches 0 as its limit[8] for $x \to \infty$, thus, being negative for every $s > s_{\text{thr}}$. As a consequence, we can write the logarithm[9] as $\log(|B(s)|) + \mathrm{i}\,\pi$, which shows that the imaginary part of the Chew-Mandelstam function is half of the two-body phase space above threshold, $\mathrm{Im}(\texttt{CM}(s > s_{\text{thr}})) = \frac{1}{16\pi} A(s) = \frac{1}{2}\Phi_2(s)$. Therefore, we can perform the metioned replacement in equations (3.34) and (3.37) as detailed later in equation (3.40).

Since $B(s > s_{\text{thr}})$ is negative, we sit exactly on the branch cut of the logarithm. This means that shifting the argument of the logarithm slightly above the real axis ($x + \mathrm{i}\,\varepsilon$ or equivalently $s + \mathrm{i}\,\varepsilon$) will result in approximately[10] $\log(|B(s)|) + \mathrm{i}\,\pi$ and shifting it slightly below ($x - \mathrm{i}\,\varepsilon$ or $s - \mathrm{i}\,\varepsilon$) will result in a jump of $-2\pi\mathrm{i}$ to approximately $\log(|B(s)|) - \mathrm{i}\,\pi$. Hence, we just located a branch cut starting at threshold and extending to infinity where $\mathrm{Im}(\texttt{CM}(s))$ will change its sign, exactly as intended. At least if we use the `Mathematica` convention for the square root inside of $A(s)$. For the physics convention, we would also expect such a jump from $A(s + \mathrm{i}\,\varepsilon)$ to $A(s - \mathrm{i}\,\varepsilon)$, so could they cancel each other out or enhance each other? No they do neither, and the reason is that we also have a square root inside of $B(s)$ which will cancel the effect of the outer square root[11], leaving us still with only the cut from the logarithm.

This leaves us only with the problem of the unphysical pseudo-threshold branch cut. Let us focus on the physics convention where this cut extends from the pseudo-threshold to the left. This means that we are looking at values $s < s_{\text{pth}}$. We can do the same as before, but using $y := s_{\text{pth}} - s \geq 0$, resulting in

$$B(y) = 1 + \frac{y}{2m_1 m_2}\left(1 + \underbrace{\sqrt{1 + \frac{4m_1 m_2}{y}}}_{>1}\right).$$

If the sign of the inner square root flips due to the corresponding branch cut, this expression will stay positive for all $s < s_{\text{pth}}$, however, it will change from $B(s + \mathrm{i}\,\varepsilon) > 1$ to $B(s - \mathrm{i}\,\varepsilon) < 1$ which means

[8] To calculate this limit, one can perform a Taylor expansion of the square root giving $1 + \frac{2m_1 m_2}{x} - O\left(\frac{1}{x^2}\right)$. Inserting this yields $0 - O\left(\frac{1}{x}\right)$, which also shows that it is approaching 0 from below.

[9] We take the principle value of the complex logarithm that has its complex argument inside the interval $(-\pi, \pi]$.

[10] We established that $B(x)$ is monotonously rising, thus with Taylor expansion we see $B(x+\mathrm{i}\,\varepsilon) = B(x) + \underbrace{B'(x)}_{>0}\,\mathrm{i}\,\varepsilon \approx B(x) + \mathrm{i}\,\varepsilon$.

[11] Here are more details: Evaluating equation (3.39) at $x \pm \mathrm{i}\,\varepsilon$ and looking at the square root, we can Taylor-expand $1 + \frac{4m_1 m_2}{x \pm \mathrm{i}\,\varepsilon} \approx 1 + \frac{4m_1 m_2}{x} \mp \mathrm{i}\,\varepsilon \frac{4m_1 m_2}{x^2}$. This shows that, with the physics convention, the square root will change sign since its argument is once slightly below and once slightly above the positive real axis, which means that the whole bracket will become negative changing the sign of the $x \pm \mathrm{i}\,\varepsilon$ in front of it as well. Thus, we flip the imaginary part inside the logarithm resulting in a flipped imaginary part outside. The square root inside of $A(s)$ will also flip sign when changing from $s + \mathrm{i}\,\varepsilon$ to $s - \mathrm{i}\,\varepsilon$, therefore, we end up with the same result as for the `Mathematica` convention.

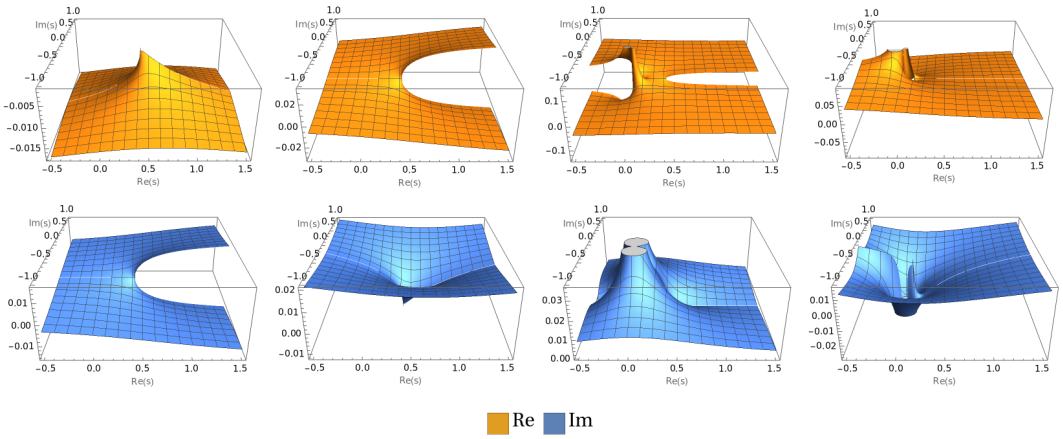

Figure 3.9: Plotted are real part (orange) and imaginary part (blue) of the Chew-Mandelstam function (left), the Chew-Mandelstam phase space (middle left), the two-body phase space (middle right), and the difference of the last two (right). All plots describe the decay $K^{*0}(892) \to K^+\pi^-$ with $\tilde{\Gamma}_{K^*} = 0.1\,\text{GeV}$ using the physics convention.

that the logarithm flips its sign. This sign flip will compensate the sign flip of the square root inside of $A(s)$, leaving the whole function unchanged. As a result, the branch cut extending from the pseudo threshold will not be present for the Chew-Mandelstam function.

The final square-root branch cut that one could investigate, is the one for $s_{\text{pth}} < s < s_{\text{thr}}$ for the `Mathematica` convention. Here we can define $z := s_{\text{thr}} - s > 0$, where the other limit of s yields the requirement $z < s_{\text{thr}} - s_{\text{pth}} = 2m_1 m_2$. Once again, one expresses $B(z)$ in a similar fashion as before and can show that the branch cut of $A(s)$ will be compensated by the logarithm.

With this, we can fully understand why the Chew-Mandelstam BW in Figure B.1 does not change for the two conventions. Figure 3.9 shows the Chew-Mandelstam function (left), the Chew-Mandelstam phase space according to equation (3.40) (middle left), the normal two-body phase space (middle right) and the difference between the two plots in the middle (right), using the physics convention for all of them. The last column shows that the real part of the Chew-Mandelstam phase space is, above threshold, indeed equal to the real part of the two-body phase space. This means that one can continue to use the simpler two-body phase space if one is only interested in this region on the real axis. However, if one needs to analytically continue the phase space into the complex plane or even integrate, one should always use the Chew-Mandelstam phase space, since its complex structure is simpler and does not have unphysical features, like the pole at $s = 0$ and the pseudo-threshold branch cut.

All this allows us to perform the following replacement in equations (3.34) and (3.37):

$$\Phi(s, m_1^2, m_2^2) \;\to\; \Phi_{\texttt{CM}}(s, m_1^2, m_2^2) := 2\mathrm{i} \cdot \left(\mathrm{Re}\left[\texttt{CM}(M^2, m_1^2, m_2^2)\right] - \texttt{CM}(s, m_1^2, m_2^2)\right). \tag{3.40}$$

Like this we still ensure that $\Phi_{\texttt{CM}}(M^2, m_1^2, m_2^2) = \Phi(M^2, m_1^2, m_2^2)$ and, thus, $\Gamma(s = M^2) = \Gamma_0$. We will call a BWM with such a replacement a Chew-Mandelstam BW.

This concludes the segment on the BWMs. How the complex structures of the previous models change if we take the invariant mass of the two-body system $M = \sqrt{s}$ as an argument, will be discussed briefly in appendix B.1. This model is suited well as long as we are dealing with isolated resonances. As soon as this is not the case anymore and we have to start adding BWs for the different resonances, we will violate unitarity and, therefore, it might be better to search for a different model like the $\boldsymbol{K}$-matrix approach mentioned in section 3.1, where unitarity is fulfilled by construction.

3.4 Partial-Wave Decomposition

We have introduced models to describe the behavior of resonances as a function of the invariant mass of the system of their corresponding decay particles. However, before one can start to fit BWMs or other amplitude models to the data, one has to disentangle resonances with different QNs. So let us take a step back and have a look at the PWD that can help with this. As a first introduction to the idea, we start with the simplest example possible.

Simple Example

The simplest case is $2 \to 2$ scattering of two scalar particles without intrinsic spin, which – according to equation (3.13) – gives us two independent variables that fully describe the process. We can choose the Mandelstam variables $s := (p_1 + p_2)^2$ and $t := (p_1 - p_3)^2$. For even more simplicity, we assume equal masses $m_i \equiv m$ of all four participants and a collider experiment, meaning we are in the Center-of-Momentum System (CMS) with $\vec{p}_1 = -\vec{p}_2$, $\vec{p}_3 = -\vec{p}_4$, and due to equal masses also $\left|\vec{p}_i\right| \equiv q$, the break-up momentum. This gives $s = 4E^2$ and $t = -2q^2(1 - \cos\theta)$, with the energy $E_i \equiv E$ of the involved particles and the scattering angle θ between particles 1 and 3.

The total spin J_X of the resonance is completely transferred into the orbital angular momentum L between the two scalar particles and the full amplitude can be decomposed into the Legendre polynomials P_L in the following way

$$A\big(s, t(\theta)\big) = \sum_{L=0}^{\infty} (2L + 1) a_L(s) P_L(\cos\theta), \tag{3.41}$$

where we split off the known angular dependence of the amplitude giving us access to the mass-dependent partial-wave amplitudes a_L that, now, only contain information from resonances with $J_X = L$.

Since the Legendre polynomials form a basis of linearly-independent functions, one can find a unique separation of the given full amplitude spectrum $A(s, t)$. However, this is only true for an infinite amount of data without experimental uncertainties. Additionally, it is computationally impossible to extend this sum to infinity. Therefore, one has to define an accepted $L_{\max}$ up to which one performs this separation. Everything with higher L will leak into the other partial-wave amplitudes. Another problem is that not only scattering through a resonance can occur. Especially with more than two final-state particles, also other background processes might be present that do not have a specific angular dependence according to the separation that we are performing. These background events will also leak into all partial waves.

Coupled-Channel K-Matrix

Considering the case where not all particles are identical[12] in the $2 \to 2$ scattering, we can couple different decay channels to each other by using the unitarity relation of $\mathcal{M}$ in equation (3.15). When inserting A from equation (3.41) for $\mathcal{M}$, we can employ orthogonality of the Legendre polynomials to perform the integration over the angular integrals of the differential phase space. This yields

$$\sum_L (2L+1)\mathrm{Im}\left[a_L^{(fi)}\right] P_L(\cos\theta) = \sum_{f'} \Phi_2^{(f')} a_L^{(ff')} a_L^{(if')*}.$$

By only considering two different intermediate states for the sum over f', one can combine $a_L^{(ij)}$ and $\Phi_2^{(j)}$ into matrices to obtain

$$\mathrm{Im}\left[a_L\right] = 2a_L^\dagger \rho a_L, \tag{3.42}$$

defining the diagonal half-phase-space matrix

$$\rho = \begin{pmatrix} \rho_1 & 0 \\ 0 & \rho_2 \end{pmatrix} := \frac{1}{2}\begin{pmatrix} \Phi_2^{(1)} & 0 \\ 0 & \Phi_2^{(2)} \end{pmatrix}. \tag{3.43}$$

This can easily be confirmed by calculating the individual components of the 2×2 matrices on both sides of the equal sign. Using $2\mathrm{i}\,\mathrm{Im}\left[a_L\right] = a_L - a_L^\dagger$ in equation (3.42) – and like this reverting the made assumption on time-reveral symmetry[13] by using the dagger instead of just the complex conjugate, making it valid not only for $2 \to 2$ scattering – we obtain

$$(a_L^\dagger)^{-1} - a_L^{-1} = 4\mathrm{i}\,\rho \tag{3.44}$$

by multiplying from the left with $(a_L^\dagger)^{-1}$ and from the right with a_L^{-1}. If we want to evaluate the partial-wave amplitude a_L in the physical regime, we have to do this at $s_+ := s + \mathrm{i}\,\varepsilon$. Using the Schwarz Reflection Principle for the daggered matrix gives $a_L^\dagger(s_+) = a_L^T(s_-)$. Since the phase space is basically a square-root function, we will have $\rho(s_+) - \rho(s_-) = 2\rho(s)$ for its discontinuity[14] along the real axis. With this, we can write equation (3.42) in the following way:

$$K_L^{-1}(s_+) := a_L^{-1}(s_+) + 2\mathrm{i}\,\rho(s_+) = (a_L^T)^{-1}(s_-) + 2\mathrm{i}\,\rho(s_-) = \left(a_L^{-1}(s_+) + 2\mathrm{i}\,\rho(s_+)\right)^\dagger, \tag{3.45}$$

making $K_L(s)$ a Hermitian matrix[15] with

$$a_L(s) = \left(K_L^{-1}(s) - 2\mathrm{i}\,\rho(s)\right)^{-1} = \left(\mathbf{1} - 2\mathrm{i}\,K_L(s)\rho(s)\right)^{-1} K_L(s). \tag{3.46}$$

[12] This only alters the formulas for s and t, otherwise, the expansion in Legendre polynomials does not change.

[13] as it was applied in equation (3.14)

[14] We have to calculate the discontinuity of the square root in equation (3.24) for $z > 0$ in the physics convention. For this, we use $\texttt{sqrt}(-z; \pi - \varepsilon)$ instead of $\sqrt{z}$, evaluating it at $-z$ since the cut will point in the other direction. This minus sign will cancel the exponential factor under the square-root symbol and the outer exponential factor yields an extra i on the left-hand side, resulting in $\mathrm{Disc}_{z>0}[\texttt{sqrt}(z; \pi - \varepsilon)] = 2\sqrt{r}$.

[15] In the last step, we make use that square root is following a slightly modified Schwarz Reflection Principle for the physics convention, equation (3.25).

For example, by parametrizing a real and symmetric matrix K_L, we can incorporate several resonances and background contributions into the scattering amplitude a_L while still obeying unitarity. Additionally, this concept allows for the coupling of different decay channels to each other and, thus, a more general description of the involved physics not only taking information from single channels into account that might lead to slightly different pole positions for the same resonance in different channels.

So much for the simple case, but before jumping into the more complicated case at COMPASS, let us review on the basic QNs that define a resonance. Table 3.1 lists formulas to calculate them for some specific cases.

3.4.1 Quantum Numbers

First of all, we have the QNs that define a resonance X in addition to its mass m_X and its decay width Γ_X or equivalently its lifetime $\tau_X = \frac{\hbar}{\Gamma_X}$. Additionally, there are the total spin J_X of the resonance and its projection $M_X \in \{-J_X, \dots, J_X\}$ to the polarization axis. A similar QN to the spin is the isospin, which has the same transformation properties. Up and down quark as well as their antiparticles all have isospin $\frac{1}{2}$, the strange quark and the other heavy quarks (c, b, t) have isospin 0. The isospin projection on the third axis I_3 is $+\frac{1}{2}$ for u and $\bar{d}$, and $-\frac{1}{2}$ for d and $\bar{u}$, and is an additive QN.

Next is the parity QN P, which is the eigenvalue of the wave function under total space inversion. The C-parity or charge conjugation turns every particle in its antiparticle. While elementary fermions such as quarks and (charged) leptons will always change their identity and, therefore, cannot be eigenstates of this operation, a pair of a quark and its own antiquark, such as the π^0, can have C as a good QN. An extension to the charged partners of the corresponding isospin multiplet, e.g. the $\pi^\pm$ in case of the π^0, is the G-parity, which combines C with a rotation in isospin space. It can be calculated via $G = C(-1)^I$, where I is the total isospin of the particle.

By using a specific basis for the parametrization of the decay amplitude, the reflectivity basis, one can introduce the reflectivity number $\epsilon = \pm 1$ which separates positive and negative spin projections resulting only in positive $M^\epsilon \in \{1^\pm, \dots, J_X^\pm\}$. The case $M = 0$ is special as we will either have only $M^\epsilon = 0^+$ if $\epsilon P(-1)^J = 1$, or $M^\epsilon = 0^-$ if $\epsilon P(-1)^J = -1$. This number is also the eigenvalue of reflections on the production plane and in the high-energy limit it is equal to the naturality of the exchange particle in a $2 \to 2$ scattering ([34], section 2.3). The naturality is +1 for scalars $J^P = 0^+$, vectors $J^P = 1^-$, tensors $J^P = 2^+$ and so on, and -1 for pseudoscalars $J^P = 0^-$, pseudo-vectors $J^P = 1^+$, pseudo-tensors $J^P = 2^-$. This means the naturality – and with this also the reflectivity – can be written as $\epsilon = P_{I\!R}(-1)^{J_{I\!R}}$ with the QNs of the exchange Reggeon $I\!R$. It allows to incorporate parity conservation into the scattering amplitude, see section 2.2 of [34].

In general, the allowed total spin J of the resonance depends on the orbital angular momentum L between the decay products and the spins of the daughter particles. In this thesis, we are experimentally dealing with the three-body final states $\pi^-\pi^+\pi^-$ and $\pi^- K_S^0 K_S^0$ which consist both of only pseudoscalar particles with QNs $J^P = 0^-$. Combining $\pi^-\pi^+$, $\pi^- K_S^0$ or $K_S^0 K_S^0$ to intermediate two-body resonances ξ, called isobars, this isobar-spin S_ξ is equal to the orbital angular momentum of their corresponding decay. The total spin J_X of the resonance X is obtained by combining this isobar-spin with the orbital angular momentum L that appears in the decay of X to the isobar ξ and the bachelor particle ζ, which is the remaining one of the three final-state particles $\zeta \in \{\pi^-, K_S^0\}$ that was not part in the two-body resonance. Such a model with an intermediate two-body resonance is called the isobar model and is motivated by experimentally seen resonance structures in the corresponding Dalitz plots

Table 3.1: Collection of QNs that are described in the text. Total spin J, spin projection M, isospin I, isospin projection I_3, orbital angular momentum L, intrinsic spin S, parity P, charge conjugation C, and G-parity. The different rows show systems of particles or decays and list the corresponding values and formulas to calculate the respective QN. "–" means that this QN is not well defined for a general "two-body system" or is not that easy to calculate in case of "$N \times \pi$". The possible values for $A \oplus B$ are $|A - B|, \ldots, A + B$, in full integer steps, with their respective strength or likelihood given by the corresponding Clebsch-Gordan coefficient. The combination $\big(\,|u\bar{u}\rangle - |d\bar{d}\rangle\,\big)/\sqrt{2}$ corresponds to the neutrally charged component of π_J, ρ_J, a_J and b_J mesons, [35]. The isospin-0 component would result in $\big(\,|u\bar{u}\rangle + |d\bar{d}\rangle\,\big)/\sqrt{2}$ and would mix with a possible $|s\bar{s}\rangle$ component.

QN	J	I	I_3
$u/d/s/\bar{u}/\bar{d}/\bar{s}$	$\frac{1}{2}$	$\frac{1}{2} \cdot (1/1/0/1/1/0)$	$\frac{1}{2} \cdot (1/-1/0/-1/1/0)$
two-body system	$L \oplus S_1 \oplus S_2$	$I_1 \oplus I_2$	$I_{3,1} + I_{3,2}$
$\pi^+ + \pi^-$	L	$0, 1, (2)$	0
$\big(\,\lvert u\bar{u}\rangle - \lvert d\bar{d}\rangle\,\big)/\sqrt{2}$	$L \oplus (0, 1)$	1	0

QN	P	C	G
$u/d/s/\bar{u}/\bar{d}/\bar{s}$	$+1/+1/+1/-1/-1/-1$	–	–
two-body system	$P_1 P_2 (-1)^L$	–	–
two eigenstates of C or G	$P_1 P_2 (-1)^L$	$C_1 C_2$	$G_1 G_2$
$\pi^+ + \pi^-$	$(-1)^L$	P	$+1$
$\big(\,\lvert u\bar{u}\rangle - \lvert d\bar{d}\rangle\,\big)/\sqrt{2}$	$(-1)^{L+1}$	$(-1)^{L+S}$	$C(-1)^I$
$N \times \pi$	–	–	$(-1)^N$

(see section 5.3.3 for examples) and will be discussed in the section 3.4.3.

So far, the label for a decay chain would be $I^G(J^{PC})M^\varepsilon\,\xi\zeta\,L$, which incorporates all QNs of the isobar into its name. We will simplify it further in section 3.4.3, once we discussed a few more details on the scattering process.

3.4.2 Differential Cross Section of Diffractive Scattering at COMPASS

At COMPASS, we are interested in diffractive scattering via Pomeron exchange, see Figure 3.10(a). The Pomeron can be interpreted as a gluon ladder and is the dominant exchange "particle" for t-channel scattering with high beam energies. Here, the beam particle b interacts with the target t and gets excited into some resonance X kicking out the target particle creating a recoil r. The target particle stays in tact which means that target and recoil are the same particle species. COMPASS used an unpolarized fixed ℓH2 target, thus, the target and the recoil are protons. In this thesis, we consider only negative pions for the beam particles although also hadron beams with kaons and (anti)proton beams are possible. The $2 \to 2$ scattering happens in the t-channel and reads $b + t \to X + r$, i.e. $\pi^- + p_{\text{target}} \to X + p_{\text{recoil}}$. In a second process, the resonance X decays further into an N-body final state in general, however, in this thesis we are only dealing with $N = 3$. The first process can be described by the Mandelstam variables s_0 and t. Since COMPASS is a fixed-target experiment with a beam energy E_b of 191 GeV, the variable $s_0 = (p_b + p_t)^2 = m_b^2 + m_t^2 + 2E_b m_t \approx (19\,\text{GeV})^2$ is the same for all events. Instead of the Mandelstam t, it is more convenient to use the reduced

four-momentum transfer

$$t' := |t| - |t|_{\min}. \tag{3.47}$$

We can calculate it using the CMS kinematics of the $2 \to 2$ scattering:

$$\begin{aligned} |t| = -t &= 2E_b E_X - m_b^2 - m_X^2 - 2\left|\vec{p}_b\right|\left|\vec{p}_X\right|\cos\theta \\ |t|_{\min} &= 2E_b E_X - m_b^2 - m_X^2 - 2\left|\vec{p}_b\right|\left|\vec{p}_X\right|, \qquad \text{since } \theta = 0 \text{ is possible in CMS} \\ t' &= 2\left|\vec{p}_b\right|\left|\vec{p}_X\right|(1-\cos\theta) = \frac{\lambda^{\frac{1}{2}}(s_0, m_b^2, m_t^2)\lambda^{\frac{1}{2}}(s_0, m_X^2, m_r^2)}{2s_0}(1-\cos\theta). \end{aligned} \tag{3.48}$$

One can observe that t' has only a weak dependence on the mass of the resonance m_X, since the second λ-function is dominated by the much larger s_0 component. It only drops by roughly 2.5 % from $m_X = 0\,\text{GeV}$ to $m_X = 3\,\text{GeV}$. What is also interesting to point out, is the similarity of this expression for t' to the one of t in the simple example with equal masses at the beginning of this section 3.4.

One ingredient in the expression of the differential cross section $\mathrm{d}\sigma$, equation (3.11), that is unspecified so far, is the flux factor of equation (3.12). Since $F = 4\sqrt{(p_b \cdot p_t)^2 - m_b^2 m_t^2}$ is Lorentz-invariant, its value is the same in every reference frame. However, the calculation in the CMS is the simplest, since we already know the formulas to calculate the energies and momenta of the involved particles (cf. equations (A.1) and equation (A.2), respectively). Inserting them and simplifying the expression yields

$$F = 2\left|\vec{p}_b\right|\sqrt{s_0} = \lambda^{\frac{1}{2}}(s_0, m_b^2, m_t^2) \approx 360\,\text{GeV}^2. \tag{3.49}$$

The full reaction is of the type $2 \to 3 + 1$, so the differential phase space factor is $\mathrm{d}\Phi_4$. Using the recursion formula for phase spaces derived in appendix A.1.3, we can rewrite this as

$$\mathrm{d}\Phi_4(P; p_1, p_2, p_3, p_r) = \int \frac{\mathrm{d}m_X^2}{2\pi} d\Phi_3(p_X; p_1, p_2, p_3)\mathrm{d}\Phi_2(P; p_X, p_r), \tag{3.50}$$

with $P = p_b + p_t$.

By taking the derivative of equation (3.48) with respect to the CMS scattering angle $\cos\theta$, yielding $\mathrm{d}\cos\theta = -\mathrm{d}t'/(2\left|\vec{p}_b\right|\left|\vec{p}_X\right|)$, we can express the differential two-body phase space from the initial $2 \to 2$ reaction in equation (3.50) in terms of t':

$$\mathrm{d}\Phi_2(P; p_X, p_r) = \frac{1}{8\pi}\frac{2\left|\vec{p}_X\right|}{\sqrt{s_0}}\frac{\mathrm{d}\cos\theta\mathrm{d}\phi}{4\pi} = \frac{1}{8\pi}\frac{1}{2\left|\vec{p}_b\right|\sqrt{s_0}}\mathrm{d}t', \tag{3.51}$$

where the minus sign in the substitution is used to correct the integration direction of t', since it goes in the opposite direction as the one of $\cos\theta$. Additionally, we do not measure the polarization of the target and the recoil particle, therefore, the squared matrix element is averaged (an additional factor of $1/2$ appears for two possible proton polarizations) and summed over their spin projection, respectively. This makes the squared matrix element independent of the azimuthal angle ϕ of the resonance X (below equation (142) of [20]), which allowed us to take out the integration over $\mathrm{d}\phi$ in equation (3.51). Using $\mathrm{d}m_X^2 = 2m_X\mathrm{d}m_X$ as well, we can put everything together by inserting this together with equation (3.51) into equation (3.50). This result, together with equation (3.49) entered

into equation (3.11), yields

$$\mathrm{d}\sigma = \overbrace{\frac{1}{2}}^{\text{averaging}} \underbrace{\frac{1}{2\left|\vec{p}_b\right|\sqrt{s_0}}}_{F=} \left|\mathcal{M}\right|^2 \overbrace{\frac{2m_X \mathrm{d}m_X}{2\pi}}^{\mathrm{d}m_X^2=} \mathrm{d}\Phi_3(p_X; p_1, p_2, p_3) \underbrace{\frac{1}{8\pi}\frac{1}{2\left|\vec{p}_b\right|\sqrt{s_0}}\mathrm{d}t'}_{\mathrm{d}\Phi_2}.$$

Cleaning things up and pulling all differentials on the left-hand side of the equation results in the intensity distribution (cf. equations (142) and (143) of [20])

$$\begin{aligned} \mathcal{I}(t', m_X, \tau) := \frac{\mathrm{d}N}{\mathrm{d}m_X \mathrm{d}t' \mathrm{d}\Phi_3(m_X, \tau)} \propto \frac{\mathrm{d}\sigma}{\mathrm{d}m_X \mathrm{d}t' \mathrm{d}\Phi_3(m_X, \tau)} &= \frac{1}{16\pi^2}\frac{1}{\lambda(s_0, m_b^2, m_t^2)} m_X \left|\mathcal{M}(t', m_X, \tau)\right|^2 \\ &\propto m_X \left|\mathcal{M}(t', m_X, \tau)\right|^2, \end{aligned} \tag{3.52}$$

where $N = \sigma \mathcal{L}_{\text{int}}$ is the number of produced events, given a constant integrated luminosity $\mathcal{L}_{\text{int}} = \int \mathcal{L} \mathrm{d}t$. τ denotes the independent kinematic variables that parametrize the 3-body phase space.

We already saw that with equation (3.13), we have two independent variables to describe the $2 \to 2$ production reaction, which we chose as s_0 and t'. We omitted the former in the dependence of I, since it has the same value for all considered processes. Due to the resonance X being off-shell, we have its mass m_X as an additional parameter. For the remaining $1 \to 3$ decay, we have an additional set of $3 \cdot 3 - 4 = 5$ independent variables τ that are needed to fully describe the matrix element. We will discuss a possible choice for τ in the next section. This amounts to 8 variables in total, perfectly fitting the expectations from a $2 \to 4$ reaction with fully known initial state and all final-state particles on mass shell according to equation (3.13). To account for the unmeasured luminosity, we will use a strength parameter for fitting the measured intensity. This will also take care of all proportionality constants and, therefore, we can omit them here.

Finally, we factor out the production component $\mathcal{P}$ of the matrix element $\mathcal{M}$. It contains all t' dependence and it is independent of the variables τ.

$$\mathcal{M}(t', m_X, \tau) = \mathcal{P}(t', m_X) \cdot A(m_X, \tau) \tag{3.53}$$

The remainder A is the three-body decay amplitude and we will discuss its construction in the next section such that it allows us to separate resonances with different QNs from each other. This will also bring us to the isobar model.

3.4.3 Isobar Model

In this thesis, we want to study two different decay channels, the 3π-channel $\pi^- + p \to X^- \to \pi^-\pi^+\pi^- + p$ and the $\pi K\bar{K}$-channel $\pi^- + p \to X^- \to \pi^- K_S^0 K_S^0 + p$. In both cases we have two identical bosons, in 3π we have two π^- and in $\pi K\bar{K}$ we have two K_S^0, therefore, the full decay amplitude has to be symmetric under exchange of these two. This symmetry can be enforced by averaging the amplitude

with exchanged 4-momenta in the following way:

$$\begin{aligned} A^{\text{sym}}_{3\pi}\left(p^{(1)}_{\pi^-}, p^{(2)}_{\pi^+}, p^{(3)}_{\pi^-}\right) &= \frac{1}{\sqrt{2}}\left(A_{3\pi}\left(p^{(1)}_{\pi^-}, p^{(2)}_{\pi^+}, p^{(3)}_{\pi^-}\right) + A_{3\pi}\left(p^{(3)}_{\pi^-}, p^{(2)}_{\pi^+}, p^{(1)}_{\pi^-}\right)\right) \\ A^{\text{sym}}_{\pi K\overline{K}}\left(p^{(1)}_{\pi^-}, p^{(2)}_{K^0_S}, p^{(3)}_{K^0_S}\right) &= \frac{1}{\sqrt{2}}\left(A_{\pi K\overline{K}}\left(p^{(1)}_{\pi^-}, p^{(2)}_{K^0_S}, p^{(3)}_{K^0_S}\right) + A_{\pi K\overline{K}}\left(p^{(1)}_{\pi^-}, p^{(3)}_{K^0_S}, p^{(2)}_{K^0_S}\right)\right). \end{aligned} \quad (3.54)$$

Such Bose symmetrization can be applied at the end after the full construction of the model, so for the moment, we do not have to worry about it and will treat all particles as distinct.

Similar to the previously discussed separation of the four-body phase space into a three-body and a two-body phase space, we can mathematically split the remaining three-body phase space into two two-body phase spaces with the same recursion formula as derived in appendix A.1.3. As mentioned before by looking at Dalitz plots for a resonance decaying into three particles, experimentally, one sees bands of increased intensity appearing in the two-body subsystems that correspond to two-body resonances, called isobars. So, by applying the phase-space recursion formula, we not only have a simpler way to calculate the three-body phase space, but it additionally allows us to incorporate these isobars into the physics model easier, see appendix A.1.4. Such a model is called an isobar model.

While being practical and comparably simple, it comes with the disadvantage of neglecting final-state interactions, meaning interactions of the final-state particles with each other before being detected in the experimental setup. A way to incorporate this into the isobar model will be discussed in section 3.6. Two further issues are the omission of direct three-body decays into the final-state particles as well as the strong model dependence on the isobar line shapes that have to be put in. While the first point seems to be of lower importance as data clearly shows a bias towards these isobar decay modes, the second point was recently addressed successfully by [36] with a so-called freed-isobar PWD. Here, one not only bins in the three-body invariant mass m_X and four-momentum transfer t', but also in the two-body invariant mass of the isobar subsystems m_ξ. However, this is only possible for huge data sets, for example as they are available for the $\pi^-\pi^+\pi^-$ final state at COMPASS of $\sim 46 \times 10^6$ events.

A visual representation of such an isobar decay can be found in Figure 3.10(b). As discussed in section 3.4.1, we can label the decay chain with $I^G(J^{PC})M^\varepsilon\,\xi\zeta\,L$. However, since the beam particle has isospin $I_{\text{beam}} = 1$ and the exchanged Pomeron is an iso-scalar, also the resonance has to have isospin $I = 1$. Similarly, also its G-parity has to be negative as for the beam pion. Thus, the resonance X has to have $I^G = 1^-$, therefore, these QNs are omitted in the notation. The resonance is negatively charged, therefore, it cannot be an eigenstate of the charge conjugation. But since we know its isospin and G-parity, we can deduce the C-parity of the corresponding neutral iso-triplet state via $C = G(-1)^I$ (cf. Table 3.1). For us, it will always be positive, however, to allow for easier identification of the possible resonances, we will still keep it inside the label. The resulting label for the partial waves is $J^{PC}M^\varepsilon\,\xi\zeta\,L$, with ζ being the remaining final-state particle that is not part of the isobar decay. For the 3π decay channel we only have isobars $\xi_{\pi\pi}$ in the $\pi^+\pi^-$ subsystem with $\zeta_{\pi\pi} = \pi^-$. On the other hand for the $\pi K\overline{K}$ decay channel, we expect isobars $\xi_{\pi\overline{K}}$ in the $\pi^-K^0_S$ subsystem with $\zeta_{\pi\overline{K}} = K^0_S$ and isobars $\xi_{K\overline{K}}$ in the $K^0_SK^0_S$ subsystem with $\zeta_{K\overline{K}} = \pi^-$.

We will go into more details on the question of which $\xi_{\pi\overline{K}}$ and $\xi_{K\overline{K}}$ isobars can appear, when we discuss the corresponding event selection in section 5.1.2. For the 3π channel, the total spin J_ξ as well as P_ξ and C_ξ of the isobar $\xi_{\pi\pi}$ are fully determined by the orbital angular momentum S between the two spinless daughter pions, $J_\xi = S$ and $P_\xi = C_\xi = (-1)^S$, cf. Table 3.1. This gives us access to

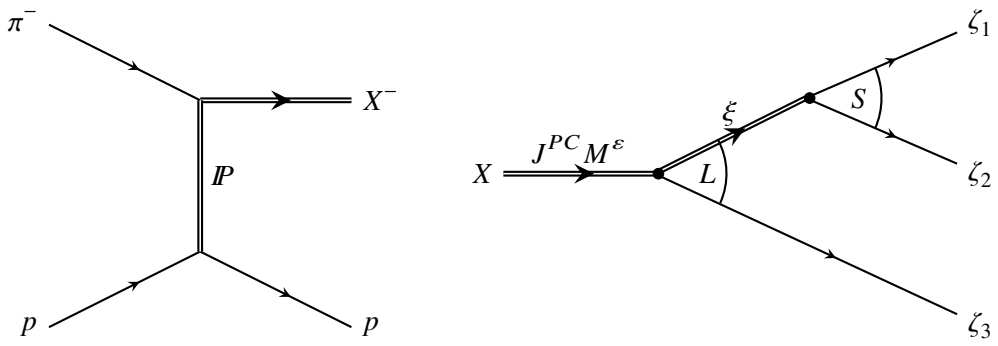

Figure 3.10: Sketch of diffractive $\pi^- + p$ scattering via Pomeron exchange (left) and the subsequent three-body decay of a resonance X with QNs $J^{PC}M^{\varepsilon}$ via the isobar model into three pseudoscalars ζ_j (right). L and S denote the orbital angular momentum between the daughter particles at the corresponding decay vertex.

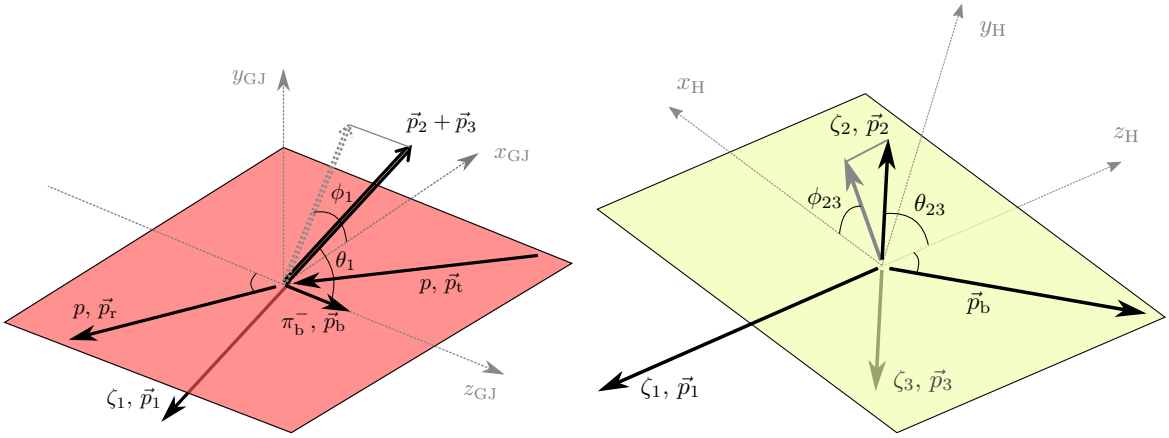

Figure 3.11: GJ frame (left) and helicity frame (right) with the definition of the relevant angles for these frames. Here, the isobar appears in the subsystem of $(\zeta_2\zeta_3)$. (Figure 5.3 from [33] with modified labels, the source files were kindly provided by the author).

$J_{\xi}^{P_\xi C_\xi} \in \{0^{++}, 1^{--}, 2^{++}, 3^{--}, \ldots\}$. The isospin can be either zero or one, however, the G-parity has to be positive due to the decay into two pions. This eliminates the iso-scalar ω_J and the iso-vector a_J particles, resulting in only $\xi_{\pi\pi} \in \{f_{\mathrm{even}}, \rho_{\mathrm{odd}}\}$ as possible isobars in the 3π channel.

3.4.4 Decay Amplitudes

A derivation of the decay amplitudes that are used in this thesis, can be found in appendix C of [33]. To understand them, we first have to define two reference frames, the Gottfried-Jackson (GJ) frame and the isobar helicity frame. A depiction of both frames can be found in Figure 3.11. Let us for now assume that we have an isobar in the (23) subsystem. But we do not have to constrain ourselves to this, since we can simply cycle the indices $1 \to 2 \to 3 \to 1$ or $1 \to 3 \to 2 \to 1$ to obtain the corresponding reference frames and angles for the other subsystems (31) and (12), respectively.

Gottfried-Jackson Frame

The GJ frame is a CMS of the resonance X. It is chosen such that the spin projection M of the total spin J of the resonance is a good QN. The z-axis is defined in the direction of the beam after boosting it into the GJ frame, $\hat{z}_{\text{GJ}} = \hat{p}_b$. One obtains the y-axis by taking the cross product of the boosted target with the boosted beam $\hat{y}_{\text{GJ}} = \frac{\vec{p}_t \times \vec{p}_b}{|\vec{p}_t \times \vec{p}_b|}$. Finally, the x-axis is defined by the right-handed Cartesian coordinate system $\hat{x}_{\text{GJ}} = \hat{y}_{\text{GJ}} \times \hat{z}_{\text{GJ}}$. The angles used to describe the particle directions in this frame are $\Omega_1 = (\theta_1, \phi_1)$, being the polar and azimuthal angles, respectively, of the momentum vector of the isobar in the (23) subsystem $\vec{p}_{23} = \vec{p}_2 + \vec{p}_3$.

Isobar Helicity Frame

The isobar helicity frame is also a CMS, but this time of the isobar, for example in the (23) subsystem. The z-axis is defined as the direction of the isobar in the GJ frame before the boost or equivalently as $\hat{z}_H = -\hat{p}_1$ after boosting into the helicity frame. Once more, we define the y-axis via a cross product, this time of the boosted momentum of particle 1 and the boosted beam, $\hat{y}_H = \frac{\vec{p}_1 \times \vec{p}_b}{|\vec{p}_1 \times \vec{p}_b|}$, and again $\hat{x}_H = \hat{y}_H \times \hat{z}_H$. In this frame, the spin projection λ of total spin S of the isobar is a well-defined QN. We choose the angles $\Omega_{23} = (\theta_{23}, \phi_{23})$ to describe the momenta in this frame, which are the polar and azimuthal angles, respectively, of $\vec{p}_2 = -\vec{p}_3$.

Set of Independent Variables

We still need a set of independent variables τ of which we will use the previously defined four angles Ω_1 and Ω_{23}. For the last one, let us consider the fact that $\cos\theta_{23}$ can be expressed as a function of the invariant masses of the two-body subsystems as derived in appendix A.4, equation (A.40).

By defining

$$\sigma_i = (p_j + p_k)^2, \quad \text{with cyclic indices } (ijk) \in \{(123), (231), (312)\} \tag{3.55}$$

as the squared invariant masse of the respective two-body subsystem (jk), we can easily relate σ_2 to the other two squared invariant masses, see equation (A.36), showing that only two of them are independent variables. Since we can express $\cos\theta_{23}$ via the σ_i as well, we see that we can choose, for example, the angle θ_{23} instead of σ_3 that can be calculated from the angle via

$$\sigma_3 = \frac{1}{2\sigma_1}\left(\sqrt{\lambda_1\lambda_{s1}}\cos\theta_{23} + (m_2^2 - m_3^2)(s - m_1^2)\right) + \frac{1}{2}\left(s + \sum m_i^2 - \sigma_1\right), \tag{3.56}$$

which is obtained by inserting equation (A.36) into equation (A.40) and solving for σ_3. Here, we define $s = m_X^2$ since we can view the reaction as an s-channel scattering of $\pi^- + I\!P \to X \to \zeta_1 + \zeta_2 + \zeta_3$ and the resonance mass would correspond to the square root of the corresponding Mandelstam variable, while m_i are the masses of the final-state particles ζ_i. The factor in front of the $\cos\theta_{23}$ is defined using the Källén function, equation (A.3), evaluated at two specific sets of masses:

$$\lambda_i := \lambda(\sigma_i, m_j^2, m_k^2), \quad \lambda_{si} = \lambda(s, \sigma_i, m_i^2), \tag{3.57}$$

with cyclic indices.

So the final set of parameters to describe the full $2 \to 4$ reaction is $(s_0, t', m_X, \underbrace{\sigma_i, \Omega_i, \Omega_{jk}}_{=:\tau_i})$ with cyclic indices for τ_i depending on which isobar-channel (jk) is currently of interest. Since in principle any set of τ_i can be used as parameters and one can transform them into each other, we will drop the index i and simply use τ, where it does not really matter which one to choose.

Defintion of Angular Functions

To obtain the decay amplitude, we describe the decay of the resonance X in the GJ frame and the decay of the isobar in the corresponding helicity frame. As shown in equation (3.4) of [33], we can expand the full decay amplitude into different partial waves depending on their QNs $w = (J, M, L, S)$ and the reflectivity ϵ:

$$A^{\epsilon}(t', m_X, \tau) = \sum_w F_w^{\epsilon}(t', m_X)\Psi_w^{\epsilon}(\tau). \tag{3.58}$$

Since different waves with different reflectivity do not interfere with each other ([20]), we can sum them up later incoherently on intensity level. Here, we also see that we can factorize the known angular dependence from the so-far unknown mass dependence. The angular term will be split in three parts according to the isobar model in the following way

$$\Psi_w^{\epsilon}(\tau) = \sum_{i=1}^{3} C_I^{(i)} Z_w^{\epsilon}(\Omega_i, \Omega_{jk}) h_L(s, \sigma_i) f_S(\sigma_i), \tag{3.59}$$

cf. equation (3.15) of [33]. Note that in [33] it explicitly only contains two terms, since specifically there, the 3π channel is discussed where one does not expect an isobar in the (31) channel with two π^- as daughters. However in the case of the $\pi K\overline{K}$ channel, isobars can occur in all three subsystems. Let us start with the coefficient $C_I^{(i)}$, which is the Clebsch-Gordan coefficient of the isospin coupling of the resonance to the isobar-bachelor system. Next, the h_L are the Blatt-Weisskopf factors, already discussed in section 3.3 and explicitly given in appendix A.2. Technically, these factors introduce some s or m_X dependence, however, since this dependence is known[16], it is factored out from the mass-dependent terms F_w^{ϵ} and omitted from the argument of the Ψ_w^{ϵ}. The factor f_S is the actual isobar parametrization where, usually, a BWM is used. Finally, the angular function is given by

$$Z_w^{\epsilon}(\Omega_i, \Omega_{jk}) := \sqrt{n_L n_S} \sum_{\lambda} \langle L0, S\lambda | J\lambda \rangle \, {}^{\epsilon}D^{J*}_{M\lambda}(\Omega_i) \, D^{S*}_{\lambda 0}(\Omega_{jk}), \quad \text{with } n_x = 2x + 1 \tag{3.60}$$

with cyclic indices, cf. equation (3.9) of [33], where ${}^{\epsilon}D^{J}_{M\lambda}(\Omega)$ is the reflectivity representation of the Wigner-D functions as detailed in appendix A.3.2, equation (A.27).

3.4.5 Fit Procedure

With equations (3.58), (3.59) and (3.60) we have a complete basis that we could use to decompose the data into its contributions from different partial waves. For this, one performs a binning of the data in t' and m_X. For each of these (t', m_X)-bins one assumes a constant $F_w^{\epsilon}(t', m_X)$ and performs such a

[16] or maybe more precise: phenomenologically modeled

decomposition. However, to do so, one has to normalize the $\Psi_w^\epsilon(\tau)$ correctly. This normalization is a free parameter of the model and has to be fixed by the data. Otherwise, fit results of separate (t', m_X)-bins do not have the correct relative strength.

Normalization

The normalization factor can be extracted from the $F_w^\epsilon(t', m_X)$ and the procedure is derived in detail in section 5.2.4 of [20]. We will summarize the end result in the following. For this, we first introduce the integral matrices

$$I_{ww'}^\epsilon(m_X) := \int \mathrm{d}\Phi_3(\tau; m_X)\Psi_w^\epsilon(\tau; m_X)\Psi_{w'}^{\epsilon *}(\tau; m_X) \tag{3.61}$$

between two partial waves w and w'. These integrals can best be calculated by drawing events distributed according to flat three-body phase space, so-called flat MC, and evaluating the Ψ on these events. Like this one can also directly and properly include the Bose symmetrization by boosting the final-state four-vectors of each flat MC event i into the corresponding GJ frame and the isobar helicity frame in order to calculate the variables τ_i of this event. Then, according to equation (3.54), one switches the two four-vectors of the particles that one wants to symmetrize and repeats the boosting and the calculation of the new $\tilde{\tau}_i$ variables. Finally, the symmetrized integral matrices are given by

$$I_{ww'}^\epsilon(m_X) := \frac{1}{2}\sum_i^{N_{\mathrm{MC}}^{\mathrm{flat}}} \Big(\Psi_w^\epsilon(\tau_i; m_X) + \Psi_w^\epsilon(\tilde{\tau}_i; m_X)\Big)\Big(\Psi_w^\epsilon(\tau_i; m_X) + \Psi_w^\epsilon(\tilde{\tau}_i; m_X)\Big)^*. \tag{3.62}$$

With this, the normalized basis functions read

$$\overline{\Psi}_w^\epsilon(\tau; m_X) := \frac{\Psi_w^\epsilon(\tau; m_X)}{\sqrt{I_{ww}^\epsilon(m_X)}}, \tag{3.63}$$

which results in

$$\int \mathrm{d}\Phi_3(\tau; m_X)\left|\overline{\Psi}_w^\epsilon(\tau; m_X)\right|^2 = 1$$

and for the interferences in

$$\int \mathrm{d}\Phi_3(\tau; m_X)\overline{\Psi}_w^\epsilon(\tau; m_X)\overline{\Psi}_{w'}^{\epsilon *}(\tau; m_X) = \frac{I_{ww'}^\epsilon(m_X)}{\sqrt{I_{ww}^\epsilon(m_X)}\sqrt{I_{w'w'}^\epsilon(m_X)}}.$$

As mentioned before, this normalization is taken from the mass-dependent factor $F(t', m_X)$ from equation (3.58) to keep the full decay amplitude A^ϵ unchanged. This brings us to the definition of the transition amplitudes

$$\mathcal{T}_w^\epsilon := \sqrt{m_X}\cdot\mathcal{P}(t', m_X)\cdot F_w^\epsilon(t', m_X)\cdot\sqrt{I_{ww}^\epsilon(m_X)}. \tag{3.64}$$

They include the m_X of equation (3.52) pulled into the squared magnitude of the matrix element, as well as the so far omitted production amplitude $\mathcal{P}$ of equation (3.53) that differentiates the matrix element $\mathcal{M}$ of equation (3.52) from the full decay amplitude A from equation (3.58) and should

parametrize the t' and m_X dependence of the $2 \to 2$ production reaction.

Spin-Density Matrix

Putting everything together, we can write the intensity from equation (3.52) as[17]

$$\mathcal{I}(t', m_X, \tau) = \sum_{\epsilon=\pm} \left| \sum_w \mathcal{T}_w^\epsilon(t', m_X) \overline{\Psi}_w^\epsilon(\tau; m_X) \right|^2 + \left| \mathcal{T}_{\text{flat}}(t', m_X) \overline{\Psi}_{\text{flat}}(m_X) \right|^2, \tag{3.65}$$

where we introduced another incoherently added wave that is "flat" in the three-body phase space to account for events with uncorrelated final-state particles, for example from other background processes. It is also a good measure for the completeness of the chosen wave set, with a large flat-wave component indicating the insufficiency of the wave set. Its basis function is

$$\overline{\Psi}_{\text{flat}}(m_X) \equiv \overline{\Psi}_{\text{flat}}(\tau; m_X) = \frac{1}{\sqrt{I_{\text{flat}}(m_X)}}, \qquad \text{with } I_{\text{flat}}(m_X) := \int \mathrm{d}\Phi_3(\tau; m_X).$$

With this normalization, we can write down the expected number of events per (t', m_X)-bin by integrating the intensity $\mathcal{I}$ over the three-body phase space:

$$\begin{aligned}
\frac{\mathrm{d}^2 N_{\text{expected}}}{\mathrm{d}m_X \mathrm{d}t'} &= \int \mathrm{d}\Phi_3(\tau; m_X) \mathcal{I}(t', m_X, \tau) && (3.66)\\
&= \sum_{\epsilon=\pm} \left(\sum_w \left|\mathcal{T}_w^\epsilon\right|^2 + \sum_w \sum_{w' \neq w} \mathcal{T}_w^\epsilon \mathcal{T}_{w'}^{\epsilon *} \frac{I_{ww'}^\epsilon}{\sqrt{I_{ww}^\epsilon I_{w'w'}^\epsilon}} \right) + \left|\mathcal{T}_{\text{flat}}\right|^2, && (3.67)\\
&= \sum_{\epsilon=\pm} \left(\sum_{i=1}^{N_{\text{waves}}^\epsilon} \rho_{ii}^\epsilon + \sum_{i=1}^{N_{\text{waves}}^\epsilon} \sum_{j=i+1}^{N_{\text{waves}}^\epsilon} 2\mathrm{Re}\left[\rho_{ij}^\epsilon \frac{I_{ij}^\epsilon}{\sqrt{I_{ii}^\epsilon I_{jj}^\epsilon}} \right] \right) + \left|\mathcal{T}_{\text{flat}}\right|^2 && (3.68)
\end{aligned}$$

where the arguments are omitted for brevity, but they should be clear from the definitions above. In the last row, we explicitly require a certain sorting and a limitation on the considered number $N_{\text{waves}}^\epsilon$ of partial waves per reflectivity, and we introduced the Hermitian Spin-Density Matrix (SDM) accordingly via

$$\varrho_{ij}^\epsilon(t', m_X) = \mathcal{T}_i^\epsilon(t', m_X) \mathcal{T}_j^{\epsilon *}(t', m_X), \qquad \varrho^\epsilon = \vec{\mathcal{T}}^\epsilon \cdot \left(\vec{\mathcal{T}}^\epsilon \right)^\dagger. \tag{3.69}$$

On its diagonal it has the (phase-space-integrated) intensity of each partial-wave, i.e. the expected number of events for a certain combination of QNs, and the complex argument of its off-diagonal elements is the relative phase between partial waves i and j.

[17] All omitted proportionality factors from equation (3.52) can simply be absorbed in the unknown transition amplitudes $\mathcal{T}$, therefore we can write "=" instead of "∝".

Chung-Trueman Vector and Rank

The vector $\vec{\mathcal{T}}^{\epsilon}$ of transition amplitudes is called Chung-Trueman vector and one can generalize it to a matrix $\mathcal{T}^{\epsilon}$ of dimension $(N^{\epsilon}_{\text{waves}}, R)$ where each additional column $\vec{\mathcal{T}}^{\epsilon,r}$ contains one "zero" more at the top, such that the resulting SDM has rank R, see appendix E of [20] for details. This is the resulting structure of the Chung-Trueman matrix for rank-3 with 5 waves as an example

$$\{\mathcal{T}_w^{\epsilon,r}\} = \begin{pmatrix} \mathcal{T}_1^{\epsilon,1} & 0 & 0 \\ \mathcal{T}_2^{\epsilon,1} & T_2^{\epsilon,2} & 0 \\ \mathcal{T}_3^{\epsilon,1} & T_3^{\epsilon,2} & T_3^{\epsilon,3} \\ \mathcal{T}_4^{\epsilon,1} & T_4^{\epsilon,2} & T_4^{\epsilon,3} \\ \mathcal{T}_5^{\epsilon,1} & T_5^{\epsilon,2} & T_5^{\epsilon,3} \end{pmatrix} \tag{3.70}$$

Calculating the SDM from this via equation (3.69) gives

$$\begin{aligned} \rho^{\epsilon} \quad = \quad & \begin{pmatrix} \left|T_1^{\epsilon,1}\right|^2 & T_1^{\epsilon,1}T_2^{\epsilon,1*} & T_1^{\epsilon,1}T_3^{\epsilon,1*} & T_1^{\epsilon,1}T_4^{\epsilon,1*} & T_1^{\epsilon,1}T_5^{\epsilon,1*} \\ T_2^{\epsilon,1}T_1^{\epsilon,1*} & \left|T_2^{\epsilon,1}\right|^2 & T_2^{\epsilon,1}T_3^{\epsilon,1*} & T_2^{\epsilon,1}T_4^{\epsilon,1*} & T_2^{\epsilon,1}T_5^{\epsilon,1*} \\ T_3^{\epsilon,1}T_1^{\epsilon,1*} & T_3^{\epsilon,1}T_3^{\epsilon,1*} & \left|T_3^{\epsilon,1}\right|^2 & T_3^{\epsilon,1}T_4^{\epsilon,1*} & T_3^{\epsilon,1}T_5^{\epsilon,1*} \\ \vdots & \ddots & \ddots & \ddots & \vdots \end{pmatrix} \\ & + \begin{pmatrix} 0 & 0 & 0 & 0 & 0 \\ 0 & \left|T_2^{\epsilon,2}\right|^2 & T_2^{\epsilon,2}T_3^{\epsilon,2*} & T_2^{\epsilon,2}T_4^{\epsilon,2*} & T_2^{\epsilon,2}T_5^{2*} \\ 0 & T_3^{\epsilon,2}T_2^{\epsilon,2*} & \left|T_3^{\epsilon,2}\right|^2 & T_3^{\epsilon,2}T_4^{\epsilon,2*} & T_3^{\epsilon,2}T_5^{\epsilon,2*} \\ \vdots & \vdots & \ddots & \ddots & \vdots \end{pmatrix} \\ & + \begin{pmatrix} 0 & 0 & 0 & 0 & 0 \\ 0 & 0 & 0 & 0 & 0 \\ 0 & 0 & \left|T_3^{\epsilon,3}\right|^2 & T_3^{\epsilon,3}T_4^{\epsilon,3*} & T_3^{\epsilon,3}T_5^{\epsilon,3*} \\ \vdots & \vdots & \vdots & \ddots & \vdots \end{pmatrix}, \end{aligned} \tag{3.71}$$

where we see that it can be decomposed into the sum of one matrix per rank with each following matrix having one line and column of zeroes more than the previous one. It also demonstrates that the $\vec{\mathcal{T}}^{\epsilon,r}$ of different ranks do not interfere with each other and due to this, it allows for the incorporation of additional incoherences into the PWD model that might come from background processes besides diffractive resonance production.

This generalization introduces many additional (complex) parameters $\mathcal{T}_w^{\epsilon,r}$, with a total[18] amount of $N^{\epsilon}_{\text{waves}}R - (R-1)R/2$, and with this, it delivers a more flexible model. In principle, all of these parameters are complex, resulting in twice as many real-valued fit parameters, $2N^{\epsilon}_{\text{waves}}R - R^2 + R$. However, the global phase is unobservable, therefore, the diagonal[19] of the Chung-Trueman matrix is

[18] We add another $R-1$ columns of size $N^{\epsilon}_{\text{waves}}$. Then, we fix $0+1+\ldots+(R-1)$ entries to zero, resulting in a subtraction of $(R-1)R/2$ entries.

[19] i.e. the first non-zero element of each column and, thus, one element for each additional incoherent sector

chosen to be real and positive, resulting in R real-valued parameters less. In total, this amounts to $2N^{\epsilon}_{\text{waves}}R - R^2$ real-valued parameters.

Extended Log-Likelihood Fit

In order to fit the model for the total intensity in equation (3.68) to the experimental data of the COMPASS experiment, we start by binning the data in (t', m_X) as already mentioned at the beginning of this section. Then, we need to find a procedure that allows for event-based fitting, since we need to evaluate the model on the individual kinematic variables of the events. Also, we need a way to correct for the detector acceptance α, which is a measure for the probability that an event inside a given volume element of the phase space is detected. Such a procedure is the extended log-likelihood fit, see section 5.2.5 of [20] for a proof of the working principle and more details. In the following, we give the general idea of the concept.

The probability to measure exactly N events follows the Poisson distribution:

$$P(N; N_{\text{pred}}) = \frac{\left(N_{\text{pred}}\right)^N}{N!} \mathrm{e}^{-N_{\text{pred}}}, \tag{3.72}$$

where

$$N_{\text{pred}}(\mathcal{T}^{\epsilon}) = \int \mathrm{d}\Phi_3(\tau)\, \alpha(\tau) \mathcal{I}(\tau; \mathcal{T}^{\epsilon}) \tag{3.73}$$

is the number of predicted events given the limited detector acceptance $\alpha(\tau)$ that provides the probability that an event with kinematic variables τ is detected by the experimental setup.

On the other hand, the probability to obtain N events with exactly the kinematic variables τ_k as measured by the experiment – given a certain set of parameters $\mathcal{T}^{\epsilon}$ – will be the product of the phase-space-integrated intensities normalized by the number of predicted events:

$$P(\tau_k; \mathcal{T}^{\epsilon}; N) = \prod_{k=1}^{N} \frac{\Phi_3(\tau_k) I(\tau_k; \mathcal{T}^{\epsilon})}{N_{\text{pred}}(\mathcal{T}^{\epsilon})}. \tag{3.74}$$

The denominator cancels exactly with the factor $\left(N_{\text{pred}}\right)^N$ if we build the product of equations (3.72) and (3.74).

Since these numbers will be very small, it is numerically better to take the logarithm of the resulting expression which also changes from a product over all events to a sum. The logarithm is a monotonous function and, thus, leaves the position of the maximum invariant. Additionally, computers usually are used to minimize rather than maximize, therefore, we take the negative logarithm:

$$-\ln \mathcal{L}_{\text{ext}} = \cancel{\ln(N!)} + N_{\text{pred}}(\mathcal{T}^{\epsilon}) - \sum_{k=1}^{N} \ln\left[\Phi_3(\tau_k) \mathcal{I}(\tau_k; \mathcal{T}^{\epsilon})\right]. \tag{3.75}$$

The first term is equal for all sets of parameters $\mathcal{T}^{\epsilon}$ and, as a consequence, will not change the position of the minimum allowing us to drop it. The number of predicted events as of equation (3.73) will be calculated using MC data. For this, one generates flat MC distributed according to three-body phase space and tracks the generated final-state particles through a virtual detector setup that describes the

actual COMPASS experiment as detailed as possible using TGEANT. Afterwards, one simulates the detector responses and reconstructs the events with CORAL in the same way as one would do it with RD. In a final step, the events go through the same PHAST event selection as RD. MC events with kinematic variables τ_k^{MC} that pass this step are called aMC and will be assigned $\alpha\big(\tau_k^{\mathrm{MC}}\big) = 1$. For all other generated MC events we set $\alpha\big(\tau_k^{\mathrm{MC}}\big) = 0$, which results in an omission from equation (3.73). However, since the integral matrices $I^{\epsilon}_{ww'}$ in equation (3.61) – that are needed for the normalization of the basis functions in equation (3.63) – are calculated without acceptance effects, they can be calculated numerically using the full MC sample. An execution of this procedure can be seen in chapter 6.

3.5 Dalitz Plots for the 1^{++} Sector

The Pomeron $I\!P$ – as the exchange particle of diffractive scattering – has QNs $J^{PC} = 2^{++}$ and, thus, positive naturality. This means that positive reflectivity $\epsilon = +$ is expected to be dominant for diffractive scattering. Additionally for this section, we only consider axial-vector resonances a_1 with QNs $J^{PC}M^{\epsilon} = 1^{++}0^{+}$. The reason is that a_0 with $J^{PC} = 0^{++}$ cannot be produced[20] and a_2 with $J^{PC} = 2^{++}$ can only appear[21] with spin projection $M \geq 1$, which is suppressed. Since no $\pi(1300)$ was observed in the $\pi^-\pi^+\pi^-$ final state by COMPASS, we can also neglect contributions from 0^{-+} for low resonance masses $m_X \lessapprox 1.5\,\mathrm{GeV}$. The J^{PC} combinations 1^{-+} and 2^{-+} as well as $J > 2$ have their ground-state resonances at masses above 1.6 GeV, which means that the 1^{++} sector clearly dominates this region.

Since all the final-state particles are spinless, the orbital angular momentum S between the isobar daughters corresponds to the total spin of the isobar. L denotes the orbital angular momentum between the isobar and the bachelor particle. The parity of the three-body system can be calculated via $P = P_{\xi}(-1)^{L+1} = (-1)^{L+S+1}$ and since we want positive parity ($J^{PC} = 1^{++}$) for our resonance, $L + S$ has to be odd. We will only consider the two possibilities $LS = 10$ and $LS = 01$ corresponding to e.g. a $[\pi\pi]_{\mathrm{S}}\,\pi$ P-wave and $[\pi\pi]_{\mathrm{P}}\,\pi$ S-wave, respectively, in case of the 3π system. We will do this, since higher orbital angular momenta in the subsystems yield isobars with higher masses and, thus, smaller available phase space, making them less likely to occur especially in the low-mass region. To avoid confusion with the variable S for the orbital angular momentum in the decay of the isobar, we will use spectral notation for its values with upright characters (S, P, D, ...).

3.5.1 Definition of Dalitz Plots

After splitting off the initial $2 \to 2$ reaction as discussed in section 3.4.2, we remain with a three-body decay which, for fixed values of t' and m_X, has two degrees of freedom. This is often depicted in form of a Dalitz plot and, apart from this context, it has many use-cases such as ω and ϕ decays to 3π or weak decays of e.g. D mesons and Λ_c baryons. A different application for a partial-wave decomposition is the prediction of such Dalitz plots for specific final-state systems, but let us revise its definition first.

[20] A beam pion with $J^{PC} = 0^{-+}$ and an exchange $I\!P$ with $J^{PC} = 2^{++}$ need orbital angular momentum $L = 2$ to form a resonance X^- with $J_X = 0$. This results in a parity of $P_X = (-1)(+1)(-1)^2 = -1$.

[21] For $M = 0$ and even resonance spin J, the corresponding Wigner-D function will vanish for positive reflectivity and positive parity, cf. equation (A.27). This is another reason, why 0^{++} resonances cannot contribute, since they can only have $M = 0$.

If we have a resonance[22] of mass m_X decaying into three particles of masses m_1, m_2 and m_3, then, one can show that the differential three-body phase space $\frac{\mathrm{d}^2\Phi_3}{\mathrm{d}\sigma_1\mathrm{d}\sigma_3}$ = const is flat (see appendix A.5). One often also writes $\sigma_3 = (p_1 + p_2)^2 =: m_{12}^2$ and $\sigma_1 = (p_2 + p_3)^2 =: m_{23}^2$.

If we plot the measured events in a two-dimensional histogram with these two squared invariant masses on the x and y axis, respectively, any deviation from a flat distribution has to come from the matrix element $\mathcal{M}$ in the relation $N \propto \sigma \sim |\mathcal{M}|^2 \Phi_3$. If the decay of a resonance can occur via an isobar ξ_{12} in the (12)-subsystem, it would manifest itself as an enhancement in form of a vertical line at the value $m_{12}^2 = m_{\xi_{12}}^2$. Vice versa, an isobar ξ_{23} in the (23)-subsystem would appear as a horizontal line at the value $m_{23}^2 = m_{\xi_{23}}^2$.

The third combination $m_{13}^2 = (p_1 + p_3)^2$ could replace any of the above as a possible axis for the Dalitz plot and isobars ξ_{13} in the 13-subsystem would appear as enhancements at the value $m_{13}^2 = m_{\xi_{13}}^2$. Since all three squared invariant masses are related in the following way

$$m_{13}^2 + m_{12}^2 + m_{23}^2 = m_X^2 + m_1^2 + m_2^2 + m_3^2, \qquad \text{(cf. equation (A.36))}$$

we can see isobars in the respectively third subsystem as diagonal lines in the Dalitz plot. For an isobar mass of $m_{13}^2 = m_{\xi_{13}}^2$, these lines can be parameterized in the following way

$$m_{23}^2(m_{12}^2) = m_X^2 + m_1^2 + m_2^2 + m_3^2 - m_{\xi_{13}}^2 - m_{12}^2.$$

Experimentally, we usually have to allow for a certain window around the resonance mass when creating the Dalitz plot. Therefore, these diagonal lines will be washed out by the size of this chosen window, since the position of the diagonal line depends on the allowed values of m_X^2.

3.5.2 Dalitz-Plot-Prediction Method

For fixed values of t' we can rewrite the partial-wave expansion in equation (3.58) in the following way

$$A^{\epsilon}(m_X, \tau) = \sum_w \Big(F_w(m_X, \sigma_1) Z_w^{\epsilon}(\Omega_1, \Omega_{23}) + F_w(m_X, \sigma_2) Z_w^{\epsilon}(\Omega_2, \Omega_{31}) + F_w(m_X, \sigma_3) Z_w^{\epsilon}(\Omega_3, \Omega_{12}) \Big). \tag{3.76}$$

Here, we collect everything other than Z_w^{ϵ} from equation (3.59) and combine it with the existing F_w of equation (3.58), allowing to distinguish them via the extra σ_i dependence

$$F_w(m_X, \sigma_i) = F_w(m_X) C_I^{(i)} h_L(s, \sigma_i) f_S(\sigma_i). \tag{3.77}$$

In the specific case at hand, namely $J^{PC} M^{\epsilon} = 1^{++}0^+$, one can easily convince oneself by looking at the definitions in equations (3.60) and (A.23) that $Z_{10LS}^{+} \equiv Z_{10LS}$, since $\epsilon P (-1)^{J-M} = -1$ in equation (A.27). While, for now, we still keep general J and M in the equations, we will already drop the ϵ index.

We will omit the contributions from the production amplitude $\mathcal{P}(t', m_X)$, since we will only create Dalitz plots for fixed value of t'. A correct relative strength between different m_X-bins is, therefore, only given if $\mathcal{P}(t', m_X) \equiv \mathcal{P}(t')$. According to equation (3.53), this makes $\mathcal{M}$ equal to the full

[22] or any three-body system with fixed invariant mass

amplitude A from equation (3.76):

$$\left|\mathcal{M}(m_X, \tau)\right|^2 = \sum_{J,J',M,M'} A^{J*}_{M}(m_X, \tau) \cdot A^{J'}_{M'}(m_X, \tau)\,, \tag{3.78}$$

where we explicitly write out the sum over M and J for the full amplitude A.

In total, we consider the following five similar three-body final-state systems (s), namely $(\pi^-\pi^+\pi^-)$, $(\pi^-\pi^0\pi^0)$, $(\pi^-K^+K^-)$, $(\pi^-\overline{K}^0K^0)$ and $(K^-\pi^0K^0)$. The reason is that they are all pseudoscalar mesons and can produce exactly the same combinations of QNs, i.e. resonances. For each of them, we can calculate the respective differential cross section via

$$\frac{\mathrm{d}^{(s)}\sigma}{\mathrm{d}m_X\,\mathrm{d}\sigma_1\,\mathrm{d}\sigma_3} \sim \frac{1}{m_X}\int \frac{\mathrm{d}\phi_1\,\mathrm{d}\cos\theta_1\,\mathrm{d}\phi_{23}}{8\pi^2}\left|{}^{(s)}\mathcal{M}(\tilde{\tau})\right|^2, \tag{3.79}$$

cf. equation (3.52) together with equation (A.46), which leads to the new set of independent variables $\tilde{\tau} = (m_X, \theta_1, \phi_1, \phi_{23}, \sigma_1, \sigma_3)$. As before, the angles (θ_1, ϕ_1) are the angles of the isobar system (23) in the GJ frame and ϕ_{23} is the azimuthal angle of particle 2 in the helicity frame of the just mentioned isobar.

We cannot directly perform the angular integrals in equation (3.79), since each isobar contribution has a different set of angles. However, equation (A.22) allows us to relate the angles $(\phi_i, \theta_i, \phi_{jk})$ from the other two isobar systems to the specific angles chosen for $\tilde{\tau}$ which we can apply to the pairs of Wigner-D matrices inside of the angular Z functions. Factoring out the now common Wigner-D matrix $D^J_{M,\nu}(\phi_1, \theta_1, \phi_{23})$ yields

$${}^{(s)}A^J_M(\tilde{\tau}) \;=\; \sum_{\nu} D^J_{M,\nu}(\phi_1, \theta_1, \phi_{23}) \sum_{S} {}^{(s)}A^J_{S\nu}(\hat{\tau})\,, \tag{3.80}$$

where we introduce the remainder $\hat{\tau} = (m_X, \sigma_1, \sigma_3)$ together with the sum over the angular momentum S in the isobar decay and

$$\begin{aligned}{}^{(s)}A^J_{S\nu}(\hat{\tau}) \;=\; \sqrt{n_J n_S}\sum_{\lambda}\Big[{}^{(s)}F^J_{S\lambda}(\sigma_1)\overbrace{d^J_{\nu,\lambda}(\theta^*_{1(1)})}^{=\delta_{\nu,\lambda}} d^S_{\lambda,0}(\theta_{23}) + {}^{(s)}F^J_{S\lambda}(\sigma_2) d^J_{\nu,\lambda}(\theta^*_{2(1)})\, d^S_{\lambda,0}(\theta_{31}) \\ + {}^{(s)}F^J_{S\lambda}(\sigma_3) d^J_{\nu,\lambda}(\theta^*_{3(1)})\, d^S_{\lambda,0}(\theta_{12})\Big].\end{aligned} \tag{3.81}$$

The angle $\theta^*_{j(i)}$ is the angle between particles j and i in the GJ frame, see equation (A.37) for its dependence on $\hat{\tau}$, and we use the abbreviation $n_x = (2x+1)$. The ${}^{(s)}F^J_{S\nu}$ are the isobar amplitudes in the helicity basis for a given final-state system (s), and $d^J_{\lambda_1,\lambda_2}$ is the Wigner-d function. For the amplitude $A^J_{S\nu}$, the spin of the system is quantized with respect to the direction of the particle 1, therefore, the trivial angle appears for the first decay chain ($\theta^*_{1(1)} = 0$), hence, the Wigner-d function can be reduced to a Kronecker-δ.

We can simplify the notation by introducing vectors:

$$ {}^{(s)}A^{J}_{S\nu}(\tilde{\tau}) = \sqrt{n_J n_S} \sum_{\lambda} {}^{(s)}\vec{F}^{J}_{S\lambda}(\vec{\sigma}) \cdot \vec{\Omega}^{JS}_{\nu\lambda}(\vec{\theta}^*, \vec{\theta}) \tag{3.82} $$

introducing ${}^{(s)}\vec{F}^{J}_{S\nu}(\vec{\sigma}) = \{{}^{(s)}F^{J}_{S\nu}(\sigma_i)\}_i$ and

$$ \vec{\Omega}^{JS}_{\nu\lambda}(\vec{\theta}^*, \vec{\theta}) = \{\delta_{\nu\lambda} d^{S}_{\nu,0}(\theta_{23}),\ \ d^{J}_{\nu,\lambda}(\theta^*_{2(1)})\, d^{S}_{\lambda,0}(\theta_{31}),\ \ d^{J}_{\nu,\lambda}(\theta^*_{3(1)})\, d^{S}_{\lambda,0}(\theta_{12})\} $$

Inserting equation (3.80) for each factor into equation (3.78) and this into equation (3.79)[23], we can use the orthogonality relation for Wigner-D matrices in equation (A.19) to perform the angular integral over the product $D^{J^*}_{M,\nu}(\phi_1, \theta_1, \phi_{23}) D^{J'}_{M',\nu'}(\phi_1, \theta_1, \phi_{23})$ which removes the sums over J', M' and ν':

$$ \frac{\mathrm{d}^{(s)}\sigma}{\mathrm{d}m_X\, \mathrm{d}\sigma_1\, \mathrm{d}\sigma_3} = \frac{1}{m_X} \sum_{J,M,\nu} \frac{1}{n_J} \sum_{S,S'} {}^{(s)}A^{J^*}_{S\nu}(\tilde{\tau}) \ \cdot {}^{(s)}A^{J}_{S'\nu}(\tilde{\tau}). \tag{3.83} $$

To enforce parity constraints, we change for the isobar amplitudes from the helicity eigenfunctions to LS functions with the following linear transformation given by a set of Clebsch-Gordan coefficients

$$ {}^{(s)}\vec{F}^{J}_{S\lambda}(\vec{\sigma}) = \sum_{L} \sqrt{\frac{n_L}{n_J}} \langle L, 0; S, \lambda | J, \lambda \rangle \, {}^{(s)}\vec{F}^{J}_{L,S}(\vec{\sigma}). \tag{3.84} $$

For the rest of this section, we only consider the case mentioned in the introduction of this section 3.5, specifically $J = 1$ and we will omit the corresponding index everywhere, e.g. $F^{1}_{L,S} \equiv F_{L,S}$. As well, we will take only $M = 0$ as mentioned before. This brings us to

$$ \frac{\mathrm{d}^{(s)}\sigma^{J=1,M=0}}{\mathrm{d}m_X\, \mathrm{d}\sigma_1\, \mathrm{d}\sigma_3} = \sum_{\nu} \left| \sum_{S,L} \sqrt{\frac{n_S n_L}{3}} \sum_{\lambda} \langle L, 0; S, \lambda | 1, \lambda \rangle \, {}^{(s)}\vec{F}_{L,S}(\vec{\sigma}) \cdot \vec{\Omega}^{S}_{\nu\lambda}(\vec{\theta}^*, \vec{\theta}) \right|^2 \tag{3.85} $$

In the considered case with $(LS) = (10)$ or $(LS) = (01)$, we can write $L = 1 - S$ making the sum over L unnecessary and the prefactor $\sqrt{n_L n_S}$ will always be $\sqrt{3}$. For $S = 0$ we have $\langle 1, 0; 0, \lambda | 1, \lambda \rangle = \delta_{\lambda 0}$, and for $S = 1$ the Clebsch-Gordan coefficient from the transformation is $\langle 0, 0; 1, \lambda | 1, \lambda \rangle = 1$ for every value of λ. This means, equation (3.85) can be written as

$$ \frac{\mathrm{d}^{(s)}\sigma^{J=1,M=0}}{\mathrm{d}m_X\, \mathrm{d}\sigma_1\, \mathrm{d}\sigma_3} = \sum_{\nu} \left| {}^{(s)}\vec{F}_{1,0}(\vec{\sigma}) \cdot \vec{\Omega}^{0}_{\nu 0}(\vec{\theta}^*, \vec{\theta}) + \sum_{\lambda} {}^{(s)}\vec{F}_{0,1}(\vec{\sigma}) \cdot \vec{\Omega}^{1}_{\nu\lambda}(\vec{\theta}^*, \vec{\theta}) \right|^2 \tag{3.86} $$

Using a specific ordering for the final-state systems (s), we can arrange the different isobar amplitudes ${}^{(s)}F_{L,S}$ in a matrix $\mathbf{F}_{L,S}$ together with their Clebsch-Gordan coefficients from combining the isospins of the involved particles accordingly, showing which partial waves are relevant in which

[23] We omit all constant prefactors since we normalize the Dalitz plots anyways.

subchannels:

$$\mathbf{F}_{L,S} = \begin{matrix} (23) \\ \downarrow \end{matrix} \quad \begin{matrix} (31) \\ \downarrow \end{matrix} \quad \begin{matrix} (12) \\ \downarrow \end{matrix} \tag{3.87}$$

$$\begin{pmatrix} \left(\sqrt{\frac{1}{3}}[\pi\pi]_S^{I=0} - \frac{1}{2}[\pi\pi]_S^{I=1}\right) \pi\, L & 0, & \left(\sqrt{\frac{1}{3}}[\pi\pi]_S^{I=0} + \frac{1}{2}[\pi\pi]_S^{I=1}\right) \pi\, L \end{pmatrix} \leftarrow (\pi^-\pi^+\pi^-)$$

$$\begin{pmatrix} -\sqrt{\frac{1}{3}}[\pi\pi]_S^{I=0}\, \pi\, L & \frac{1}{2}[\pi\pi]_S^{I=1}\, \pi\, L & -\frac{1}{2}[\pi\pi]_S^{I=1}\, \pi\, L \end{pmatrix} \leftarrow (\pi^-\pi^0\pi^0)$$

$$\begin{pmatrix} \left(\sqrt{\frac{1}{2}}[K\overline{K}]_S^{I=0} + \frac{1}{2}[K\overline{K}]_S^{I=1}\right) \pi\, L & 0, & -\sqrt{\frac{2}{3}}[\pi K]_S^{I=1/2}\overline{K}\, L \end{pmatrix} \leftarrow (\pi^-K^+K^-)$$

$$\begin{pmatrix} \left(\sqrt{\frac{1}{2}}[\overline{K}K]_S^{I=0} + \frac{1}{2}[\overline{K}K]_S^{I=1}\right) \pi\, L & 0, & -\sqrt{\frac{2}{3}}[\pi\overline{K}]_S^{I=1/2}\, K\, L \end{pmatrix} \leftarrow (\pi^-\overline{K}^0K^0)$$

$$\begin{pmatrix} \sqrt{\frac{1}{3}}[\pi K]_S^{I=1/2}\overline{K}\, L & \sqrt{\frac{1}{2}}[K\overline{K}]_S^{I=1}\, \pi\, L & -\sqrt{\frac{1}{3}}[\overline{K}\pi]_S^{I=1/2}\, K\, L \end{pmatrix} \leftarrow (K^-\pi^0K^0)$$

Each row corresponds to[24] the vector ${}^{(s)}\vec{F}_{L,S}(\vec{\sigma})$ for the corresponding final-state system (s), which means that each column will be evaluated on σ_1, σ_2 or σ_3, respectively. Note that we omitted π^-K^0 and π^-K^- combinations as well as isospins $I = \frac{3}{2}$ since they would manifestly involve four-quark states. Additionally, the order inside the square brackets is as presented to make an identification of particles and the determination of the corresponding Clebsch-Gordan coefficients easier. Since the correct isobar couplings are already incorporated into equation (3.87), it will not matter for the line-shape parametrization. This means for example, we will use the same one for $[\pi\overline{K}]_\mathrm{S}$ and $[\overline{K}\pi]_\mathrm{S}$, only adjusting the masses of the involved particles accordingly depending on their charge.

We do not[25] expect isobars for $[\pi\pi]_\mathrm{S}^{I=1}$, $[\pi\pi]_\mathrm{P}^{I=0}$, $[K\overline{K}]_\mathrm{S}^{I=1}$ and $[K\overline{K}]_\mathrm{P}^{I=0}$. This makes the isospin index unambiguous ($I = S$), so we omit it. In addition the first kinematically allowed isobar in $[K\overline{K}]_\mathrm{P}$ would be $\rho(1450)$ which is heavier than the considered mass range and will be neglected. This

[24] modulo the m_X-dependent three-body-resonance amplitude contribution $R_\nu(m_X)$ as it is factored out and appears later in equation (3.90)

[25] The G-parity of the listed isobars has to be positive, since the resonance as well as the bachelor pion both have negative G-parity. This means the isobars have to fulfill the condition $C = (-1)^I$. For $[\pi\pi]_\mathrm{S}^{I=1}$, we need $C = -$ which is already violated for a $(\pi^0\pi^0)$-pair. For a $(\pi^+\pi^-)$-pair, the C-parity is equal to the involved orbital angular momentum. So also here with $L = 0$, we have a contradiction. For $[\pi\pi]_\mathrm{P}^{I=0}$, we need $C = +$ which is contradicted for a $(\pi^+\pi^-)$-pair since they would have $C = -$ for $L = 1$. It would work for a $(\pi^0\pi^0)$-pair, however here, Bose symmetrization makes odd isobar spins impossible, compare with section 5.1.3.

simplifies the matrix $\mathbf{F}_{L,S}$ for specific values of S:

$$\mathbf{F}_{1,0} = \begin{array}{c} \begin{matrix} (23) & (31) & (12) \\ \downarrow & \downarrow & \downarrow \end{matrix} \\ \begin{pmatrix} \sqrt{\frac{1}{3}}[\pi\pi]_{\mathrm{S}}\,\pi\,\mathrm{P} & 0 & \sqrt{\frac{1}{3}}[\pi\pi]_{\mathrm{S}}\,\pi\,\mathrm{P} \\ -\sqrt{\frac{1}{3}}[\pi\pi]_{\mathrm{S}}\,\pi\,\mathrm{P} & 0 & 0 \\ \sqrt{\frac{1}{2}}[K\overline{K}]_{\mathrm{S}}\,\pi\,\mathrm{P} & 0 & -\sqrt{\frac{2}{3}}[\pi K]_{\mathrm{S}}\overline{K}\,\mathrm{P} \\ \sqrt{\frac{1}{2}}[\overline{K}K]_{\mathrm{S}}\,\pi\,\mathrm{P} & 0 & -\sqrt{\frac{2}{3}}[\pi\overline{K}]_{\mathrm{S}}\,K\,\mathrm{P} \\ \sqrt{\frac{1}{3}}[\pi K]_{\mathrm{S}}\overline{K}\,\mathrm{P} & 0 & -\sqrt{\frac{1}{3}}[\overline{K}\pi]_{\mathrm{S}}\,K\,\mathrm{P} \end{pmatrix} \end{array} \begin{array}{l} \leftarrow \\ \leftarrow \\ \leftarrow \\ \leftarrow \\ \leftarrow \end{array} \begin{array}{l} (\pi^-\pi^+\pi^-) \\ (\pi^-\pi^0\pi^0) \\ (\pi^-K^+K^-) \\ (\pi^-\overline{K}^0K^0) \\ (K^-\pi^0K^0) \end{array} \tag{3.88}$$

$$\mathbf{F}_{0,1} = \begin{array}{c} \begin{matrix} (23) & (31) & (12) \\ \downarrow & \downarrow & \downarrow \end{matrix} \\ \begin{pmatrix} -\frac{1}{2}[\pi\pi]_{\mathrm{P}}\,\pi\,\mathrm{S} & 0 & \frac{1}{2}[\pi\pi]_{\mathrm{P}}\,\pi\,\mathrm{S} \\ 0 & \frac{1}{2}[\pi\pi]_{\mathrm{P}}\,\pi\,\mathrm{S} & -\frac{1}{2}[\pi\pi]_{\mathrm{P}}\,\pi\,\mathrm{S} \\ 0 & 0 & -\sqrt{\frac{2}{3}}[\pi K]_{\mathrm{P}}\overline{K}\,\mathrm{S} \\ 0 & 0 & -\sqrt{\frac{2}{3}}[\pi\overline{K}]_{\mathrm{P}}\,K\,\mathrm{S} \\ \sqrt{\frac{1}{3}}[\pi K]_{\mathrm{P}}\overline{K}\,\mathrm{S} & 0 & -\sqrt{\frac{1}{3}}[\overline{K}\pi]_{\mathrm{P}}\,K\,\mathrm{S} \end{pmatrix} \end{array} \begin{array}{l} \leftarrow \\ \leftarrow \\ \leftarrow \\ \leftarrow \\ \leftarrow \end{array} \begin{array}{l} (\pi^-\pi^+\pi^-) \\ (\pi^-\pi^0\pi^0) \\ (\pi^-K^+K^-) \\ (\pi^-\overline{K}^0K^0) \\ (K^-\pi^0K^0) \end{array} \tag{3.89}$$

Inserting these matrix expressions for $\mathbf{F}_{L,S}$ into equation (3.86), we see that we can simply perform a matrix multiplication and directly obtain $\mathrm{d}\boldsymbol{\sigma} = \{\mathrm{d}^{(s)}\sigma\}_{(s)}$ for all final-state systems at once. However, we have to define a component-wise absolute value $|\vec{x}|_\odot = \{|x_i|\}_i$:

$$\frac{\mathrm{d}\boldsymbol{\sigma}^{J=1,M=0}}{\mathrm{d}m_X\,\mathrm{d}\sigma_1\,\mathrm{d}\sigma_3} = \sum_\nu \left|R_\nu(m_X)\right|^2 \left|\mathbf{F}_{1,0}(\vec{\sigma})\cdot\vec{\Omega}^0_{\nu 0}(\vec{\theta}^*,\vec{\theta}) + \sum_\lambda \mathbf{F}_{0,1}(\vec{\sigma})\cdot\vec{\Omega}^1_{\nu\lambda}(\vec{\theta}^*,\vec{\theta})\right|^2_\odot , \tag{3.90}$$

where we include the three-body-resonance amplitude $R_\nu(m_X)$ that can be pulled out of the squared magnitude since it is independent of $\vec{\sigma}$ (cf. footnote 24).

As a next step, we have to express the angles $\vec{\theta}^*$ and $\vec{\theta}$ through the kinematic invariants σ_1, σ_3 and s (see appendix A.4) which requires us to expand $\vec{\Omega}^S_{\nu\lambda}$ to a matrix $\boldsymbol{\Omega}^S_{\nu\lambda} = \{({}^{(s)}\vec{\Omega}^S_{\nu\lambda})^{\mathrm{T}}\}_{(s)}$ as well where we have the vector for each system in the corresponding row. The reason is that the expressions for the angles contain the final-state-particle masses and, therefore, are different for the individual systems. This brings us to the final result:

$$\frac{\mathrm{d}\boldsymbol{\sigma}^{J=1,M=0}}{\mathrm{d}m_X\,\mathrm{d}\sigma_1\,\mathrm{d}\sigma_3} = \left|R_\nu(m_X)\right|^2 \sum_\nu \left|\mathbf{F}_{1,0}(\vec{\sigma})\odot\boldsymbol{\Omega}^0_{\nu 0}(\vec{\sigma}) + \sum_\lambda \mathbf{F}_{0,1}(\vec{\sigma})\odot\boldsymbol{\Omega}^1_{\nu\lambda}(\vec{\sigma})\right|^2_\odot . \tag{3.91}$$

where we define a row-wise scalar product for two matrices $A\odot B = \{\sum_j A_{ij}B_{ij}\}_i$ resulting in a vector.

3.5.3 Production of Dalitz Plots

We can use equation (3.91) to calculate Dalitz plots. For this, we choose a fixed value for m_X and pick two of the three two-body invariant masses, e.g. σ_1 and σ_3, on a grid. The remaining two-body invariant mass can be calculated using relation (A.36). To obtain the correct border of the Dalitz plot, we can use the Kibble function in equation (A.35), since it is zero on the border and positive inside of the physical decay region.

We limited ourselves to $J^{PC} = 1^{++}$ and $S \in \{0, 1\}$, therefore, the accessible isobars are limited as well. Using the notation from equations (3.88) and (3.89), we constrain ourselves to a broad $(\pi\pi)_S$ (also known as σ or $f_0(500)$) and $f_0(980)$ for the $[\pi\pi]_S$ component and the $\rho(770)$ for the $[\pi\pi]_P$, while due to the higher mass threshold only the $f_0(980)$ will be used for the $[K\overline{K}]_S$. The $[\overline{K}\pi]_S$ will be the $(K\pi)_S$ component (also known as κ or $K_0^*(700)$) and the $[\overline{K}\pi]_P$ will be modeled using the $K^*(892)$. Their line shapes are presented in section 6.2.1 and normalized such that the maximum lies at 1.

We have two experimental $\pi^-\pi^+\pi^-$ Dalitz plots ([31], FIG. 6) that we can compare the predictions with in order to validate the algorithm, one at $m_X = 1.318\,\text{GeV}$ (Figure 3.12(b)) and one at $m_X = 1.672\,\text{GeV}$ (Figure 3.13(b)), each with a mass window of $\pm 100\,\text{MeV}$. The strength for each $(\pi\pi)$-isobar can be estimated by looking at the intensities of the respective partial waves at the given resonance mass. For the Dalitz plots at $m_X = 1.318\,\text{GeV}$ we use the values $\left|A_{(\pi\pi)_S}\right|^2 = 0.16 \times 10^6$ (FIG 25(f) of [31]), $\left|A_{f_0(980)}\right|^2 = 1 \times 10^3$ (FIG 25(e) of [31]), $\left|A_\rho\right|^2 = 1.2 \times 10^6$ (FIG 14(a) of [31]). The phase of the ρ is fixed to $\phi_\rho = 0$, while the phases of the other two isobars can be taken from the relative phases extracted by the PWD, namely $\phi_{(\pi\pi)_S} = -420°$ and $\phi_{f_0(980)} = 270°$ ([31]).

In order to take the m_X window into account that was used for the COMPASS data, one has to integrate the prediction over all included values. Otherwise the top-right border of the Dalitz plot will be wrong, since its position – and with this also the size of the physically accessible area – depend on m_X, see equation (A.36). We perform this integration numerically by calculating the Dalitz plots in steps of 1 MeV for $m_X \in [1.218\,\text{GeV}, 1.418\,\text{GeV}]$ and adding them all up. Finally, we normalize this integrated prediction to its maximum. The result can be found in Figure 3.12(a). Here, we made the assumption of a mass-independent production amplitude $\mathcal{P}(t', m_X) \equiv \mathcal{P}(t')$ that we mentioned already at the beginning, since otherwise the normalization between different m_X values is not correct. A bigger problem is that we neglect an m_X dependence of $\mathcal{M}$ due to the line shape of the three-body resonance within the integrated resonance mass window of the Dalitz plot, i.e. we set $R_\nu(m_X) = \text{const}$ in equation (3.91). This latter assumption is the weakest link in the prediction, since for a simple BWM with constant width (cf. equation (3.27)) of an $a_1(1260)$ resonance[26] one can expect a drop of 15 % in intensity towards the left border of the interval and almost 30 % towards the right border. Luckily, this can be incorporated easily into the model during the integration by weighting the Dalitz plots with the intensity of the corresponding resonance model, but for a first proof-of-principle this is not necessary.

Figure 3.12 shows a very good agreement between the model calculation and the experimental data despite its simplifications. In both cases, we see a very strong $\rho(770)$ band and even the enhancement towards the top-right of the central maximum is reproduced. Due to the performed integration of the mass window, also the borders of the Dalitz plot match. This integration also explains the diagonal band that mimics an isobar in the forbidden $(\pi^-\pi^-)$-system. The line appears where the Dalitz plot for

[26] Using $m_{a_1(1260)} = 1.299\,\text{GeV}$ and $\Gamma_{a_1(1260)} = 280\,\text{MeV}$ as determined by COMPASS in [37].

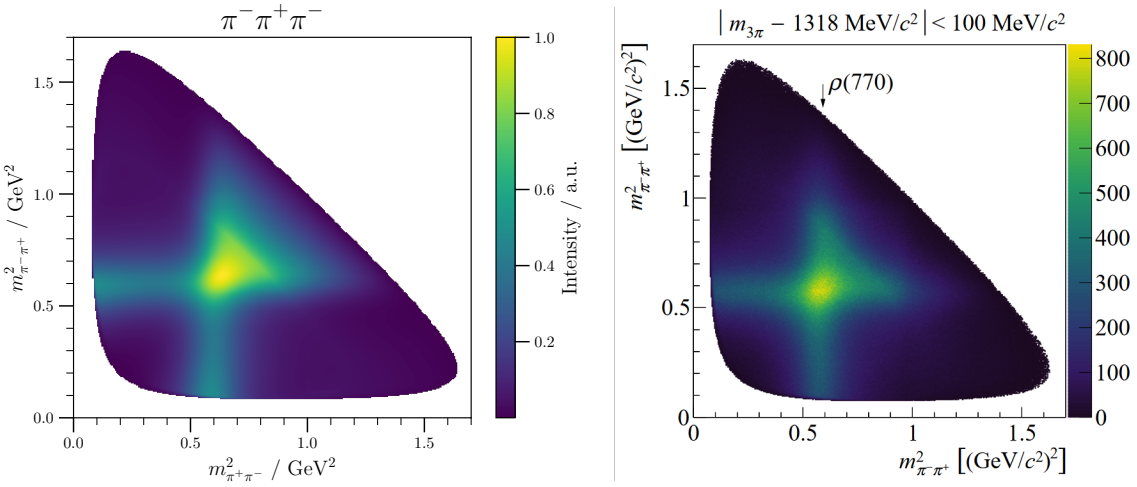

(a) Prediction

(b) COMPASS data, FIG. 6(a) of [31]

Figure 3.12: Comparison between the Dalitz-plot prediction for $\pi^-\pi^+\pi^-$ (left) integrated over the mass range as indicated in the plot of the COMPASS data (right) for a resonance mass of $m_X = 1.318\,\text{GeV}$.

the smallest included $m_X = 1.218\,\text{GeV}$ would end. From this point on, only higher mass bins can contribute, which creates a continuous drop in intensity towards the top-right resulting in this diagonal edge.

To summarize, the proof-of-principle was very successful, especially since the model only considers resonance QNs $J^{PC}M^{\epsilon} = 1^{++}0^+$. There might also be contributions from higher M, although this is less likely due to their reduction in production strength. This might also be the reason why the $a_2(1320)$ resonance, which also lies in this window, does not create too much disturbance, since it can only be produced in an $M \geq 1$ wave for positive reflectivity as discussed at the beginning of this section 3.5.

In order to test the limits of this model, we do the same for the Dalitz plots at $m_X = 1.672\,\text{GeV}$ using the values $\left|A_{(\pi\pi)_S}\right|^2 = 0.03 \times 10^6$, $\left|A_{f_0(980)}\right|^2 = 4.0 \times 10^3$, $\left|A_\rho\right|^2 = 0.1 \times 10^6$, and phases $\phi_{(\pi\pi)_S} = -400°$ and $\phi_{f_0(980)} = 500°$, again extracted from the COMPASS PWD in [31]. Similarly, we sum the calculated Dalitz plots for $m_X \in [1.572\,\text{GeV}, 1.772\,\text{GeV}]$ in steps of 1 MeV. We obtain Figure 3.13, where we seem to overestimate the contribution from the $(\pi\pi)_S$ isobar indicated by the local maxima at low $m^2_{\pi^+\pi^-}$ of the ρ-bands. On the other hand, we see a small effect of the $f_0(980)$ at roughly $m^2_{\pi^+\pi^-} = 1\,\text{GeV}$, which is a bit more enhanced in the COMPASS data. Since we constrain the model to isobar spins of $S < 2$, we do not see the contributions from the $f_2(1270)$ which makes the shortcomings of this simplified model and its restrictions to low resonance masses very obvious. Especially here, other J^{PC} than the considered 1^{++} will contribute, since we are sitting at the mass of the $\pi_2(1670)$ with QNs $J^{PC} = 2^{-+}$ (producible in an $M = 0$ wave). This can and will lead to different isobar fractions and different relative phases and, now, it will be especially important to incorporate a proper description of the three-body-resonance line shape. One interesting feature that could be reproduced, is the diagonal line which connects the two maxima created by the $f_2(1270)$ in the COMPASS data. As before, such a line would hint to an isobar in the $(\pi^-\pi^-)$ subsystem, impossible

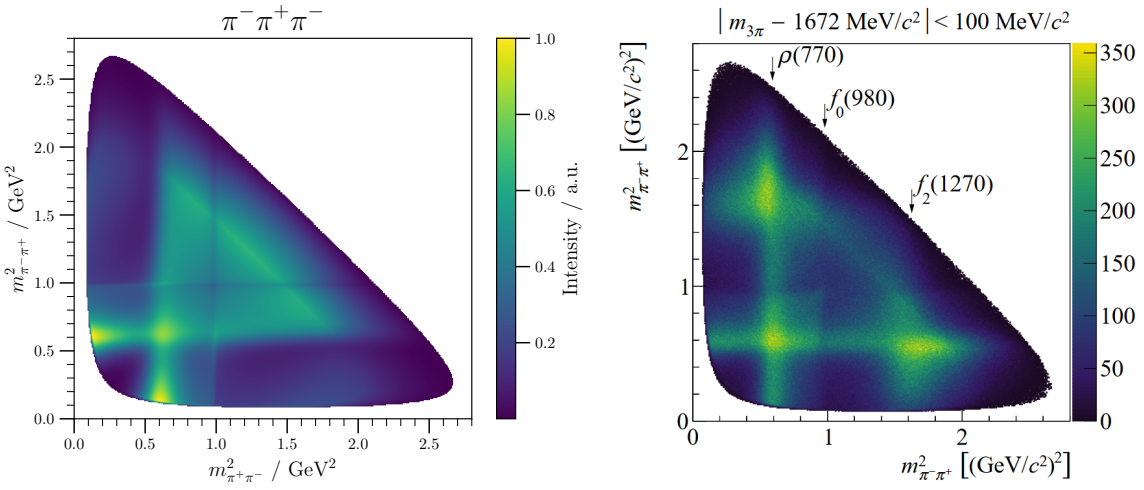

(a) Prediction

(b) COMPASS data, FIG. 6(b) of [31]

Figure 3.13: Comparison between the Dalitz-plot prediction for $\pi^-\pi^+\pi^-$ (left) integrated over the mass range as indicated in the plot of the COMPASS data (right) for a resonance mass of $m_X = 1.672\,\text{GeV}$.

for a simple $q\bar{q}$ state. And again, the reason for this line is the intensity drop at the top-right border due to the integration over the experimental three-body mass window. Due to its clear spatial separation from the existing isobar lines, it is better visible than it was in Figure 3.12.

As part of the analysis[27] of [39], a Dalitz plot for $\pi^-\pi^0\pi^0$ at $m_X = 1.318\,\text{GeV}$ was produced. Using the same values for the relative strengths and phases as for the low-mass $\pi^-\pi^+\pi^-$ Dalitz plot, we obtain Figure 3.14, where we adjust the color scale to be equal to the one of [39] for easier comparison. Once more, the calculated Dalitz plots are added for $m_X \in [1.211\,\text{GeV}, 1.425\,\text{GeV}]$ in steps of 1 MeV. One slight difference compared to the final state with three charged pions in Figure 3.12(b) is the tilt in the ρ band at the lower and the left border of the Dalitz plot towards higher squared masses. The Dalitz-plot calculation also exhibits this feature showing fair agreement in general. However, looking a bit more closely, we see that the ρ bands appear at slightly higher squared invariant masses and are a bit less pronounced, which could hint to a difference in the relative phase between interfering ρ and $(\pi\pi)_S$ waves. Some difference might also come from the fact that the COMPASS data plot on the right is not acceptance-corrected, meaning that some regions might be underpopulated due to having a smaller probability of being detected in the first place. For such a final state with neutral particles, the acceptance is usually also a lot worse than for a case with only charged particles like the $\pi^-\pi^+\pi^-$ final state. The main reason is that the photons from the π^0-decay can be directly detected only in one detector, the `ECAL`, while the track of the charged particles is obtained from many small and also more precise measurements from a whole array of tracking detectors. Additionally, if a photon at these energies ($\sim$ GeV) interacts with matter, it produces an e^+e^--pair, i.e. it is "gone". On the other hand, a charged particle will most likely only perform multiple scattering just leading to a slightly larger uncertainty on its track definition.

Having seen the power, but also the restrictions that this model brings, we can still use it to plot

[27] It is also presented in Figure 5.2 of [38].

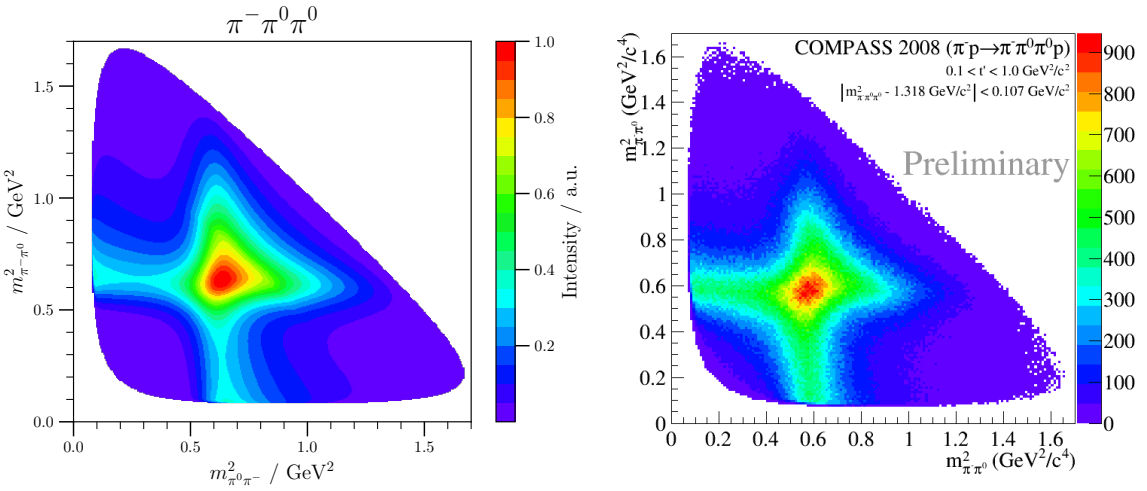

(a) Prediction

(b) COMPASS data, [39]

Figure 3.14: Comparison between the Dalitz-plot prediction for $\pi^-\pi^0\pi^0$ (left) integrated over the mass range as indicated in the plot of the COMPASS data (right) for a resonance mass of $m_X = 1.318\,\text{GeV}$.

the other three final states. However, since they are involving kaons, we will slightly increase the three-body invariant mass to $m_X = 1.41\,\text{GeV}$ in order to still have a sufficiently large Dalitz plot. Regarding the relative strengths, we make the assumption that the ratio between $(\pi\pi)_S$ and $\rho(770)$ is the same as between $(K\pi)_S$ and $K^*(892)$ (we use the same for both charge configurations K^{*0} and K^{*-} despite the slightly different mass), since in both cases we are dealing with a pseudoscalar meson and the corresponding vector meson in the meson octets, additionally exhibiting a similar mass difference of roughly $\sim 200\,\text{MeV}$. But for the $f_0(980)$ production, we cannot simply use the same relative strength, since it is known that the $f_0(980)$ couples stronger to $K\overline{K}$ than to $\pi\pi$. Here, we simply set it to equal strength as the $K^*(892)$ for a very first look, also setting all relative phases to zero. In the end all these values are free parameters of the model that have to be determined by experiments.

The resulting distribution can be found in Figure 3.15. As expected, we see a clear $K^*(892)$ band in the π^-K^+ (top left), $\pi^-\overline{K}^0$ (top right), $K^-\pi^0$ and π^0K^0 (bottom left) squared invariant masses. By construction it is absent in the π^-K^- and π^-K^0 systems (no diagonal bands in the top row plots). In Figure 3.15(a) we can barely see the $f_0(980)$ as a horizontal band right at threshold. In Figure 3.15(b) this is even harder due to the very slightly higher mass of the neutral kaons and, thus, a slightly higher threshold for the Dalitz plot.

Since the $\pi^-\overline{K}^0K^0$ final state is experimentally not observable, we have to somehow change it to the physical $\pi^-K_S^0K_S^0$ final state (or one involving K_L^0). If we also allow the third two-body configuration π^-K^0 to form isobars by effectively replacing the K^0 by a $\overline{K}^0$ where it is needed[28], we can mimic $\pi^-K_S^0K_S^0$ without changing the discussed model too drastically. The only adjustments are in the fourth row and second column of the matrices in equations (3.88) and (3.89), entry $\left(\mathbf{F}_{L,S}\right)_{4,2}$. We simply

[28] Both K_S^0 and K_L^0 consist to 50 % of K^0 and $\overline{K}^0$, therefore, such a replacement makes sense. One should consider this percentage as well in the overall strength of the final state, but since we normalize the Dalitz plots to their maximum here, anyways, this is not needed. Also in a $K_S^0K_S^0$ or $K_L^0K_L^0$ system, no isobars with odd spin are allowed due to Bose symmetrization, see section 5.1.3. Fortunately, we did not include an isobar for $[K^0\overline{K}^0]_P$.

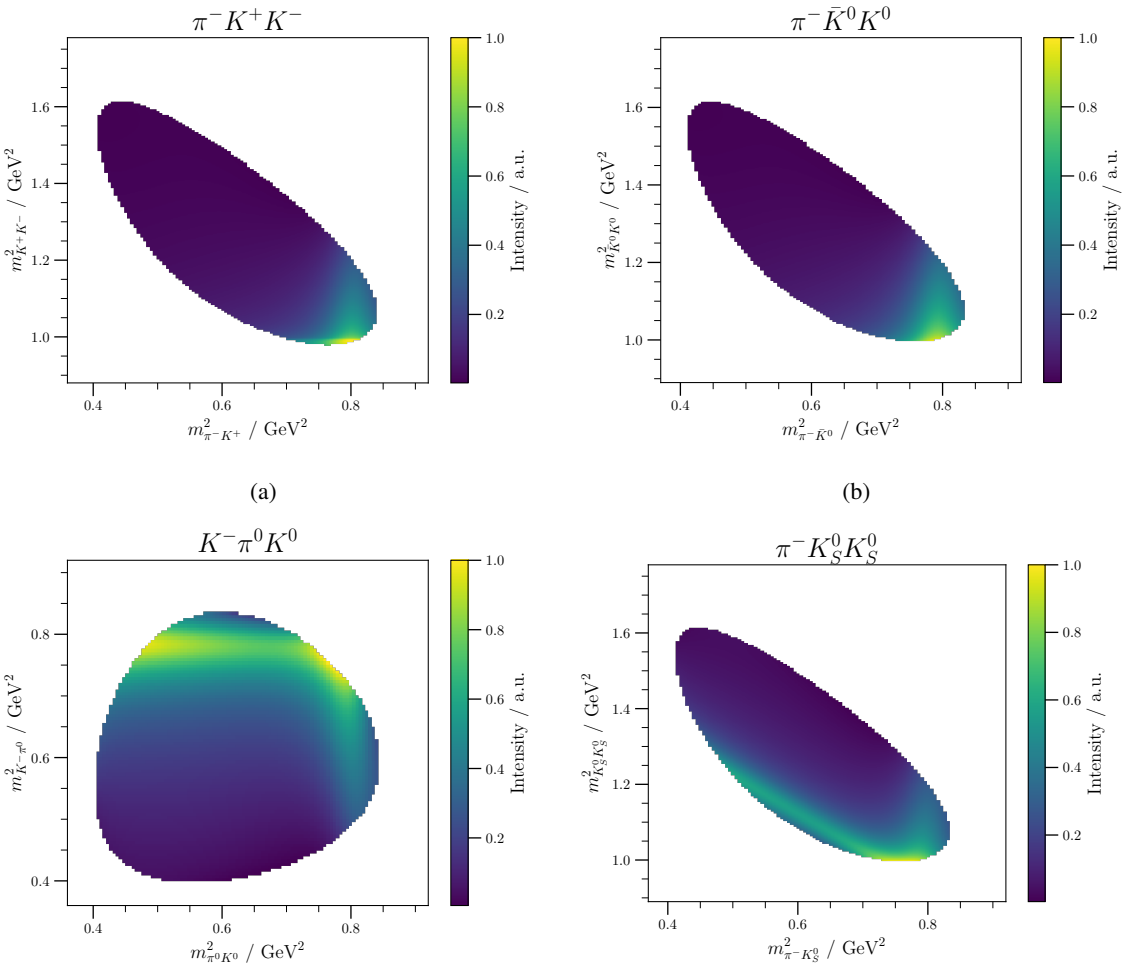

(a) (b)

(c) (d)

Figure 3.15: Predictions for the final states $\pi^- \overline{K}^0 K^0$ (top left), $\pi^- \overline{K}^0 K^0$ (top right) and $K^- \pi^0 K^0$ (bottom left) at a fixed resonance mass of $m_X = 1.41$ GeV. The plot on the bottom right is an approximation to the $\pi^- K_S^0 K_S^0$ final state as discussed in the main text.

replace the 0 by the entry on the right, $\left(\mathbf{F}_{L,S}\right)_{4,3}$, with flipped sign due to the change from $\pi^-\overline{K}^0$ to $\overline{K}^0\pi^-$ in the Clebsch-Gordan coefficients for the isospin coupling[29] from channel (12) (third column) to channel (31) (second column). The result can be found in Figure 3.15(d). Both $K^*(892)$ bands are overlapping exactly where the $f_0(980)$ band will be, making a PWD inevitable to disentangle these contributions in an experiment. We will compare this model calculation with COMPASS data for the $\pi^- K_S^0 K_S^0$ final state (Figure 5.36) later in section 5.4.

Keep in mind that, especially in the last case involving kaons, a lot of not fully justified simplifications entered. This should merely yield as a first look and demonstrate that the model can calculate these Dalitz plots. If an actual comparison to real data is the goal, one has to estimate or determine the free model parameters in a more sophisticated manner.

3.6 Partial-Wave Projection

So far we only considered independent final-state systems. The method of partial-wave projections as introduced in [33] allows us not only to include rescattering within a final-state system (s), but also from one final-state system to another. In the course of the here presented studies, the derivations of [33] were generalized from the there mainly discussed 3π final-state system with equal final-state-particle masses to a final-state system where all particles might have different masses. For this, we start once more from equation (3.76). And since we will also mainly focus on $J^{PC}M^{\epsilon} = 1^{++}0^+$ QNs later, the ϵ index is omitted. The only used feature of the angular functions is their orthogonality, and since this relation also holds for Z_w^{ϵ} (see section A.3.3), the following is also true when using the reflectivity basis. But one should not sum over ϵ, since this sum has to be performed incoherently. The Partial-wave-projection method in this form only applies for projection to waves with equal reflectivity. Now, projecting the full amplitude $A(s,\tau)$ from equation (3.76) onto a single partial wave with QNs $w = (J, M, L, S)$ in the (i) isobar channel with cyclic indices via the integral

$$\mathrm{d}Z_w^{(i)} := \frac{\mathrm{d}\Omega_i}{4\pi}\frac{\mathrm{d}\Omega_{jk}}{4\pi}Z_w^{(i)*}, \quad \text{with } Z_w^{(i)} := Z_w(\Omega_i, \Omega_{jk}) \tag{3.93}$$

we obtain a single partial-wave amplitude

$$A_w(s,\sigma_i) \;=\; \int \mathrm{d}Z_w^{(i)} A(s,\tau) \;=\; F_w(s,\sigma_i) + \hat{F}_w(s,\sigma_i), \quad \text{with} \tag{3.94}$$

$$\hat{F}_w(s,\sigma_i) \;:=\; \int \mathrm{d}Z_w^{(i)} \sum_{w'} \Big(F_{w'}(s,\sigma_j) Z_{w'}^{(j)} + F_{w'}(s,\sigma_k) Z_{w'}^{(k)} \Big). \tag{3.95}$$

Due to orthogonality $\int \mathrm{d}Z_w^{(i)} Z_{w'}^{(i)} = \delta_{ww'}$ for different QNs w and w' as given in equation (A.24), of isobar channel (i) in equation (3.94) only the $F_w(s,\sigma_i)$ with the projected QNs w remains of the (in principle infinite) sum of partial waves in equation (3.76). For the angular functions of the other two isobar channels (j) and (k) this orthogonality is not given since the integration happens via different

[29] According to the PDG, the formula for an exchange of the involved particles inside a Clebsch-Gordan coefficient is

$$\langle j_1 m_1, j_2 m_2 | JM \rangle = (-1)^{J - j_1 - j_2} \langle j_2 m_2, j_1 m_1 | JM \rangle, \tag{3.92}$$

which gives an extra -1 factor when applied to the here discussed combination of isospins $I = \frac{1}{2}$, $I_1 = 1$ and $I_2 = \frac{1}{2}$.

angles than the relevant ones for the specific isobar channel. Therefore, we still have the full sum over all w' and we simply summarize the terms from the isobar cross channels into $\hat{F}_w$ in equation (3.95). It will still be a function of σ_i though, since the angular integral over $\mathrm{d}Z_w^{(i)}$ will integrate out all σ_j and σ_k dependence of $Z_{w'}^{(j)}$ and $Z_{w'}^{(k)}$, respectively.

Note that we can also introduce contributions from other final-state systems through $\hat{F}$ by effectively performing the projection on the partial-wave sum of the other system. This will become more clear once we actually calculate the projection integral (cf. equation (A.26)) and apply it to the physics case of interest in section 4.3.4.

By employing unitarity, [33] derived in equation (4.25) that the discontinuity of the partial-wave amplitude with respect to σ_i, denoted by $\mathrm{Disc}_{\sigma_i}[A_w](s,\sigma_i)$, is dependent on the amplitude itself in the following way

$$\mathrm{Disc}_{\sigma_i}[A_w](s,\sigma_i) = \mathrm{i}\, f_S^\dagger(\sigma_i)\rho(\sigma_i)A_w(s,\sigma_i),$$

where f_S is again the two-body scattering amplitude of the corresponding isobar channel (i) and $\rho = \frac{1}{2}\Phi_2$ is half of the respective two-body phase space, cf. equation (A.8). Inserting equation (3.94) into this and making the assumption that $\hat{F}_w(s,\sigma_i)$ does not have a discontinuity in σ_i, we obtain

$$\mathrm{Disc}_{\sigma_i} F_w(s,\sigma_i) = \mathrm{i}\, f_S^\dagger(\sigma_i)\rho(\sigma_i)\Big(F_w(s,\sigma_i) + \hat{F}_w(s,\sigma_i)\Big), \tag{3.96}$$

which is known as the inhomogeneous Omnès problem [40] and it has the following formal solution (equation (4.26) of [33])

$$F_w(s,\sigma_i) = f_S(\sigma_i)\left(C_w(s,\sigma_i) + \frac{1}{2\pi}\int_{(m_j+m_k)^2}^{\infty}\frac{\rho(\sigma)\hat{F}_w(\sigma)}{\sigma-\sigma_i}\mathrm{d}\sigma\right), \tag{3.97}$$

where $C_w(s,\sigma_i)$ is an entire function in σ_i, meaning a function that is holomorphic for all possible complex values σ_i. Additional assumptions needed for this result are according to [33]

1. $f_S(\sigma_i)$ cannot have a left-hand cut
   $\rightsquigarrow$ use Chew-Mandelstam BW as detailed in section 3.3.3,
2. $\hat{F}_w(s,\sigma_i)\cdot\sigma_i \overset{\sigma_i\to\infty}{\longrightarrow} 0$
   $\rightsquigarrow$ one can perform so-called subtractions (cf. equation (3.22)) if needed,
3. $F_w(s,\sigma_i)$ as well as $f_S(\sigma_i)$ do not have kinematic singularities
   $\rightsquigarrow$ see equation (3.99) in the next section 3.6.1 for a method to deal with them.

3.6.1 Dealing with Kinematic Singularities

Previously we mentioned that F_w can have kinematic singularities, but this would be a problem for the derivation of equation (3.97). Let us assume that the angular functions $Z_w^{(i)}$ have kinematic singularities in the form of $1/K(s,\sigma_i)$ with the additional condition that $K^2(s,\sigma_i)$ does not have a discontinuity in σ_i.

Looking back at the very beginning, equation (3.76), we have $A(s,\tau) \sim F_w(s,\sigma_i)Z_w^{(i)}$. But the full amplitude A cannot have kinematic singularities, therefore, F_w has to cancel the ones of $Z_w^{(i)}$,

meaning $F_w(s,\sigma_i) \sim K(s,\sigma_i)$. This cancellation of singularities will always happen when they appear together, e.g. for the cross-channel contributions inside of $\hat{F}_w$, but this imposes a problem once we try to separate F_w and $Z_w^{(i)}$ from each other as it happens during the definition of the partial-wave projected amplitude $A_w(s,\sigma_i)$ in equation (3.94), where we see that also A_w inherits these kinematic singularities from F_w. But luckily this can be solved quite easily by simply defining $G_w(s,\sigma_i) = F_w(s,\sigma_i)/K(s,\sigma_i)$ and accordingly $\hat{G}_w(s,\sigma_i) = \hat{F}_w(s,\sigma_i)/K(s,\sigma_i)$, and using them instead of the F_w and $\hat{F}_w$ in equation (3.94):

$$\tilde{A}_w(s,\sigma_i) := \frac{A_w(s,\sigma_i)}{K(s,\sigma_i)} = G_w(s,\sigma_i) + \hat{G}_w(s,\sigma_i).$$

Like this, $\tilde{A}_w$ and G_w are kinematic-singularity-free in σ_i. However, $\hat{G}_w$ will have a K^{-2} dependence, one coming from this substitution and the other one from the $Z_w^{(i)*}$ of the projection integral $\mathrm{d}Z_w^{(i)}$ in the definition[30] of $\hat{F}_w$, equation (3.95). Here, the additional condition enters that K^2 does not have a discontinuity and, thus, $\hat{G}_w$ will not have one as well, allowing us to reach the corresponding version of equation (3.96). Solving this equation will result in

$$G_w(s,\sigma_i) = f_S(\sigma_i)\left(C_w(s,\sigma_i) + \frac{1}{2\pi}\int_{(m_j+m_k)^2}^{\infty} \frac{\rho(\sigma_i')\hat{G}_w(\sigma_i')}{\sigma_i' - \sigma_i}\mathrm{d}\sigma_i'\right). \tag{3.98}$$

Now, we only have to replace G_w and $\hat{G}_w$ back to F_w and $\hat{F}_w$, respectively, resulting in a corrected formula

$$F_w(s,\sigma_i) = K(s,\sigma_i) f_S(\sigma_i)\left(C_w(s,\sigma_i) + \frac{1}{2\pi}\int_{(m_j+m_k)^2}^{\infty} \frac{\rho(\sigma_i')\hat{F}_w(\sigma_i')/K(\sigma_i')}{\sigma_i' - \sigma_i}\mathrm{d}\sigma_i'\right). \tag{3.99}$$

This formula can also be used if no kinematic singularities would be present, since one can simply set $K(s,\sigma_i) \equiv 1$ which brings us back to equation (3.97). An example for a determination of this kinematic factor K will be discussed in section 4.3.4.

3.6.2 Iteration Procedure

Inspecting equation (3.99), we see that F_w depends on $\hat{F}_w$ and while looking at the definition of $\hat{F}_w$ in equation (3.95), we observe that, in return, it depends on F_w (of the isobar cross channels). This means that we have to solve an integral equation in order to actually calculate F_w.

The zeroth-order approximation is obtained by setting ${}^{(0)}\hat{F}_w \equiv 0$ and choosing $C_w(s,\sigma_i) \equiv C_w(s)$ constant in σ_i. This allows us to view ${}^{(0)}F_w = f_S(\sigma_i)C_w(s)$ as simply the product of the resonance propagator $C_w(s)$ multiplied by the isobar propagator $f_S(\sigma_i)$, the simplest model for a decay via the isobar model. Having the iteration start $n = 0$ fixed, we can write down the iteration steps $n \to n+1$

[30] As mentioned before, the kinematic singularities in the products of $F_w \cdot Z_w$ in the integrand cancel.

next:

$$
{}^{(n+1)}\hat{F}_w(s,\sigma_i) = \int \mathrm{d}Z_w^{(i)} \sum_{w'} \left({}^{(n)}F_{w'}(s,\sigma_j) Z_{w'}^{(j)} + {}^{(n)}F_{w'}(s,\sigma_k) Z_{w'}^{(k)} \right), \tag{3.100}
$$

$$
{}^{(n+1)}F_w(s,\sigma_i) = K(s,\sigma_i) f_S(\sigma_i) \left(C_w(s) + \frac{1}{2\pi} \int_{(m_j+m_k)^2}^{\infty} \frac{\rho(\sigma)\, {}^{(n+1)}\hat{F}_w(\sigma) \big/ K(s,\sigma)}{\sigma - \sigma_i - \mathrm{i}\,\varepsilon} \mathrm{d}\sigma \right) \tag{3.101}
$$

By introducing the $\mathrm{i}\,\varepsilon$ in the denominator of the integral, we ensure that we do not encounter a pole on the integration path. Its sign convention, i.e. $\sigma_i + \mathrm{i}\,\varepsilon$, ensures that we stay in the physical regime slightly above the real axis (also see [22] on additional reasons for the $+\mathrm{i}\,\varepsilon$ prescription than the more phenomenological one given here).

In principle, this iteration procedure allows for corrections of the simplest model up to arbitrary order from every final-state to the other as long as they share an isobar. Therefore, it can be applied on the Dalitz-plot prediction method from section 3.5.2 to incorporate rescattering and cross-channel effects. An explicit application of this partial-wave projection will be performed in section 4.3.3, however already after the first iteration, we stop after projecting the $\pi K \overline{K}$ final state onto the 3π channel. Higher orders would modify the K^* parametrization in the triangular loop, however, they are expected to be small.

CHAPTER 4

The Curious Case of the $a_1(1420)$

Already using only a simple Constituent-Quark Model (CQM) and looking at the excitation spectrum of a $q\bar{q}'$-pair[1] yields a huge amount of possible states. Many of these were already found and could be assigned to these CQM states. However, there are some states still experimentally missing in this simple picture and some supernumerous states were found, that do not match with the predictions. The latter might be a bit more interesting, because they directly point to the short-comings of this simple model.

There are different possibilities to extend this model which enables us to explain more particles, one of which is the introduction of more than $q\bar{q}$ within a Meson. If we allow for constituent gluons[2] ($q\bar{q}g$) the resulting particle would be called "hybrid" and if we allow for additional (anti)quarks we would classify them as tetraquarks ($qq\bar{q}\bar{q}$) or pentaquarks ($q\bar{q}qqq$) bound by color-force. The former would be expected to appear in meson spectroscopy due to its integer spin and baryon number $\mathcal{B} = 0$ and the latter in baryon spectroscopy with half-integer spin and baryon number $\mathcal{B} = 1$. Another option is a molecule built from two color-neutral mesons or baryons and bound by light-meson exchange, similar to the deuteron where the biggest contribution to its binding of the constituent proton and neutron originates from pion-exchange.

While molecules are more likely to appear in the heavy-quark sector due to the stronger binding potential, some of the light mesons are already discussed as tetraquarks. In addition to new particles there also exist some kinematic phenomena that can create resonance-like signals.

This chapter will focus on one of the resonance-like signals that does not fit the CQM, the $a_1(1420)$. Why this is the case will be discussed in the following sections.

4.1 The Signal in 3π at COMPASS

In 2015 the COMPASS experiment observed a narrow structure with QNs $I^G(J^{PC}) = 1^-(1^{++})$ in the decay to $f_0(980)\pi^-$ in a P-wave, [6]. Being found at a mass of roughly 1.42 GeV and due to its QNs it was assigned the name $a_1(1420)$. In Figure 4.1 on the left you can see a fit with a simple BWM to the intensity of this partial wave. Here, the blue line represents the signal contribution from a relativistic Breit-Wigner, the green line a phenomenological background model and the red line is the coherent

[1] For simplicity of the notation I leave away the $'$ from now on, but in principle all (anti)quarks could be of different flavor.

[2] Or one should rather say that one allows for excitations of the gluonic string that connects the two constituent quarks.

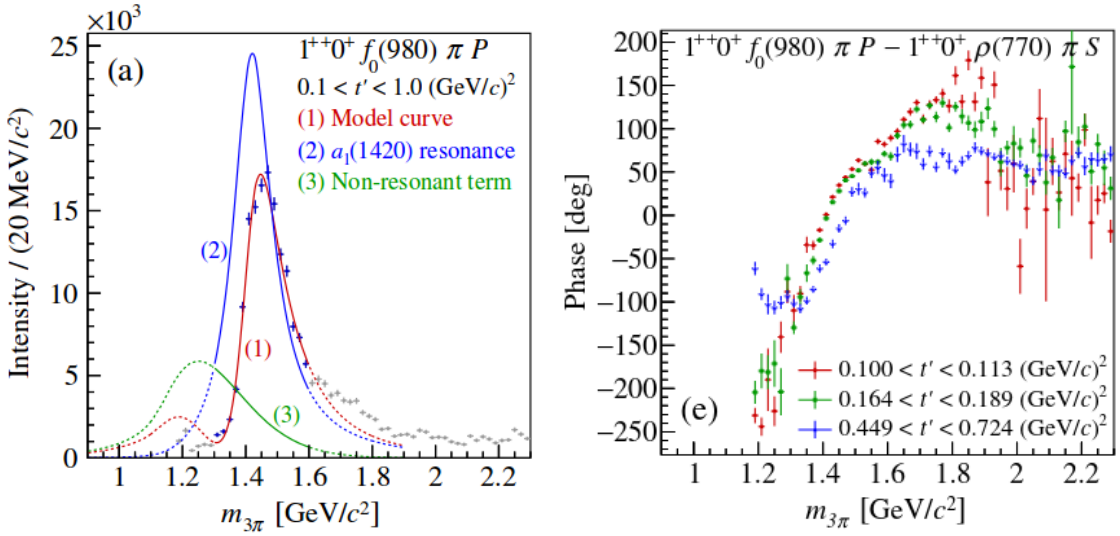

Figure 4.1: The left plot shows the intensity of the $1^{++}0^+$ $f_0(980)\pi$ P wave and on the right you see its interference with the $1^{++}0^+$ $\rho(770)\pi$ S wave published in [6]. The data points come from a PWD with 88 waves (statistic uncertainties only). On the left plot, the data of the full t' range of the analysis is combined, while the right plot shows three sub-ranges. On the left plot, the full model curve is displayed in red. It is constructed as the coherent sum of a BWM (blue) together with a non-resonant background (green). The data is grayed out and the fit lines are dotted outside of the fit region.

sum of both. As we see, we do not only have a signal in the intensity spectrum, but also a very sharp phase motion in the interference with the $I^G(J^{PC}) = 1^-(1^{++})$ $\rho(770)\pi$ S-wave on the right plot, both of which are usually a very good argument for a resonance. This strong phase motion is also visible throughout all slices in the t' range (of which three are displayed here) showing the robustness of the signal. The next section will deal with possible explanations for such kind of signal.

4.2 Possible Explanations

We need to find explanations for not only the peak in the intensity spectrum, but also for the rapid phase motion in the relative phase. In the following, several options will be discussed.

4.2.1 New Genuine Resonance

Let us start with the most straight forward one: a narrow intensity peak with rapid phase motion speaks for the interpretation as a resonance. The problem with this interpretation is that the CQM does not predict a state here. The ground state with $I^G(J^{PC}) = 1^-(1^{++})$ is the well-established $a_1(1260)$ with a width of roughly 300 MeV. This means that the $a_1(1420)$ still lies within one width of the ground state. In addition the width of the $a_1(1420)$ is actually only half as big with 150 MeV which would be very unusual for a radial excitation.

The next candidate for such a radial excitation of the $a_1(1260)$ is the $a_1(1640)$. Not only is the mass difference of $\sim$ 420 MeV closer to expectations from other resonances, e.g. in the $I^G(J^{PC}) = 1^-(2^{++})$

sector[3], but also their width is comparable, the heavier one being 250 MeV wide.

From theory it is expected that radial and orbital excitations lie on straight lines, so-called Regge trajectories, with either the intrinsic orbital-angular-momentum QN L or the radial-excitation QN n. A simple derivation of the first dependence $L \sim M^2$ can be found in appendix C.1.1. In [41], they derive the mentioned functional dependence as given in equation (C.3), which we can reformulate for the following as

$$n + L = \text{slope} \cdot M^2 - \frac{1}{2}. \tag{4.1}$$

Since we are interested in a_J resonances with QNs $J^{PC} = J^{++}$, we need odd orbital angular momentum due to $P = (-1)^{L+1} \stackrel{!}{=} +1$ for a $q\bar{q}$ pair and, therefore, also odd intrinsic spin as follows from $C = (-1)^{L+S} \stackrel{!}{=} +1$ with odd L, cf. Table 3.1. With two spin-$\frac{1}{2}$ particles, odd intrinsic spin means $S = 1$. With this, we can determine L of the a_J resonances. We obtain $L = 1$ for a_0, a_1 and a_2. The latter one could also be constructed with $L = 3$, however usually, higher orbital angular momenta have a reduced likelihood. A small admixture of an $L = 3$ component to the a_2 could actually be responsible for the slightly heavier mass than the a_1 ground state. The a_3 and a_4 involve $L = 3$, while we need at least $L = 5$ for the a_6.

If we plot the Regge trajectories, one for each total spin J, we expect to see the lines for the a_0, a_1 and a_2 to be closer together, since they should share a similar offset according to equation (4.1). Afterwards, we expect a gap before the lines of a_3 and a_4, and another one till the a_6.

All resonances are also listed in Table 4.1 with a proposed assignment for the radial-excitation QN n. The $a_1(1420)$ is the signal in question and only $n = 2$ makes sense here, since the ground state $a_1(1260)$ is very well established. For the heavier a_1 resonances we consider two assignments, one excluding the $a_1(1420)$ and continuing with $n = 2$ for the $a_1(1640)$ (Table 4.1 and light blue solid line in Figure 4.2), and one including the $a_1(1420)$ as $n = 2$ and continuing with $n = 3$ for the $a_1(1640)$ (red dotted line in Figure 4.2). Since the masses of the $a_2(1950)$, $a_2(1990)$ and $a_2(2030)$ all lie within 80 MeV – and they also have a similar decay width – they are grouped together to $n = 3$. Having experimental uncertainty of 20 to 70 MeV on their mass, makes using three separate states for this simplified picture unreasonable.

The lightest a_0 resonances are currently discussed as a candidates for tetraquarks [42] and, therefore, we do not include them in Figure 4.2.

Note that this assignment of the radial-excitation QNs is most likely wrong and by far not the only possibility. In general, experimental uncertainties, missing undiscovered states and also the fluctuations in masses where different experiments see these resonances make a final statement on the assignment of radial-excitation QNs hard if not impossible. A more detail study regarding the Regge trajectories was performed in [43], showing how well it works, also for other QN combinations than the here discussed a_J states.

Let us now have a closer look at the Regge-trajectory plot in Figure 4.2. The lines are a linear fit to the respective group of the same color. In the legend, one can see the corresponding linear fit function describing the dependence of $n(M^2)$ for fixed J and, thus, also fixed L.

Resonances with equal J are depicted in the same color, while same L assignment as discussed before uses similar colors. All solid-line fits exhibit a slope of $\sim 1\,\text{GeV}^{-2}$, qualitatively agreeing with

[3] The ground state $a_2(1320)$ and the first radial excitation $a_2(1700)$ have a mass difference of ~ 380 MeV.

Table 4.1: Particle masses and their uncertainties were taken from PDG. If statistical and systematic uncertainty were given, the larger one is shown here. If no official average was stated although there was more than one experiment, the range of values is listed here. The assignment of the radial-excitation QN n is a proposal based on the expected distance from and the proximity to previous/later states. The corresponding particles are listed in the column **comment** with arrows pointing to the other states. The column **established** shows if they are included by the PDG in "Particle Listings" under "Light Unflavored Mesons" (✓) or in the section "Other Mesons" under "Further States" (✗).

resonance	M/GeV	J	n	**established**	**comment**
$a_0(980)$	0.980 ± 0.020	0	1	✓	tetraquark candidate, see 4.2.3
$a_0(1450)$	1.474 ± 0.019	0	2	✓	tetraquark candidate, see 4.2.3
$a_0(1950)$	1.931 ± 0.022	0	3	✓	
$a_0(2020)$	2.025 ± 0.030	0	4	✗	
$a_1(1260)$	1.230 ± 0.040	1	1	✓	
$a_1(1420)$	1.411 ± 0.005	1	2?	✗	resonance-like signal in question
$a_1(1640)$	1.655 ± 0.016	1	2	✓	
$a_1(1930)$	1.930 ± 0.070	1	3	✗	
$a_1(2095)$	2.096 ± 0.131	1	4	✗	
$a_1(2270)$	2.270 ± 0.055	1	5	✗	
$a_2(1320)$	1.318 ± 0.001	2	1	✓	
$a_2(1700)$	1.698 ± 0.044	2	2	✓	
$a_2(1950)$	1.950 ± 0.070	2	3	✗	close to $a_2(1990) \downarrow$ and $a_2(2030) \Downarrow$
$a_2(1990)$	$2.003 - 2.050$	2	3	✗	close to $a_2(1950) \uparrow$ and $a_2(2030) \downarrow$
$a_2(2030)$	2.030 ± 0.020	2	3	✗	close to $a_2(1950) \Uparrow$ and $a_2(1990) \uparrow$
$a_2(2175)$	2.175 ± 0.040	2	4	✗	
$a_2(2255)$	2.255 ± 0.020	2	5	✗	
$a_3(1875)$	1.874 ± 0.096	3	1	✗	
$a_3(2030)$	2.031 ± 0.012	3	2	✗	
$a_3(2275)$	2.275 ± 0.035	3	3	✗	
$a_4(1970)$	1.967 ± 0.016	4	1	✓	
$a_4(2255)$	$2.237 - 2.255$	4	2	✗	
$a_6(2450)$	2.450 ± 0.130	6	1	✗	

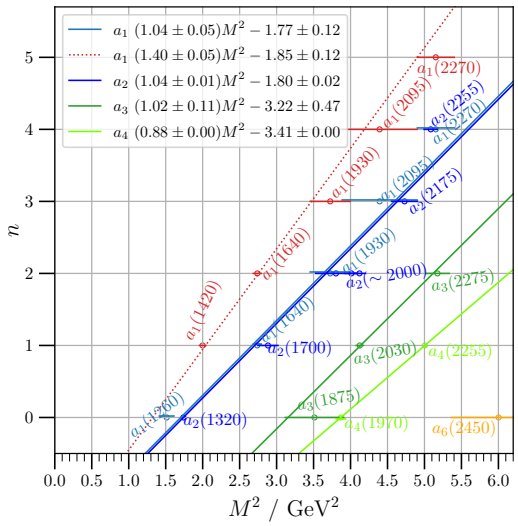

Figure 4.2: Plot with Regge trajectories for the a_J resonances. The relation from equation (4.1) with the radial-excitation QN n is plotted. The lines are a fit to all resonances of the same group, indicated by the same color. The legend shows the fit function, where the slopes are given in the unit GeV^{-2}. The red dotted line shows the case where we assume the $a_1(1420)$ to be an ordinary radial excitation with $n = 2$ and heavier a_1 resonances shown in red with their n accordingly increased by 1.

the value of 0.84 GeV^{-2} as estimated at the end of appendix C.1.1. Also the ordinates of the two blue $L = 1$ lines and the two green $L = 3$ lines are close to the expectation of -1.5 and -3.5 from equation (4.1), respectively. The red dotted line on the other hand shows a 40 % larger slope raising strong doubts to the adjusted assignment of n.

While we see that these Regge trajectories are not perfect[4], we can definitely conclude that seeing the $a_1(1420)$ as the first radial excitation of the $a_1(1260)$ would make matters a lot worse. Additionally, there would be no direct reason for an ordinary CQM resonance to appear in the $f_0(980)\pi$ P-wave, while being absent in the $\rho(770)\pi$ S or the $(\pi\pi)_S\pi$ P waves as it is the case in the COMPASS data.

4.2.2 $K^*\overline{K}$ Molecule

Meson molecules are always a possibility when a decay threshold is close by. In the case of the $a_1(1420)$ this would be the $K^*\overline{K}$ threshold at ~ 1.39 GeV. Here appears already the first problem with this interpretation, because usually the mass of a molecule is slightly below the threshold[5] which increases the lifetime of the molecular state due to its inability to decay immediately via this channel. The reason is that a higher molecule mass $m_{K^*\overline{K}} > m_{K^*} + m_{\overline{K}}$ corresponds to a positive binding energy $E_{\text{bind}} := m_{K^*\overline{K}} - m_{K^*} - m_{\overline{K}} = +22$ MeV using $m_{K^*\overline{K}} = m_{a_1(1420)}$, so basically no binding at all.

In [44], the hypothesis of a hadronic molecule is compared to a diquark-antidiquark structure (tetraquark). They state that the former explanation provides a better agreement with the COMPASS results. However, they also mention that the branching of $a_1(1420) \to f_0(980)\pi$ is significantly

[4] Also by considering the fact that many of these resonances are not yet fully established.

[5] Most prominent example is the deuteron as a proton-neutron molecule.

suppressed in comparison to $a_1(1420) \to K^*\overline{K}$ modes by one order of magnitude. In chapter 6, section 6.3.1, we compare the partial waves of a resonance with $J^{PC} = 1^{++}$ decaying into $K^*(892)K_S^0$ and into $f_0(980)\pi$. We see a strong $a_1(1420)$ signal in the $f_0(980)\pi$ wave while there is almost no intensity at 1.4 GeV for the $K^*(892)K_S^0$ wave. This stands in contradiction with the expectations from a hadronic molecule, making this interpretation unlikely.

Additionally, [44] do not give reasons for the absence of the $a_1(1420) \to \rho\pi$ or $a_1(1420) \to (\pi\pi)_S\pi$ decay channels. These decay modes come with a larger phase space than $f_0(980)\pi$ since these isobars are lighter, thus, something would have to prevent these specific decays, which is simply not given in a molecular description.

4.2.3 Tetraquark

While a meson molecule consists of two color-singlet states that would be bound by meson exchange, e.g. by pion exchange as for the deuteron, a tetraquark will be bound by color force. [42] introduces the concept of $[qq']$ diquarks with two versions, a spin-0 diquark being a color-antitriplet with antialigned quark spins and a spin-1 diquark being a color-sextuplet with aligned quark spins, both being a flavor-antitriplet.

As derived by [42] as well as in appendix C.2, combining a spin-0 diquark with a spin-0 antidiquark results in a scalar tetraquark nonet, and combining a spin-1 diquark with a spin-1 antidiquark yields a tetraquark nonet as well, however this time with three possible spins 0, 1 or 2.

According to [42], the ground-state scalar tetraquark nonet built by a spin-0 diquark and spin-0 antidiquark can be filled by three $a_0(980)$ mesons, four $K_0^*(700)$ mesons also known as κ, the $f_0(500)$ also known as σ, and finally the $f_0(980)$. While the $a_0(980)$ and the $f_0(980)$ have quite small widths of less than 100 MeV, κ and σ are a lot broader despite their small mass. This can be understood if we look at the assumed quark content in the diquark-antidiquark picture. $f_0(500)$ and $f_0(980)$ are assumed to be mixed from the pure diquark-antidiquark states, similar to the $q\bar{q}$ equivalent of η and η' that come from the corresponding singlet and octet states. Assuming ideal mixing, one can infer $f_0(500)$ to be made up of $[ud][\bar{u}\bar{d}]$ and, thus, being very light while the heavier partner $f_0(980)$ consists of $\frac{1}{\sqrt{2}}\Big([ds][\bar{d}\bar{s}] + [su][\bar{s}\bar{u}]\Big)$. On one hand, this can explain the strong coupling of the $f_0(980)$ to kaons due to its inherent $s\bar{s}$ content. And on the other hand this also can help to understand the broadness of the $f_0(500)$, since it consists only of u and d quarks and it is expected that tetraquarks with heavier quarks are more strongly bound. The $K_0^*(700)$ is composed out of $[nn'][\bar{n}\bar{s}]$ and its complex conjugate (c.c.) for different combinations of $n, n' \in \{u, d\}$ with $n \neq n'$, e.g. $[du][\bar{d}\bar{s}]$ for the K_0^{*+}. Having only one strange quark also makes it broader than the heavier particles of the nonet. Both $f_0(980)$ and $a_0(980)$ have two strange quarks inside resulting in a stronger expected binding and, therefore, a smaller width.

There would also be a heavier nonet of scaler tetraquarks involving spin-1 (anti)diquarks coupling to total spin 0, which can be assigned to three $a_0(1450)$ states, four $K_0^*(1430)$ mesons and the $f_0(1370)$ mixing again with the $f_0(1500)$.

For the case of the $a_1(1420)$, the more interesting candidates are, however, the tetraquarks with total spin 1. Here, [42] showed from considerations of the diquark-antidiquark wave functions that the expected QNs would be $J^{P(C)} = 1^{+(-)}$, which would narrow it down to K_1, b_1 and h_1 mesons. This would actively render the $a_1(1420)$ impossible to be a tetraquark within this framework.

But so far, only states with no intrinsic orbital angular momentum were considered. Bringing a non-vanishing L into the mix can certainly open up to other QNs. However, this should come with increased masses and, therefore, also broader states while the $a_1(1420)$ signal is very narrow compared to similarly heavy resonances, e.g. the $a_1(1260)$. Additionally, it would introduce a huge amount of new possible states that are simply not observed, creating more problems than it would actually solve. And as mentioned before, [44] showed that, actually, the experimental data prefers a molecular interpretation over the one of a tetraquark, making the tetraquark interpretation even more unlikely.

4.2.4 Unitary Coupled Channel

Another possibility is an interference effect of background processes with the existing resonance $a_1(1260)$. In [45] and [46], Basdevant and Berger investigated the $\rho(770)\pi$ and $f_0(980)\pi$ final states in a coupled-channel analysis. They showed that one can obtain a peak at the $a_1(1420)$ mass in the $f_0(980)\pi$ channel if one incorporates unitarity properly, while combining the $a_1(1260)$ decay with the so-called Deck process. This process is a t-channel exchange instead of the production of a resonance, see Figure 4.15, and it is known for its leakage into almost all partial waves of the 3π channel as demonstrated by [47].

However, the argument that speaks against this model as the cause for the $a_1(1420)$, is the fact that this model produces a phase motion at the ground-state $a_1(1260)$ mass only, but not at 1.4 GeV where we see it in the data (compare Figure 4.1 with the purple line in Figure 4.12(b), which corresponds to FIG. 4 of [45]). Another new argument against this interpretation, is the fact that, meanwhile, first hints of the $a_1(1420)$ signal were observed in τ decays [8]. If this turns out to be true, it excludes the interpretation as a dynamic effect of the Deck-like background, since this background is not present there. Although this effect might not be the actual cause for the $a_1(1420)$ signal, nevertheless, this study shows the importance of incorporating background processes in a unitary way when fitting models to mass distributions.

4.2.5 Triangle Singularity

The last possibility, and the one that we will focus on for the rest of this chapter, is a rescattering effect at the origin of the $a_1(1420)$. Here, starting with the ground-state meson $a_1(1260)$ as a source, one considers it decaying into $K^*\overline{K}$ or its c.c. Subsequently, the K^* will decay into $K + \pi$ and this K together with the $\overline{K}$ from the initial decay will meet to rescatter through an $f_0(980)$ isobar into two pions. If such a rescattering process is kinematically possible with involved particles on mass shell, Landau showed that this will produce a singularity close to the physical region [48]. Since the involved process has a diagram in shape of a triangle (see Figure 4.3), such a singularity is called Triangle Singularity (TS). In this case, it is a logarithmic branch point ([21]) that can create a peaking structure together with a phase motion mimicking a resonance behavior. It was first proposed as an explanation by [49], where they also estimated its strength from the involved couplings compared to the decay $a_1(1260) \to \rho(770)\pi$, finding good agreement with the experimental results. Details on the calculations can be found in the next section. A fit of an earlier version of this theoretical model to the COMPASS data was already published in [50].

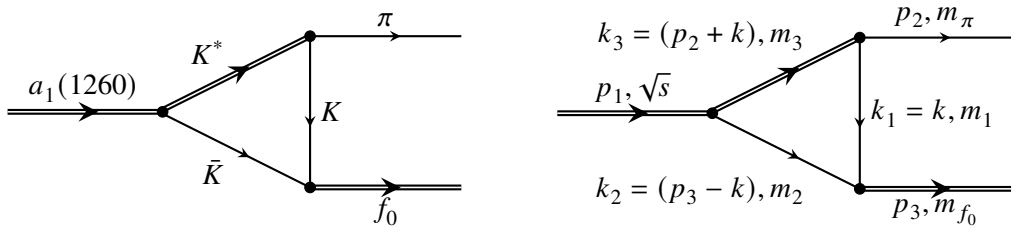

Figure 4.3: Triangle diagram with particles (left) and their momenta and masses (right). Arrows indicate the flow of momentum, and double lines indicate unstable particles.

4.3 Rescattering

There are several ways how to calculate the amplitude of a rescattering process. We will start with the simplest case, where we assume all particles to be spinless and use Feynman rules with scalar propagators for all involved internal particle lines. Since the data that we are analyzing, is the result of a PWD, the contributions from different isobars were already separated from each other. Thus, we are dealing with only a single isobar decay – meaning $X^- \to f_0(980)\pi^-$ – and, therefore, we will treat the $f_0(980)$ as a quasi-stable particle and set it on mass shell. Its comparably narrow width of roughly $\Gamma_{f_0} = 50\,\text{MeV}$ allows for this as well, since mathematically a BW becomes a δ-distribution for vanishing width, $\texttt{BW}(s; m, \Gamma) \xrightarrow{\Gamma \to 0} \delta(s - m^2)$. Also we will simply call it f_0, removing its mass from the name. To avoid confusions with the other states from the rich $[\pi\pi]_S$ spectrum, the $f_0(500)$ will be named σ and heavier f_0 will keep their mass in the name, e.g. the $f_0(1500)$.

The rescattering process is depicted in Figure 4.3 on the left. It takes the $a_1(1260)$ as a source which decays into $K^*\bar{K}$. The K^* further decays into $K\pi$. Now, the rescattering happens where the $\bar{K}$ from the initial decay fuses with the K from the second decay to form the f_0 isobar that can finally decay into two pions, resulting in the observed 3π final state. This triangle can have two different charge modes $K^{*0}K^-K^+$ and $K^{*-}K^0\overline{K}^0$ that come with the same Clebsch-Gordan coefficients on the vertices. Therefore, the overall relative strength for these amplitudes will be equal, only the masses of the involved particles will change slightly. The Clebsch-Gordan coefficients will be omitted since they can be absorbed by the strength parameter used during fitting.

4.3.1 Scalar Case

This case was first studied in [51], where the authors also gave ideas on how to incorporate the width and the spins. Detailed calculations can be found in [26], so we will only discuss the recipe here and present the results for later comparison. The notation used for this calculation can be found in Figure 4.3 on the right.

The steps of the calculation are as follows:

1. Construct the matrix element $\mathcal{M}$ consisting of three scalar propagators and an integration over the momentum inside the triangular loop: $\mathcal{M}_\Delta \sim \int \mathrm{d}^4k \prod_{i=1}^{3} \frac{1}{m_i^2 - k^2 - \mathrm{i}\,\varepsilon}$
2. Use the Feynman trick to replace $\frac{1}{ABC} = 2 \iiint_0^1 \frac{\delta(x+y+z-1)}{(Ax+By+Cz)^3} \mathrm{d}x\,\mathrm{d}y\,\mathrm{d}z$
3. Perform a linear substitution $K = k - yp_3 + zp_2$ to remove terms linear in k.

4. Change from the Minkowski integral of the four-momentum K to an Euclidean integral by performing a Wick rotation, effectively replacing $K^2 \to -K^2$ and $\mathrm{d}^4K \to \mathrm{i}\,\mathrm{d}^4K$.

5. Solve the K-integral by changing to 4-dimensional spherical coordinates.

6. Solve the z-integral by using the δ distribution and write the integrand as $\frac{1}{s(y-y_+)(y-y_-)}$, with $y_\pm$ as in equation (4.3).

7. Split the product of fractions into a sum of fractions via partial fraction decomposition, leading to the sum of logarithms after solving the y-integral.

8. Solve the remaining x-integral numerically by replacing $s \to s + \mathrm{i}\,\varepsilon$ to be in the physical regime slightly above the real axis and to avoid possible singularities on the integration path.

The final expressions read as follows:

$$\begin{aligned}
\mathcal{M}_\Delta &\sim \frac{1}{s}\int_0^1 \mathrm{d}x \frac{1}{y_+ - y_-}\left[\log\left(\frac{1-x-y_+}{-y_+}\right) - \log\left(\frac{1-x-y_-}{-y_-}\right)\right], \text{ with} && (4.2)\\
y_\pm &= A_y \pm \sqrt{A_y^2 + B_y} && (4.3)\\
A_y &= \frac{(m_3^2 - m_2^2 + s) - (s + m_\pi^2 - m_{f_0}^2)x}{2s}\\
B_y &= \frac{m_3^2 + (m_1^2 - m_3^2 - m_\pi^2)x + m_\pi^2 x^2}{s}.
\end{aligned}$$

Note that $y_\pm$ is dependent on x and s making the final integration highly non-trivial, therefore, we perform it numerically. However already before, we can extract some interesting information from it, namely the position of the TS.

For this, we see that the integrand has a pole when $y_+ = y_- =: y_s$. This happens for two different values of x:

$$\begin{aligned}
x_\pm &= A_x \pm \sqrt{A_x^2 - B_x} && (4.4)\\
A_x &= \frac{2s(m_1^2 - m_3^2 - m_\pi^2) - (m_3^2 - m_2^2 + s)(m_{f_0}^2 - s - m_\pi^2)}{\lambda(s, m_\pi^2, m_{f_0}^2)}\\
B_x &= \frac{\lambda(s, m_2^2, m_3^2)}{\lambda(s, m_\pi^2, m_{f_0}^2)}.
\end{aligned}$$

Now, the TS occurs when these two poles meet in a so-called pinch singularity. This means that for some specific values of the incoming squared invariant mass s we have $x_+ = x_- =: x_s$. Here, one finds two points $\sqrt{s} = 1.4168\,\mathrm{GeV}$ and $\sqrt{s} = 1.4699\,\mathrm{GeV}$, of which only the first one fulfills $x_s + y_s < 1$ (and both x_s and y_s being positive), which is a requirement coming for the original $\delta(x + y + z - 1)$. As a result, we expect some enhancement at 1.4168 GeV coinciding well with the position where the $a_1(1420)$ was found.

From this result we can also infer some information on the type of the TS. In equation (4.2) we see that we are basically dealing with a first-order pole when viewing the integrand as a function of

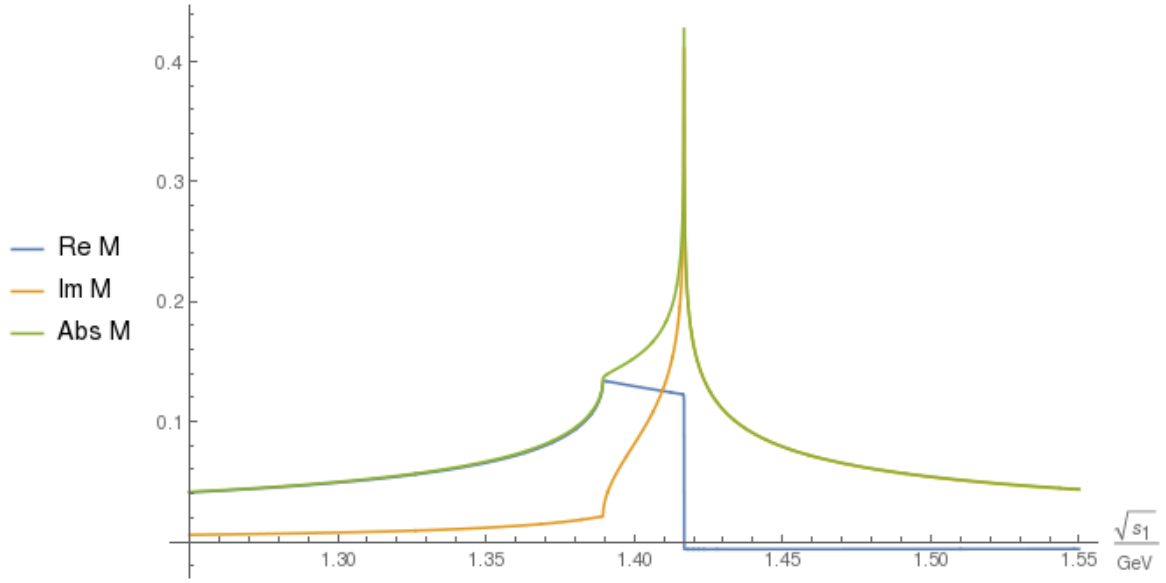

Figure 4.4: Real part (blue), imaginary part (orange) and absolute value (green) of the matrix element $\mathcal{M}_\Delta$ for the triangle diagram, calculated using equation (4.2). Taken from [26] (Figure 3.8), with $\sqrt{s_1}$ being equivalent to $\sqrt{s}$ as mentioned in this work.

x, in a very simplified manner we have something like $\sim \frac{1}{x}$. Integrating this will result in $\sim \log(x)$, which has a logarithmic singularity where the integrand has a pole. This means that the TS will be a logarithmic branch point, at least in the case of only scalar particles. That it really is a logarithmic branch point also in the physically correct configuration was shown by Gribov (section 2.4.5 of [21]).

The resulting complex amplitude as a function of $\sqrt{s}$ is presented in Figure 4.4. We see some enhancement at the calculated position of the TS, however, the function is not very smooth. The reason for this is, that we did not include the finite width of the K^* into the calculations. We will see a method to do this in a mathematically sound way in the next section 4.3.2.

4.3.2 Dispersive Approach

So far we treated everything as scalar particles with infinitesimally small decay width Γ. We will address now the latter simplification by showing a way to incorporate the width of the unstable K^* that appears inside the triangle loop. This procedure was also already presented in [26], thus once more, we will only sketch the calculations. The general idea is, to add another loop in the K^* propagator to accommodate for its decay into $K\pi$, as can be seen in Figure 4.5.

The steps to calculate the amplitude of the triangle diagram are:

1. Cut the diagram along the dashed line in Figure 4.5 and write down the matrix elements for the left and right side of the line, respectively named $\mathcal{M}_{\text{left}}$ and $\mathcal{M}_{\text{right}}$.

2. Use a BW with energy-dependent width according to equation (3.34) as the propagator[6] in the scalar propagator $(m_3^2 - k_3^2 - \mathrm{i}\,\varepsilon)^{-1}$ for the K^*. In principle one would have to use a Flatté

[6] This means, we replace $\varepsilon = m_3\Gamma_3(k_3)$.

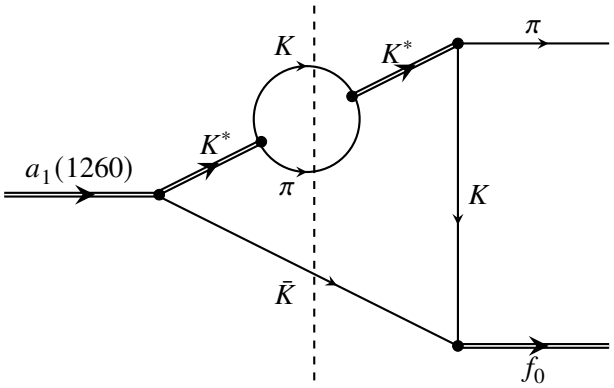

Figure 4.5: Triangle diagram as it is used for the dispersive calculation. The dashed line indicates where the diagram will be cut during the calculation of the discontinuity of the triangle amplitude.

parametrization (cf. equation (3.37)) since the K^* has two different decay modes[7]. But since their masses are similar and since they have equal Clebsch-Gordon coefficients for the isospin couplings, we can take the average mass μ_K for the kaons and μ_π for the pions, and the full decay width of the K^* to simplify the expressions.

3. Use the cutting rules developed by Cutkosky [52] and specifically derived for this case in [26] to write down the formula to calculate the discontinuity of the triangle amplitude via

$$\mathrm{Disc}\mathcal{M}_\Delta \sim \mathrm{i} \int \mathcal{M}_{\mathrm{left}} \mathcal{M}^*_{\mathrm{right}} \mathrm{d}\Phi_3,$$

where we integrate over the phase space of the three cut propagator lines.

4. Replace $\mathrm{d}\Phi_3$ according to the phase-space recursion formula (see appendix A.1.3) by an integral over intermediate K^* squared invariant mass $\int \mathrm{d}k_3^2$ and the product of the corresponding two two-body phase spaces.

5. Calculate the $\mathrm{d}k_3^2$ integral inside the expression of the discontinuity numerically.

6. Insert the result into a dispersion relation $\mathcal{M}(s) = \dfrac{1}{2\pi\mathrm{i}} \displaystyle\int_{s_{\mathrm{th}}}^{\infty} \frac{\mathrm{Disc}\mathcal{M}(s')}{s' - s - \mathrm{i}\,\varepsilon} \mathrm{d}s'$ and calculate the integral numerically.

The resulting triangle amplitude of the dispersive approach is shown in Figure 4.6. It turns out that the result is very similar to the case discussed in section 4.3.1 if we replace there $m_3^2 \to m_3^2 - \mathrm{i}\, m_3 \Gamma_3$, showing that this simple way of incorporating a width of a particle is a good approximation.

4.3.3 Application of the Partial-Wave Projection

There is one simplification left that could create some changes in the resulting triangle amplitude, and this is the proper inclusion of spin and orbital angular momentum. For this, we will employ the

[7] The decays $K^{*-} \to \overline{K}^0 + \pi^-$ and $K^{*-} \to K^- + \pi^0$ exist, or in case of the neutral one, we have $K^{*0} \to K^0 + \pi^0$ and $K^{*0} \to K^+ + \pi^-$.

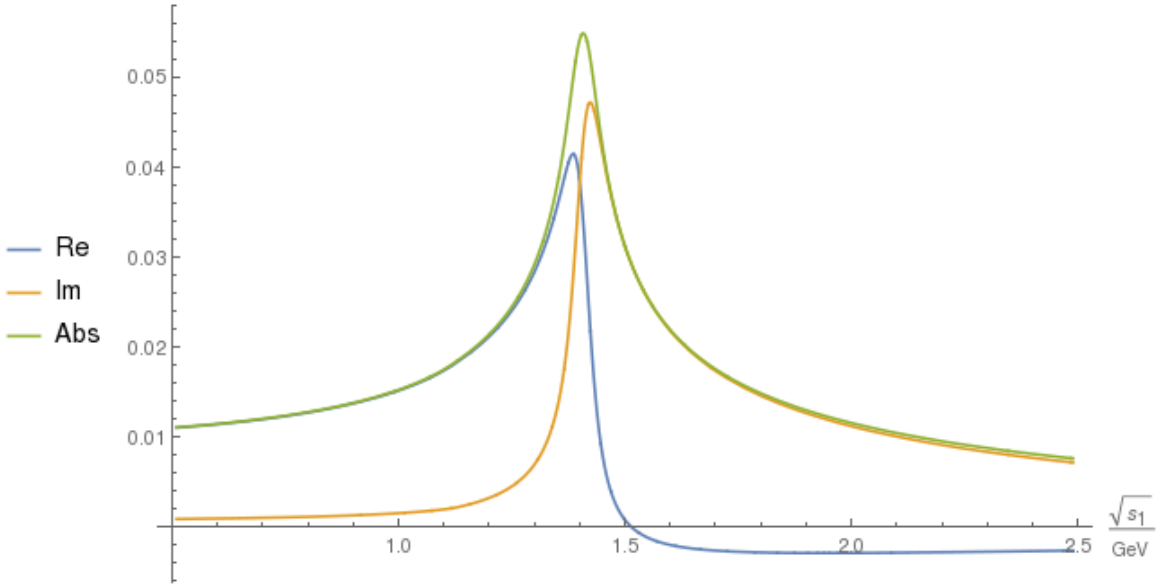

Figure 4.6: Real part (blue), imaginary part (orange) and absolute value (green) of the triangle amplitude calculated using the dispersive approach with a proper inclusion of the finite width of the K^*. Taken from [26] (Figure 3.12), with $\sqrt{s_1}$ being equivalent to $\sqrt{s}$ as mentioned in this work

partial-wave-projection mechanism introduced in section 3.6. We start with the iteration procedure from equations (3.100) and (3.101). As mentioned in the text above these equations, we will start the iteration $n = 0$ by setting ${}^{(0)}\hat{F}_w \equiv 0$.

For the function $C_w(s)$ we use a BWM with energy-dependent width according to equation (3.34) as it is used as well by COMPASS during mass-dependent fits after the PWD. We give it the name $\mathtt{BW}_{a_1}(s)$.

The two-body scattering amplitude will be the one of the K^* in the (12) isobar channel[8], see Figure 4.7(a). We label it with $f_{K^*}(\sigma_3)$ and use a Chew-Mandelstam BW as introduced in section 3.3.3. This will make sure that we have the correct complex structure, since every additional branch cut, as it is present for the normal two-body phase space due to the pseudo threshold, will create problems during integrations in the complex plane. This wave has the QNs $w' = (J'M'L'S') = (1001)$ and with this we can write down the expression for F:

$$ {}^{(0)}F_{(1001)}(s, \sigma_3) = f_{K^*}(\sigma_3)\mathtt{BW}_{a_1}(s). \tag{4.5} $$

Now, this partial wave will be projected onto the $f_0\pi$ P wave (see Figure 4.7(b)) where we observe the $a_1(1420)$ signal, neglecting all other possible waves. This reduces the sum over w' in equation (3.100) to only the wave with QNs $w = (JMLS) = (1010)$. Since we do not expect to see any contributions coming from isobars in the $\pi^-\pi^-$ subsystem, we only consider the term dependent on σ_1 and drop the one with σ_2. This gives us the final expression for ${}^{(1)}\hat{F}$:

$$ {}^{(1)}\hat{F}_{1010}(s, \sigma_1) = \int \mathrm{d}Z^{(1)}_{(1010)}\, {}^{(0)}F_{(1001)}(s, \sigma_3) Z^{(3)}_{(1001)}, \tag{4.6} $$

[8] This means the index on the left-hand side of equation (3.100) is $i = 3$ and, therefore, $j = 1$ and $k = 2$.

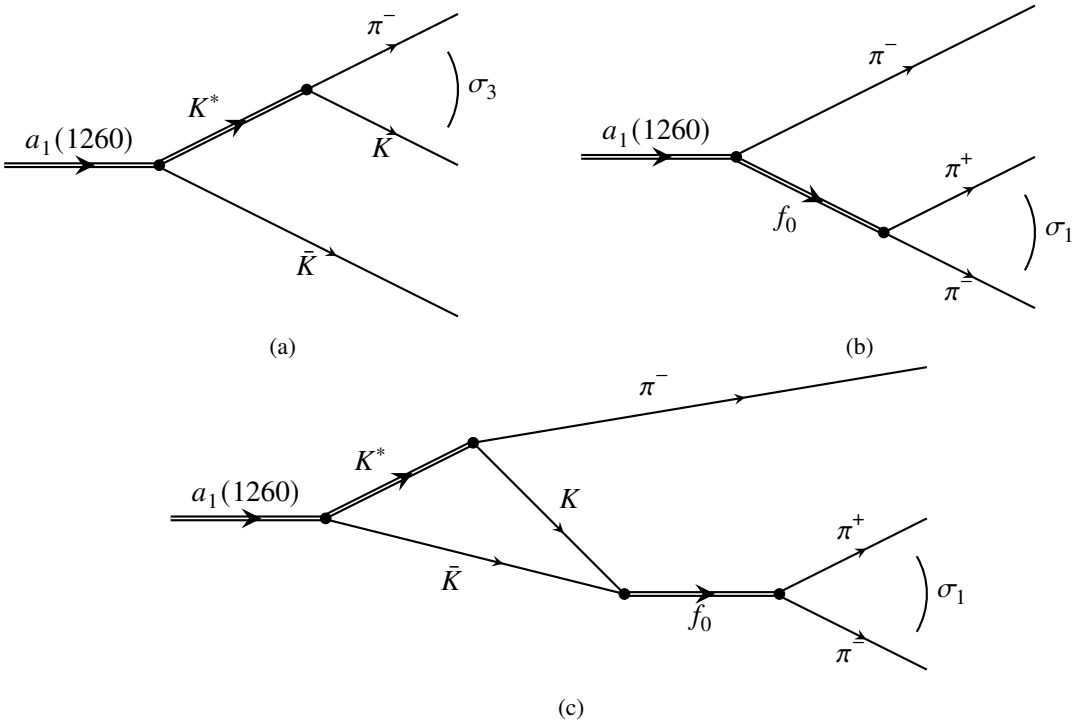

Figure 4.7: Diagrams to visualize the partial-wave-projection method. One starts with the partial wave indicated by diagram 4.7(a) and projects it on the partial wave indicated by diagram 4.7(b). The result is the diagram 4.7(c).

where $\mathrm{d}Z_w^{(i)}$ was defined in equation (3.93).

Coming to equation (3.101), we choose $C(s) \equiv 0$ this time, which means that we neglect a direct production of the $f_0\pi$ P wave. The two-body scattering amplitude will be the one of the f_0, where we stick to the COMPASS convention and use a Flatté parametrization as in equation (3.36) and detailed in section 6.2.1. However, this choice does not matter at this point, since we will see later that this factor can be absorbed into a quasi-two-body phase space. This gives us the final expression for F:

$$ {}^{(1)}F_{(1010)}(s,\sigma_1) = K(s,\sigma_1) f_{f_0}(\sigma_1) \frac{1}{2\pi} \int_{4m_\pi^2}^{\infty} \frac{\rho_{f_0}(\sigma_1')\, {}^{(1)}\hat{F}_{(1010)}(s,\sigma_1') \,/\, K(s,\sigma_1')}{\sigma_1' - \sigma_1 - \mathrm{i}\,\varepsilon} \mathrm{d}\sigma_1'. \tag{4.7} $$

Inserting now equation (4.5) into equation (4.6), and the result of that into equation (4.7), we see that we can simply pull out the $\mathtt{BW}_{a_1}(s)$, since it does not depend on the integration variables. This shows that we can view the triangle calculation just as a modification of the decay vertex for $a_1(1260) \to f_0\pi$:

$$ F_{(1010)}(s,\sigma_1) = \mathtt{BW}_{a_1}(s) f_{f_0}(\sigma_1) \cdot \frac{K(s,\sigma_1)}{2\pi} \int\limits_{4m_\pi^2}^{\infty} \frac{\rho_{f_0}(\sigma_1') \int \mathrm{d}Z_{(1010)}^{(1)} f_{K^*}(\sigma_3) Z_{(1001)}^{(3)} \,/\, K(s,\sigma_1')}{\sigma_1' - \sigma_1 - \mathrm{i}\,\varepsilon} \mathrm{d}\sigma_1'. \tag{4.8} $$

The next step will be the actual calculation of the double integral.

4.3.4 Calculation of the Triangle Amplitude

We have to start with the inner integral of equation (4.8). Some general transformations using properties of the Wigner-D functions are performed in appendix A.3.2 and we will apply equation (A.26) to our case.

$$\begin{aligned} B^{\lambda\lambda'}_{1,10,01} &= 1 \cdot \underbrace{\langle 10, 0\lambda | 1\lambda\rangle}_{=\delta_{\lambda 0}} \underbrace{\langle 00, 1\lambda' | 1\lambda'\rangle}_{=1} \\ \mathrm{d}Z^{(1)}_{(1010)} \cdot Z^{(3)}_{(1001)} &= \frac{\mathrm{d}\cos\theta_{23}}{2} \sum_{\lambda'} \underbrace{d^0_{00}(\theta_{23})}_{=1} d^1_{0\lambda'}(\theta_{3(1)}) d^1_{\lambda' 0}(\theta_{12}) \\ &= \frac{\mathrm{d}\cos\theta_{23}}{2} \cos(\theta_{3(1)} + \theta_{12}), \end{aligned}$$

where the last step is obtained by explicitly writing out the sum[9] over $\lambda' \in \{-1, 0, 1\}$ and inserting the respective Wigner-d functions. Now, the remaining angles have to be expressed in terms of σ_i in order to perform the final integral. The corresponding formulas are derived in appendix A.4.

Looking back at equation (4.8) the projection integral also contained the isobar propagator $f_{K^*}(\sigma_3)$, however, this is independent of the three angles that we already integrated out. We have to perform a substitution of the final angle $\cos\theta_{23}$ to σ_3 in order to be able to integrate f_{K^*}, see equation (A.45). We get $\cos(\theta_{3(1)} + \theta_{12})$ from equation (A.43), giving us the full inner integral to solve:

$$\hat{F}_{(1010)}(s, \sigma_1) = \int \mathrm{d}Z^{(1)}_{(1010)} \cdot Z^{(3)}_{(1001)} f_{K^*}(\sigma_3) = \int_{\sigma_3^-(s,\sigma_1)}^{\sigma_3^+(s,\sigma_1)} \mathrm{d}\sigma_3 \frac{\sigma_1 \cdot W(\sqrt{s}, \sqrt{\sigma_1}, \sqrt{\sigma_3}) \cdot f_{K^*}(\sigma_3)}{\left((\sqrt{s} + \sqrt{\sigma_3})^2 - m_3^2\right) \lambda_{s1} \sqrt{\lambda_1 \lambda_3}}, \tag{4.9}$$

with W as defined in equation (A.42) and the integration limits given by

$$\sigma_3^{\pm}(s, \sigma_1) = \frac{1}{2}\left(s + \sum m_i^2 - \sigma_1 + \frac{(m_2^2 - m_3^2)(s - m_1^2)}{\sigma_1} \pm \frac{\sqrt{\lambda_1 \lambda_{s1}}}{\sigma_1}\right), \tag{4.10}$$

which is obtained by inserting the limits $\cos\theta_{23} = \pm 1$ into equation (3.56).

Kinematic Factor

We have to determine the kinematic factor $K(s, \sigma_1)$ that is introduced in section 3.6.1. For this, we have to think where it actually comes from. Although the argument σ_1 might suggest that it comes from $F_{(1010)}(s, \sigma_1)$ this is not the case. We have to remove the kinematic factor from the first $F_{(1001)}$, since this enters in the derivations of the partial-wave projection formula. This means that we have to determine the part of $Z^{(3)}_{(1001)}$ that is singular in σ_1.

[9] From a conceptual point of view such a sum over the product of two Wigner-d functions – each corresponding to a specific rotation matrix – is equivalent to the Wigner-d function corresponding to the product of these rotation matrices, thus, the sum of their rotation angles.

Proceeding exactly as in the derivation of equation (A.26) we obtain

$$Z^{(3)}_{(1001)} = Z_{(1001)}(\Omega_3, \Omega_{12}) = \sqrt{3} \sum_{\lambda,\nu} D^{1*}_{0\nu}(\phi_1, \theta_1, \phi_{23}) \underbrace{d^1_{\nu\lambda}(\theta^*_{3(1)})}_{\sim \frac{1}{\sqrt{\lambda_{s1}\lambda_{s3}}}} \underbrace{d^1_{\lambda 0}(\theta_{12})}_{\sim \frac{1}{\sqrt{\lambda_3\lambda_{s3}}}}. \tag{4.11}$$

The dependencies below are obtained from the fact that $d^1_{\nu\lambda}$ is simply a first-order polynomial in sine or cosine of the argument. These are calculated in appendix A.4 and have equal denominators for a specific angle as indicated in the equation above. Of these dependencies, only one factor is dependent on σ_1 and exhibits square-root branch-point singularities. Therefore, we can identify

$$K(s, \sigma_1) = \sqrt{\lambda_{s1}}. \tag{4.12}$$

Note that this kinematic factor also fulfills the required condition – as detailed in the text before equation (3.98) – that $K^2(s, \sigma_1) = \lambda_{s1}$ does not exhibit a discontinuity. Inserting it into equation (4.8) yields

$$F_{(1010)}(s, \sigma_1) = \mathtt{BW}_{a_1}(s) f_{f_0}(\sigma_1) q_{f_0}(s, \sigma_1) \cdot \underbrace{\frac{2s}{2\pi} \int_{4m_\pi^2}^{\infty} \frac{\rho_{f_0}(\sigma_1') \int \mathrm{d}Z^{(1)}_{(1010)} f_{K^*}(\sigma_3) Z^{(3)}_{(1001)} / \sqrt{\lambda'_{s1}}}{\sigma_1' - \sigma_1 - \mathrm{i}\,\varepsilon} \mathrm{d}\sigma_1'}_{=: \mathcal{M}_\Delta}, \tag{4.13}$$

where we define $\lambda'_{si} = \lambda(s, \sigma_i', m_i^2)$. Here, we introduced an extra $2s$ factor in order to transform the $\sqrt{\lambda_{s1}}$ into the corresponding break-up momentum q_{f_0} of the decay $a_1 \to f_0\pi$. This dependence is also expected as we are dealing with a P-wave decay that should come with one additional power in the break-up momentum, see equation (3.32). Another benefit of this kinematic factor is that the integrand gets additional damping from the $(\lambda'_{s1})^{-\frac{1}{2}} \sim (\sigma_1')^{-1}$ that helps with the convergence of the outer σ_1'-integral.

Limit Behavior of the Inner Integral

The next step is the actual calculation of the triangle amplitude $\mathcal{M}_\Delta$ that modifies the decay vertex of $a_1 \to f_0\pi$. For this, we look how the integration limits $\sigma_3^\pm$ in equation (4.10) of the inner integral (cf. equation (4.9)) behave for fixed $s = (1.4168\,\mathrm{GeV})^2$ as a function of the integration variable σ_1 of the outer integral. In general $\sigma_3^\pm$ are complex quantities, thus, an integration will have to happen along a path in the complex plane. Figure 4.8 shows their behavior as functions of σ_1. The blue circles indicate the pseudo-threshold and the threshold of the K^* decay. Using a Chew-Mandelstam BW, we only expect to have one branch cut extending from the threshold to infinity along the real axis. By adding some small imaginary quantity $\mathrm{i}\,\varepsilon$ to $\sqrt{s}$, we can uncover on which side of this branch cut the integration paths lie. Now, we have to make sure that the integration path does not cross this branch cut, therefore, simply using straight lines connecting the two limiting values $\sigma_3^\pm$ is not an option, since they will cross the branch cut for some values of σ_1 as can best be seen in Figure 4.8(b). The simplest solution to this problem is, that we always go in a straight line from σ_3^- to some midpoint between the pseudo-threshold and the threshold – e.g. $0.2\,\mathrm{GeV}^2$ – and, then, continue to σ_3^+. The advantage of the Chew-Mandelstam parametrization over a simple energy-dependent width using the two-body phase

space (cf. equation (3.34)) is that it does not have the cut starting at the pseudo-threshold which could be crossed by accident if one does not take care of rotating the branch cuts of the phase space properly as discussed and derived in section 3.3.3. The absence of a left-hand cut is also a requirement for the derivation of the partial-wave projection method.

Such a linear integration path from point a to point b in the complex plane can be parametrized in the following way

$$\ell(t; a, b) = a + t(b - a), \qquad \text{with } t \in [0, 1] \tag{4.14}$$

with the complex integration being calculated accordingly via

$$\int\limits_{\ell(a\to b)} f(z)\mathrm{d}z := \int_0^1 f(\ell(t; a, b))\dot{\ell}(t; a, b)\mathrm{d}t = \int_0^1 f(\ell(t; a, b))(b - a)\mathrm{d}t. \tag{4.15}$$

K^* Scattering Amplitude

As mentioned already, we use a Chew-Mandelstam BW in order to have the correct complex structure with only the relevant branch cuts for the BWM. Since the K^* has spin $S_{K^*} = 1$ and both daughters are scalars, we will have orbital angular momentum $L = 1$ in the decay. This would mean that the barrier factors are non-trivial, but this would introduce more complex structures that would complicate the integration process. Therefore, we only take the p^L-dependence to have the correct behavior at threshold as mentioned in section 3.3.1, equation (3.32). This means the used expression is

$$\begin{aligned} f_{K^*}(\sigma_3) &= p_3 \hat{f}_{K^*}(\sigma_3), \quad \text{with} \\ \hat{f}_{K^*}(\sigma_3) &= m_{K^*}\Gamma_{K^*} \Bigg/ \left(m_{K^*}^2 - \sigma_3 + m_{K^*}\Gamma_{K^*} \frac{\mathrm{Re}[2\mathtt{CM}(m_{K^*}^2, m_K^2, m_\pi^2)] - 2\mathtt{CM}(\sigma_3, m_K^2, m_\pi^2)}{\Phi_2(m_{K^*}^2, m_K^2, m_\pi^2)} \right). \end{aligned}$$

The $\sqrt{\lambda_3}$ of $p_3 = \sqrt{\lambda_3}/(2\sqrt{\sigma_3})$ will cancel with the corresponding factor in the denominator of the integrand in equation (4.9) removing its branch cuts as a direct consequence, which keeps the complex structure in σ_3 simple. We can rewrite equation (4.9) slightly, pulling everything independent of σ_3 out of the integral:

$$\hat{F}_{(1010)}(s, \sigma_1) = \frac{\sigma_1}{\lambda_{s1}\sqrt{\lambda_1}} \int_{\sigma_3^-(s,\sigma_1)}^{\sigma_3^+(s,\sigma_1)} \mathrm{d}\sigma_3 \underbrace{\frac{W(\sqrt{s}, \sqrt{\sigma_1}, \sqrt{\sigma_3}) \cdot \hat{f}_{K^*}(\sigma_3)}{\left((\sqrt{s} + \sqrt{\sigma_3})^2 - m_3^2\right) \cdot 2\sqrt{\sigma_3}}}_{=: g(s, \sigma_1, \sigma_3)}.$$

Splitting the integration path into two linear paths $\sigma_3^- \to \sigma_3^m$ and $\sigma_3^m \to \sigma_3^+$ via some midpoint between pseudo-threshold and threshold, e.g $\sigma_3^m = 0.2\,\mathrm{GeV}^2$, and employing equation (4.15), we have to calculate

$$\int g(s, \sigma_1) = \int_0^1 \mathrm{d}t \left[g\big(s, \sigma_1, \ell(\sigma_3; \sigma_3^-, \sigma_3^m)\big)(\sigma_3^m - \sigma_3^-) + g\big(s, \sigma_1, \ell(\sigma_3; \sigma_3^m, \sigma_3^+)\big)(\sigma_3^+ - \sigma_3^m) \right].$$

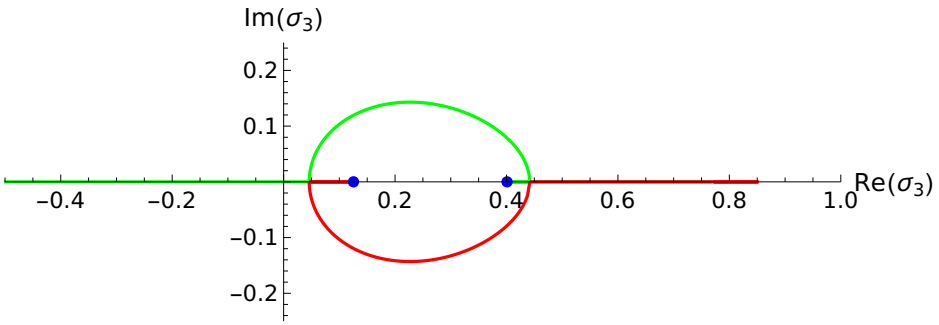

(a) $\varepsilon = 0\,\text{GeV}$

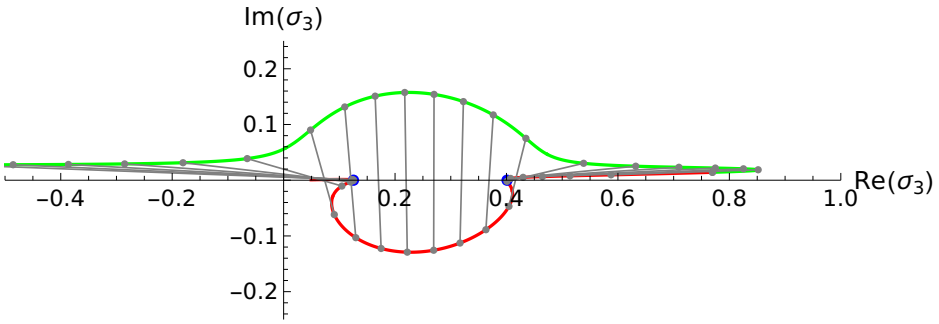

(b) $\varepsilon = 1/100\,\text{GeV}$

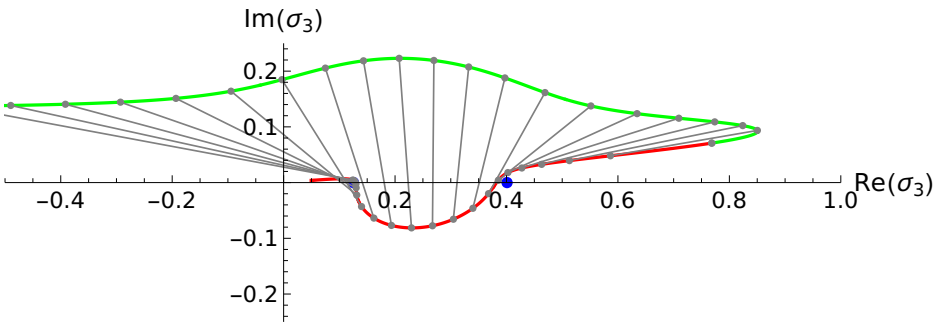

(c) $\varepsilon = 1/20\,\text{GeV}$

Figure 4.8: Parametric plot of σ_3^- (green) and σ_3^+ (red) as a function of σ_1 for fixed $s = (1.4168\,\text{GeV} + \mathrm{i}\,\varepsilon)^2$ for different values of ε as indicated in the corresponding captions. Both curves start on the right where they touch for $\sigma_1 = 4m_K^2$ (best visible in Figure 4.8(c)). The gray dots in the lower two plots indicate steps of $0.2\,\text{GeV}^2$ in σ_1 and the points for equal values are connected by a straight gray line. The two blue points indicate the pseudo-threshold $(m_K - m_\pi)^2$ and threshold $(m_K + m_\pi)^2$ for the decay of a K^*. This plot was created with `Mathematica`.

This lets us write down the expression for $\mathcal{M}_\Delta$ in the following way:

$$\mathcal{M}_\Delta(s,\sigma_1) = \frac{s}{\pi}\int_{4m_\pi^2}^{\infty} \frac{\rho_{f_0}(\sigma_1')\overbrace{\frac{\sigma_1'}{\lambda_{s1}'\sqrt{\lambda_1'}}\int g(s,\sigma_1')/\sqrt{\lambda_{s1}'}}^{\hat{F}_{(1010)}=}}{\sigma_1'-\sigma_1-\mathrm{i}\,\varepsilon}\mathrm{d}\sigma_1' = \frac{s}{16\pi^2}\int_{4m_\pi^2}^{\infty}\frac{(\lambda_{s1}')^{-3/2}\int g(s,\sigma_1')}{\sigma_1'-\sigma_1-\mathrm{i}\,\varepsilon}\mathrm{d}\sigma_1',$$

where inserting the half-phase-space factor $\rho_{f_0}(\sigma_1') = \frac{1}{16\pi}\frac{\sqrt{\lambda_1'}}{\sigma_1'}$ canceled some terms in the second step.

One can precalculate the inner integral on a two-dimensional (s,σ_1) grid and interpolate it between these grid points in order to calculate the outer σ_1' integral of $\mathcal{M}_\Delta$ later. However, this outer integral goes up to infinity, therefore, we have to perform a substitution to a finite interval in order for the precalculations to work. We choose the following

$$\frac{\sigma_1'}{1\,\mathrm{GeV}^2} = \tan(y), \quad \frac{\mathrm{d}\sigma_1'}{1\,\mathrm{GeV}^2} = \big(1+\tan^2(y)\big)\mathrm{d}y,$$
$$y_- = y(\sigma_1'=4m_\pi^2) = \arctan\left(\frac{4m_\pi^2}{1\,\mathrm{GeV}^2}\right), \quad y_+ = y(\sigma_1'=\infty) = \frac{\pi}{2}$$

and evaluate $\int g(s,\tan(y))$ already during the precalculations for values $y\in[y_-,y_+]$ for equidistant steps of 0.001. Inserting this substitution results in the final expression

$$\mathcal{M}_\Delta(s,\sigma_1) = \frac{s}{16\pi^2}\int_{y_-}^{y_+}\frac{\left(\lambda_{s1}'\big|_{\sigma_1'=\tan(y)}\right)^{-3/2}\left[\int g(s,\tan(y))\right]\big(1+\tan^2(y)\big)}{\tan(y)-\sigma_1-\mathrm{i}\,\varepsilon}\mathrm{d}y.$$

The whole numerator of the integrand is independent of the actual value of σ_1, therefore, we can also include the other two factors into the precalculation of $\int g$ for different values of s. Afterwards, we can perform the outer integration numerically for each of these values s and $\sigma_1 = m_{f_0}^2$.

4.3.5 Triangle-Amplitude Result

The result can be found in Figure 4.9 (solid lines) together with a comparison of the scalar case (dashed lines) from the dispersive approach, section 4.3.2. We see that the peak is at the same place as expected, but that the shape of the partial-wave-projected amplitude is slightly different. The left plot shows the calculations for a rescattering via a triangle with $K^{*0}K^+K^-$, while the right plot displays the result for a triangle with $K^{*-}K^0\overline{K}^0$. Since both these triangles come with the same Clebsch-Gordan coefficients[10] on the vertices, we will simply add them up for the theoretical model of the rescattering process.

Figure 4.10 shows the effect of slightly adjusting σ_1 by using different $f_0(980)$ masses. The result using the nominal PDG mass is plotted with solid lines. For simplicity we only show the

[10] Both the K^{*0} and the K^{*-} are the lower component of the respective isospin doublets, containing a d-quark and a $\bar{u}$-quark, respectively.

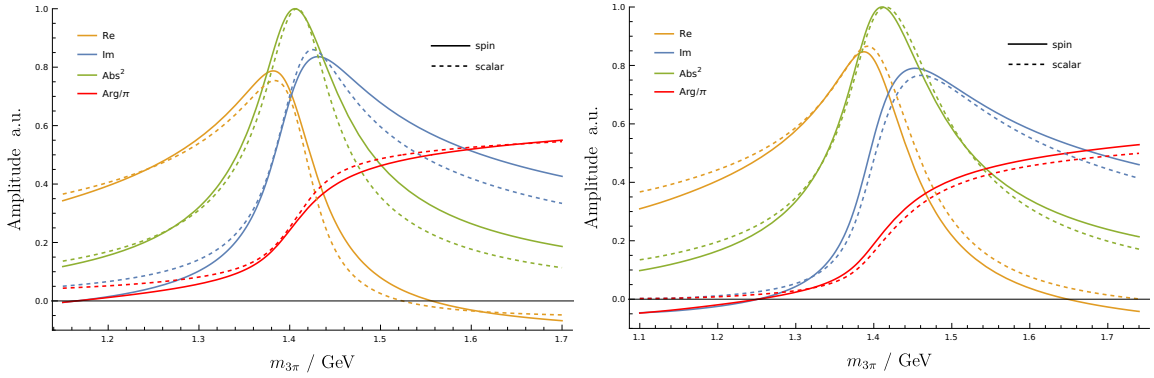

(a) $\pi^- K^+ K^-$ projection (b) $\pi^- K^0 \overline{K}^0$ projection

Figure 4.9: Comparison of the scalar triangle amplitude from the dispersive approach (dashed) to the result for the partial-wave projection approach including all spins and orbital angular momenta (solid). The colors indicate which function is applied on the triangle amplitude as detailed in the top-left legend. On the left the result is plotted for neutral $K^{*0}(892)$ and on the right for negatively charged $K^{*-}(892)$. The calculations and the creation of this plot are done with `Mathematica`.

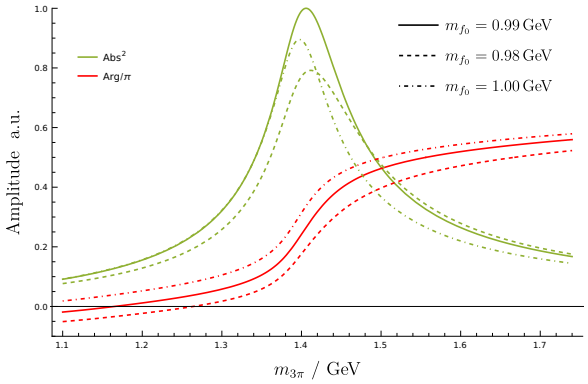

Figure 4.10: Comparison of the squared magnitude (green) and the complex phase (red) of the triangle amplitude $\mathcal{M}_\Delta$ for different $f_0(980)$ masses as indicated by the legend inside the plot. The calculations and the creation of this plot are done with `Mathematica`.

squared magnitude (green) and the complex phase (red) of the triangle amplitude $\mathcal{M}_\Delta$. Everything is normalized to the maximum of the nominal-mass amplitude.

Finally, we can have a look at the Argand diagram in Figure 4.11. We see that both the scalar model from the dispersive approach (dashed) and the one coming from the partial wave projection (solid) describe almost a full circle as it is the case for a normal resonance (dot-dashed green). This is true for the triangle amplitude alone (blue) and especially true for the full amplitude including the propagator of the source (red), here, a BWM for the $a_1(1260)$.

4.3.6 Other Triangles

The rescattering via a triangle diagram can create a signal that is very similar to an ordinary resonance. But the question arises, why this triangle involving kaons is so special. One can create such a

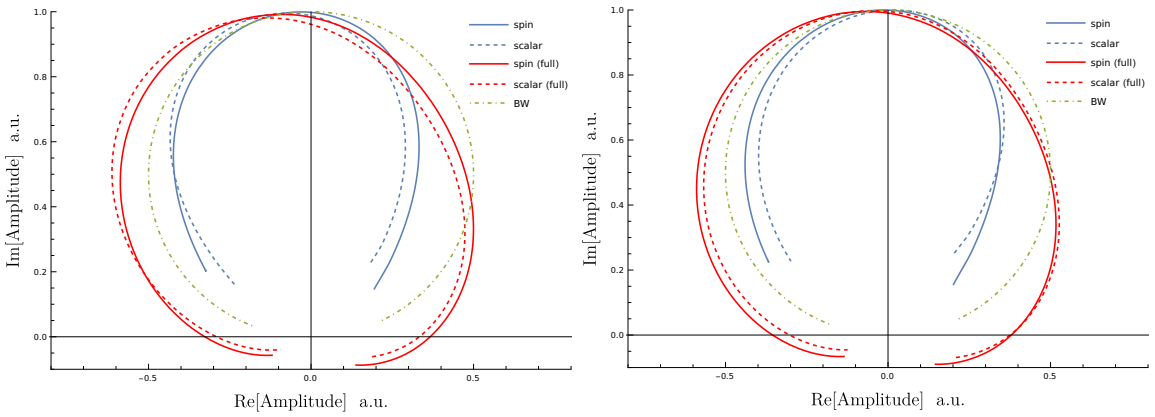

(a) $\pi^- K^+ K^-$ projection (b) $\pi^- K^0 \overline{K}^0$ projection

Figure 4.11: Argand diagrams of the scalar triangle amplitude from the dispersive approach (dashed) and the result for the partial-wave-projection approach including all spins and orbital angular momenta (solid), once alone (blue) and once multiplied by a BWM for the $a_1(1260)$ source (red). They are compared to the Argand diagram of a BWM for a hypothetical $a_1(1420)$ resonance (dot-dashed green). For easier comparison, rotations are applied to the Argand diagrams such that they all lie approximately at the same place. On the left the result is plotted for neutral $K^{*0}(892)$ and on the right for negatively charged $K^{*-}(892)$. The calculations and the creation of this plot are done with `Mathematica`.

rescattering process with any isobar ξ that the $a_1(1260)$ can decay into. First, we have the decay $a_1^-(1260) \to \xi\pi^-$, subsequently follows the decay $\xi \to \pi^+\pi^-$, and finally, the initial π^- can merge with the π^+ from the decay of the isobar to form the $f_0(980)$ of the final state, leaving the π^- of the isobar-decay as the bachelor particle.

Since calculations with the partial-wave-projection method are different if the spin of the isobar changes, we calculate their amplitudes with the method from the scalar case from section 4.3.1. There, we incorporate the width of the intermediate isobar via the replacement $m_\xi^2 \to m_\xi^2 - \mathrm{i}\, m_\xi \Gamma_\xi$, as it was mentioned at the end of section 4.3.2. In Figure 4.12, the resulting amplitudes (various grey dashed lines) are compared to the kaonic triangle (blue). In all cases we multiply the corresponding triangle amplitude with a BWM for the initial $a_1(1260)$ propagator. In case of the intensity (Figure 4.12(a)), we take the squared magnitude of the amplitude and multiply it by the corresponding two-body phase space. All triangles are compared to a simple model for the direct decay $a_1(1260) \to f_0\pi$ (red) and to a non-resonant background model (green) as it will be discussed in section 4.4.2. One observes that all other triangles as well as the direct decay show a similar behavior in the intensity as can be modeled by the non-resonant contribution. In the complex phase (Figure 4.12(b)), only the triangle involving kaons has a phase motion at 1.4 GeV. All other triangles obtain their phase motion from the multiplied $a_1(1260)$ propagator, which already starts to level off at the location of the $a_1(1420)$. Therefore, the non-resonant background model – that itself does not have a phase motion – should be able to take these other effects into account.

One important feature is the normalization. All triangles[11] are divided by the height of the scalar triangle involving kaons. Therefore, the y-axis shows the relative strength of these other triangles

[11] All, except the one calculated with the partial-wave-projection method. It is normalized to 1, since its model is quite different while the other triangles are all calculated with the same model and, therefore, the same prefactors.

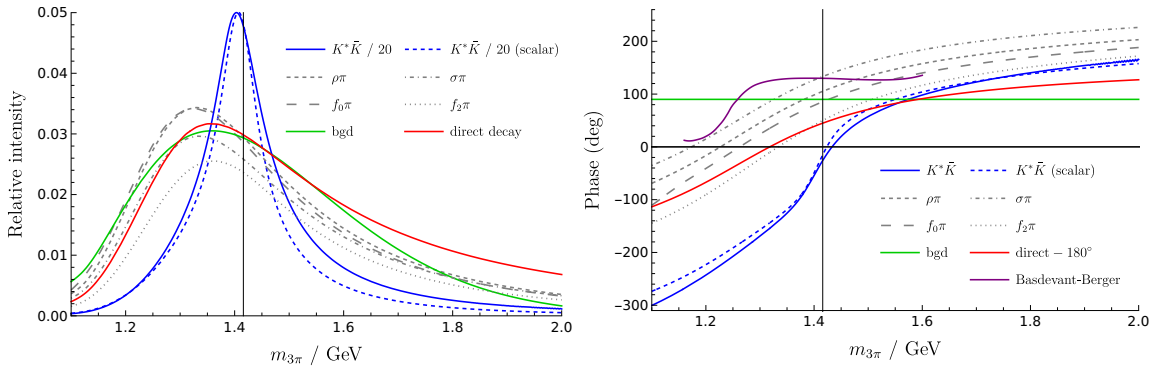

(a) (b)

Figure 4.12: Comparison of different triangles as indicated by the legend, always listing the initial decay before the rescattering. The left plot shows the expected intensity, i.e. the quasi-two-body phase space of the $f_0(980)\pi$ channel times the squared magnitude of the product of a BWM with energy-dependent width for the $a_1(1260)$ with the triangle amplitude of the respective channel. It is compared to the direct decay (red), i.e. the same quantity just without the triangle amplitude, and a phenomenological model for the non-resonant background (green), see equation (4.19). The right plot shows the complex phase of the respective amplitudes. The purple line indicates the predictions from the Basdevant-Berger model discussed in section 4.2.4 (FIG. 4 of [45]).

compared to the kaonic triangle. We see that one has to divide the kaonic triangle by a factor of 20 to be able to plot all of them at the same time. This factor will come in addition to the product of involved couplings in the triangle diagram if one wants to estimate the branchings of the different contributions.

If we want to understand, why the other triangles behave so differently, we have to investigate the complex structure of such a triangle amplitude, see Figure 4.13. First, we can use the definition of $x_\pm$ in equation (4.4) for the scalar triangle in section 4.3.1 and calculate the position of the triangle singularities by finding the two values $\sqrt{s}$ such that $x_+ = x_- =: x_p$. Note that these singularities move downwards into the complex plane if the intermediate isobar has a finite width $\Gamma_\xi > 0$. One can calculate the complex position of the singularity, by performing the replacement $m_\xi^2 \to m_\xi^2 - \mathrm{i}\, m_\xi \Gamma_\xi$, affecting the real part of it only slightly.

Since they are logarithmic branch points (empty and filled circles), we know that they must have branch cuts (dotted and zigzag lines), which we can choose such that they connect the branch points to each other. To find out on which Riemann sheet they live, we can calculate the corresponding $y_+ = y_- =: y_p$ with equation (4.3) for each given singularity and check the conditions $x_p > 0, y_p > 0, x_p + y_p < 1$. Only if all three conditions are met, we will have a pinch singularity during the final integration and, thus, a singularity on the second Riemann sheet (filled circle). This only happens for one of the singularities of the kaonic triangle. Otherwise it has to be located on a higher Riemann sheet (empty circle) and, therefore, its tail has to propagate around the corresponding branch point of the two-body phase space of the initial decay, whose branch cut creates the higher Riemann sheets.

Speaking of phase spaces, we have to consider several ones here. First of all, we have the unitarity cut starting at the 3π threshold $3m_\pi$. This splits the complex plane and opens a gate to the second Riemann sheet, where the pole of the $a_1(1260)$ resonance lies. When using a BWM with energy-dependent width for the $a_1(1260)$ or a Chew-Mandelstam BW, we have the two-body phase space of its decay into the isobar-bachelor system appearing in its denominator, which creates a branch point at

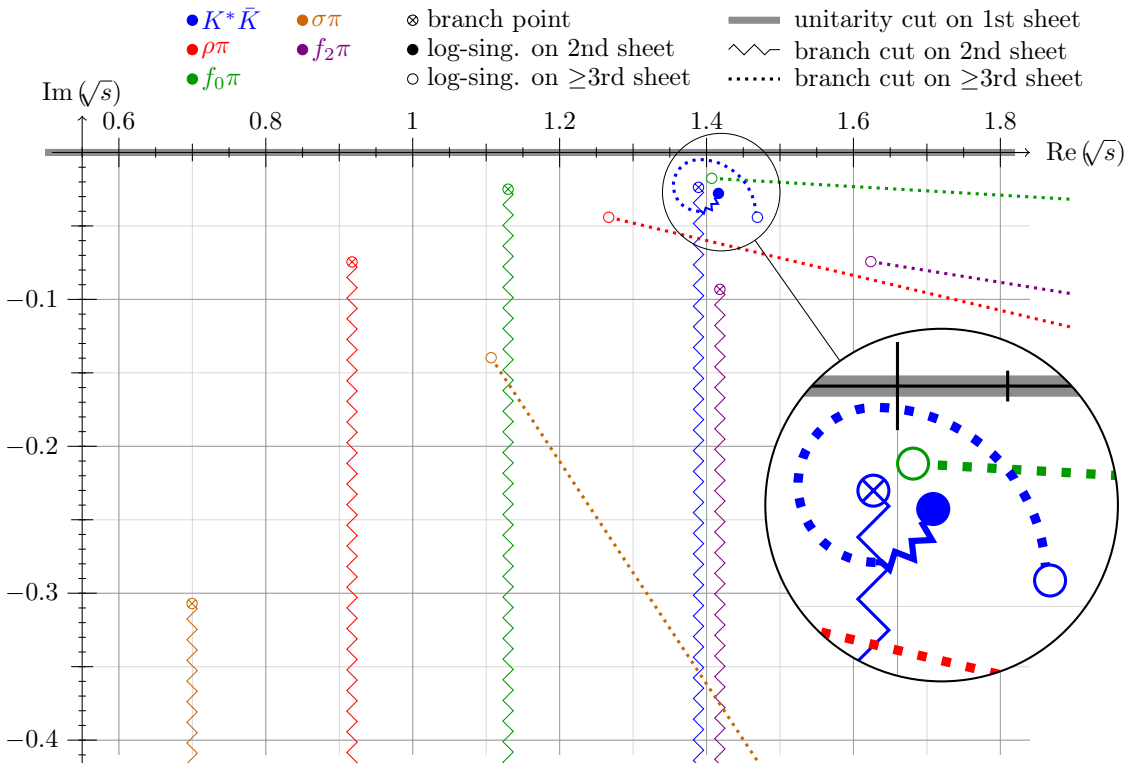

Figure 4.13: Sketch of the location of the singularities from triangle diagrams. Different colors represent complex structures coming from the indicated initial decay of a rescattering to $f_0\pi$. Points and lines are explained in the main text.

$m_\xi + m_\zeta$. However, if the isobar is an unstable particle, this branch point moves downwards into the complex plane, similar to the singularities before. One can calculate the position again by replacing $m_\xi^2 \to m_\xi^2 - \mathrm{i}\, m_\xi \Gamma_\xi$ and finding the zero of the Källén function inside the two-body phase space, equation (A.7). The location of these branch points is indicated by crossed circles in Figure 4.13 and the corresponding branch cuts (thin zigzag lines) are rotated downwards to reduce the amount of overlapping lines in the picture.

Figure 4.13 only provides an artistic view of the complex structures, but indeed, when comparing with the squared magnitude of the triangle amplitudes for the different rescattering processes, see Figure 4.14, we see that the other triangles all peak slightly left of where their corresponding phase-space branch point lies (crossed circles in Figure 4.13 correspond to vertical lines in Figure 4.14). The only exception is the kaonic triangle that peaks on the right, where the real part of its singularities lies.

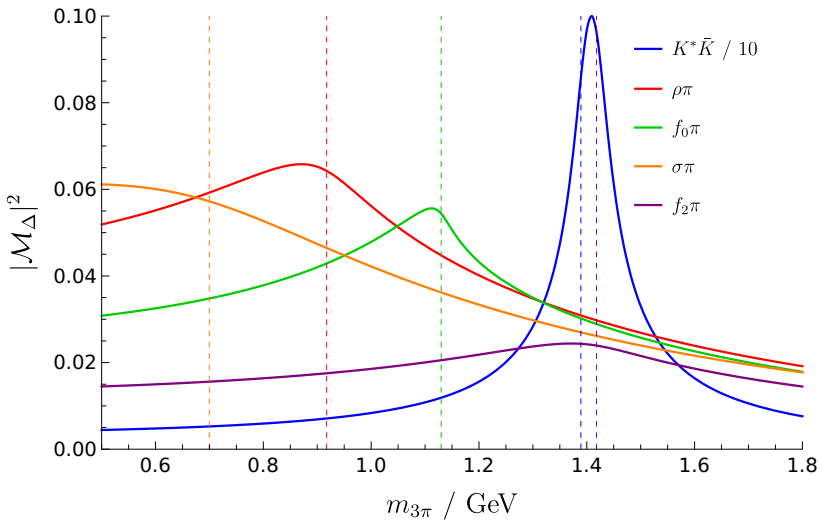

Figure 4.14: Comparison of the squared magnitude of the bare triangle amplitude calculated for scalar triangles according to section 4.3.1 for different involved particles as indicated by the legend.

4.4 Fit Model

Now, we want to fit the previously calculated theoretical model to the COMPASS data to see if it can describe the observed resonance-like $a_1(1420)$ signal. Such a fit with a slightly different model was already published in [50]. Fitting the complete set of all 88 waves extracted by the corresponding 3π PWD would be not advisable, since we would drown in systematic uncertainties from fitting all other waves. Therefore, we have to make a selection with as few waves as possible, one of which definitely has to be the $1^{++}0^+ f_0(980)\pi$ P wave where the $a_1(1420)$ signal was found, using the labelling of partial waves as introduced in section 3.4.3. Since the $a_1(1260)$ is the source for the rescattering, we also need a wave that contains this resonance, namely the $1^{++}0^+ \rho(770)\pi$ S wave. However, this wave also contains a huge amount of background coming from Deck-like processes, where no resonance is produced and instead a t-channel exchange of the isobar or a pion takes place (see Figure 4.15). This means that we need another wave which can serve as an interferometer to fix the relative phases between signal and background. We choose the $2^{++}1^+ \rho(770)\pi$ D wave containing a very clean signal of the $a_2(1320)$ resonance with very little background contamination.

4.4.1 General Fit Model

According to equation (3.52), the number of events in a partial wave (w) for a given (m_X, t') slice can be calculated via

$$\frac{\mathrm{d}N_{(w)}}{\mathrm{d}m_X \mathrm{d}t'} \propto m_X \int \mathrm{d}\tau \left|\mathcal{M}_{(w)}\right|^2 \Phi_3(\tau). \tag{4.16}$$

Employing the isobar model allows us to split off the two-body scattering amplitude f_ξ of the isobar from the matrix element $\mathcal{M}$ which makes the remainder $\tilde{\mathcal{M}}$ independent of the kinematic variables τ. Therefore, we can perform the τ-integral beforehand, resulting in the quasi-two-body phase space $\tilde{\Phi}_2$

(see appendix A.1.4 for details)

$$\frac{\mathrm{d}N_{(w)}}{\mathrm{d}m_X \mathrm{d}t'} \propto m_X \left|\tilde{\mathcal{M}}_{(w)}\right|^2 \underbrace{\int \mathrm{d}\tau \left|f_\xi\right|^2 \Phi_3(\tau)}_{=:\tilde{\Phi}_2} =: \mathcal{F}_{(w)}(m_X, t'), \tag{4.17}$$

where one can also already incorporate the Bose symmetrization due to having two identical bosons in the final state.

But the advantage of a PWD is that it does not only provide us with intensities of partial waves, but also with interferences between different partial waves. Let us assume that we have interference between wave (w_1) and wave (w_2). Than we can model this interference with

$$\mathcal{F}^{(w_2)}_{(w_1)}(m_X, t') := m_X \tilde{\mathcal{M}}^*_{(w_1)} \tilde{\mathcal{M}}_{(w_2)} \sqrt{\tilde{\Phi}_2^{(w_1)} \tilde{\Phi}_2^{(w_2)}}, \tag{4.18}$$

where we use the same models for $\tilde{\mathcal{M}}_{(w_i)}$ as for the intensities of the respective partial waves.

This means that in total we can fit one intensity for each wave and one real and one imaginary part for each pair of waves. Therefore, for the chosen set of three partial waves we will have a total of 9 data sets to fit. And this for each of the 11 t' slices.

As for the model of the remaining matrix element $\tilde{\mathcal{M}} = \mathcal{M}_{\text{sig}} + \mathcal{M}_{\text{bgd}}$, we can further split this into a signal component $\mathcal{M}_{\text{sig}}$ and a background component $\mathcal{M}_{\text{bgd}}$ that will be added coherently, allowing for constructive and destructive interference. In the following we will specify the models that are used for the three selected partial waves.

Nomenclature and Jargon

The quantity $\mathcal{F}_{(w)}$ as defined in equation (4.17) is technically the phase-space-integrated intensity as of equation (3.66) and corresponds to the diagonal elements of the SDM of equation (3.69). However, in reality the prefix "phase-space-integrated" is usually dropped and we will do so from now on as well simply calling it intensity.

Additionally, $\mathcal{F}^{(w_1)}_{(w_2)}$ of equation (4.18) that corresponds to the off-diagonal elements of the SDM sometimes is referred to as "relative phase" since one usually plots only its complex argument to see the relative phase motion between two partial waves.

Considering the transition amplitude $\mathcal{T}^{\epsilon}_{w}$ as defined in equation (3.64), we see that the quasi-two-body phase space $\tilde{\Phi}_2^{(w)}$ of partial wave (w) directly corresponds to the respective diagonal element of the integral matrix I^{ϵ}_{ww} as defined in equation (3.61). This equation also highlights once more the connection between the matrix element $\tilde{\mathcal{M}}_{(w)}$ and the product of the production amplitude $\mathcal{P}$ with the mass-dependent part of the decay amplitude F^{ϵ}_{w}. As before, we will however neglect the m_X dependence of the production amplitude $\mathcal{P}$ and take its t' dependence into account by using independent fit parameters for the signal strength of each t' slice.

4.4.2 Phenomenological Deck-Background Model

Before we go into detail on the specific amplitude model for each wave, let us discuss the general structure of the background model. The so-called Deck process is depicted in Figure 4.15 and also

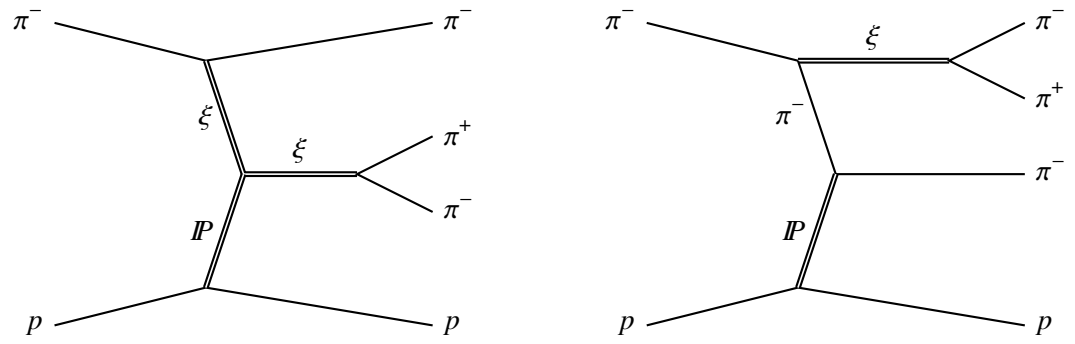

Figure 4.15: Two diagrams for a Deck-like background for the $\pi^-\pi^+\pi^-$ final state without an intermediate three-body resonance.

appears for a $\pi^-\pi^+\pi^-$ final state, but instead of producing a three-body resonance, we will have a t-channel exchange of either the pion that absorbs the Pomeron from the proton target producing the isobar at the upper vertex, or the pion continues at the upper vertex and we exchange the isobar that absorbs the Pomeron.

It is not possible to kinematically separate this process from the resonance production that we are interested in. Additionally, it was shown by [47] that this background contributes to almost all partial waves. Therefore, a phenomenological description is used as it is described in [53] (section 3.4.1). It has the following parametrization that is flexible enough to capture the effect, but not too flexible to be able to describe the waves without resonances:

$$\texttt{Bgd}(m_X; a, b, \{c_n\}) = a(t') \left(\frac{m_X - m_{\text{thr}}}{m_{\text{thr}}} \right)^b \exp\left(-\tilde{q}^2 \sum_n c_n \cdot (t')^n \right). \tag{4.19}$$

First, we have a complex parameter a that provides the possibility to scale the amplitude, while also allowing to change the interference of the background with the signal. For each t' slice we will have a different set of two real parameters, magnitude and phase of a. The second factor serves as a threshold term, where $m_{\text{thr}} = 0.5\,\text{GeV}$ is fixed to a value slightly higher than the $m_{3\pi}$ threshold at 0.42 GeV, and b being a and positive real fit parameter (~ 1), equal for all t' slices. The last term has the purpose of damping the background amplitude at higher masses, which is achieved by the squared break-up momentum $\tilde{q}$ calculated from the quasi-two-body phase space of the current partial wave. It gets multiplied to a polynomial in t', of which the fit parameters c_i are real valued and the same for all t' slices. It allows for the background shape to change with t', while the signal models are independent of it.

4.4.3 $1^{++}0^+\,\rho(770)\pi\,\text{S}$ Signal Model

This wave, which we will call $\rho\pi$ S-wave from now on, contains the $a_1(1260)$ as the main resonance. We model this with a BWM with energy-dependent width using the quasi-two-body phase space of the $\rho(770)\pi$ S decay channel in the denominator of the BW. This model comes with two real-valued parameters, the mass and the width of the resonance. Additionally, a strength parameter $A(t')$ enters as a different set of two parameters for each t' slice, the magnitude and the complex argument of A.

For the background we use a second order polynomial in t' meaning we have in total four parameters

that are independent of t', specifically b, c_0, c_1 and c_2. For each t' slice we have two real parameters from a.

In total we will have $2 + 2 \cdot 11 = 24$ signal parameters and $4 + 2 \cdot 11 = 26$ background parameters for this wave.

4.4.4 $1^{++}0^+$ $f_0(980)\pi$ P Signal Model

In the following, we will call this one the $f_0\pi$ P-wave, and we use the same $a_1(1260)$ BWM for the source of the rescattering as for the $\rho\pi$ S-wave. Since the $\rho\pi$ S-wave has a much stronger intensity – and with this also a lot smaller error bars – the $a_1(1260)$ mass and width will mostly be fixed by that wave. Therefore, we will not count them as parameters for the $f_0\pi$ P-wave. This BWM will be multiplied by the theoretical amplitude calculated in section 4.3.3 (the sum of both charge configurations in the loop, since the involved isospin couplings are equal) that by itself comes without parameters[12]. Since the possible fit range of this wave is smaller and we still need eleven complex strength parameters $A(t')$ for each t' slice, we will simplify the background model to only contain the exponential factor constant in t', meaning only the forced-positive parameter $c_0 > 0$ besides of the complex $a(t')$.

This wave will add $2 \cdot 11 = 22$ signal parameters and $1 + 2 \cdot 11 = 23$ background parameters.

4.4.5 $2^{++}1^+$ $\rho(770)\pi$ D Signal Model

This wave will be simply called $\rho\pi$ D-wave and due to the fact that the global complex phase of the full amplitude is unobservable, we will fix the strength parameters $A(t')$ of the signal to be positive real. Other than that the signal will be a Flatté BWM as described in section 3.3.2, with $a_2(1320)$ mass and width as free parameters, where we will use the $\rho\pi$ D channel with a fixed branching of $r = 80\,\%$ and the $\eta\pi$ D channel with the remaining fraction of $(1 - r) = 20\,\%$ in equation (3.37). The quasi-two-body phase space appears for the first component of the width and for the $\eta\pi$ D-channel component we will use the normal two-body phase space together with a Blatt-Weisskopf factor for $L = 2$.

The background will be the full model as for the $\rho\pi$ S-wave. This brings us to a total of $2+1\cdot 11 = 13$ signal parameters and $4 + 2 \cdot 11 = 26$ background parameters.

All three waves together amount to $50 + 45 + 39 = 134$ real-valued fit parameters.

4.4.6 $a_1(1420)$ Breit-Wigner Model

Since we need a second fit model to be able to compare it with the rescattering interpretation in form of the previously defined Triangle-Singularity Model (TSM), we will replace the $f_0\pi$ P-wave signal parametrization by a BWM for the $a_1(1420)$. Since we do not want to imply any knowledge on the possible decay channels of a hypothetical new resonance $a_1(1420)$, we will use a BW with fixed width. This means we will have two parameters more compared to the rescattering model, the mass and the width of the $a_1(1420)$, giving us a total of 136 real-valued fit parameters. The background models as well as the signal models for the other two waves will not be changed.

[12] The masses and widths of the particles in the loop are taken from the PDG and all omitted couplings will be absorbed by the strength parameter of the BWM.

4.4.7 Fitting Procedure

We will use the usual definition of a χ^2 for the fitting procedure, since it provides us with a simple way of comparing a model to the data while incorporating the uncertainty of the data as well:

$$\chi^2 = \sum_i \left(\frac{\mathcal{F}(x_i) - y_i}{\sigma_i} \right)^2 . \tag{4.20}$$

The sum will go over all data points (x_i, y_i) of the previously discussed 9 data sets, where x_i is given by the corresponding (m_X, t')-bin of the PWD results and y_i denotes the corresponding value of the intensity or the real and imaginary part of the interference with its experimental uncertainty σ_i. $\mathcal{F}$ is the model of the corresponding data set evaluated for a given set of fit parameters.

We use the minimizer `MINUIT2` to find the optimal solution for $\mathcal{F}$ that minimizes the χ^2. Since during this procedure we might run in a local minimum, it is common practice to perform the fit several times with random starting parameters and take the minimum with the smallest χ^2 as the best fit. However, we have a lot of fit parameters which makes convergence of the fit unlikely. We solve this by using the following fit strategy:

1. We fit only the first t' slice using random starting parameters for the common parameters of all t' slices (m, Γ, b, $\{c_i\}$) as well as the parameters specific for this slice (A and a).

2. We temporarily fix the common parameters of all t' slices (m, Γ, b, $\{c_i\}$).

3. We fit the other t' slices one-by-one, always using the slice-specific parameters of the previous slice as starting parameters.

4. After fitting all slices separately like this, we release all fit parameters and do a final fit over all t' slices combined.

If at any point during this procedure the χ^2 value get larger than the arbitrarily set limit of 10^{10}, or any of the fit parameters results in "not a number" (`NaN`), the fit attempt will be discarded and a new attempt with new random starting parameters will be started.

Usually, one would expect the $\chi^2_{\text{red}} = \chi^2 / N_{\text{dof}}$ of a fit to reach 1 at the end of a fit. However, this is only true for independent data points which is not the case here, since the three interferences are dependent on each other and on the intensities via

$$\mathcal{F}^{(2)}_{(1)} + \mathcal{F}^{(3)}_{(2)} + \mathcal{F}^{(1)}_{(3)} = 0 \qquad \text{and} \qquad \left| \mathcal{F}^{(j)}_{(i)} \right|^2 = \mathcal{F}_{(i)} \cdot \mathcal{F}_{(j)} .$$

Additionally, looking at the data itself and the provided statistical uncertainties coming from the previously performed PWD, we see some places where these uncertainties are obviously underestimated resulting in a too large χ^2_{red}. Let us slightly jump ahead and shortly discuss two regions in the first t' slice where this is very obvious. For this, we have a look at Figure 4.16, where so far only the black data points coming from the PWD are of interest for us.

The first one appears in the complex phase of the interference between the $\rho\pi$ S wave and the $f_0\pi$ P wave, i.e. the plot in the first row and second column of Figure 4.16. In the region $m_{3\pi} \leq 1.5\,\text{GeV}$ we see a continuously rising relative phase. Then, in the range between 1.5 GeV and 1.6 GeV, we see that the relative phase starts to drop for two data points and suddenly jumps up again continuing its

rise. This jump corresponds to ~ 33 deg or $\sim 9.7\sigma$, where σ denotes the uncertainty of the data point before the jump.

The second location can be found in the plot directly to the left, the intensity of the $\rho\pi$ S wave, directly at the peak. The data points at 1.13 GeV and 1.17 GeV lie both approximately at 215 k events. The point in between, at 1.15 GeV, as well as the two points to the left and right of this region lie at ~ 205 k events. The uncertainty of these points is given as roughly $\sigma \sim 1.6$ k events, which means that we jump up by 10 k events or 6.3σ, then, down by the same amount, and up and down again. A fit model might be able to describe the outer four points, however the central point will always be far away from a continuous model curve.

4.4.8 Fit Quality

Since we want to compare two competing models, we need to define something that quantifies the goodness of the fit. For this, we will use a similar construction to the χ^2 as defined in the previous section 4.4.7. However, since both fit models are very similar, it does not make sense to include all data points here. Therefore, we will restrict the sum in equation (4.20) only to the data points directly related to the $a_1(1420)$ signal, meaning the intensity of the $f_0\pi$ P-wave and the interference of it with the $\rho\pi$ S-wave. In principle also the interference between $f_0\pi$ P-wave and $\rho\pi$ D-wave contains information of the $a_1(1420)$ signal. But the sum of all three interferences is zero by construction and since the interference between the $\rho\pi$ S-wave and the $\rho\pi$ D-wave can be assumed to be almost completely fixed by their respective models due to the smaller experimental uncertainties, we will not gain extra information by including both $f_0\pi$ P interferences. Also we will not use real and imaginary part of the interference, but instead only the complex phase[13], since this is what we use for plotting of the fit results and, thus, only what we display will be used to determine the quality of the fit.

Since the rescattering model has two parameters less than the $a_1(1420)$ BWM, we will divide the quantity by the number of degrees of freedom $N_{\text{dof}}^{a_1(1420)}$, specifically the number of included data points minus the number of fit parameters related directly to the $f_0\pi$ P-wave as defined in sections 4.4.4 and 4.4.6. Here is the final expression of the reduced-χ^2 equivalent:

$$\mathcal{R}^2_{\text{red}} := \frac{1}{N_{\text{dof}}^{a_1(1420)}} \sum_{a_1(1420)} \left(\frac{\mathcal{F}(m_X, t') - y_i(m_X, t')}{\sigma_i} \right)^2 . \tag{4.21}$$

We still should not expect this number to be equal to 1, however its size will provide a good measure of compatibility and we can consider a model to fit the data better than another model if its $\mathcal{R}^2_{\text{red}}$ is smaller.

Considering only the two mentioned data sets, we have a total of $2 \times 25 \times 11 = 550$ fitted data points. Reducing them by 45 or 47 fit parameters for the TSM and the BWM, respectively, leads to $N_{\text{dof}}^{\text{TSM}} = 505$ and $N_{\text{dof}}^{\text{BWM}} = 503$.

[13] Since the complex phase is periodic, the points at +180 deg and −180 deg are close to each other. To take this into account, we will always calculate the contribution from a data point y_i to $\mathcal{R}^2_{\text{red}}$ with the values y_i, $y_i + 360$ deg and $y_i - 360$ deg, and use the minimum.

4.5 Fit Results

We will now discuss the results of the model fit as described in the previous section. A comparison of the TSM (solid lines) with the BWM (dashed lines) for the first of the eleven t' slices can be found in Figure 4.16, the remaining ten in appendix C.3. The signal contribution (blue) is obtained by setting the strength parameter of the background to zero. On the other hand, the non-resonant background contribution (green) is obtained by setting the strength parameter of the signal function to zero. The full fit model (red) is the coherent sum of these two contributions. Therefore – due to interference – it can be in some regions larger than the separate contributions and in other regions smaller. The diagonal plots show the intensities $\mathcal{F}_{(w)}$ and on the off-diagonal one can find the complex phase of the interference $\mathcal{F}^{(w_2)}_{(w_1)}$.

As a first observation, we can see that the fit models do not differ much for the $\rho\pi$ S and $\rho\pi$ D waves. This shows that the assumption was valid according to which the resonance parameters of the $a_1(1260)$ are almost fully determined by the fit to the $\rho\pi$ S wave and can, therefore, be omitted during the determination of the number of degrees of freedom for equation (4.21).

Secondly, we see that both models describe the $f_0\pi$ P wave similarly well by eye. Calculating the $\mathcal{R}^2_{\text{red}}$ according to equation (4.21) yields $\mathcal{R}^2_{\text{red,TSM}} = 4.59$ for the TSM and $\mathcal{R}^2_{\text{red,BWM}} = 4.87$ for the BWM. Remember that these values also include the contributions from the central column of plots of the other ten t' slices in appendix C.3. This means that the TSM shows a slightly better compatibility with the data than the opposing BWM. This is even more striking since the TSM does not have a fit parameter that lets us adjust the position and width of the signal peak (solid blue line). It is completely determined by the particles involved in the triangular loop. On the other hand, the peak of the BWM signal (dashed blue line) can be shifted by adjusting the mass parameter and broadened or narrowed by its width parameter.

Having a look at the other t' slices we see that especially in the third one (the central pad of the second Figure in appendix C.3) the peak in the $f_0\pi$ P intensity is not very well described by the TSM. Not even the BWM describes it very well despite its capability of shifting the position of the peak freely (although not differently for each t' slice) which could indicate the presence of systematic problems of the underlying PWD as already discussed with the two regions in the first t' slice at the end of section 4.4.7. Having said that, the fit – and with this the $\mathcal{R}^2_{\text{red}}$ – is mainly dominated by the corresponding relative phase with the $\rho\pi$ S wave, since it has much smaller uncertainties than the $f_0\pi$ P intensity due to its relation to the $\rho\pi$ S intensity: $\left|\mathcal{F}^{f_0\pi\,\text{P}}_{\rho\pi\,\text{S}}\right|^2 = \mathcal{F}_{\rho\pi\,\text{S}}\mathcal{F}_{f_0\pi\,\text{P}}$. Thus, although the deviation at the peak seems to be striking, it only contributes minorly to the overall $\mathcal{R}^2_{\text{red}}$.

In the following, we discuss some performed systematic studies in order to confirm that the slightly favored TSM is not just a coincidence due to systematic uncertainties of the PWD or the resonance-model fit.

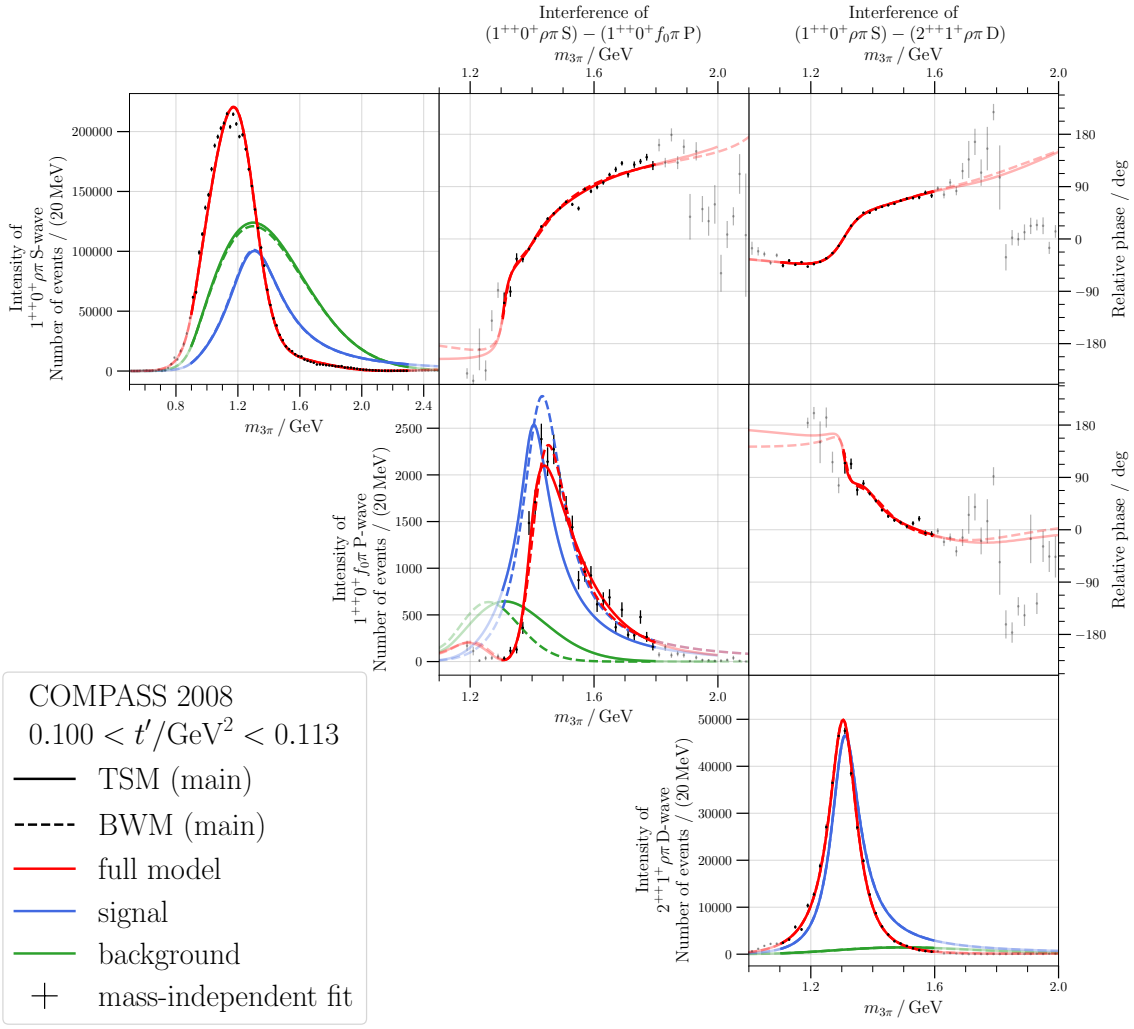

Figure 4.16: Result of the main fit as described in 4.4. The TSM (solid) is compared to the BWM (dashed). The signal and background separation of the BWM is indicated by the same colors as for the TSM. Displayed are the coherently added contributions of the signal (blue) and the non-resonant background (green). The full fit function is displayed with the red curve. The diagonal plots show the intensities of the respective waves as indicated by the labels. The off-diagonal plots show the relative phase between the corresponding waves on the corresponding row and column. The transparent lines indicate the extrapolation of the fit function outside of the fit range.

4.6 Systematic Studies

Since the $\rho\pi$ S and $\rho\pi$ D waves are very similar for the two competing models, we will only focus on the central column of plots in Figure 4.16 and will only compare the competing models via these two plots. For easier comparison, we will only display the $f_0\pi$ P intensity of the first t' slice due to it having the smallest uncertainties and, thus, having a higher impact on $\mathcal{R}^2_{\text{red}}$. We do not split the relative phase into its separate model components because the non-resonant background does not have a mass-dependent phase. So we will show a selection of three t' slices, specifically slices 1, 4 and 7. This style is inspired by the original publication of the $a_1(1420)$ signal, see [6] and Figure 4.1.

For the intensity plot, we use the same color code as before: red for the full fit model, blue for the signal contribution, and green for the non-resonant background. Its legend indicates which model corresponds to the solid lines and which to the dashed lines. We either compare the main TSM with a slightly modified version of it, or we compare the TSM to the BWM after changing the general fit model or the underlying fitted data. For the relative phase the different colors always indicate the data points as well as the full fit model for one of the three displayed t' slices. To make them more visible, the first slice is shifted up by 45 deg and the last displayed slice is shifted down by 45 deg as also indicated by the legend.

Figure 4.17 shows how this representation looks like for the comparison of the main fit with the TSM and the BWM as presented in the previous section.

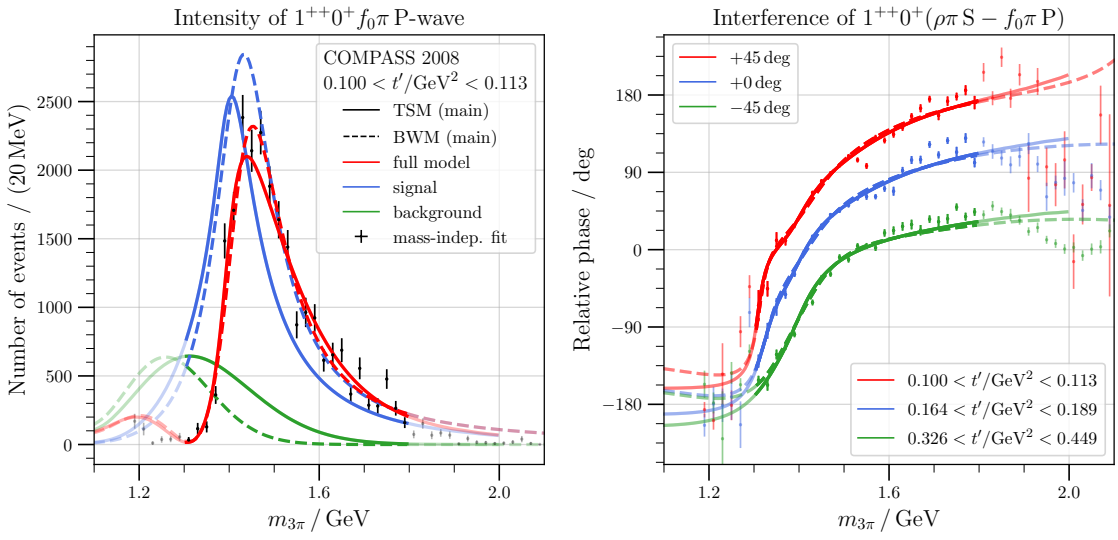

Figure 4.17: Compact representation of Figure 4.16 and the plots in appendix C.3. For explanations on the color code and what is plotted refer to the plot legends as well as the main text.

The comparison of the $\mathcal{R}^2_{\text{red}}$ values for the different models can be found in Figure 4.24 at the end of this section, as well as in Table C.1 in appendix C.4.

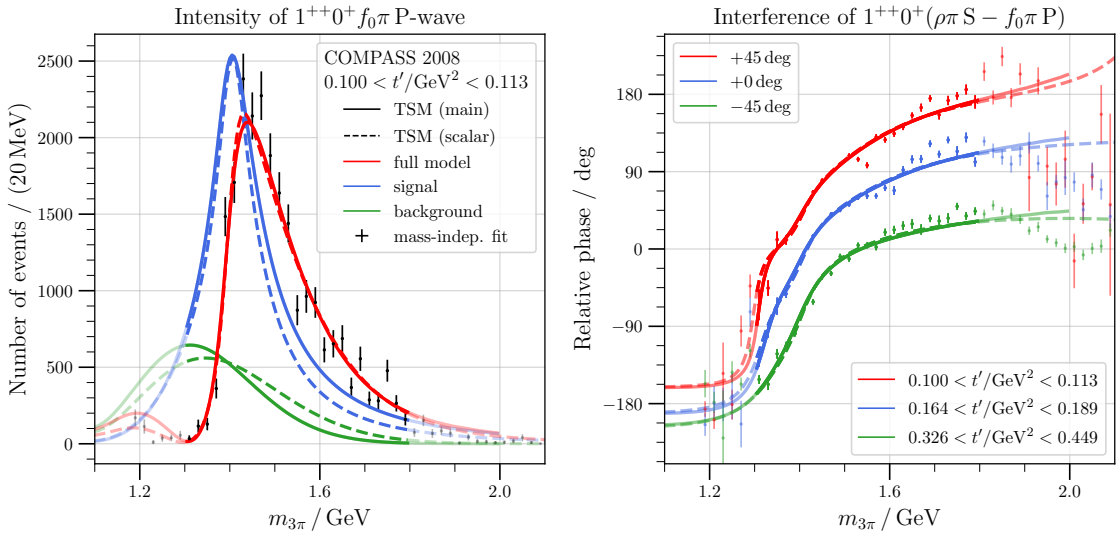

Figure 4.18: Comparison between main TSM (solid) and scalar TSM (dashed).

4.6.1 Variation of the Fit Model

In this section, we vary the fit model slightly to see how it affects the fit quality. The resulting $\mathcal{R}^2_{\mathrm{red}}$ comparisons of these models are depicted as green points in Figure 4.24.

Dispersive Scalar Triangle Model

As a first study, we perform the resonance-model fit using the scalar model from the dispersive approach, section 4.3.2, and compare it to the main TSM, see Figure 4.18. A similar fit was already performed in [26] as a first test of the rescattering interpretation.

We see that both fit models show very similar agreement with the data. This demonstrates that the much easier calculable scalar model provides a good approximation for first investigations. However, we see that the proper model, which includes the involved spins and orbital angular momenta, moves the needed background contribution slightly further to lower resonance masses outside of the peak region. This is possible due to the slower fall-off of the high-mass tail of the triangle amplitude. Regarding the phase motion, no major differences between the two models can be observed.

Include Direct Decay

As a next study, we also include the so far neglected direct decay of $a_1(1260) \to f_0\pi$ without intermediate rescattering. However, this comes with an increase in the amount of fit parameters, since each t' slice brings two more real parameters, the strength of the direct production and its complex phase. Although it brings a reduction in the $\mathcal{R}^2_{\mathrm{red}}$ value compared to the main fit simply due to the bigger flexibility of the model, it also comes with a reduction in fit stability.

The comparison between the TSM (solid lines) and the BWM (dashed lines) each with an added direct-decay component in the $f_0\pi$ P wave can be found in Figure 4.19. There, the two signal

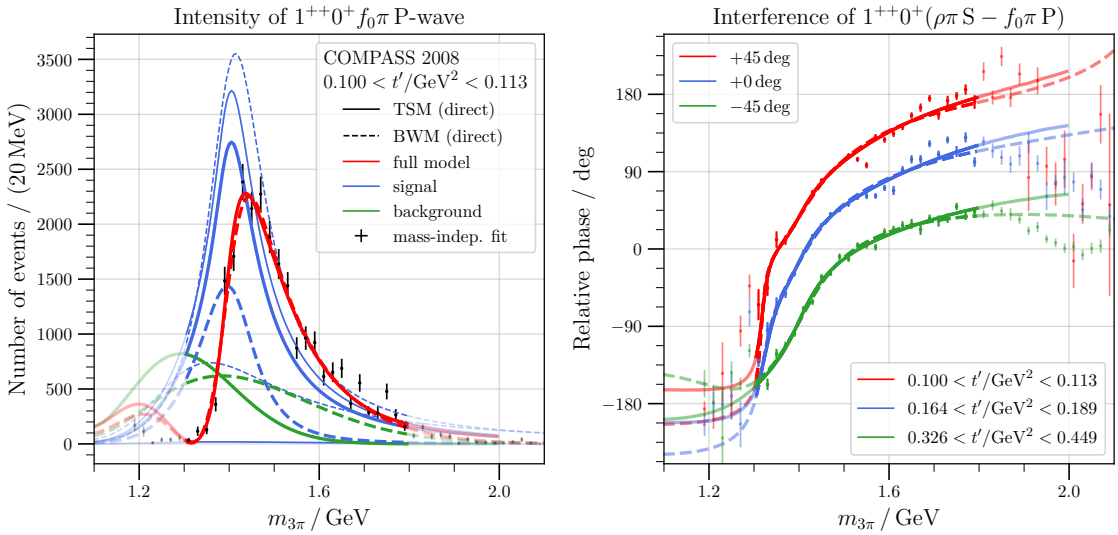

Figure 4.19: Comparison between TSM (solid) and BWM (dashed) where both include an extra component for the direct decay $a_1(1260) \to f_0\pi$. The thinner blue lines correspond to the two components of the signal as discussed in the main text.

components are depicted with the thinner blue lines and the thick line corresponds to their coherent sum. In case of the TSM (solid lines), the line close to zero corresponds to the direct decay $a_1(1260) \to f_0\pi$ and the stronger one to the component including the rescattering. On the other hand for the BWM (dashed lines) the direct-decay component behaves very similar to the non-resonant background component (dashed green) and the full signal component is only twice as large, indicating strong destructive interference between the very strong $a_1(1420)$ component and the $a_1(1260)$ component.

While the TSM model does not change drastically compared to the main model in Figure 4.17, the BWM does. It gets more similar to the TSM (red lines are overlapping strongly) and the background peak moves inside of the fit region. This indicates that the fit has troubles separating the signal from the background, showing that the initial assumption was accurate that the background can also incorporate the direct decay.

Non-Symmetrized Phase Space

This is a simplification of the fit model and it was done in order to see how important a proper treatment of the quasi-two-body phase space is. Here, we calculate the quasi-two-body phase space according to appendix A.1.4 without symmetrization of the amplitude with respect to the exchange of the two π^- of the final state, instead of normally taking the integral matrices as introduced in section 3.4.5.

Comparing Figure 4.20 with the main fit in Figure 4.17, we see that with the non-symmetrized phase space both TSM and BWM get very slightly closer to each other. Although the $\mathcal{R}^2_{\mathrm{red}}$ increases slightly for the non-symmetrized approximation, the general differences compared to the symmetrized case is not very big, thus, it can serve as a good approximation for first tests.

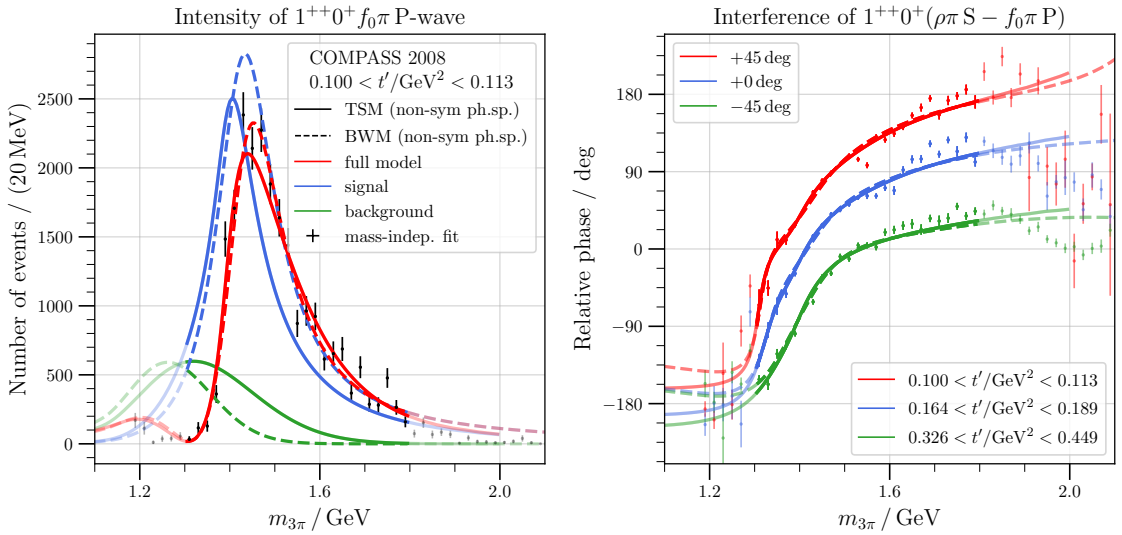

Figure 4.20: Comparison between TSM (solid) and BWM (dashed) where both use a non-symmetrized quasi-two-body phase space as a simplification.

More Flexible Background

The simplified parametrization for the non-resonant background of the main fit was chosen in order to have a similar fit model compared to the initial $a_1(1420)$ publication [6]. So as an additional systematic study we also use the full background parametrization as described in section 4.4.2 for the $f_0\pi$ P wave. This increases the amount of fit parameters and, thus, decreases the amount of degrees of freedom by three while giving the background model and with this also the whole fit model an explicit t' dependence besides the complex strength parameters of the separate components.

The $\mathcal{R}^2_{\mathrm{red}}$ decreases in both cases, we see however in Figure 4.21 that the background of the BWM changes stronger compared to the previous studies and its relative phase exhibits an additional motion towards zero when the model is extrapolated towards lower resonance masses. Also the high-mass region experiences some stronger deviations of the relative phase from the data points, in general hinting towards an instability of the BWM.

Include Excited States

As a final modification of the general fit model, we include the first radial excitations $a_1(1640)$ and $a_2(1700)$ in the models of the $\rho\pi$ S and $\rho\pi$ D wave, respectively. With this introduction, we also increase the fit range of the $\rho\pi$ D wave until 1.9 GeV.

Since we do not want to extract resonance parameters of these excitations with this study, we fix their mass and width to values as they were extracted by the COMPASS collaboration in [37] in order to stabilize the fit. The inclusion of these excitations introduces 44 new fit parameters to the complete fit, however, the number of parameters for the $f_0\pi$ P wave and thus the number of degrees of freedom for the determination of $\mathcal{R}^2_{\mathrm{red}}$ do not change. But its value gets significantly smaller due to a better description of the high-mass region for the relative phase, see Figure 4.22.

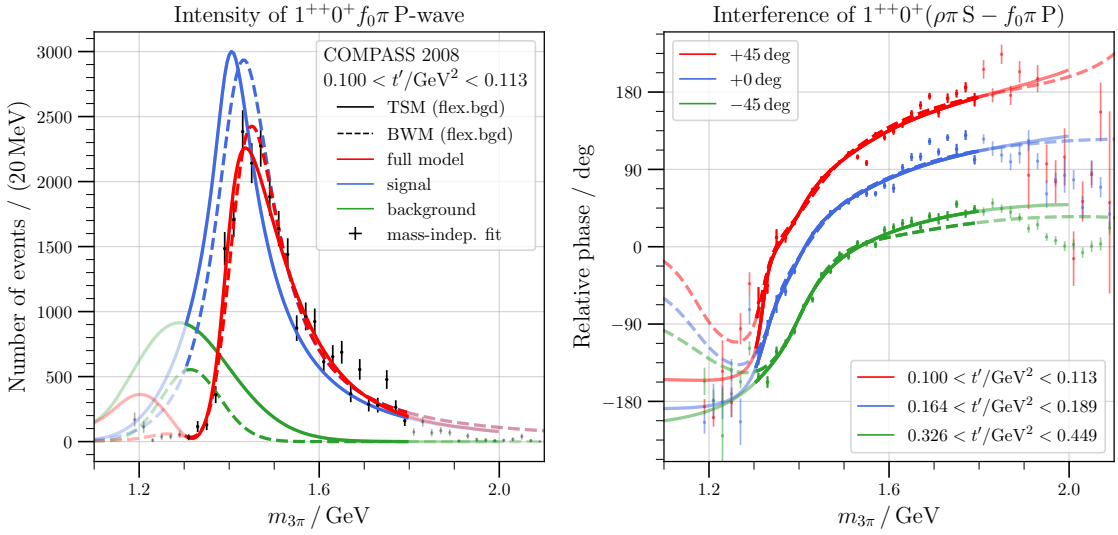

Figure 4.21: Comparison between TSM (solid) and BWM (dashed) where both use a more flexible model for the non-resonant background.

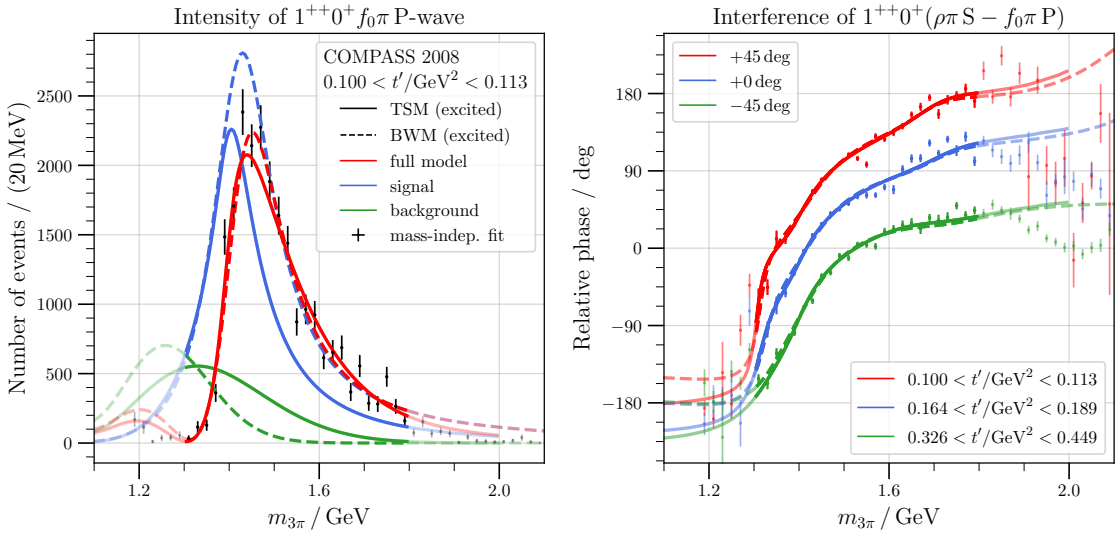

Figure 4.22: Comparison between TSM (solid) and BWM (dashed) where the $a_1(1640)$ and the $a_2(1700)$ are included as additional resonances into the $\rho\pi$ S and $\rho\pi$ D wave models, respectively.

4.6.2 K* Parameters

A small modification of the K^* resonance parameters, i.e. its mass and width, can give a measure for the impact of higher-order rescattering. For this, we have a look at the measurements that are taken into account by the PDG in the determination of the average mass and width. Different production mechanisms could all contribute in some way or form in such a rescattering of the K^* and, therefore, we take the maximum and minimum of these measurements. This means that once, we increase the mass of the charged K^{*-} to $m_{K^{*-}} + 3.8\,\text{MeV}$, and once we decrease it to $m_{K^{*-}} - 5.1\,\text{MeV}$. Similary for the width, we take a slightly broader K^{*-} with $\Gamma_{K^{*-}} + 3.0\,\text{MeV}$ and, then, a slightly narrower one with $\Gamma_{K^{*-}} - 5.6\,\text{MeV}$. Accordingly, the mass of the neutral K^{*0} in the other charge combination of the triangle diagram is adjusted to $m_{K^{*0}} + 2.9\,\text{MeV}$ and $m_{K^{*0}} - 1.9\,\text{MeV}$, and its width to $\Gamma_{K^{*0}} + 8.5\,\text{MeV}$ and $\Gamma_{K^{*0}} - 3.3\,\text{MeV}$.

We study in total four cases, where both K^* are made heavier, both are made lighter, both are made wider, and both are made narrower. The resulting fits can be found in appendix C.4.1. They show only minor differences. The fit quality is compared with the main BWM and depicted as yellow diamonds in Figure 4.24, from left to right heavier, narrower, wider and lighter K^*. One can observe that changing the width of the K^* does not affect the $\mathcal{R}^2_{\text{red}}$ strongly (the two inner points), while changing the mass does (the two outer points). In summary, a narrower and heavier K^* seems to be of advantage to the fit quality.

4.6.3 Variation of the Data

Blue crosses indicate the $\mathcal{R}^2_{\text{red}}$ comparison for the following studies in Figure 4.24. They are systematic studies of the underlying PWD as they were published in [31] and more details on them can be found there. Here is a short summary of what distinguishes each of them from the main PWD:

- Coarse event selection, i.e. use more relaxed cuts during the selection of the $\pi^-\pi^+\pi^-$ final state
- No negative-reflectivity waves were used during the fit
- Smaller wave set with only 53 waves
- Change $(\pi\pi)_S$ parametrization from the modified M-parametrization (see appendix A.6.1) to the K_1-parametrization of [54]
- Use a BW instead of a Flatté for the line shape of the $f_0(980)$
- Allow for more incoherent contributions by changing to a rank-2 fit

For all except one, we see a better fit quality for the TSM over the BWM. The outlier is the one with the changed $(\pi\pi)_S$ parametrization. That this one has the biggest impact is also to be expected, since it directly affects the way how the PWD can separate its contributions from the $f_0(980)$ isobar due to having exactly the same QNs and therefore interfering strongly with each other. Also changing the parametrization of the $f_0(980)$ from a Flatté to a simple BW negatively impacts the fit quality of the TSM. This is however also problematic in of itself, since the simple BW neglects the decay of $f_0(980) \to K\bar{K}$ which is an active requirement for the TSM to allow for the $K\bar{K} \to \pi\pi$ rescattering. The comparison plots for all these studies can be found in appendix C.4.2.

4.6.4 Bootstrap

Bootstrapping is a good numerical method to estimate the statistical uncertainties of a complicated functional dependence. As a basis for this bootstrap study, a reanalysis of the COMPASS PWD for 3π was performed by [55]. Afterwards the underlying selected events that enter the PWD are reshuffled in such a way that some events are used more than once and other events are discarded, effectively changing the weight that each event carries during the fit. 500 of such shuffled data sets were created and the PWD was performed for all of these. Taking the Root Mean Square, i.e. the square root of the arithmetic mean of the squares (RMS), of the resulting PWD data points can be used to obtain asymmetric 68 % quantiles as uncertainties. The study showed that the uncertainties increase, however, the jumps in the data as mentioned at the end of section 4.4.7 can still not completely be explained by them. [55] concluded from this study that most likely a production of a larger MC data set for the acceptance correction is needed.

Nevertheless, we can use these results as a systematic study of the TSM fit. In the following, we deal with the asymmetric uncertainties in a rather phenomenological way. If the experimental data point lies below the fit model, we use its upper error and if it lies above the fit model, we instead use its lower uncertainty limit. The result of this fit can be found in Figure 4.23 for the first t' slice and in appendix C.5. Again, we fit with the TSM and the BWM and can compare their $\mathcal{R}^2_{\text{red}}$ values, the red point in Figure 4.24. But we can even go one step further. Using the fit parameters of this new main bootstrap result as a starting point, we can fit each of the 500 bootstrap PWDs with the two models and compare their $\mathcal{R}^2_{\text{red}}$ values as well. They correspond to the tiny gray points[14] in Figure 4.24. The red ellipse corresponds to their 68 % confidence ellipse (1σ) and the green one to their 95 % confidence ellipse (2σ). All of these fits show a systematic preference of the TSM model regarding their fit quality.

4.6.5 Summary of Systematic Studies

In the previous sections we discussed the origin of every point in Figure 4.24. The grey dashed line indicates the points where both the TSM and the BWM have an equal fit quality. As mentioned before, only one single systematic study lies on the bottom right of this grey line, therefore, we can state a general systematic preference of the TSM over the BWM.

Considering the values of the determined $\mathcal{R}^2_{\text{red}}$ for each of the systematic studies, we can determine a systematic uncertainty for this quantity. Since we see a clear tendency towards lower values for both the TSM and the BWM, we want to do it in an asymmetric manner as well. For this we split the $\mathcal{R}^2_{\text{red}}$ values of the systematic studies in two groups: all values above the value of the main fit model and all values below. For each of these groups, we determine the RMS of their difference to the main fit model. The RMS of the first group defines the upper systematic uncertainty and the RMS of the second group yields the lower systematic uncertainty. This results in $\mathcal{R}^2_{\text{red,TSM}} = 4.59^{+0.13}_{-0.40}$ and $\mathcal{R}^2_{\text{red,BWM}} = 4.87^{+0.09}_{-0.48}$. Counting how many studies lie inside of this interval yields for the TSM $\frac{11}{16} = 68.8\,\%$. For a 2σ interval we have $\frac{15}{16} = 93.8\,\%$. Both findings agree well with the interpretation of Gaussian errors that amount to 68.3 % and 95.4 %, respectively. For the BWM we obtain $\frac{6}{11} = 54.5\,\%$ for a 1σ interval

[14] The fits to the bootstrap attempts experience a systematic shift of roughly the number of degrees of freedom of the fit towards a higher χ^2 compared to the main bootstrap fit. In order to be able to compare these results, all gray points were shifted such that their mean coincides with the value of the main bootstrap result.

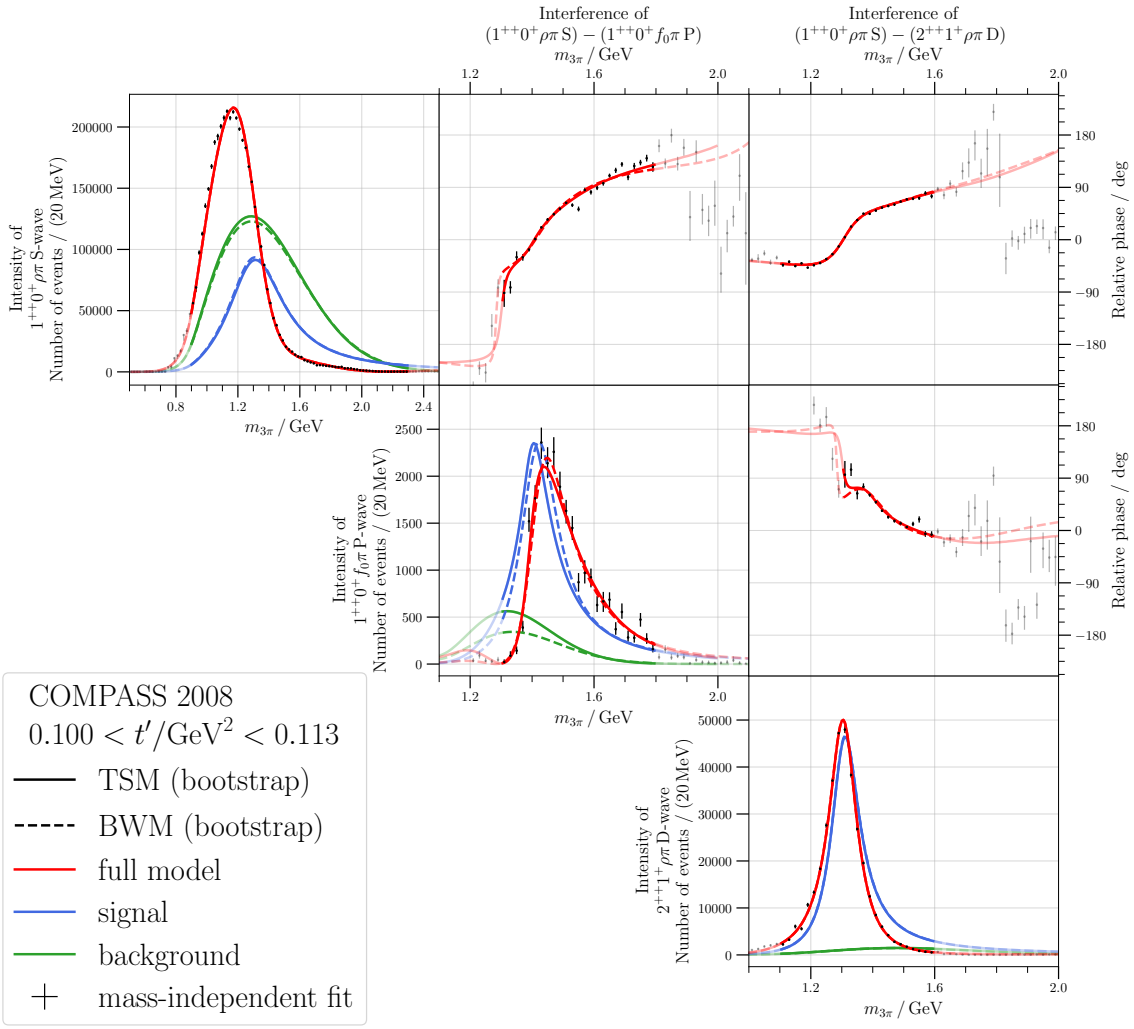

Figure 4.23: First t' slice of the reanalysis of the COMPASS PWD with asymmetric uncertainties fitted by the main fit model.

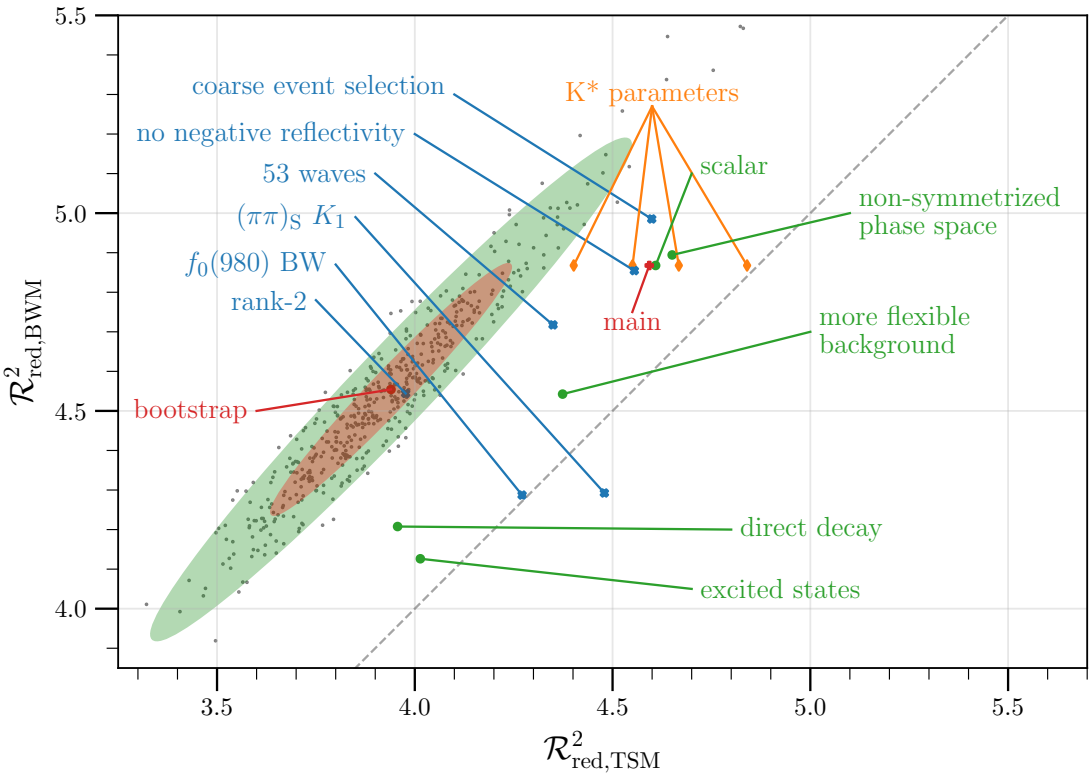

Figure 4.24: Comparison of the fit quality of all systematic studies described in section 4.6. Plotted is always the $\mathcal{R}^2_{\text{red}}$ value of the BWM against the one of the corresponding TSM. The red plus indicates the main fit model, blue crosses correspond to systematic studies with variation of the underlying PWDs, green points label systematic studies of the fit model, and orange diamonds show the impact of modified K^* parameters during the calculation of the triangle amplitude (from left to right with heavier, narrower, wider and lighter K^*). The red circle corresponds to the main minimum of a reanalysis of the PWD. For this analysis, a bootstrap study with 500 attempts (small grey dots) was performed. The red ellipse indicates the 68 % (1σ) and the green ellipse the 95 % (2σ) quantiles. The grey dashed line shows the points where TSM and BWM would have equal fit quality. The values are given in Table C.1.

and $\frac{11}{11} = 100\,\%$ for a 2σ interval. This does not fit as nicely as for the TSM, but we also have less studies to evaluate, therefore, this was expected.

In general, we see that these two uncertainty intervals overlap, making a definite statement difficult from this data alone. However, we observe that all systematic studies of the TSM are better than the main fit model of the BWM. This, together with the general bias towards the TSM, are strong arguments in favor of the rescattering interpretation.

Occam's razor principle states: if two theories explain a situation equally well, the easier one that uses fewer assumptions should always be preferred. In this case this is definitely the TSM, since we do not need additional resonance parameters to describe the $a_1(1420)$ signal, and we also know from scattering theory that the rescattering has to be present. While on the other hand, the introduction of a new resonant state modeled by a BWM, let it be a new genuine resonance, a hadronic molecule or a tetraquark, comes with additional problems as stated in section 4.2 that have to be addressed.

Since the resonant contributions cannot be completely ruled out, also a fit with the TSM together with a coherently added BWM for the $a_1(1420)$ was tested. But no stable minimum could be found.

4.6.6 t' Dependence of the Signal Amplitude

For diffractive production one expects the strength of a resonance to follow an exponential decay law as a function of t' of the following form (compare to equation (46) in [31], but with only one exponential component, since we do not want to account for the coherently-added non-resonant background):

$$\left|A(t')\right|^2 \sim (t')^M \exp(-bt'), \tag{4.22}$$

with A being the strength parameter of the signal model for a given partial wave, and b being a characteristic slope parameter for a given resonance. Note that after proper normalization the t' dependence is approximately equal for the squared fit parameter, for the maximal height of the signal, as well as for the m_X-integral of the signal model, since the signal model itself does not have an explicit t' dependence besides the one of the strength parameter.

As a result of the resonance-model fit of 14 partial waves by the COMPASS collaboration in [37], it was found that the $a_1(1260)$ signal component and the $a_1(1420)$ signal component have similar slope parameters. This would also be expected for an interpretation as a rescattering effect, since the origin is the same resonance. However, due to deviations of the fit curve from the data for some of the higher t' slices as mentioned earlier, such a slope determination was not possible for this fit. In future studies one has to adjust the fit model such that a consistent description of all t' slices is obtained and a reliable t'-dependence of the signal strength can be determined.

One possible idea could be the combination of a TSM with a unitary-coupled-channel treatment of the non-resonant background as it was proposed by Basdevant and Berger [45, 46] and is shortly discussed in section 4.2.4. A second ingredient for a better description could be the introduction of the $a_1(1640)$ into the $f_0\pi$ P wave which should also come with a rescattering component: it has the same QNs as the ground state $a_1(1260)$, its width also extends down to 1.42 GeV where the triangle-singularity amplitude peaks, and in chapter 6 we see clear evidence for the necessary $K^*\overline{K}$ decay channel.

4.7 The Signal in Other Channels

The rescattering interpretation of the $a_1(1420)$ signal does not forbid the presence of an additional resonance pole in form of an $a_1(1420)$ resonance. In order to find more clues on the actual nature of the $a_1(1420)$ one has to look for it also in other final states.

4.7.1 τ Decays

One of them is again the 3π final state, but this time in the decay of τ leptons. The $a_1(1260)$ resonance as a source of the rescattering can also be produced in these decays ([56]) and, thus, a rescattering from its $\pi K\overline{K}$ decay mode to the 3π final state should also be possible there. While the τ decays come with a decreased kinematically available range due to the finite mass of the mother lepton, they have the big advantage that there are no other background reactions. This means that the explanation as a unitary-coupled-channel effect (see section 4.2.4) is definitely off the table if the $a_1(1420)$ signal would be observed in the $f_0\pi$ P wave of the $J^{PC} = 1^{++}$ sector in τ decays. The reason is that there does not exist a Deck-like process as in Figure 4.15 that the $\rho\pi$ S wave could couple to in order to create a peak at 1.4 GeV. Since τ decays happen via the weak interaction, they provide a very gluon-poor environment (in contrast to the gluon-rich diffractive production at COMPASS) which makes productions of meson molecules or tetraquarks probably unlikely as well.

These very promising τ-decays are currently investigated by the BELLE collaboration [7], already presenting hints for the $a_1(1420)$ in preliminary results of a partial-wave analysis [8].

4.7.2 The $\pi K\overline{K}$ Final State

If the rescattering interpretation is correct, the $a_1(1420)$ should also appear in the $J^{PC} = 1^{++}$ $f_0\pi$ P wave of the $\pi K\overline{K}$ final state, since the $f_0(980)$ can not only rescatter to 2π as it was needed for the 3π final state, but also back to $K\overline{K}$. Here, we would also have the opportunity to directly observe the impact of such a rescattering on the source channel, the $K^*\overline{K}$ partial wave. Since events from the $K^*\overline{K}$ final state rescatter to the $f_0(980)\pi$ final state, we should expect some decrease in the intensity at 1.4 GeV of the $J^{PC} = 1^{++}$ $K^*\overline{K}$ S wave. Having said that, interference with the ground state $a_1(1260)$ and its radial excitation $a_1(1640)$ also play an important role, making an exact statement very difficult at this stage.

The COMPASS experiment is the perfect place to study this final state, therefore, the next chapter 5 will discuss the event selection of the $\pi K\overline{K}$ final state and chapter 6 will provide a first look at the subsequent PWD.

4.8 Conclusion

To conclude this chapter, let us summarize the results again. First, we demonstrated that interpretations of the $a_1(1420)$ as a radial excitation, a hadronic molecule, a tetraquark, or an effect from a unitary incorporation of the Deck background all come with problems, making them unlikely. We discuss the interpretation as a triangle singularity from a rescattering process through the intermediate $K^*\overline{K}$ state and present different methods to calculate the corresponding amplitude. We successfully demonstrated that the resulting TSM shows a better fit quality compared to a BWM of a hypothetical new $a_1(1420)$ resonance. This is true for all but one of the systematic studies, despite the fact that the BWM has

two parameters more that can directly modify the actual line shape of the resonance, while for the TSM, this line shape is completely determined by the particles involved in the rescattering process. At the same time, all systematic studies of the TSM are performing better than the main fit model of the BWM. We estimate the systematic uncertainties for the two models to be $\mathcal{R}^2_{\text{red,TSM}} = 4.59^{+0.13}_{-0.40}$ and $\mathcal{R}^2_{\text{red,BWM}} = 4.87^{+0.09}_{-0.48}$. The asymmetric uncertainties are obtained by calculating the RMS of the difference to the main fit model of all systematic studies with larger $\mathcal{R}^2_{\text{red}}$ value than the main fit model for the upper uncertainty and all systematic studies with a lower value for the lower uncertainty.

The experimental uncertainties and the nature of the problem itself make it impossible to prove the origin of the signal with certainty from this decay channel alone, therefore, other reactions like τ decays or the $\pi^- K^0_S K^0_S$ final state have to be investigated. Following Occam's razor principle, we should favor the explanation as a triangle singularity, since it does not need extra assumptions and describes the data even slightly better than competing models. Due to the recent publication of an earlier stage of these studies [50], the $a_1(1420)$ is now omitted from the particle listings of the PDG since it is interpreted as the manifestation of the $a_1(1260)$ in the $f_0(980)\pi$ decay channel.

CHAPTER 5

Kaons at COMPASS

The COMPASS experiment gives access to many different final states. The biggest dataset for diffractive $\pi^- + p$ scattering was obtained in the $\pi^-\pi^+\pi^- + p$ final state[1] [31] and some results were already discussed in the previous chapter. In the past, also investigations of the $\pi^-\pi^0\pi^0$ final state were performed [39, 57], coming with a strong reduction in the number of selected events due to shortcomings in the photon-detection acceptance. But in addition to purely pionic final states, also many studies with final-state kaons (some with pion beam and some with kaon beam) were already performed, such as $K^-\pi^+\pi^-$ [58], $\pi^-K^+K^-$ [9], $\pi^-K_S^0$ and $K^-K_S^0$ [59]. The last two use the same skimming for events with K_S^0 that is described in section 5.2.1. But also a first look at the here discussed $\pi^-K_S^0K_S^0$ final state was already performed in [9]. Note that we consider only strong interaction at the production vertex. The effects from em and weak interaction are only relevant for the decays of the mentioned final-state particles, i.e. the decay of the π^0 and the kaons, respectively, since they cannot decay strongly.

5.1 Possibilities at the COMPASS Experiment

The COMPASS experiment provides huge amounts of data containing many different final states. Most of them originate from a pion beam, where this beam pion is excited to some resonance by exchanging a Pomeron with the target proton. However, since COMPASS uses a secondary beam, some small fraction of 2.4 % is kaons ([11], Table 2), providing access to excited kaons as well, though with drastically reduced statistics. Another way on how to access kaon resonances is by looking at final states with two kaons and a pion. Here, the beam is also required to be a pion beam due to the zero net-strangeness in the final state.

5.1.1 Final States with Charged Kaons

Already analyzed was the final state with two oppositely charged kaons and a negative pion. However, the accessible resonance mass region only starts at roughly 1.5 GeV ([9], FIGURE 4), so one will not be able to look for the $a_1(1420)$ in this final state. The main reason is the necessity to positively identify at least one of the negatively charged particles as a kaon, but the RICH only allows for the

[1] The final states discussed in this chapter all include the recoil proton, which is vital for the determination of the reaction. But since it is the same for all final states, we will omit it from now on for brevity.

identification of kaons in a very restricted momentum range. Here, the idea came up to look for neutral kaons instead and by this circumventing the restrictions of the RICH detector.

Neutral kaons have a finite life time, therefore, they can be detected as a displaced Secondary Vertex (SV) of two charged tracks, a so-called $V0$ particle[2]

5.1.2 The $\pi^-\overline{K}^0K^0$ Final State

This final state is very similar to the huge 3π data set that was analyzed thoroughly by the COMPASS collaboration some of which's results were published in [31]. In both cases we deal with three pseudoscalar particles.

Possible Resonances

The beam pion has isospin $I_\pi = 1$ and since the exchanged Pomeron $I\!P$ does not have quark content[3] – and with this no isospin, $I_{I\!P} = 0$ – the resonance X^- is required to have isospin $I_X = 1$ as well.

Since the Pomeron has isospin $I_{I\!P} = 0$, it would have to decay into at least two pions, resulting in a G-parity $G_{I\!P} = +$. This means for the resonance X^- follows $G_X = -$. From this we can extrapolate to the C-parity of the neutral isospin-triplet partner of the resonance via $G := C(-1)^I \Rightarrow C_X = G_X(-1)^{I_X} = +$. QNsn summarize some of the possible QNs of the resonance:

$$I^G[J^{PC}](X) = 1^-[J^{P+}].$$

For positive parity this results in $a_J := 1^-[J^{++}]$ and for negative parity we obtain $\pi_J := 1^-[J^{-+}]$. Before we can make any statements on possible decay chains, let us first have a look at the two-body subsystems.

Possible Isobars

We have the following QNs for the final-state particles $\pi^-\overline{K}^0K^0$:

$$I^G[J^P](\pi^-) = 1^-[0^-], \qquad I^G[J^P](K^0) = I^G[J^P](\overline{K}^0) = \frac{1}{2}[0^-].$$

Combining the isospins of the two kaons yields

$$\overline{K}^0 \otimes K^0 = \left|\tfrac{1}{2}, +\tfrac{1}{2}\right\rangle \otimes \left|\tfrac{1}{2}, -\tfrac{1}{2}\right\rangle = \frac{1}{\sqrt{2}}\left|1, 0\right\rangle \oplus \frac{1}{\sqrt{2}}\left|0, 0\right\rangle,$$

[2] "V", since its visible decay topology has the shape of the letter "V": no visible incoming track, but two visible outgoing tracks. And "0", because the particle must have no charge, otherwise it would leave a track in the detectors and could not decay into two charged particles that create tracks (no doubly-charged mesons were found, yet, and they would contradict the simple $q\bar{q}'$ quark model, requiring at least an extension to tetraquarks).

[3] In first order approximation the Pomeron can be understood as a two-gluon exchange, or for higher order as a gluon ladder. This "state" is possible to achieve, because gluons can interact with each other, since they carry color charge themselves unlike their Quantum Electro Dynamics (QED) equivalent, the photon.

and of the pion with one of the kaons yields

$$\pi^- \otimes \overline{K}^0 = \left|1,-1\right\rangle \otimes \left|\tfrac{1}{2},+\tfrac{1}{2}\right\rangle = \frac{1}{\sqrt{3}}\cancel{\left|\tfrac{3}{2},-\tfrac{1}{2}\right\rangle} \oplus \left(-\sqrt{\frac{2}{3}}\right)\left|\tfrac{1}{2},-\tfrac{1}{2}\right\rangle,$$

or

$$\pi^- \otimes K^0 = \left|1,-1\right\rangle \otimes \left|\tfrac{1}{2},-\tfrac{1}{2}\right\rangle = \cancel{\left|\tfrac{3}{2},-\tfrac{3}{2}\right\rangle},$$

of which in both cases the $I = \frac{3}{2}$ states will not contribute, since a simple $q\bar{q}$-meson can only have $I \leq 1$. It follows that only the $\overline{K}^0$ can form an isobar resonance together with the pion.

For the total spin J, we have to combine the spins S_1 and S_2 of the daughter particles with the orbital angular momentum L between the two. Since all three particles are pseudoscalars, their combined spin is $S = 0$ in both possible isobar subsystems $K^0\overline{K}^0$ and $\pi^-\overline{K}^0$, resulting in $J = L$. For the parity we obtain the expression $P = P_1 P_2 (-1)^L = (-1)^L$, since all three particles have negative parity.

For the C-parity we can first note that the $\pi^-\overline{K}^0$ system is not an eigenstate of this QN, simply due to its negative net charge. For $K^0\overline{K}^0$ we have to use a trick, similar to a $\pi^+\pi^-$ system. Switching the places of the two particles, i.e. acting with the parity operator on them, does exactly the same as turning each particle into its antiparticle, i.e. acting with the charge-conjugation operator on them[4], thus, $C = P = (-1)^L$.

$$J^{PC}(K^0\overline{K}^0) = [\text{even}]^{++} \text{ or } [\text{odd}]^{--} \qquad J^{PC}(\pi^-\overline{K}^0) = [\text{even}]^{+} \text{ or } [\text{odd}]^{-}.$$

Now, we have to combine these J^{PC} states with the possible isospin states from above. In the case of $\pi^-\overline{K}^0$ we only have one possibility, giving us:

$$I[J^{PC}](\pi^-\overline{K}^0) = \tfrac{1}{2}[\text{even}]^{+} \text{ or } \tfrac{1}{2}[\text{odd}]^{-} =: K_J^{*-}.$$

For $K^0\overline{K}^0$ we have four possible combinations. Here, the G-parity QN helps to decide which ones are possible. Since the resonance has $G_X = -$ and the bachelor particle is a π^- with $G_\pi = -$ as well, we know that the G-parity of the isobar system has to be positive, $G = +$. For isospin $I = 1$ it follows now $C = G(-1)^I = -$ and for $I = 0$ we obtain in the same way $C = +$, leaving only two of the four combinations:

$$I^G[J^{PC}](K^0\overline{K}^0) = 1^+[\text{odd}^{--}] \text{ or } 0^+[\text{even}^{++}] = \rho_{\text{odd}} \text{ or } f_{\text{even}}.$$

We will constrain ourselves for now to a total spin of $S_\xi \leq 4$ for the isobar ξ and, therefore, to the particles:

$$\xi_{K^0\overline{K}^0} \in \{f_0, f_2, f_4, \rho, \rho_3\} \qquad \text{and} \qquad \xi_{\pi^-\overline{K}^0} \in \{K_0^{*-}, K^{*-}, K_2^{*-}, K_3^{*-}, K_4^{*-}\}.$$

Possible Decay Channels

Now, we have to figure out which of the possible resonances can decay to which possible isobars and with which orbital angular momentum. For this, we constrain ourselves to an orbital angular momentum $L \leq 4$. The procedure to determine the possible final states is the following:

We start with the decay channel $\xi\zeta$, where ξ is the isobar $K^0\overline{K}^0$ or $\pi^-\overline{K}^0$ and ζ is the bachelor

[4] None of them has spin, which would have to be swapped as well

Table 5.1: Possible resonances for the channels $f_{\text{even}}\pi^-$ and $K^{*-}_{\text{even}}K^0$ (left) and $\rho_{\text{odd}}\pi^-$ and $K^{*-}_{\text{odd}}K^0$ (right) for any possible $L \leq 4$.
Note: The channels $\rho_{\text{odd}}\pi^-$ are not possible within the final state $\pi^- K^0_S K^0_S$, see section 5.1.3 for an explanation.

$\xi\zeta$	${S_\xi}^{P_\xi}$	L	P_X	J_X	X^-
$f_0\pi^-$ $K^{*-}_0 K^0$	0^+	0	−	0	π
		1	+	1	a_1
		2	−	2	π_2
		3	+	3	a_3
		4	−	4	π_4
$f_2\pi^-$ $K^{*-}_2 K^0$	2^+	0	−	2	π_2
		1	+	1, 2, 3	a_1, a_2, a_3
		2	−	0, ..., 4	$\pi, ..., \pi_4$
		3	+	1, ..., 5	$a_1, ..., a_5$
		4	−	2, ..., 6	$\pi_2, ..., \pi_6$
$f_4\pi^-$ $K^{*-}_4 K^0$	4^+	0	−	4	π_4
		1	+	3, 4, 5	a_3, a_4, a_5
		2	−	2, ..., 6	$\pi_2, ..., \pi_6$
		3	+	1, ..., 7	$a_1, ..., a_7$
		4	−	0, ..., 8	$\pi, ..., \pi_8$

$\xi\zeta$	${S_\xi}^{P_\xi}$	L	P_X	J_X	X^-
$(\rho\pi^-)$ $K^{*-}K^0$	1^-	0	+	1	a_1
		1	−	0, 1, 2	π, π_1, π_2
		2	+	1, 2, 3	a_1, a_2, a_3
		3	−	2, 3, 4	π_2, π_3, π_4
		4	+	3, 4, 5	a_3, a_4, a_5
$(\rho_3\pi^-)$ $K^{*-}_3 K^0$	3^-	0	+	3	a_3
		1	−	2, 3, 4	π_2, π_3, π_4
		2	+	1, ..., 5	$a_1, ..., a_5$
		3	−	0, ..., 6	$\pi, ..., \pi_6$
		4	+	1, ..., 7	$a_1, ..., a_7$

particle π^- or K^0, respectively. Here, we take the total spin of the isobar S_ξ and its parity P_ξ and use them to calculate the parity P_X for any possible orbital angular momentum L via $P_X = -P_\xi(-1)^L$. Then, we combine S_ξ and L to any possible combination of J_X using the fact that the bachelor spin is always 0. And finally, we can identify the resulting resonance from the list of the possible resonances. Table 5.1 shows the results of these calculations for all possible decay channels.

This table is nice, because one can directly read off where and how each resonance can be produced. However, it might be more useful to invert this table and show for all resonances how their respective decay channels look like. This can be found in table 5.2, where we use the spectral notation for the orbital angular momentum. We again constrain ourselves to $L \leq 4$ and also $J \leq 4$.

We see that this data set is very rich and would allow for a detailed investigation of these resonances in several different decay channels as well as a direct extraction of the relative branching-fraction ratios of all these channels.

Sadly, the a_0 resonance is not accessible via this reaction, but on the other hand the explicitly spin-exotic candidate π_1 is.

The higher the orbital angular momentum, the more suppressed the corresponding decay channel will be. Therefore, in the Dalitz plots we will most likely only be able to see S and P waves. Also the ground states in the radial excitation spectra of K^{*-}_3, K^{*-}_4 and f_4 will most likely be already too heavy to be observed as an isobar in the decay of a resonance. The lightest f_4 meson would be the $f_4(2050)$ according to the PDG making it visible as an $f_4(2050)\pi^-$ isobar decay only for resonances with masses $\gtrsim 2.2\,\text{GeV}$. For K^{*-}_3 we would see the $K^{*-}_3(1780)K^0_S$ isobar decay only for resonances with masses $\gtrsim 2.28\,\text{GeV}$ and for K^{*-}_4 it would be the $K^{*-}_4(2045)K^0_S$ isobar decay for resonances with

Table 5.2: Resonances with their respective decay channels. Each column corresponds to an isobar-bachelor pair and each entry of the matrix corresponds to the allowed orbital angular momentum $L \leq 4$ in spectroscopic notation S, P, D, F, G.
Note: The channels $\rho_{\text{odd}}\pi^-$ are not possible within the final state $\pi^- K_S^0 K_S^0$, see section 5.1.3 for an explanation.

$X^- \to \xi\zeta$	$f_0\pi^-$, $K_0^{*-}K^0$	$(\rho\pi^-,)\ K^{*-}K^0$	$f_2\pi^-$, $K_2^{*-}K^0$	$(\rho_3\pi^-,)\ K_3^{*-}K^0$	$f_4\pi^-$, $K_4^{*-}K^0$
a_1	P	S, D	P, F	D, G	F
a_2	$--$	D	P, F	D, G	F
a_3	F	D, G	P, F	S, D, G	P, F
a_4	$--$	G	F	D, G	P, F
π	S	P	D	F	G
π_1	$--$	P	D	F	G
π_2	D	P, F	S, D, G	P, F	D, G
π_3	$--$	F	D, G	P, F	D, G
π_4	G	F	D, G	P, F	S, D, G

masses $\gtrsim 2.55\,\text{GeV}$. For these reasons we will strengthen the constraint on the isobar spin to $S_\xi \leq 2$.

5.1.3 The Physical $\pi^- K_S^0 K_S^0$ Final State

So far we only considered the pure isospin states K^0 and $\overline{K}^0$. However, in nature theses are not the states that are actually observed. They mix to form the physical states K_S^0 and K_L^0 which consist each to 50 % out of K^0 and $\overline{K}^0$. So by requiring both final state kaons to be a K_S^0 we have a 50 % chance for the K^0 to be a K_S^0 and another 50 % for the $\overline{K}^0$ to be a K_S^0, as stated by the PDG. Therefore, only 25 % of the $\pi^- \overline{K}^0 K^0$ final state result in the physically observed state of interest, $\pi^- K_S^0 K_S^0$. Similarly, one would obtain the $\pi^- K_L^0 K_L^0$ final state in 25 % of all cases and the $\pi^- K_S^0 K_L^0$ final state in the remaining 50 %.

No ρ_J Isobars

Since the final-state kaons are identical, they have to follow the Bose statistics. This means that the full wave function has to be symmetric under exchange of these two particles. We start with the symmetrized wave function

$$\frac{1}{\sqrt{2}}\Big(|p_1, p_2\rangle + |p_2, p_1\rangle\Big),$$

where p_i denotes the four-momentum of the corresponding K_S^0. If we expand each component into its partial waves, we obtain

$$\begin{aligned} |p_1, p_2\rangle &= \sum_{J,M} \sqrt{2J+1}\, D^J_{M,0}(\phi_1, \theta_1, 0)\, |J, 0\rangle, \\ |p_2, p_1\rangle &= \sum_{J,M} \sqrt{2J+1}\, D^J_{M,0}(\phi_2, \theta_2, 0)\, |J, 0\rangle, \end{aligned}$$

where $D^J_{M,0}$ denotes the Wigner-D matrices as detailed in appendix A.3.

Since both daughters are scalars and the spin projection M is an additive QN, it has to be $M = 0$ for the ρ_J meson. This simplifies the expression because the ϕ_i dependence drops out due to $D^J_{0,0}(\phi_i, \theta_i, 0) \equiv d^J_{0,0}(\theta_i)$. Now, we can relate the two θ_i angles via $\theta_2 = \pi - \theta_1$, since they are produced back-to-back in the helicity frame where this partial-wave decomposition is performed. Using the following property of the d-function $d^J_{0,0}(\pi - \theta) = (-1)^J d^J_{0,0}(\theta)$ brings us to

$$D^J_{0,0}(\phi_2, \theta_2, 0) = d^J_{0,0}(\theta_2) = d^J_{0,0}(\pi - \theta_1) = (-1)^J d^J_{0,0}(\theta_1).$$

For the symmetrized wave function follows accordingly

$$\frac{1}{\sqrt{2}}\Big(|p_1, p_2\rangle + |p_2, p_1\rangle\Big) = \frac{1}{\sqrt{2}} \sum_J \sqrt{2J+1} \underbrace{\Big(1 + (-1)^J\Big)}_{0 \text{ for odd } J} d^J_{0,0}(\theta_1)\, |J, 0\rangle.$$

This expression shows that for odd total spin J the corresponding partial wave vanishes. Therefore, the decay $\rho_{\text{odd}} \to K^0_S K^0_S$ is forbidden.

Average Flight Distance of Neutral Kaons

We observe this final state through diffractive scattering of a 190 GeV π^- beam off of a fixed liquid-hydrogen target. The recoiling proton only takes a few hundred MeV of energy, leaving each of the three remaining final-state particles on average with roughly 60 GeV. A lot of simplifications play inside here, but at this stage we are only interested in a rough estimate for the flight path of the neutral kaons. For a Lorentz-boosted particle one can calculate its average flight path in the LAB system via $\ell = \beta\gamma c\tau$, however this is a statistical process following an exponential decay law. According to the PDG for K^0_S we have $c\tau = 2.6844\,\text{cm}$, therefore, at the given energy it will fly a distance of approximately 3.24 m on average before decaying and creating a SV. Evaluating the Cumulative Distribution Function (CDF) of the exponential distribution for a mean of 3.24 m gives us approximately 95.4 % of all K^0_S decaying within $\leq 10\,\text{m}$. Already at 40 m there are basically no K^0_S left making it very unlikely that one of them might escape the detector setup in longitudinal direction[5].

For the K^0_L we have $c\tau = 15.34\,\text{m}$ resulting in an average flight length of 1.8 km for the given energy, while the COMPASS detector spans roughly 50 m from the target to the last tracking detector. Using this as a mean value for the CDF, only ≤ 3 % of all K^0_L will decay within the whole COMPASS spectrometer rendering it basically impossible to detect them via the presence of a SV.

K^0_S Decays

Constraining us to K^0_S gives us another restriction on the detectability: According to the PDG a K^0_S will decay in ~ 70 % of all cases into a pair of charged pions, $\pi^+\pi^-$, the other ~ 30 % will be $\pi^0\pi^0$

[5] The center of the target cell is located at approximately −48 cm in the COMPASS reference system. The first tracking detector after the target is the silicon detector `SI04` and lies at roughly −12 cm and the last tracking detector is the `GEM GM11` at roughly 48 m or, more likely, the `MWPC PB06` at roughly 46.3 m due to its generally larger areal coverage. It is also centered on the beam while `GM11` was placed away from the beam and, thus, only covers a small asymmetric range in the azimuthal angle.

which immediately[6] decay each into a pair of photons. Since neither the K_S^0 nor the photons leave a track in the tracking detectors, it is nearly impossible to find the position of the SV.

In case of exactly one K_S^0 decaying to two neutral pions, one would require exactly four photon clusters coming from the same SV. Then, one would have to guess the correct position of the SV such that two pairs of photons would result in an invariant mass of a π^0, and the combined invariant mass of these two π^0 would be the mass of a K_S^0. The position of the SV has three unknowns (x, y and z position) which can be fixed by the mass constraints for twice $m_{2\gamma} = m_{\pi^0}$ and once $m_{4\gamma} = m_{K_S^0}$. However, this would obviously work for all three combinations of combining four photons to two pairs. So one will have to do this calculation for all combinations. The correct one could be determined by the remaining constraint that the resulting K_S^0 momentum direction has to cross with the Primary Vertex (PV). This makes the system of equations overdetermined and allows to reject false combinations. More details on how this procedure would mathematically work can be found in appendix D.1.

In case both K_S^0 would decay to neutral pions, the situation would be even more complicated because now, one has to deal with eight photon clusters. This would be a combinatorial nightmare.

Requiring both K_S^0 to decay into charged pions reduces the detectible $\pi^- \overline{K}^0 K^0$ events further to 49 %. Taking one charged and one neutral decay mode would yield 42 %, leaving the remaining 9 % for twice the neutral mode. Therefore, by selecting only $\pi^- K_S^0 K_S^0$ where both K_S^0 decay into charged pions, we have a total reduction down to approximately 12.25 % of all $\pi^- \overline{K}^0 K^0$ events.

Although it seems that one could gain a lot more data by including these other possibilities, the unification of all of them into one big data set is highly questionable. While the last case with eight photons is definitely not worth the effort, already using the final state with only one K_S^0 decaying via its neutral charge mode would change the detector acceptance drastically by requiring information from ECALs, most likely making it worse. One would also have to create two different samples of MC data for the acceptance determination, and in addition the background processes would be completely different.

5.1.4 Final States with K_L^0

The $\pi^- K_S^0 K_L^0$ final state would yield additional 35 % of $\pi^- \overline{K}^0 K^0$ events (50 % for the $\pi^- K_S^0 K_L^0$ final state itself and of this 70 % by looking only for the charged decay mode of the K_S^0.) One could try to use the HCALs in order to identify K_L^0 as a cluster of deposited energy without a track leading to it. However, the energy resolution of the HCAL is not very good[7] leading to a bad determination of the K_L^0 energy and momentum.

However, using the HCALs only as a trigger (one cluster without assigned track) one could determine the K_L^0 momentum from the missing momentum of a well-reconstructed $\pi^- K_S^0$ subsystem. Its momentum direction could be obtained, similarly to the case of photons, by taking the connecting line of the HCAL cluster with the PV. This could be used as a crosscheck for the direction of the missing momentum. Its energy would be obtained from its momentum by assuming the nominal K_L^0 mass, since

[6] The PDG lists $c\tau = 25.3$ nm for the π^0, resulting in an average flight path of $\sim 19\,\mu$m for an energy of 100 GeV. With a vertex resolution in the order of a few mm along the beam direction, this becomes impossible to resolve. Therefore, it can be assumed that the decay vertex of the π^0 is located directly at its creation point for all practical purposes.

[7] For a particle with energy of 60 GeV, the uncertainty of the measurement would be ~ 9 GeV for HCAL1 and ~ 8 GeV for HCAL2, according to [11].

a single neutron[8] in the final state would basically be impossible. It would have to be accompanied by an antiproton[9] (negatively charged particle from the PV) to fulfill baryon-number conservation, however, antiprotons are quite well identified by the RICH detector over a large momentum range (within $18\,\text{GeV} < p_{\bar{p}} < 100\,\text{GeV}$) and can be excluded almost completely by performing a veto cut on the required negatively charged primary track. Also, final states with baryons come with a very high mass threshold of $\sim 2.4\,\text{GeV}$ reducing their likelihood even further.

This final state would start with roughly three times more events than $\pi^- K_S^0 K_S^0$ (only considering charged decay modes for K_S^0 in both cases), however, its acceptance and purity will most likely be worse. Similarly to the $\pi^- K_S^0 K_S^0$ events with neutral K_S^0 decay mode, also here the event topology would be quite different requiring also different MC data with different background contributions. Additionally, this final state would allow for the $\rho_{\text{odd}}\pi^-$ decay channels, since the neutral kaons are now distinguishable and the argument with Bose symmetrization does apply here anymore. A combined treatment of $\pi^- K_S^0 K_L^0$ events with $\pi^- K_S^0 K_S^0$ events will therefore be questionable, however, it could be an interesting project on its own.

The final state $\pi^- K_L^0 K_L^0$ cannot be studied without direct energy measurements from the HCALs, because both K_L^0 would only appear as missing energy and missing momentum, rendering it impossible to assign an individual value to each of them.

5.2 Event Selection of $\pi^- K_S^0 K_S^0$

At COMPASS, the data taking is split into runs, each consisting of at most 200 spills. One such spill is a short period of roughly 5 s where the COMPASS experiment receives beam from the SPS. During each spill in the order of 10^5 triggered diffractive events are recorded. The data taking is, then, separated into periods of two consecutive weeks where no work on the setup was allowed in between the runs to ensure consistent data. During the years 2008 and 2009, there were recorded six such periods with negatively charged secondary hadron beam in total: `2008_W33`, `2008_W35`, `2008_W37`, `2009_W25`, `2009_W27` and `2009_W35`.

Then, the production of the data is done in an iterative procedure, where one checks the quality of the resulting events, identifies issues and reproduces all data again. Such a production at COMPASS is called `Slot` and it performs tracking, vertexing, clustering and so forth, such that the user does not have to deal with the individual detector responses and their caveats during the event selection, but can focus on the specifics of the final state of interest. The first one for hadron beam on a proton target that was used for analyses leading to publications was `Slot3`. From this the big analysis of the $\pi^-\pi^+\pi^-$ final state was performed, e.g. see [31]. Looking at final states with neutral pions, one identified problems with the calibrations of the ECALs, therefore, a reproduction `Slot4` was performed. However, when repeating the analysis of the $\eta^{(\prime)}\pi^-$ final state, more issues were found and fixed, leading to the current `Slot5` production with the following additional changes:

- The π^0-calibration of the ECALs was improved where one adjusts the response of individual calorimeter cells such that the π^0 peak in the $\gamma\gamma$ invariant-mass spectrum is centered at the nominal π^0 mass.

[8] This is the lightest neutral hadron next to the K_L^0 that lives long enough to reach the HCALs before decaying.

[9] Also an antineutron would be possible, however, this could be excluded by requiring only one HCAL cluster without assigned track.

- The first few runs showed a shift in the trigger timing. In `Slot4` analyses, this could be cured by shifting the beam time for the first few runs accordingly during the event selection and before applying any cuts on it. Before performing the new reproduction, the trigger timing was recalibrated such that a beam-time shift is not necessary anymore.

- A run-by-run time calibration of the `RPD` was performed and a new procedure to cut on "good" proton track was implemented [60].

In order to make the enormous amount of data easier accessible, the usual practice is to perform a rough skimming of the data, where one focusses on a specific trait of the events, e.g. the number of charged tracks coming from the PV. For the selection of $\pi^- K_S^0 K_S^0$ such a trait is the existence of a SV, which in PHAST is defined as any crossing of a positive and negative track. The decision on which cuts to apply during the skimming was still done on `Slot4`. The skimming itself and also the following studies and selection steps were repeated for the new `Slot5` production. This analysis is the first to use this new `Slot5` production and a comparison with the new and the old production was performed during the internal COMPASS release procedure, see appendix D of [61]. Besides an increase of roughly 10 % in selected events due to the improved `RPD` treatment, no major difference in the kinematic distributions could be found.

5.2.1 Skimming for K_S^0

To determine the best set of cuts for the skimming, two runs of 2008 were chosen, run `69595`[10] and run `69754`. As mentioned in the introduction of this section, this decision was made on the `Slot4` production. However, since the cuts are very basic and they only serve for a first reduction of the data, the main statements still hold. In total the file size of these two runs is 77 GB and the total file size for the year 2008 amounts to 34.6 TB, approximately double for both years 2008 and 2009 combined. To reach the goal of a reduction to $\sim$ 6 TB for both years combined, similar to the skimming for three charged hadrons that was used for the $\pi^-\pi^+\pi^-$ and $\eta^{(\prime)}\pi^-$ final states, one needs a reduction down to $\sim$ 6.7 GB for the two analyzed runs.

The final requirements of the skimming are the following:

- It has to exist a Best Primary Vertex (BPV) in the event, which is defined in PHAST as the PV with the lowest χ^2 during the vertex fitting. A PV is any crossing of the beam with an arbitrary amount of charged tracks measured by the COMPASS spectrometer.

- The BPV has to lie roughly within the target region, specifically between -100 cm and 0 cm in the COMPASS reference system where the 40 cm long target cell is centered at -48 cm.

- At least one negatively charged track has to leave the BPV. This is needed in order to have the primary π^- from the $\pi^- K_S^0 K_S^0$ final state.

- At most five charged tracks leave the BPV. Five tracks would correspond to the case where the two K_S^0 decay almost immediately after creation and still within the vertexing resolution of the BPV.

[10] Only the first 10 files of this run were taken.

- At least one SV has to exist, which is any crossing of a positively charged track with a negatively charged one (excluding beam tracks, i.e. tracks with an assigned detector hit upstream of the target). Assigning the mass of a pion to the daughter particles, the invariant mass of the two-pion system has to lie within 50 MeV of the nominal K_S^0 mass as stated by the PDG. This big window still leaves the possibility to fit the mass spectrum and obtain a good separation of the K_S^0 signal and the underlying background. By only requiring "at least one" SV, one also allows for subsequent selection of final states with exactly one K_S^0, e.g. [59], or more than two K_S^0, making the skimming more versatile.

The usage of these requirements yielded a reduction to 7.7 GB and a resulting estimate of 3.5 TB for the year 2008. The actual file size after the skimming on `Slot4` data amounts to 3.4 TB for 2008, showing that the estimation worked quite well. For the skimming of `Slot5` the full file size for both years combined is 6.7 TB. The total amount of events remaining after the skimming is 1.07×10^9.

5.2.2 Preselection for $\pi^- K_S^0 K_S^0$

First, a preselection is performed, where we try to reduce the background by applying all cuts that do not require a good definition of a K_S^0. The resulting events can, then, be used to determine the requirements on the SVs. A subsequent fine selection will ensure the quality of the data, meaning correct particle ID, exclusivity and four-momentum conservation.

During the studies it turned out that the inclusion of events with more than two charged tracks leaving the BPV resulted in only few events and in addition a distorted shape of the invariant-mass spectra, see appendix D.2. Therefore, it was decided to already cut accordingly during the preselection.

Styles for Histograms

There are two ways to show the impact of a cut on an event selection. For one of them one applies the cuts one after another and directly sees the impact of each of them. In the following, this style will be called "Waterfall-Style" and has the advantage that it follows the natural flow of how one develops an event selection. One starts with everything, looks at a specific distribution, e.g. the z_{BPV}-position of the BPV inside the target, and cuts on it. The disadvantage is that for the decision on how to actually perform the cut one might be biased from the huge amount of background that is still present in the data.

The second way is to look at a given spectrum after applying all cuts that do not influence the spectrum directly. In the example of the position of the BPV one would look at the corresponding z_{BPV}-distribution after applying all other cuts – e.g. on the number of charged tracks and exclusivity of the event – and, then, decide on where to put the cut ranges on z_{BPV} accordingly. Like this one has the lowest possible background when making a decision on where to place the cuts. However, events that are thrown by more than one cut will never appear in any of the histograms. This can hide some problems with the detectors that might still be solvable otherwise. Also the determination of a cut depends on the definition of all other cuts, therefore, one will need to perform it iteratively to find the optimum for all cuts. For previous analyses at the Technical University of Munich (TUM) a tool called Antok was created. In order to be able to perform independent crosschecks, the idea was to implement such a Bonn Event Selection Tool (`BEST`) for Bonn. But since the implementation of the ongoing event selections at Bonn was quite different, everybody at Bonn created their own version of it and an "official" `BEST` was not created. A description on the working principle of the version

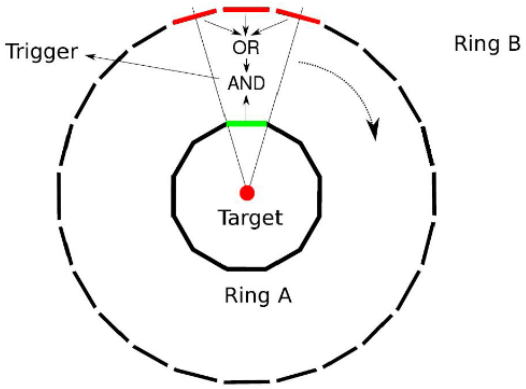

Figure 5.1: Schematic view of the RPD, [63]

implemented for this project can be found in appendix E. It also serves as a guide on how to transform an existing Waterfall-Style selection into a BEST-Style selection. Accordingly, the corresponding histograms will be labeled with "BEST-Style".

A summary of all cuts can be found at the end of this section 5.2.2.

Trigger

First, we want to make sure that the physics of interest is present in the data. For this, the DT0 trigger was created as a coincidence of several different detector signals, with a detailed description in [62].

- The aBT has to trigger, which ensures that a particle of the beam is coming towards the target and a scattering event happened. It is a coincidence of the SciFi FI01X and the Beam Counter (BC). The latter is a small scintillating disc of 32 mm diameter directly placed in the beam.

- The RPD, used for tracking and identification of recoil protons, has to have a coincidence between one slab of the inner ring and one of three outer slabs that could be hit afterwards from a particle flying in a straight line from the target through the hit slab of the inner ring as depicted in Figure 5.1.

- The veto system, which consists of several detectors, should not trigger. First, no hit in the hodoscope veto system is allowed, which ensures that we do not have particles from hadronic interactions in the beam line or particles that are too far away from the actual beam line. Next is the sandwich veto, which is a calorimeter with a circular hole in the center situated downstream of the RPD. It guarantees that no particles leave the angular acceptance of the COMPASS spectrometer. Finally, no coincidence in the two Beam Killers (BKs) is allowed. They are two scintillating discs located after SM2, separated by a few meters, and similar in design to the BC. We do not want to select events in which the beam did not interact with the target, which would be the case if it passes through both of the BKs. The coincidence is important, since otherwise events would also be discarded where one final-state particle hits one of the BKs by chance.

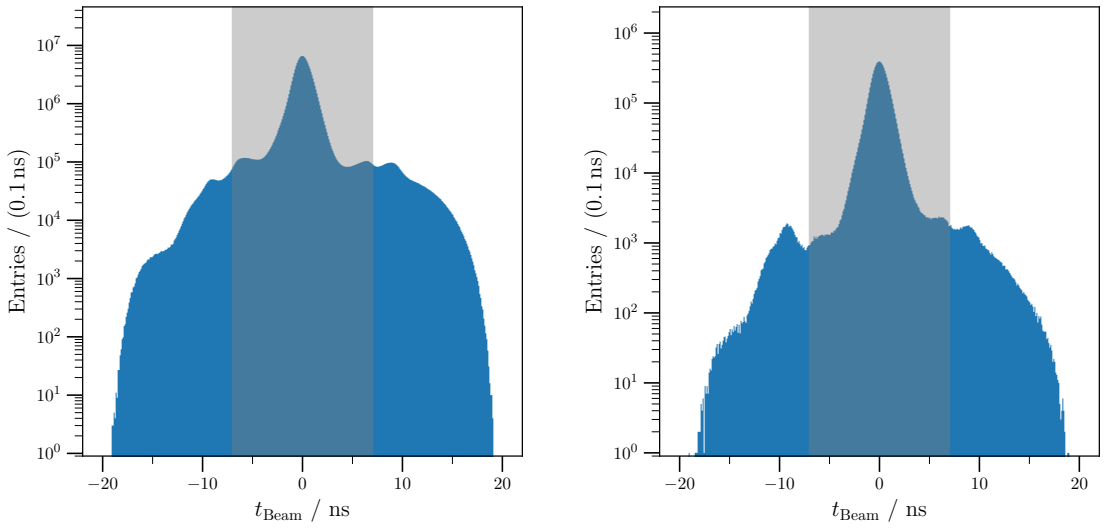

(a) Waterfall-Style

(b) BEST-Style

Figure 5.2: Beam-time distribution. The gray band denotes the accepted range.

Beam Properties

In order to avoid overlapping events one has to perform a cut on the beam time, meaning the main trigger time of the event to which all other detectors are tuned to during the beginning of a time period. This beam time has to be around zero and in the corresponding spectrum in Figure 5.2 one can clearly identify the main peak and in addition some smaller local maxima in both directions. In order to already cut most of these pile-up events away, we perform a very rough cut of $|t_{\text{beam}}| \leq 7$ ns symmetrically around zero. A more refined cut will be performed later during the fine selection, see section 5.2.3.

For the final state we want to ensure that the beam is a pion in order to be able to employ strangeness conservation at the PV and, thus, deduce the identity of the charged particle leaving from there without the kinematic constraints coming from the RICH detector (more on these in section 5.2.3). For this, we use the CEDARs that are placed in the beam line a few meters in front of the target, which were calibrated using a likelihood approach, see [64] for details. They also provide a C++ library (PaCEDARDetector and PaCEDARLikelihood) to extract the relevant information from the PHAST event tree.

First, we want to make sure that the calibration of the CEDARs exists for the given run. Therefore, we cut events away where either the current run number does not appear in the calibration file, or if one or both of the detector-IDs are missing (equal 0) in the calibration file for the given run. This can either be because there was not enough data in the given run to perform the calibrations, or due to one or both of the CEDARs not working properly or being excluded from the data taking for the given run.

After this, one can obtain the likelihood $\mathcal{L}_X^i$ for a given particle species $X \in \{\pi, K\}$ and each of the

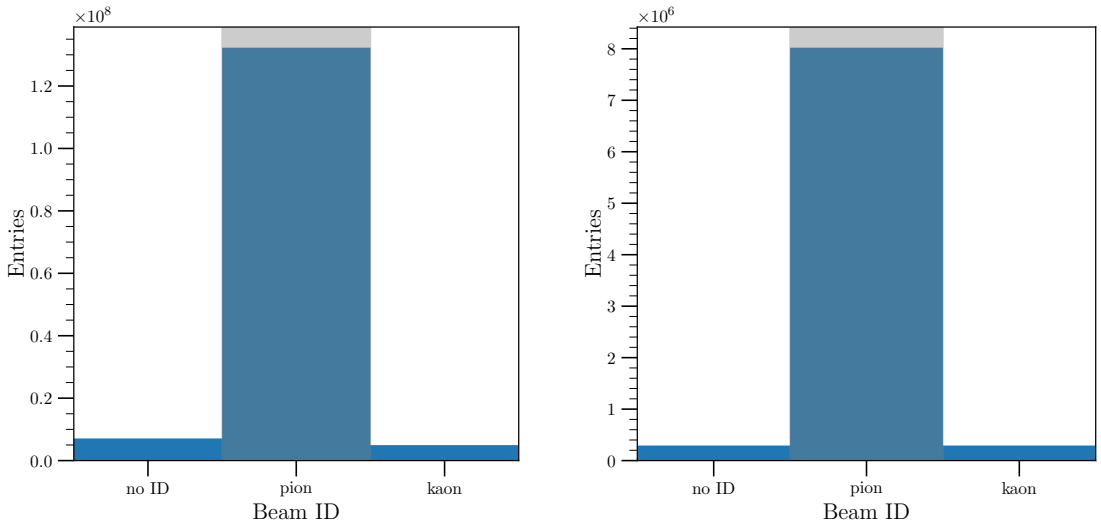

(a) Waterfall-Style

(b) BEST-Style

Figure 5.3: Particle IDentification (PID) of the beam particle as determined by the CEDARs. Only pions are accepted.

two CEDARs $i \in \{1, 2\}$. These likelihoods are, then, combined to

$$\mathcal{R} = \log_{10}\left(\frac{\mathcal{L}_K^1 \cdot \mathcal{L}_K^2}{\mathcal{L}_\pi^1 \cdot \mathcal{L}_\pi^2}\right).$$

From this definition it is obvious that $\mathcal{R} < 0$ corresponds to a higher pion likelihood while $\mathcal{R} > 0$ corresponds to a higher kaon likelihood. In the end, adjusting these thresholds will always be a compromise between efficiency, how well a real pion is actually identified as such, and impurity, how often a real kaon is misidentified as a pion. Therefore, it might be better to cut a bit stronger to achieve a better purity. In [64] this was studied and it was found out that with the cut $\mathcal{R} < 0$ we obtain a pion efficiency of roughly 99 % with an impurity of 0.005 %. With roughly 240 000 selected events in the end, this results in only 12 events where the beam was actually a kaon. Although this is already very small, the actual number will most likely be even smaller if not zero, since also other cuts like exclusivity and the RICH veto on the identity of the primary particle (that has to have the same identity as the beam if exclusivity holds and strangeness conservation is applied) during the fine selection will also help to throw these "bad" events.

For kaons we would set the cut at $\mathcal{R} > 4$ resulting in an efficiency of roughly 85 % while having an impurity of 3 %. For everything in between these two cut values no ID will be assigned to the beam particle. The distribution of beam-particle IDs can be found in Figure 5.3. Besides of a reduction in the total number of events not much changes between the two selection-styles.

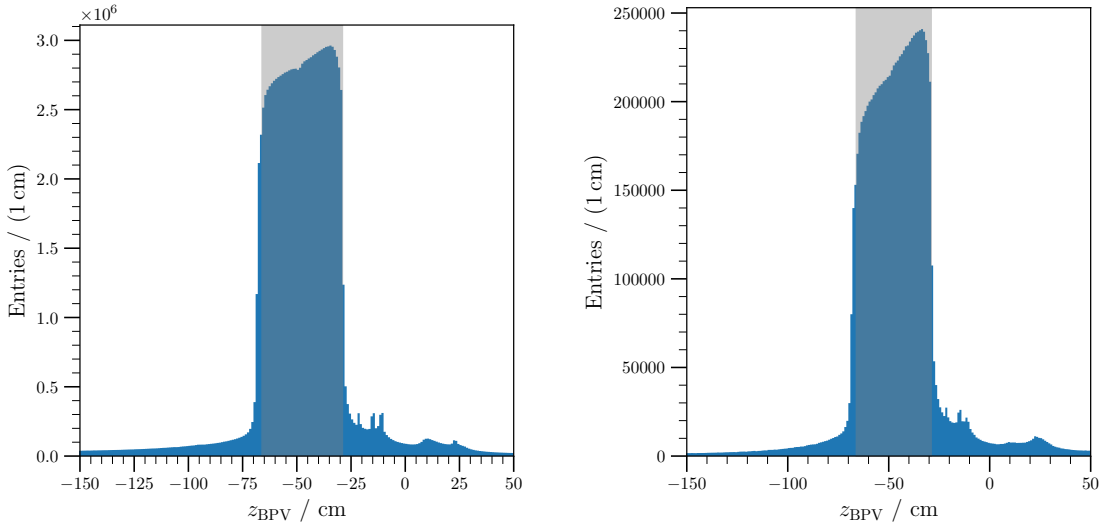

(a) Waterfall-Style

(b) BEST-Style

Figure 5.4: z-position of the BPV. The gray band denotes the accepted range.

Properties of the BPV

As mentioned in the introduction of this section, we decided to discard events with more than two outgoing charged tracks from the BPV, requiring $N_{\text{out}}^{\text{BPV}} \leq 2$. This cut reduces the amount of data drastically, but also the amount of background that might come from e.g. events with five charged pions in the final state.

Next we want to make sure that the BPV actually lies within the target cell and, therefore, a scattering of the pion off a proton took place during the event. This cut is purely driven by the geometry of the target cell and, therefore, no further fine tuning is needed. For this, we require

$$-66\,\text{cm} < z_{\text{BPV}} < -29\,\text{cm}.$$

Like this we cut a bit tighter than actually necessary in order to avoid the inclusion of events where a scattering happened at the windows of the target cell that are smeared out due to the resolution of the vertexing.

Another condition is put on the transversal distance of the BPV from the beam axis

$$r_{\text{BPV}} := \sqrt{x_{\text{BPV}}^2 + y_{\text{BPV}}^2} < 1.55\,\text{cm}.$$

These cuts are in accordance with previous selections [59, 65]. The corresponding histograms can be found in Figures 5.4 and 5.5.

One can see a small dip in the z-distribution right in the middle of the broad peak representing the target cell. [66] showed with MC studies that it can be reproduced by including small Light-Emitting Diode (LED)s placed in the center of each RPD-slab that were used for the calibration of the detector during the data taking.

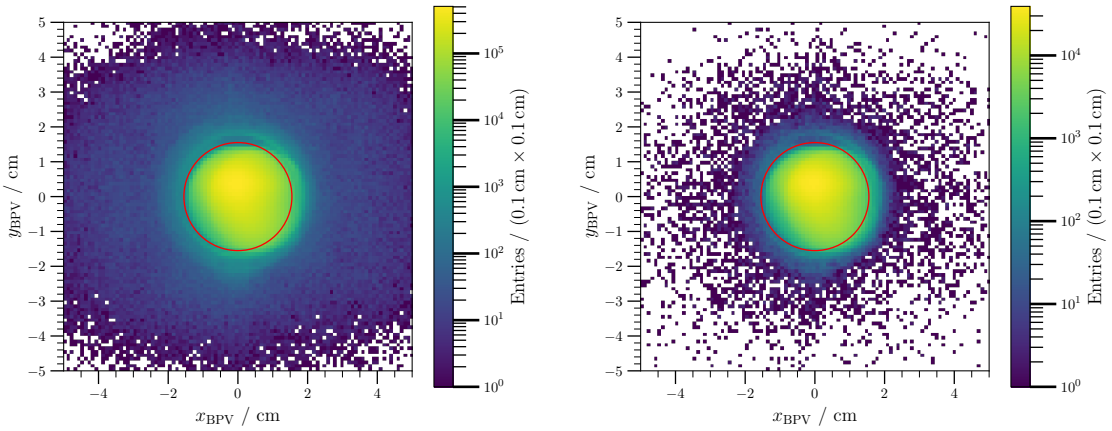

(a) Waterfall-Style

(b) BEST-Style

Figure 5.5: (x, y)-position of the BPV. Everything inside the red circle is accepted.

Number of Proton Tracks

For the reaction of interest we require exactly one "good" track measured by the RPD. Also for the RPD a corresponding C++ library exists (`RPD_Helper` by [63]). The RPD measures the azimuthal angle ϕ_p of the proton track through the slabs that are hit. The angular uncertainty depends on which outer slab is hit, since for every odd outer slab half of it lies in a straight line with one inner slab and the other half with the neighboring inner slab, see Figure 5.1. This reduces the possible size of the slab in which a hit could have occurred by a factor 2. More on this in the fine selection during the description of the planarity cut, section 5.2.3.

Since the slabs are read out with Photo-Multiplier Tube (PMT) on both sides, one can obtain the polar angle θ_p of the proton track by measuring the time difference in which the signal arrives at both ends. A run-by-run `t0`-calibration was performed and is described here [60]. This calibrates the RPD for signals coming from proton tracks. In the note the feature `EnableCutOnSlapZPos(-120, 20, -140, 70)` is recommended. If a fake hit e.g. created by noise in the readout of a single slab occurs, it can create a reconstructed hit position that actually would lie outside of the physical position of the RPD slabs. Such hits are thrown away by enabling this cut which reduces the number of events with more than one possible recoil-proton track. All remaining hits are, then, combined to recoil-proton tracks. For this, we require that every track has one hit in the inner and one hit in one of the three geometrically-possible outer-ring slabs that lie on a straight line with the PV, see Figure 5.1. These tracks are called `goodProtonTracks` and, now, we require the events to have exactly one such track. If it has zero or more than one, we discard the event. The amount of `goodProtonTracks` is displayed in Figure 5.6, where we obtain a strong maximum at 1 with a sharp drop afterwards. Surprisingly, we have quite a lot of events at the %-level with more than 3 proton tracks for both selection styles.

K_S^0 Candidates

The final cut of the preselection will reduce a huge amount of unwanted data by requiring at least two K_S^0-candidates. Such candidates are defined as a SV where the invariant mass of the two daughter

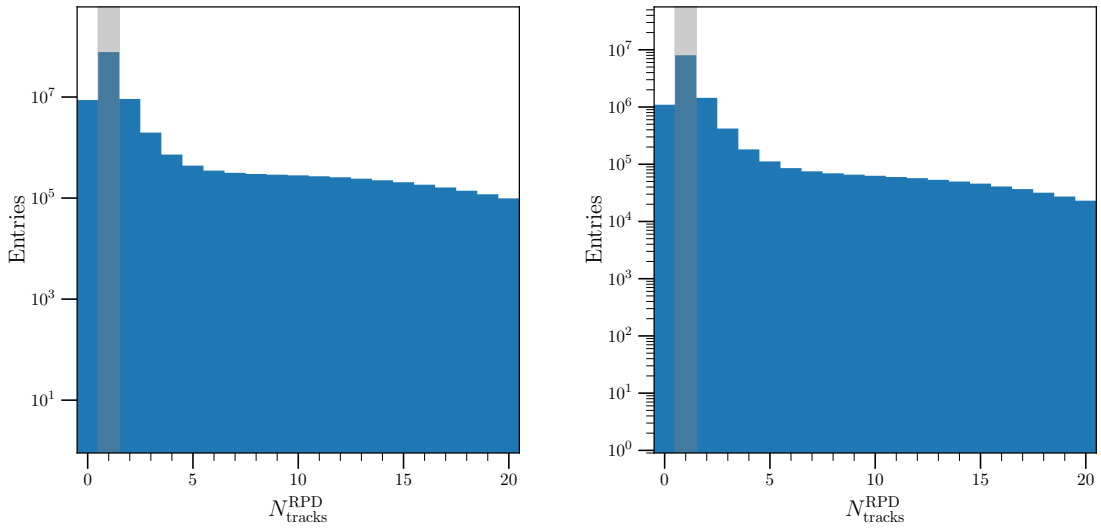

(a) Waterfall-Style

(b) BEST-Style

Figure 5.6: Number of `goodProtonTracks` measured by the RPD. Only events with exactly one are accepted.

particles, each with mass hypothesis of a charged pion, lies within ±50 MeV around the nominal PDG mass of a K^0_S. This window is still broad enough to separate the contributions for the actual K^0_S and the underlying background during later detailed studies. The number of K^0_S-candidates is depicted in Figure 5.7(a), which shows a very rapid drop-off. Next to it in Figure 5.7(b) one can see the resulting invariant mass of the K^0_S-candidates after the preselection. It has a very sharp peak that is very slightly shifted to higher masses. But we also still see quite a substantial background contribution below.

Cut-Flow Diagram

Finally, a summary of all of the mentioned cuts is presented in Figure 5.8 in a cut-flow diagram, also known as waterfall plot since it shows the flow of the selection and one can directly see how many events are successively removed by each cut.

We see that the biggest impact comes from the cut on $N^{\text{BPV}}_{\text{out}} \leq 2$, but this is also expected since a lot more "background" final states become available if we allow for a bigger number. This was one of the reasons why it was decided to cut on this number already here. The cut on the PID of the beam reduces the amount of events by $\sim 8\,\%$. This is a bit more than the $\sim 2.4\,\%$ of kaons in the beam, however, this number is obviously impacted by other quantities as well, like the presence of a K^0_S in the final state that is required by the previously discussed skimming. This increases the chance of beam-kaons, since with at least one kaon in the final state this either means we have another kaon in the final state or the beam needs to contain an s-quark as well to conserve strangeness. The final heavy hitter is the cut on at least two K^0_S which is split in two parts, first cutting on at least two SVs and, then, on at least two K^0_S-candidates, which makes the previous cut obsolete, but shows that there is a substantial amount of SVs that come from other $V0$ particles e.g. photons producing an e^+e^--pair in the close proximity of detector material or are just coincidental crossings of oppositely charged tracks.

However, this style of representing the reduction of events might also lead to slightly wrong

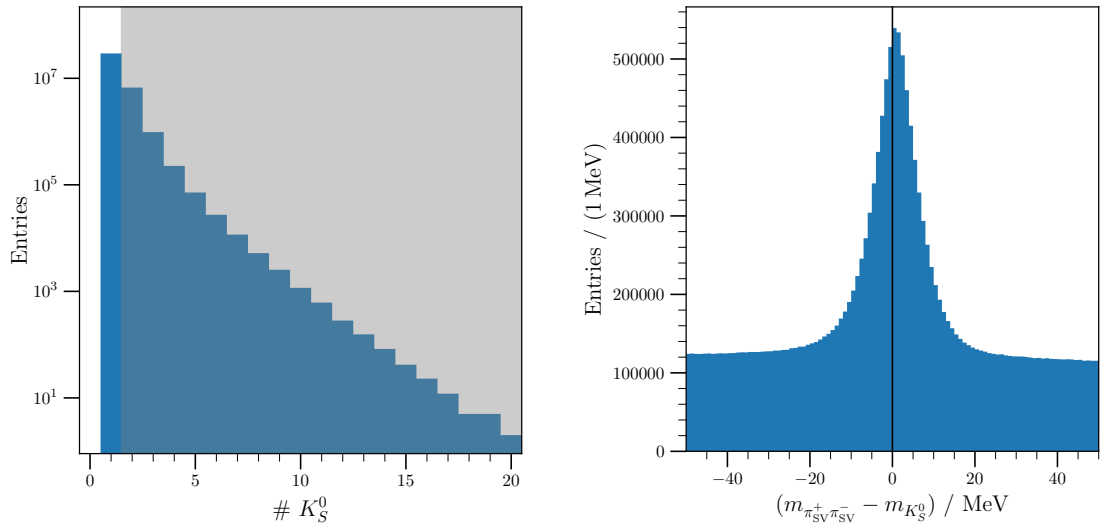

(a) (b)

Figure 5.7: **Left:** Number of K_S^0-candidates before the cut on the number of SVs. The gray area shows the accepted events. **Right:** Invariant-mass distribution of the K_S^0-candidates at the end of the preselection (including the cut on at least two K_S^0-candidates)

conclusions, especially since cuts at the beginning might seem to remove a lot, but the removed events could also haven been removed by some other cuts later down the line. Therefore, one can also look at the BEST-Style version of this plot in Figure 5.9, where we display only the events that are exclusively removed by a specific cut, in other words the number of events that would still be there if we would not apply the corresponding cut. Also here we see immediately that the cut on $N_{\text{out}}^{\text{BPV}}$ has as expected the biggest impact, followed by the cut on requiring more than one K_S^0-candidate. We do not see any entries for the cut on the number of SVs because it is a requirement for the cut on K_S^0-candidates. Similarly, the existence of a CEDAR calibration is needed for the cut on the beam PID, therefore, its entry is zero as well.

5.2.3 Fine Selection of $\pi^- K_S^0 K_S^0$

Before we continue with the selection, we have to properly define the criteria when we want to accept a SV as a K_S^0.

K_S^0 Selection

First, we have a look at different criteria in order to classify the SVs. Initially, we included events with five outgoing charged particles from the BPV, in order to allow for a selection of the case where both K_S^0 decay within the vertexing resolution. Such a class will be called "close" K_S^0. An even amount of charged particles coming from the BPV cannot conserve the negative charge of the beam particle and, therefore, it is forbidden. However, if the extrapolated trajectory of one of the two daughters of the K_S^0 is closely passing by the BPV within the vertexing resolution, this charge conservation can

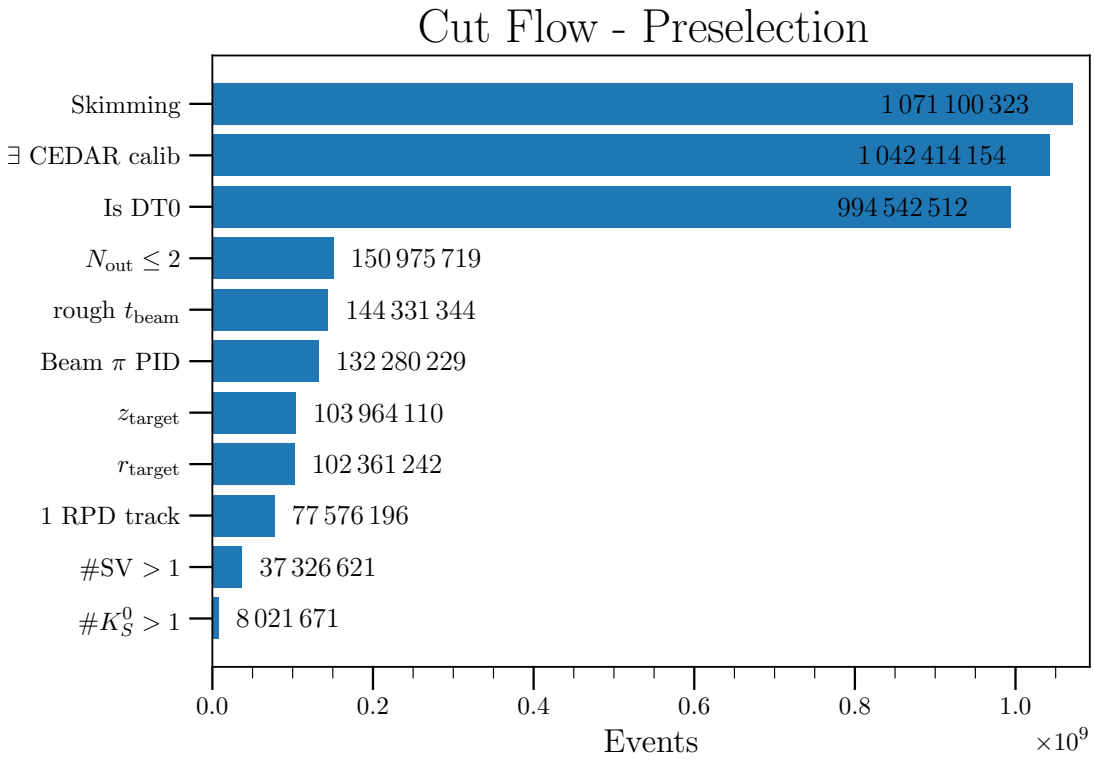

Figure 5.8: Cut-flow diagram of the preselection.

still be achieved. This defines the second class of "shared" K_S^0, where one of the daughter tracks is also associated with BPV by PHAST. The third and final class are the "far" K_S^0, where none of the daughters comes from the BPV. Depending on $N_{\text{out}}^{\text{BPV}}$, we have to require a certain amount of each of the three different classes to accommodate for all outgoing tracks from the BPV:

$N_{\text{out}}^{\text{BPV}} = 1$: two "far" K_S^0

$N_{\text{out}}^{\text{BPV}} = 2$: one "far" K_S^0 and one "shared" K_S^0

$N_{\text{out}}^{\text{BPV}} = 3$: one "far" K_S^0 and one "close" K_S^0
or: two "shared" K_S^0

$N_{\text{out}}^{\text{BPV}} = 4$: one "shared" K_S^0 and one "close" K_S^0

$N_{\text{out}}^{\text{BPV}} = 5$: two "close" K_S^0

Let us have a look at two quantities that let us differentiate between the three classes. First in mind comes the separation of the SV from the BPV. Using the simple picture from above, one would expect a "close" K_S^0 to also be geometrically close to the BPV in order to be able to have both daughter particles in common. Similarly for the "shared" K_S^0 one also needs some closeness in order for one

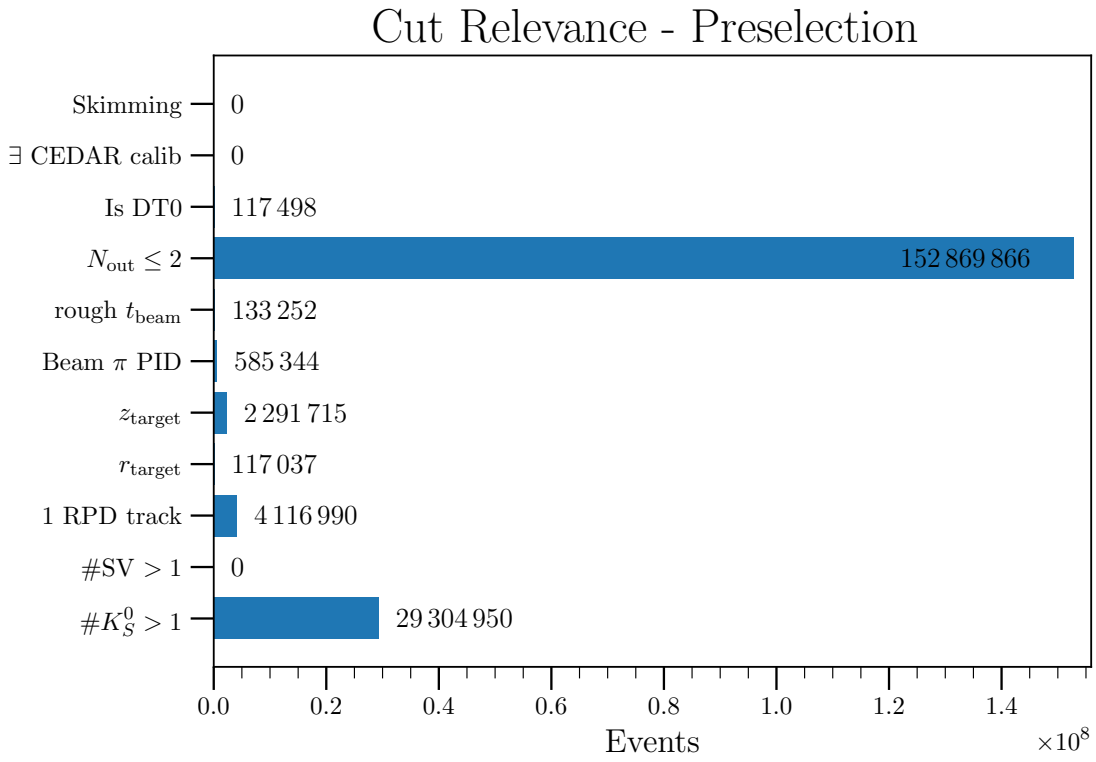

Figure 5.9: Number of events that are cut by only the respective cut during the preselection.

of them to be able to pass by the BPV within the vertexing resolution. However, for "far" K_S^0 one expects some distance to the BPV. Since the vertex resolution in transversal direction only amounts to $\sim 10\,\mu\text{m}$, while in longitudinal direction[11] we have something in the order of 10 mm, we will only look at the difference between the z coordinates of the BPV and the SV instead of calculating the actual distance. If we perform the same preselection as described in section 5.2.2, just leaving away the cut on $N_{\text{out}}^{\text{BPV}} \leq 2$, we obtain Figure 5.10(a). Here, we see a clear separation of the three classes. There are substantially more "far" K_S^0 with large $\Delta z := z_{\text{SV}} - z_{\text{BPV}}$ than for the other two classes. For both "shared" K_S^0 and "close" K_S^0 we see a sharp peak at $\Delta z = 0\,\text{cm}$, with a slightly slower drop-off for "shared" K_S^0.

Let us shortly discuss the other peaking structures in Figure 5.10(a). The first peak at $\Delta z \approx -260\,\text{cm}$ most likely corresponds to scattering or the production of secondary particles in the `Silicons` `SI02` and `SI03`. The detector thickness is broadened by not only the vertexing resolution, but more dominantly due to the size of the target cell in which the BPV is located. This creates a $\sim 20\,\text{cm}$ window around the actual detector position making an exact statement impossible at this stage of

[11] In [11] values are stated for a 5π final state of $13 - 16\,\mu\text{m}$ transversal vertexing resolution and $0.75 - 4.7\,\text{mm}$ longitudinal vertexing resolution, but it is expected that these values worsen drastically if one reduces the amount of outgoing tracks to 1 as in our case. However, the order of magnitude should still be valid, especially the big difference between transversal and longitudinal resolution.

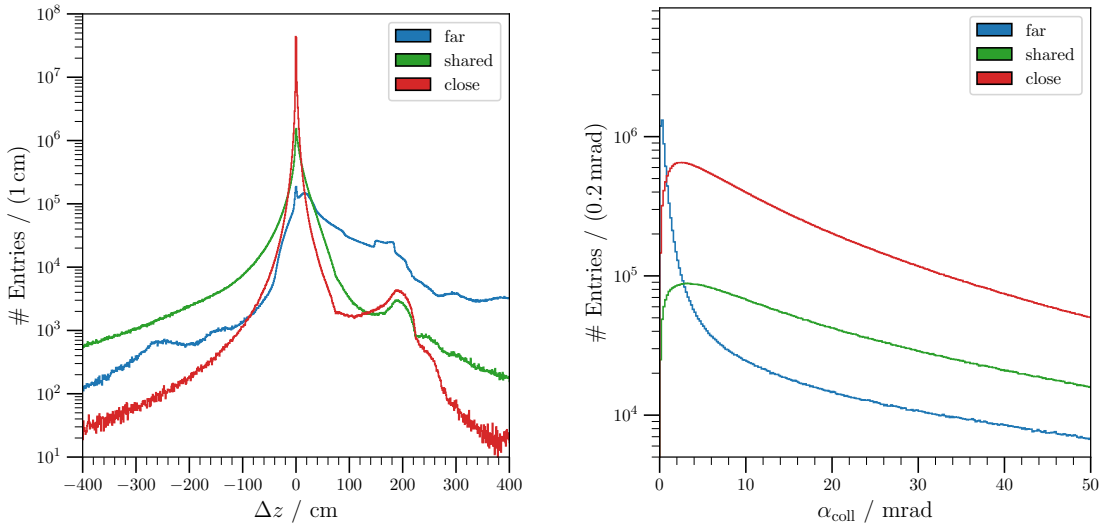

(a) Vertex separation

(b) collinearity angle

Figure 5.10: Separation of "far" K_S^0 (blue), "shared" K_S^0 (green) and "close" K_S^0 (red) visualized for the vertex separation $\Delta z = z_{\text{SV}} - z_{\text{BPV}}$ (left) and the collinearity angle (right). This plot was produced after the preselection using `Slot4` data without the cut on $N_{\text{out}}^{\text{BPV}} \leq 2$.

the selection[12]. The structures on the other side of the main peak at $\sim 200\,\text{cm}$ could originate from scattering on the `MicroMEGAS` `MM01` and the `DC00`.

Secondly, we can compare the direction of the reconstructed K_S^0 momentum with its expected flight direction determined from the connecting line between the BPV and its SV. The angle between these two quantities is called the collinearity angle:

$$\alpha_{\text{coll}} = \angle(\vec{p}_{K_S^0}, \vec{r}_{\text{SV}} - \vec{r}_{\text{BPV}}). \tag{5.1}$$

The corresponding distribution can be found in Figure 5.10(b). Here, we see that the angle is generally a lot smaller for "far" K_S^0. This can be understood, since for larger distances Δz the resolution of the vertexing has a smaller impact on the definition of the connecting line between BPV and SV, resulting also in a smaller effect on the collinearity angle.

These two quantities show that such a classification makes sense, at least the "far" K_S^0 are behaving quite different than the other two classes. Now, we have to determine the optimal cut criteria for these quantities. As always, one has to find a compromise between quantity and quality, therefore, we can perform a significance study. The significance is defined by

$$\mathcal{S} = \frac{S}{\sqrt{S+B}} = s \cdot \sqrt{N}, \qquad \text{where } N = S + B, \tag{5.2}$$

with S denoting the amount of signal events, B is the background and $s = \frac{S}{N}$ is the relative signal strength. The advantage of optimizing the significance over an optimization of the signal-to-background

[12] One would have to cut stronger on the BPV position, in order to see the full tomography of the spectrometer.

ratio is, that the significance rises linearly with the relative signal strength, $\mathcal{S} \propto s$, and additionally with the square root of the total amount of data, $\mathcal{S} \propto \sqrt{N}$. During this optimization we try to reduce the background as much as possible. Therefore, estimating its value results in bigger relative uncertainties and, thus, more fluctuations in the determination of the quantity B and accordingly in the signal-to-background ratio S/B. On the other hand, we try to keep as much as possible of the signal component. With this, s will be big and with small relative uncertainty, resulting in a very stable determination of the significance $\mathcal{S}$.

The different components S and B can only be determined with a fit to the K_S^0-mass spectrum. Looking at Figure 5.7(b), we see that we still have a huge amount of background left after the preselection. Therefore, it was decided to perform the fine selection with different cut-off values for Δz_{min} and α_{coll} and perform a significance study with the results of all these fine selections, always looking at the K_S^0-mass spectrum at the very end after all cuts are applied. The signal component is modeled with a double-Gaussian

$$\mathcal{DG}(x; A, r, \mu, \sigma_1, \sigma_2) = A \cdot \Big[r \cdot \mathcal{N}(x; \mu, \sigma_1) + (1 - r) \cdot \mathcal{N}(x; \mu, \sigma_2) \Big], \tag{5.3}$$

with

$$\mathcal{N}(x; \mu, \sigma) := \frac{1}{\sqrt{2\pi\sigma^2}} \exp\left(-\frac{(x-\mu)^2}{2\sigma^2} \right). \tag{5.4}$$

The background on the other hand is simply modeled by a polynomial, since its real functional form is unknown. We determine the cut values for the K_S^0 invariant mass as 3σ intervals around the mean μ, where we combine the two widths in the following weighted way

$$\sigma = r \cdot \sigma_1 + (1 - r) \cdot \sigma_2, \tag{5.5}$$

where r is the fraction of the first Gaussian with width σ_1, and accordingly $(1 - r)$ is the fraction of the second Gaussian with width σ_2. Then, the signal contributions is obtained from an integral of the double-Gaussian

$$S = \int_{\mu-3\sigma}^{\mu+3\sigma} \mathcal{DG}(x) \mathrm{d}x.$$

The background contribution B is obtained from the integral over the same range of the corresponding polynomial model.

It turned out that it was not possible to perform the significance study for "close" K_S^0, since the background was too huge and the fit could not reliably extract a signal component. Also when simply using $\Delta z_{\text{min}} = 0$ for all classes of K_S^0, the resulting invariant-mass distribution of the $\pi^- K_S^0 K_S^0$ system looked quite different when including cases with $N_{\text{out}}^{\text{BPV}} > 2$ which always involve "close" K_S^0, see appendix D.2. This lead to the decision of excluding these cases in the preselection, already.

Therefore, we will focus only on the two classes of "far" K_S^0 and "shared" K_S^0.

At first, a one-dimensional significance study was performed, where we change $\Delta z_{\text{min}}^{\text{far}}$ and $\Delta z_{\text{min}}^{\text{shared}}$ simultaneously in steps of 0.5 cm, without cut on the collinearity angle. Separately, also the collinearity cut-off angles $\alpha_{\text{coll,max}}^{\text{far}}$ and $\alpha_{\text{coll,max}}^{\text{shared}}$ are simultaneously changed in steps of 0.05 mrad. The resulting mass distributions are fitted with the previously described model and the significance is calculated. The result can be found in Figures 5.11 and 5.12.

In Figure 5.12 we see that the significance is steadily increasing with increasing maximally allowed

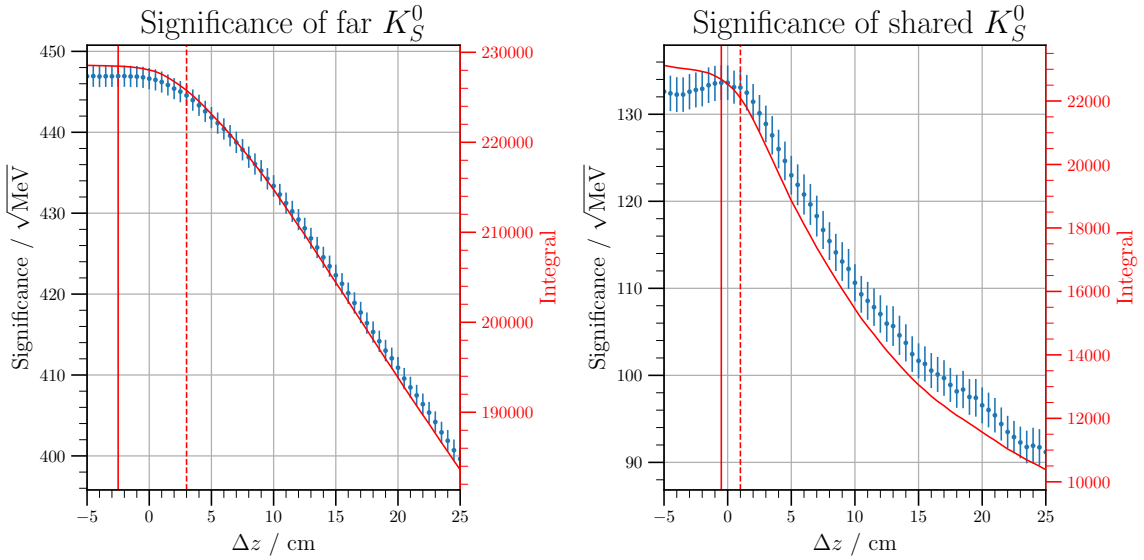

(a) "far" K^0_S (b) "shared" K^0_S

Figure 5.11: Result of the one-dimensional significance study, varying Δz_{min}. The solid vertical line corresponds to the position of the maximum, while the dashed vertical line is the chosen limit from the two-dimensional significance (cf. Figure 5.13). The red curve together with the axis on the right side of each plot shows the integral of the full fit function (signal + background) and is an indication for the total number of events N.

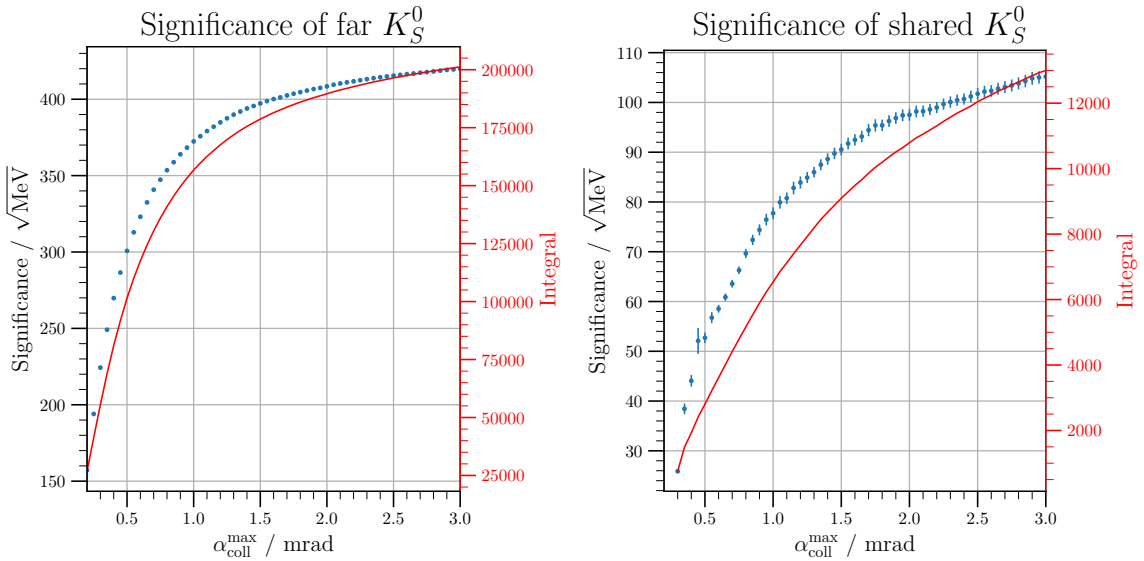

(a) "far" K^0_S (b) "shared" K^0_S

Figure 5.12: Result of the one-dimensional significance study, varying $\alpha^{\text{max}}_{\text{coll}}$. The solid vertical line corresponds to the position of the maximum, while the dashed vertical line is the chosen limit from the two-dimensional significance (cf. Figure 5.13).

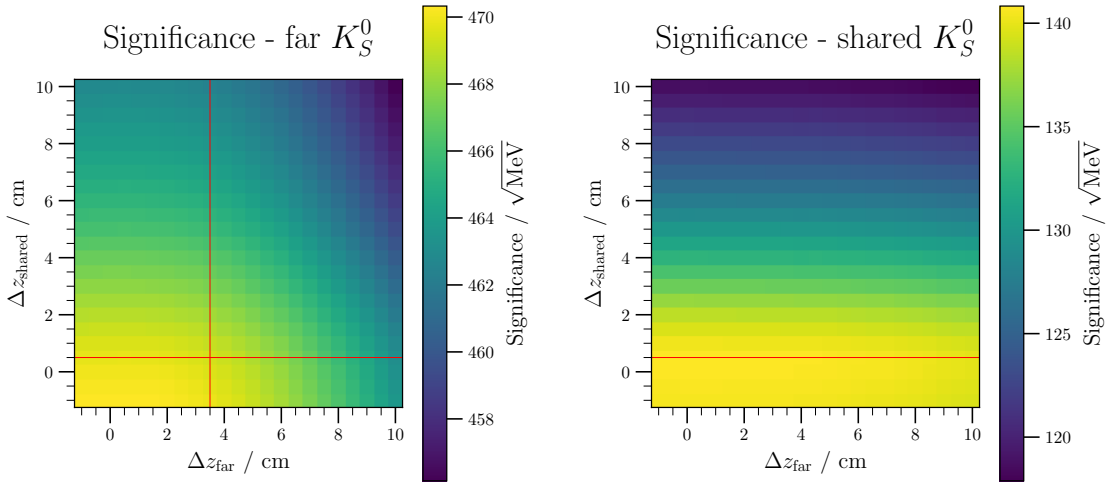

(a) "far" K_S^0 (b) "shared" K_S^0

Figure 5.13: Result of the two-dimensional significance study, varying $\Delta z_{\text{min}}^{\text{far}}$ independently of $\Delta z_{\text{min}}^{\text{shared}}$.

α_{coll}. Since also the spectrum of the collinearity angle does not show any structures besides a strong peak at 0 mrad, it was decided to not cut on this quantity. For the study on Δz_{min} however, Figure 5.11, we see a steady drop-off for "far" K_S^0 and even a peak at ~ 0 cm for "shared" K_S^0. Both classes of K_S^0 have their maximal significance for values below 0 cm, which is obviously unphysical for a K_S^0 coming from the BPV.

Even if we would put this fact aside by trying to explain it with a bad vertexing resolution, the so far presented way of performing the significance study has a problem. The criterion on choosing "far" K_S^0 directly affects the amount of allowed "shared" K_S^0 and vice versa, since we always require exactly two K_S^0 in the final state during the fine selection. Therefore, a two-dimensional significance study is the correct way of determining the final cut criteria. Here, we combine each tested value of $\Delta z_{\text{min}}^{\text{far}}$ with each value of $\Delta z_{\text{min}}^{\text{shared}}$, basically using a grid of values. The resulting significance can be found in Figure 5.13.

On Figure 5.13(b) we see that the significance of "shared" K_S^0 is constant in $\Delta z_{\text{min}}^{\text{far}}$. Therefore, we can choose the value $\Delta z_{\text{min}}^{\text{shared}} = 0.5$ cm at the place where the significance starts to drop, indicated by the horizontal red line. If we now look at Figure 5.13(a), we see some dependence on both cut-off values. Since we fixed the value of $\Delta z_{\text{min}}^{\text{shared}}$ with Figure 5.13(b), we can choose $\Delta z_{\text{min}}^{\text{far}} = 3.5$ cm now again as the value where the significance starts to drop at the given horizontal red line. The chosen value is indicated by a vertical red line.

From the corresponding fit of the K_S^0 mass spectrum, we can also obtain the cut-values for the K_S^0 invariant mass, see Figure 5.14. The values are

$$-15.00\,\text{MeV} \leq (m_{\pi\pi}^{\text{far}} - m_{K_S^0}^{\text{PDG}}) \leq 16.50\,\text{MeV}, \qquad -18.24\,\text{MeV} \leq (m_{\pi\pi}^{\text{shared}} - m_{K_S^0}^{\text{PDG}}) \leq 17.15\,\text{MeV}. \tag{5.6}$$

A K_S^0-candidate fulfilling these stronger mass requirements of equation (5.6), which also has a vertex

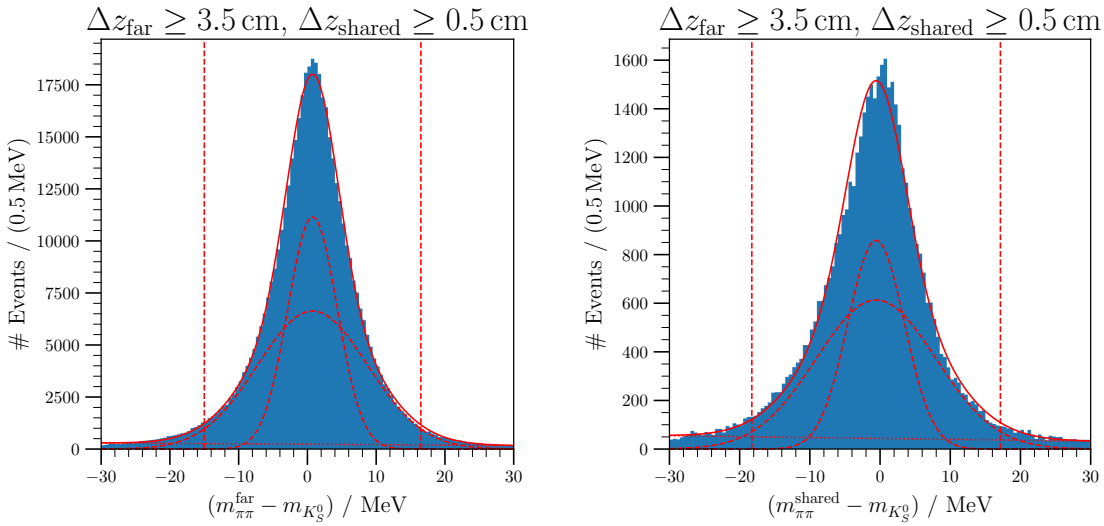

(a) "far" K^0_S (b) "shared" K^0_S

Figure 5.14: Invariant-mass spectrum of K^0_S-candidates at the determined cut-off values for Δz_{min}. The red dashed vertical lines indicate the cut interval. The full fit function is depicted as a red solid curve, the signal contributions from the double-Gaussian are the red dashed curves and the background is the red dotted curve.

separation of

$$\Delta z^{\text{far}} \geq \Delta z^{\text{far}}_{\text{min}} = 3.5\,\text{cm}, \qquad \Delta z^{\text{shared}} \geq \Delta z^{\text{shared}}_{\text{min}} = 0.5\,\text{cm} \tag{5.7}$$

according to its classification, is considered a "true" K^0_S. For the cut on exactly two K^0_S, now we demand exactly two "true" "far" K^0_S for $N^{\text{BPV}}_{\text{out}} = 1$, and exactly one "true" "far" K^0_S together with exactly one "true" "shared" K^0_S for $N^{\text{BPV}}_{\text{out}} = 2$. This is also a hard cut, meaning that all other cuts are automatically set to "failed" if this requirement is not met. The reason is, that for most of the following cuts, we need to have a well-defined final state with one primary track and two "true" K^0_S.

Not only can a SV share outgoing particles with the BPV, but it can also do so with any other SV. Therefore, we have to make sure that we actually have five distinct tracks in our event, two from each "true" K^0_S and one negatively charged track from the BPV. In the case of $N^{\text{BPV}}_{\text{out}} = 2$ we have to make sure that the one track of the BPV that is not part of the "shared" K^0_S, has negative charge. We assign the mass of a pion to this negatively charged track and call the resulting particle primary pion π^-_{prim}, because it originates from a PV. Accordingly, the daughters of the "true" K^0_S are called secondary pions $\pi^{\pm}_{\text{sec}}$. The cut on a "healthy" BPV takes care of all this. Figure 5.15 shows the number of unique tracks for such a selected $\pi^- K^0_S K^0_S$ event.

RICH-Veto Cuts

So far we simply assumed that all outgoing tracks are pions. However, also other final states might contribute such as $\Lambda K^0_S \bar{p}$, where not only the primary particle would be an antiproton, but additionally one of the SV would be a Λ baryon. Also $\Lambda\bar{\Lambda}\pi^-$ would be possible where both SV would be baryons. The (anti-)Λ baryon would decay into an (anti-)proton and an oppositely charged pion. Due to the

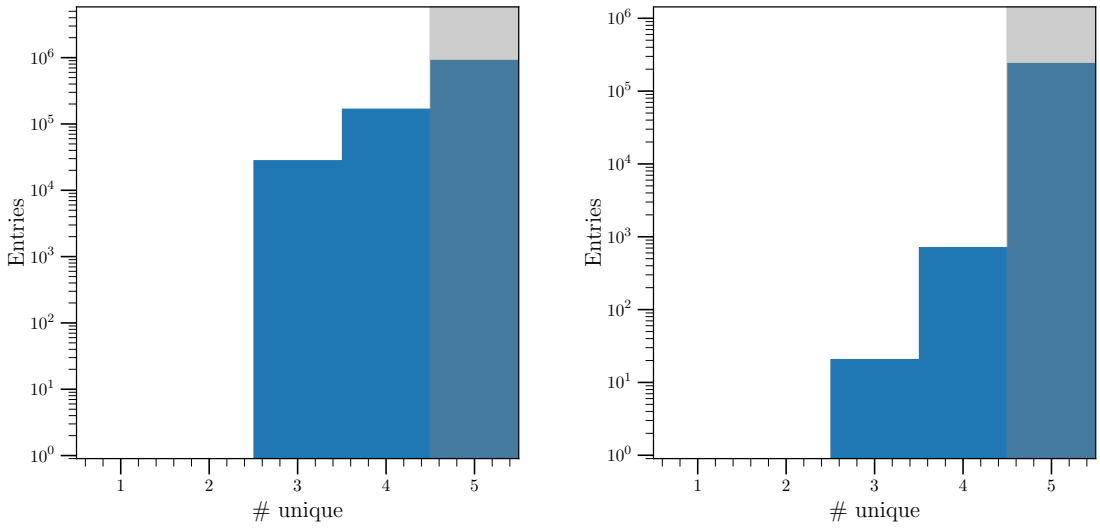

(a) Waterfall-Style

(b) BEST-Style

Figure 5.15: Number of unique tracks in the $\pi^- K_S^0 K_S^0$ event. We require exactly five unique tracks and in addition the remaining outgoing track from the BPV needs to have negative charge.

different masses of the daughter particles the invariant mass with pion assumption for both daughters could be within the window of equation (5.6), whilst assuming pion and proton mass for the daughters might also be close to the Λ mass. Due to the high mass of the involved baryons, these final states have a very high mass threshold of $> 2\,\text{GeV}$, but the slightly longer lifetime of the Λ baryon compared to the K_S^0 also allows for a displaced vertex, mimicking a very similar event topology.

Although the RICH detector only has a very limited momentum range in which it can distinguish the long-lived charged particles, we can still use it as a veto if it identifies any of the outgoing tracks as either kaons or (anti-)protons. The following procedure was developed and calibrated by [58]. The momentum ranges, where the RICH detector can positively identify particles are:

$$\pi\text{:}\ \ 3\,\text{GeV} \leq p_{\text{track}}^{@RICH} \leq 60\,\text{GeV}$$

$$K\text{:}\ \ 10\,\text{GeV} \leq p_{\text{track}}^{@RICH} \leq 60\,\text{GeV}$$

$$p\text{:}\ \ 18\,\text{GeV} \leq p_{\text{track}}^{@RICH} \leq 100\,\text{GeV}$$

For this we extrapolate the tracks to the position of the RICH detector at $z_{\text{RICH}} = 615.5\,\text{cm}$ in the COMPASS reference system. In addition to these momentum constraints, we also have to make sure that the tracks actually go through the active volume of the detector. This means that the transversal distance of the track from the beam axis has to be $r_{\text{track}}^{@RICH} > 5\,\text{cm}$ and the polar angle of the track has to fulfill $0\,\text{rad} < \theta_{\text{track}}^{@RICH} < 0.25\,\text{rad}$.

If these requirements are met, we can extract the likelihood of each particle species $\mathcal{L}_X$ with $X \in \{\pi, K, p, \text{bgd}\}$ and define a likelihood-ratio $\mathcal{R} := \dfrac{\mathcal{L}_X}{\max_{Y \neq X} \mathcal{L}_Y}$. If $\mathcal{R}_X > 1.15$, we assign the PID X to the particle. For the edge cases $\mathcal{L}_X \leq 0$, meaning no likelihood could be determined for PID X,

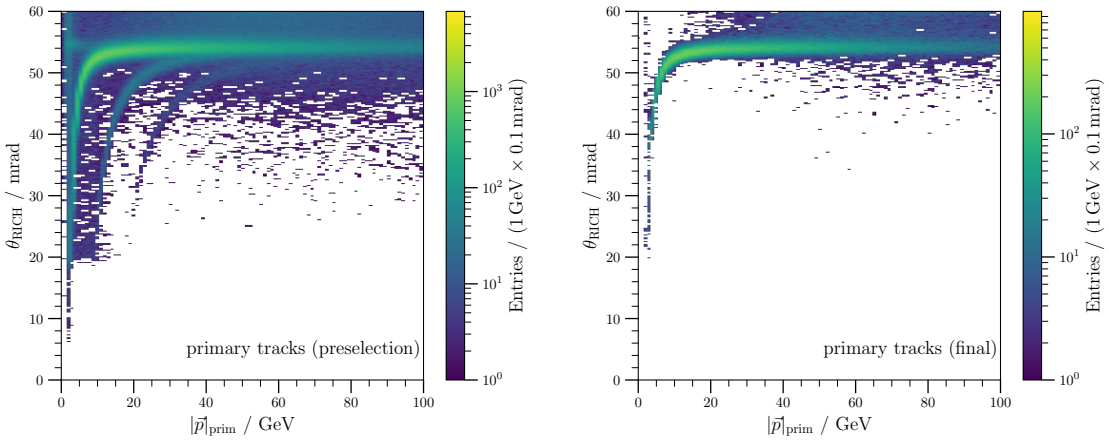

(a) Before the RICH-veto cuts.

(b) At the end of the fine selection

Figure 5.16: Cherenkov angle θ_{RICH} plotted against the momentum of the π^-_{prim}.

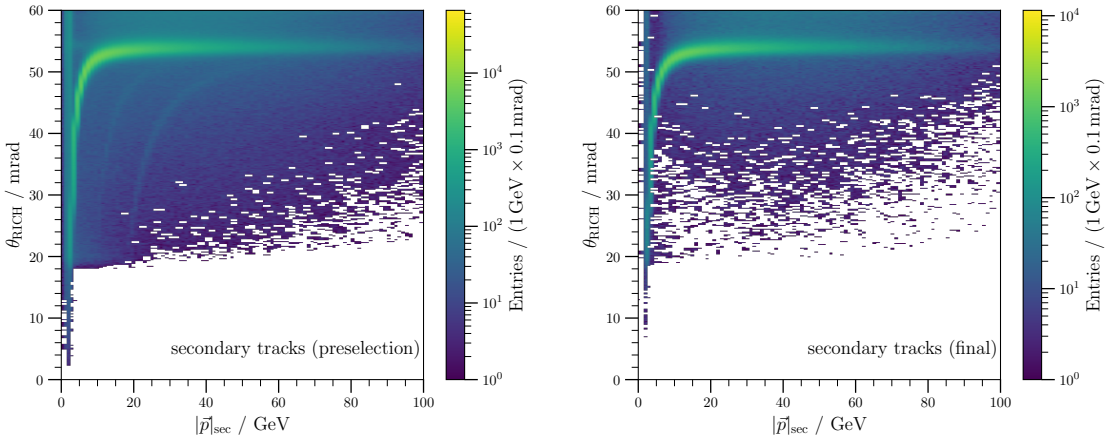

(a) Before the RICH-veto cuts.

(b) At the end of the fine selection

Figure 5.17: Cherenkov angle θ_{RICH} plotted against the momentum of the $\pi^{\pm}_{\mathrm{sec}}$.

we assign $\mathcal{R}_X = -1$ definitely resulting in a non-X PID. And if $\mathcal{L}_X > 0$, but $\max_{Y \neq X} \mathcal{L}_Y \leq 0$, we set $\mathcal{R}_X = 10$ leading to a positive identification as X.

If we plot the Cherenkov angle θ_{RICH} measured by the RICH detector against the momentum of the track at the position of the RICH, we should be able to see three different bands, corresponding from left to right to π, K and p. We can do this for the π^-_{prim}, see Figure 5.16, as well as for the $\pi^{\pm}_{\mathrm{sec}}$, see Figure 5.17.

In Figures 5.16(a) and 5.17(a) we see that there are three distinct bands visible as expected. However, at the end of the fine selection in Figures 5.16(b) and 5.17(b) the two rightmost ones corresponding to K and p are gone. These two bands were already a lot less visible for the $\pi^{\pm}_{\mathrm{sec}}$ due to the mass-constraint that is applied to the "true" K^0_S. Looking at the number of different particles before the RICH-veto cuts

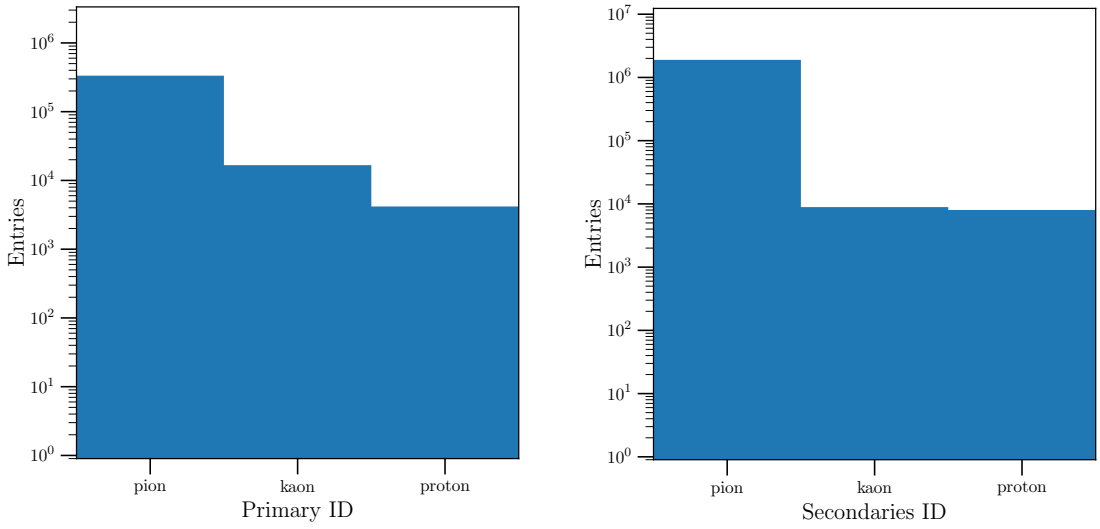

(a) π^-_{prim} (b) $\pi^{\pm}_{\text{sec}}$

Figure 5.18: Number of positively identified pions, kaons and (anti-)protons before the RICH-veto cuts.

in Figure 5.18, we see that the number of (anti-)protons is bigger for the $\pi^{\pm}_{\text{sec}}$ than for the π^-_{prim}, which hints to the presence of (anti-)Λ baryons before the RICH-veto cuts.

We can test this by simply assigning a proton mass to one and a pion mass to the other of the secondary tracks of the "true" K_S^0. If we assign the proton mass to the positively charged track, we should see a peak for the Λ baryon, while assigning it to the negatively charged track making it a $\overline{p}$, we have access to the $\bar{\Lambda}$ baryon. The corresponding invariant-mass distributions can be found in Figure 5.19, where we clearly can see a peak in each spectrum at the (anti-)Λ mass before the RICH-veto cuts, and at the end of the fine selection this peak is gone without strongly disturbing the "background" shape.

The peak of the Λ candidates in Figure 5.19(a) is slightly higher than the one of the $\bar{\Lambda}$ candidates in Figure 5.19(b), which might be explained by the fact that the $\bar{\Lambda}$ can only be created in the final state $\bar{\Lambda}\Lambda\pi^-$ while the Λ can additionally appear in $\Lambda K_S^0 \overline{p}$. Looking at the "charge-conjugated" final state $\bar{\Lambda} K_S^0 p$ the primary proton has the wrong charge, therefore, this final state is not possible, making the Λ more likely to occur.

Tight Beam-Time Cut

We already performed a rough cut on the beam time t_{beam} during the preselection to cut away all events that are definitely out-of-time. This cut will now be refined in the fine selection. Since the triggers are very sensitive, it is very likely that the timing will change slightly between different data-taking periods. Therefore, a fit to the BEST-Style distribution of the beam time was done period-by-period for all six data-taking periods. The signal was modeled with a single-Gaussian

$$\mathcal{G}(x; A, \mu, \sigma) = A \cdot \mathcal{N}(x; \mu, \sigma), \tag{5.8}$$

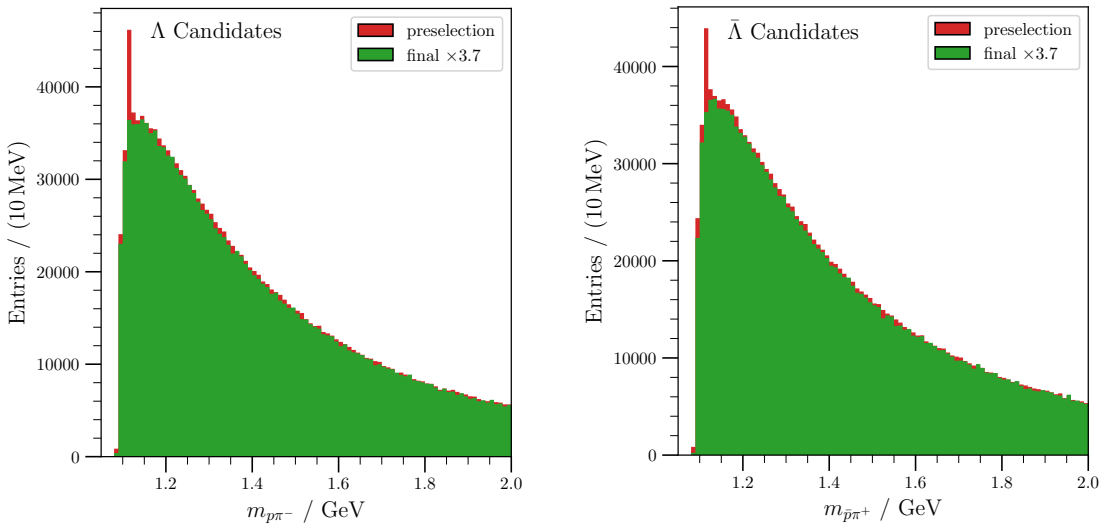

(a) $m_{p\pi^-}$ invariant-mass distribution.

(b) $m_{\bar{p}\pi^+}$ invariant-mass distribution.

Figure 5.19: Invariant-mass distributions of "true" K^0_S, while assigning the proton mass to one of the two daughter tracks and the pion mass to the other daughter track. The distribution before the RICH-veto cuts (red) is compared to the one after the fine selection (green). The latter is scaled by a factor of 3.7 to facilitate the comparison.

Table 5.3: Cut values for the beam time for the different data-taking periods with $t_\pm = \mu \pm 3\sigma$. They are obtained via a fit to the data, see Figure 5.20.

Period	A	μ / ns	σ / ns	t_- / ns	t_+ / ns
all	11895.35	0.00658	0.69404	-2.07553	2.0887
2008_W33	1476.54	0.01585	0.70377	-2.09545	2.12714
2008_W35	2364.5	0.06414	0.67785	-1.9694	2.09769
2008_W37	3598.84	0.10065	0.67337	-1.91946	2.12076
2009_W25	700.89	-0.20865	0.64451	-2.14218	1.72488
2009_W27	945.87	0.39336	0.75605	-1.87478	2.66149
2009_W35	3316.71	-0.19586	0.73719	-2.40744	2.01572

where $\mathcal{N}$ is the normal distribution as defined in equation (5.4). Again, the background shape is unknown, therefore, a second-order polynomial is used. In Figure 5.20, we can see that the determined mean values differ strongly[13] between the different data-taking periods, therefore, each of them has a slightly different accepted timing window as listed in Table 5.3.

[13] The maximal difference of the mean values μ is similar to the width σ of the distribution.

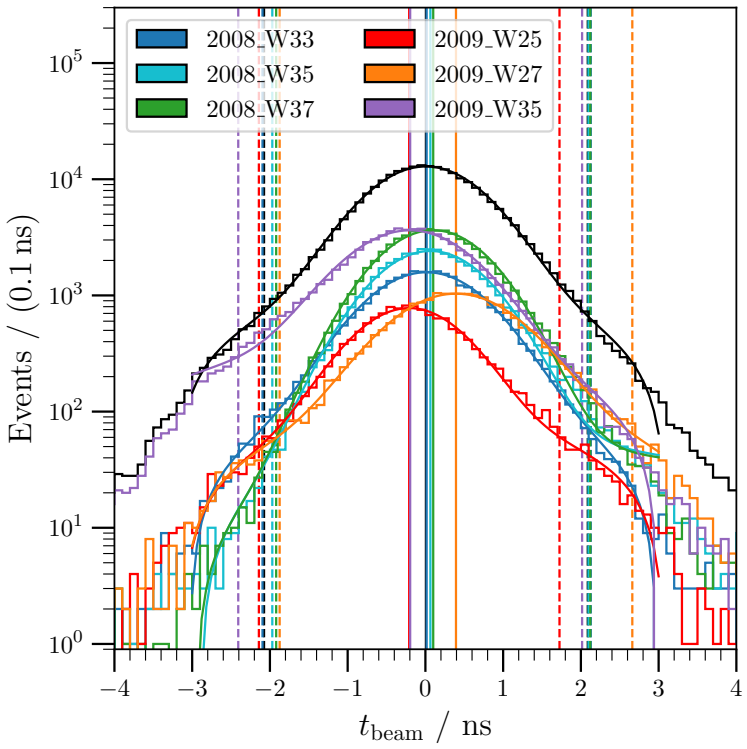

Figure 5.20: Fit to the beam time with a single-Gaussian as a model for the signal and a second-order polynomial for the background. Different colors correspond to different data-taking periods as indicated in the legend, while black corresponds to the combined data set. The colored vertical lines correspond to the mean μ (solid) and the 3σ intervals (dashed) of the respective period.

Kinematic Fit

At the end of the fine selection the invariant-mass distribution in Figure 5.21 has a lot smaller background compared to the one after the preselection in Figure 5.7(b), however, the mass of the "true" K_S^0 still deviates slightly from their nominal mass as stated by the PDG. This deviation purely comes from the detector resolution, since the decay width of the K_S^0 is negligible. We can correct for this resolution by performing a kinematic fit, which is a special case of constrained fitting [67]. To summarize it in one sentence, it is an iterative procedure that modifies the 4-vectors of the daughter particles slightly within their experimental uncertainties such that the invariant mass of the two-body system is exactly the nominal PDG K_S^0 mass. Details on the procedure can be found in appendix D.3.

Exclusivity and 4-Momentum Conservation

So far we did not ensure that the final state is complete, especially since we only throw events, where we have more or less than two "true" K_S^0. This does not exclude the possibility that there might be other `V0` particles that do not fulfill the requirements as discussed at the beginning of this section 5.2.3. We would simply miss these particles, but still would consider it a good event. However, this would

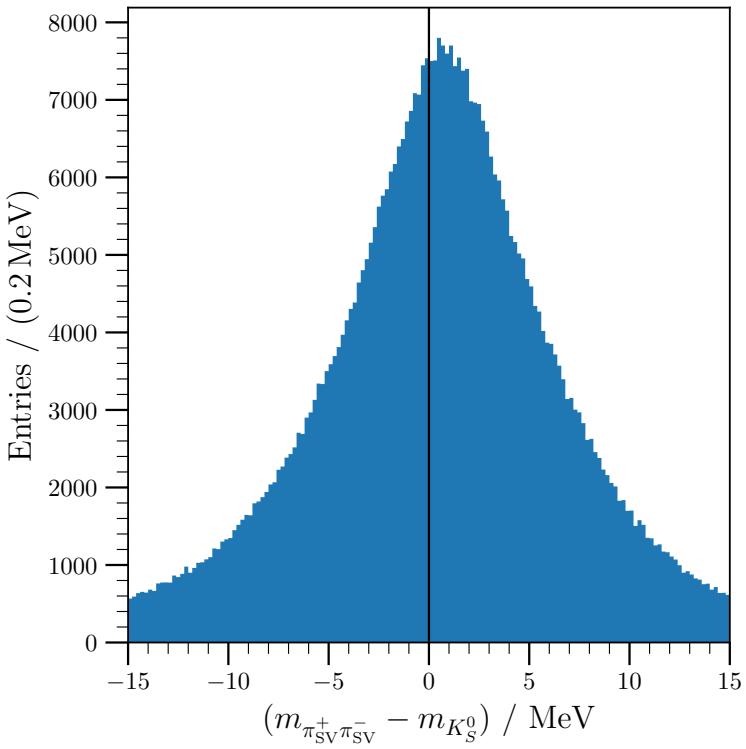

Figure 5.21: Invariant-mass distribution of "true" K^0_S at the end of the fine selection, but without applying the kinematic fit. It has to be successful though and the exclusivity cuts have to be fulfilled for final state with the kinematically fit K^0_S.

result in missing momentum and missing energy, thus, we perform the following two cuts to make sure that everything is conserved and the event is exclusive, meaning that no final-state particles are lost. In both calculations the kinematically fit 4-momenta of the "true" K^0_S enter.

First, we have the planarity cut. For both recoil momentum and resonance momentum we determine the components transverse to the direction of the beam, $\vec{p}^{\,\perp}_{\mathrm{recoil}}$ and $\vec{p}^{\,\perp}_{\mathrm{X}}$ respectively. The planarity angle ϕ_{recoil} is the angle between these two transverse momentum components. More details on how to calculate it can be found in appendix D.4.

The expectation for an exclusive event is 180°, since the transverse components of the recoil momentum and the resonance momentum have to be back-to-back in order to be able to cancel each other out. Therefore, we look at $\Delta\phi_{\mathrm{recoil}} = \phi_{\mathrm{recoil}} - 180°$ instead to obtain a spectrum centered around 0°, see Figure 5.22. In accordance with previous event selections at COMPASS and as determined by [68], we use $\left|\Delta\phi^{\mathrm{even}}_{\mathrm{recoil}}\right| \leq 8.432°$ and $\left|\Delta\phi^{\mathrm{odd}}_{\mathrm{recoil}}\right| \leq 5.377°$ as cut intervals for the planarity angle, respectively for even and odd RPD-slabs. These values are obtained by not only taking into account the dimensions of the slabs, but also multiple scattering in the scintillator material.

For the second cut to ensure exclusivity, we reconstruct the beam energy from our final-state particles $\pi^- K^0_S K^0_S$. This can be achieved by equating $t = (p_{\mathrm{target}} - p_{\mathrm{recoil}})^2 = (p_{\mathrm{beam}} - p_X)^2$, employing

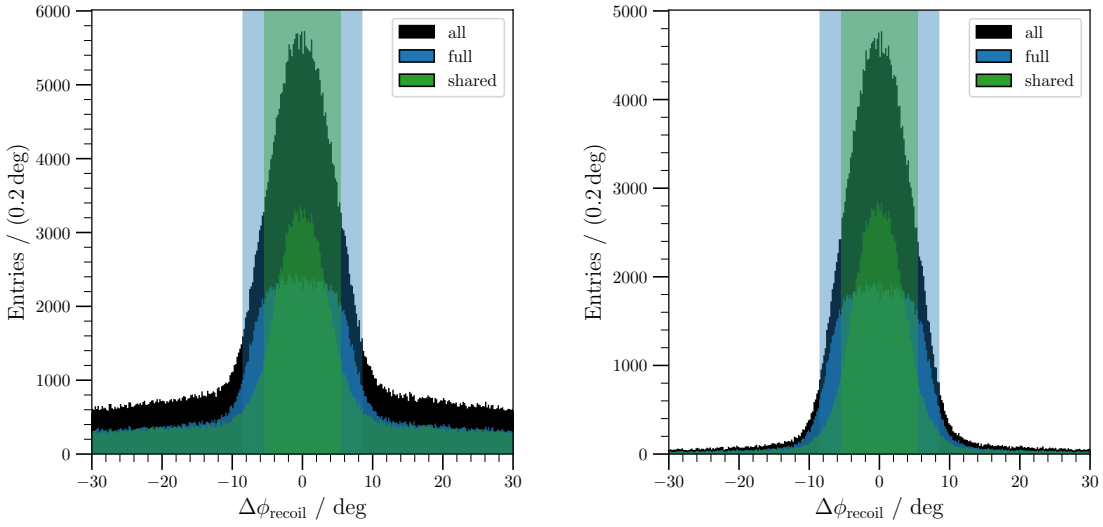

(a) Waterfall-Style

(b) BEST-Style

Figure 5.22: Deviation from the expectation of the planarity angle. The full spectrum is plotted in black, but no cuts were performed directly on this spectrum. Instead, a separation of the two different cases is plotted, where either an "even" (green) or an "odd" slab (blue) of the outer RPD-ring was hit. The corresponding cut intervals are highlighted with the same color code.

energy conservation to replace E_{recoil} by the other involved energies[14] and solving for $|\vec{p}_{\text{beam}}|$. From this we can calculate the beam energy via $E_{\text{beam}} = \sqrt{|\vec{p}_{\text{beam}}|^2 + m_{\text{beam}}^2}$. The details on the calculation can be found in appendix D.5.

In order to extract meaningful cut ranges, the resulting beam-energy spectrum is fitted with a single-Gaussian, see equation (5.8), for the signal and a second-order polynomial for the background. Events with a reconstructed beam energy within a 3σ interval around the mean value are accepted. The fit to the BEST-Style distribution can be found in Figure 5.23 and the resulting fit parameters are presented in Table 5.4. Similarly to the beam time, a separate fit for all data-taking periods was performed. However, the spread is not that big[15], which means, in the end, the values extracted from the fit over all periods combined are used.

Bad Runs

During previous event selections it was found out that some runs have differences in kinematic distributions that most likely come from malfunctioning detector equipment. An extensive bad-run analysis was performed by Simon Havemann and is described in appendix C of [65]. There, simple quantities like mean and standard deviation of kinematic distributions are taken and a run-by-run

[14] The energy resolution of the RPD is not very good, therefore, we do not use it for these calculations.

[15] The maximal difference of the mean values μ is $\sim 200\,\text{MeV}$, while the width σ of the distribution is almost one order of magnitude bigger with $\sim 1.7\,\text{GeV}$.

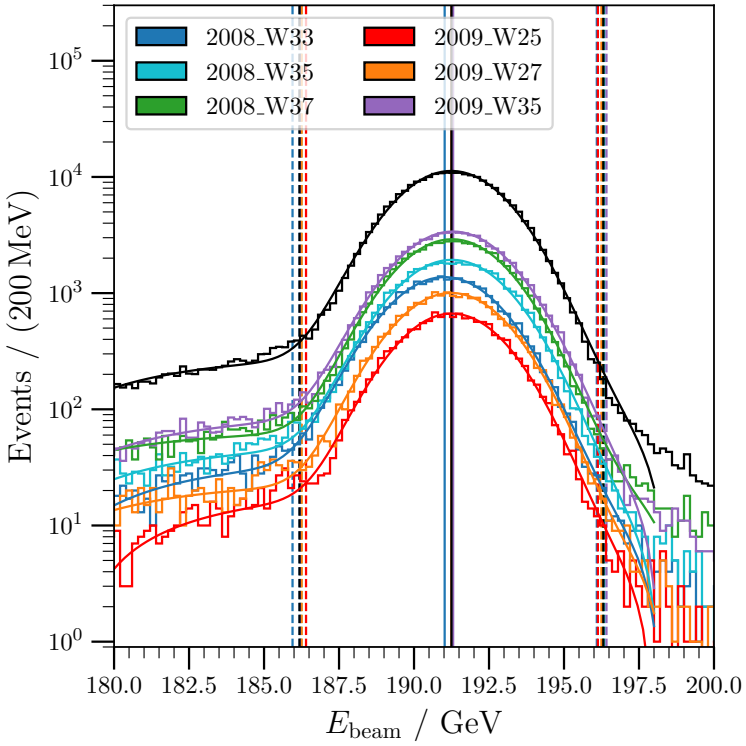

Figure 5.23: Fit to reconstructed beam-energy distribution

Table 5.4: Possible cut values for the beam energy for the different data-taking periods with $E_{\pm} = \mu \pm 3\sigma$. They are obtained via a fit to the data, see Figure 5.23. In the end, the values in the first row are taken for all periods.

Period	A	μ / GeV	σ / GeV	E_- / GeV	E_+ / GeV
`all`	11047.85	191.248	1.688	186.184	196.312
`2008_W33`	1345.24	191.021	1.691	185.95	196.093
`2008_W35`	1897.09	191.267	1.694	186.185	196.348
`2008_W37`	2858.84	191.271	1.676	186.242	196.3
`2009_W25`	651.71	191.264	1.621	186.4	196.129
`2009_W27`	986.0	191.25	1.666	186.252	196.248
`2009_W35`	3323.01	191.304	1.704	186.191	196.416

comparison was performed[16]. Outliers of this comparison were investigated in more detail. Also the logbook of the data taking was consulted to find reasons for these outliers. The opposite direction was also done, i.e. if the logbook lists problems with detectors, a more detailed look at the distributions affected by these detectors were checked for problems. Then, the problems are categorized, since not all selections might be affected by problems of a specific detector type.

For this selection, all runs that show up in the categories "General", "RICH" and "CEDAR" are excluded by this bad-run cut. Since we do not use the information of the ECALs, problems of the corresponding category should not directly impact the selection at hand and therefore, they are still accepted.

In Figure 5.26 we see that the selection in general is quite good in excluding these runs, since only roughly 5 000 events are excluded only due to this cut. However, this also shows that such a bad-run analysis is an important step during such a selection, since without it we would most likely have roughly 2 % more background in the final data sample.

True Primary Vertex

The final cut is about the number of PVs in the event. In principle, we should have only one PV to be sure that this is the place, where the beam interacted with the target. But especially in the case where we have displaced SVs in the final state, a coincidental crossing of one of the corresponding daughter particles with the direction of the beam can occur. Therefore, we will not cut on the number of PV directly, but define a "true" PV, instead.

First of all, we define the BPV as a "true" PV. For all other PV-candidates of the event as provided by PHAST, we compare their outgoing charged tracks with the final-state tracks, meaning the tracks of the π^-_{prim} and the $\pi^\pm_{\text{sec}}$. If all outgoing tracks of the PV under investigation are also part of the final-state tracks, the PV is discarded. Now, if all other PVs than the BPV can be discarded accordingly, the event will be accepted. But if at least one of the other PVs has a track that is not part of the final state, this PV is considered a "true" PV and the event will be discarded. Figure 5.24 shows the amount of such "true" PVs. Since we consider the BPV as "true", only all events with exactly one "true" PV are accepted. Since this is the last cut of the fine selection, both Waterfall-Style and BEST-Style histograms are the same. The difference in the bin "1" is 1 143, which means we gain this amount of events at the end of the selection compared to when simply cutting on the number of all PVs.

Cut-Flow Diagram

In the cut-flow diagram of the fine selection in Figure 5.25 we can clearly see that the biggest impact comes from the first cut on the two K_S^0. This is understandable since it requires a much tighter mass cut compared to the preselection, as well as a cut on the minimal vertex separation. This cut is also a hard requirement for all other cuts, therefore, its entry in Figure 5.26 is zero, since all other cuts will be set to "failed" once we do not have exactly two K_S^0.

After the "healthy" BPV cut, the set of final-state particles is complete and the following cuts guarantee the quality of the events. The subsequent RICH-cuts do not have a big impact, since they are just vetoes. The cut on the beam time exclusively removes roughly 6 600 events, showing that there is

[16] If a run showed differences with respect to the other ones, a spill-by-spill analysis was performed for this run to see if parts of it were recoverable.

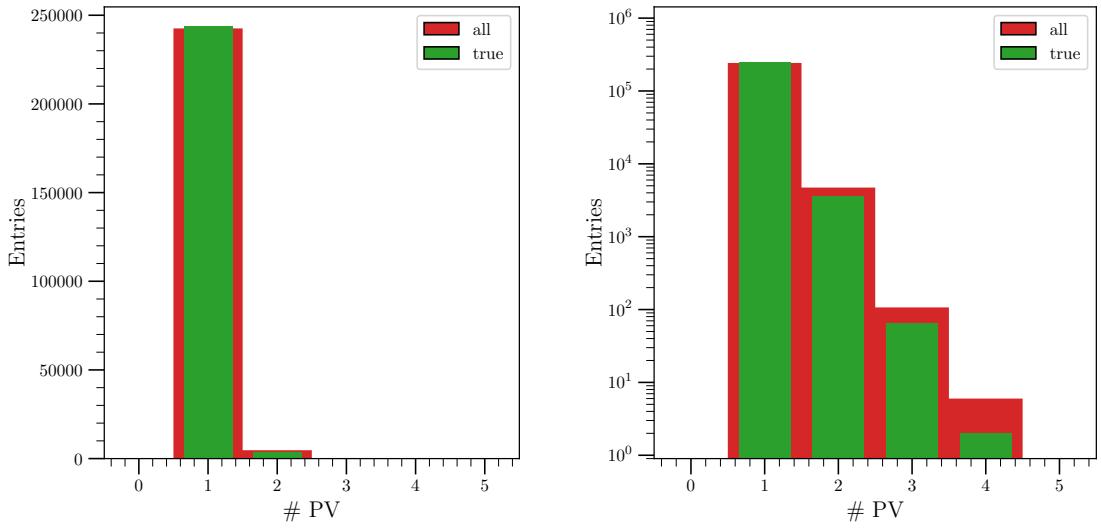

(a) Linear scale

(b) Logarithmic scale

Figure 5.24: Number of "true" PVs (green) compared to number of all PVs (red). Only events with exactly one "true" PV are accepted. Since the corresponding cut is the last one, BEST-Style and Waterfall-Style are the same for this distribution.

still quite some overlap of events present that has to be removed. On the other hand, the kinematic fit only fails for 8 events, showing the stability of the fit procedure.

A big impact comes from the planarity cut as well as from the cut on the beam energy. Figure 5.25 suggests that the planarity cut has a much stronger effect, however, Figure 5.26 indicates that both cuts are of similar order. Since not many other cuts come afterwards, we can deduce that many events also fail to fulfill the requirements on the planarity angle when they violate the cut on the beam energy and vice versa. This shows that these two cuts are strongly connected to each other.

At the end of the fine selection we are left with 243 722 exclusive $\pi^- K_S^0 K_S^0$ events.

5.2.4 t' Distribution

Before we discuss the results of the event selection, let us have a look at the reduced four-momentum transfer t'. Figure 5.27 shows an exponential drop as it is expected from theory. A fit with the sum of two exponential functions was performed. This parametrization can later be used in order to optimize the generation of MC data that is needed to determine the acceptance of the COMPASS spectrometer for the $\pi^- K_S^0 K_S^0$ final state.

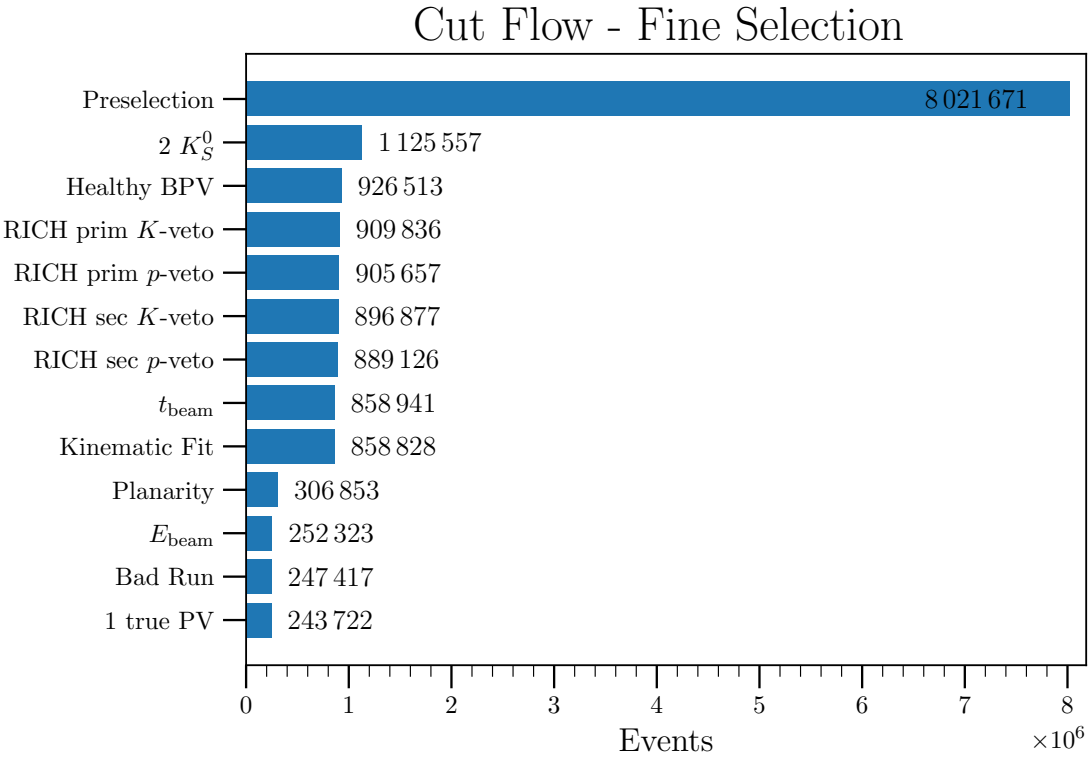

Figure 5.25: Cut-flow diagram of the fine selection.

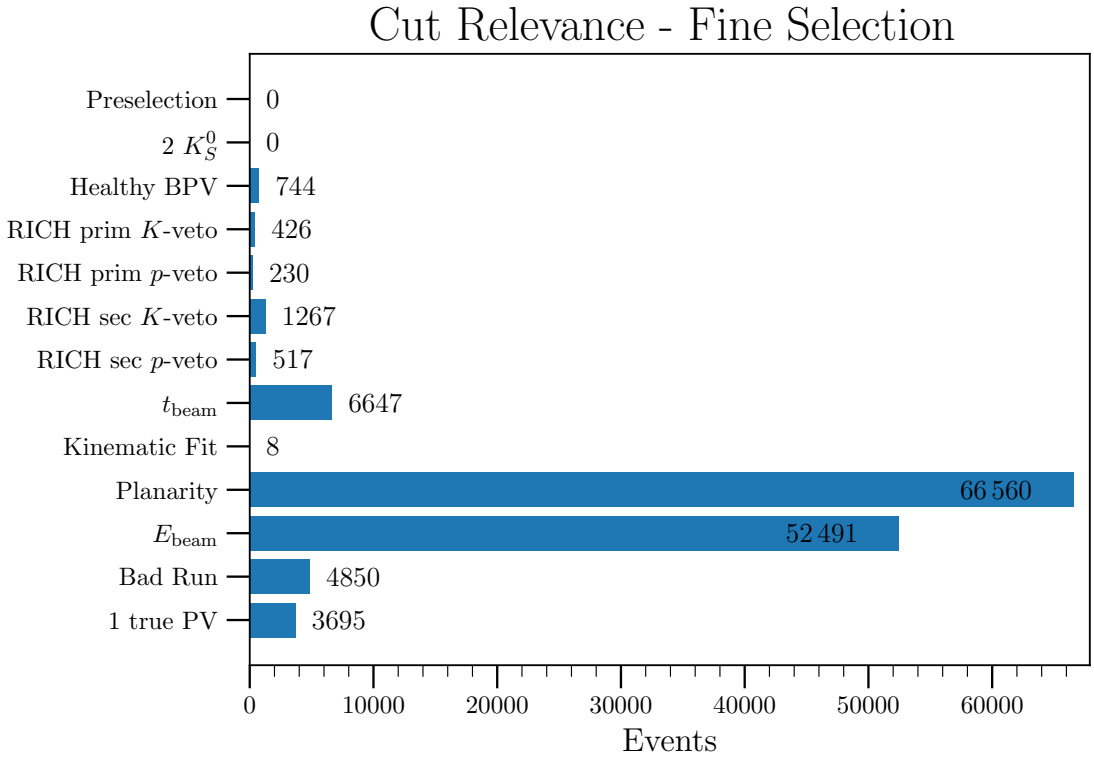

Figure 5.26: Number of events that are cut by only the respective cut during the fine selection.

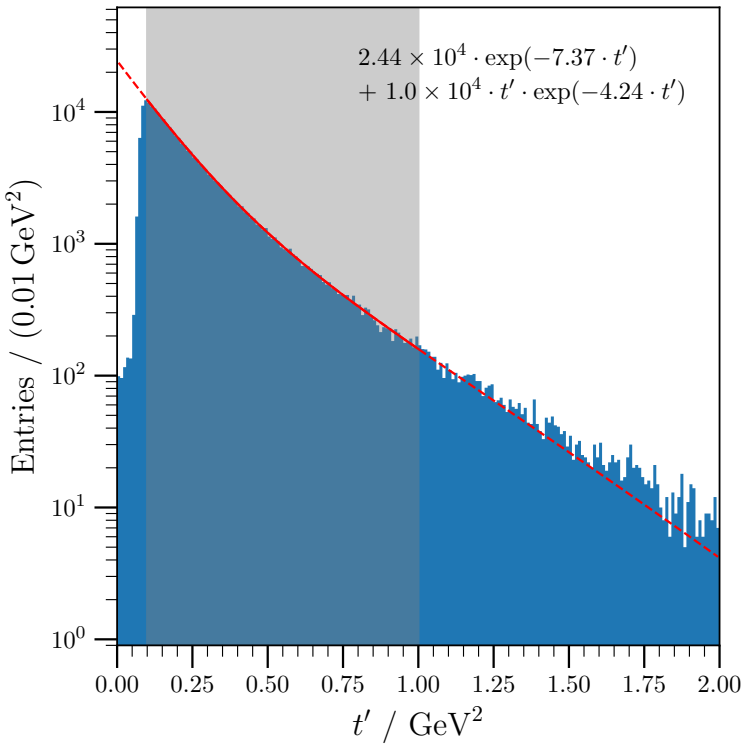

Figure 5.27: Distribution of the reduced four-momentum transfer t' at the end of the fine selection. The red line indicates a fit with the sum of two exponential functions as indicated in the plot. Note that the units of the provided fit parameters are GeV^{-2}.

5.3 Invariant-Mass Distributions and Dalitz Plots

Before we finally can discuss the results of the event selection, let us define our expectations on what we could and should see on the mass distributions and the Dalitz plots.

5.3.1 Identifying possible Resonances

From Table 5.2 we can read off the dominant decay modes for each resonance. Usually, decays with higher orbital angular momentum are suppressed, which means that we most likely will only see S-waves if their decay modes are kinematically possible. This is obviously a simplification since a stronger coupling to an isobar candidate could compensate this effect. Anyways, let us now have a look at each resonance one by one and discuss the likelihood of identifying it on the Dalitz plots by eye.

$J^{PC} = 1^{++}$: a_1

The dominant S-channel decay goes via $K^{*-}K^0_S$. Therefore, the PDG-established states $a_1(1260)$ and $a_1(1640)$ should have the $K^*(892)$ as the dominant isobar contribution, with the former sitting right at threshold. For the heavier PDG-listed states $a_1(1930)$, $a_1(2095)$ and $a_1(2270)$ also the heavier $K^*(1410)$ could be contributing, additionally. The heaviest one could even have $K^*(1680)$ as an isobar. However, heavier states corresponding mostly to higher radial excitations usually come with a reduction in intensity.

$J^{PC} = 2^{++}$: a_2

The a_2 resonances cannot decay via an S-channel, making them very unlikely to be visible by eye on the Dalitz plots. On top of that they require $M \geq 1$, reducing their strength even further.

$J^{PC} = 3^{++}$: a_3

The PDG does not list any established a_3 resonances, however there are some listings that we will discuss now. The a_3 resonances would dominantly decay via the $K^{*-}_3 K^0_S$ S-channel. The lightest PDG-established isobar candidate would be the $K^*_3(1780)$ making this decay mode kinematically impossible for the $a_3(1875)$ and the $a_3(2030)$. The $a_3(2275)$ would, however, sit right at the threshold. In any case, an observation will only be possible with a PWD by also looking at other decay channels with higher orbital angular momentum.

$J^{PC} = 4^{++}$: a_4

Similar to the a_2 resonances also the a_4 resonances cannot decay via an S-channel and require $M \geq 1$, therefore, one will need to look at the results of the PWD to identify any contributions here.

$J^{PC} = 0^{-+}$: π

Here, the $f_0\pi^-$ and the $K^{*-}_0 K^0_S$ channels would be dominant S-wave decays. This gives us a big quantity of possible isobars namely the $f_0(980)$, $f_0(1500)$ and $f_0(1710)$ on one side and the $K^*_0(700)$ and $K^*_0(1430)$ on the other. The lightest K^*_0 is very broad, therefore, we do not expect to see it by eye. The

PDG also lists the $f_0(1370)$, but we do not see it in the $K_S^0 K_S^0$ invariant-mass spectrum and it was also not seen in the $\pi^-\pi^+\pi^-$ final state of COMPASS [31]. The non-strange cousin of the $K_0^*(700)$, the $f_0(500)$ also known as σ, is too light to decay into two kaons. However, it is quite broad such that its high-mass tail could actually contribute, which still does not make it very likely to be visible.

Let us now come to the resonances. The $\pi(1300)$ could only decay to the lightest isobar of each channel, but it sits right at threshold. The next candidate is the $\pi(1800)$, where only the $f_0(1710)$ and the $K_0^*(1430)$ are too heavy to appear as possible isobars. Further listings include the $\pi(2070)$ and the $\pi(2369)$ that could decay via all isobar channels listed above.

$J^{PC} = 1^{-+}$: π_1

These QNs are spin-exotic, meaning that they cannot be produced by a simple $q\bar{q}$-pair making them a candidate for a so-called hybrid meson, where in addition also a constituent gluon contributes to its QNs. Sadly, no S-wave decay will be possible and similarly to the a_{even} resonances only $M \geq 1$ is allowed, therefore, we have to wait for the PWD to see its contributions.

$J^{PC} = 2^{-+}$: π_2

Isobar candidates for S-channel decays with a mass below 2 GeV are $f_2(1270)$, $f_2'(1525)$ and $f_2(1950)$, as well as $K_2^*(1430)$ and $K_2^*(1980)$. For the lightest resonance $\pi_2(1670)$ only the $f_2(1270)$ would be possible. The $\pi_2(1880)$ could additionally have contributions from the $f_2'(1525)$. The PDG-listed $\pi_2(2285)$ would also allow for the $f_2(1950)\pi^-$ channel.

$J^{PC} = 3^{-+}$: π_3

This case is similar to the π_1, however, the PDG does not list any resonance candidates so far.

$J^{PC} = 4^{-+}$: π_4

The dominant S-wave decay would go via the $f_4\pi^-$ and $K_4^{*-}K_S^0$ channels. But for the listed $\pi_4(2250)$, only the $f_4(2050)$ would be light enough to be an isobar in the decay. The $K_4^*(2045)$ would require a mass of more than 2.5 GeV to become possible.

Summary

To summarize, only the decay channels $a_1(1640) \to K^*(892)K_S^0, \pi_2(1670) \to f_2(1270)\pi, \pi(1800) \to f_0(980)\pi$ and maybe $\pi(1800) \to f_0(1500)\pi$ might be visible by eye when looking at the Dalitz plots. For the rest, a PWD has to be performed to separate the different contributions by using the angular information between the final-state particles.

5.3.2 Invariant-Mass Distributions

Now, we can finally look at the invariant-mass distributions and see if we can confirm our expectations from section 5.3.1.

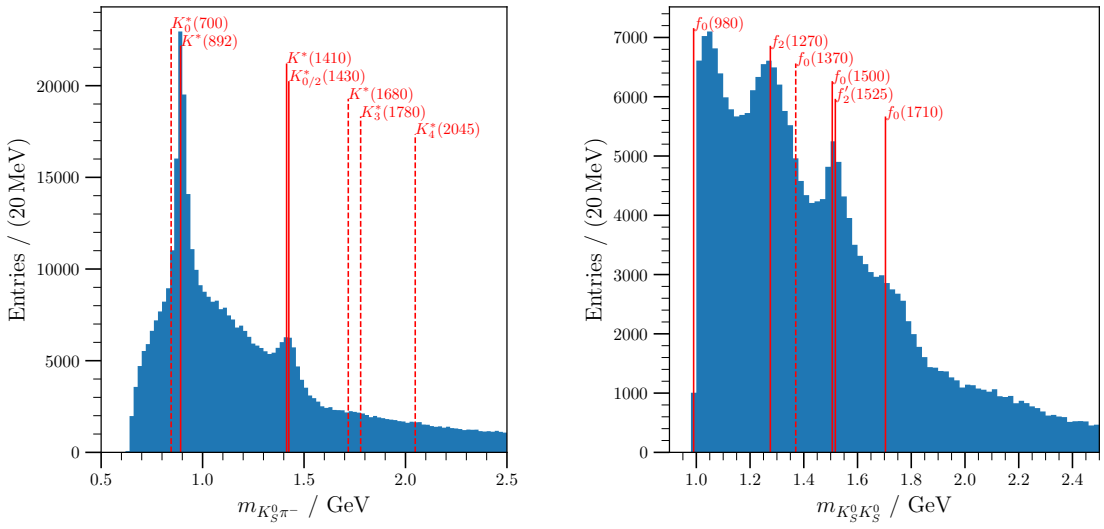

(a) $\pi^- K_S^0$ invariant mass

(b) $K_S^0 K_S^0$ invariant mass

Figure 5.28: Isobar invariant-mass spectra of the two-body subsystems $\pi^- K_S^0 K_S^0$ (left) and $K_S^0 K_S^0$ (right). Solid lines indicate isobars visible in the data and isobars with dashed lines are either absent or no strong indication is present in the data. Note that on the left plot, both $\pi^- K_S^0$ combinations are filled, therefore, the total amount of entries is double of the ones on the right.

Two-Body Subchannels

Let us start with the two-body subsystems. One can find the invariant-mass distributions in Figure 5.28. We see some peaking structure right at threshold in the $K_S^0 K_S^0$-invariant-mass spectrum in Figure 5.28(b) that could be related to the high-mass tail of the $f_0(980)$ meson. Also, there is a very strong peak at the mass of the $f_2(1270)$ suggesting its presence in the data. At roughly 1.5 GeV we have the $f_0(1500)$ and the $f_2'(1525)$ that could be contributing to the visible structure. At 1.7 GeV we see a clear shoulder that might come from the $f_0(1710)$. However, we do not see any structure at the mass of the $f_0(1370)$ indicating its absence in the data, as it is also the case for the $\pi^-\pi^+\pi^-$ final state at COMPASS [31].

As discussed in section 5.1.3, we do not expect ρ_J isobars to appear. And indeed, there is no sign of a $\rho(1450)$ or a $\rho_3(1670)$.

Looking at the $\pi^- K_S^0$ subsystem in Figure 5.28(a), we see a very broad bump below the narrow $K^*(892)$ peak. Besides of background from e.g. the cross-channel decay via $f_J\pi^-$, also the very broad $K_0^*(700)$ could contribute here. However, one will only be able to extract its contributions with a PWD. We see a second peak at the mass of the $K^*(1410)$, the $K_0^*(1430)$ and the $K_2^*(1430)$. Disentangling which of these resonances contributes how much will also only be possible with a PWD.

These isobar spectra are integrated over all three-body invariant masses, therefore, a lot of additional information is lost when looking at them. A better way to represent them is, by showing their evolution as a function of $m_{\pi^- K_S^0 K_S^0}$, see Figure 5.29. Here, we see the strong $K^*(892)$ peak starting to appear at $m_{\pi^- K_S^0 K_S^0} = 1.4$ GeV, loosing its strength around $m_{\pi^- K_S^0 K_S^0} = 1.8$ GeV, where the $\pi(1800)$ would be

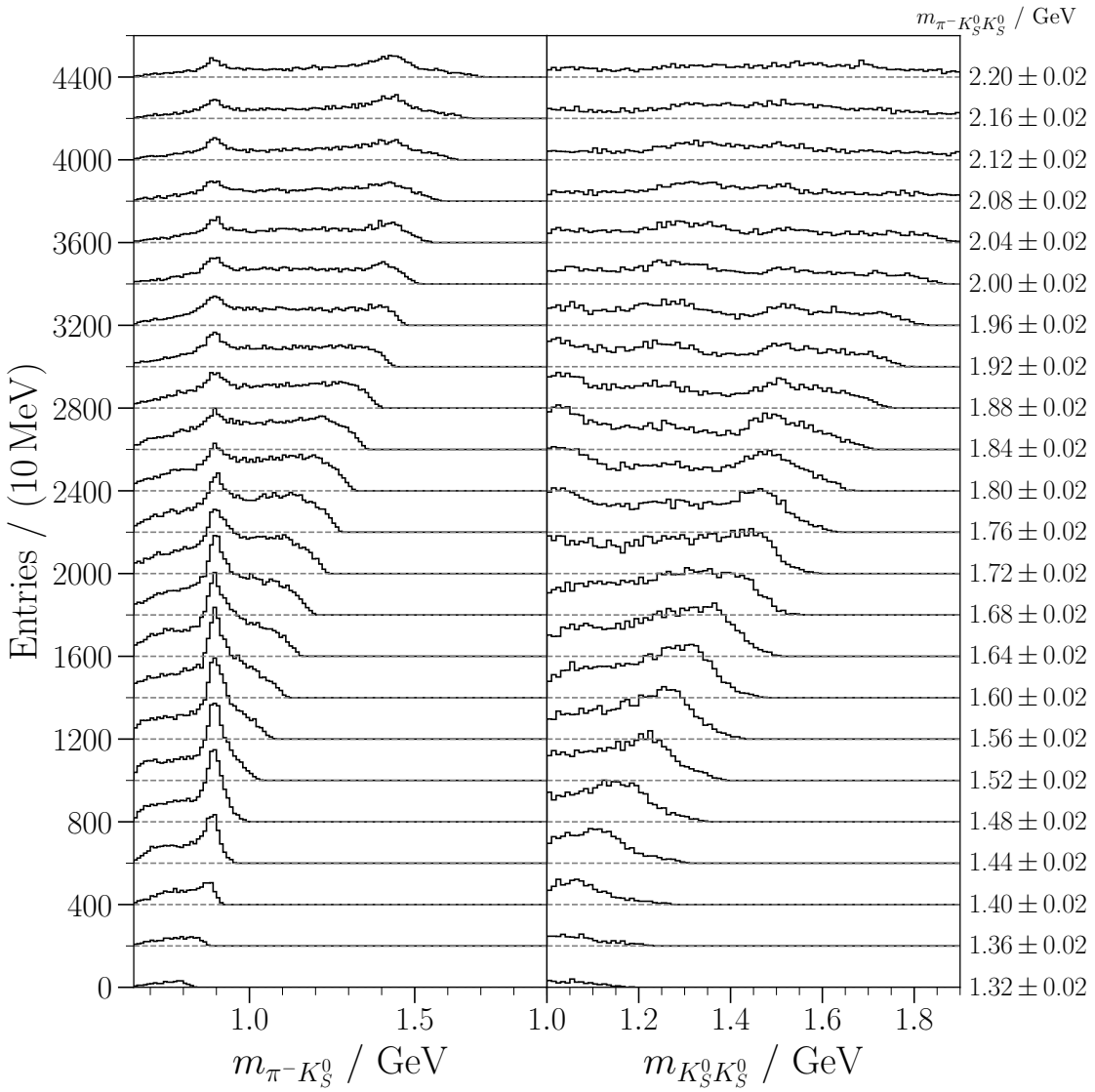

Figure 5.29: Invariant-mass spectra for the two-body subsystems $\pi^- K_S^0$ (left) and $K_S^0 K_S^0$ (right) for different bins of $m_{\pi^- K_S^0 K_S^0}$ as indicated by the axis on the right. Note that for the $\pi^- K_S^0$ system, the combinations with both K_S^0 are filled with a weight of 0.5 in order to have comparable hights on both isobar spectra.

expected to decay predominantly into f_0 isobars. And indeed, at that three-body invariant mass, peaks at the masses of the $f_0(980)$ and the $f_0(1500)$ appear on the right column. Around $m_{\pi^- K_S^0 K_S^0} = 1.68\,\text{GeV}$, we see a peak at the $f_2(1270)$ mass which could hint towards the $\pi_2(1670) \to f_2(1270)\pi$ decay in an S-wave. Regarding higher resonance masses, no dominating peak structures emerge for the $K_S^0 K_S^0$ subsystem, however, in the $\pi^- K_S^0$ system a second peak at the mass of the heavier K_J^* isobars appears at $m_{\pi^- K_S^0 K_S^0} \geq 2\,\text{GeV}$.

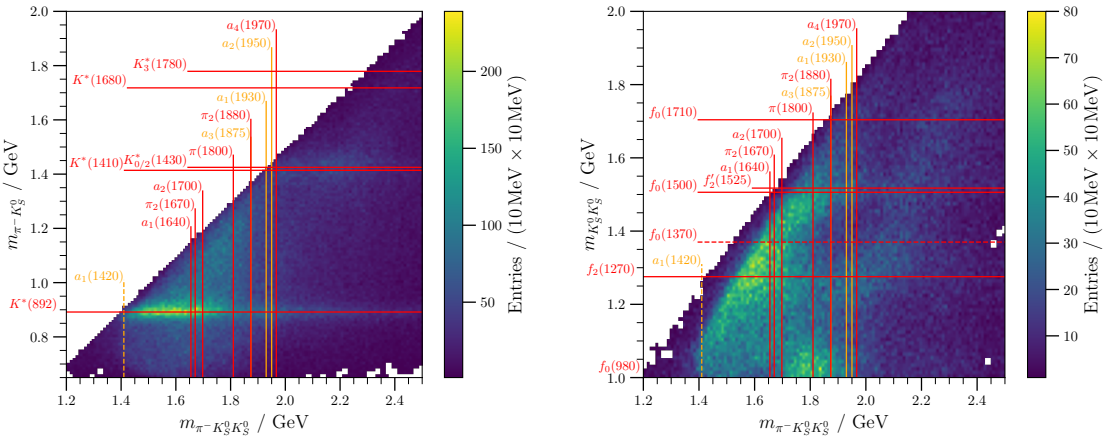

(a) (b)

Figure 5.30: Two-body invariant mass of the $\pi^- K_S^0$ (left) and the $K_S^0 K_S^0$ subsystems (right) plotted against the three-body invariant mass. Red lines indicate established states according to the PDG and orange lines label states that still need confirmation. Note that on the left plot, both $\pi^- K_S^0$ combinations are filled, therefore, the total amount of entries is double of the ones on the right.

A different visualization of this evolution can be found in Figure 5.30 leading to similar conclusions. We see a strong $K^*(892)$ band on the left that looses its strength at $m_{\pi^- K_S^0 K_S^0} = 1.8\,\text{GeV}$. At that mass we see an enhancement on the right at the bottom, where the $f_0(980)$ lies.

$\pi^- K_S^0 K_S^0$ Invariant-Mass Spectrum

If we have a look at the three-body invariant-mass spectrum in Figure 5.31(a), we see a broad bump at $\sim 1.75\,\text{GeV}$ and a shoulder at $\sim 2.2\,\text{GeV}$. If we draw lines for all allowed resonances in this final state, we see that they are all very close to each other. This also becomes obvious if we look at Figure 5.31(b). There we see that the resonances overlap heavily within their decay widths. This will make it difficult to cut on the three-body invariant mass to look for possible decay channels on the Dalitz plots. However, we can still try to confirm our expectations from the summary of section 5.3.1.

5.3.3 Dalitz Plots

The concept of Dalitz plots was introduced in section 3.5.1. Applying it to our specific final state, we choose $m^2_{\pi^- K_S^0}$ on the x-axis resulting in K_J^* isobars appearing as vertical bands, and $m^2_{K_S^0 K_S^0}$ on the y-axis which gives us f_J isobars as horizontal lines. Diagonal lines will correspond to the other $\pi^- K_S^0$ combination meaning that K_J^* isobars will also appear as diagonal lines. Since we cannot distinguish the two K_S^0 from each other, we will symmetrize the Dalitz plot by filling it with both $\pi^- K_S^0$ combinations. As a result, we will have two entries per event.

In order to test the hypotheses of the summary of section 5.3.1, we have a look at the Dalitz plots with a 20 MeV window around the PDG value of the $a_1(1640)$ (band "2" in Figure 5.31(b)) and the $\pi(1800)$ (band "3" in Figure 5.31(b)). As mentioned at the end of section 3.5.1, this mass window

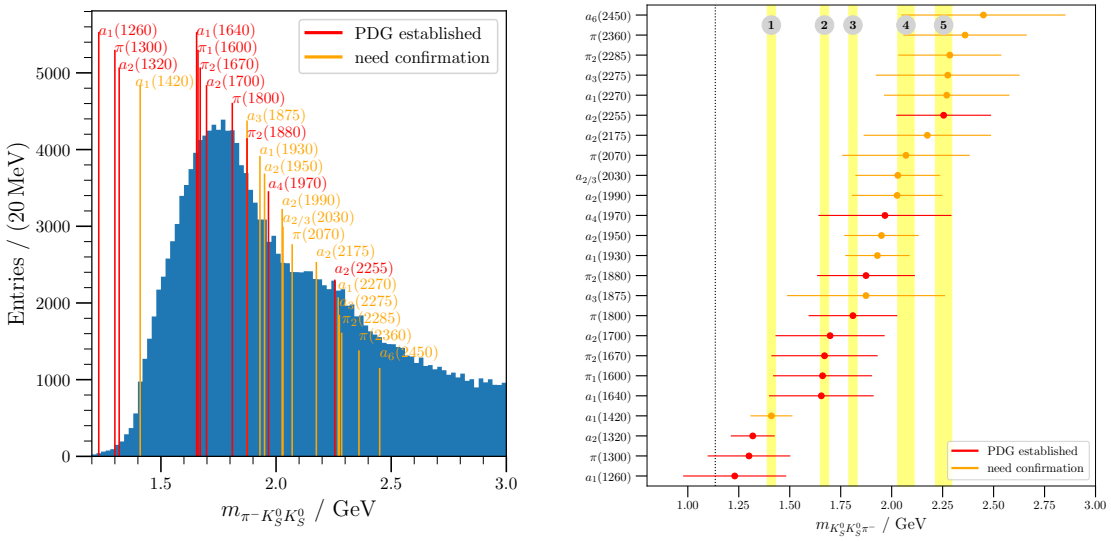

(a) $\pi^- K_S^0 K_S^0$ spectrum

(b) Overlap of resonances

Figure 5.31: The left plot shows the resonance-mass spectrum for the $\pi^- K_S^0 K_S^0$ final state. The plot on the right plots the mass of all allowed resonances according to the PDG. The horizontal lines correspond to the decay width of the corresponding resonance. The vertical yellow bands indicate the regions for which we will create Dalitz plots.

will wash out the diagonal bands slightly, which is why we choose it that narrow.

Let us begin with the Dalitz plot around the $a_1(1640)$ mass. Our expectation was to have the dominant decay via $a_1(1640) \to K^*(892)K_S^0$, and indeed we see a very strong vertical and diagonal $K^*(892)$ band in the Dalitz plot in Figure 5.32. In principle, the mentioned $\pi_2(1670) \to f_2(1270)\pi$ decay channel should also be dominant, however, due to the strong and overlapping $K^*(892)$ bands in this region, it is hard to tell by eye if there is a horizontal line present in the Dalitz plot.

The next Dalitz plot around the $\pi(1800)$ mass in Figure 5.33 should have a dominant decay via $\pi(1800) \to f_0\pi$, and indeed, we can see that the $K^*(892)$ band is strongly suppressed coming along with an enhancement at the lower $m^2_{K_S^0 K_S^0}$ threshold, indicating the presence of the $f_0(980)$ isobar. We also see a hint for a horizontal line at the $f_0(1500)$ mass, however, the vertical and diagonal $K^*(892)$ bands overlap at this position which makes a definitive statement on its presence impossible. There might also be a very faint line coming from the $f_2(1270)$ which could be a hint towards the presence of the decay $\pi_2(1880) \to f_2(1270)\pi^-$ or it also could simply be the high-mass tail of the decay from the $\pi_2(1670) \to f_2(1270)\pi^-$ that was not hardly visible in Figure 5.32 due to the overlapping $K^*(892)$ bands.

In order to also explore the broad high-mass shoulder in the $\pi^- K_S^0 K_S^0$ spectrum, we also look at two higher-mass regions (bands "4" and "5" in Figure 5.31(b)). They are centered around the $\pi(2070)$ and the $a_2(2255)$. However, there are many very broad resonances that all contribute to these regions, thus, predicting dominant decay channels is very difficult. The Dalitz plots can be found in Figures 5.34 and 5.35, respectively. Since the Dalitz plots become bigger, we also have to increase the resonance-mass window to 40 MeV to have sufficiently populated distributions.

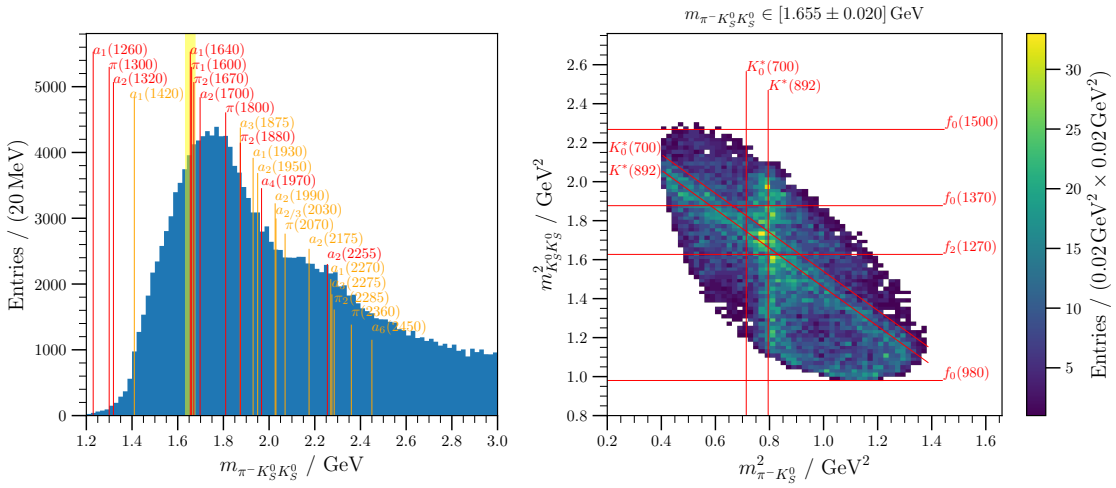

Figure 5.32: The left plot shows the invariant-mass distribution of the $\pi^- K^0_S K^0_S$ final state. The yellow band indicates the mass region that was used to create the Dalitz plot on the right. The mass region around the $a_1(1640)$ mass is spelled out in the title of the Dalitz plot and corresponds to band number 2 in Figure 5.31(b). The Dalitz plot has two entries per selected event.

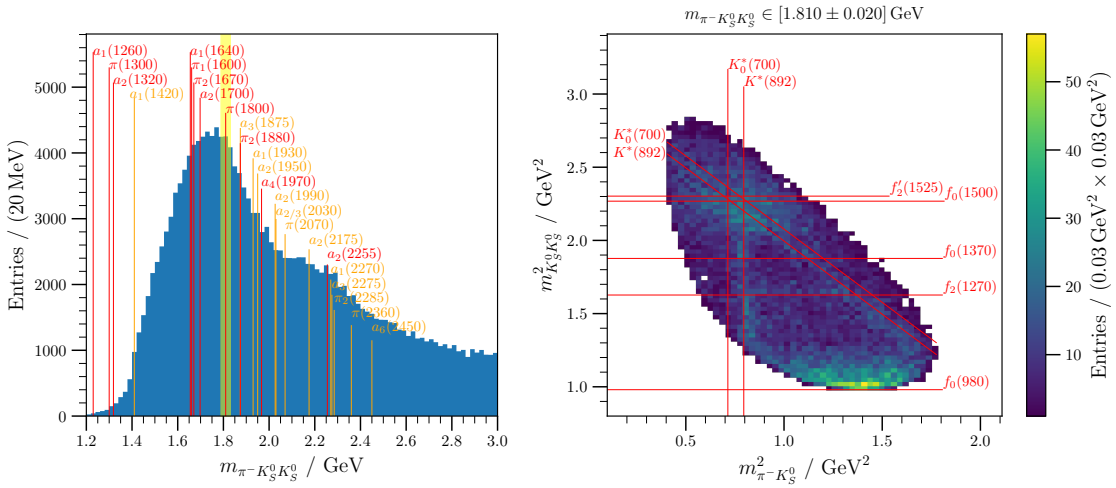

Figure 5.33: The left plot shows the invariant-mass distribution of the $\pi^- K^0_S K^0_S$ final state. The yellow band indicates the mass region that was used to create the Dalitz plot on the right. The mass region around the $\pi(1800)$ mass is spelled out in the title of the Dalitz plot and corresponds to band number 3 in Figure 5.31(b). The Dalitz plot has two entries per selected event.

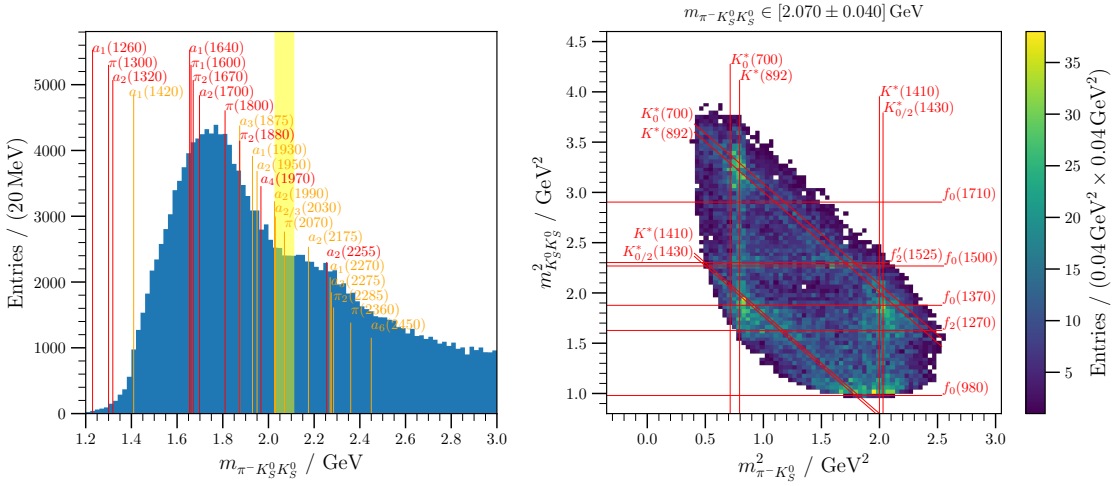

Figure 5.34: The left plot shows the invariant-mass distribution of the $\pi^- K^0_S K^0_S$ final state. The yellow band indicates the mass region that was used to create the Dalitz plot on the right. The mass region around the $\pi(2070)$ mass is spelled out in the title of the Dalitz plot and corresponds to band number 4 in Figure 5.31(b). The Dalitz plot has two entries per selected event.

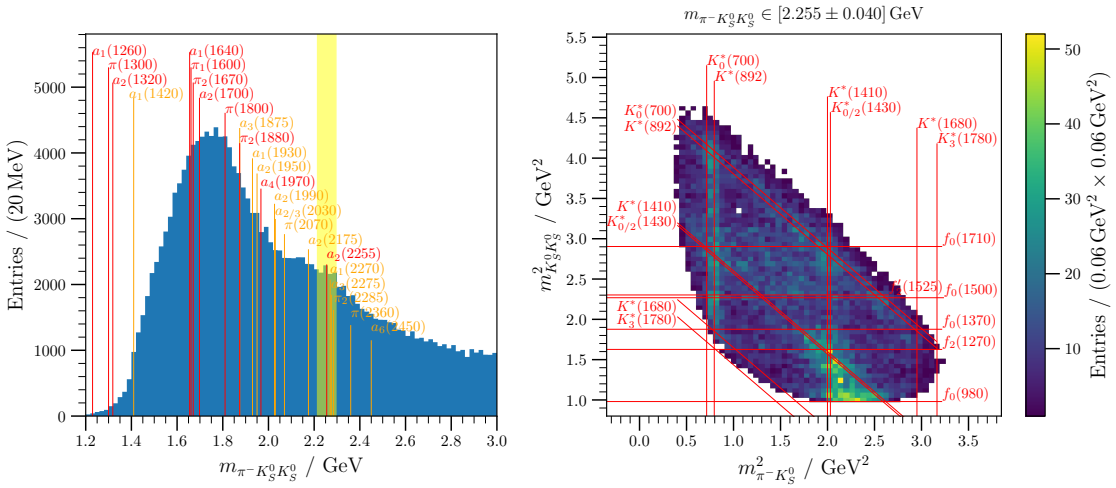

Figure 5.35: The left plot shows the invariant-mass distribution of the $\pi^- K^0_S K^0_S$ final state. The yellow band indicates the mass region that was used to create the Dalitz plot on the right. The mass region around the $\pi_2(2255)$ mass is spelled out in the title of the Dalitz plot and corresponds to band number 4 in Figure 5.31(b). The Dalitz plot has two entries per selected event.

In addition to the vertical and diagonal $K^*(892)$ band, for the first time we also see an enhancement at the higher K^*_J mass region with three candidates as discussed for Figure 5.28(a). In the horizontal direction, we can more clearly see a band at the $f_0(1500)$ and $f_2'(1525)$ mass region. The reduction in intensity at the $f_0(1370)$ mass where no diagonal lines are passing through, highlights its absence again while hinting stronger to the presence of the $f_2(1270)$ at the same time.

5.4 Hints for the $a_1(1420)$ in $\pi^- K^0_S K^0_S$

Since we are partly doing these investigations in order to see if the $a_1(1420)$ is present in the $\pi^- K^0_S K^0_S$ final state, it is just fair to ask how the Dalitz plot looks like in the expected resonance-mass region. For this, refer to Figure 5.36. Here we see very strong vertical and diagonal bands of the $K^*(892)$. These most likely come from the high-mass tail of the $a_1(1260)$ decaying to $K^*(892)K^0_S$. However, this makes it impossible to see if the isobar $f_0(980)$ is present in the Dalitz plot, since the two $K^*(892)$ bands cross exactly at the location where the horizontal line of the $f_0(980)$ would be. Therefore, it is also impossible to select for the $f_0(980)\pi$ decay channel by cutting away the $K^*(892)$ bands. Only with a PWD it might be possible to disentangle the corresponding distributions.

Comparing the theoretical calculation of the Dalitz plot in Figure 3.15(d), which was discussed in section 3.5.2, to the Dalitz plot in Figure 5.36, we see some similarity in form of two $K^*(892)$ bands that overlap at the expected position of the $f_0(980)$. But, the enhancement at the overlap of these bands is stronger in the predictions than in the data, which shows instead more homogeneous isobar bands. We perform another model calculation of the Dalitz plot, but this time without the $f_0(980)$ and the $(K\pi)_S$ isobars. The enhancement at the lower right corner is still present, as can be seen in Figure 5.37 when comparing it directly to the real data. This means that either one of the removed

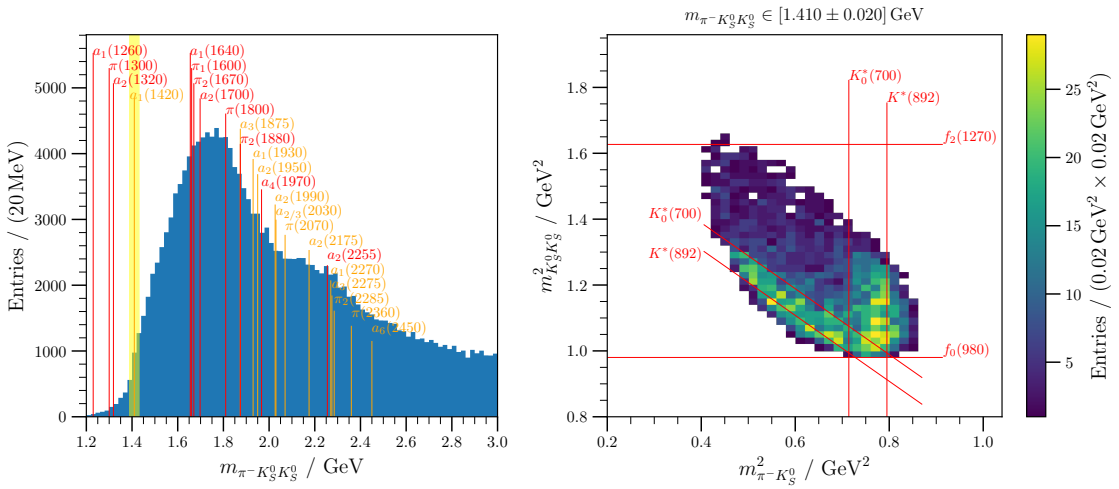

Figure 5.36: The left plot shows the invariant-mass distribution of the $\pi^- K^0_S K^0_S$ final state. The yellow band indicates the mass region that was used to create the Dalitz plot on the right. The mass region around the $a_1(1420)$ mass is spelled out in the title of the Dalitz plot and corresponds to band number 1 in Figure 5.31(b). The Dalitz plot has two entries per selected event.

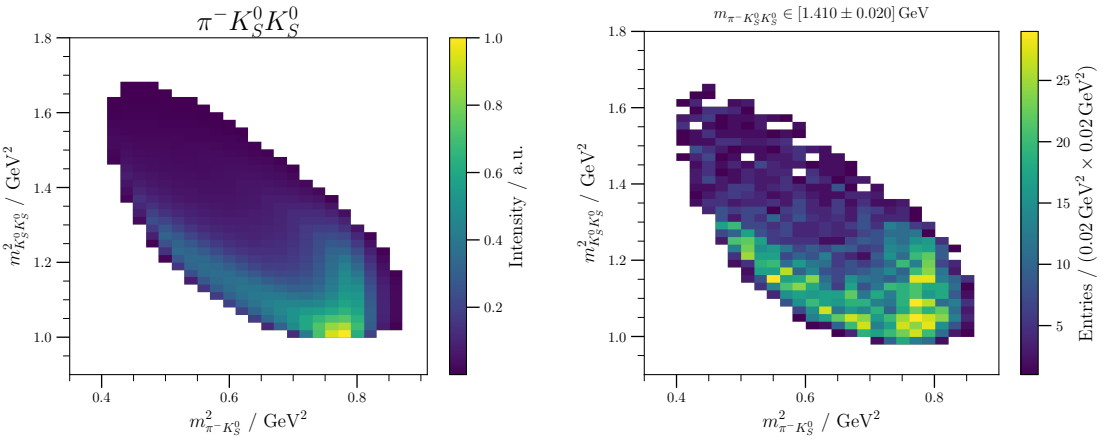

(a) Prediction with only $K^*(892)$.

(b) Result of this event selection.

Figure 5.37: **Left:** Dalitz-plot prediction as described in section 3.5.2. The difference to Figure 3.15(d) besides the adjusted binning is the removal of the $(K\pi)_S$ as well as the $f_0(980)$ isobar. Additionally, the prediction is obtained by adding the Dalitz plots for all values $m_X \in [1.39\,\mathrm{GeV}, 1.43\,\mathrm{GeV}]$ in steps of 1 MeV in order to account for the finite mass window of the data on the right.
Right: Dalitz plot for the indicated mass region around the $a_1(1420)$ as written in the title. The Dalitz plot has two entries per selected event and is the same as in Figure 5.36, just with adjusted axes and removed isobar lines.

isobars, or both, have to be present to allow for destructive interference.

5.5 Momentum Distributions

Up to this point, the event selection was crosschecked by Julien Beckers, documented in [61], and released by the COMPASS collaboration. Before continuing with the PWD and the subsequent resonance-model fit we still want to try to reduce the background from other non-resonant reactions as much as possible. For this, we have a look at Figure 5.38(a), where we see that the momentum of the π^-_{prim} peaks at roughly 10 GeV and again at 170 GeV. Figure 5.38(b) also shows a peak for the K^0_S momentum at roughly 10 GeV and, then, a broad shoulder at $\sim$ 60 GeV.

Appendix D.6 presents some simple phase-space MC, where we can see that the low-momentum peak of the π^-_{prim} and the broad shoulder of the K^0_S can be explained with resonance production. Using specific isobar masses for the two-body subsystems, one can see that the distributions can be shifted to slightly higher masses, however, they cannot produce the high-momentum peak in the π^-_{prim} spectrum or the low-momentum peak in the K^0_S spectrum. These most likely come from a different process, where the pion keeps almost all its momentum and the K^0_S-pair is centrally produced with very low momentum, e.g. from double-Pomeron, double-Reggeon or Pomeron-Reggeon fusion (see Figure 5.39).

If we have a look at the momentum distributions in Figure 5.38 once more, we see that the high-momentum peak of the π^-_{prim} and the low-momentum peak of the K^0_S vanish if we cut on the three-body invariant mass. We expect the resonance production to be dominant at small masses, therefore, it confirms that these additional peaks are coming from non-resonant backgrounds.

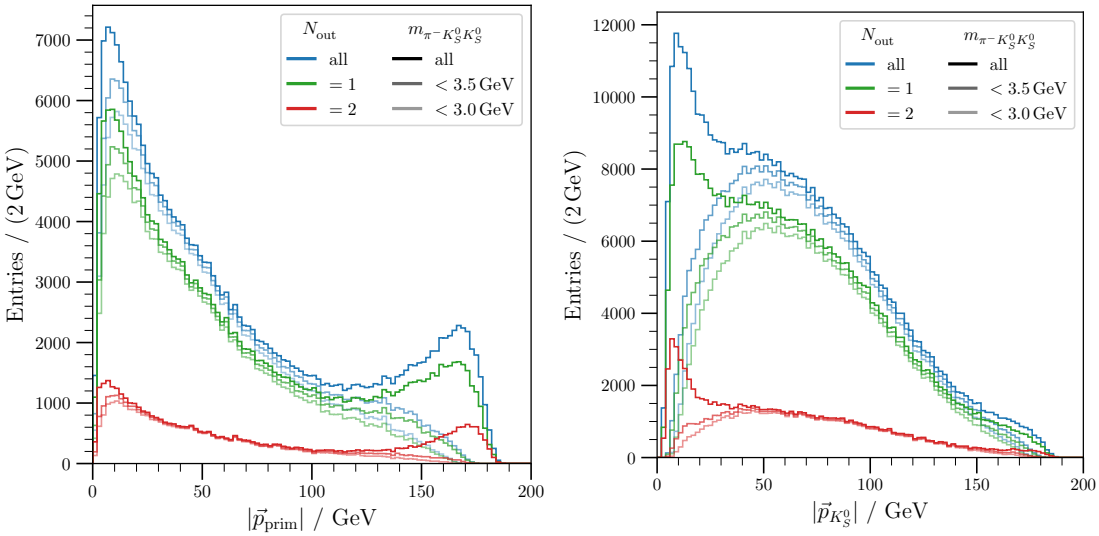

(a) π^-_{prim} momentum

(b) K^0_S momentum

Figure 5.38: Momentum distributions at the end of the full selection (solid) for different number of outgoing particles from the BPV as indicated by the legend. The additional transparent lines indicate the distributions for cuts on the maximal three-body invariant mass.

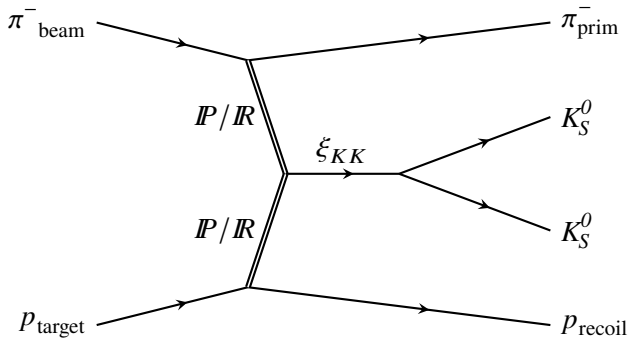

Figure 5.39: Central pair production of slow K^0_S

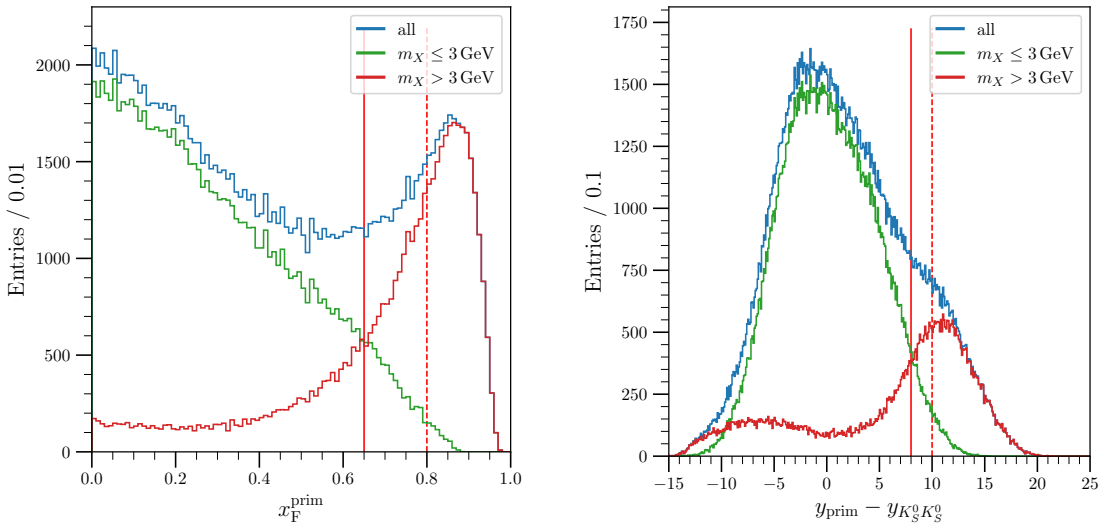

(a) x_F distribution

(b) Rapidity gap

Figure 5.40: Distribution of the x_F^{prim} of the π^-_{prim} (left) and the rapidity gap calculated from the rapidity-difference between π^-_{prim} and the (K_S^0, K_S^0) system. Different colors show the distributions after a cut on the three-body invariant mass as indicated by the legend. Dashed red lines display the conservative cuts and solid red lines indicate the strong cuts on these quantities.

Following the idea of [69] (Section 5.1.7), we will try to exclude this background with a cut on the "centrality" of the event. For this, we introduce two variables, the rapidity

$$y = \frac{1}{2} \ln \frac{E + p_z}{E - p_z} \tag{5.9}$$

and the Feynman-x

$$x_F \approx \frac{2p_z}{\sqrt{s}}, \tag{5.10}$$

where the kinematic variables E and p_z are determined in the GJ frame. The corresponding distributions can be found in Figure 5.40. We see that the events with high three-body invariant mass dominantly have high values for x_F^{prim} and the rapidity gap $\Delta y := y_{\mathrm{prim}} - y_{K_S^0 K_S^0}$, which confirms the difference in the production mechanism and gives us a method to remove the background.

In order to find the optimal cut values for x_F^{prim} and Δy, we perform a simple flat MC simulation. Here, we draw 10 M values for the resonance mass according to the RD distribution (cf. solid black line in Figure 5.41(c)), give it 190 GeV momentum in z-direction, and let it decay into the $\pi^- K_S^0 K_S^0$ final state distributed according to flat three-body phase space. The resulting distributions are normalized such that they match the falling edge of the K_S^0-momentum distribution, since it is neither affected by a cut on m_X (see Figure 5.38) nor on x_F^{prim} and Δy (see Figure 5.41). Interestingly, with this normalization we match almost exactly with the $N_{\mathrm{out}}^{\mathrm{BPV}} = 1$ case in the resonance-mass distribution, Figure 5.41(c), but this just shows how similar it is to the combined resonance-mass spectrum for both

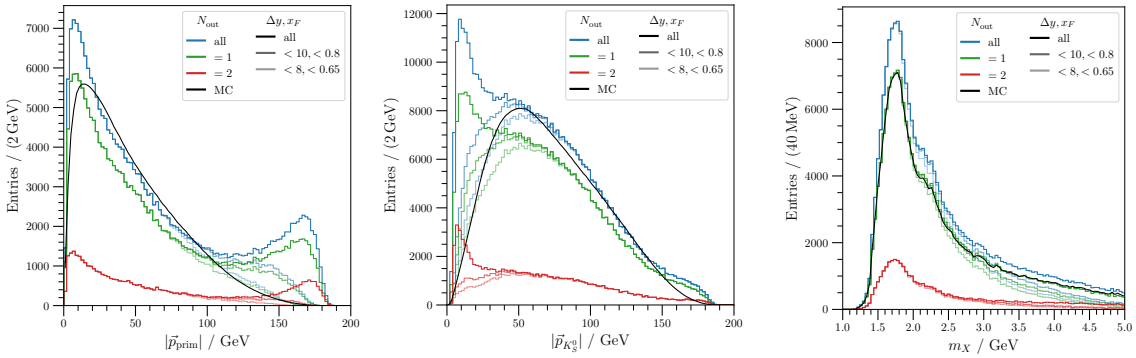

(a) π^-_{prim} momentum (b) K^0_S momentum (c) Invariant mass of the resonance

Figure 5.41: Momentum distributions for π^-_{prim} (left) and both K^0_S (middle) of the final state, as well as the resonance-mass distribution (right) for the three $N^{\text{BPV}}_{\text{out}}$ cases differentiated by color and for three different combinations of cuts on x_F^{prim} and Δy, differentiated by transparency as indicated by the legends.

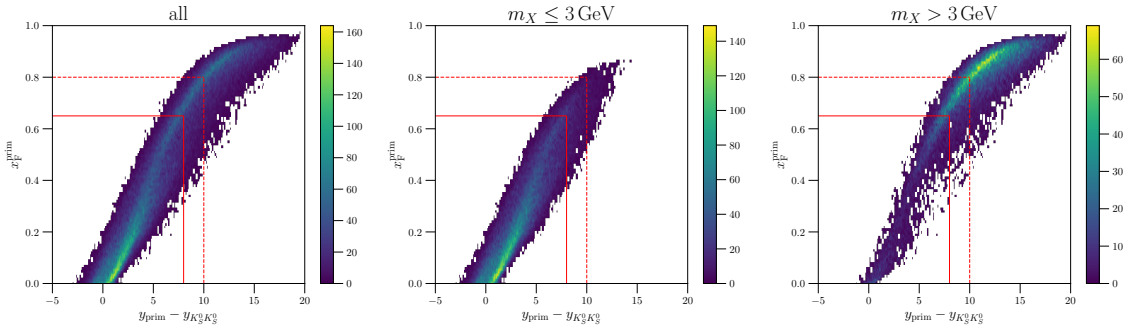

Figure 5.42: x_F^{prim} plotted against the rapidity gap Δy for all events (left), for events with resonance mass below (middle) and above 3 GeV (right). Dashed red lines indicate the conservative cuts and solid red lines display the strong cuts. Accepted is the bottom left box enclosed by these lines.

$N^{\text{BPV}}_{\text{out}}$ cases. In the end the normalization is just a global factor multiplied to the spectrum, where the amount of additional events from the central production approximately matches with the fraction of events in the $N^{\text{BPV}}_{\text{out}} = 2$ case, coincidentally.

We plot the momentum distributions of the final-state particles (Figures 5.41(a) and 5.41(b)) with various cuts on x_F^{prim} and Δy. One conservative cut was chosen with $\Delta y < 10$ and $x_F^{\text{prim}} < 0.8$ where the respective distributions for $m_X \leq 3\,\text{GeV}$ are almost zero, and a stronger cut with $\Delta y < 8$ and $x_F^{\text{prim}} < 0.65$ where the distributions for $m_X \leq 3\,\text{GeV}$ and $m_X > 3\,\text{GeV}$ are approximately equal. A two-dimensional representation of these cuts can be found in Figure 5.42.

While the conservative cut already shows a reduction of the unwanted peaks, we see that the strong cut removes them completely, making the flat MC match the momentum distributions almost perfectly. At the same time the resonance-mass spectrum almost stays the same, especially for low masses.

Although this study does not change much, since we cut away the high-mass region for the PWD,

anyways, it demonstrates the separation power of these two quantities nicely. As a starting point for the PWD, we use the strong cuts on $x_F^{\text{prim}} < 0.65$ and $\Delta y < 8$, and we constrain $m_X \leq 3\,\text{GeV}$ and $0.1\,\text{GeV}^2 \leq t' \leq 1.0\,\text{GeV}^2$, since the latter is the acceptance[17] of the RPD. After these additional cuts, we are left with 150 153 exclusive events to enter the PWD that is discussed in the next chapter.

5.6 Conclusion

In this chapter, we started with a look at the possibilities for final states with kaons in diffractive pion-proton scattering at COMPASS that could give access to the $a_1(1420)$ signal in the $\pi K\overline{K}$ sector. The $\pi^- K^+ K^-$ final state cannot be detected below 1.5 GeV due to shortcomings in the PID of high-momentum charged particles by the RICH detector. This renders a search for the $a_1(1420)$ impossible in this final state. Going to neutral kaons circumvents this problem, due to the identification via a displaced decay vertex from the initial interaction inside of the target. Since, K_L^0 live too long to decay within the dimensions of the spectrometer, we focus on the $\pi^- K_S^0 K_S^0$ final state.

For this, a first rough skimming for the existence of K_S^0-candidates in the COMPASS data was developed, which can and already was used for other final states involving K_S^0. Next, the event selection of the $\pi^- K_S^0 K_S^0$ final state was performed, where the optimal minimal vertex separation of the displaced K_S^0 decay vertices was determined by means of a significance study. At the end of this event selection, roughly 240 000 exclusive $\pi^- K_S^0 K_S^0$ events were selected, which is more than 240 times the amount of the, up to now, largest data set of $\pi^- K_S^0 K_S^0$ from diffractive scattering collected by the E580 experiment at Fermilab [71].

When looking at the isobar subsystems, we see in the $\pi^- K_S^0$ invariant mass a clear $K^*(892)$ peak and another enhancement at the mass of the $K^*(1410)$ that could have contributions from the $K_0^*(1430)$ and the $K_2^*(1430)$. The $K_S^0 K_S^0$ subsystem shows clear evidence for the $f_0(980)$ and the $f_2(1270)$ as well an enhancement at the mass of the $f_0(1500)$ and the $f_2'(1525)$. The three-body invariant mass shows a broad peak at 1.7 GeV with a shoulder at 2.1 GeV. We discussed possible resonances and their isobar-decay channels. By looking at the Dalitz plots for narrow windows in the three-body invariant mass, we can identify evidence for the decay channels $a_1(1640) \to K^*(892) K_S^0$, $\pi(1800) \to f_0(980)\pi$ and $\pi_2(1670) \to f_2(1270)\pi$. Additionally, we observe a well populated Dalitz plot at a resonance mass around 1.4 GeV. By only looking at the data, we cannot confirm the presence of the $f_0(980)\pi$ decay channel due to overlapping $K^*(892)$ bands in the cross-channels. However, by performing a theoretical calculation of the Dalitz plot with only $K^*(892)$ as a possible isobar, we see clear deviations from the experimental findings. This demonstrates that the $f_0(980)$ or the $(K\pi)_S$ isobars have to be present as well.

By comparing the momentum distributions of the selected $\pi^- K_S^0 K_S^0$ events with a simple MC simulation, we are able to identify contributions from centrally produced K_S^0-pairs from double-Regge exchange. Cutting on the Feynman-x of the π^-_{prim} as well as on its rapidity-difference to the $K_S^0 K_S^0$ subsystem, we are able to reduce this background to the resonance-production process. This yields in total roughly 150 000 exclusive $\pi^- K_S^0 K_S^0$ events that can be used for the subsequent PWD.

[17] [70] states that $t' \geq 0.07\,\text{GeV}^2$ is the smallest four-momentum transfer at which a recoiling proton can be detected by the RPD. But still, we see an increase of the selected number of events up to roughly $0.1\,\text{GeV}^2$, although an exponential drop is expected. This hints towards an inhomogeneous acceptance. For values larger than $1.0\,\text{GeV}^2$ also inhomogeneities in the acceptance are observed as stated by [70].

CHAPTER 6

PWD of the $\pi^- K^0_S K^0_S$ Final State

In this chapter, we will take the event selection of the previous chapter 5 as a starting point. Since a full-fledged PWD is a thesis project on its own, this chapter will only provide a first look, highlighting the performed simplifications in each step and discussing a method in order to address them in the future. In the end, we will give a summary of these next steps that have to be performed in order to finalize the project.

6.1 Monte Carlo Production with TGEANT

As a first step after an event selection, a MC production has to be performed. This process was already introduced in section 2.2 and we see its application in the following section. On one hand, it is needed to correct for the detector acceptance and is entering the PWD on an event-by-event basis, specifically in the calculation of N_{pred} in equation (3.73) as it appears in equation (3.75). And on the other hand the gMC can be used to precalculate the integral matrices of equation (3.61) that are needed for the correct normalization.

We produce so-called "signal MC", since we want to know how many physics events of the reaction of interest with certain kinematic variables are detected by the experiment. For this, we start by taking the four-momentum of a beam particle from the TGEANT beam file. This file contains reconstructed beam particles from the $\pi^-\pi^+\pi^-$ final state, since it has very large statistics and a good detector acceptance. This beam particle is extrapolated by TGEANT to the virtual ℓH2 target and a random position inside the target cell is drawn where the interaction with the target is supposed to happen. As well, a random resonance mass is chosen (we discuss details on this later) and a reduced four-momentum transfer t' is generated according to the distribution[1] as extracted by the fit to the RD, see section 5.2.4. They are used to determine the four-momenta of the recoil proton and the resonance. Now, the "signal" part of the MC comes into play, since we are artificially producing the $\pi^- K^0_S K^0_S$ final state by distributing the final-state four-momenta according to flat three-body phase space in the rest frame of the resonance. In a next step, these are boosted into the lab frame by using the previously determined four-momentum of the resonance. And finally, the three final-state particles and the recoil proton are handed over to GEANT, which handles their extrapolation through the virtual COMPASS

[1] The only reason for this is that we do not want to create too much MC in kinematic regions where one does not expect many events anyways.

spectrometer and the interaction with material.

There is one caveat regarding the two K_S^0, since they will decay within the COMPASS detector. This decay will also be handled by GEANT, however, since the K_S^0 decays to two charged pions only in 70 % of all cases, we artificially set its probability to 100 %, at the same time disabling the decay mode into two neutral pions. All of these simulated events are called gMC.

The deposited energy in the active detector material is fed to CORAL, where the response of the single detectors is simulated and the event reconstruction is performed in the same way as for RD. Then, these rMC events are send through the same event selection[2] as the one discussed in the previous chapter, and the events that pass all selection criteria make up the aMC. The ratio $\frac{\#\text{aMC}}{\#\text{gMC}}$ defines the overall acceptance of the COMPASS detector for a given final state. In case of the $\pi^- K_S^0 K_S^0$ final state this total acceptance amounts to $\frac{5959481}{45392059} = 13.1\,\%$, determined with ~ 45 M gMC events in a non-uniformly distributed mass range from 1.2 to 3.5 GeV. This is also the reason why this overall acceptance is not a very useful quantity. It only serves as a first rough estimate on how many gMC have to be produced to reach a certain amount of aMC.

For the $\pi^-\pi^+\pi^-$, PWD approximately ten times as many aMC events were produced than RD events of this final state. In section 4.4.7 we already mentioned some problematic regions, where the resulting data points from the PWD were jumping strongly from bin to bin. With a statistical reanalysis of the data in form of a bootstrap study as discussed in section 4.6.4, slightly bigger uncertainties were obtained. However, the observed jumps in the data are still not explainable as statistical fluctuations. In the bootstrap analysis of [55], they concluded that the origin of these fluctuations might lie in not sufficient aMC. Since we have a lot less data for the $\pi^- K_S^0 K_S^0$ final state compared to the $\pi^-\pi^+\pi^-$ final state, we can directly produce twenty times as many aMC than RD events. To see if this is sufficient is already the first point that should be studied in more detail when finalizing the project.

Some regions of the three-body invariant mass are stronger populated than others, as one can see in Figure 5.31(a), therefore, we will divide it in sections containing roughly equal amounts of events and, there, produce MC data with uniformly distributed $m_{\pi^- K_S^0 K_S^0}$. Since the detector acceptance might vary for different values of $m_{\pi^- K_S^0 K_S^0}$, we will plot this acceptance as well as the amount of aMC to identify regions of too few MC. For these regions, we produce more MC and repeat the process until the whole $m_{\pi^- K_S^0 K_S^0}$ spectrum is covered with at least twenty times as much aMC data.

This is presented in Figure 6.1, where the blue histogram corresponds to the RD distribution of Figure 5.31(a), but now with the additionally applied cuts as discussed at the end of section 5.5. The red line indicates the acceptance as a function of $m_{\pi^- K_S^0 K_S^0}$, i.e. as the previously discussed ratio of aMC over gMC for all events that fall in the corresponding resonance-mass bin of the RD histogram. And finally, the grey transparent histogram indicates the amount of aMC divided by a factor of twenty. This means that if the gray histogram is above the blue histogram we have at least the required multiple of aMC. We see that the acceptance is slowly and very smoothly increasing over the whole mass range and ranges from 9 % at 1.2 GeV up to 17 % at 3.5 GeV.

This plot cannot only be created for the invariant mass of the full $\pi^- K_S^0 K_S^0$ system, but also for the two subsystems $\pi^- K_S^0$ and $K_S^0 K_S^0$, see Figure 6.2. Here, we see that most of the spectra are covered by the gray histogram. Only the K^* peak and the high-mass region in the $\pi^- K_S^0$ spectrum as well as the

[2] There are only some differences regarding particle-identification detectors such as the RICH and the CEDARs. For each of them, an efficiency study was performed in [58] and [64], respectively, and the MC particles are identified as pions according to the corresponding experimental efficiency for the given kinematics.

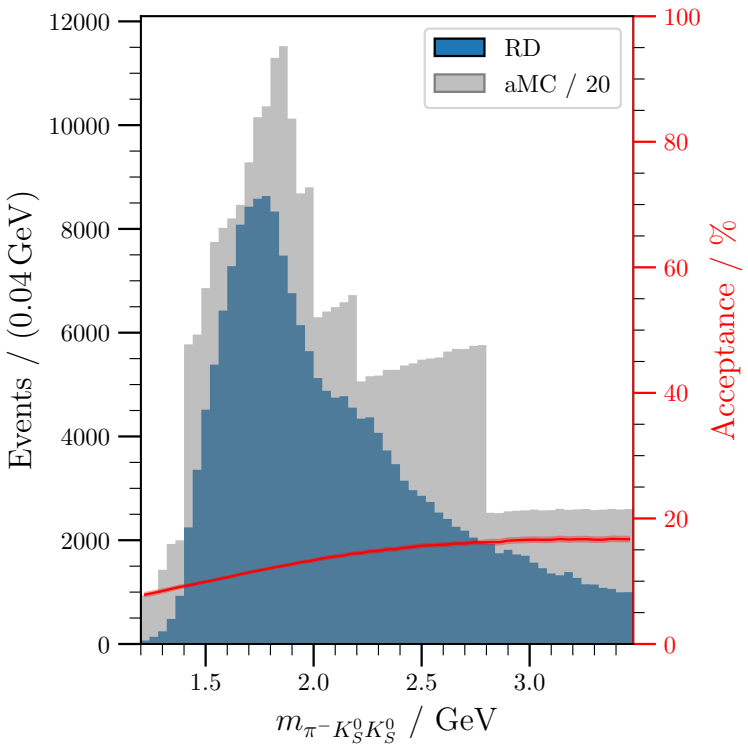

Figure 6.1: RD distribution of the $\pi^- K^0_S K^0_S$ invariant mass (blue histogram) overlaid with the amount of aMC divided by twenty (gray histogram). The acceptance as the ratio of aMC over gMC in each of the histogram bins is plotted as the red line with a 1σ uncertainty band.

low mass threshold of the $K^0_S K^0_S$ spectrum are not fully covered. This is the second point that should be addressed before a publication, for example by simply producing more MC data, but for now this coverage is sufficient. Also here, it is important that the acceptance is smooth and rather constant in the two-body-subsystem invariant masses, such that we cannot produce artifacts in certain partial waves due to artificially increasing the importance of an isobar as an effect of an increased acceptance correction in its mass range.

A last thing that we can check is, how this acceptance behaves for the Dalitz plots. This can be seen in Figure 6.3 for two different three-body mass ranges, one where the $a_1(1420)$ is expected to appear and one around the mass of the $\pi(1800)$. In general also there, the acceptance function is very smooth. We see a lower acceptance for smaller invariant masses of the $(K^0_S K^0_S)$ subsystem, which is the case for lower particle momenta in the LAB System (LAB). A K^0_S with a low momentum is expected to decay closer to the PV, thus, this acceptance drop is most likely related to the cut on the required minimal vertex separation of the SVs from the PV. At the other borders of the Dalitz plot only one of the K^0_S has a small LAB momentum. Here, the inclusion of "shared" K^0_S could be the reason why not such a strong acceptance drop is observed. To solve the problems at the lower border, the final state would need two "shared" K^0_S, which is excluded during the event selection, so far. These are interesting studies that could also be addressed when working towards a publication.

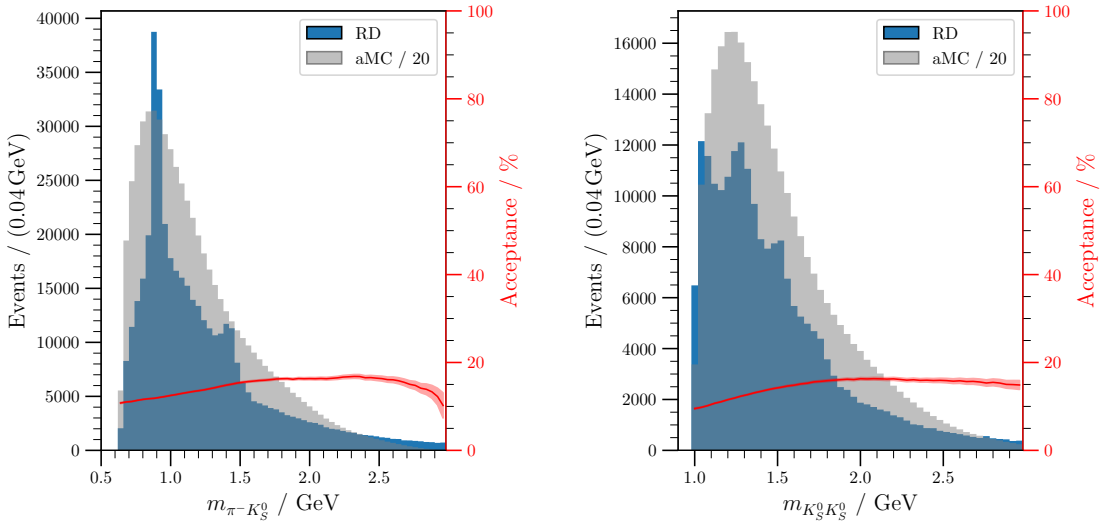

(a) (b)

Figure 6.2: Acceptance with a 1σ uncertainty band (red line) plotted for the $\pi^- K_S^0$ two-body system (left) and the $K_S^0 K_S^0$ two-body system (right). The RD is depicted by the blue histogram, while the gray transparent histogram shows the amount of produces aMC divided by twenty.

6.1.1 Fine Selection of the MC Data

Not only the acceptance is an interesting quantity to look at for MC data. We can also compare the histograms obtained during the event selection of the MC data with the ones from RD. However, we have to keep in mind that we have slightly different distributions for the kinematics due to a different shape of the resonance-mass distribution in MC.

One quantity that is not directly affected by this, is the invariant-mass distribution of the secondary pions. During the creation of the gMC, we created the $\pi^- K_S^0 K_S^0$ final state according to phase space. The propagation and the decay of the K_S^0 are than handled by GEANT, thus, a comparison of the vertex separation and the vertexing resolution in form of the width of the K_S^0 peak is very interesting.

Let us start with the latter. In Figure 6.4, we see a comparison of the K_S^0 peak before the kinematic fit for MC (left) and RD (right). For MC, the peak is perfectly centered on the nominal K_S^0 mass, which shows that the shift towards higher masses in RD does not originate from artifacts in the vertexing or the track reconstruction. The width of the peak is a bit narrower for MC, demonstrating that there is not much background contributing to the K_S^0 peak. Otherwise the resolution in MC should be better, since there, we know for sure that we have K_S^0.

Figure 6.5 shows the vertex separation between SVs and the BPV. In both cases we see a falling distribution with changes in the slope at 100 cm and 300 cm.

Next, we have a look at the momentum distributions of the final-state particles, see Figure 6.6. One has to compare with the corresponding RD distributions in Figure 5.41 that have the strongest cuts on centrality and the rapidity gap, since they have no background from central production which does not follow the used flat-three-body-phase space distributions. We not only see a similar shape between MC and RD, but we also have a similar ratio of the compared cases $N_{\text{out}}^{\text{BPV}} = 1$ and $N_{\text{out}}^{\text{BPV}} = 2$. This not

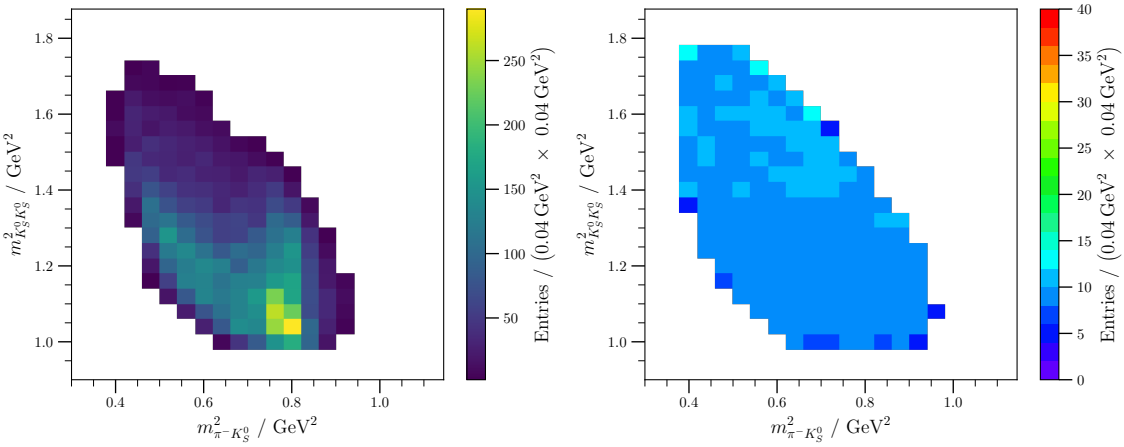

(a) $m_{\pi^- K_S^0 K_S^0}$ = 1.37 to 1.47 GeV

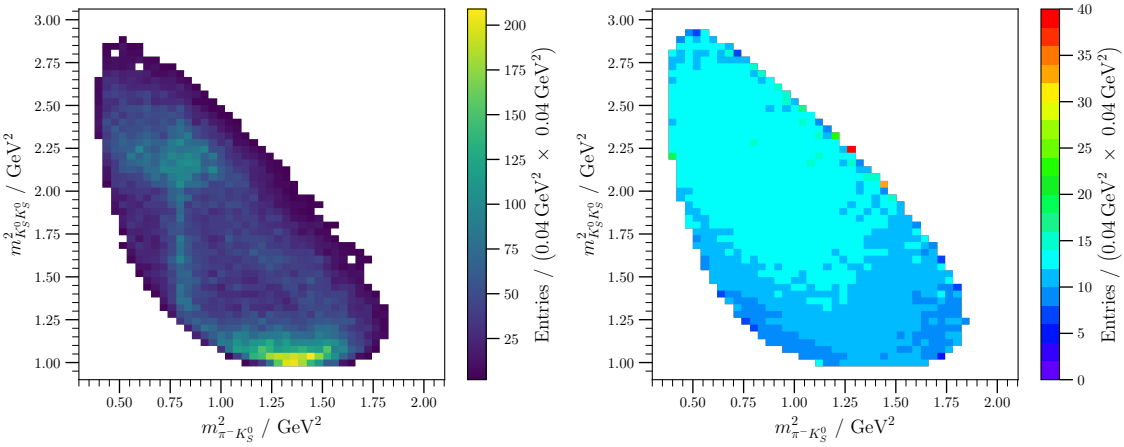

(b) $m_{\pi^- K_S^0 K_S^0}$ = 1.75 to 1.85 GeV

Figure 6.3: RD Dalitz plot (left column) for two different three-body mass ranges as indicated by the captions (rows). The right column shows the corresponding acceptance in each of the Dalitz-plot bins. Outliers of very high (red) or very low (dark blue) acceptance on the border of the MC Dalitz plot originate from the small number of gMC events that enter these bins.

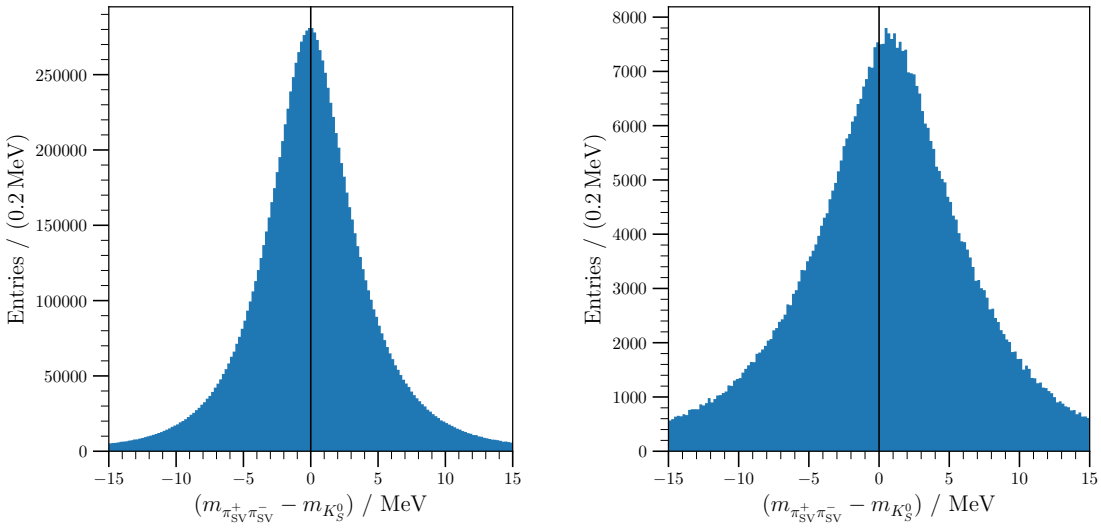

(a) MC (b) RD

Figure 6.4: Invariant-mass distribution of pairs of $\pi^{\pm}_{\mathrm{sec}}$ for MC (left) and RD (right).

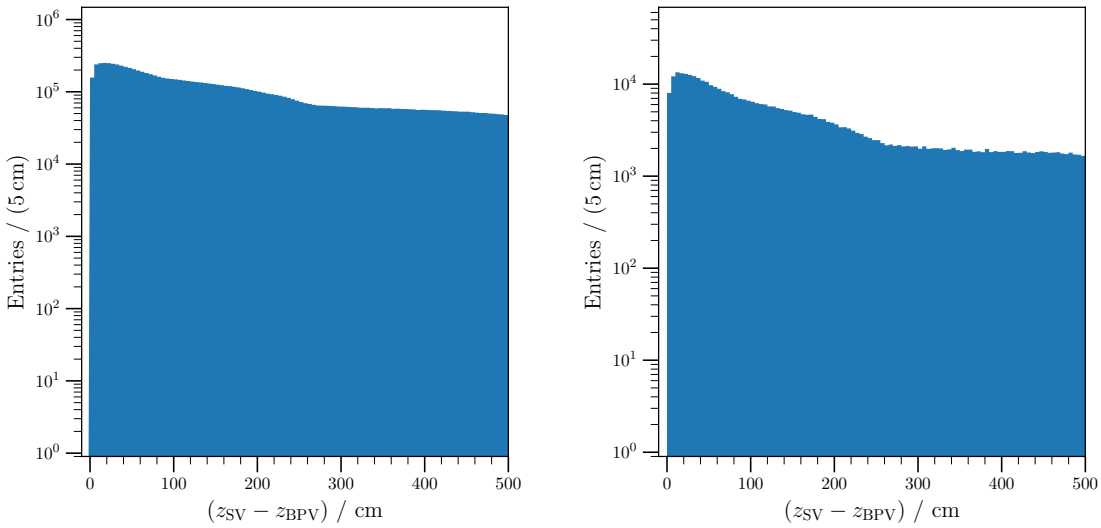

(a) MC (b) RD

Figure 6.5: Vertex separation between SV and BPV for MC (left) and RD (right).

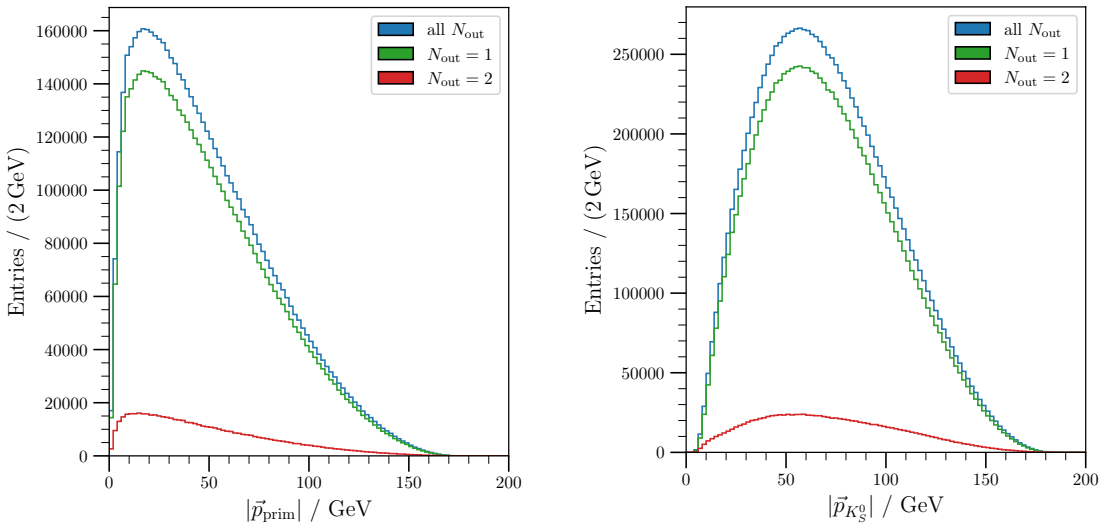

(a) π^-_{prim} momentum

(b) K^0_Smomentum

Figure 6.6: Momentum distributions for the π^-_{prim} momentum (left) and K^0_S momentum (right). To be compared with the most transparent lines in Figure 5.41.

only confirms the existence of "shared" K^0_S in MC, but also that their inclusion is possible and useful.

6.2 Wave Selection

As mentioned already when discussing the simplest possible example of a PWD in section 3.4, one has to cut off the sum over all partial waves w in equation (3.65) due to the finite amount of available RD. As a first simplification, we restrict ourselves to only positive reflectivity $\varepsilon = +1$, since it is expected to strongly dominate the total intensity at these large beam energies and as it is confirmed by the $\pi^-\pi^+\pi^-$ analysis of COMPASS. This removes the outer incoherent sum and for the inner sum we allow for a maximum of total resonance spin $J \leq 6$, resonance spin projection $M \leq 2$ and orbital angular momentum $L \leq 6$ in the resonance decay. With these, we take all physically allowed combinations of the isobar spin S such that $|L - S| \leq J \leq L + S$. As discussed in section 3.4.1, $M = 0$ is only possible if $\varepsilon P(-1)^J = 1$, which means for positive reflectivity that $P = (-1)^J$. This removes the zero spin projections for resonances with $J^{PC} \in \{(\text{odd})^{-+}, (\text{even})^{++}\}$. Allowing for the $[K\overline{K}]_S$ isobars $f_0(980)$, $f_2(1270)$, $f_0(1500)$, $f_2'(1525)$ and $f_0(1710)$ as well as for the $[K\pi]_S$ isobars $(K\pi)_S$, $(K\eta)_S$, $K^*(892)$, $K^*(1410)$ and $K_2^*(1430)$, with their parametrization as detailed in section 6.2.1, results in a wave set of 365 waves in total, plus one flat wave.

All of the following analysis was performed with the PWD program Wave Analysis Software Tool [72] (`WASP`) developed by our working group in Bonn. Details of the working principle and the implementation will be presented in the theses of my coworkers [66, 73].

6.2.1 Isobar Line Shapes

In the following, the line shapes of the isobars are presented as they are entering the PWD model. Resonance parameters as well as information about the dominant decay channels are taken from the PDG. Isobars in the $(K\overline{K})$ subsystem will be grouped together into $[K\overline{K}]_S$ indicating the isobar spin S, and with this also the orbital angular momentum in its decay, as an index in spectral notation (upright letters). Similarly, isobars in the $(K\pi)$ subsystem will be grouped together into $[K\pi]_S$.

$[K\overline{K}]_S$ Isobars

Note that we do not include a broad $(\pi\pi)_S$ component into the isobar model. A parametrization that could be use in the future to study its effect on the PWD is presented in appendix A.6.1, but due to its broad shape extending far below the $K\overline{K}$ threshold, it is omitted from $[K\overline{K}]_S$. And an additional reason is that during the PWD many isobars are contributing to the $J^{PC} = 0^{-+}$ sector, so an inclusion would mean a lot more possibilities for strong interferences, making it harder for the fit to converge.

The $f_0(980)$ is modeled using a Flatté width for its decay modes to $\pi\pi$ and $K\overline{K}$ as in equation (3.36) with $\frac{g_1^2}{16\pi} = 0.165\,\text{GeV}^2$ and $\frac{g_2^2}{g_1^2} = 4.21$ as determined[3] by the BES collaboration [74]. It is analytically continued below threshold, i.e. $q \to \mathrm{i}\,|q|$ is used for the $K\overline{K}$ phase-space term below $s < 4m_K$.

Both $f_0(1500)$ and $f_0(1710)$ are described with a BWM with energy-dependent width according to equations (3.34) and (3.35). For the $f_0(1500)$, we only use the 2π phase space in its energy-dependent width, since this is the strongest two-body contribution with $\sim 35\,\%$. It is only surpassed by the 4π contribution with $\sim 50\,\%$, which is hard to include into the energy-dependent-width formalism. In the case of the $f_0(1710)$, we use its decay to $K\overline{K}$ in the denominator of the BWM. However at these isobar masses, we are far away from the corresponding thresholds, therefore, the BW with energy-dependent width will not differ that much from the one with constant width due to $\Phi_2(s) \overset{s\to\infty}{\longrightarrow} \text{const} < \infty$.

All line shapes and their complex phase, as well as the corresponding Argand diagram, can be found in Figure 6.7.

[3] Note that in the cited article g_1 and g_2 are defined differently, but converting their notation to the one that is used here, we obtain the detailed expressions.

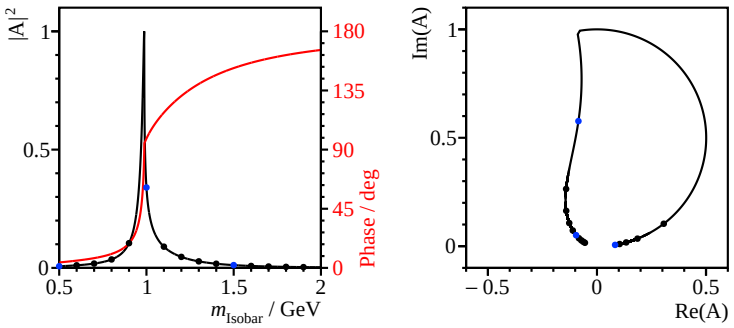

(a) $f_0(980)$ Flatté parametrization

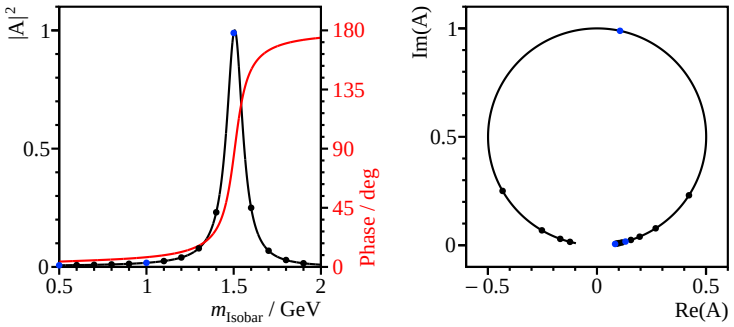

(b) $f_0(1500)$ BWM with energy-dependent width

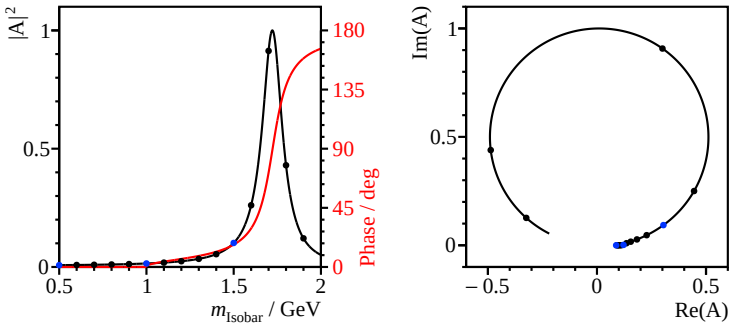

(c) $f_0(1710)$ BWM with energy-dependent width

Figure 6.7: Each row represents the parametrization of the line shape of one isobar as indicated in the caption. The left plot shows the line shape (black) and the complex phase (red), while the right shows the Argand diagram of the complex amplitude. The dots indicate steps in 0.1 GeV. For an easier relation of the plots to each other, multiples of 0.5 GeV are indicated with a blue dot.

$[K\bar{K}]_D$ Isobars

Here, we model the $f_2(1270)$ and the $f_2'(1525)$ with an energy-dependent width according to equations (3.34) and (3.35) using the 2π channel for the energy-dependent width of the former and the $K\bar{K}$ channel for the latter, since these are their respective dominant decay modes. The line shapes are presented in Figure 6.8.

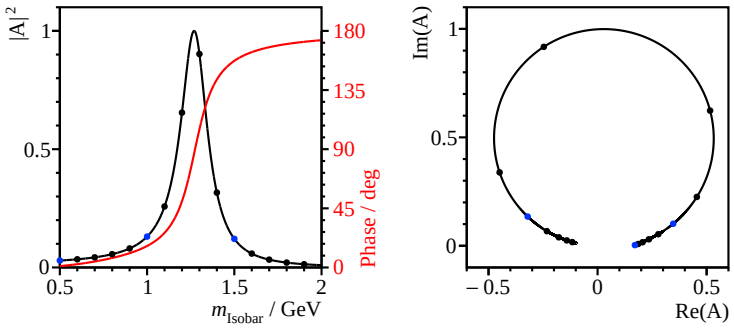

(a) $f_2(1270)$ BWM with energy-dependent width

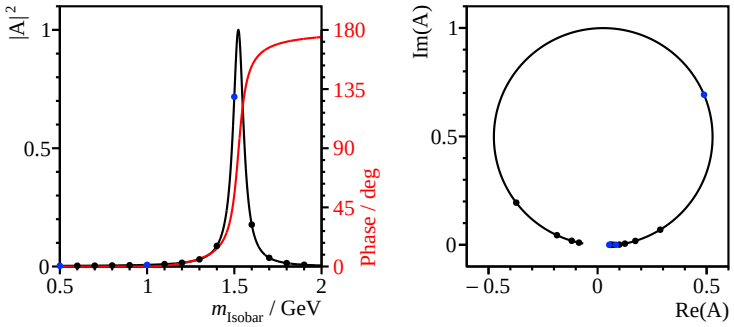

(b) $f_2'(1525)$ BWM with energy-dependent width

Figure 6.8: Each row represents the parametrization of the line shape of one isobar as indicated in the caption. The left plot shows the line shape (black) and the complex phase (red), while the right shows the Argand diagram of the complex amplitude. The dots indicate steps in 0.1 GeV. For an easier relation of the plots to each other, multiples of 0.5 GeV are indicated with a blue dot.

$[K\pi]_S$ Isobars

Similar to the $[\pi\pi]_S$ sector, we have a very broad state here at low masses, the $K_0^*(700)$ aka κ. Here, a coupled-channel $\boldsymbol{K}$-matrix fit was performed by [75] including three poles, i.e. resonances. We use two "isobars", the matrix elements T_{11} for the $K\pi \to K\pi$ channel, called $(K\pi)_S$, and T_{12} coming from the $K\eta \to K\pi$ channel, called $(K\eta)_S$. Although in principle both could contribute to the PWD model, the $(K\pi)_S$ was removed during the automatic wave selection due to its strong destructive interference with the other waves. Figure 6.9 displays their line shape. Their implementation is described in detail in section 5.1.4 of [58], therefore, it is omitted here.

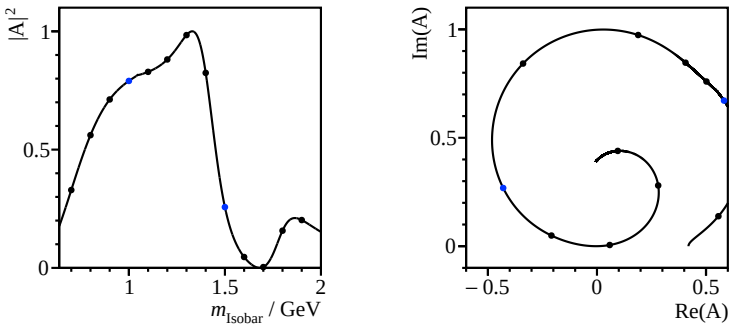

(a) $(K\pi)_S$ Palano-Pennington parametrization

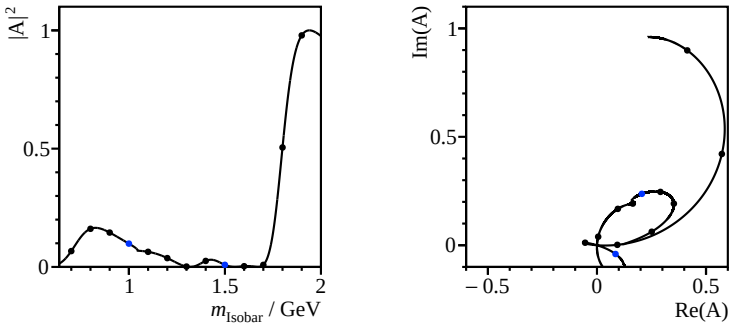

(b) $(K\eta)_S$ Palano-Pennington parametrization

Figure 6.9: Each row represents the parametrization of the line shape of one isobar as indicated in the caption. The left plot shows the line shape, while the right shows the Argand diagram of the complex amplitude. The dots indicate steps in 0.1 GeV. For an easier relation of the plots to each other, multiples of 0.5 GeV are indicated with a blue dot.

$[K\pi]_P$ Isobars

Here, we only consider the $K^*(892)$ and the $K^*(1410)$, both modeled with a BWM with energy-dependent width, see Figure 6.10.

$[K\pi]_D$ Isobars

The only candidate for this isobar in the mass range of interest is the $K_2^*(1430)$ modeled with a BWM with energy-dependent width, see Figure 6.11.

6.2.2 Thresholding

In order to reduce this huge amount of waves, an automatic thresholding procedure was developed by Florian Kaspar[4] for the $\pi^-\pi^+\pi^-$ final state and already implemented in the $\omega\pi^-\pi^0$ analysis of [77].

[4] Details of the procedure will be published in the PhD thesis of [76].

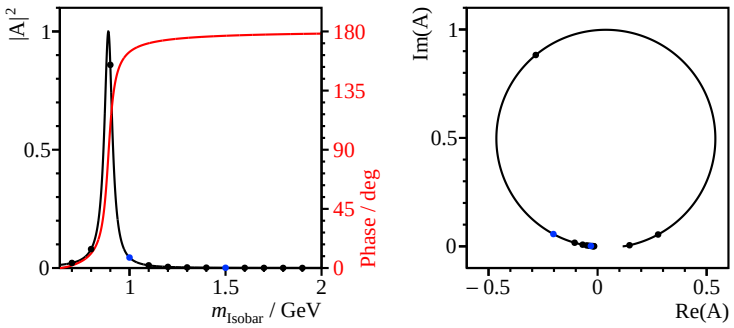

(a) $K^*(892)$ BWM with energy-dependent width

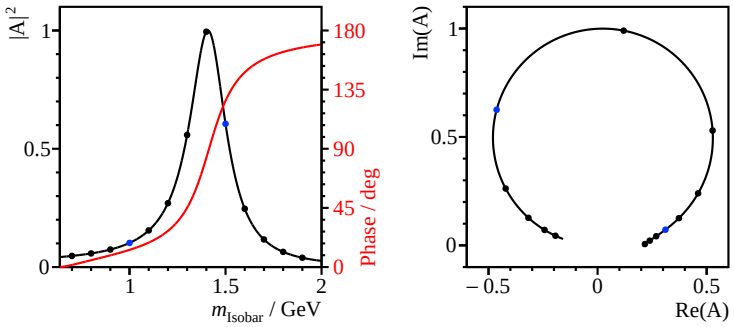

(b) $K^*(1410)$ BWM with energy-dependent width

Figure 6.10: Each row represents the parametrization of the line shape of one isobar as indicated in the caption. The left plot shows the line shape (black) and the complex phase (red), while the right shows the Argand diagram of the complex amplitude. The dots indicate steps in 0.1 GeV. For an easier relation of the plots to each other, multiples of 0.5 GeV are indicated with a blue dot.

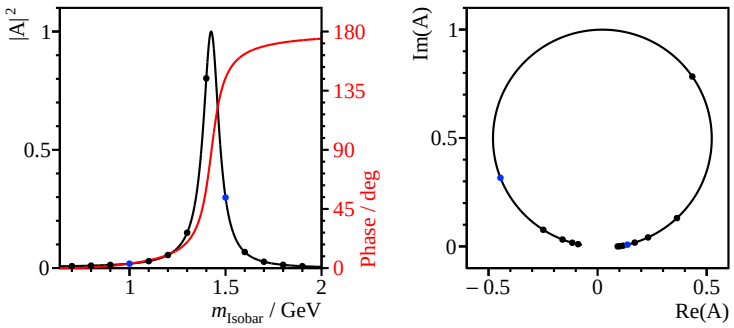

Figure 6.11: Parametrization of the line shape of the $K_2^*(1430)$. The left plot shows the line shape (black) and the complex phase (red), while the right shows the Argand diagram of the complex amplitude. The dots indicate steps in 0.1 GeV. For an easier relation of the plots to each other, multiples of 0.5 GeV are indicated with a blue dot.

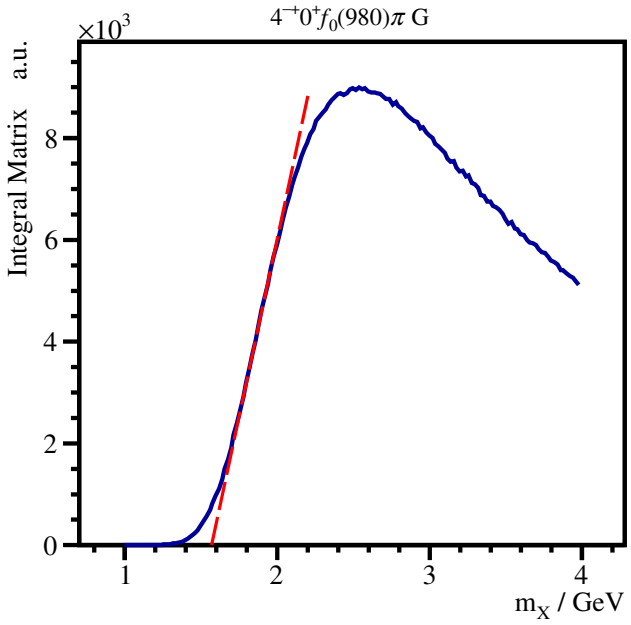

Figure 6.12: Integral matrix for the $4^{-+}0^{+}f_0(980)\pi$ G wave as a function of the resonance mass m_X (blue solid line) plotted together with an extrapolation of the steepest slope down to the x-axis (red dashed line). The rough threshold of this wave is set to a value 0.3 GeV more to the left of the zero-crossing of the red dashed line.

We will follow this recipe by starting with a rough thresholding of the partial waves.

Rough Thresholding

For this, we calculate the diagonal elements of the integral matrix of equation (3.61) for different values of m_X via the MC-integration method as described below that equation. The resulting function of m_X will start rising when the phase space for this specific partial wave starts to open up. The maximal slope of this rising edge is extrapolated down to the x-axis and the threshold of this particular wave is set to this axis crossing minus 0.3 GeV to give it a bit of a safety margin. The execution of this procedure can be seen for the $4^{-+}0^{+}f_0(980)\pi$ G wave in Figure 6.12.

Tight Thresholding

Next, a stronger thresholding is performed to remove waves that strongly interfere destructively. For this, the partial waves are sorted according to the previously determined rough thresholding. Then, one starts from the highest mass bin (at this moment set to 3 GeV) going bin-by-bin downwards to the lowest mass bin at 1.2 GeV. During each step, one adds partial waves one-by-one according to their sorting and for each such set of partial waves one determines the acceptance integral matrix I_{ij}^{acc}, i.e. the MC-integrated $\Psi_i \Psi_j^*$ only using accepted MC events. Then, this complex integral matrix is

normalized via $\bar{I}_{ij}^{\text{acc}} = \frac{I_{ij}^{\text{acc}}}{\sqrt{I_{ii}^{\text{acc}} I_{jj}^{\text{acc}}}}$ and inverted via the algorithm described in [78]. According to [76, 77], the maximal diagonal entry $I_{\text{max}}^{-1} := \max_i \{ \left| \left(\bar{I}_{ii}^{\text{acc}} \right)^{-1} \right| \}$ of this inverse matrix is a measure for the largest overlap between the so far included waves. If this value fulfills $I_{\text{max}}^{-1} \geq 2$, the last-added wave will be removed from the wave set of this current mass bin and all smaller mass bins. This means that the wave set can only increase for increasing resonance mass.

The result of this tight thresholding is summarized in Figure 6.13. Looking first at the black line that corresponds to all waves and is equal in both plots, we see a jump in the amount of added partial waves happening at ~ 2.4 GeV and another jump shortly before the end of the plot at 3 GeV. It jumps from ~ 15 % of all waves to ~ 30 % and, then, to ~ 50 % defining three distinct regions where the number of waves is rather constant. At the end we will constrain the resonance-mass bins to values up to 2.5 GeV and, thus, only the ~ 60 first partial waves will remain. But at this stage we will not cut on the number of waves, yet. Everything that remains after this step will enter in the next wave-selection stage.

But before we continue with this, let us have a more detailed look at the results. On the left, in Figure 6.13(a), one can see that partial waves with isobars $f_0(1710)$ and $K_2^*(1430)$ are basically removed from the wave pool, since they only start to contribute at the position of the second jump. The isobars $f_0(1500)$, $f_2'(1525)$ and $K^*(1410)$ start in the central region, only the $2^{-+}2^+ f_2'(1525)\pi$ S wave starts already at ~ 1.6 GeV. The corresponding $M = 0$ and $M = 1$ waves and the also possible D-waves and G-waves start later, showing that there would be a lot of destructive interference between the $f_2^{(\prime)}$-waves. The same is also true for the partial waves with the K^* isobars, basically removing the $K^*(1410)$ due to strong interference otherwise.

A second not so obvious problem of this kind appears regarding the spin-0 isobars. While the heavy $f_0(1500)$ and $f_0(1710)$ are completely removed below 2.4 GeV as already mentioned, also the other spin-0 isobars are strongly suppressed. Only the $f_0(980)\pi$ channels start strong with a 50 % survival rate. The two kaonic isobars $(K\pi)_{\text{S}}$ and $(K\eta)_{\text{S}}$ start with 2 and 4 partial waves, respectively. A jump occurs at 1.94 GeV which is directly correlated with the jump in the 1^{++} sector in Figure 6.13(b). And slightly later we see a jump in the 0^{-+} sector coinciding with an inclusion of a corresponding $(K\pi)_{\text{S}}$ wave. And indeed looking at the actual resulting list of partial waves, both kaonic spin-0 isobars only contribute to partial waves with $J \geq 2$. All of this is most likely related to the Bose symmetrization that is affecting both $\pi^- K_S^0$ and $K_S^0 K_S^0$ isobars, effectively doubling the number of partial-waves amplitudes that can interfere with each other.

Looking more closely at Figure 6.13(b), we see that the J^{PC} spin sector 6^{++} is completely removed, and 5^{-+} as well as 6^{-+} only start to contribute in the final region. At the first jump in the total amount of waves the spin sectors 4^{++}, 4^{-+} and 5^{++} kick in, with the last two only having few waves starting already very early. This means in conclusion that for a PWD up to only 2.5 GeV almost only resonances with $J \leq 3$ will be accessible when using these thresholds. But as mentioned earlier, we will continue with this complete mass range entering into the following "automatic" part of the wave-selection procedure.

6.2.3 Wave-Selection Fit

So far we did not use the actual PWD formalism, but this will change now. By introducing an extra penalty term into the likelihood function [58] demonstrated for the $K^- \pi^- \pi^+$ final state and [77] for the $\omega \pi^- \pi^0$ final state that the PWD framework will be able to actively set certain partial waves to zero, if

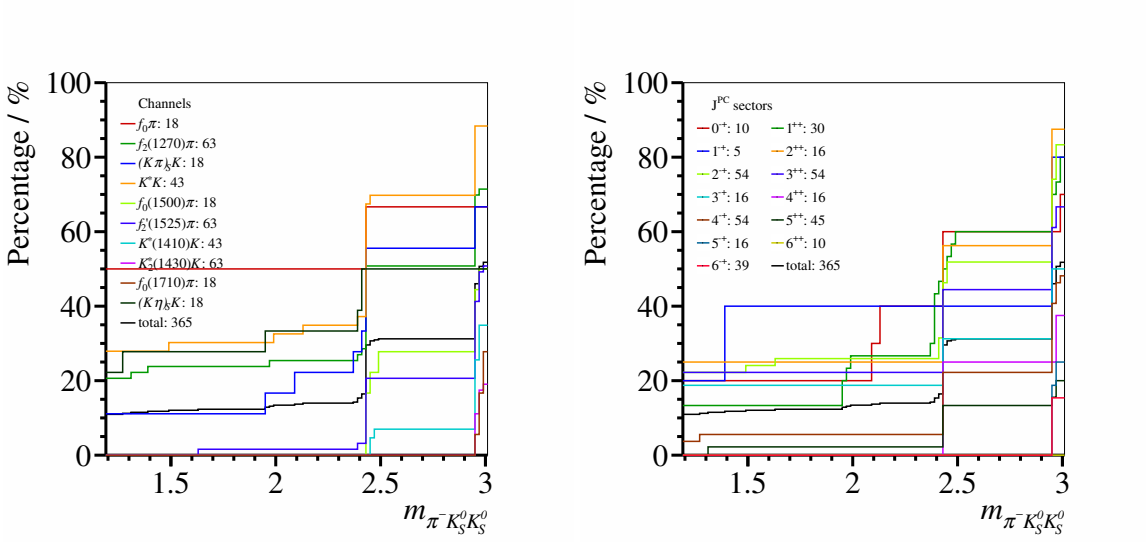

(a) (b)

Figure 6.13: Result of the tight thresholding, the partial waves are grouped according to the decay channel (left) and the J^{PC} sector (right). The number behind each component in the legends is the total amount of waves for this group and defines the 100 % for the corresponding colored line.

they are not needed to describe the full intensity. The procedure is also described in [20, 79]. The corresponding term, that will be added to the negative-log-likelihood function, is

$$-\ln \mathcal{L}_{\text{Cauchy}} = \sum_w \ln\left(1 + \frac{\left|T_{ww}\right|^2 I_{ww}^{\text{acc}}}{\gamma^2}\right), \tag{6.1}$$

where the sum extends over all partial waves and all incoherent sectors, i.e. positive-reflectivity waves, negative-reflectivity waves (which we neglect here) and the flat wave. The parameter γ or rather its inverse is a measure for the wave-suppression power of this additional term[5] and is chosen as $\gamma = 0.3$, the smaller γ the more low-intensity waves will be set to zero. This is definitely another place where additional studies could be performed to find the optimal value.

Since normally, all mass bins are fitted separately during a PWD without any knowledge of each other, such a wave-selection fit could result in only single isolated bins for a specific partial-wave being present in a certain mass range. This is not very helpful and, therefore following [**\cite {wallner:phdthesis}**], an additional term can be added to the negative-log-likelihood function which allows to incorporate a continuity condition between neighboring bins for each partial wave w:

$$(-\ln \mathcal{L}_{\text{comb}})_w(m_j) = \sum_{i=-N_{\frac{1}{2}}}^{N_{\frac{1}{2}}-1} \left|\mathcal{T}_{ww}(m_{j+i}) - \mathcal{T}_{ww}(m_{j+i+1})\right|^2, \qquad \text{with } N_{\frac{1}{2}} := (N_{\text{comb}} - 1)/2 \tag{6.2}$$

[5] [58] writes that each wave would need its own γ_w as they have different acceptances. He suggests to use the acceptance integral matrix to incorporate this difference and to allow for the usage of just one common hyperparameter for all partial waves.

where N_{comb} is the number of bins to combine[6]. Increasing N_{comb} increases the runtime of a fit drastically, thus, for now we choose $N_{\text{comb}} = 7$, i.e. we always fit each mass bin together with the three previous and the three following mass bins. If the specific partial wave w does not exist in the wave set of a mass bin, the corresponding terms, where it appears, will be omitted. Otherwise, we would always force the amplitudes to start at zero from their corresponding threshold.

For one mass bin m_j, the full negative-log-likelihood for this automatic wave selection is given by

$$(-\ln \mathcal{L}_{\text{full}})(m_j) = \sum_{i=-N_{\frac{1}{2}}}^{N_{\frac{1}{2}}} \Big((-\ln \mathcal{L})(m_{j+i}) + (-\ln \mathcal{L}_{\text{Cauchy}})(m_{j+i}) \Big) + \beta \sum_w (-\ln \mathcal{L}_{\text{comb}})_w(m_j), \quad (6.3)$$

with the strength β of this additional continuity constraint, which we set to $\beta = 0.2$ for this first test study. For each of such a fit, only the transition amplitudes $\mathcal{T}$ of the central mass bin m_j are saved, the rest is discarded. In the future, the parameters β and N_{comb} should be studied together with the choice of γ in order to see how they affect the resulting wave set.

Usually, one sorts the waves according to their intensity, separately for each mass bin. Plotting this intensity against the position of the wave in this sorting results, by construction, in a falling curve. This curve will experience a sudden drop at some wave index from where on the intensities of the partial waves become small. This defines a cut-off value for the intensities of this mass bin. Only waves with an intensity larger than this cut-off value would be added to the wave set of this particular mass bin. However, using this automatic wave selection can result in holes in the intensity spectrum for some partial waves, thus, we change here to a more hands-on method. We look at partial-wave intensity plots and discard waves completely if

- they contribute with less than 0.05 % to the full intensity,
- only few subsequent mass bins have non-vanishing intensity ($\lessapprox 7$),
- the threshold of a wave, roughly defined as the mass bin where the intensity consistently does not vanish for several subsequent mass bins, lies above 1.9 GeV.

The last requirement is not really necessary, but for the moment we want to focus on small resonance masses. For the high-mass region more heavy isobars and higher total spins as well as orbital angular momenta start to contribute which increases the amount of allowed QN combinations drastically, making the wave selection more involved. These criteria result in the wave set as detailed in Table 6.1.

The extracted intensities and interferences of the wave-selection fit are only useful to find the thresholds for partial waves, since the penalty factor together with the combined-bins term can strongly affect the position and shape of peaks in the intensity. Thus, we summarize the results in words.

Firstly, one can observe that all waves with isobars $f_0(1500)$, $f_0(1710)$, $f_2'(1525)$, $(K\pi)_S$, $K^*(1410)$ and $K_2^*(1430)$ are completely excluded from the wave pool due to either a too high threshold, in case of the $(K\pi)_S$, or no intensity at all, for the other ones. Regarding the J^{PC} QNs of the resonance, we notice consistently dominant contributions from the 0^{-+}, 1^{++} and 2^{-+} spin sectors. The sectors with QNs 1^{-+}, 2^{++} and 3^{++} are small. All other sectors are negligible. The only exception is the $4^{-+}0^+ (K\eta)_S K_S^0$ G wave, but more on that later.

[6] We only consider odd values of N_{comb} in order to have symmetric intervals around the central bin.

Table 6.1: Wave set determined by the wave-selection method as described in section 6.2.3. Partial waves with grey text are separately discussed in section 6.2.4.

J^{PC}	M^{ϵ}	$\xi\zeta\, L$	**rel. intensity**	**threshold** / GeV
1^{++}	0^+	$f_0(980)\pi$ P	11.8 %	1.28
0^{-+}	0^+	$f_0(980)\pi$ S	11.0 %	1.20
2^{-+}	0^+	$(K\eta)_S K_S^0$ D	5.2 %	1.36
1^{++}	0^+	$K^*(892)K_S^0$ S	4.8 %	1.36
2^{-+}	0^+	$f_0(980)\pi$ D	4.3 %	1.48
2^{-+}	0^+	$K^*(892)K_S^0$ P	3.0 %	1.40
2^{-+}	1^+	$K^*(892)K_S^0$ P	2.1 %	1.48
1^{++}	1^+	$K^*(892)K_S^0$ S	1.8 %	1.44
1^{++}	1^+	$f_0(980)\pi$ P	1.7 %	1.36
2^{++}	1^+	$K^*(892)K_S^0$ D	1.6 %	1.48
2^{-+}	1^+	$f_0(980)\pi$ D	1.5 %	1.48
1^{-+}	1^+	$K^*(892)K_S^0$ P	1.4 %	1.40
3^{++}	$0^+, 1^+$	$f_0(980)\pi$ F	0.5 %, 0.7 %	1.48
3^{++}	$0^+, 1^+$	$(K\eta)_S K_S^0$ F	0.7 %, 0.5 %	1.48
4^{-+}	0^+	$(K\eta)_S K_S^0$ G	1.0 %	1.44
0^{-+}	0^+	$f_2(1270)\pi$ D	0.9 %	1.32
3^{++}	$0^+, 1^+$	$K^*(892)K_S^0$ D	0.4 %, 0.4 %	1.60
2^{-+}	1^+	$K^*(892)K_S^0$ F	0.7 %	1.52
1^{-+}	1^+	$f_2(1270)\pi$ D	0.6 %	1.40
2^{-+}	1^+	$(K\pi)_S K_S^0$ D	0.6 %	1.40
2^{-+}	0^+	$f_2(1270)\pi$ S	0.5 %	1.56
2^{++}	1^+	$f_2(1270)\pi$ P	0.07 %	1.48
flat wave			31.5 %	1.36

However, the biggest contribution comes from the flat wave, which has the shape of the acceptance-corrected total intensity, see Figure 6.14. This shows that the fit is not able to separate the contributions properly. It turns out that this problem can be solved by increasing the rank of the PWD model as introduced in section 3.4.5. Higher rank introduces additional incoherences into the model and can help to disentangle contributions from different production processes. Due to the event topology of displaced vertices for the two K_S^0 in the final state, also other backgrounds might still be present in the data, one of which might be for example a 5π final state. This has to be studied in the future, e.g. by producing signal MC for these background processes and performing the $\pi^- K_S^0 K_S^0$ event selection on them to see how big their contribution to the current data set is.

6.2.4 Final Adjustment of the Wave Set

The determined thresholds of the previously detailed wave set (see Table 6.1) are all relatively small. Since a change in the amount of waves impacts all other partial waves and can create artifacts in the resulting resonance-mass distributions, we let all selected waves start at the minimal value of 1.2 GeV.

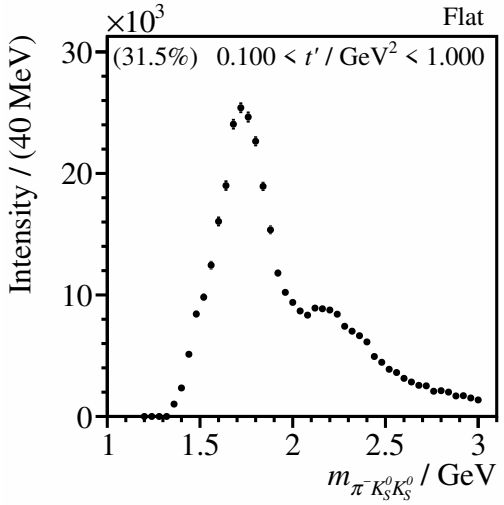

Figure 6.14: Flat wave as extracted by the wave-selection fit.

In order to see if this has a negative effect on the stability of the fit, we start with the strongest waves with a relative intensity above 4 % as determined by the wave-selection fit and add the following waves one-by-one in the order as they are listed in Table 6.1.

Also similar to the wave-selection fit, we observe a strong contribution from the flat wave in shape of the total intensity during the standard PWD fit. Increasing the rank shows that the threshold of the flat wave increases as well, together with an overall decrease in its relative intensity. Also the fit results become a lot more stable, therefore, we use a rank-3 fit for this next step. It turns out that the fit model is very stable when it comes to adding new partial waves. This impacts the shape of the previously already included partial waves only weakly. In the following we discuss the problematic cases.

For the three 3^{++} waves only the theoretically most dominant $M = 0$ partial wave is added to reduce the amount of waves. Additionally, the two waves, whose $M = 0$ component was removed by the automatic wave selection but the $M = 1$ component survived, are excluded as well. These are the $K^*(892)K_S^0$ F-wave and the $(K\pi)_S K_S^0$ D-wave of the $J^{PC} = 2^{-+}$ sector.

When including the partial wave $4^{-+}0^+$ $(K\eta)_S K_S^0$ G to the wave pool, it develops an unphysical peak at 1.65 GeV that seems to be leakage from the 2^{-+} sector where the $\pi_2(1670)$ is expected to contribute strongly at this resonance mass. This 2^{-+} sector is also heavily impacted by the inclusion of this wave. One could give this wave a higher threshold to solve this issue, but since we are focussing only on the low-mass region, we simply exclude the wave.

The inclusion of the $0^{-+}0^+$ $f_2(1270)\pi$ D-wave has a very strong impact on all waves with $f_0(980)$ as an isobar. The reason is probably that, so far, $f_0(980)$ was the only isobar in the $(K_S^0 K_S^0)$ system. The wave was excluded for the moment, but we will address it again later.

The $K^*(892)K_S^0$ D-wave of the 3^{++} sector develops an unphysical peak starting already at 1.45 GeV, thus, we do not include it.

Next in line is the spin-exotic $1^{-+}1^+$ $f_2(1270)\pi$ D wave. This partial wave has a two-peak structure with an enhancement at 1.65 GeV, a dip down to zero at 1.9 GeV and another peak at 2 GeV. This structure is expected for the 2^{-+} sector where the $\pi_2(1670)$, the $\pi_2(1880)$ and the $\pi_2(2005)$ should

appear. This indicates that these structure might simply be leakage from the not yet included $2^{-+}0^+ f_2(1270)\pi$ S-wave. But even after its inclusion this structure still remains in the corresponding 1^{-+} wave. Since the $\pi_1(1600)$ hybrid candidate is not predicted to decay into this specific final state according to ℓQCD, at least not with a substantial strength ([10], FIG. 16), we exclude the wave for now.

When adding the just mentioned $2^{-+}0^+ f_2(1270)\pi$ S-wave to the wave set, we see the previously described two-peak structure. Its inclusion affects the $0^{-+}0^+ f_0(980)\pi$ S-wave by introducing some overall background, but not as strongly as the respective 0^{-+} wave with the $f_2(1270)$ isobar did. Since the π_2 resonances are expected to decay to $f_2(1270)\pi$, we include this wave nevertheless.

Incorporating the $2^{++}1^+ f_2(1270)\pi$ P-wave into the wave set does not affect the other waves, thus, we keep it inside.

When using the resulting wave set, we experience a lot of bin-wise jumps in the relative phases with the $0^{-+}0^+ f_0(980)\pi$ S-wave indicating the presence of mathematical ambiguities in the fit model. This means that there are different solutions that result in the same negative log-likelihood value and, thus, the fit cannot distinguish which of them is the correct one. However, if we try to add single waves to the 0^{-+} sector, this always creates strong destructive interference between these two 0^{-+} waves, especially when adding the $(K\pi)_S$ isobar. If we add two waves, namely the $f_2(1270)\pi$ D-wave and the $K^*(892)K_S^0$ P wave, the destructive interference is strongly reduced and it even reduces again the background that the inclusion of the $2^{-+}0^+ f_2(1270)\pi$ S-wave created in the $0^{-+}0^+ f_0(980)\pi$ S-wave. The resulting resonance-mass spectra of these two additionally included partial waves are not very convincing, however, it gives stability to the relative phases involving the $f_0(980)\pi$ S-wave. Therefore, we keep them even though the $K^*K_S^0$ P-wave was originally already excluded by the tight thresholding discussed in section 6.2.2. Additionally, the inclusion of these two waves reduces the relative intensity of the flat wave drastically to 7.9 % and its intensity starts to rise at 1.78 GeV.

The final wave set is listed in Table 6.2 (without the greyed out rows) and we will discuss the results of the corresponding PWD in the next section.

6.3 Partial-Wave Decomposition of the $\pi^- K_S^0 K_S^0$ Final State

For the final PWD fit to the data, a rank-4 model was used in order to smoothen the complex phase of the interference terms further. Each additional rank allows for another incoherent sector. This can be necessary if there are different final states contributing, for example due to misidentification of final-state particles. The biggest contribution will most likely come from a 5π final state with charged pions. Such a final state could be reduced by requiring a larger vertex separation between the BPV and the SVs of the K_S^0, however, at the cost of signal events as well. This should be studied in the future by create signal MC for such a $\pi^-\pi^-\pi^-\pi^+\pi^+$ final state and determining the leakage through the $\pi^- K_S^0 K_S^0$ event selection discussed in chapter 5.2. Similarly, also a final state with three charged pions together with two charged kaons could be possible, where the kaons are not correctly identified by the `RICH` cut. They could originate from a ϕ-meson decaying in close proximity of the BPV and being identified as a "shared" K_S^0, where the invariant mass of the kaon pair lies in the accepted mass range of the K_S^0 when applying the wrong pion-hypothesis. Furthermore, final states with soft π^0 could contribute, where the missing momentum and energy are small enough for the event to pass the exclusivity cuts discussed in section 5.2.3, e.g. the G-parity violating 6π final state originating from the G-parity allowed $3\pi\eta$. According to [34] (section 2.2), also an integration over a large t' range – as we are

doing it here – can make a higher rank necessary. Lastly, we observe a strong flat wave for smaller rank. This could indicate the insufficiency of the chosen set of partial waves. When increasing the rank (see appendix F.1), we observe a reduction of the relative intensity of the flat wave, as well as an increase of its threshold. With these reasons, a rank-4 fit can be justified for a first attempt, however, we note that this is definitely a point that should be investigated further in the future.

The used wave set is detailed in Table 6.2. The last column shows which of the waves were used during the resonance-model fit of the $\pi^-\pi^+\pi^-$ analysis of COMPASS as described in reference [37] together with the respective relative intensity of that wave. If these waves were excluded by the previously discussed wave-selection procedure for this $\pi^- K_S^0 K_S^0$ analysis, they have the entry "–" and the lines are greyed out.

Note that the $\rho(770)\pi$ waves from the $\pi^-\pi^+\pi^-$ analysis are listed in the corresponding row of the $K^*(892)K_S^0$ wave in this analysis solely due to the similarity of the involved QNs. However, a comparison of the relative intensities is not useful since the coupling ratio of the decays $\rho(770) \to \pi^+\pi^-$ and $f_0(980) \to \pi^+\pi^-$ is different than the one of the decays $K^*(892) \to K_S^0 K_S^0$ and $f_0(980) \to K_S^0 K_S^0$.

The $0^{-+}0^+ f_0(980)\pi$ S obtains intensity over a large range of the resonance mass, thus, it is chosen as the reference wave. This means that its transition amplitude is chosen to be positive real and fixes the free global phase. Future studies should test the effect that this choice has on the wave selection procedure and the stability of the PWD.

In order to find the correct minimum for each of the separate m_X-bin fits, for each of these bins, we perform 500 fit attempts with random starting parameters and take the one with the lowest negative log-likelihood. To test for ambiguities, we plot all results with a negative log-likelihood close to the minimal value at the same time. Ambiguous solutions should manifest themselves as separated continuous lines in the spectra, however, in each intensity and relative phase only one such line was observed. This does not completely exclude the existence of ambiguities, since it could be the case that it is simply more likely for the fitter to end up in one specific solution or that they have a slightly higher negative-log-likelihood value, however, it definitely confirms the stability of the procedure.

Additionally, the same model is used for a fit where the binning in the resonance mass is made finer. Again, the best of 500 attempts for each of these mass bins is plotted and the results can be found in appendix F.4. The pots will be cross-referenced for easier comparison.

Since the heavier isobars were excluded by the wave-selection procedure, we can omit the mass from their names, i.e. $f_0(980) \equiv f_0$, $K^*(892) \equiv K^*$ and finally $f_2(1270) \equiv f_2$. Additionally, we will shorten the wave label, by giving the name of the expected resonance X as a subscript to the orbital angular momentum L in the decay. And if it is necessary to distinguish the spin projections M, the higher ones will be given as a superscript to L. For direct reference, this short notation is given in Table 6.2.

To summarize the fit results beforehand, we can have a look at the overview plots once more, where contributions to the different decay channels or J^{PC} sectors are added coherently. These can be found in Figure 6.15. The first observation is that some error bars extend below zero. We use the Gaussian approximation, what means that we are determining the Covariance matrix from the analytically calculated inverse Hessian matrix of the fit model. This covariance matrix is then propagated to the uncertainty of the coherent sum of all contributions to the corresponding isobar or spin sectors, according appendix C of to [80]. It seems as if this approximation is not completely valid, therefore, the uncertainties are slightly overestimated. In Figure 6.15(a), we observe a broad peak at 1.6 GeV in the $K^* K_S^0$ channels (blue), which indicates the presence of the $a_1(1640)$, since this is its dominant

Table 6.2: Final wave set for the PWD. The last colum indicates if the corresponding partial wave was used for the resonance-model fit in the $\pi^-\pi^+\pi^-$ final state together with the respective relative intensity as listed in Table 2 of [37]. The $\rho(770)\pi$ waves of the $\pi^-\pi^+\pi^-$ final state are listed in the row of the corresponding $K^*(892)K_S^0$ wave. Grey text indicates that the corresponding wave is not used and is just listed for comparison with the $\pi^-\pi^+\pi^-$ analysis.

full wave label			**short notation**	**rel. intensity**	3π	**rel. intensity**
J^{PC}	M^ϵ	$\xi\zeta\, L$	$\xi\zeta\, L_X^{(M)}$			
0^{-+}	0^+	$f_0(980)\pi\,\mathrm{S}$	$f_0\pi\,\mathrm{S}_\pi$	12.9 %	✓	2.4 %
0^{-+}	0^+	$K^*(892)K_S^0\,\mathrm{P}$	$K^*K_S^0\,\mathrm{P}_\pi$	9.6 %	✗	
0^{-+}	0^+	$f_2(1270)\pi\,\mathrm{D}$	$f_2\pi\,\mathrm{D}_\pi$	4.4 %	✗	
1^{++}	0^+	$f_0(980)\pi\,\mathrm{P}$	$f_0\pi\,\mathrm{P}_{a_1}$	9.1 %	✓	0.3 %
1^{++}	1^+	$f_0(980)\pi\,\mathrm{P}$	$f_0\pi\,\mathrm{P}^1_{a_1}$	3.5 %	✗	
1^{++}	0^+	$K^*(892)K_S^0\,\mathrm{S}$	$K^*K_S^0\,\mathrm{S}_{a_1}$	5.0 %	✓	32.7 %
1^{++}	1^+	$K^*(892)K_S^0\,\mathrm{S}$	$K^*K_S^0\,\mathrm{S}^1_{a_1}$	2.2 %	✗	
1^{++}	0^+	$f_2(1270)\pi\,\mathrm{P}$	–	–	✓	0.4 %
1^{-+}	1^+	$K^*(892)K_S^0\,\mathrm{P}$	$K^*K_S^0\,\mathrm{P}_{\pi_1}$	3.0 %	✓	0.8 %
2^{++}	1^+	$K^*(892)K_S^0\,\mathrm{D}$	$K^*K_S^0\,\mathrm{D}_{a_2}$	3.3 %	✓	7.7 %
2^{++}	2^+	$K^*(892)K_S^0\,\mathrm{D}$	–	–	✓	0.3 %
2^{++}	1^+	$f_2(1270)\pi\,\mathrm{P}$	$f_2\pi\,\mathrm{P}_{a_2}$	1.6 %	✓	0.5 %
2^{-+}	0^+	$f_0(980)\pi\,\mathrm{D}$	$f_0\pi\,\mathrm{D}_{\pi_2}$	8.4 %	✗	
2^{-+}	1^+	$f_0(980)\pi\,\mathrm{D}$	$f_0\pi\,\mathrm{D}^1_{\pi_2}$	2.2 %	✗	
2^{-+}	0^+	$(K\eta)_\mathrm{S}K_S^0\,\mathrm{D}$	$(K\eta)_\mathrm{S}K_S^0\,\mathrm{D}_{\pi_2}$	11.3 %	✗	
2^{-+}	0^+	$K^*(892)K_S^0\,\mathrm{P}$	$K^*K_S^0\,\mathrm{P}_{\pi_2}$	5.5 %	✓	2.2 %
2^{-+}	1^+	$K^*(892)K_S^0\,\mathrm{P}$	$K^*K_S^0\,\mathrm{P}^1_{\pi_2}$	2.4 %	✗	
2^{-+}	0^+	$f_2(1270)\pi\,\mathrm{S}$	$f_2\pi\,\mathrm{S}_{\pi_2}$	2.1 %	✓	6.7 %
2^{-+}	1^+	$f_2(1270)\pi\,\mathrm{S}$	–	–	✓	0.9 %
2^{-+}	0^+	$f_2(1270)\pi\,\mathrm{D}$	–	–	✓	0.9 %
3^{++}	0^+	$f_0(980)\pi\,\mathrm{F}$	$f_0\pi\,\mathrm{F}_{a_3}$	2.5 %	✗	
3^{++}	0^+	$(K\eta)_\mathrm{S}K_S^0\,\mathrm{F}$	$(K\eta)_\mathrm{S}K_S^0\,\mathrm{F}_{a_3}$	5.5 %	✗	
4^{++}	1^+	$K^*(892)K_S^0\,\mathrm{G}$	–	–	✓	0.8 %
4^{++}	1^+	$f_2(1270)\pi\,\mathrm{F}$	–	–	✓	0.2 %
flat wave, starts at 1.78 GeV			–	7.9 %	✗	

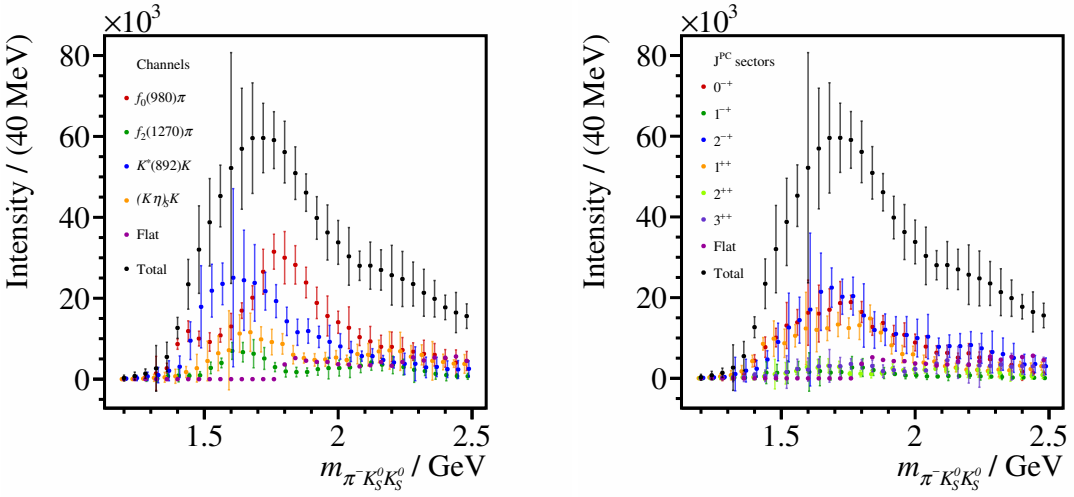

(a) (b)

Figure 6.15: Overview of which decay channels (left) and which J^{PC} sectors (right) contribute during the main fit. Displayed is the coherent sum of all partial waves that belong to the sectors as indicated by the legend. The same result for the fit with finer mass binning can be found in Figure F.6. The colored data points are slightly shifted sideways in order to make the error bars visible. All colored points actually lie where the corresponding black dot is located. Note that some uncertainty bands extend below zero. This is unphysical and shows that the used Gaussian approximation to propagate the uncertainties from the fit parameters to the intensities is not completely valid.

S-wave decay channel. A shoulder on the falling edge at 1.9 GeV could originate from the $a_1(1930)$. Next, we see a bump at 1.6 GeV in the $f_2\pi$ channels (dark green), where the $\pi_2(1670)$ has its dominant S-wave decay. Then, we see a dip at $\sim$ 1.8 GeV with another rise afterwards, which could indicate a $\pi_2(1880)$, interfering destructively, and a $\pi_2(2005)$. The $(K\eta)_S$ channel also behaves similarly, where one should note that it is only included with $J \geq 2$ partial waves. Finally, the $f_0\pi$ channels (red) have a strong peak at 1.8 GeV coming most likely from the $\pi(1800)$. In addition, we see an enhancement at 1.4 GeV already hinting strongly to the presence of the $a_1(1420)$.

Figure 6.15(b) shows a small enhancement at 1.8 GeV in the 0^{-+} sector (red) on top of a very broad hill. This broad component could originate from a Deck-like non-resonant background. A similarly broad hill is observed in the 1^{++} sector (orange), probably containing non-resonant background as well. The 2^{-+} sector (dark blue) shows a clear but also broad peak at 1.7 GeV that should come from the $\pi_2(1670)$. The remaining J^{PC}-sectors are only contributing weakly.

Before we start to look at the results in detail, let us discuss their presentation first. We will use a similar style as for the display of the TSM and BWM fit discussed in section 4.5, Figure 4.16. This means that we select a subset of the full list of fitted waves and plot the intensities of these waves on the diagonal, while the off-diagonal shows the interference terms. There, we always display the relative phase between the partial wave in the row and the one in the column. This means that resonances in the intensity on the left side should appear as rising phases, while resonances in the intensity below

should fall. The reason is that the complex phase of a pole in form of a BWM always rises (row) and its complex conjugate always drops (column). If a resonance appears in both partial waves, the relative phase should rather stay constant. Having said that this is only true for an isolated resonance without background contribution. As soon as one adds two or more components coherently in one partial wave, things can change drastically and even change the phase motion to go in the other direction[7], making predictions from the data alone is difficult without performing a resonance-model fit.

We draw vertical lines at the resonance masses where resonances are expected to appear, in order to indicate where peaks in the intensity and rapid motion in the phase would be expected. Each combination of J^{PC} gets its own color as indicated by the respective legends. In the 0^{-+} sector, we draw lines for the $\pi(1300)$, the $\pi(1800)$ and the $\pi(2070)$ in blue. The indicated 1^{++} resonances are $a_1(1260)$, $a_1(1670)$ and $a_1(1930)$. For 2^{-+}, we show lines for the $\pi_2(1670)$, $\pi_2(1880)$ and the $\pi_2(2005)$. And in the case of 2^{++}, we expect the $a_2(1320)$, the $a_2(1700)$ and the $a_2(1950)$. For the spin-exotic QNs 1^{-+}, we give the location of the $\pi_1(1600)$ and the $\pi_1(2015)$. Finally for 3^{++}, we only show the $a_3(1875)$. If available, we use their mass values as determined by COMPASS in [37], otherwise, the values are taken from the PDG.

In the top-left corner of each diagonal plot, we will show the relative intensity that this partial wave obtained from the acceptance-corrected total intensity. While this relative intensity refers to the complete fitted mass range $m_{\pi^- K_S^0 K_S^0}$ from 1.2 to 2.5 GeV, we will restrict the range for plotting to 1.25 to 2.05 GeV, since outside, the amount of RD decreases drastically, resulting in very large uncertainties. In addition the PWD model is definitely incomplete for higher masses. Heavier isobars as well as higher resonance spins would start to contribute there, thus, the results are not reliable. This is also the reason, why we do not discuss the 2^{-+} and 3^{++} waves in the main part of the thesis. A short discussion and the corresponding plots can be found in appendix F.3. A compilation of all extracted partial waves is presented in appendix F.5, however, this is probably only readable in the digital version of this thesis.

Since the relative phase is periodic, points slightly below 180° and points slightly above −180° are close to each other. To facilitate the identification of a phase motion, we additionally plot all data points of the relative phases shifted by ±360° in grey.

6.3.1 Evidence for the $a_1(1420)$ in $\pi^- K_S^0 K_S^0$

Let us start the result discussion with a look at the $a_1(1420)$ partial wave, i.e. the $1^{++}0^+ f_0(980)\pi$ P-wave or for short the $f_0\pi\,\mathrm{P}_{a_1}$-wave. To show the similarity to the $\pi^-\pi^+\pi^-$ analysis, we compare it to the $K^* K_S^0\,\mathrm{S}_{a_1}$-wave as a second component. And as a third component we choose the strongest a_2 wave, namely $K^* K_S^0\,\mathrm{D}_{a_2}$. With all three together, we can recreate Figure 4.16 for this analysis and the result can be found in Figure 6.16.

The top-left plot corresponds to the intensity of the $K^* K_S^0\,\mathrm{S}_{a_1}$-wave and exhibits a broad peak at roughly 1.6 GeV. This peak is at slightly below the mass of the $a_1(1640)$ resonance indicated by the second green line. However, this could easily explained by a background component that interferes constructively with the $a_1(1640)$ on its low-mass tail and destructively on its high-mass tail. In order to explain the full peak, we need a large background component which can drastically change the behavior of the relative phases in this region. We do not see a distinct peak neither for the $a_1(1260)$

[7] This is even true for a background without own phase motion as the phenomenological Deck background described in section 4.19.

nor for the $a_1(1930)$. The former sits right at the threshold of the $\pi^- K_S^0 K_S^0$ final state and, thus, is kinematically suppressed. The latter is expected to be less pronounced than the $a_1(1640)$, since it is a radial excitation.

The $f_0\pi\,\mathrm{P}_{a_1}$-wave in the central pad of Figure 6.16 shows a two-peak structure. One where the $a_1(1420)$ should show up, indicated by the dashed green line, and one between the $a_1(1640)$ and the $a_1(1930)$. The second peak could be created by two comparably strong BWM that are subtracted from each other, i.e. with a relative phase of 180°, since this would change the interference such that the two contributions interfere coherently in the range between their maxima. We see a strong falling phase slightly before the position of the $a_1(1420)$ and afterwards a small rise. Since the phase is changing there, it indicates that there has to be something other than background. Otherwise the phase would be constant.

Now, looking at the third partial wave, the $K^* K_S^0\,\mathrm{D}_{a_2}$-wave at the bottom-right pad, we see two small bumps in the data where the $a_2(1700)$ and the $a_2(1950)$ are expected. However, the uncertainties are very large, thus, a definitive statement is impossible to make. The ground state, the $a_2(1320)$, has the same problem as the $a_1(1260)$ in the 1^{++} sector that it sits directly at the threshold. At the position of the $a_2(1700)$, we see a rise when looking at the relative phase with the $K^* K_S^0\,\mathrm{S}_{a_1}$-wave. However, this would rather indicate the presence of the $a_1(1640)$ in the latter wave. On the other hand, there is almost no relative phase motion with the $f_0\pi\,\mathrm{P}_{a_1}$-wave, which could indicate the presence of either none or both of the resonances. Their resonance parameters are similar, therefore, their phase motion could simply cancel out.

Only with a full-fledged resonance-model fit, one will be able to see if the resonances are present in the data or if it can be solely described by a non-resonant background. And especially the $K^* K_S^0\,\mathrm{D}_{a_2}$-wave demonstrates that more data is necessary to make stronger claims of the presence of resonances.

Appendix F.2 shows the $f_0\pi\,\mathrm{P}^1_{a_1}$-wave with spin projection $M = 1$, where we also see a small bump at 1.4 GeV together with phase motion in the relative phase to the $K^* K_S^0\,\mathrm{S}_{a_1}$-wave and the $K^* K_S^0\,\mathrm{D}_{a_2}$.

Throughout all test, there was always a clear peaking structure at 1.4 GeV. Since it appears in both spin projections and does not appear in the other 1^{++} waves, we can affirm evidence for the presence of the $a_1(1420)$ consistent with the interpretation as a rescattering effect.

6.3.2 The Pseudoscalar Sector

As a second subset, we want to focus on the 0^{-+} waves. Here, we choose again the same format as before, just with all spins reduced by one. This means that we take the $K^* K_S^0\,\mathrm{P}_{\pi}$-wave, the reference wave $f_0\pi\,\mathrm{S}_{\pi}$ and once more the $K^* K_S^0\,\mathrm{S}_{a_1}$-wave in order to have a known component that helps to relate the additional plots to the already discussed ones.

In the first panel of Figure 6.17, we again see a similar structure in the $K^* K_S^0\,\mathrm{P}_{\pi}$-wave as we already had for the $K^* K_S^0\,\mathrm{S}_{a_1}$-wave (here as well presented in the bottom-right plot): We see a broad bump slightly before the location where the $\pi(1800)$ would be expected. This indicates that, also here, a large background contribution is present that could interfere with a possible resonant signal.

The $f_0\pi\,\mathrm{S}_{\pi}$-wave in the central pad, however, shows a clear peak at 1.8 GeV for the $\pi(1800)$. But only a slight phase motion is visible in the relative phase with the other two waves. While the $\pi(1800)$ as a hybrid candidate is also very interesting, we observe a new peaking signal at 1.4 GeV. And in the two corresponding relative phases, we also see a strong motion of the phase in the surrounding bins. A peak with a phase motion are usually strong hints for a resonance, but here it could be

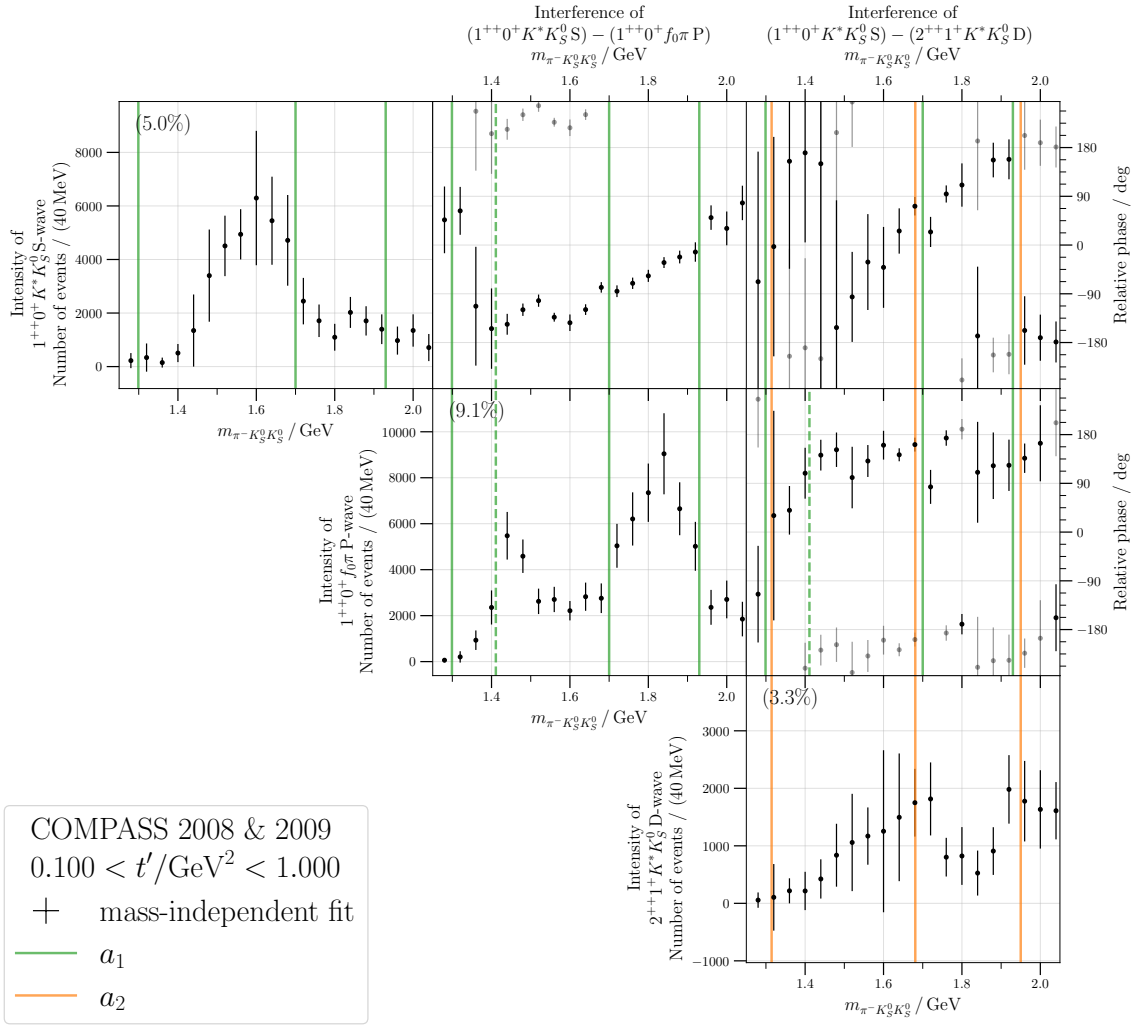

Figure 6.16: Result of the $\pi^- K_S^0 K_S^0$ PWD presented as described in the main text. Displayed are the partial waves $K^* K_S^0\,\mathrm{S}_{a_1}$ (first row/column), $f_0\pi\,\mathrm{P}_{a_1}$ (second row/column) and $K^* K_S^0\,\mathrm{D}_{a_2}$ (third row/column). The same result for the fit with finer mass binning can be found in Figure F.7.

something different. It shows many similarities to the $a_1(1420)$, for example also the fact that we see neither a peak in the corresponding $K^* K_S^0 \, \mathrm{P}_\pi$-wave nor a phase motion in its relative phase with the $K^* K_S^0 \, \mathrm{S}_{a_1}$-wave. Could this be another triangle singularity causing this effect? Or maybe even the same one? We will elaborate on that later in section 6.4. Due to its similarities, we will call it $\pi(1420)$ from now on.

While the $a_1(1420)$ signal was persisting and strong throughout all performed fits, this new $\pi(1420)$ was sometimes not that strongly visible and vanished in the destructive interference with the other 0^{-+} waves that was mentioned in section 6.2.4. Especially when only including the $f_2\pi \, \mathrm{D}_\pi$-wave, the dip between the two peaks in the central panel of Figure 6.17 is filled up. As mentioned earlier, this is most likely coming from destructive interference between the two waves, which gets cured or at least reduced when add the $K^* K_S^0 \, \mathrm{P}_\pi$-wave. Keeping this in mind, it is still possible that this peaking structure is only an artifact of the wave selection, however, this artifact would also have to create a phase motion in almost all relative phases. See also appendix F.5 for a complete presentation of all discussed partial waves together, where the first row of all plots corresponds to the reference wave $f_0\pi \, \mathrm{S}_\pi$.

6.3.3 The Spin-Exotic $\pi_1(1600)$ in $\pi^- K_S^0 K_S^0$

The final partial-wave that we will discuss, is the spin-exotic $K^* K_S^0 \, \mathrm{P}_{\pi_1}$-wave where we hope to see the $\pi_1(1600)$. This wave only obtains 3 % of the full intensity. This means it is similar in strength than the already discussed $K^* K_S^0 \, \mathrm{D}_{a_2}$-wave. And also here, see the top-left panel in Figure 6.18, we have large uncertainties that make a clear statement impossible. We observe a broad peak extending from 1.4 to 1.9 GeV and the relative phases are nearly constant at 1.6 GeV. In case of the relative phase to the $K^* K_S^0 \, \mathrm{P}_\pi$-wave we see a hint of a slow rising phase which turns into a drop where the $\pi(1800)$ lies. In the interference with the $K^* K_S^0 \, \mathrm{S}_{a_1}$-wave, no phase motion is observed. The reason could be that the phase motions of the $\pi_1(1600)$ and the $a_1(1640)$ compensate each other. A similar behavior was observed during the analysis of the $\eta\pi^+ \pm \pi^-$ final state by the E852 collaboration (see Figure 4e of [81]). This is also the case for the results with finer binning in the resonance mass, see Figure F.10. This together does not give convincing arguments for the presence of a $\pi_1(1600)$. But given the small amount of data, as well as maybe an insufficient wave set to properly select waves with such small relative intensities, we can neither make a definite statement on its absence. If a large background contribution would be present in this partial wave, it could strongly reduce the visibility of the phase motion.

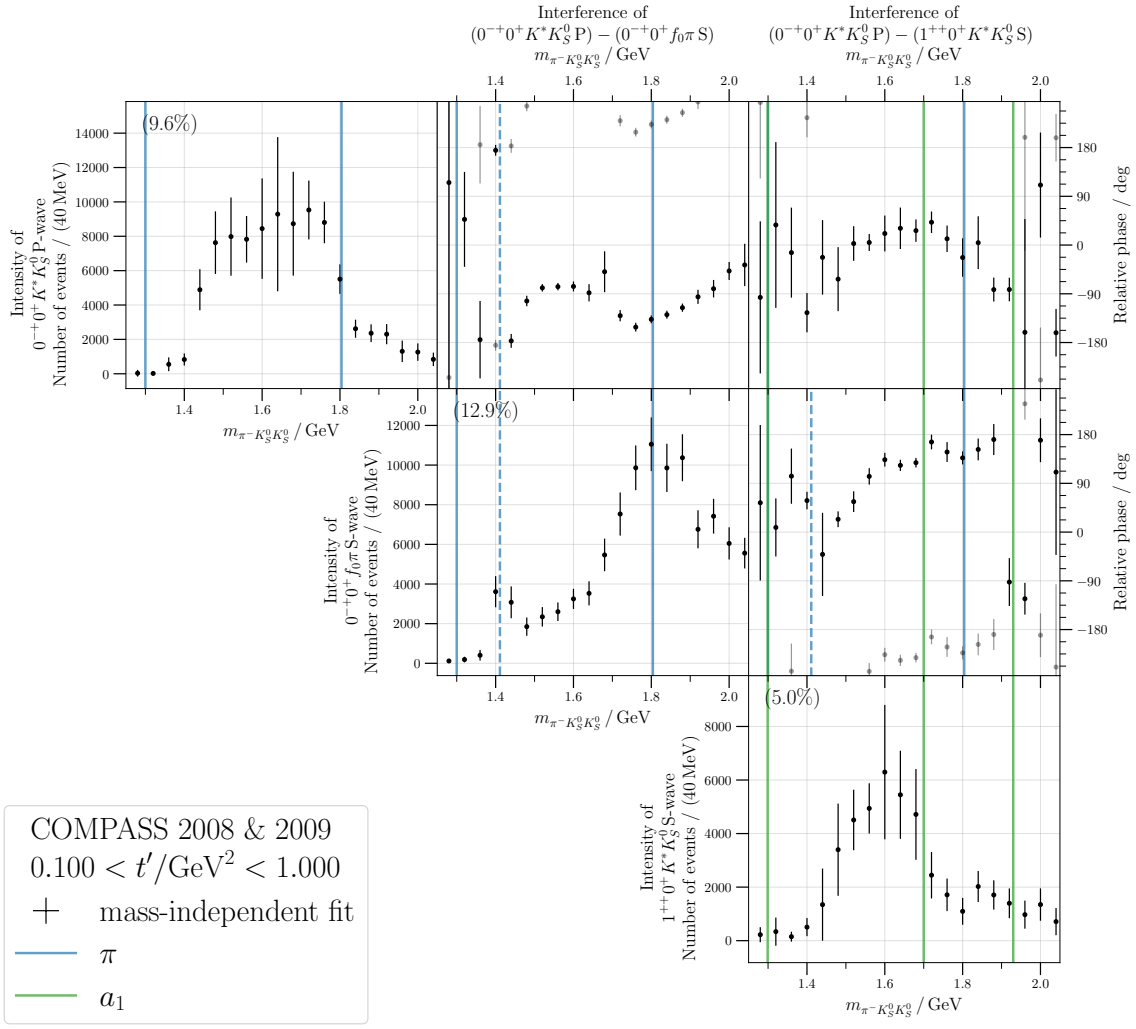

Figure 6.17: Result of the $\pi^- K_S^0 K_S^0$ PWD presented as described in the main text. Displayed are the partial waves $K^* K_S^0\,\mathrm{P}_\pi$ (first row/column), $f_0\pi\,\mathrm{S}_\pi$ (second row/column) and $K^* K_S^0\,\mathrm{D}_{a_1}$ (third row/column). The same result for the fit with finer mass binning can be found in Figure F.9.

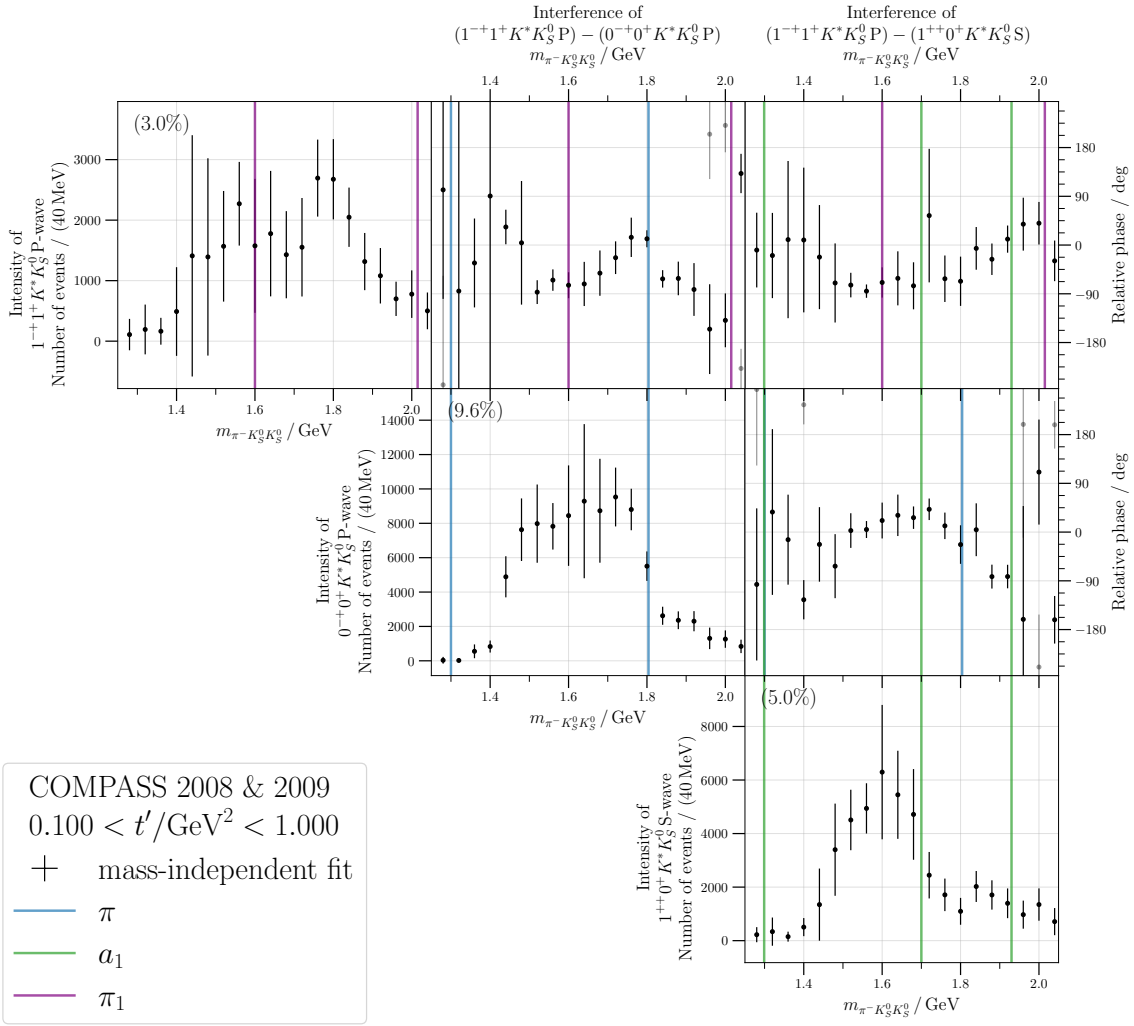

Figure 6.18: Result of the $\pi^- K_S^0 K_S^0$ PWD presented as described in the main text. Displayed are the partial waves $K^* K_S^0\,\mathrm{P}_\pi$ (first row/column), $K^* K_S^0\,\mathrm{P}_\pi$ (second row/column) and $K^* K_S^0\,\mathrm{D}_{a_1}$ (third row/column). The same result for the fit with finer mass binning can be found in Figure F.10.

6.4 The $\pi(1420)$ as a Triangle Singularity

As already discussed, the new $\pi(1420)$ signal shows many similarities to the $a_1(1420)$. To summarize them again we have

- a narrow peak in the intensity of the $f_0\pi\,\mathrm{S}_\pi$ wave,
- a phase motion in the relative phase with all other waves,
- no peak at 1.4 GeV of the other 0^{-+} partial waves and also no phase motion with other waves except with the $f_0\pi\,\mathrm{S}_\pi$-wave and the $f_0\pi\,\mathrm{P}_{a_1}$-wave (which would rather come from the $a_1(1420)$).

The QNs of the resonance do not enter directly in the calculations of the triangle amplitude. Especially the scalar case does not require any input other than the masses and decay widths of the particles involved in the triangular loop. This means for the triangle singularity that it should also manifest itself for other resonance QNs than 1^{++}. In principle not even a resonance has to be present.

The difference is here now that we start from a $K^*K_S^0$ P wave and go to a $f_0\pi$ S wave which means that we start from the QNs $w = (JMLS) = (0011)$ and go to $w = (JMLS) = (0000)$. This simplifies the equations for a partial-wave projection. Following section 4.3.3 for the case at hand, we can set

$$^{(0)}F_{(0011)}(s,\sigma_3) = f_{K^*}(\sigma_3)\mathtt{BW}_\pi(s). \tag{6.4}$$

As a source for the rescattering, the $\pi(1300)$ comes to mind. But so far, no decay channel involving kaons was observed for this resonance and also here, we do not see direct evidence for it. Nevertheless, we can continue with the calculations and think of possible source resonances later.

Comparing with equation (4.8), the final expression changes here to

$$F_{(1010)}(s,\sigma_1) = \mathtt{BW}_\pi(s) f_{f_0}(\sigma_1)\cdot\frac{K(s,\sigma_1)}{2\pi}\int\limits_{4m_K^2}^{\infty}\frac{\rho_{f_0}(\sigma_1')\int \mathrm{d}Z^{(1)}_{(0000)} f_{K^*}(\sigma_3) Z^{(3)}_{(0011)}\,/\,K(s,\sigma_1')}{\sigma_1'-\sigma_1-\mathrm{i}\,\varepsilon}\mathrm{d}\sigma_1'. \tag{6.5}$$

Next, we want to determine the kinematic factor. For this, we look at

$$Z^{(3)}_{(0011)} = Z_{(0011)}(\Omega_3,\Omega_{12}) = 3\sum_{\lambda,\nu} D^{0*}_{0\nu}(\phi_1,\theta_1,\phi_{23})\underbrace{d^0_{\nu\lambda}(\theta^*_{3(1)})}_{=\delta_{\nu0}\delta_{\lambda0}} d^1_{\lambda0}(\theta_{12}) = 3\cos(\theta_{12}) \sim \frac{1}{\sqrt{\lambda_3\lambda_{s3}}},$$

which is a lot simpler than the corresponding version for the 1^{++} sector in equation (4.11). Additionally, the argument of the square root in the denominator does not depend on σ_1, therefore, we can set the kinematic factor to $K(s,\sigma_1)\equiv 1$.

Also the projection integral becomes a lot simpler with $B^{\lambda\lambda'}_{0,00,11} = 3\delta_{\lambda0}\delta_{\lambda'0}$ from equation (A.26):

$$\mathrm{d}Z^{(1)}_{(0000)} Z^{(3)}_{(0011)} = \frac{\mathrm{d}\cos\theta_{23}}{2} 3\cos\theta_{12}.$$

The rest of the calculations work in a similar manner to section 4.3.4. But the final dispersive integral in σ_1' will not converge. Therefore, one has to perform a subtraction as introduced in equation (3.22).

With this, the final expression is

$$F_{(0000)}(s,\sigma_1) = \mathtt{BW}_\pi(s) f_{f_0}(\sigma_1) \underbrace{\left[C(s) + \frac{\sigma_1}{2\pi} \int_{4m_K^2}^{\infty} \frac{\rho_{f_0}(\sigma_1') \int \mathrm{d}Z^{(1)}_{(0000)} f_{K^*}(\sigma_3) Z^{(3)}_{(0011)}}{\sigma_1'(\sigma_1' - \sigma_1 - \mathrm{i}\,\varepsilon)} \mathrm{d}\sigma_1' \right]}_{=:\mathcal{M}_{\Delta,\pi}}, \quad (6.6)$$

where $C(s)$ is the subtraction constant that could still be a function of s.

Performing the numerical integrations, we obtain Figure 6.19 for $\sigma_1 = m_{f_0}^2$ after adjusting the (complex) subtraction constant $C(s) \equiv \text{const} \in \mathbb{C}$ to receive a similar signal compared to the $a_1(1420)$ case. We see a similar peaking structure with an asymmetry in the opposite direction than for the 1^{++} case, i.e. a steeper fall off of the high-mass tail. The subtraction constant would be a free parameter of the theoretical model if one decides to fit this amplitude to the results of the PWD.

In conclusion, such a rescattering could be the origin of this new signal, however, the question of the source has to be answered still. The $\pi(1800)$ would be an obvious candidate since we clearly see it in the data, but this signal would be $1.8\Gamma_{\pi(1800)}$ away from the peak. This means that the triangle have only $\sim 9\,\%$ of its maximal strength due to sitting on the tail of the $\pi(1800)$ propagator[8] that would have to be multiplied to the triangle amplitude. Using a $\pi(1300)$ with a width of 400 MeV as central value of the interval provided by the PDG, we would get $\sim 72\,\%$, but we do not see a convincing sign of the $\pi(1300)$ in the data. This reduction is only part of the story, since one would obviously have to include all the involved couplings for a proper estimation of the relative strength. Future studies have to investigate this by performing a resonance-model fit to the results of the presented PWD.

[8] We use a relativistic BW with constant width for this simple estimation.

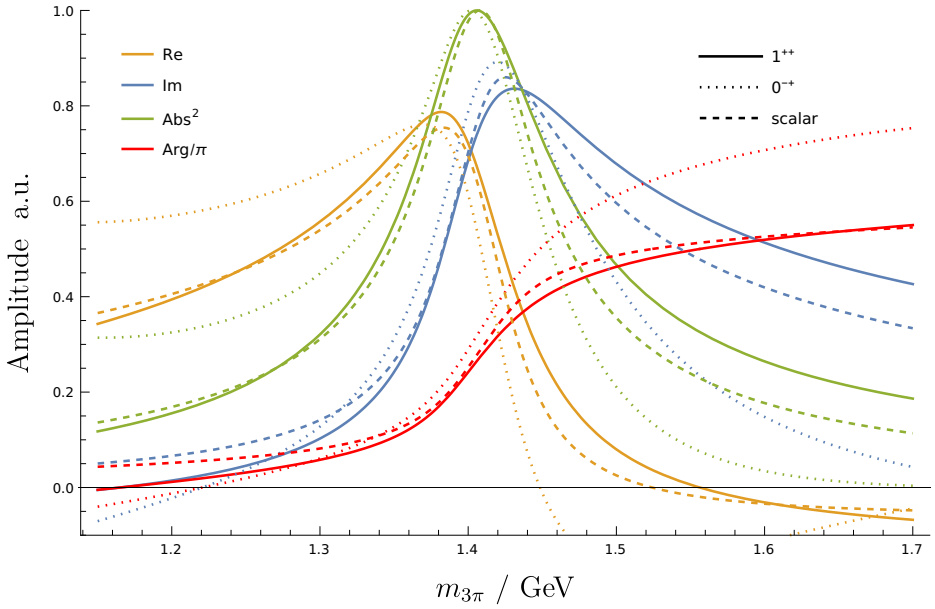

Figure 6.19: Comparison of the scalar triangle amplitude from the dispersive approach (dashed) to the result for the partial-wave projection approach including all spins and orbital angular momenta for 1^{++} (solid) and 0^{-+} (dotted). The colors indicate which function is applied on the triangle amplitude as detailed in the top-left legend. Calculations are performed for $K^{*0}(892)$, K^{+} and K^{-} involved in the rescattering. The calculations and the creation of this plot are done with `Mathematica`.

6.5 Next Steps

As already mentioned several times throughout this chapter, the here presented results are only a first attempt. In order to draw final conclusions, there are many things on the agenda. Let us summarize them here.

- Perform the event selection with different cuts on the vertex separation to see how this impacts the background in the partial waves.
- Test, how the exclusion of "shared" K_S^0 or the inclusion of events with two "shared" K_S^0 affect the results of the PWD.
- Produce more aMC in the regions of the K^* and the $f_0(980)$, where we do not have twenty times as much aMC as RD.
- Test if the amount of produced aMC is sufficient by slowly decreasing it to find out when the jumps in the data become too large. If a small reduction shows an immediate effect, we can be sure that we need more aMC.
- Create signal-MC for other processes, such as 5π, $3\pi + 2K$, $3\pi\eta$,...Perform the $\pi^- K_S^0 K_S^0$ event selection on them. Like this, one can determine the size of the background coming from these processes. One can also perform the PWD on these results, to see which partial waves are affected the strongest.

- Similarly to [47], one can produce MC events distributed according to the intensity of the Deck amplitude and feed it through the whole analysis chain to see where the strongest contribution from the Deck background is observed.
- Vary the parameterization of the isobar line shapes described in section 6.2.1 to estimate their impact on the partial-wave decomposition.
  - Especially the $K^*(892)$ might profit strongly from a change in its parametrization. The reason is that it has very large uncertainties at the tips of the peaks in all its partial waves, where one would usually expect the smallest uncertainties due to the larger amount of available data.
  - [75] provides different options for the parametrization of the $(K\pi)_S$ and the $(K\eta)_S$ that could be tested here. Maybe this could also reduce the destructive interference that we observe regarding the $(K\pi)_S$ partial waves, especially with the $f_0\pi\,S_\pi$-wave.
- With an optimized wave set, one can try to fit with lower rank.
- Include negative-reflectivity waves to test their importance.
- Try different values for the free parameters of the automatic wave selection as discussed in section 6.2.3. Also, try to follow the automatic-wave-selection procedure till the end, for example by allowing for gaps in the mass distribution.
- Perform weighting of the MC data with the obtained fit result and compare the resulting kinematic and angular distributions to RD in order to see how well the fit was able to separate the contributions.
- Perform a bootstrap analysis similar to the one discussed in section 4.6.4 to get a better estimate on the uncertainties. This is needed, since we see uncertainties extending below zero in the intensity. This happens if there is not enough data and, therefore, the Gaussian uncertainties are not a good approximation anymore.
- Extend the PWD to higher resonance masses and include heavier isobars. This could be relevant, since we see, for example, bands in the Dalitz plots where the heavier K^* isobars start to contribute, see Figures 5.34 and 5.35.
- Try to bin as well in t' in order to be able to separate signal from background better during a resonance-model fit. However, due to the already large uncertainties, it is very unlikely that such an additional binning would work. We already observe that the uncertainties are huge if we double the amount of bins in m_X, especially for the partial waves with small relative intensity. It seems as if the available data is simply not sufficient.

We see that there is still a lot of work needed, but the current status of the PWD already gives the opportunity for a resonance-model fit in the low-mass region. This would allow to test the rescattering interpretation for the $a_1(1420)$ similarly to chapter 4 and as well for the newly observed $\pi(1420)$, a resonance-model fit could give further insights on its origin.

From such a resonance-model fit, one can not only extract the mass and the decay width of the resonances, but one will also be able to compare with the results obtained by the $\pi^-\pi^+\pi^-$ analysis

in [37]. This allows to determine branching-fraction ratios, once the relative normalization is fixed. Since the coupling of $X \to f_J \pi$ is independent on the decay of f_J, one can select an isobar whose branching to $\pi\pi$ and $K\overline{K}$ is known (e.g. the $f_0(980)$) for which follows

$$\frac{\mathcal{M}_{X\to 3\pi}}{\mathcal{M}_{X\to \pi K\overline{K}}} \stackrel{!}{=} \frac{g_{X\to f_0\pi} g_{f_0\to\pi\pi}}{g_{X\to f_0\pi} g_{f_0\to K\overline{K}}}. \tag{6.7}$$

With equation (3.52), we can relate the number of events, or equivalently the height of the resonance signal, to the squared magnitude of the matrix element. By measuring one resonance-height ratio, we can determine the unknown ratio of proportionality constants in equation (3.52) and, thus, can correct all other branching-fraction ratios with this.

6.5.1 Possibilities with AMBER

We discussed that the data might not be sufficient to extend the PWD to higher resonance masses or to perform an additional binning in t'. Therefore, it would be good to increase the amount of available data. The AMBER experiment is one candidate that can provide this additional data with the planned spectroscopy run. The focus will lie on a kaon beam, however, there will still always be a large beam-pion fraction that one can select as well. This would allow for an increase of the $\pi^- K_S^0 K_S^0$ data set if it is possible to combine it with the current one. Differences in the experimental setup can affect the acceptance, which can make a merging of the data sets difficult.

A more promising path is the $\pi^- K^+ K^-$ final state though. At COMPASS, the acceptance of this final state was zero for low resonance masses and even for higher masses it was non-uniform due to the limited momentum range, in which the RICH detector can distinguish pions from kaons. AMBER tries to improve the PID before and after the target, which means that this final state might become reasonable again. Some reasons why this final state is better than the $\pi^- K_S^0 K_S^0$ final state once the PID is guaranteed, are

- a better constrained PV due to three outgoing charged particles,
- no necessity for additional vertexing for SVs
- a smaller chance of particles escaping the geometrical acceptance of the spectrometer.

Currently, MC studies are ongoing that try to optimize the setup for the spectroscopy program of AMBER.

6.6 Conclusion

To summarize this chapter, we presented the signal-MC production for the $\pi^- K_S^0 K_S^0$ final state at COMPASS including its fine selection and comparison to the RD. We obtained an overall acceptance of roughly 13 %, rather uniformly distributed as a function of the three-body invariant mass as well as the invariant mass of the two-body subsystems. Also, the Dalitz plots around 1.4 GeV and 1.8 GeV showed a flat acceptance.

As a next step, a wave selection was performed with a final wave set of 18 partial waves and a flat wave. Here, the focus was put to the low-mass region to search for the $a_1(1420)$ in $\pi^- K_S^0 K_S^0$, thus, the wave set for higher masses needs to be refurbished if one wants to extend the fit range to values

above 1.9 GeV. Having a look at the results of a rank-4 fit with the determined wave set, we see a clear signal of the $a_1(1420)$ in both $1^{++}M^+$ $f_0(980)\pi$ P-waves with $M \in \{0, 1\}$. It also shows phase motion in the interference with other waves, while at the same time, no intensity peak as well as no phase motion is observed at 1.4 GeV for the $1^{++}0^+$ $K^*(892)K_S^0$ S. This makes an interpretation of the $a_1(1420)$ as a hadronic molecule unlikely, since then, it should have a dominant decay via $K^*\overline{K}$ according to [44]. On the other hand, we see a broad peak in the $1^{++}0^+$ $K^*(892)K_S^0$ S-wave where the $a_1(1640)$ sits, strengthening the indications of the $a_1(1640) \to K^*(892)K_S^0$ decay mode that we observed in the corresponding Dalitz plot.

Looking at the 0^{-+} sector, we see a clear peak for the $\pi(1800)$ decaying to $f_0(980)\pi$ as expected from the analysis of the Dalitz plot around a resonance mass of 1.8 GeV. Additionally to the $\pi(1800)$, we see a new and narrow peak at 1.4 GeV that comes with phase motion in the relative phases to other partial waves. No signal is observed in the corresponding $K^*(892)K_S^0$ P-wave at this mass. While we cannot exclude that this is an artifact of the PWD, it bares many similarities to the case of the $a_1(1420)$, therefore, we explore the possibilities of a triangle singularity in the 0^{-+} sector. And indeed, when calculating the corresponding amplitude, we observe a peak with phase motion at 1.4 GeV. However, the source of the rescattering is unclear, since the $\pi(1800)$ might be too far away and no convincing sign of the $\pi(1300)$ is observed at COMPASS, neither in the $\pi^- K_S^0 K_S^0$ final state discussed here, nor in the $\pi^-\pi^+\pi^-$ final state investigated in the past.

While we see a clear signal for the $\pi_2(1670)$ in the corresponding partial waves, we cannot make a clear statement on the existence of the $\pi_2(1880)$ hybrid candidate due to apparent insufficiencies of the current wave set at higher masses.

Finally, the spin-exotic $\pi_1(1600)$ is expected to make an appearance in the $1^{-+}1^+$ $K^*(892)K_S^0$ P-wave. This partial wave takes roughly 3 % of the total intensity and we see a broad peak extending from 1.4 to 1.9 GeV. The relative phase to other waves does not exhibit a strong phase motion, therefore, a conclusive statement on the presence of the $\pi_1(1600)$ cannot be made, yet.

Besides of many studies that can still be performed on the PWD, the next step is a resonance-model fit. This can shed light on some of the remaining open questions.

CHAPTER 7

Summary, Conclusion and Outlook

In this work, we try to answer the question for the origin of the supernumerous $a_1(1420)$ signal that was discovered by the COMPASS collaboration in 2014. For this, we started in chapter 1 with a short description of the standard model of particle physics and the quark model, introducing as well the concept of exotic mesons. Chapter 2 was dedicated to the COMPASS experiment and its analysis framework, focussing on diffractive pion-proton scattering. An introduction to scattering theory followed in chapter 3, together with a detailed look on Breit-Wigner Models (BWMs) and their complex structures. The principle of Partial-Wave Decompositions (PWDs) was summarized and a method to calculate Dalitz plots from isobar parametrizations was discussed. The end of the chapter was dedicated to partial-wave projections that allow the incorporation of resonance spins and orbital angular momenta into a rescattering model.

At the beginning of chapter 4, several different interpretations for the $a_1(1420)$ signal are discussed. The interpretation as a triangle singularity, originating from a rescattering of the $K^*(892)\overline{K}$ intermediate state to the $f_0(980)\pi$ final state, was the focus of the rest of the chapter, introducing several methods to calculate the corresponding triangle amplitude, one of which was the application of the previously introduced partial-wave-projection method. The obtained Triangle-Singularity Model (TSM) was fitted to the COMPASS data from the $\pi^-\pi^+\pi^-$ PWD and its fit quality was compared to the one of a BWM of a hypothetical new $a_1(1420)$ resonance. Finally, several systematic studies were performed.

In the next chapter 5, the event selection of the $\pi^- K_S^0 K_S^0$ final state was presented, discussing general possibilities for diffractive pion-proton scattering with kaons in the final state first. A skimming for events with at least one K_S^0-candidate was developed and the optimal vertex separation for a K_S^0 from the primary interaction vertex was determined with a significance study. After the fine selection of the $\pi^- K_S^0 K_S^0$ final state, which ensured exclusivity of the events, the results of the event selection were discussed by looking at invariant-mass spectra of the two-body systems and the Dalitz plots for certain resonance masses. In the end, a method to reduce background coming from central production via double-Regge exchange was executed.

The final chapter 6 started by determining the acceptance of the COMPASS detector for the $\pi^- K_S^0 K_S^0$ final state via the production and processing of signal Monte-Carlo (MC) data. Next, a wave-selection procedure was introduced and executed. The resulting set of partial waves was used to perform a rank-4 Partial-Wave Decomposition (PWD). In the end, the extracted partial-wave intensities and their interference with other partial waves were examined. Here, the focus was put on waves containing the $a_1(1420)$, the $\pi(1800)$ and the $\pi_1(1600)$. A possible interpretation of a

newly found signal in the pseudoscalar sector as a triangle singularity similar to the $a_1(1420)$ was discussed and further steps towards a resonance-model fit were listed together with a short outlook to the possibilities that the AMBER experiment can provide in the future for spectroscopy involving kaons.

We try to make a case for the interpretation of the $a_1(1420)$ as a rescattering effect. For this, we start by finding arguments against possible other explanations. The first one is the interpretation as a radial excitation of the $a_1(1260)$. The resulting Regge trajectory shows a slope of $(1.40 \pm 0.05)\,\mathrm{GeV}^{-2}$ when including the $a_1(1420)$ as a first radial excitation, while the slope without the $a_1(1420)$ yields $(1.05 \pm 0.05)\,\mathrm{GeV}^{-2}$ which is in agreement with the slopes from the other a_J trajectories. The second possibility is a hadronic $K^*(892)\overline{K}$ molecule, which is problematic since the mass of the $a_1(1420)$ is larger than sum of the constituent masses. Additionally according to [44], this interpretation predicts a larger branching ratio for the decay to $K^*(892)\overline{K}$ than for the decay to $f_0(980)\pi$ – by one order of magnitude. When looking at the results of the $\pi^- K_S^0 K_S^0$ PWD, we see a clear signal for the $a_1(1420)$ in the $f_0(980)\pi$ P-wave while the intensity is almost 0 at 1.4 GeV for the $K^*(892)K_S^0$ S-wave. This makes the hadronic-molecule interpretation very unlikely. In [44], the tetraquark-hypothesis was tested against the molecule-hypothesis, showing a better compatibility with the COMPASS data for the latter one. This makes the interpretation as a tetraquark even less likely than the one as a hadronic molecule. It was demonstrated by [42] that a diquark-antidiquark pair without involved orbital angular momentum would yield the Quantum Numbers (QNs) 1^{+-} for spin-1 tetraquarks. Therefore, higher orbital angular momentum would be needed in this model to allow for the $a_1(1420)$ as a tetraquark, which would increase the amount of possible states drastically. This stands in contradiction with the number of presently known states. Lastly, an interference effect with the Deck background was proposed by Basdevant and Berger in [45]. They could demonstrate that a unitary treatment of the Deck amplitude in a coupled-channel analysis of the $\rho(770)\pi$ and the $f_0(980)\pi$ channels can reproduce both intensity distributions. However, the relative phase between the two partial waves has its strongest rise at the mass of the $a_1(1260)$ and not at 1.4 GeV, where we observe it in the COMPASS data. In the meantime, first results from the PWD of the τ decays at Belle [8] were presented that show a clear $a_1(1420)$ signal. This exclude the explanation via interference with the Deck-background, since this background is not present in τ decays.

Now, we come to the interpretation as a triangle singularity originating from a rescattering of the intermediate $K^*(892)\overline{K}$ channel to the observed $f_0(980)\pi$ channel. We demonstrated that a fit with the TSM shows a better fit quality compared to a BWM of a hypothetical new $a_1(1420)$ resonance, manifested by a smaller $\mathcal{R}^2_{\mathrm{red}}$ value that is conceptionally similar to a reduced χ^2. All but one of the performed systematic studies show this tendency and all systematic studies of the TSM describe the COMPASS data better than the main fit model of the $a_1(1420)$ BWM. Determining systematic uncertainties from these studies by taking the RMS of the difference to the main model of all systematic studies with larger $\mathcal{R}^2_{\mathrm{red}}$ than the main model as the upper uncertainty and the one of all studies with smaller $\mathcal{R}^2_{\mathrm{red}}$ as the lower uncertainty, we obtain $\mathcal{R}^2_{\mathrm{red,TSM}} = 4.59^{+0.13}_{-0.40}$ and $\mathcal{R}^2_{\mathrm{red,BWM}} = 4.87^{+0.09}_{-0.48}$. Since these uncertainty intervals are overlapping, one cannot make a definite statement with this fit alone, but one needs information from other channels to strengthen the case of the rescattering interpretation.

One such channel is the $\pi^- K_S^0 K_S^0$ final state of which we performed an event selection in the course of this work, resulting in the worlds largest data set of diffractively produced $\pi^- K_S^0 K_S^0$. We could confirm the findings of the E580 experiment at Fermilab [71] and greatly expand on them due to more than 240 times the amount of exclusive events. We see clear evidence for the isobars $f_0(980)$ and $f_2(1270)$ in the $K_S^0 K_S^0$ subsystem that could be confirmed with the subsequent PWD. Additionally, we see a peak

at 1.5 GeV, where the $f_0(1500)$ and the $f_2'(1525)$ are located, and a shoulder at 1.7 GeV where the $f_0(1710)$ is expected. During the PWD, the focus was put on low resonance masses, therefore, no conclusive statement on the existence of these heavier isobars can be made, since the threshold of their decay channels starts only at $\sim$ 1.7 GeV. In the $\pi^- K_S^0$ subsystem we see a strong and narrow $K^*(892)$ peak, as well as another peak at 1.4 GeV where the $K^*(1410)$, the $K_0^*(1430)$ and the $K_2^*(1430)$ are expected. Here, only the lightest K^* could be confirmed with the PWD since the thresholds of the other channels are even higher than for the heavier f_J isobars. The $K_0^*(700)$ could contribute to the broad underground, however, due to strong destructive interference, especially with the $f_0(980)$ channels, it could not be included in the current PWD model. By looking at the Dalitz plots, we could predict the presence of the decay channels $a_1(1640) \to K^*(892)K_S^0$, $\pi(1800) \to f_0(980)\pi$ and $\pi_2(1670) \to f_2(1270)\pi$, which could all be confirmed by the PWD. By calculating the Dalitz plot around 1.4 GeV for a model with only the $K^*(892)$ isobar and comparing it to the COMPASS data, we could argue for the presence of one or both of the $f_0(980)$ and the $K_0^*(700)$ due to strong deviations of the distributions.

Enough signal MC data was produced to obtain at least twenty times as many accepted MC events as we have real data in each resonance-mass bin. For the $\pi^-\pi^+\pi^-$ final state, only ten times as much accepted MC was produced. Artifacts in the resulting PWD could be attributed to this insufficiency of the MC sample, therefore, we produced twice as much here. In the future, it should be studied if the amount is sufficient. However, the kinematic distributions of these accepted MC events show, in general, a fair agreement with the real-data distributions. More importantly, it could be demonstrated that the detector acceptance is smooth and uniformly distributed as a function of the three-body invariant mass and as a function of the invariant mass of the two-body subsystems. The acceptance displayed on the Dalitz plots around 1.4 GeV and 1.8 GeV also shows no structures. This demonstrates that no artifacts should be introduced into the PWD due to the acceptance correction of the data.

By employing an automatic wave-selection procedure, we were able to select a wave set of 18 partial waves plus one flat wave. The procedure guaranteed low destructive interference between partial waves, removing in the process the $(K\pi)_S$ and $(K\eta)_S$ isobars – which represent the K_0^* isobars – for resonance spins of $J < 2$ and masses below 2 GeV. And indeed, including these by hand, results in unphysically[1] large $f_0(980)\pi$ and $(K\pi)_S K_S^0$ intensities, hinting to the presence of mathematical ambiguities in the model. Future studies should investigate this behavior further and one has to find a method to resolve these ambiguities if one wants to include these additional isobars. Coming now to the results, we observe clear signal of the $a_1(1420)$ in both $f_0(980)\pi$ P-waves with $M \in \{0, 1\}$. As already mentioned before, no intensity peak – or rather almost no intensity at all – was observed for the $K^*(892)K_S^0$ S-wave at 1.4 GeV. This could indicate that, due to the rescattering, the events from the $K^*(892)K_S^0$ S-wave were redistributed into the $f_0(980)\pi$ P-waves. Additionally to this signal in the intensity of the $f_0(980)\pi$ P-wave, also a rapid change in the relative phase to other partial waves is observed. All of this agrees well with the interpretation of the $a_1(1420)$ signal as a rescattering effect, therefore, it strengthens the case for it. With a resonance-model fit, one will be able to test if the triangle amplitude can describe the $\pi^- K_S^0 K_S^0$ data as well. The $K^*(892)K_S^0$ S-wave for $J^{PC} = 1^{++}$ exhibits a broad peak around the mass of the $a_1(1640)$. The broadness indicates the presence of some possible non-resonant background that interferes, similar as it is the case for the $\rho(770)\pi$ S-wave in the $\pi^-\pi^+\pi^-$ final state. Also here, a resonance-model fit will provide clarity. Next, having a look at the 0^{-+} sector, we observe a strong peak for the $\pi(1800)$ in the $f_0(980)\pi$ S-wave as expected from looking

[1] Each of them approximately twice as large as the total intensity

at the corresponding Dalitz plot after the event selection. Additionally, a first sighting of a small and narrow peak is located at 1.4 GeV. It does not appear in the corresponding $K^*(892)K_S^0$ P-wave for 0^{-+} and also its relative phase to other waves shows resonant behavior. Since this resonance-like signal has a very similar signature compared to the $a_1(1420)$, we call it $\pi(1420)$ and investigate the possibility for a triangle singularity as the origin. Calculating the corresponding triangle amplitude with the partial-wave-projection method, we indeed see a peak and a rising phase at 1.4 GeV. However, as for the $a_1(1420)$, we need a source for the rescattering in form of, for example, a resonance. The $\pi(1800)$ could be too far a way and we do not see a sign of a possible $\pi(1300)$ resonance in the COMPASS data. The Deck-process could serve as a source of such a rescattering as well, but at this stage of the analysis, we cannot exclude the possibility of an artifact of the PWD due to the absence of the $(K\pi)_S K_S^0$ waves. The $1^{-+}1^+K^*(892)K_S^0$ is – with only roughly 3 % of the total intensity – definitely one of the weaker partial waves. It has a broad peak extending from 1.4 to 1.9 GeV, which could inhabit the spin-exotic $\pi_1(1600)$. However, no striking motion in the relative phase to other waves is observed. In case of the interference with 1^{++} partial waves containing the $a_1(1640)$, this could be explainable by a compensation of their phase motion, as it was also observed by the E852 collaboration [81]. Another reason for a reduced phase motion could be the presence of a strong non-resonant-background component inside of the broad peak, since such an interference can reduce the strength of the phase motion of the resonance. Again, with a resonance-model fit, one will be able to test its presence. While we see strong indications for a $\pi_2(1670)$ in the 2^{-+} partial waves, we have to refurbish the wave set for higher masses with the inclusion of heavier isobars in order to allow for statements on the presence of the hybrid candidate $\pi_2(1880)$ or heavier states.
Regarding the origin of the $a_1(1420)$, this work could provide a lot more arguments in favor of the rescattering interpretation. Additionally, a contradiction to the expectation for a hadronic molecule to appear dominantly in the $K^*\overline{K}$ channel, could be demonstrated. First signs of the $a_1(1420)$ in τ decays by [8] give further arguments against the interpretation as an interference effect with the Deck background beside the wrong location of the resonant behavior of the relative phase. But final results of the corresponding PWD with a resonance-model fit using the TSM are highly anticipated and are needed to strengthen the already strong case of the $a_1(1420)$ as a rescattering effect further. Not only in τ decays but also in diffractive scattering, there are more final states that could allow for the rescattering of $K^*\overline{K}$ to $f_0\pi$. The AMBER experiment could allow for the detection of the $\pi^-K^+K^-$ final state if its particle identification is improved compared to COMPASS. But also with COMPASS data, we can look into the $\pi^-K_S^0K_L^0$ final state by following the recipe described in this thesis. All of these additional puzzle pieces can provide further insight into the identity of the $a_1(1420)$.

But the $a_1(1420)$ does not need to be the only triangle singularity. For each of the pentaquark-candidates from [82] discovered by LHCb, a triangle singularity is present and close to the physical sheet. However, when incorporating the decay width of the involved particles, the triangle amplitudes become too broad to yield a satisfying description of the data. At lower energies, in the reaction $\gamma p \to p\pi^0\eta$, the CBELSA/TAPS collaboration found a peculiar structure in the $M_{p\eta}$ invariant mass distribution [83]. Here, the involvement of a triangle singularity through the reaction chain $\gamma p \to pa_0 \to p\pi^0\eta$ was able to provide a good description of the data. The BGOOD experiment also could successfully apply the concept of a triangle singularity in the reaction chain $\gamma p \to K^+\Lambda(1405) \to K^+\pi^0\Sigma^0$ where the $N^*(2030)$ was the source for such a rescattering [84].

Regarding the presented PWD of the $\pi^-K_S^0K_S^0$ final state, there are many additional studies needed, some of which were already mentioned. The most important problem to solve, is the strong unphysical

interference of the partial waves involving the $(K\pi)_S$ isobar for which we gave a mathematical ambiguity as one possible origin. But the effect of its parametrization has to be tested as well, since this can change the way how the isobar interferes with other partial waves. An investigation of background processes via MC production could help to rework some of the selection criteria in order to have a cleaner data sample. This might allow for a reduction of the rank of the PWD model, since we observe an increase in the experimental uncertainties if we increase the rank. Once a complete model of the PWD is obtained, one can perform a resonance-model fit. It can directly provide branching-fraction ratios of the decay channels $f_J\pi$ and $K_J^*K_S^0$. By comparing the obtained signal strengths of a resonance with equal isobar-decay mode between the $\pi^-K_S^0K_S^0$ and the $\pi^-\pi^+\pi^-$ final state, e.g. the $\pi(1800) \to f_0(980)\pi$ or the $\pi_2(1670) \to f_2(1270)\pi$ decays, one can obtain a global relative normalization constant that allows to relate the strengths of all other resonances to each other. This would give access to the branching-fraction ratios of $\pi_1(1600) \to K^*\overline{K}$ and $\pi_1(1600) \to \rho\pi$ which can be compared to the predictions of ℓQCD. This could provide valuable information for the model that is used to calculate the hybrid-meson spectrum.

To conclude, this work provided strong new evidence for the $a_1(1420)$ as a triangle singularity by presenting its first observation in the $\pi^-K_S^0K_S^0$ final state. It pioneers in the field of partial-wave projections by using the obtained model for a first time in a fit to data, showing even better compatibility with the data than a more flexible BWM. This can serve as a recipe for other occurrences of triangle singularities in order to incorporate spins and orbital angular momenta in a sophisticated manner. With the event selection of the $\pi^-K_S^0K_S^0$ final state, many new and exciting paths open up to extract resonance parameters, branching fraction ratios, and more insights to hybrid candidates such as the $\pi_1(1600)$ and the $\pi(1800)$. Finally, the first observation of a narrow resonance-like signal in the $0^{-+}0^+$ $f_0(980)\pi$ S-wave was observed that could originate from the same triangle singularity as the $a_1(1420)$ which provides even more arguments in favor of the rescattering interpretation.

Bibliography

[1] M. Valente, "The Standard Model of Particle Physics",
Supersymmetric Beasts and Where to Find Them: From Novel Hadronic Reconstruction Methods to Search Results in Large Jet Multiplicity Final States at the ATLAS Experiment,
Springer International Publishing, 2022 5, ISBN: 978-3-030-94047-8,
URL: https://doi.org/10.1007/978-3-030-94047-8_2 (cit. on p. 2).

[2] S.-K. Choi et al.,
Observation of a Narrow Charmoniumlike State in Exclusive $B^{\pm} \to K^{\pm}\pi^{+}\pi^{-}J/\psi$ Decays,
Phys. Rev. Lett. **91** (26 2003) 262001,
URL: https://link.aps.org/doi/10.1103/PhysRevLett.91.262001 (cit. on p. 4).

[3] B. Aubert et al.,
Observation of a Broad Structure in the $\pi^{+}\pi^{-}J/\psi$ Mass Spectrum around 4.26 GeV/c^2,
Phys. Rev. Lett. **95** (14 2005) 142001,
URL: https://link.aps.org/doi/10.1103/PhysRevLett.95.142001 (cit. on p. 4).

[4] T. Xiao et al., *Observation of the charged hadron $Z_c^{\pm}(3900)$ and evidence for the neutral $Z_c^0(3900)$ in $e^{+}e^{-} \to \pi\pi J/\psi$ at $\sqrt{s} = 4\,170$ MeV*, Physics Letters B **727** (2013) 366,
ISSN: 0370-2693,
URL: https://www.sciencedirect.com/science/article/pii/S0370269313008484
(cit. on p. 4).

[5] M. Ablikim et al., *Observation of $Z_c(3900)^0$ in $e^{+}e^{-} \to \pi^0\pi^0 J/\psi$*,
Phys. Rev. Lett. **115** (11 2015) 112003,
URL: https://link.aps.org/doi/10.1103/PhysRevLett.115.112003 (cit. on p. 4).

[6] C. Adolph et al., *Observation of a New Narrow Axial-Vector Meson $a_1(1420)$*,
Phys. Rev. Lett. **115** (2015) 082001, arXiv: 1501.05732 [hep-ex]
(cit. on pp. 4, 63, 64, 93, 96).

[7] A. Rabusov, D. Greenwald, and S. Paul, *Partial wave analysis of $\tau^{-} \to \pi^{-}\pi^{+}\pi^{-}\nu_{\tau}$ at Belle*,
2022, arXiv: 2211.11696 [hep-ex] (cit. on pp. 5, 103).

[8] A. Rabusov, D. Greenwald, and S. Paul, *Partial-wave analysis of $\tau^{-} \to \pi^{-}\pi^{-}\pi^{+}\nu_{\tau}$ at Belle*,
Talk at the DPG - Spring meeting, Dresden, Germany, 2023,
URL: https://www.dpg-verhandlungen.de/year/2023/conference/smuk/part/hk/session/29/contribution/2 (cit. on pp. 5, 69, 103, 192, 194).

[9] T. Schlüter and T. C. collaboration, *Study of kaonic final states in $\pi - p$ at 190 GeV*,
AIP Conference Proceedings **1257** (2010) 462, ISSN: 0094-243X,
URL: https://doi.org/10.1063/1.3483372 (cit. on pp. 5, 105).

[10] A. J. Woss et al., *Decays of an exotic 1^{-+} hybrid meson resonance in QCD*, Phys. Rev. D **103** (5 2021) 054502, URL: https://link.aps.org/doi/10.1103/PhysRevD.103.054502 (cit. on pp. 5, 175).

[11] P. Abbon et al., *The COMPASS setup for physics with hadron beams*, Nuclear Instruments and Methods in Physics Research Section A: Accelerators, Spectrometers, Detectors and Associated Equipment **779** (2015) 69, ISSN: 0168-9002, URL: https://www.sciencedirect.com/science/article/pii/S0168900215000662 (cit. on pp. 7, 8, 105, 111, 123, 244).

[12] M. Meyer-Conde, *Drell-Yan measurements at the COMPASS experiment*, Proceedings of Science **390** (2021) 488 (cit. on p. 9).

[13] J. M. Friedrich and on behalf of the COMPASS collaboration, *Pion-photon reactions and chiral dynamics in Primakoff processes at COMPASS*, AIP Conference Proceedings **1701** (2016) 040006, eprint: https://pubs.aip.org/aip/acp/article-pdf/doi/10.1063/1.4938623/13467948/040006_1_online.pdf, URL: https://doi.org/10.1063/1.4938623 (cit. on p. 9).

[14] S. Huber, *Measurement of the Pion Polarizability at COMPASS*, 2014, arXiv: 1401.4760 [hep-ex] (cit. on p. 9).

[15] D. Ecker, "Testing Predictions of the Chiral Anomaly in Primakoff Reactions at COMPASS", *20th International Conference on Hadron Spectroscopy and Structure*, 2023, arXiv: 2310.09138 [hep-ph] (cit. on p. 9).

[16] O. Kouznetsov, *GPD study programme of COMPASS at CERN*, Nuclear and Particle Physics Proceedings **270-272** (2016) 36, 18th Montpellier International Conference on Quantum Chromodynamics (QCD 15), ISSN: 2405-6014, URL: https://www.sciencedirect.com/science/article/pii/S2405601416000109 (cit. on p. 9).

[17] A. Sandacz and on behalf of the COMPASS Collaboration, *COMPASS results on DVCS and exclusive π^0 production*, Journal of Physics: Conference Series **938** (2017) 012015, URL: https://dx.doi.org/10.1088/1742-6596/938/1/012015 (cit. on p. 9).

[18] C. Adolph et al., *Sivers asymmetry extracted in SIDIS at the hard scales of the Drell-Yan process at COMPASS*, Physics Letters B **770** (2017) 138, ISSN: 0370-2693, URL: https://www.sciencedirect.com/science/article/pii/S0370269317303167 (cit. on p. 9).

[19] B. Adams et al., *Letter of Intent: A New QCD facility at the M2 beam line of the CERN SPS (COMPASS++/AMBER)*, (2019), arXiv: 1808.00848 [hep-ex] (cit. on p. 9).

[20] B. Ketzer, B. Grube, and D. Ryabchikov, *Light-Meson Spectroscopy with COMPASS*, Prog. Part. Nucl. Phys. **113** (2020) 103755, arXiv: 1909.06366 [hep-ex] (cit. on pp. 11, 28, 30, 38, 39, 43, 44, 46, 47, 171, 213).

[21] V. Gribov, *Strong Interactions of Hadrons at High Energies*, Cambridge University Press, 2022, ISBN: 978-1-00-929022-7 (cit. on pp. 11, 15, 69, 72).

[22] R. J. Eden et al., *The Analytic S-Matrix*, 5th ed., Cambridge University Press, 1966, ISBN: 978-0-521-04869-9 (cit. on pp. 11, 15, 17, 62).

[23] C. Berger, *Elementarteilchenphysik*, Springer, 2006, ISBN: 978-3-54-023143-1 (cit. on p. 13).

[24] D. I. Olive, *Unitarity and the evaluation of discontinuities*, Il Nuovo Cimento (1955-1965) **26** (1 1962) 73, ISSN: 1827-6121, URL: https://doi.org/10.1007/BF02754344 (cit. on p. 14).

[25] W. R. Inc., *Mathematica, Version 12.3*, Champaign, IL, 2021, URL: https://www.wolfram.com/mathematica (cit. on p. 16).

[26] M. Wagner, *Study of Rescattering Effects in Diffractive Production in COMPASS - The Case of the $a_1(1420)$*, MA thesis: Rheinische Friedrich-Wilhelms Universität Bonn, 2017 (cit. on pp. 18, 70, 72–74, 94).

[27] T. Åkesson et al., *A search for glueballs and a study of double pomeron exchange at the CERN intersecting storage rings*, Nuclear Physics B **264** (1986) 154, ISSN: 0550-3213, URL: https://www.sciencedirect.com/science/article/pii/0550321386904773 (cit. on p. 27).

[28] F. Von Hippel and C. Quigg, *Centrifugal-barrier effects in resonance partial decay widths, shapes, and production amplitudes*, Phys. Rev. D **5** (1972) 624 (cit. on pp. 28, 30).

[29] P. D. Group et al., *Review of Particle Physics*, Progress of Theoretical and Experimental Physics **2022** (2022), 083C01, ISSN: 2050-3911, eprint: https://academic.oup.com/ptep/article-pdf/2022/8/083C01/49175539/ptac097.pdf, URL: https://doi.org/10.1093/ptep/ptac097 (cit. on pp. 28, 299).

[30] J. M. Blatt and V. F. Weisskopf, *Theoretical Nuclear Physics*, ed. by Wiley, Springer New York, 1979, ISBN: 978-0-471-08019-0 (cit. on p. 28).

[31] C. Adolph et al., *Resonance production and $\pi\pi$ S-wave in $\pi^- + p \to \pi^-\pi^-\pi^+ + p_{recoil}$ at 190 GeV/c*, Phys. Rev. D **95** (3 2017) 032004, URL: https://link.aps.org/doi/10.1103/PhysRevD.95.032004 (cit. on pp. 30, 54–56, 98, 102, 105, 106, 112, 143, 144).

[32] J.-L. Basdevant and E. L. Berger, *Unstable-particle scattering and an analytic quasi-unitary isobar model*, Phys. Rev. D **19** (1 1979) 239, URL: https://link.aps.org/doi/10.1103/PhysRevD.19.239 (cit. on p. 31).

[33] M. Mikhasenko, *Three-pion dynamics at COMPASS: resonances, rescattering and non-resonant processes*, PhD thesis: Rheinische Friedrich-Wilhelms Universität Bonn, 2019, URL: https://bonndoc.ulb.uni-bonn.de/xmlui/handle/20.500.11811/8115 (cit. on pp. 31, 41, 43, 59, 60, 212).

[34] T. Schlüter,
The $\pi^-\eta$ and $\pi^-\eta'$ Systems in Exclusive 190 GeV $\pi^- p$ *Reactions at COMPASS (CERN)*,
PhD thesis: Ludwig-Maximilians-Universität München, 2012,
URL: https://edoc.ub.uni-muenchen.de/15867/1/Schlueter_Tobias.pdf
(cit. on pp. 36, 175).

[35] Particle Data Group, K. Nakamura, et al., *Review of Particle Physics*,
J. Phys. G **37** (2010) 075021, URL: http://pdg.lbl.gov (cit. on p. 37).

[36] F. M. Krinner, *Freed-Isobar Partial-Wave Analysis. Freiisobarische Partialwellenanalyse*,
Presented 04 Jul 2018, PhD thesis, 2018, URL: https://cds.cern.ch/record/2783415
(cit. on p. 40).

[37] M. Aghasyan et al., *Light isovector resonances in $\pi^- p \to \pi^-\pi^-\pi^+ p$ at* 190 GeV/c,
Phys. Rev. D **98** (9 2018) 092003,
URL: https://link.aps.org/doi/10.1103/PhysRevD.98.092003
(cit. on pp. 54, 96, 102, 176, 177, 179, 189).

[38] S. Uhl, *Photon Reconstruction and Partial-Wave Analysis of Three-Body Final States with Neutral Particles at COMPASS*, PhD thesis: Technische Universität München, 2016,
URL: https://mediatum.ub.tum.de/1303717 (cit. on p. 56).

[39] S. Uhl et al., *Diffractive Production of Final States decaying to $\pi^-\pi^0\pi^0$*,
Internal COMPASS Note (2013), URL: http://wwwcompass.cern.ch/compass/results/2013/october_hadron_3pi_neutral/releasenote.pdf (cit. on pp. 56, 57, 105).

[40] E. Omnès, *On the solution of certain singular integral equations of quantum field theory*,
Il Nuovo Cimento (1955-1965) **8** (2 1958) 316,
URL: https://doi.org/10.1007/BF02747746 (cit. on p. 60).

[41] H. Forkel, M. Beyer, and T. Frederico, *Linear Meson and Baryon Trajectories in ADS/QCD*,
International Journal of Modern Physics E **16** (2007) 2794,
URL: https://doi.org/10.1142%2Fs0218301307008422 (cit. on pp. 65, 226).

[42] H. Kim et al., *Tetraquark mixing framework for isoscalar resonances in light mesons*,
Phys. Rev. D **97** (9 2018) 094005,
URL: https://link.aps.org/doi/10.1103/PhysRevD.97.094005
(cit. on pp. 65, 68, 192, 227, 228, 294).

[43] A. V. Anisovich, V. V. Anisovich, and A. V. Sarantsev,
Systematics of $q\overline{q}$ states in the (n, M^2) and (J, M^2) planes, Phys. Rev. D **62** (5 2000) 051502,
URL: https://link.aps.org/doi/10.1103/PhysRevD.62.051502 (cit. on p. 65).

[44] T. Gutsche et al., *Test of the multiquark structure of $a_1(1420)$ in strong two-body decays*,
Phys. Rev. D **96** (11 2017) 114004,
URL: https://link.aps.org/doi/10.1103/PhysRevD.96.114004
(cit. on pp. 67–69, 190, 192).

[45] J.-L. Basdevant and E. L. Berger, *Peak Locations and Relative Phase of Different Decay Modes of the a_1 Axial Vector Resonance in Diffractive Production*,
Phys. Rev. Lett. **114** (19 2015) 192001,
URL: https://link.aps.org/doi/10.1103/PhysRevLett.114.192001
(cit. on pp. 69, 83, 102, 192).

[46] J.-L. Basdevant and E. L. Berger,
The twofold emergence of the a_1 axial vector meson in high energy hadronic production, 2015,
arXiv: 1501.04643 [hep-ph] (cit. on pp. 69, 102).

[47] D. Ryabchikov, *Modeling of non-resonant Deck-like contributions in diffractive-dissociation reactions at COMPASS*, Talk at the DPG - Spring meeting, Munich, Germany, 2016,
URL: https://wwwcompass-private.cern.ch/compass/publications/talks/t2016/locked/ryabchikov_dpg2016.pdf (cit. on pp. 69, 87, 188).

[48] L. Landau, *On analytic properties of vertex parts in quantum field theory*,
Nuclear Physics **13** (1959) 181, ISSN: 0029-5582,
URL: https://www.sciencedirect.com/science/article/pii/0029558259901543 (cit. on p. 69).

[49] M. Mikhasenko, B. Ketzer, and A. Sarantsev, *Nature of the $a_1(1420)$*,
Physical Review D **91** (2015), URL: https://doi.org/10.1103/PhysRevD.91.094015 (cit. on p. 69).

[50] G. D. Alexeev et al., *Triangle Singularity as the Origin of the $a_1(1420)$*,
Phys. Rev. Lett. **127** (8 2021) 082501,
URL: https://link.aps.org/doi/10.1103/PhysRevLett.127.082501 (cit. on pp. 69, 85, 104).

[51] M. Mikhasenko, B. Ketzer, and A. Sarantsev, *Nature of the $a_1(1420)$*,
Phys. Rev. D **91** (9 2015) 094015,
URL: https://link.aps.org/doi/10.1103/PhysRevD.91.094015 (cit. on p. 70).

[52] R. Cutkosky, *Singularities and discontinuities of Feynman amplitudes*,
J. Math. Phys. **1** (1960) 429 (cit. on p. 73).

[53] B. Grube, *Study of 2π and 3π resonances in diffractively produced $\pi^-\pi^-\pi^+$*,
habilitation: Technische Universität München, 2018, URL: https://wwwcompass.cern.ch/compass/publications/theses/2018_hab_grube.pdf (cit. on p. 87).

[54] K. L. Au, D. Morgan, and M. R. Pennington,
Meson dynamics beyond the quark model: Study of final-state interactions,
Phys. Rev. D **35** (5 1987) 1633,
URL: https://link.aps.org/doi/10.1103/PhysRevD.35.1633 (cit. on pp. 98, 220).

[55] S. Sehgal and M. Mikhasenko,
Analysing Bootstrap Errors for the PWA Analysis of the 3π-System,
Private communication, talk at internal COMPASS meeting, 08.10.2019,
URL: https://indico.cern.ch/event/849809/contributions/3571209/attachments/1911010/3177794/Bootstrap_PWA.pdf (cit. on pp. 99, 158).

[56] M. Mikhasenko et al., *Pole position of the $a_1(1260)$ from τ-decay*,
Phys. Rev. D **98** (9 2018) 096021,
URL: https://link.aps.org/doi/10.1103/PhysRevD.98.096021 (cit. on p. 103).

[57] F. Nerling, D. I. Ryabchikov, et al.,
First results on $\pi^-\pi^0\pi^0$ in comparison to $\pi^-\pi^+\pi^-$ final states (diffractively produced on proton),
Internal COMPASS Note (2011), URL: http://wwwcompass.cern.ch/compass/results/2011/june_hadron_pipi0pi0/releasenote_3pi_neutral.pdf (cit. on p. 105).

[58] S. Wallner,
Exploring the Strange-Meson spectrum with COMPASS in the reaction $K^- + p \to K^-\pi^-\pi^+ + p$,
PhD thesis: Technische Universität München, 2022 414,
URL: https://cds.cern.ch/record/2802793 (cit. on pp. 105, 129, 158, 166, 170, 171).

[59] J. Beckers, M. Wagner, and the Hadron Subgroup, *Event Selection of the Reactions $\pi^- + p \to K^0_S K^- + p$, $K^- + p \to K^0_S \pi^- + p$, and $K^- + p \to \Lambda\bar{p} + p$*,
Internal COMPASS Note (2022),
URL: https://wwwcompass.cern.ch/compass/results/2022/january_KsPi/KsPi_Event_Selection_COMPASS_release_note.pdf (cit. on pp. 105, 114, 118, 257).

[60] S. Havemann and H. Pekeler, *COMPASS-TN-2023-001*, Internal COMPASS Note (2023),
URL: https://twiki.cern.ch/twiki/bin/view/Compass/HadronAnalysis/RPD
(cit. on pp. 113, 119).

[61] M. Wagner, J. Beckers, and the hadron analysis Subgroup, *Event Selection of $K^0_S K^0_S pi^-$*,
Internal COMPASS Note (2023), URL: https://twiki.cern.ch/twiki/pub/Compass/HadronAnalysis/PimBeamKsKsPim/COMPASS-RN-2023-003_v3.pdf
(cit. on pp. 113, 151, 257).

[62] J. Bernhard, *Hadron Trigger*,
https://twiki.cern.ch/twiki/bin/view/Compass/Trigger/HadronTrigger, 2012-09-13
(cit. on p. 115).

[63] J. Bernhard, *Exclusive vector meson production in pp collisions at the COMPASS experiment*,
PhD thesis: Johannes Gutenberg Universität Mainz, 2014, URL: https://www.blogs.uni-mainz.de/fb08-kph-compass/files/2019/07/diss_bernhard.pdf
(cit. on pp. 115, 119).

[64] S. Wallner et al., *CEDAR PID using the Likelihood Approach for the Hadron-Beam*,
Internal COMPASS Note (2017),
URL: https://wwwcompass.cern.ch/compass/notes/2017-1/2017-1.pdf
(cit. on pp. 116, 117, 158).

[65] D. Spülbeck et al., *Event Selection of the Diffractive Reaction $\pi^- + p \to \pi^-\pi^+\pi^-\gamma\gamma + p$ Recorded in 2008 and 2009*, Internal COMPASS Note (2022),
URL: https://wwwcompass.cern.ch/compass/results/2022/february_evtsel_3Pi2G/Event_Selection_3Pi2G_06_04.pdf (cit. on pp. 118, 135).

[66] H. C. Pekeler, *Working title: Analysis of the $\eta\pi$ and $\eta'\pi$ final states at COMPASS*,
PhD thesis: Rheinische Friedrich-Wilhelms Universität Bonn, expected 2024
(cit. on pp. 118, 163).

[67] *Statistical Methods in Experimental Physics*,
second edition of the homonymous book by W.T. Eadie et al., World Scientific, 2006
(cit. on pp. 133, 246).

[68] K. A. Bicker, *Model Selection for and Partial-Wave Analysis of a Five-Pion Final State at the COMPASS Experiment at CERN*, PhD thesis: Technische Universität München, 2016, URL: https://mediatum.ub.tum.de/1297640 (cit. on p. 134).

[69] F. Haas, *Two-Dimensional Partial-Wave Analysis of Exclusive* 190 GeV $\pi^- p$ *Scattering into the* $\pi^-\pi^-\pi^+$ *Final State at COMPASS (CERN)*, PhD thesis: Technische Universität München, 2013, URL: https://mediatum.ub.tum.de/doc/1186008/1186008.pdf (cit. on p. 153).

[70] C. Dreisbach, *Study of elastic* $\pi^- p$ *scattering at COMPASS - Squared four-momentum transfer* $|t|$ *and Regge theory*, MA thesis: Technische Universität München, 2014, URL: https://wwwcompass.cern.ch/compass/publications/theses/2014_dpl_dreisbach.pdf (cit. on p. 155).

[71] T. Y. Chen et al., *Diffractive production of* $K^0_S K^0_S \pi^-$ *in* $\pi^- N$ *interactions at 200 GeV/c*, Phys. Rev. D **28** (9 1983) 2304, URL: https://link.aps.org/doi/10.1103/PhysRevD.28.2304 (cit. on pp. 155, 192).

[72] H. Pekeler, D. Spülbeck, and M. Wagner, *Wave Analysis Software Package (WASP)*, Bonn, Germany, 2023, URL: http://fsketzer.cb.uni-bonn.de/gitlab/pekeler/PiPiPiGG_PWA (cit. on pp. 163, 298).

[73] D. B. Spülbeck, *Working title: Analysis of the* $\pi^-\pi^-\pi^+\eta$ *final state at COMPASS*, PhD thesis: Rheinische Friedrich-Wilhelms Universität Bonn, expected 2025 (cit. on p. 163).

[74] M. Ablikim et al., *Resonances in* $J/\psi \to \phi\pi^+\pi^-$ *and* ϕK^+K^-, Physics Letters B **607** (2005) 243, ISSN: 0370-2693, URL: https://www.sciencedirect.com/science/article/pii/S0370269304017265 (cit. on p. 164).

[75] S. Descotes-Genon and B. Moussallam, *The* $K_0^*(800)$ *scalar resonance from Roy–Steiner representations of* πK *scattering*, The European Physical Journal C - Particles and Fields **48** (2 2006) 553 (cit. on pp. 166, 188).

[76] F. Kaspar, private communication, to be published in form of a PhD thesis, 2023 (cit. on pp. 167, 170).

[77] P. Haas et al., *Partial-Wave Decomposition of* $\omega\pi\pi$ *at COMPASS*, Internal COMPASS Note (2023), URL: https://twiki.cern.ch/twiki/pub/Compass/HadronAnalysis/Diffraction_omegapipi/COMPASS-RN-2023-001_v6.pdf (cit. on pp. 167, 170).

[78] Z. Dai, L.-H. Lim, and K. Ye, *Complex matrix inversion via real matrix inversions*, 2023, arXiv: 2208.01239 [math.NA] (cit. on p. 170).

[79] F. M. Kaspar et al., "Wave-selection techniques for partial-wave analysis in light-meson spectroscopy", *Hadron Spectroscopy and Structure* 471, eprint: https://www.worldscientific.com/doi/pdf/10.1142/9789811219313_0079, URL: https://www.worldscientific.com/doi/abs/10.1142/9789811219313_0079 (cit. on p. 171).

[80] S. Neubert,
First Amplitude Analysis of Resonant Structures in the 5-Pion Continuum at COMPASS,
PhD thesis: Technische Universität München, 2012,
URL: https://mediatum.ub.tum.de/doc/1108179/1108179.pdf (cit. on p. 176).

[81] J. Kuhn et al., *Exotic meson production in the $f_1(1285)\pi^-$ system observed in the reaction $\pi^- p \to \eta\pi^+\pi^-\pi^- p$ at 18 GeV/c*, Physics Letters B **595** (2004) 109, ISSN: 0370-2693,
URL: https://www.sciencedirect.com/science/article/pii/S0370269304007798
(cit. on pp. 182, 194).

[82] M. Mikhasenko, *Heavy Pentaquarks at LHCb*,
Talk at the Quarkonium Working Group meeting, 2021, URL: https://cds.cern.ch/record/2757285/files/pentaquarks.LHCb.mikhasenko.pdf
(cit. on p. 194).

[83] V. Metag, M. Nanova, J. Hartmann, et al., *Observation of a structure in the $M_{p\eta}$ invariant mass distribution near 1700 MeV/c^2 in the $\gamma\mathbf{p} \to \mathbf{p}\pi^0\eta$ reaction*,
The European Physical Journal A **57** (2021) 325,
URL: https://doi.org/10.1140/epja/s10050-021-00634-1 (cit. on p. 194).

[84] G. Scheluchin, T. Jude, S. Alef, et al., *Photoproduction of $K^+\Lambda(1405) \to K^+\pi^0\Sigma^0$ extending to forward angles and low momentum transfer*, Physics Letters B **833** (2022) 137375,
ISSN: 0370-2693,
URL: https://www.sciencedirect.com/science/article/pii/S0370269322005093
(cit. on p. 194).

[85] A. Martin and T. Spearman, *Elementary Particle Theory*,
North-Holland Publishing Company, 1970, ISBN: 9780720401578,
URL: https://books.google.de/books?id=sxAzAAAAMAAJ (cit. on p. 211).

[86] L. D. Landau and E. M. Lifshitz, *Quantum Mechanics, Non-relativistic Theory*, vol. 3,
Pergamon Press Ltd., 1977, ISBN: 0-08-020940-8 (cit. on p. 215).

[87] T. W. B. Kibble,
Kinematics of General Scattering Processes and the Mandelstam Representation,
Phys. Rev. **117** (4 1960) 1159,
URL: https://link.aps.org/doi/10.1103/PhysRev.117.1159 (cit. on p. 216).

[88] A. Davydychev and R. Delbourgo, *Explicitly symmetrical treatment of three-body phase space*,
Journal of Physics A: Mathematical and General **37** (2003) (cit. on p. 216).

[89] I. Kachaev, *Modified S-wave $\pi\pi$ scattering amplitude for multiparticle PWA*, (2023),
arXiv: 2305.11711 [hep-ph] (cit. on p. 220).

[90] M. Thomson, *Modern Particle Physics*, 5th ed., Cambridge University Press, 2016,
ISBN: 978-1-107-03426-6 (cit. on p. 225).

[91] P. D. Group, C. Amsler, et al., *Review of Particle Physics*, Physics Letters B (2008),
URL: https://pdg.lbl.gov/2009/reviews/rpp2009-rev-young-diagrams.pdf
(cit. on p. 226).

[92] N. Brambilla, S. Eidelman, B. K. Heltsley, et al.,
Heavy quarkonium: progress, puzzles, and opportunities,
The European Physical Journal C **71** (2 2011) 1434 (cit. on p. 228).

[93] T. Schlüter, *A code for kinematic fitting with constraints from intermediate particle masses*,
Internal COMPASS Note **10** (2007),
URL: https://wwwcompass.cern.ch/compass/notes/2007-10/2007-10.pdf
(cit. on pp. 246, 247).

[94] WikiSysop et al., *cppreference*, 2023, URL: https://en.cppreference.com/mwiki/index.php?title=cpp/language/types&oldid=155947 (cit. on p. 266).

APPENDIX A

Further Details on Kinematics

A.1 Kinematics of Two-Body Decays

For a decay of some resonance it usually makes sense to do the calculations in the CMS where the resonance is at rest, meaning $\vec{P} = 0$. If needed, one can perform a Lorentz boost afterwards to go back to the LAB. In the following, an asterisk $(*)$ will denote quantities that are calculated in the CMS of the resonance.

A.1.1 CMS Energy and Break-Up Momentum

If a resonance decays in two particles with momenta $\vec{p}_1^* = -\vec{p}_2^*$, one can derive expressions for their respective energies and momenta in the following way:

$$m_2^2 = p_2^2 = (P - p_1)^2 = s + m_1^2 - 2\sqrt{s}E_1^*,$$

which we can easily solve for the energy

$$E_1^* = \frac{s - m_2^2 + m_1^2}{2\sqrt{s}}, \qquad E_2^* = \frac{s - m_1^2 + m_2^2}{2\sqrt{s}}, \tag{A.1}$$

where the formula for the second energy can be obtained by exchanging all indices $1 \leftrightarrow 2$ in the expression. The momentum can be obtained using $\left|\vec{p}_i^*\right| = \sqrt{E_i^{*2} - m_i^2}$ and can be shortened to

$$q \equiv \left|\vec{p}_i^*\right| = \frac{\lambda^{\frac{1}{2}}(s, m_1^2, m_2^2)}{2\sqrt{s}}, \tag{A.2}$$

by using the Källén function

$$\begin{aligned} \lambda(x, y, z) &= x^2 + y^2 + z^2 - 2xy - 2xz - 2yz & \text{(A.3)} \\ &= \left(x - (\sqrt{y} + \sqrt{z})^2\right)\left(x - (\sqrt{y} - \sqrt{z})^2\right) & \text{(A.4)} \\ &= (x + y - z)^2 - 4xy & \text{(A.5)} \end{aligned}$$

Note that this expression has to be symmetric in the indices 1 and 2, since this so-called break-up momentum has to be equal for both particles. This symmetric nature of the Källén function under exchange of any two arguments can be best seen in its first form in equation (A.3), while from its second form in equation (A.4) one can immediately identify the regions where it is positive, where it is negative, and the two points where it vanishes. For the break-up momentum in equation (A.2) these two points are called threshold $s_{\text{th}} := (m_1 + m_2)^2$ and pseudo threshold $s_{\text{pth}} := (m_1 - m_2)^2$. Its third form (A.5) is useful for numeric calculations, since it involves the least amount of arithmetic operations.

A.1.2 Two-Body Phase Space

The two-body phase space can be calculated in the following way. We start at the definition

$$\Phi_2 = (2\pi)^4 \int \frac{\mathrm{d}^3\vec{p}_1}{(2\pi)^3 2E_1} \frac{\mathrm{d}^3\vec{p}_2}{(2\pi)^3 2E_2} \delta^{(4)}(P - p_1 - p_2),$$

which is a Lorentz-invariant quantity. Therefore, we can perform the calculations in the CMS. In the first step, we use the three-dimensional $\delta^{(3)}(\vec{p}_1^* + \vec{p}_2^*)$ to get rid of one of the integrals:

$$\Phi_2 = \frac{1}{16\pi^2} \int \frac{\mathrm{d}^3\vec{p}_1^*}{E_1^* \cdot E_2^*(\vec{p}_1^*)} \delta(M - E_1^* - E_2^*(\vec{p}_1^*)).$$

Be aware that we have to replace $\vec{p}_2^*$ by $-\vec{p}_1^*$ in the calculation of the energy resulting in $E_2^*(\vec{p}_1^*) = \sqrt{m_2^2 + \left|\vec{p}_1^*\right|^2}$. We can go over to spherical coordinates $\mathrm{d}^3\vec{p}_1^* = p^2 \mathrm{d}p\, \mathrm{d}\cos\theta\, \mathrm{d}\phi$ and since everything only depends on the magnitude of the momenta, we can perform the angular integral resulting in a factor of 4π:

$$\Phi_2 = \frac{1}{4\pi} \int \frac{p^2 \mathrm{d}p}{E_1^* \cdot E_2^*(p)} \delta(M - E_1^* - E_2^*(p)).$$

From $2E\frac{\mathrm{d}E}{\mathrm{d}p} = \frac{\mathrm{d}}{\mathrm{d}p}E^2 = \frac{\mathrm{d}}{\mathrm{d}p}(p^2 + m^2) = 2p$, we deduce $\frac{\mathrm{d}p}{E} = \frac{\mathrm{d}E}{p}$ and replace $p = \sqrt{E_1^{*2} - m_1^2}$, which gives

$$\Phi_2 = \frac{1}{4\pi} \int \frac{p \mathrm{d}E_1^*}{E_2^*(E_1^*)} \delta\left(M - E_1^* - \sqrt{m_2^2 + E_1^{*2} - m_1^2}\right).$$

Since inside the δ-distribution we have a slightly more complicated function of E_1^*, we have to use the following property[1] of the δ-distribution

$$\delta(f(x)) = \sum_{x_j} \frac{\delta(x - x_j)}{\left|f'(x_j)\right|}, \quad x_j\text{: first order zeroes of } f. \tag{A.6}$$

[1] We will not provide a detailed proof of this property, but here is the general idea: We have to integrate a function with full support together with this expression – this is how distributions work. Then, we split this integral into small intervals $x_j \pm \varepsilon$ around the zeroes of f – which explains the sum – since in between these intervals, the integral is zero due to the δ. Finally, we perform a substitution $u = f(x), x = f^{-1}(u), \mathrm{d}x = \mathrm{d}u/f'(x)$, which explains the fraction. The absolute value in the denominator appears due to the change of the direction of integration after the substitution in case of $f'(x) < 0$, because for this, we have $f(x + \varepsilon) < f(x - \varepsilon)$. All of this works, since x_j are first order zeroes and, therefore, $f' \not\equiv 0$ in close proximity of x_j, resulting in a monotonous f that has a unique inverse f^{-1}.

The zero of the expression inside the δ-distribution is exactly the CMS energy as given in equation (A.1), and the derivative corresponds to $\left|-1 - \frac{E_1^*}{E_2^*}\right| = \frac{M}{E_2^*(E_1^*)}$. Inserting this leads to

$$\Phi_2 = \frac{1}{4\pi} \int \frac{p \, \mathrm{d}E}{M} \delta(E - E_1^*),$$

and the application of the final δ-distribution makes out of p the break-up momentum from equation (A.2):

$$\Phi_2(M^2, m_1^2, m_2^2) = \frac{1}{8\pi} \frac{2q}{M} = \frac{1}{8\pi} \frac{\lambda^{\frac{1}{2}}(M^2, m_1^2, m_2^2)}{M^2}, \tag{A.7}$$

or we can recover the angles $\mathrm{d}\Omega = \mathrm{d}\cos\theta \, \mathrm{d}\phi$ and write it in its differential form

$$\mathrm{d}\Phi_2(M^2, m_1^2, m_2^2) = \frac{1}{8\pi} \frac{2q}{M} \frac{\mathrm{d}\Omega}{4\pi}. \tag{A.8}$$

A.1.3 Phase Space Recursion Relation

We want to prove the phase space recursion formula as it is given in equation (3.50), but we do the slightly more general case of splitting Φ_{N+1} into Φ_N and Φ_2, allowing us to use the relation also for values other than $N = 3$:

$$\Phi_{N+1}(P; p_1, ..., p_N, p_r) = \int \frac{\mathrm{d}m_X^2}{2\pi} d\Phi_N(p_X; p_1, ..., p_N) \mathrm{d}\Phi_2(P; p_X, p_r). \tag{A.9}$$

For this, we start on the right-hand side and simply insert the definition of the N-body and 2-body phase spaces according to equation (3.10). We can immediately see that already everything of the $(N+1)$-body phase space is present:

$$\begin{aligned}
&\int \frac{\mathrm{d}m_X^2}{2\pi} d\Phi_N(p_X; p_1, ..., p_N) \mathrm{d}\Phi_2(P; p_X, p_r) \\
&= \underbrace{(2\pi)^4 \delta^{(4)}\left[p_X - \sum_{k=1}^{N} p_k\right] \prod_{k=1}^{N} \frac{\mathrm{d}^3\vec{p}_k}{(2\pi)^3 2E_k} \cdot \frac{\mathrm{d}^3\vec{p}_r}{(2\pi)^3 2E_r}}_{=\Phi_{N+1}(P; p_1, ..., p_N, p_r)} \int \frac{\mathrm{d}m_X^2}{2\pi} \frac{\mathrm{d}^3\vec{p}_X}{(2\pi)^3 2E_X} (2\pi)^4 \delta^{(4)}\left[P - p_X - p_r\right] \\
&= \Phi_{N+1}(P; p_1, ..., p_N, p_r) \int \frac{\mathrm{d}m_X^2}{2\sqrt{m_X^2 + \left|\vec{P} - \vec{p}_r\right|^2}} \delta\left[E - \sqrt{m_X^2 + \left|\vec{P} - \vec{p}_r\right|^2} - E_r\right] \\
&= \Phi_{N+1}(P; p_1, ..., p_N, p_r) \underbrace{\int \mathrm{d}m_X^2 \, \delta\left[m_X^2 - m_{X,0}^2\right]}_{=1}.
\end{aligned}$$

In the first step, we replace p_X by $P - p_r$ in the first $\delta^{(4)}$-distribution which is allowed because of the second $\delta^{(4)}$-distribution. In the second step we use the $\delta^{(3)}$ component of the remaining

distribution to remove the $\mathrm{d}^3\vec{p}_X$ integration, replacing $\vec{p}_X$ by $\vec{P} - \vec{p}_r$ inside $E_X = \sqrt{m_X^2 + \left|\vec{p}_X\right|^2}$. Then, we use (A.6), where the inner derivative exactly cancels the denominator and the zero is given by $m_{X,0}^2 = (E - E_r)^2 - \left|\vec{P} - \vec{p}_r\right|^2$. Finally, we use the new δ to get rid of the final integration, concluding the proof.

A.1.4 Quasi-Two-Body Phase Space

With the just defined recursion formula, one can express any phase space as a factor of two-body phase spaces always integrating over the squared-invariant mass of the respective two-body system that was split off in each step. Executed for the three-body phase space in the isobar model, we can define the quasi-two-body phase space as a simplification of this. Let us start with the formula for the differential decay width of a decay $X \to \xi + \zeta_1$ parametrized by the matrix element $\mathcal{M}_X$ and $\xi \to \zeta_2 + \zeta_3$ with the line shape $\mathcal{M}_\xi$. Factorizing the full matrix element in equation (3.31) accordingly, we can rewrite it as

$$\mathrm{d}\Gamma(s) = \frac{1}{m_X} |\mathcal{M}|^2 \,\mathrm{d}\Phi_3(s) = \frac{1}{m_X} \left|\mathcal{M}_X\right|^2 \frac{\mathrm{d}\sigma_\xi}{2\pi} \left|\mathcal{M}_\xi\right|^2 \mathrm{d}\Phi_2(s, \sigma_\xi, m_1^2)\mathrm{d}\Phi_2(\sigma_\xi, m_2^2, m_3^2).$$

Integrating everything out gives us

$$\begin{aligned} \Gamma(s) &= \frac{1}{M} \left|\mathcal{M}_X\right|^2 \tilde{\Phi}_2(s), \text{ with} \\ \tilde{\Phi}_2(s) &:= \int_{(m_2+m_3)^2}^{(\sqrt{s}-m_1)^2} \frac{\mathrm{d}\sigma_\xi}{2\pi} \left|\mathcal{M}_\xi\right|^2 \Phi_2(s, \sigma_\xi, m_1^2)\Phi_2(\sigma_\xi, m_2^2, m_3^2), \end{aligned} \tag{A.10}$$

which has the same structure as the formula we started from, equation (3.31). For a narrow isobar with $\Gamma_\xi \approx 0$, its line shape becomes approximately a δ-distribution, $\left|\mathcal{M}_\xi\right|^2 \rightsquigarrow \delta(\sigma_\xi - m_\xi^2)$ and, therefore, we would obtain the simple two-body phase space for the decay $X \to \xi + \zeta_1$, at least modulo some normalization. The proper normalization would be

$$N_\xi(s) = \int_{(m_2+m_3)^2}^{(\sqrt{s}-m_1)^2} \frac{\mathrm{d}\sigma_\xi}{2\pi} \left|\mathcal{M}_\xi\right|^2 \Phi_2(\sigma_\xi, m_2^2, m_3^2).$$

It depends on s and would have to be done for every value that one evaluates the quasi-two-body phase space at, therefore, it is highly unpractical. Instead, a simpler normalization with the integral over the complete isobar line shape up to infinity can be performed

$$N_\xi = \int_{(m_2+m_3)^2}^{\infty} \frac{\mathrm{d}\sigma_\xi}{2\pi} \left|\mathcal{M}_\xi\right|^2.$$

In case of Bose symmetrization one would have to add the corresponding isobar line shapes on amplitude level, evaluated on the respective two-body invariant masses. However, the integral has to be performed only over one of the invariant masses and the angles in the helicity frame of the corresponding isobar system. Here, the angles calculated in appendix A.4, equations (A.39) and (A.40), can help to provide the necessary dependencies.

Another easier way to calculate the quasi-two-body phase space is by using the MC-integration

method, where we draw MC events distributed flat in the three-body phase space and evaluate the expression for the quasi-two-body phase space on all of them, always boosting the event in the respective rest frames as needed. This corresponds to the integral matrices that are needed for the acceptance correction during the PWD, see section 3.4.5.

A.2 Blatt-Weisskopf Factors

Here is the used parametrization of the Blatt-Weisskopf barrier factors as they appear e.g. in equation (3.34):

$$h_0^2(z) = 1, \tag{A.11}$$

$$h_1^2(z) = \frac{2z}{z+1}, \tag{A.12}$$

$$h_2^2(z) = \frac{13z^2}{z^2+3z+9}, \tag{A.13}$$

$$h_3^2(z) = \frac{277z^3}{z^3+6z^2+45z+225}, \tag{A.14}$$

$$h_4^2(z) = \frac{12746z^4}{z^4+10z^3+135z^2+1575z+11025}, \tag{A.15}$$

$$h_5^2(z) = \frac{998881z^5}{z^5+15z^4+315z^3+6300z^2+99225z+893025}, \tag{A.16}$$

$$h_6^2(z) = \frac{118394977z^6}{z^6+21z^5+630z^4+18900z^3+496125z^2+9823275z+108056025}, \tag{A.17}$$

with $z = (qR)^2$ being the squared product of the break-up momentum of equation (A.2) with some range parameter $R = 5\,\mathrm{GeV}^{-1} \approxeq 1\,\mathrm{fm}$, which is chosen to be of the order of the range of the strong interaction. Note that in the main text, usually only $h_L^2(q)$ is written, however, this is done to show the dependence on the break-up momentum and to indicate which value to insert in case there is more than one possible decay involved. In the end, $z = (qR)^2$ has to be inserted always.

A.3 Wigner-D Functions

A.3.1 Definitions and Basic Relations

We take the definitions and relations from [85]. For direct reference, we detail the relevant information in the following.

First of all, we can relate the Wigner-D functions to the small Wigner-d functions as follows:

$$D^j_{mn}(\alpha,\beta,\gamma) = \mathrm{e}^{-\mathrm{i}m\alpha} d^j_{mn}(\beta) \mathrm{e}^{-\mathrm{i}n\gamma}. \tag{A.18}$$

They fulfill the following orthogonality relation

$$\int \frac{\mathrm{d}\alpha}{2\pi} \frac{\mathrm{d}\cos\beta}{2} \frac{\mathrm{d}\gamma}{2\pi} D^{j*}_{mn}(\alpha,\beta,\gamma) D^{j'}_{m'n'}(\alpha,\beta,\gamma) = \frac{\delta_{mm'}\delta_{jj'}\delta_{nn'}}{2j+1}. \tag{A.19}$$

Usually, we deal with angles $\Omega = (\phi, \theta)$ where we introduce a short-hand notation

$$D^{j}_{mn}(\Omega) := D^{j}_{mn}(\phi,\theta,0), \qquad \int \frac{\mathrm{d}\Omega}{4\pi} D^{j*}_{mn}(\Omega) D^{j'}_{m'n}(\Omega) = \frac{\delta_{jj'}\delta_{mm'}}{2j+1}. \tag{A.20}$$

Note that the third index (n) has to be equal for both of the Wigner-D function for the orthogonality relation to hold, since the third angle is zero.

Using the definition in equation (A.18), we see that

$$D^{J}_{M\lambda}(\Omega) D^{S}_{\lambda 0}(\Omega') = D^{J}_{M\lambda}(\phi,\theta,\phi') d^{S}_{\lambda 0}(\theta'). \tag{A.21}$$

During the partial-wave-projection procedure as introduced in section 3.6 we have to integrate the product of two angular functions of different isobar channels. However, the angles are not the same, which is why we cannot use the orthogonality relation, yet. Equation (C.31) of [33] transforms the Wigner-D function such that one can relate the angles (Ω_k, Ω_{ij}) of isobar channel (ij) to the angles (Ω_i, Ω_{jk}) of isobar channel (jk) (using cyclic indices):

$$D^{J}_{M\lambda}(\Omega_k) D^{S}_{\lambda 0}(\Omega_{ij}) = \sum_{\nu} D^{J}_{M\nu}(\phi_i,\theta_i,\phi_{jk}) d^{J}_{\nu\lambda}(\theta^{*}_{k(i)}) d^{S}_{\lambda 0}(\theta_{ij}), \tag{A.22}$$

where the angle $\theta^{*}_{j(i)}$ is defined as the angle between the momentum vectors $\vec{p}_j$ and $\vec{p}_i$ in the GJ frame.

A.3.2 Relations for Angular Functions Z_w

The angular functions for a three-body decay are given by

$$Z_w(\Omega,\Omega') := \sqrt{n_L n_S} \sum_{\lambda} \langle L0, S\lambda | J\lambda \rangle \, D^{J*}_{M\lambda}(\Omega) \, D^{S*}_{\lambda 0}(\Omega'), \qquad \text{with } w = (JMLS) \tag{A.23}$$

and fulfill the following orthogonality relation:

$$\int \frac{\mathrm{d}\Omega}{4\pi} \frac{\mathrm{d}\Omega'}{4\pi} Z_w(\Omega,\Omega') Z_{w'}(\Omega,\Omega') = \delta_{ww'} = \delta_{JJ'}\delta_{MM'}\delta_{LL'}\delta_{SS'}. \tag{A.24}$$

This can be seen by employing orthogonality of equation (A.20) on the second Wigner-D function with the $\mathrm{d}\Omega'$ integral, which already gives $\delta_{SS'}$ and removes the sum over λ' with the $\delta_{\lambda\lambda'}$, so only a single sum over λ remains. The n_S factor also cancels. Now, the second lower index of the first Wigner-D functions is equal and we can also employ orthogonality with the $\mathrm{d}\Omega$ integral leading to $\delta_{JJ'}$ and $\delta_{MM'}$ with an additional n_J^{-1}. The still missing $\delta_{LL'}$ is obtained via the following orthogonality relation for the Clebsch-Gordan coefficients (derived in section A.3.4):

$$\sqrt{n_L n_{L'}} \sum_{\lambda} \langle L0, S\lambda | J\lambda \rangle \, \langle L'0, S\lambda | J\lambda \rangle = n_J \delta_{LL'}, \tag{A.25}$$

which eats the remaining prefactor involving L and L' and cancels the previously obtained n_J^{-1} factor as well, leaving us only with the Kronecker-δ product as stated in equation (A.24).

Next, we want to simplify the projection integral $\mathrm{d}Z_w^{(i)} Z_{w'}^{(k)}$ defined via equation (3.93). For this, we use equation (A.21) inside of $Z_w^{(i)*}$ and equation (A.22) inside of $Z_{w'}^{(k)}$:

$$\begin{aligned}
\mathrm{d}Z_w^{(i)} Z_{w'}^{(k)} &= \frac{\mathrm{d}\Omega_i}{4\pi}\frac{\mathrm{d}\Omega_{jk}}{4\pi} \sum_{\lambda,\lambda',\nu} B_{ww'}^{\lambda\lambda'} \underbrace{D_{M\lambda}^{J*}(\phi_i,\theta_i,\phi_{jk}) D_{M'\nu}^{J'}(\phi_i,\theta_i,\phi_{jk})}_{\int \mathrm{d}\Omega_i \mathrm{d}\phi_{jk} \;\rightsquigarrow\; n_J^{-1}\delta_{JJ'}\delta_{MM'}\delta_{\lambda\nu}} d_{\lambda 0}^{S*}(\theta_{jk}) d_{\nu\lambda'}^{J'}(\theta_{k(i)}^*) d_{\lambda' 0}^{S'}(\theta_{ij}) \\
&\qquad \text{with} \quad B_{ww'}^{\lambda\lambda'} = \sqrt{n_L n_{L'} n_S n_{S'}}\, \langle L0, S\lambda | J\lambda\rangle \, \langle L'0, S'\lambda' | J'\lambda'\rangle \\
&= \delta_{JJ'}\delta_{MM'} \frac{\mathrm{d}\cos\theta_{jk}}{2} \sum_{\lambda\lambda'} B_{J,LS,L'S'}^{\lambda\lambda'} d_{\lambda 0}^{S}(\theta_{jk}) d_{\lambda\lambda'}^{J}(\theta_{k(i)}^*) d_{\lambda' 0}^{S'}(\theta_{ij}) \qquad \text{(A.26)} \\
&\qquad \text{with} \quad B_{J,LS,L'S'}^{\lambda\lambda'} = \frac{\sqrt{n_L n_{L'} n_S n_{S'}}}{n_J} \, \langle L0, S\lambda | J\lambda\rangle \, \langle L'0, S'\lambda' | J\lambda'\rangle \,,
\end{aligned}$$

where we used the orthogonality of the full Wigner-D functions from equation (A.19) to perform three of the four integrations. We also removed the complex conjugation of the little Wigner-d function, since they are all real-valued functions. The two Kronecker-δs show that the partial-wave projection will only affect single J and M, meaning that a resonance can only be affected by its own cross channels and not by other resonances as expected for a rescattering. For the remaining integral one has to express all angles in terms of squared two-body invariant masses σ_i, which can be found in appendix A.4.

A.3.3 Wigner-D Functions in Reflectivity Basis

As derived in [20], the Wigner-D functions expressed in the reflectivity basis read as follows:

$$^{\epsilon}D_{MM'}^{J}(\Omega) = N_M \left(D_{MM'}^{J}(\Omega) - \epsilon P (-1)^{J-M} D_{(-M)M'}^{J}(\Omega) \right), \text{ with } N_M := \begin{cases} \frac{1}{\sqrt{2}}, & M > 0 \\ \frac{1}{2}, & M = 0 \\ 0, & M < 0 \end{cases}. \qquad \text{(A.27)}$$

From this equation we can see that the case $M = 0$ will only be non-zero if $\epsilon P(-1)^J = -1$. For positive reflectivity this will be the case if $P = (-1)^{J+1}$, which means that resonances with QNs $J^{PC} \in \{\text{odd}^{-+}, \text{even}^{++}\}$ will not have partial waves with $M = 0$ reducing their likelihood compared to the other J^{PC} combinations.

The angular functions in this reflectivity basis as discussed in section 3.4.4 and defined in equation (3.60) also fulfill the orthogonality relation (A.24) with an additional $\delta_{\epsilon\epsilon'}$. To see this, we multiply out the term from equation (A.27) in the product of angular functions – assuming equal arguments (Ω, Ω') and omitting them – to obtain

$$\begin{aligned}
Z_{JMLS}^{\epsilon *} Z_{J'M'L'S'}^{\epsilon'} &= N_M N_{M'} \Big(Z_{JMLS}^* Z_{J'M'L'S'} + \epsilon\epsilon' P P' Z_{J(-M)LS}^* Z_{J'(-M')L'S'} \\
&\quad - \epsilon P (-1)^{J-M} Z_{J(-M)LS}^* Z_{J'M'L'S'} - \epsilon' P' (-1)^{J'-M'} Z_{JMLS}^* Z_{J'(-M')L'S'} \Big).
\end{aligned}$$

Performing the integral over all four angles, we can use the orthogonality relation for "normal" angular functions (A.24) on each of the terms separately. This yields the common factor $\delta_{JJ'}\delta_{LL'}\delta_{SS'}$. Due to the last two Kronecker-δs, we know that the parities will be equal due to $P = (-1)^{L+S+1}$ simplifying things even further to

$$\int (...) Z^{\epsilon *}_{JMLS} Z^{\epsilon'}_{J'M'L'S'} = N_M N_{M'} \delta_{JJ'}\delta_{LL'}\delta_{SS'} \Big(\delta_{MM'}(1 + \epsilon\epsilon') - P(-1)^{J+M} \delta_{(-M)M'} \underbrace{(\epsilon + \epsilon')}_{\epsilon(1+\epsilon\epsilon')} \Big), \tag{A.28}$$

where we inserted a $\epsilon^2 = 1$ in the last bracket to factor out one ϵ. We know that

$$(1 + \epsilon\epsilon') = 2\delta_{\epsilon\epsilon'}, \qquad \text{since } \epsilon = \pm 1. \tag{A.29}$$

To finish, we have to study the cases $M = 0$ and $M \neq 0$ separately.

Starting with $M \neq 0$, we see that $\delta_{(-M)M'} = 1$ if – and only if – one of them is negative which automatically means that either N_M or $N_{M'}$ will be zero. Thus, the second term vanishes and the $N_M N_{M'} = \frac{1}{2}$ prefactor cancels with the 2 from equation (A.29), giving us the expected result

$$\int \frac{\mathrm{d}\Omega}{4\pi} \frac{\mathrm{d}\Omega'}{4\pi} Z^{\epsilon *}_{JMLS}(\Omega, \Omega') Z^{\epsilon'}_{J'M'L'S'}(\Omega, \Omega') = \delta_{ww'}\delta_{\epsilon\epsilon'}. \tag{A.30}$$

On the other hand, for $M = 0$ we know that $\epsilon P(-1)^J = -1$ since otherwise equation (A.27) would simply be zero and the orthogonality is automatically fulfilled. Inserting this into equation (A.28) gives us equation (A.29) twice and this factor of 4 will be cancelled by the $N_0^2 = \frac{1}{4}$. This shows that equation (A.30) is also valid for $M = 0$.

Special Case for Scalar Isobars

For scalar isobars ($S = 0$) we can simplify the angular functions in reflectivity basis of equation (3.60) in the following way:

$$\begin{aligned} Z^{\epsilon}_{w,S=0}(\Omega, \Omega') &= \sqrt{n_L} \sum_{\lambda} \underbrace{\langle L0, 0\lambda | J\lambda \rangle}_{\delta_{\lambda 0}\delta_{JL}} {}^{\epsilon}D^{J*}_{M\lambda}(\Omega) D^{0*}_{\lambda 0}(\Omega') \\ &= \delta_{JL} \sqrt{n_J}\, {}^{\epsilon}D^{J*}_{M0}(\Omega) \underbrace{d^{0*}_{00}(\theta')}_{\equiv 1}. \end{aligned}$$

Inserting the definition of the Wigner-D function of equation (A.18), we see

$$\begin{aligned}
{}^{\epsilon}D^{J}_{M0}(\Omega) &= N_M \left(\mathrm{e}^{-\mathrm{i}M\phi} d^{J}_{M0}(\theta) - \epsilon P (-1)^{J-M} \mathrm{e}^{\mathrm{i}M\phi} \underbrace{d^{J}_{(-M)0}(\theta)}_{(-1)^{M} d^{J}_{M0}(\theta)} \right) \\
&= N_M \left(\mathrm{e}^{-\mathrm{i}M\phi} - \epsilon P (-1)^{J} \mathrm{e}^{\mathrm{i}M\phi} \right) d^{J}_{M0}(\theta) \\
Z^{\epsilon}_{w,S=0}(\Omega, \Omega') &= \delta_{JL} \sqrt{n_J} N_M \left(\mathrm{e}^{\mathrm{i}M\phi} - \epsilon P (-1)^{J} \mathrm{e}^{-\mathrm{i}M\phi} \right) d^{J}_{M0}(\theta).
\end{aligned}$$

For a three-body decay into pseudoscalars, the parity of the resonance will be $P = (-1)^3 (-1)^{L+S} = (-1)^{J+1}$ for scalar isobars. Inserting this yields

$$\begin{aligned}
Z^{\epsilon}_{w,S=0}(\Omega, \Omega') &= \delta_{JL} \sqrt{n_J} N_M \left(\mathrm{e}^{\mathrm{i}M\phi} + \epsilon \mathrm{e}^{-\mathrm{i}M\phi} \right) d^{J}_{M0}(\theta) \\
&= 2\delta_{JL} \sqrt{n_J} N_M d^{J}_{M0}(\theta) \cdot \begin{cases} \cos(M\phi), & \epsilon = +1 \\ \mathrm{i}\,\sin(M\phi), & \epsilon = -1. \end{cases}
\end{aligned} \tag{A.31}$$

This means that the angular functions will be purely real for positive reflectivity and purely imaginary for negative reflectivity.

A.3.4 Derivation of Clebsch-Gordan Orthogonality

We use the $3j$-symbols and their relations as they are given by [86] in order to prove the orthogonality relation in equation (A.25). For this, we make it a bit more complicated by introducing another sum first:

$$\sqrt{n_L n_{L'}} \sum_{\lambda} \langle L0, S\lambda | J\lambda \rangle \langle L'0, S\lambda | J\lambda \rangle = \sqrt{n_L n_{L'}} \sum_{\lambda,\mu} \langle L0, S\lambda | J(-\mu) \rangle \langle L'0, S\lambda | J(-\mu) \rangle \delta_{\lambda(-\mu)}. \tag{A.32}$$

Here we see that the Kronecker-δ at the end can be omitted since, anyways, the Clebsch-Gordan coefficient will be zero if $\lambda \neq -\mu$. Next, we transform the Clebsch-Gordan coefficients into the $3j$-symbols using their definition in equation (106.10) of [86] and their behaviour under exchange of columns in equation (106.5) which gives an additional $(-1)^{L+S+J}$:

$$\langle L0, S\lambda | J(-\mu) \rangle = (-1)^{L-S-\mu} \sqrt{n_J} \begin{pmatrix} L & S & J \\ 0 & \lambda & \mu \end{pmatrix} = (-1)^{J-\mu} \sqrt{n_J} \begin{pmatrix} J & S & L \\ \mu & \lambda & 0 \end{pmatrix}. \tag{A.33}$$

Doing this for both coefficients in equation (A.32) gives us

$$\text{(A.32)} = n_J \sqrt{n_L n_{L'}} \sum_{\lambda,\mu} \begin{pmatrix} J & S & L \\ \mu & \lambda & 0 \end{pmatrix} \begin{pmatrix} J & S & L' \\ \mu & \lambda & 0 \end{pmatrix} = n_J \sqrt{n_L n_{L'}} \frac{1}{n_L} \delta_{LL'}, \tag{A.34}$$

where we used the orthogonality relation of the $3j$-symbols from equation (106.12) of [86] in the last step. The n_L^{-1} together with the Kronecker-δ cancels the $\sqrt{n_L n_{L'}}$, giving us the expected $n_J \delta_{LL'}$ as a final result.

A.4 Calculation of the Dalitz-Angles

Before we start, let us define the Kibble function

$$\begin{aligned}\phi(s;\sigma_1,\sigma_3) &= \sigma_1\sigma_2\sigma_3 - \sigma_1(m_2^2m_3^2+sm_1^2) - \sigma_2(m_3^2m_1^2+sm_2^2) - \sigma_3(m_1^2m_2^2+sm_3^2) \\ &\quad +2(m_1^2m_2^2m_3^2+sm_1^2m_2^2+sm_2^2m_3^2+sm_3^2m_1^2), \end{aligned} \tag{A.35}$$

$$\text{with } \sigma_2 = s + \sum_i m_i^2 - \sigma_1 - \sigma_3. \tag{A.36}$$

The border of the Dalitz plot is given by the points that fulfill $\phi \equiv 0$. We are inside the Dalitz region, where $\phi > 0$. This function was originally introduced in [87], but a form more similar to the one given here, is derived in [88][2].

Calculation of $\cos\theta^*_{3(1)}$

The angle $\cos\theta^*_{3(1)}$ is defined in the CMS of a three-body resonance X with mass $\sqrt{s}$ as the angle of particle 3 with respect to particle 1, see Figure A.1(a). Thus, $s = p_X^2 = (p_1^* + p_2^* + p_3^*)^2$ and $\vec{p}_1^* + \vec{p}_2^* + \vec{p}_3^* = 0$. We can interpret this as a two-body decay with particle i with mass m_i and momentum $\vec{p}_i$, and particle (jk) with squared mass $\sigma_i = (p_j + p_k)^2$ and momentum $-\vec{p}_i = (\vec{p}_j + \vec{p}_k)$ as daughters[3]. Therefore, we can employ equations (A.1) and (A.2) and simply replace one of the masses by the invariant mass of the respective two-body subsystem:

$$E_i^* = \frac{s-\sigma_i+m_i^2}{2\sqrt{s}}, \quad \text{and} \quad \left|\vec{p}_i^*\right| = \frac{\lambda^{\frac{1}{2}}(s,\sigma_i,m_i^2)}{2\sqrt{s}} =: \frac{\sqrt{\lambda_{si}}}{2\sqrt{s}}.$$

Using

$$\sigma_2 = (p_1+p_3)^2 = m_1^2 + m_3^2 + 2E_1^*E_3^* - 2\left|\vec{p}_1^*\right|\left|\vec{p}_3^*\right|\cos\theta^*_{3(1)},$$

we can solve for the angle and, after inserting all energies and momenta, obtain

$$\cos\theta^*_{3(1)} = \frac{2s(m_1^2+m_3^2-\sigma_2) + (s+m_1^2-\sigma_1)(s+m_3^2-\sigma_3)}{\sqrt{\lambda_{s1}\lambda_{s3}}}. \tag{A.37}$$

In the same way by starting with σ_3 we can obtain $\cos\theta^*_{2(1)}$, effectively replacing $3 \leftrightarrow 2$ everywhere. Since $\sin\theta^*_{3(1)} \geq 0$ because $\theta^*_{3(1)} \in [0,\pi]$, we can calculate it via:

$$\sin\theta^*_{3(1)} = \sqrt{1-\cos^2\theta^*_{3(1)}} = \frac{2\sqrt{s}\sqrt{\phi}}{\sqrt{\lambda_{s1}\lambda_{s3}}}, \tag{A.38}$$

[2] There, it is given in equation (2.15). To obtain the version in equation (A.35) of this thesis, one has to replace $s \to \sigma_3$, $t \to \sigma_1$, $u \to \sigma_2$ and $p^2 \to s$.

[3] We use distinct, cyclic indices $(ijk) \in \{(123),(231),(312)\}$ and all following equations are cyclic in these indices as well, e.g. by performing the replacement $1 \to 2 \to 3 \to 1$ we obtain a valid formula. However, be aware that this will also change the considered CMS accordingly, transforming the (12)-subsystem into a (23)-subsystem in the given example. Only the rest frame of the resonance (123) stays invariant under such a replacement.

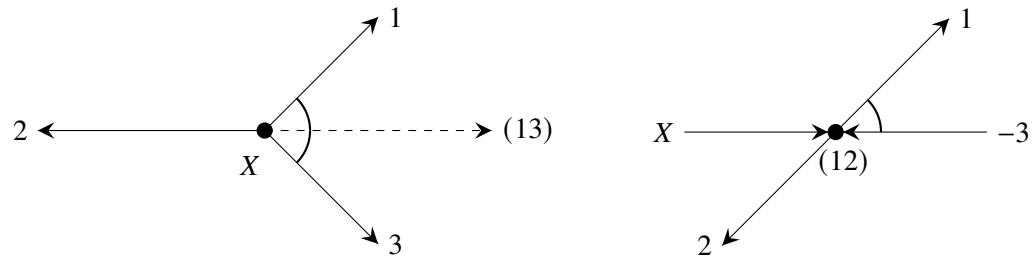

(a) $\theta^*_{3(1)}$ in CMS of X (b) θ_{12} in CMS of (12)

Figure A.1: Depiction of the angles that are calculated in this section A.4 and are needed for the partial-wave projection. Each caption shows the angle that is depicted in the respective diagram.

where the last equality is by far not trivial to show. The easiest way is to use some algebraic tool, like `Mathematica`. Here, one has to replace σ_2 everywhere via equation (A.36), square equation (A.38), multiply it by the denominator, and look at the difference of both sides of the equal-sign:

$$\lambda_{s1}\lambda_{s3} - \texttt{Numerator}\left[\cos\theta^*_{3(1)}\right]^2 - 4s\phi = 0$$

This expression can be simplified by `Mathematica` and will result in 0, showing that equation (A.38) holds.

Calculation of $\cos\theta_{12}$

θ_{12} is the angle of particle p_1 with respect to $-p_3 = p_X$ in the CMS of the (12)-subsystem, meaning the corresponding helicity frame, with invariant mass σ_3, as depicted in Figure A.1(b). We are in some rest frame, but not the one of the resonance X, therefore, we do not use the asterisk for the quantities involved to differentiate them from the previous case. Instead, the two indices denote the CMS while the first index gives the reference particle for the angle with respect to the particle of the third index which is not appearing. Equivalently, $\cos\theta_{31}$ would be the angle of particle 3 with respect to -2 in the CMS of the (31)-subsystem.

We can use equations (A.1) and (A.2) once more to calculate the involved energies and momenta in such a systems. For the CMS of system (jk) with invariant mass σ_i follows:

$$E_{j/k} = \frac{\sigma_i + m^2_{j/k} - m^2_{k/j}}{2\sqrt{\sigma_i}}, \qquad \left|\vec{p}_j\right| = \left|\vec{p}_k\right| = \frac{\lambda^{\frac{1}{2}}(\sigma_i, m_j^2, m_k^2)}{2\sqrt{\sigma_i}} =: \frac{\sqrt{\lambda_i}}{2\sqrt{\sigma_i}}.$$

The remaining final-state energy can be obtained from $s = p_X^2 = (p_i + [p_j + p_k])^2 = m_i^2 + \sigma_i + 2E_i\sqrt{\sigma_i}$ by using that $\vec{p}_j + \vec{p}_k = 0$, resulting in

$$E_i = \frac{s - \sigma_i - m_i^2}{2\sqrt{\sigma_i}}, \qquad \left|\vec{p}_X\right| = \left|\vec{p}_i\right| = \frac{\sqrt{\lambda_{si}}}{2\sqrt{\sigma_i}}.$$

Again starting from $\sigma_2 = (p_1 + p_3)^2 = m_1^2 + m_3^2 + 2E_1E_3 + 2\left|\vec{p}_1\right|\left|\vec{p}_3\right|\cos\theta_{12}$, we have to be careful with the sign in front of the cosine, since $\vec{p}_3$ points in the opposite direction compared to the previous

case. Solving for the angle and inserting all involved energies and momenta, we end up at

$$\begin{aligned}\cos\theta_{12} &= \frac{2\sigma_3(\sigma_2 - m_1^2 - m_3^2) - (\sigma_3 + m_1^2 - m_2^2)(s - \sigma_3 - m_3^2)}{\sqrt{\lambda_3\lambda_{s3}}} \\ &= \frac{\sigma_3(\sigma_2 - \sigma_1) - (m_1^2 - m_2^2)(s - m_3^2)}{\sqrt{\lambda_3\lambda_{s3}}}.\end{aligned} \tag{A.39}$$

The second equality can be obtained by multiplying out both σ_3 terms from the product of the second term, already giving us the second term in the final expression. To obtain the first term, we factor out σ_3 of all remaining expressions and replace s according to equation (A.36). Now, we just have to simplify everything, resulting in the first term $\sigma_3(\sigma_2 - \sigma_1)$. This expression especially is nice, since we can directly see the property $\cos\theta_{21} = \cos(\pi - \theta_{12}) = -\cos(\theta_{12})$, where we calculate the angle between p_2 and $-p_3$ instead, which is also achieved by the replacement $p_1 \leftrightarrow p_2$ and, therefore, as well $m_1 \leftrightarrow m_2$ and $\sigma_1 = (p_2 + p_3)^2 \leftrightarrow (p_1 + p_3)^2 = \sigma_2$ leaving $\sigma_3 = (p_1 + p_2)^2$ untouched. By accordingly cycling the indices we can obtain the angles of the other helicity frames

$$\cos\theta_{23} = \frac{\sigma_1(\sigma_3 - \sigma_2) - (m_2^2 - m_3^2)(s - m_1^2)}{\sqrt{\lambda_1\lambda_{s1}}}, \qquad \cos\theta_{31} = \frac{\sigma_2(\sigma_1 - \sigma_3) - (m_3^2 - m_1^2)(s - m_2^2)}{\sqrt{\lambda_2\lambda_{s2}}}. \tag{A.40}$$

Similarly to before, we can also calculate the sine of the angle

$$\sin\theta_{12} = \sqrt{1 - \cos^2\theta_{12}} = \frac{2\sqrt{\sigma_3}\sqrt{\phi}}{\sqrt{\lambda_3\lambda_{s3}}}. \tag{A.41}$$

The derivation of the second equality is very complicated again, however, we can show its validity with `Mathematica` once more.

Calculation of $\cos\left(\theta^*_{3(1)} + \theta_{12}\right)$

Finally, we have all ingredients that are needed to calculate the expression of interest

$$\cos\left(\theta^*_{3(1)} + \theta_{12}\right) = \cos\theta^*_{3(1)}\cos\theta_{12} - \sin\theta^*_{3(1)}\sin\theta_{12}.$$

After inserting the trigonometric functions from equations (A.37), (A.38), (A.39) and (A.41), we have $\lambda_{s3}\sqrt{\lambda_{s1}}\sqrt{\lambda_3}$ as common denominator. The first factor λ_{s3} has two zeroes, corresponding to two poles in the cosine, one of which lies in the region of integration. The zeroes of the other Källén functions appear under a square root, not resulting in poles but in branch points instead. With equation (A.4) we can write $2\sqrt{s}\lambda_{s3} = \left((\sqrt{s} - \sqrt{\sigma_3})^2 - m_3^2\right)\cdot\left((\sqrt{s} + \sqrt{\sigma_3})^2 - m_3^2\right)$. The second factor of this expression will always be positive, since $\sqrt{s} + \sqrt{\sigma_3} > m_3$. Therefore, possible zeroes can only come from the first factor which, surprisingly[4], can be factored out of the numerator of the cosine, cancelling them out

[4] Or actually not surprisingly, since we would not expect the cosine to have poles in the first place, meaning that they have to cancel out.

completely. The remaining expression in the numerator is as follows:

$$\begin{aligned}
\lambda_{s3}\sqrt{\lambda_{s1}\lambda_3}\cos\left(\theta^*_{3(1)}+\theta_{12}\right) &= \left((\sqrt{s}-\sqrt{\sigma_3})^2-m_3^2\right)\cdot W(\sqrt{s},\sqrt{\sigma_1},\sqrt{\sigma_3}),\\
W\left(\sqrt{s},\sqrt{\sigma_1},\sqrt{\sigma_3}\right) &= 2\sqrt{\sigma_3}\sqrt{s}\Big(m_1^2w_2^+ + m_2^2w_1^+ + m_1^2w_3^- - \sigma_3 w_1^+\Big),\\
&\quad -2s\lambda_3 - w_1^+\big(\sigma_3(\sigma_2-\sigma_1)-(m_1^2-m_2^2)(s-m_3^2)\big)\\
\text{with}\qquad w_i^\pm &= s\pm m_i^2\mp\sigma_i. \qquad\qquad (A.42)
\end{aligned}$$

Since this expression is even more complicated, one can use `Mathematica` again, in order to confirm the equality.

The final expression reads

$$\cos\left(\theta^*_{3(1)}+\theta_{12}\right) = \frac{W(\sqrt{s},\sqrt{\sigma_1},\sqrt{\sigma_3})}{\left((\sqrt{s}+\sqrt{\sigma_3})^2-m_3^2\right)\sqrt{\lambda_{s1}\lambda_3}}. \qquad (A.43)$$

A.5 Flatness of Dalitz Plot

We want to show that $\frac{\mathrm{d}^2\Phi_3}{\mathrm{d}\sigma_1\mathrm{d}\sigma_3}$ is flat, i.e. does not depend on σ_1 and σ_3. Since Φ_3 is Lorentz-invariant, we can perform the calculations in any frame. We will choose the helicity frame of the (23) system. Now, we start with the phase-space recursion formula of equation (A.9) for $N = 2$:

$$\Phi_3(p_X;p_1,p_2,p_3) = \int \frac{\mathrm{d}\sigma_1}{2\pi}\mathrm{d}\Phi_2(m_X^2,\sigma_1,m_1^2)\mathrm{d}\Phi_2(\sigma_1,m_2^2,m_3^2),$$

where we can insert the differential two-body phase spaces from equation (A.8) and integrate out both angles of the first one and ϕ_{23} of the second one, keeping only $\mathrm{d}\cos\theta_{23}$. Additionally, we already pull the $\mathrm{d}\sigma_1$ on the other side:

$$\frac{\mathrm{d}\Phi_3}{\mathrm{d}\sigma_1} = \frac{1}{2\pi(8\pi)^2}\frac{\sqrt{\lambda_{s1}}}{s}\frac{\sqrt{\lambda_1}}{\sigma_1}\frac{\mathrm{d}\cos\theta_{23}}{2}, \qquad (A.44)$$

where λ_{s1} and λ_1 are defined in equation (3.57).

Next, we have to perform a substitution of $\cos\theta_{23}$ to σ_3. This substitution can be calculated from the left equation of (A.40) and reads

$$\mathrm{d}\cos\theta_{23} = \frac{2\sigma_1}{\sqrt{\lambda_1\lambda_{s1}}}\mathrm{d}\sigma_3. \qquad (A.45)$$

Note that the factor of 2 comes about because we have to replace σ_2 with equation (A.36).

Inserting this substitution into equation (A.44) shows that almost everything cancels out, and after moving $\mathrm{d}\sigma_3$ on the other side we get the final expression:

$$\frac{\mathrm{d}^2\Phi_3}{\mathrm{d}\sigma_1\mathrm{d}\sigma_3} = \frac{1}{2\pi(8\pi)^2 s}. \qquad (A.46)$$

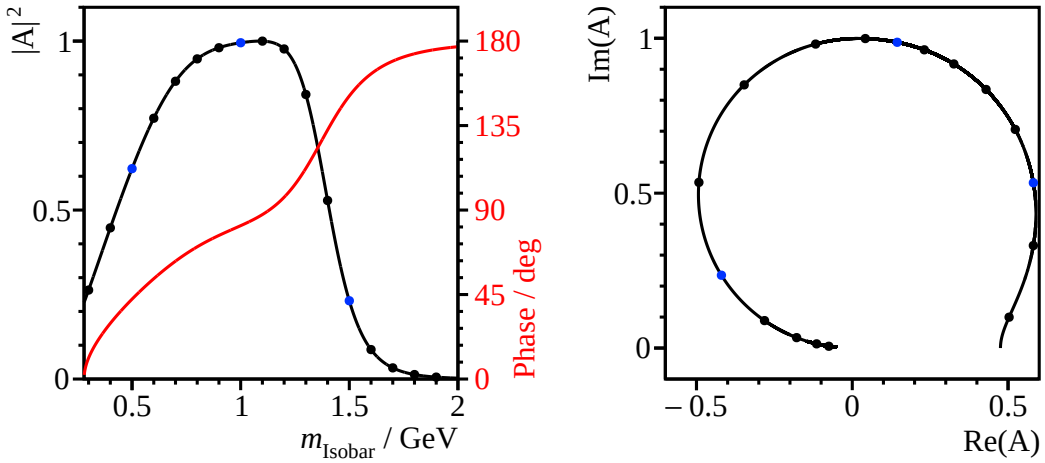

Figure A.2: Modified Au-Morgan-Pennington parametrization of the line shape of the $(\pi\pi)_S$. On the left, the line shape (black) and the phase (red) are plotted, while the right plot shows the complex amplitude in an Argand diagram.

A.6 Additional Isobar Line Shapes

A.6.1 Line Shape of the Broad $(\pi\pi)_S$

For the $f_0(500)$ aka σ aka $(\pi\pi)_S$ parametrization we use the M-solution from [54] with its modifications as detailed in [89]. It is obtained from a $\pi\pi - K\bar{K}$ coupled-channel $\boldsymbol{K}$-matrix fit and modified in order to remove contributions from the $f_0(980)$ and $f_0(1500)$. The resulting formula reads

$$f_\sigma(s) = \Big(M_{11}(s) - \mathrm{i}\,\rho_1(s)\Big)^{-1}, \quad M_{11}(s) = \frac{a_{11}}{s - s_0} + \sum_{n=0}^{3} c_{11}^{(n)} \left(\frac{s}{4m_K^2} - 1\right)^n, \tag{A.47}$$

with the average kaon mass m_K, the constants $s_0 = -0.0074\,\mathrm{GeV}^2$, $a_{11} = 0.1131\,\mathrm{GeV}^2$, $c_{11}^{(0)} = 0.0337$, $c_{11}^{(1)} = -0.3185$, $c_{11}^{(2)} = -0.0942$, $c_{11}^{(3)} = -0.5927$, and $\rho_1(s)$ being the average of the phase space (equation (A.7) without prefactor) over both charge modes $\pi^+\pi^-$ and $\pi^0\pi^0$.

Note that in this modified parametrization all $\pi\pi \to K\bar{K}$ and $K\bar{K} \to K\bar{K}$ contributions are removed. Its squared magnitude, complex phase and the corresponding Argand diagram are shown in Figure A.2.

A.6.2 $[\pi\pi]_P$ and $[K\bar{K}]_P$ Isobars

For the $[\pi\pi]_P$ sector the only considered isobar is the $\rho(770)$ modeled with a BWM with energy-dependent width according to equations (3.34) and (3.35). Since we only consider $K_S^0 K_S^0$, no $[K\bar{K}]_P$ isobars are allowed, see section 5.1.3.

APPENDIX B

Additional Plots for Complex Structures

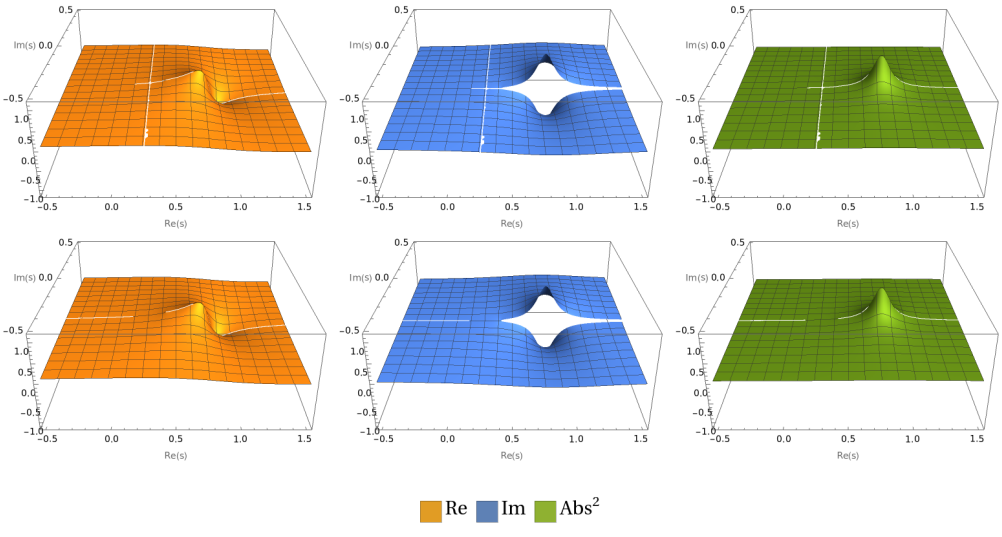

Figure B.1: Chew-Mandelstam BW for complex arguments s for the decay $K^{*0}(892) \to K^+\pi^-$ with $\tilde{\Gamma}_{K^*} = 0.1\,\text{GeV}$. Plotted are real part (orange), imaginary part (blue) and squared magnitude (green) for `Mathematica` convention (top) and physics convention (bottom).

B.1 M instead of s

In section 3.3, we only look at the functions with s as an argument. However, usually the mother mass $M = \sqrt{s}$ is used. For a simple BW, this already creates problems, since we will obtain a second pole at $-m_p + \mathrm{i}\,\Gamma_p/2$ making everything symmetric with respect of a rotation by the angle π around the point $M = 0$. Here, we use the definition of pole mass and pole width in equation (3.28). The lower contour plots of Figure B.2 shows this nicely.

Looking at the BW with energy-dependent width as a function of M in Figure B.3 reveals that we do not only double the amount of poles, but also the branch cuts and the unphysical poles from the phase space. Additionally, the cuts are curved for the `Mathematica` convention (left). Still, using the physics convention (middle) gives the simplest complex structure by hiding all poles on the second Riemann sheet. However, we obtain a small discontinuity of the imaginary part on the real axis between $-\sqrt{s_{\mathrm{pth}}} < M < \sqrt{s_{\mathrm{pth}}}$. The second Riemann sheet of the physics convention shows the full extend of the nightmare, we have four branch cuts (two of them merging at $M = 0$ and extending to $\pm\mathrm{i}\,\infty$), four BW poles and four unphysical poles.

Finally, evaluating the Chew-Mandelstam BW on M instead of s results in Figure B.4. We see that the logarithmic branch cut is still able to hide the poles and all unphysical features are removed, although `Mathematica` shows white lines at all four possible square-root branch-cut locations. However, when integrating in complex plane one would usually do this in s and not M, therefore, these plots are only presented for completeness.

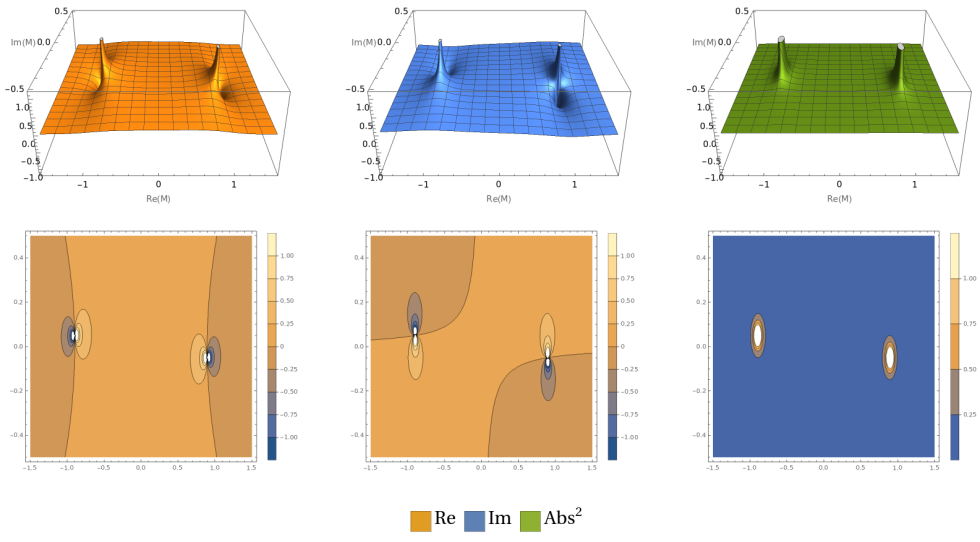

Figure B.2: Relativistic BW as a function of complex-valued $M = \sqrt{s}$ for the decay $K^{*0}(892) \to K^+\pi^-$ with $\tilde{\Gamma}_{K^*} = 0.1\,\mathrm{GeV}$. Plotted are real part (orange, left), imaginary part (blue, middle) and squared magnitude (green, right) with the corresponding contour plots in the second row.

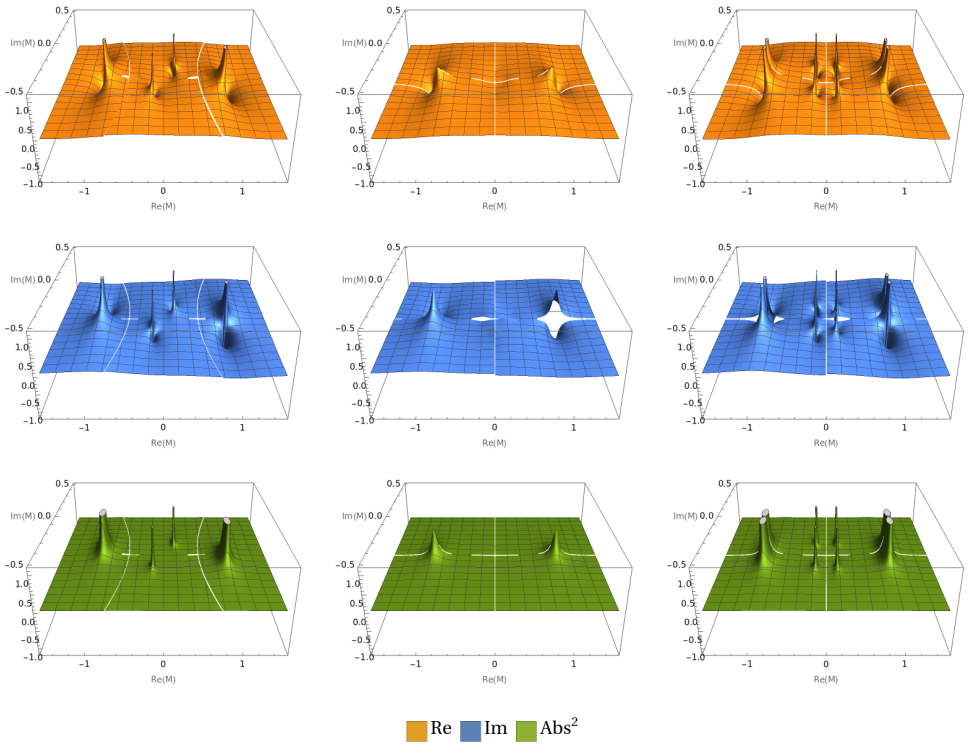

Figure B.3: BW with energy-dependent width as a function of complex-valued $M = \sqrt{s}$ for the decay $K^{*0}(892) \to K^+\pi^-$ with $\tilde{\Gamma}_{K^*} = 0.1\,\text{GeV}$. Plotted are real part (orange), imaginary part (blue) and squared magnitude (green) of the `Mathematica` convention (left), the physics convention (middle), and the second Riemann sheet of the physics convention (right) obtained by a rotation of $\phi = -\pi$.

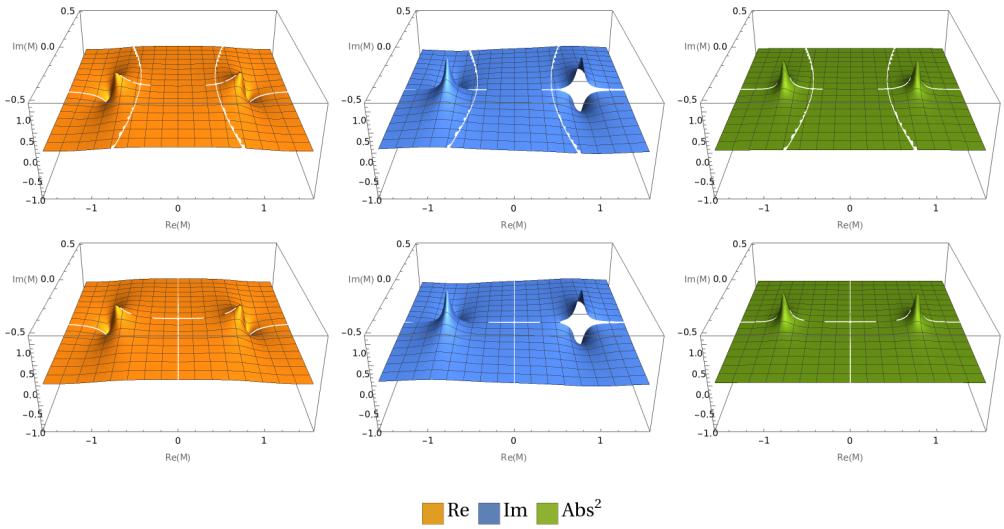

Figure B.4: Chew-Mandelstam BW as a function of complex-valued $M = \sqrt{s}$ for the decay $K^{*0}(892) \to K^+\pi^-$ with $\tilde{\Gamma}_{K^*} = 0.1\,\text{GeV}$. Plotted are real part (orange), imaginary part (blue) and squared magnitude (green) for `Mathematica` convention (top) and physics convention (bottom).

APPENDIX C

Further Details on the $a_1(1420)$

C.1 Regge Trajectories

C.1.1 Simple Regge Model

We try to derive the relation $\ell \sim M^2$ as stated in section 4.2.1. Any textbook about particle physics (e.g. equation (10.40) of [90]) will tell you that the non-relativistic potential of Quantum Chromo Dynamics (QCD) follows the form

$$V_{q\bar{q}}(r) = -\frac{4}{3}\frac{\alpha_S}{r} + kr, \tag{C.1}$$

where the constant in front of the linear term is basically the energy density between the two bound quarks, similar to the linear potential of a classical spring. With a value of $k \sim 1\ \frac{\text{GeV}}{\text{fm}}$, the predicted charmonium ($c\bar{c}$ mesons) and bottomonium ($b\bar{b}$ mesons) excitation spectra show a fairly good agreement with the measured meson masses.

The linear term in equation (C.1) has its origin in the following simplified model, which also allows us to obtain a simple relation between the mass of the meson M and its intrinsic orbital angular momentum L. For this, we assume that we have two massless quarks at a distance $2r_0$ rotating around each other at the speed of light[1]. They are attached to each other by a string with constant energy density k. The angular velocity of the whole string is fixed by this to $\omega = \frac{c}{r_0}$. The speed $v(r)$ of the string at a given distance r from the center will be accordingly $v(r) = \omega r$ and, thus, $\beta(r) = \frac{v(r)}{c} = \frac{r}{r_0}$. In order to calculate the full energy stored in the binding, we have to integrate the constant energy density k over the full length of the string. However, the further away we get from the center, the more non-relativistic the system gets, resulting in the inclusion of a factor $\gamma(r) = \frac{1}{\sqrt{1-\beta^2(r)}}$:

$$E_{\text{tot}} = 2\int_0^{r_0} k\gamma(r)\mathrm{d}r \overset{r=r_0\sin(x)}{=} 2\int_0^{\frac{\pi}{2}} k\frac{r_0\cos(x)\mathrm{d}x}{\sqrt{1-\sin^2(x)}} = 2kr_0x\Big|_{x=0}^{\frac{\pi}{2}} = \pi k r_0 \tag{C.2}$$

Since the meson is at rest, the full energy has to amount to its rest mass $E_{\text{tot}} = Mc^2$. This relates the

[1] In order to make the quantities in the following calculations more obvious, we will keep all c factors in the equations throughout this section.

radius of the meson to its mass via $r_0 = \frac{Mc^2}{\pi k}$.

Classically, we have $\vec{L} = \vec{r} \times \vec{p}$. $\vec{r}$ and $\vec{p}$ are always orthogonal, simplifying things to $L = rp$, where we have to include proper Lorentz factors by replacing $p \to \beta(r)\gamma(r)mc$. The mass density in this expression can be substituted by the energy density via $m \to \frac{k}{c^2}$. In order to obtain a dimensionless QN, we furthermore extract $\hbar$ from the orbital angular momentum L. Putting everything together results in the following integral

$$L\hbar = 2\int_0^{r_0} r\beta(r)\gamma(r)\frac{k}{c^2}c\mathrm{d}r = 2\frac{k}{c}\int_0^{\frac{\pi}{2}} r_0^2\sin^2(x)\mathrm{d}x = 2\frac{k}{c}r_0^2\frac{1}{2}\left(x - \sin(x)\cos(x)\right)\Big|_{x=0}^{\frac{\pi}{2}} = \frac{\pi k r_0^2}{2c},$$

where we used the same substitution as in (C.2), but now we have a factor $\frac{r^2}{r_0}$ more resulting in a slightly more complicated but known integral of $\sin^2(x)$.

Replacing now r_0 with the help of (C.2), we finally obtain $L = \frac{M^2c^4}{\pi k\hbar c} \sim M^2$.

The problem with this relation is that $L = 0$ corresponds to a radius $r_0 = 0$. This results in $M = 0$, which is not what we observe in nature. One of the reasons is that we fully ignored the spin of the quarks. If one properly includes all involved spins as well as other QCD corrections into the calculations, [41] showed that one obtains $L + \frac{1}{2} \sim M^2$ for mesons with both $S = 0$ and $S = 1$ intrinsic spin, moreover they state also the linear dependence on the radial excitation number n and argument for a common slope for all mesons:

$$M^2 = 4\lambda^2\left(n + L + \frac{1}{2}\right). \tag{C.3}$$

They estimate the value for λ from the mass of the ρ meson via this relation, inserting $n = L = 0$ and obtaining $\lambda = M_\rho/\sqrt{2} \approx 0.55\,\mathrm{GeV}$. This will result in a slope of $(4\lambda^2)^{-1} = 0.83\,\mathrm{GeV}^{-2}$ in equation (4.1) of $n(M^2)$ and $L(M^2)$ in Figure 4.2.

C.2 Young Tableaux for Tetraquarks

We can use Young tableaux to derive the relations as discussed in section 4.2.3. For this, we note that a quark in $SUf(3)$-flavor corresponds to $\square$ and an antiquark to $\begin{array}{l}\square\\\square\end{array}$. In the (p, q) notation they correspond to $(1, 0)$ and $(0, 1)$, respectively, where p is the number of boxes that row #1 has more than row #2, and q the number of boxes that row #2 has more than row #3. If $p > q$ we are dealing with a multiplet and if $p < q$ it is an antimultiplet denoted by the bar over the bold number. The number of elements represented by a Young tableau can be calculated with

$$N(p, q) = (p + 1)(q + 1)\frac{p + q + 2}{2}. \tag{C.4}$$

So for the quark, we obtain $N(1, 0) = 3$, i.e. a triplet $\mathbf{3}_f$, and for the antiquark we get $N(0, 1) = 3$ as well, but an antitriplet $\overline{\mathbf{3}}_f$. According to the rules of [91], we can combine two quarks into a diquark via

$$\square \otimes \square \;=\; \begin{array}{l}\square\\\square\end{array} \oplus \square\square \;=\; (0,1) \oplus (2,0) \;=\; \overline{\mathbf{3}}_f \oplus \mathbf{6}_f,$$

and similarly for the antidiquark two antiquarks via

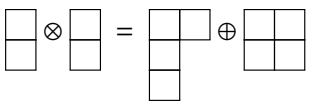

Note that the vertical column of three boxes (the dimension of the $SU(3)$ group) in the antidiquark case can be crossed out leaving only  . With this we see that the diquark has a $\bar{\mathbf{3}}_f$ component similar to an antiquark and the antidiquark has a $\mathbf{3}_f$ component similar to a quark. For the diquark, the $\bar{\mathbf{3}}_f$ will have an antisymmetric flavor wave function (only vertical boxes) and the $\mathbf{6}_f$ will have a symmetric one (only horizontal boxes). With this symmetry we can identify the diquark-triplet states as $[us]_{\text{asym}}$, $[ud]_{\text{asym}}$ and $[sd]_{\text{asym}}$, and the diquark sextuplet as $[us]_{\text{sym}}$, $[ud]_{\text{sym}}$, $[sd]_{\text{sym}}$, $[uu]$, $[dd]$ and $[ss]$, with

$$[qq']_{\text{asym}} = \frac{1}{\sqrt{2}}(qq' - q'q) \qquad \text{and} \qquad [qq']_{\text{sym}} = \frac{1}{\sqrt{2}}(qq' + q'q).$$

The $SU(3)$-color composition of the diquark can be determined exactly the same way. Combining two color-triplets yields as well $\mathbf{3}_c \otimes \mathbf{3}_c = \bar{\mathbf{3}}_c \oplus \mathbf{6}_c$ with the same symmetry behavior.

Looking at ground states with $L = 0$ and, therefore, a symmetric spatial wave function, we can combine an antisymmetric flavor wave function with an antisymmetric color wave function and an antisymmetric spin wave function, such that the wave function is antisymmetric under exchange of two fermions. As introduced in [42], we will call this a spin-0 diquark $(\bar{\mathbf{3}}_f, \bar{\mathbf{3}}_c, \mathbf{1}_s)$. On the other hand, combining the antisymmetric flavor triplet with the symmetric color sextuplet and the symmetric spin triplet also yields an antisymmetric wave function with respect to the exchange of two fermions. This is called a spin-1 diquark $(\bar{\mathbf{3}}_f, \mathbf{6}_c, \mathbf{3}_s)$.

To form tetraquarks, we need the diquark-antidiquark in a color-singlet configuration. Luckily for both the $\bar{\mathbf{3}}_c \otimes \mathbf{3}_c$ and the $\mathbf{6}_c \otimes \bar{\mathbf{6}}_c$ combinations we obtain a singlet:

$\bar{\mathbf{3}} \otimes \mathbf{3}$ = 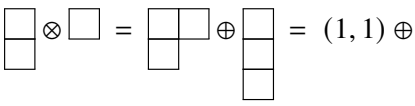

$\mathbf{6} \otimes \bar{\mathbf{6}}$ = 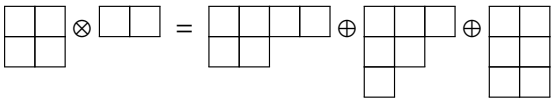

The first row also applies to the flavor component of the diquark-antidiquark combination. Therefore, we get a nonet in form of an octet and a singlet in both cases when combining a spin-0 diquark with a spin-0 antidiquark and when combining a spin-1 diquark with a spin-1 antidiquark. While combining two spin-0 (anti)diquarks will always result in scalar (spin-0) tetraquarks, with two spin-1 (anti)diquarks we can additionally also create vector (spin-1) and tensor (spin-2) tetraquarks.

One could try to also combine a spin-0 diquark with a spin-1 antidiquark and vice versa, however,

the combination of their color-components will not form the needed singlet

$\overline{\mathbf{3}} \otimes \overline{\mathbf{6}}$ = 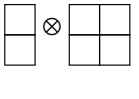 = 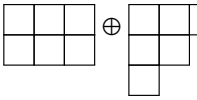 = $(0,3) \oplus (1,1)$ = $\overline{\mathbf{10}} \oplus \mathbf{8}$

$\mathbf{3} \otimes \mathbf{6}$ = 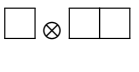 = 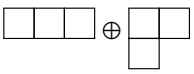 = $(3,0) \oplus (1,1)$ = $\mathbf{10} \oplus \mathbf{8}$,

making it unphysical.

With the arguments above, we expect nine scalar tetraquarks coming from spin-0 (anti)diquarks, and nine scalar tetraquarks from spin-1 (anti)diquarks. In [42] they derive that these tetraquarks will have $J^{PC} = 0^{++}$ leading to the particle assignment with the particles a_0, f_0 and K_0^* as mentioned in section 4.2.3. For the nonet of spin-1 tetraquarks from combining spin-1 (anti)diquarks, [42] derives $J^{PC} = 1^{+-}$ for the spin-1 tetraquarks, resulting in b_1, h_1 and K_1 as candidates. And for the nonet of spin-2 tetraquarks they find $J^{PC} = 2^{++}$, which means a_2, f_2 and K_2^*. While their assignment for the scalar nonets works very well including the predicted mass hierarchy, [42] states problems for the spin-1 tetraquarks while also giving a possible solution. For the spin-2 tetraquarks there are many candidates making an assignment somewhat arbitrary according to [42].

So far we only used the diquark flavor-antitriplet, but one might also think of using the diquark flavor-sextuplet. This would introduce a second kind spin-1 diquark with $(\mathbf{6}_f, \overline{\mathbf{3}}_c, \mathbf{3}_s)$. In order to obtain a color-singlet, one has to combine it with a spin-0 antidiquark (and vice versa). However, this would very drastically increase the amount of expected tetraquark candidates, therefore, we do not continue this path. Another reason is that according to section 2.9.4 of [92] such flavor-sextuplet diquarks would have a smaller binding energy than the flavor-antitriplet diquarks.

C.3 Remaining t' Slices

An explanation of the following plots can be found in section 4.5 and the first t' slice in Figure 4.16, therefore, we omit the captions to save space.

2)

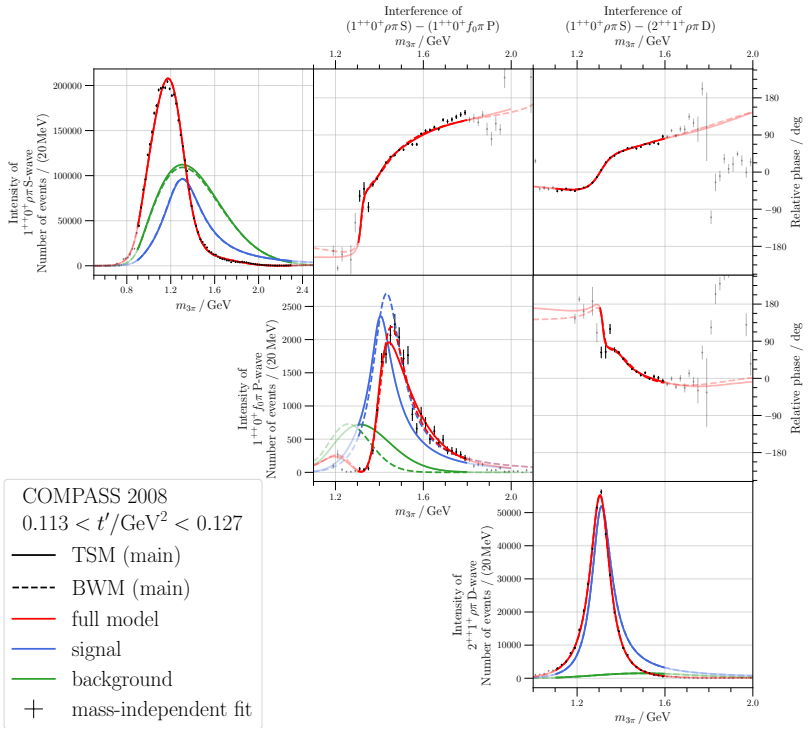

3)

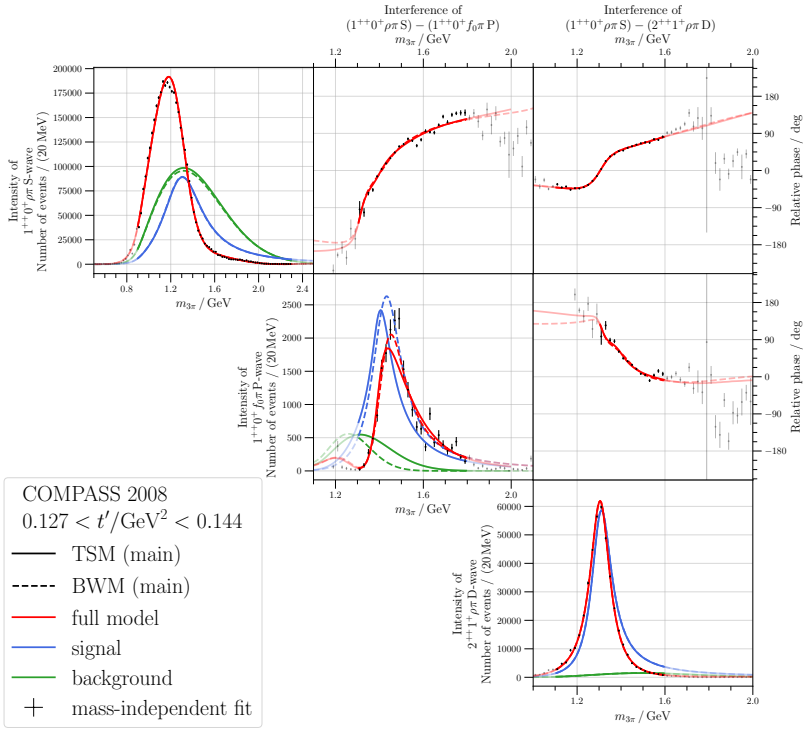

4)

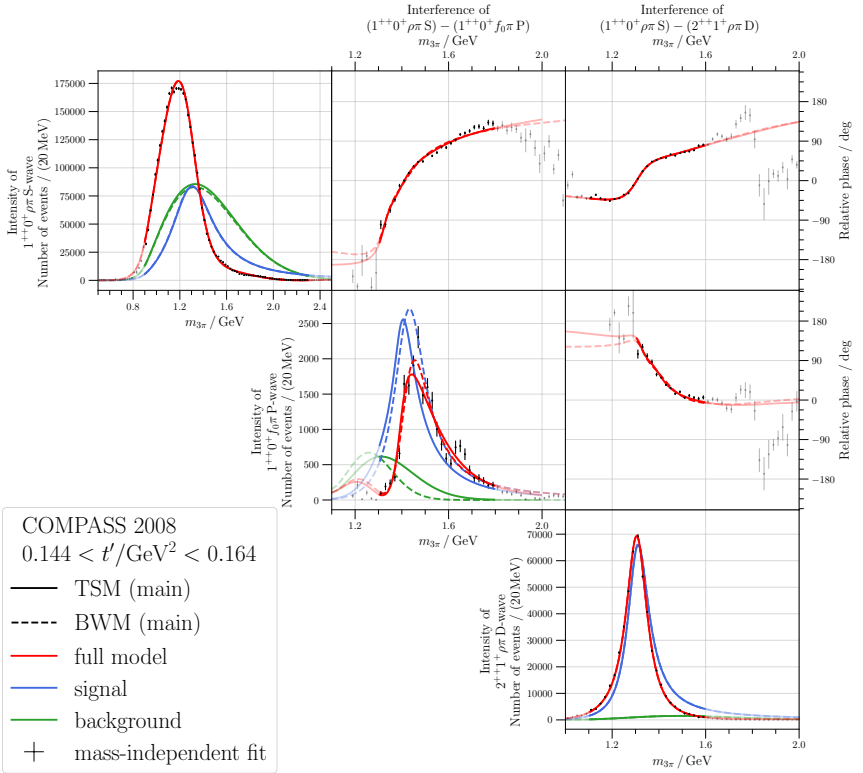
Interference of
$(1^{++}0^+\rho\pi\,\mathrm{S}) - (1^{++}0^+f_0\pi\,\mathrm{P})$
$m_{3\pi}$ / GeV
Interference of
$(1^{++}0^+\rho\pi\,\mathrm{S}) - (2^{++}1^+\rho\pi\,\mathrm{D})$
$m_{3\pi}$ / GeV
Intensity of
$1^{++}0^+\rho\pi$ S-wave
Number of events / (20 MeV)
$m_{3\pi}$ / GeV
Intensity of
$1^{++}0^+f_0\pi$ P-wave
Number of events / (20 MeV)
$m_{3\pi}$ / GeV
Intensity of
$2^{++}1^+\rho\pi$ D-wave
Number of events / (20 MeV)
$m_{3\pi}$ / GeV
Relative phase / deg
Relative phase / deg
COMPASS 2008
$0.144 < t'/\mathrm{GeV}^2 < 0.164$
TSM (main)
BWM (main)
full model
signal
background
mass-independent fit

5)

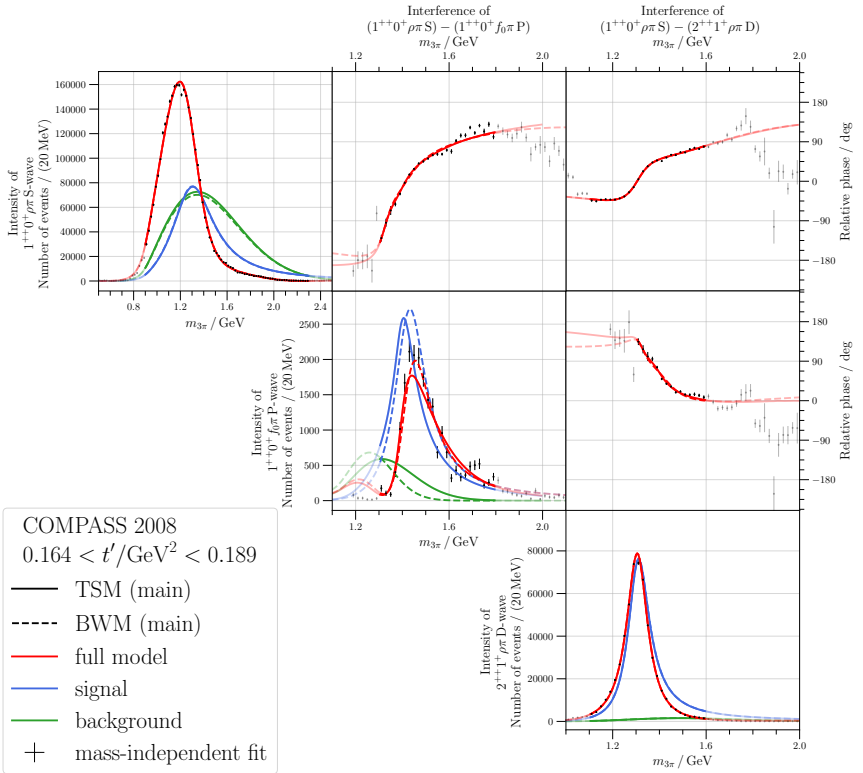
Interference of
$(1^{++}0^+\rho\pi\,\mathrm{S}) - (1^{++}0^+f_0\pi\,\mathrm{P})$
$m_{3\pi}$ / GeV
Interference of
$(1^{++}0^+\rho\pi\,\mathrm{S}) - (2^{++}1^+\rho\pi\,\mathrm{D})$
$m_{3\pi}$ / GeV
Intensity of
$1^{++}0^+\rho\pi$ S-wave
Number of events / (20 MeV)
$m_{3\pi}$ / GeV
Intensity of
$1^{++}0^+f_0\pi$ P-wave
Number of events / (20 MeV)
$m_{3\pi}$ / GeV
Intensity of
$2^{++}1^+\rho\pi$ D-wave
Number of events / (20 MeV)
$m_{3\pi}$ / GeV
Relative phase / deg
Relative phase / deg
COMPASS 2008
$0.164 < t'/\mathrm{GeV}^2 < 0.189$
TSM (main)
BWM (main)
full model
signal
background
mass-independent fit

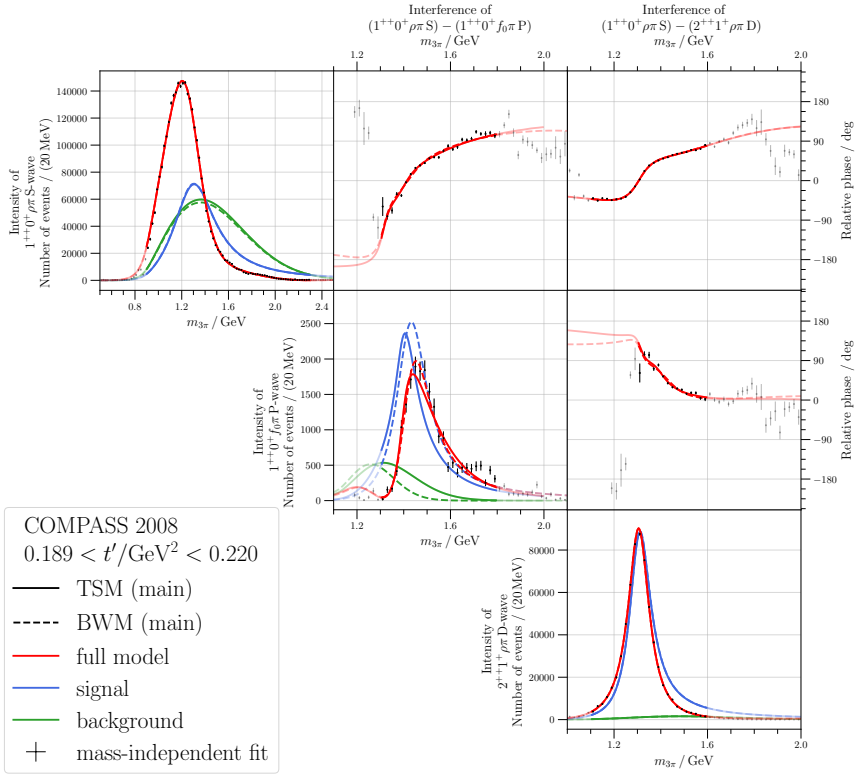
Interference of
$(1^{++}0^+\rho\pi\,\mathrm{S}) - (1^{++}0^+f_0\pi\,\mathrm{P})$
$m_{3\pi}$ / GeV
Interference of
$(1^{++}0^+\rho\pi\,\mathrm{S}) - (2^{++}1^+\rho\pi\,\mathrm{D})$
$m_{3\pi}$ / GeV
Intensity of
$1^{++}0^+\rho\pi$ S-wave
Number of events / (20 MeV)
$m_{3\pi}$ / GeV
Intensity of
$1^{++}0^+f_0\pi$ P-wave
Number of events / (20 MeV)
$m_{3\pi}$ / GeV
Intensity of
$2^{++}1^+\rho\pi$ D-wave
Number of events / (20 MeV)
$m_{3\pi}$ / GeV
Relative phase / deg
Relative phase / deg
COMPASS 2008
$0.189 < t'/\mathrm{GeV}^2 < 0.220$
TSM (main)
BWM (main)
full model
signal
background
mass-independent fit

6)

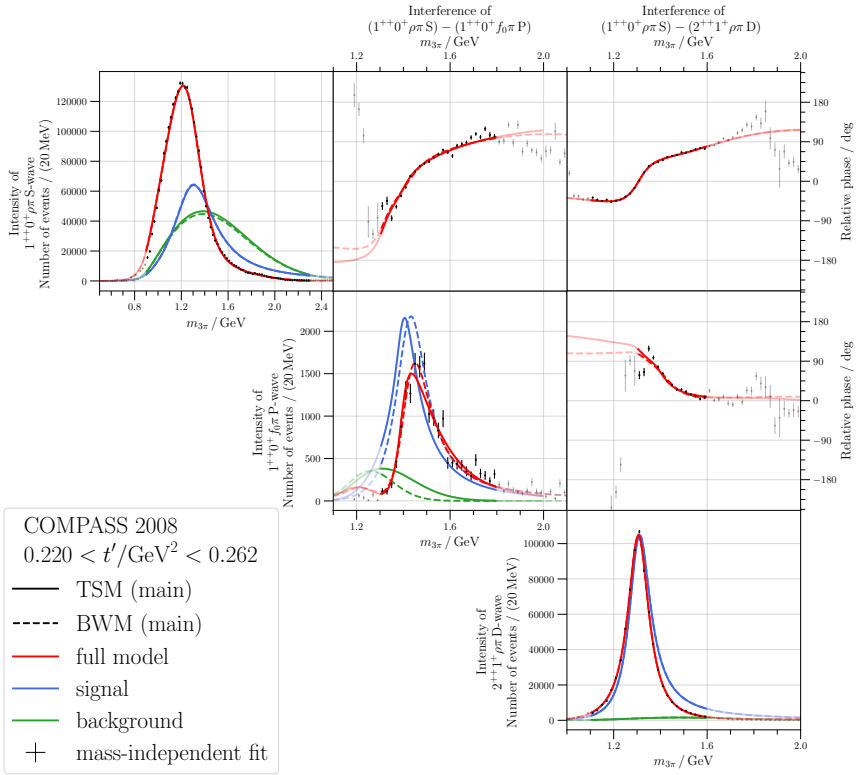
Interference of
$(1^{++}0^+\rho\pi\,\mathrm{S}) - (1^{++}0^+f_0\pi\,\mathrm{P})$
$m_{3\pi}$ / GeV
Interference of
$(1^{++}0^+\rho\pi\,\mathrm{S}) - (2^{++}1^+\rho\pi\,\mathrm{D})$
$m_{3\pi}$ / GeV
Intensity of
$1^{++}0^+\rho\pi$ S-wave
Number of events / (20 MeV)
$m_{3\pi}$ / GeV
Intensity of
$1^{++}0^+f_0\pi$ P-wave
Number of events / (20 MeV)
$m_{3\pi}$ / GeV
Intensity of
$2^{++}1^+\rho\pi$ D-wave
Number of events / (20 MeV)
$m_{3\pi}$ / GeV
Relative phase / deg
Relative phase / deg
COMPASS 2008
$0.220 < t'/\mathrm{GeV}^2 < 0.262$
TSM (main)
BWM (main)
full model
signal
background
mass-independent fit

7)

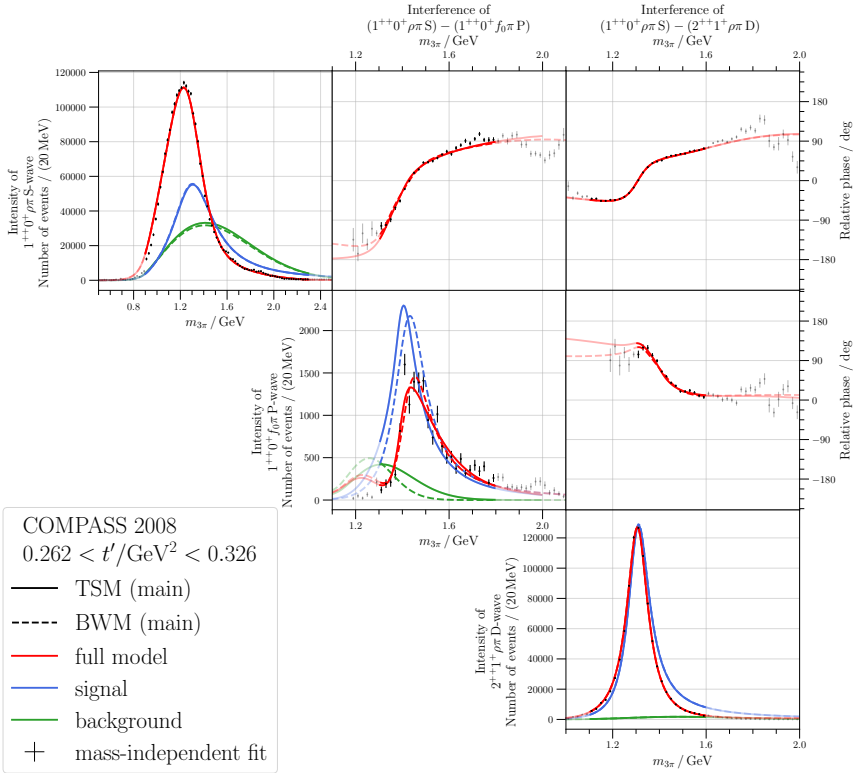
Interference of
$(1^{++}0^+\rho\pi\,\mathrm{S}) - (1^{++}0^+f_0\pi\,\mathrm{P})$
$m_{3\pi}$ / GeV
Interference of
$(1^{++}0^+\rho\pi\,\mathrm{S}) - (2^{++}1^+\rho\pi\,\mathrm{D})$
$m_{3\pi}$ / GeV
Intensity of
$1^{++}0^+\rho\pi$ S-wave
Number of events / (20 MeV)
$m_{3\pi}$ / GeV
Intensity of
$1^{++}0^+f_0\pi$ P-wave
Number of events / (20 MeV)
$m_{3\pi}$ / GeV
Intensity of
$2^{++}1^+\rho\pi$ D-wave
Number of events / (20 MeV)
$m_{3\pi}$ / GeV
Relative phase / deg
COMPASS 2008
$0.262 < t'/\mathrm{GeV}^2 < 0.326$
TSM (main)
BWM (main)
full model
signal
background
mass-independent fit

8)

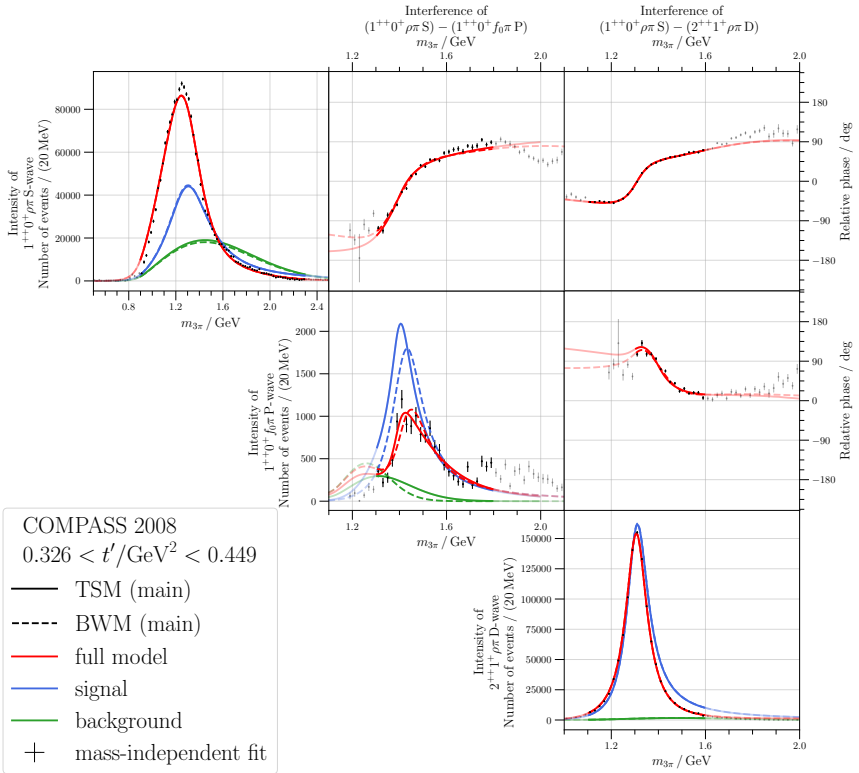
Interference of
$(1^{++}0^+\rho\pi\,\mathrm{S}) - (1^{++}0^+f_0\pi\,\mathrm{P})$
$m_{3\pi}$ / GeV
Interference of
$(1^{++}0^+\rho\pi\,\mathrm{S}) - (2^{++}1^+\rho\pi\,\mathrm{D})$
$m_{3\pi}$ / GeV
Intensity of
$1^{++}0^+\rho\pi$ S-wave
Number of events / (20 MeV)
$m_{3\pi}$ / GeV
Intensity of
$1^{++}0^+f_0\pi$ P-wave
Number of events / (20 MeV)
$m_{3\pi}$ / GeV
Intensity of
$2^{++}1^+\rho\pi$ D-wave
Number of events / (20 MeV)
$m_{3\pi}$ / GeV
Relative phase / deg
COMPASS 2008
$0.326 < t'/\mathrm{GeV}^2 < 0.449$
TSM (main)
BWM (main)
full model
signal
background
mass-independent fit

9)

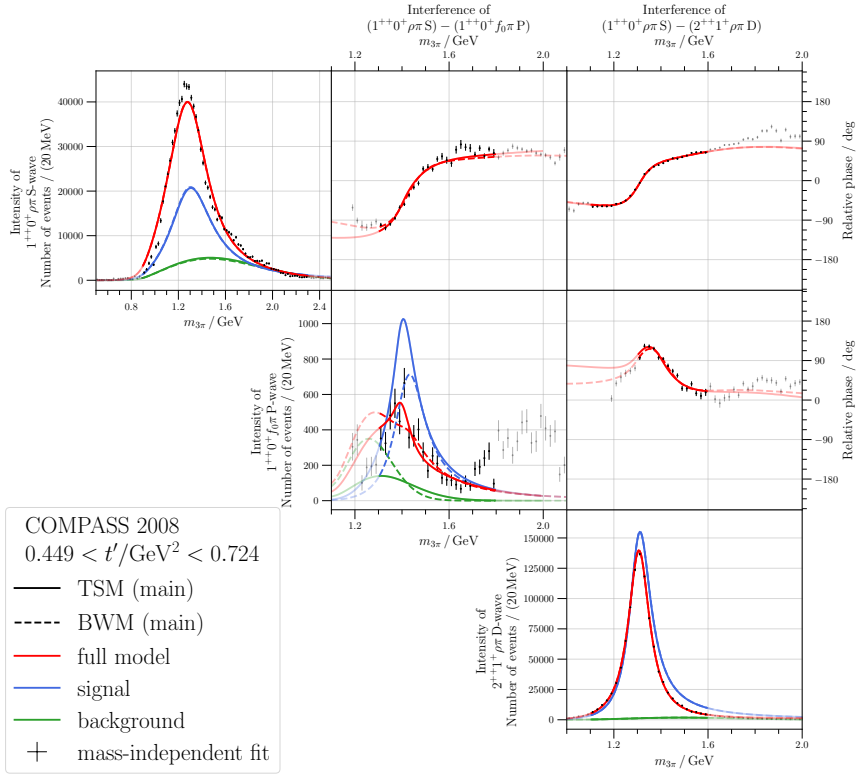
Interference of
$(1^{++}0^+\rho\pi\,\mathrm{S}) - (1^{++}0^+f_0\pi\,\mathrm{P})$
$m_{3\pi}$ / GeV
Interference of
$(1^{++}0^+\rho\pi\,\mathrm{S}) - (2^{++}1^+\rho\pi\,\mathrm{D})$
$m_{3\pi}$ / GeV
Intensity of
$1^{++}0^+\rho\pi$ S-wave
Number of events / (20 MeV)
Intensity of
$1^{++}0^+f_0\pi$ P-wave
Number of events / (20 MeV)
Intensity of
$2^{++}1^+\rho\pi$ D-wave
Number of events / (20 MeV)
Relative phase / deg
$m_{3\pi}$ / GeV
COMPASS 2008
$0.449 < t'/\mathrm{GeV}^2 < 0.724$
TSM (main)
BWM (main)
full model
signal
background
mass-independent fit

10)

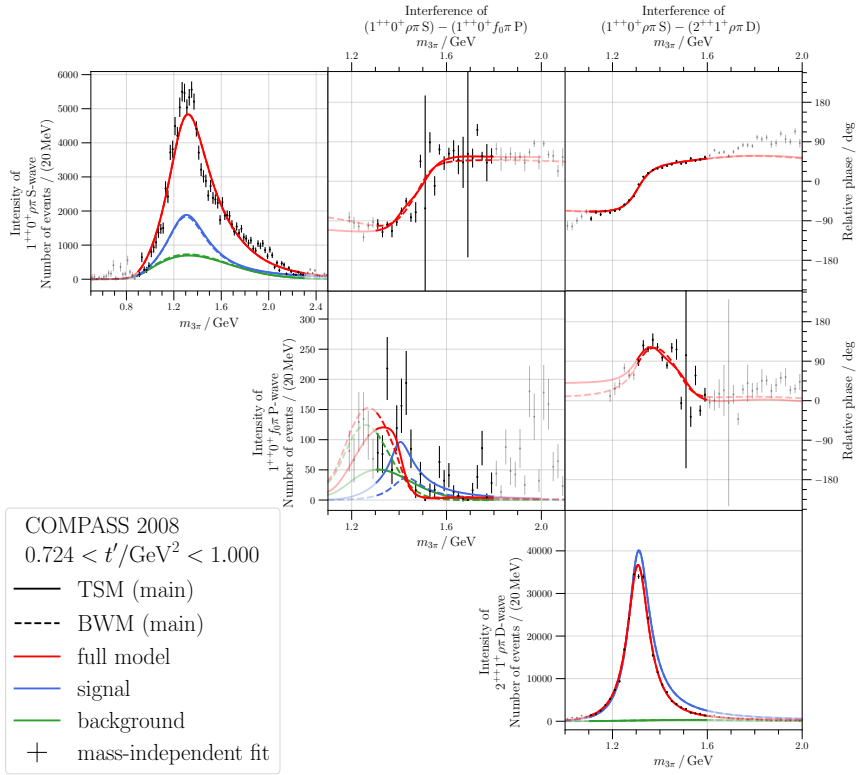
Interference of
$(1^{++}0^+\rho\pi\,\mathrm{S}) - (1^{++}0^+f_0\pi\,\mathrm{P})$
$m_{3\pi}$ / GeV
Interference of
$(1^{++}0^+\rho\pi\,\mathrm{S}) - (2^{++}1^+\rho\pi\,\mathrm{D})$
$m_{3\pi}$ / GeV
Intensity of
$1^{++}0^+\rho\pi$ S-wave
Number of events / (20 MeV)
Intensity of
$1^{++}0^+f_0\pi$ P-wave
Number of events / (20 MeV)
Intensity of
$2^{++}1^+\rho\pi$ D-wave
Number of events / (20 MeV)
Relative phase / deg
$m_{3\pi}$ / GeV
COMPASS 2008
$0.724 < t'/\mathrm{GeV}^2 < 1.000$
TSM (main)
BWM (main)
full model
signal
background
mass-independent fit

11)

C.4 Remaining Plots for Systematic Studies

The structure of the following plots in this appendix are described in detail in section 4.6, therefore, we omit the captions to save space.

Table C.1: Comparison of the fit quality for the different systematic studies as described in section 4.6 and depicted in Figure 4.24.

Study	**TSM**				**BWM**			
	χ^2	$\mathcal{R}^2$	#dof	$\mathcal{R}^2_{\text{red}}$	χ^2	$\mathcal{R}^2$	#dof	$\mathcal{R}^2_{\text{red}}$
main	19831	2319	505	4.59	19977	2448	503	4.87
scalar triangle	19942	2327	505	4.61	same as main			
direct decay	19063	1911	483	3.96	19239	2024	481	4.21
flexible bgd	19478	2196	502	4.37	19639	2271	500	4.54
excited states	18298	2027	505	4.01	18419	2075	503	4.13
non-sym. ph. sp.	18470	2349	505	4.65	18624	2462	503	4.89
wider K^*	19909	2357	505	4.67	same as main			
narrower K^*	19799	2298	505	4.55	same as main			
heavier K^*	19671	2298	505	4.40	same as main			
lighter K^*	20053	2444	505	4.84	same as main			
53 waves	21903	2146	505	4.35	21911	2373	503	4.72
no neg.-refl. waves	20843	2300	505	4.56	20985	2442	503	4.85
coarse ev. sel.	21653	2322	505	4.60	21910	2508	503	4.99
rank-2	17328	2008	505	3.98	17739	2286	503	4.54
$(\pi\pi)_S$ K1	19812	2262	505	4.48	19563	2159	503	4.29
$f_0(980)$ Breit-Wigner	20494	2157	505	4.27	20341	2156	503	4.29
bootstrap	16501	1990	505	3.94	16807	2291	503	4.55

C.4.1 Variation of K* Parameters

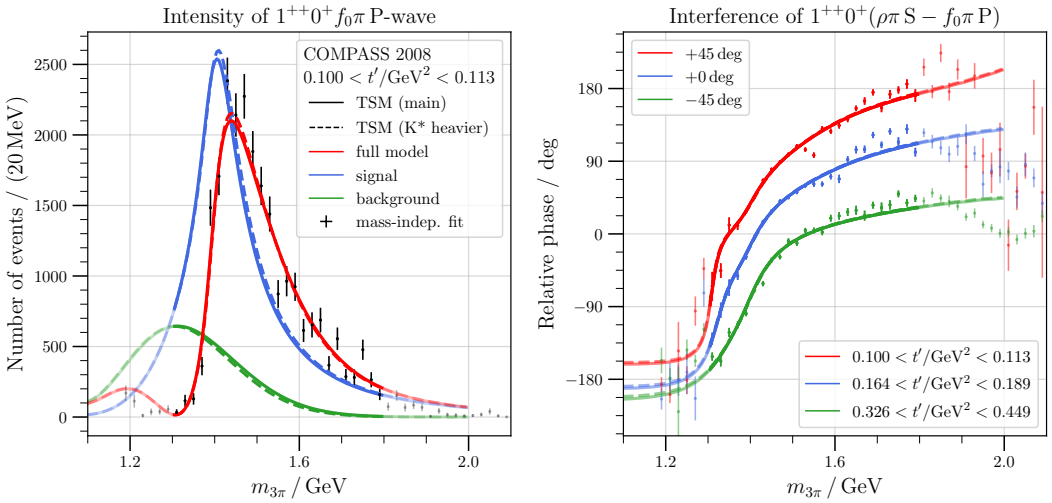

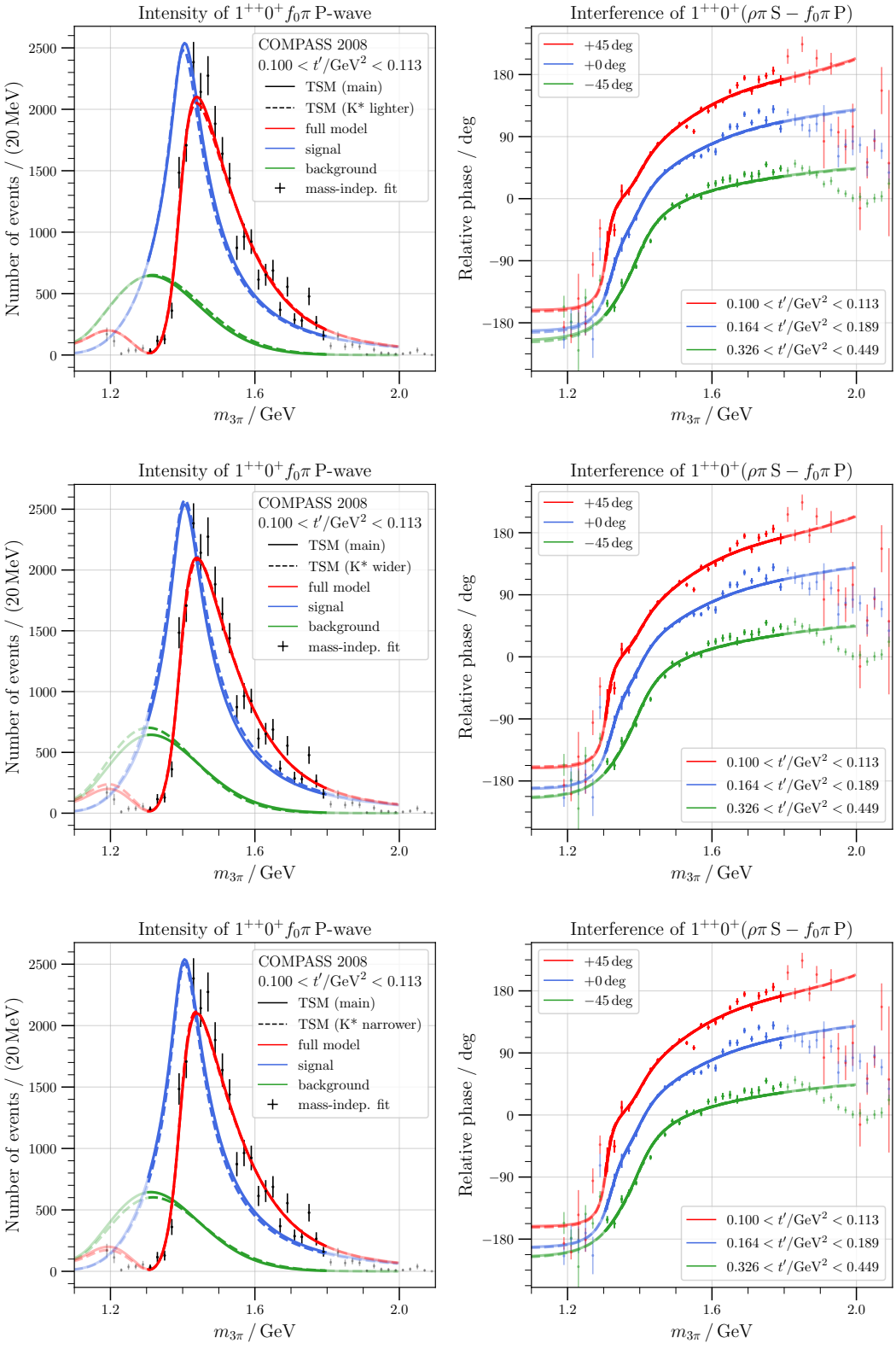
Intensity of $1^{++}0^+ f_0\pi$ P-wave
COMPASS 2008
$0.100 < t'/\mathrm{GeV}^2 < 0.113$
TSM (main)
TSM (K* lighter)
full model
signal
background
mass-indep. fit
Number of events / (20 MeV)
$m_{3\pi}$ / GeV
Interference of $1^{++}0^+(\rho\pi\,\mathrm{S} - f_0\pi\,\mathrm{P})$
+45 deg
+0 deg
−45 deg
$0.100 < t'/\mathrm{GeV}^2 < 0.113$
$0.164 < t'/\mathrm{GeV}^2 < 0.189$
$0.326 < t'/\mathrm{GeV}^2 < 0.449$
Relative phase / deg
Intensity of $1^{++}0^+ f_0\pi$ P-wave
COMPASS 2008
$0.100 < t'/\mathrm{GeV}^2 < 0.113$
TSM (main)
TSM (K* wider)
full model
signal
background
mass-indep. fit
Number of events / (20 MeV)
$m_{3\pi}$ / GeV
Interference of $1^{++}0^+(\rho\pi\,\mathrm{S} - f_0\pi\,\mathrm{P})$
+45 deg
+0 deg
−45 deg
$0.100 < t'/\mathrm{GeV}^2 < 0.113$
$0.164 < t'/\mathrm{GeV}^2 < 0.189$
$0.326 < t'/\mathrm{GeV}^2 < 0.449$
Relative phase / deg
Intensity of $1^{++}0^+ f_0\pi$ P-wave
COMPASS 2008
$0.100 < t'/\mathrm{GeV}^2 < 0.113$
TSM (main)
TSM (K* narrower)
full model
signal
background
mass-indep. fit
Number of events / (20 MeV)
$m_{3\pi}$ / GeV
Interference of $1^{++}0^+(\rho\pi\,\mathrm{S} - f_0\pi\,\mathrm{P})$
+45 deg
+0 deg
−45 deg
$0.100 < t'/\mathrm{GeV}^2 < 0.113$
$0.164 < t'/\mathrm{GeV}^2 < 0.189$
$0.326 < t'/\mathrm{GeV}^2 < 0.449$
Relative phase / deg

C.4.2 Variation of the Underlying PWD

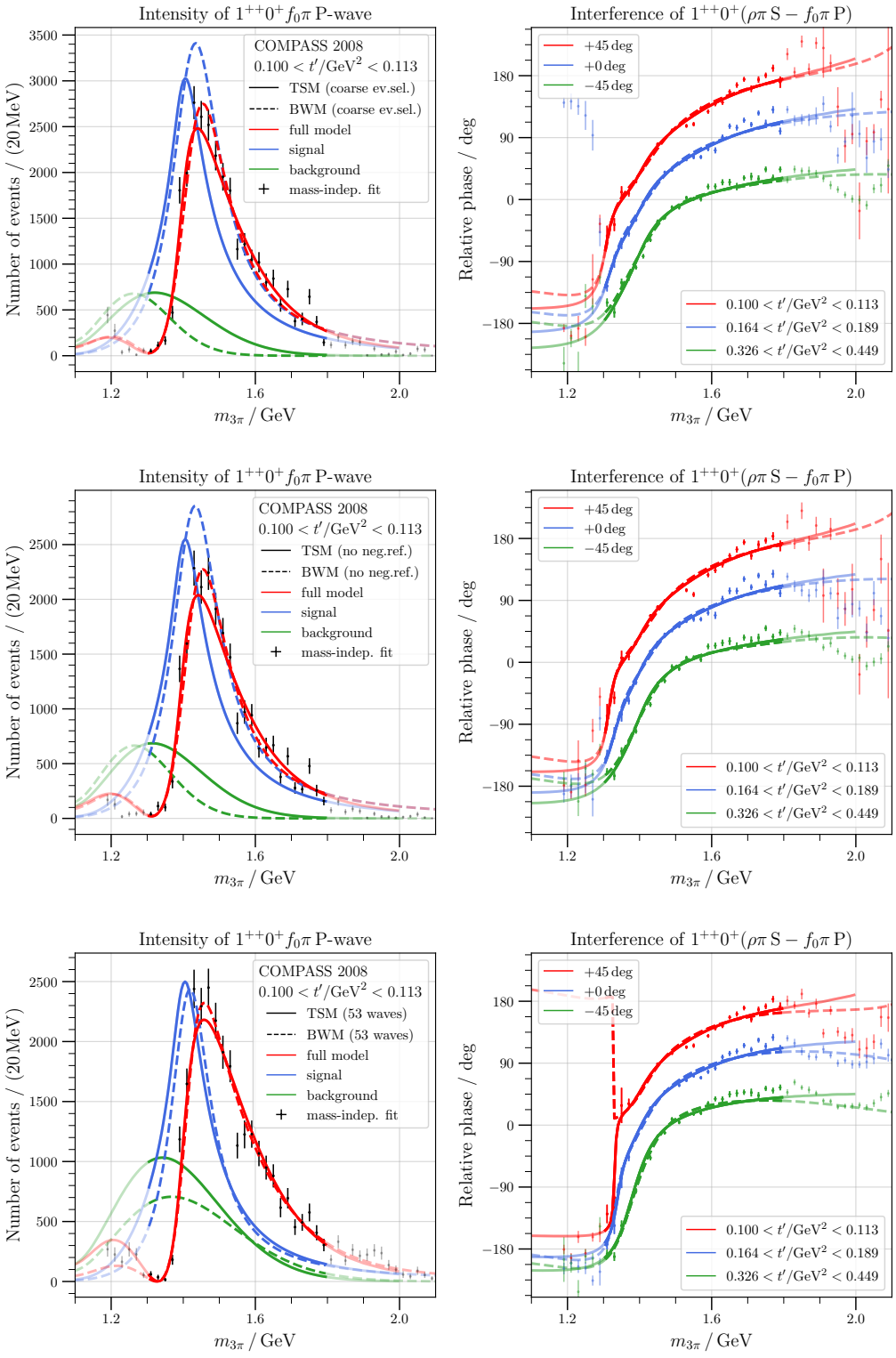

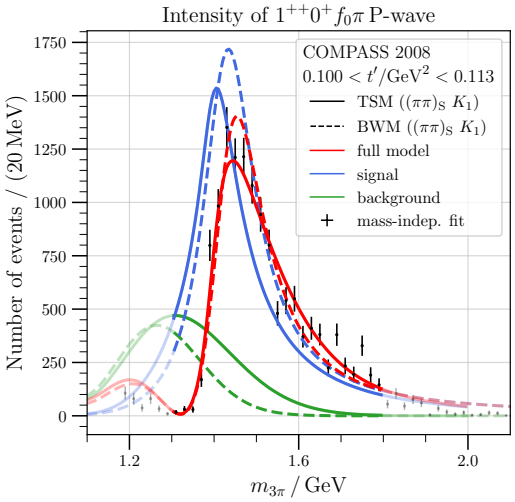
Intensity of $1^{++}0^+ f_0\pi$ P-wave
COMPASS 2008
$0.100 < t'/\mathrm{GeV}^2 < 0.113$
TSM $((\pi\pi)_S\ K_1)$
BWM $((\pi\pi)_S\ K_1)$
full model
signal
background
mass-indep. fit
Number of events / (20 MeV)
$m_{3\pi}$ / GeV

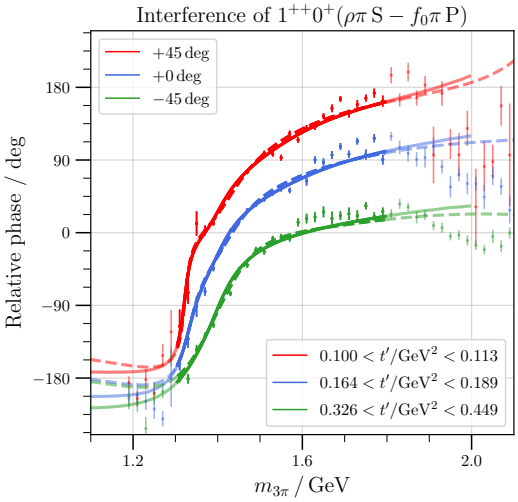
Interference of $1^{++}0^+(\rho\pi\,\mathrm{S} - f_0\pi\,\mathrm{P})$
+45 deg
+0 deg
−45 deg
$0.100 < t'/\mathrm{GeV}^2 < 0.113$
$0.164 < t'/\mathrm{GeV}^2 < 0.189$
$0.326 < t'/\mathrm{GeV}^2 < 0.449$
Relative phase / deg
$m_{3\pi}$ / GeV

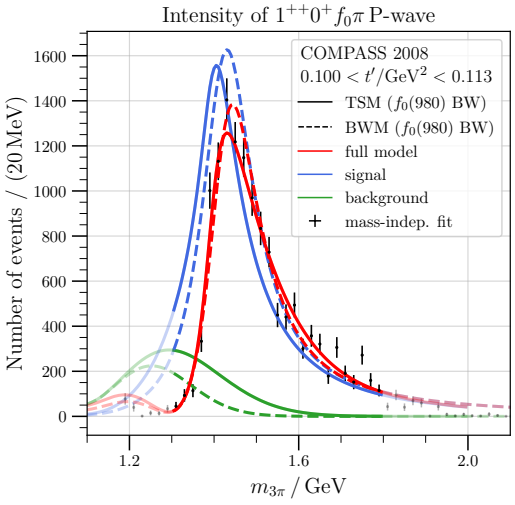
Intensity of $1^{++}0^+ f_0\pi$ P-wave
COMPASS 2008
$0.100 < t'/\mathrm{GeV}^2 < 0.113$
TSM ($f_0(980)$ BW)
BWM ($f_0(980)$ BW)
full model
signal
background
mass-indep. fit
Number of events / (20 MeV)
$m_{3\pi}$ / GeV

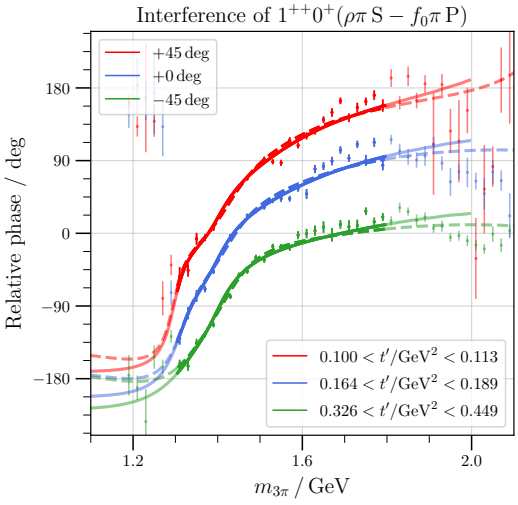
Interference of $1^{++}0^+(\rho\pi\,\mathrm{S} - f_0\pi\,\mathrm{P})$
+45 deg
+0 deg
−45 deg
$0.100 < t'/\mathrm{GeV}^2 < 0.113$
$0.164 < t'/\mathrm{GeV}^2 < 0.189$
$0.326 < t'/\mathrm{GeV}^2 < 0.449$
Relative phase / deg
$m_{3\pi}$ / GeV

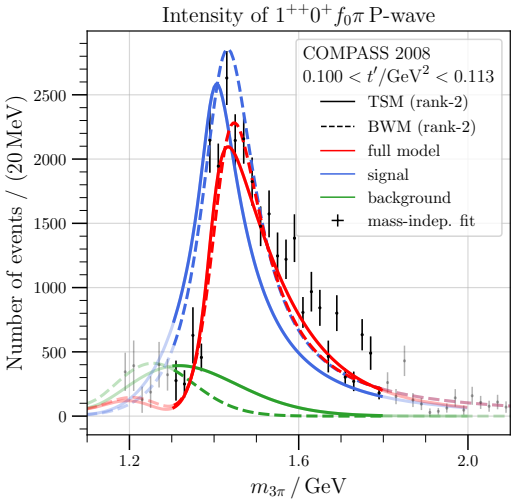
Intensity of $1^{++}0^+ f_0\pi$ P-wave
COMPASS 2008
$0.100 < t'/\mathrm{GeV}^2 < 0.113$
TSM (rank-2)
BWM (rank-2)
full model
signal
background
mass-indep. fit
Number of events / (20 MeV)
$m_{3\pi}$ / GeV

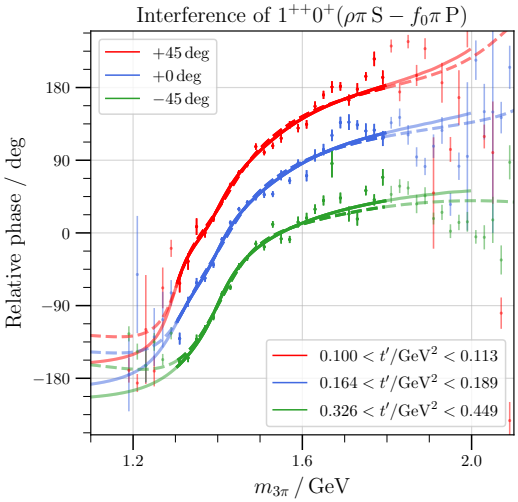
Interference of $1^{++}0^+(\rho\pi\,\mathrm{S} - f_0\pi\,\mathrm{P})$
+45 deg
+0 deg
−45 deg
$0.100 < t'/\mathrm{GeV}^2 < 0.113$
$0.164 < t'/\mathrm{GeV}^2 < 0.189$
$0.326 < t'/\mathrm{GeV}^2 < 0.449$
Relative phase / deg
$m_{3\pi}$ / GeV

C.5 Remaining t' Slices for the Bootstrap Fit

An explanation of the following plots can be found in section 4.6.4 and the first t' slice in Figure 4.23, therefore, we omit the captions to save space.

2)

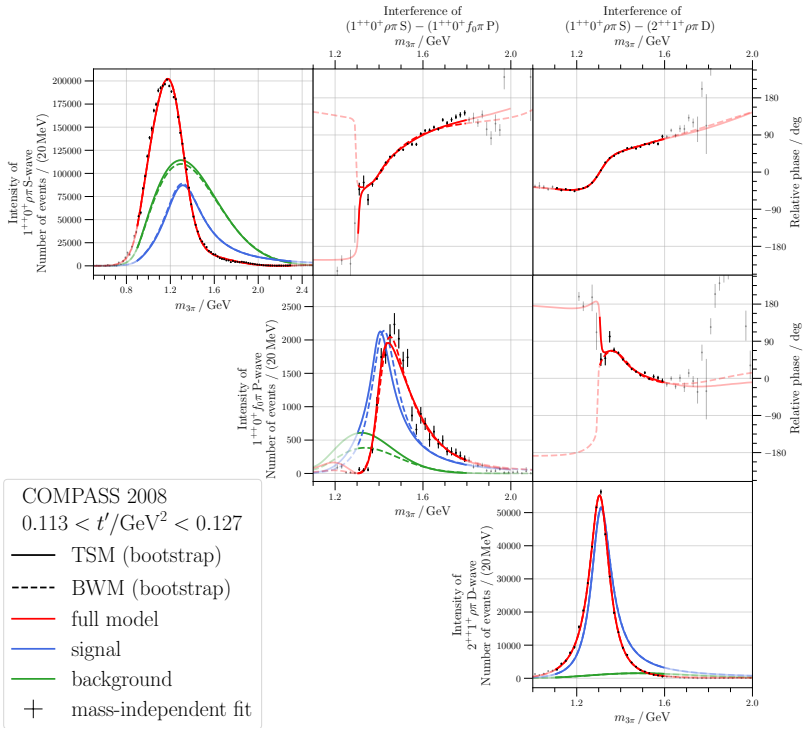

3)

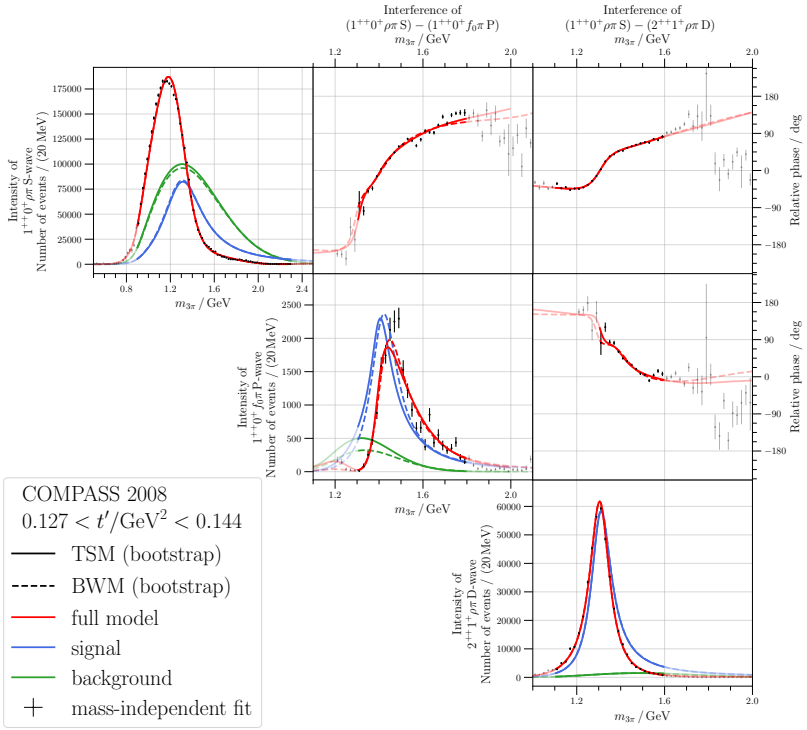

4)

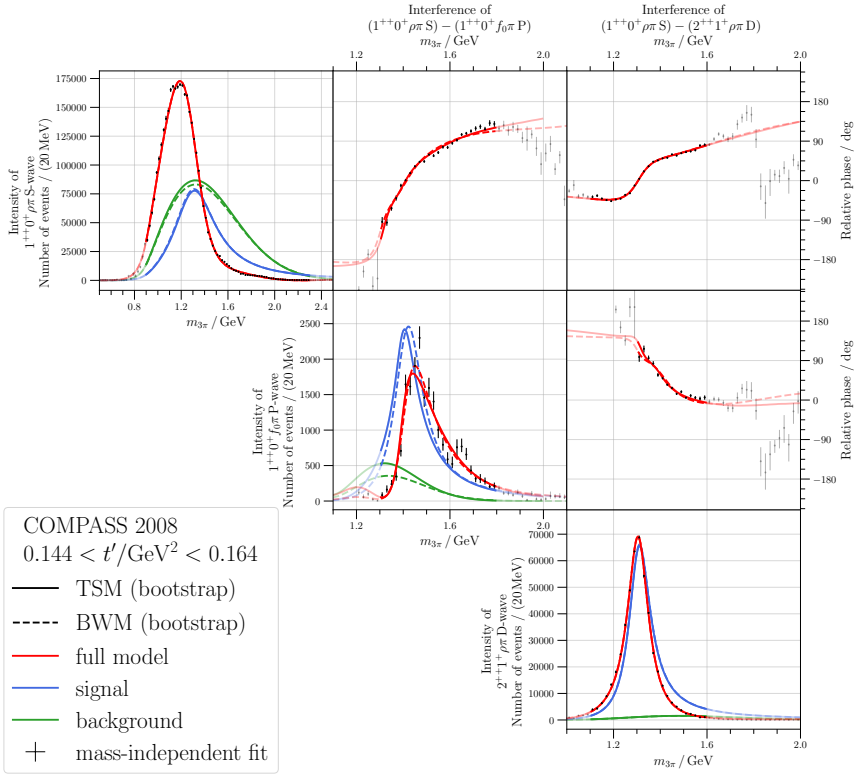
Interference of
$(1^{++}0^+\rho\pi\,\mathrm{S}) - (1^{++}0^+f_0\pi\,\mathrm{P})$
$m_{3\pi}$ / GeV
Interference of
$(1^{++}0^+\rho\pi\,\mathrm{S}) - (2^{++}1^+\rho\pi\,\mathrm{D})$
$m_{3\pi}$ / GeV
Intensity of
$1^{++}0^+\rho\pi$ S-wave
Number of events / (20 MeV)
Intensity of
$1^{++}0^+f_0\pi$ P-wave
Number of events / (20 MeV)
Intensity of
$2^{++}1^+\rho\pi$ D-wave
Number of events / (20 MeV)
Relative phase / deg
$m_{3\pi}$ / GeV
COMPASS 2008
$0.144 < t'/\mathrm{GeV}^2 < 0.164$
TSM (bootstrap)
BWM (bootstrap)
full model
signal
background
mass-independent fit

5)

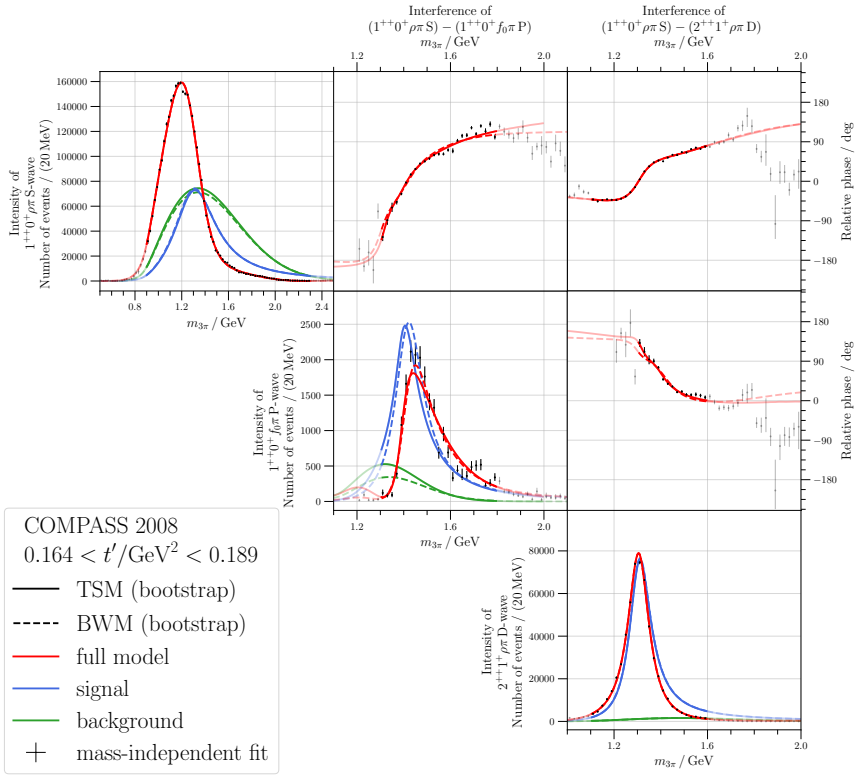
Interference of
$(1^{++}0^+\rho\pi\,\mathrm{S}) - (1^{++}0^+f_0\pi\,\mathrm{P})$
$m_{3\pi}$ / GeV
Interference of
$(1^{++}0^+\rho\pi\,\mathrm{S}) - (2^{++}1^+\rho\pi\,\mathrm{D})$
$m_{3\pi}$ / GeV
Intensity of
$1^{++}0^+\rho\pi$ S-wave
Number of events / (20 MeV)
Intensity of
$1^{++}0^+f_0\pi$ P-wave
Number of events / (20 MeV)
Intensity of
$2^{++}1^+\rho\pi$ D-wave
Number of events / (20 MeV)
Relative phase / deg
$m_{3\pi}$ / GeV
COMPASS 2008
$0.164 < t'/\mathrm{GeV}^2 < 0.189$
TSM (bootstrap)
BWM (bootstrap)
full model
signal
background
mass-independent fit

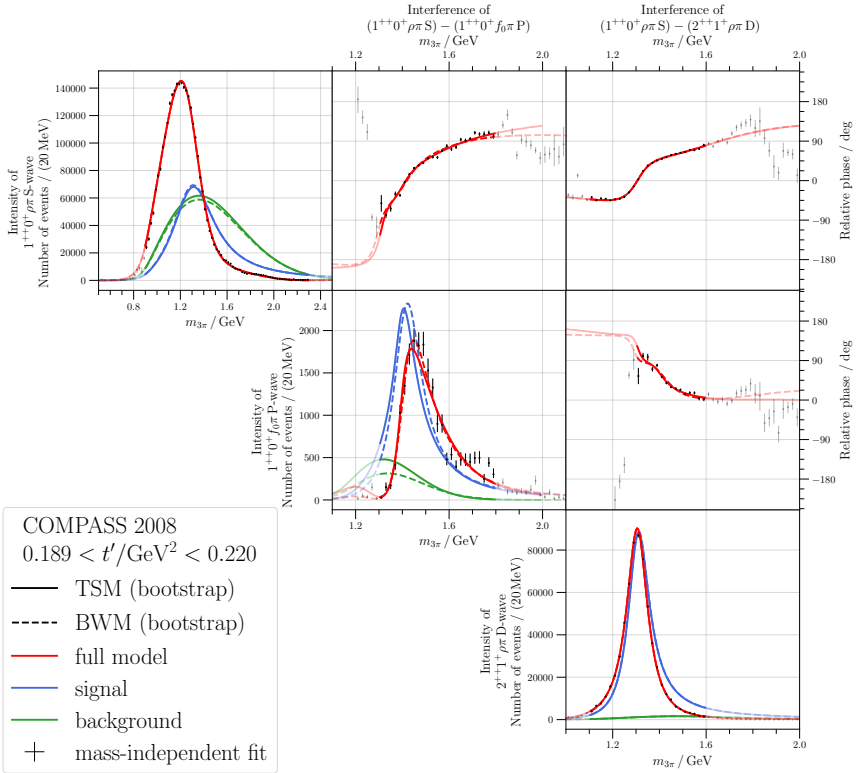
Interference of
$(1^{++}0^+\rho\pi\,\mathrm{S}) - (1^{++}0^+f_0\pi\,\mathrm{P})$
$m_{3\pi}$ / GeV
Interference of
$(1^{++}0^+\rho\pi\,\mathrm{S}) - (2^{++}1^+\rho\pi\,\mathrm{D})$
$m_{3\pi}$ / GeV
Intensity of
$1^{++}0^+\rho\pi$ S-wave
Number of events / (20 MeV)
$m_{3\pi}$ / GeV
Intensity of
$1^{++}0^+f_0\pi$ P-wave
Number of events / (20 MeV)
$m_{3\pi}$ / GeV
Intensity of
$2^{++}1^+\rho\pi$ D-wave
Number of events / (20 MeV)
$m_{3\pi}$ / GeV
Relative phase / deg
Relative phase / deg
COMPASS 2008
$0.189 < t'/\mathrm{GeV}^2 < 0.220$
TSM (bootstrap)
BWM (bootstrap)
full model
signal
background
mass-independent fit

6)

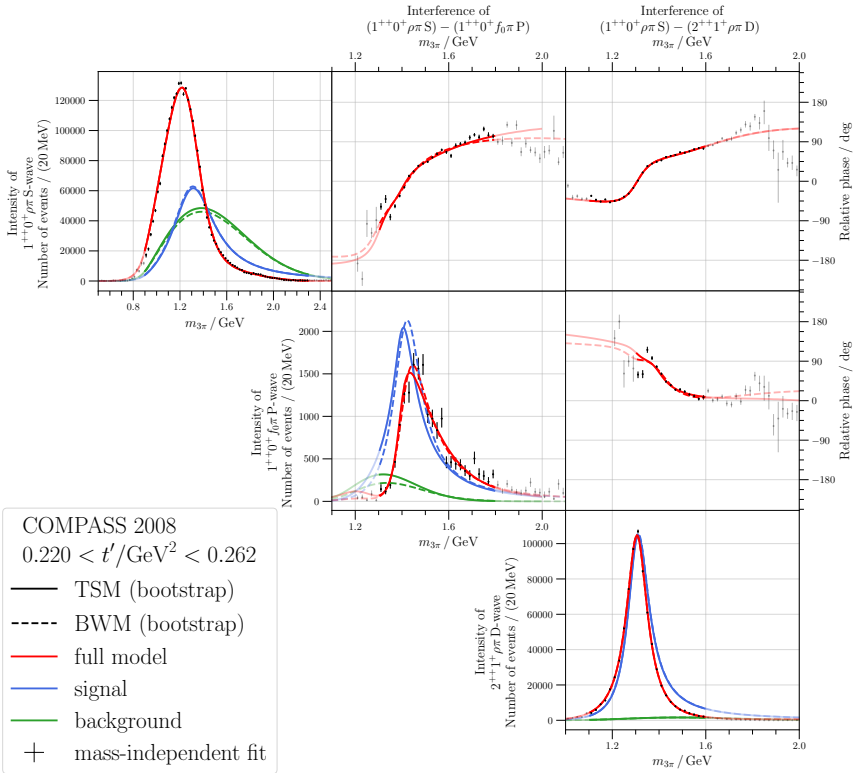
Interference of
$(1^{++}0^+\rho\pi\,\mathrm{S}) - (1^{++}0^+f_0\pi\,\mathrm{P})$
$m_{3\pi}$ / GeV
Interference of
$(1^{++}0^+\rho\pi\,\mathrm{S}) - (2^{++}1^+\rho\pi\,\mathrm{D})$
$m_{3\pi}$ / GeV
Intensity of
$1^{++}0^+\rho\pi$ S-wave
Number of events / (20 MeV)
$m_{3\pi}$ / GeV
Intensity of
$1^{++}0^+f_0\pi$ P-wave
Number of events / (20 MeV)
$m_{3\pi}$ / GeV
Intensity of
$2^{++}1^+\rho\pi$ D-wave
Number of events / (20 MeV)
$m_{3\pi}$ / GeV
Relative phase / deg
Relative phase / deg
COMPASS 2008
$0.220 < t'/\mathrm{GeV}^2 < 0.262$
TSM (bootstrap)
BWM (bootstrap)
full model
signal
background
mass-independent fit

7)

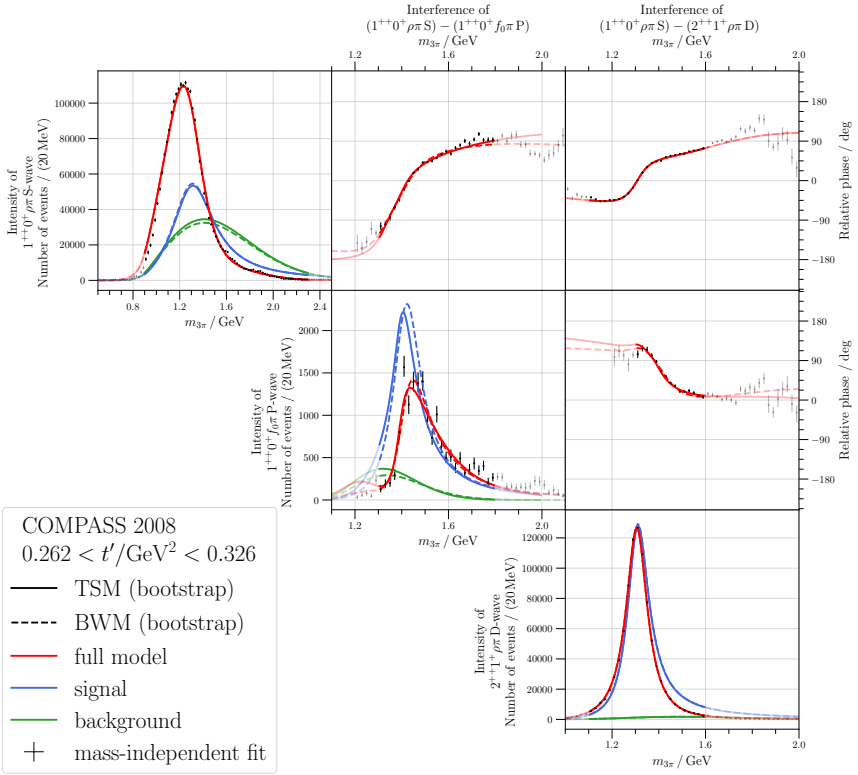
Interference of
$(1^{++}0^+\rho\pi\,\mathrm{S}) - (1^{++}0^+f_0\pi\,\mathrm{P})$
$m_{3\pi}$ / GeV
Interference of
$(1^{++}0^+\rho\pi\,\mathrm{S}) - (2^{++}1^+\rho\pi\,\mathrm{D})$
$m_{3\pi}$ / GeV
Intensity of
$1^{++}0^+\rho\pi$ S-wave
Number of events / (20 MeV)
$m_{3\pi}$ / GeV
Intensity of
$1^{++}0^+f_0\pi$ P-wave
Number of events / (20 MeV)
$m_{3\pi}$ / GeV
Intensity of
$2^{++}1^+\rho\pi$ D-wave
Number of events / (20 MeV)
$m_{3\pi}$ / GeV
Relative phase / deg
COMPASS 2008
$0.262 < t'/\mathrm{GeV}^2 < 0.326$
TSM (bootstrap)
BWM (bootstrap)
full model
signal
background
mass-independent fit

8)

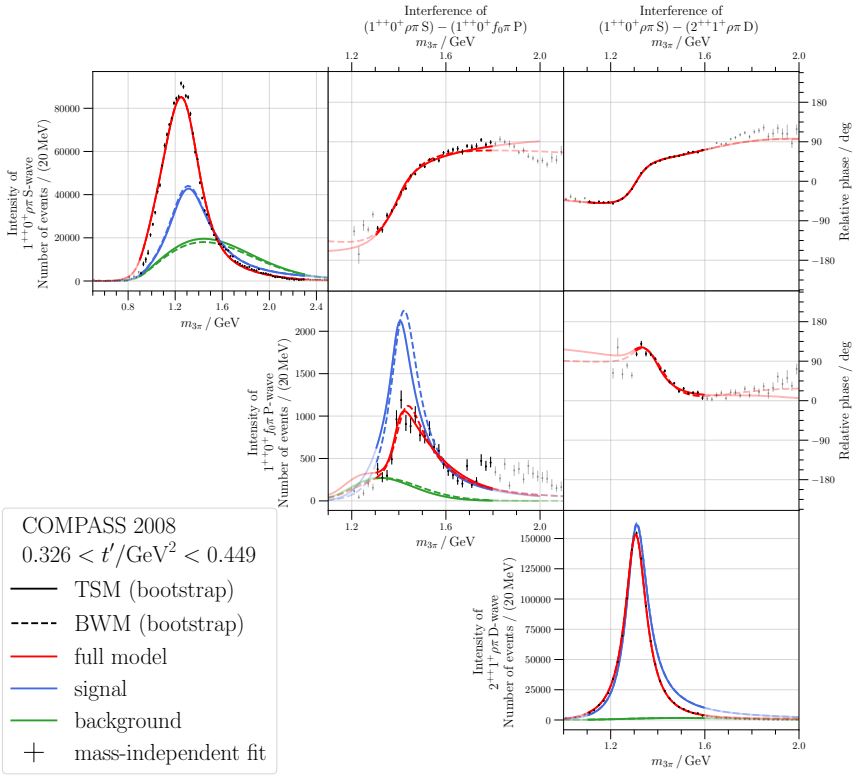
Interference of
$(1^{++}0^+\rho\pi\,\mathrm{S}) - (1^{++}0^+f_0\pi\,\mathrm{P})$
$m_{3\pi}$ / GeV
Interference of
$(1^{++}0^+\rho\pi\,\mathrm{S}) - (2^{++}1^+\rho\pi\,\mathrm{D})$
$m_{3\pi}$ / GeV
Intensity of
$1^{++}0^+\rho\pi$ S-wave
Number of events / (20 MeV)
$m_{3\pi}$ / GeV
Intensity of
$1^{++}0^+f_0\pi$ P-wave
Number of events / (20 MeV)
$m_{3\pi}$ / GeV
Intensity of
$2^{++}1^+\rho\pi$ D-wave
Number of events / (20 MeV)
$m_{3\pi}$ / GeV
Relative phase / deg
COMPASS 2008
$0.326 < t'/\mathrm{GeV}^2 < 0.449$
TSM (bootstrap)
BWM (bootstrap)
full model
signal
background
mass-independent fit

9)

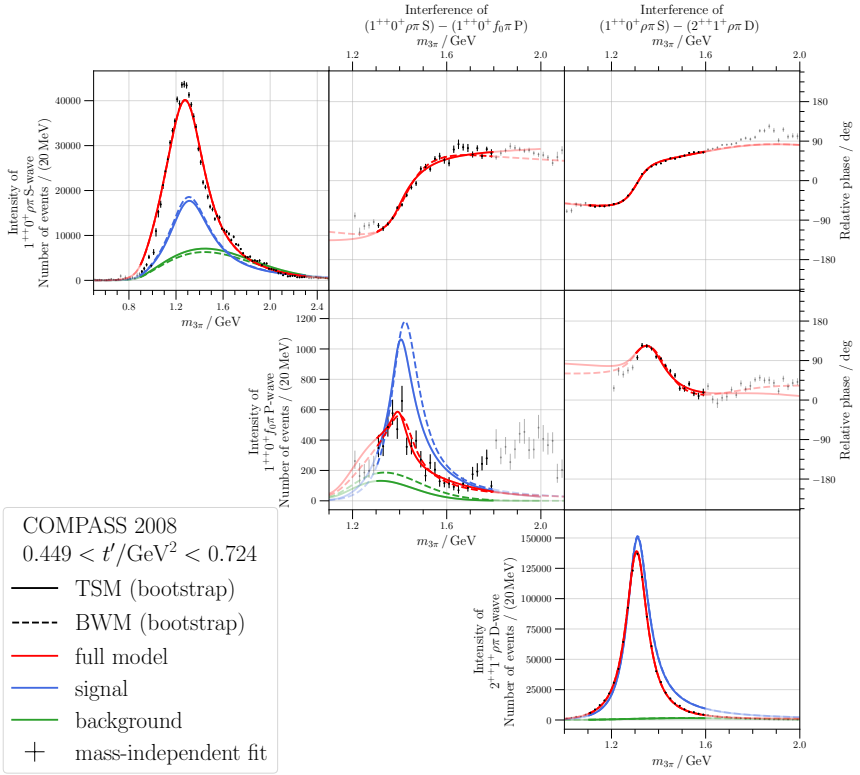
Interference of
$(1^{++}0^+\rho\pi\,\mathrm{S}) - (1^{++}0^+f_0\pi\,\mathrm{P})$
$m_{3\pi}$ / GeV
Interference of
$(1^{++}0^+\rho\pi\,\mathrm{S}) - (2^{++}1^+\rho\pi\,\mathrm{D})$
$m_{3\pi}$ / GeV
Intensity of
$1^{++}0^+\rho\pi$ S-wave
Number of events / (20 MeV)
Intensity of
$1^{++}0^+f_0\pi$ P-wave
Number of events / (20 MeV)
Intensity of
$2^{++}1^+\rho\pi$ D-wave
Number of events / (20 MeV)
Relative phase / deg
$m_{3\pi}$ / GeV
COMPASS 2008
$0.449 < t'/\mathrm{GeV}^2 < 0.724$
TSM (bootstrap)
BWM (bootstrap)
full model
signal
background
mass-independent fit

10)

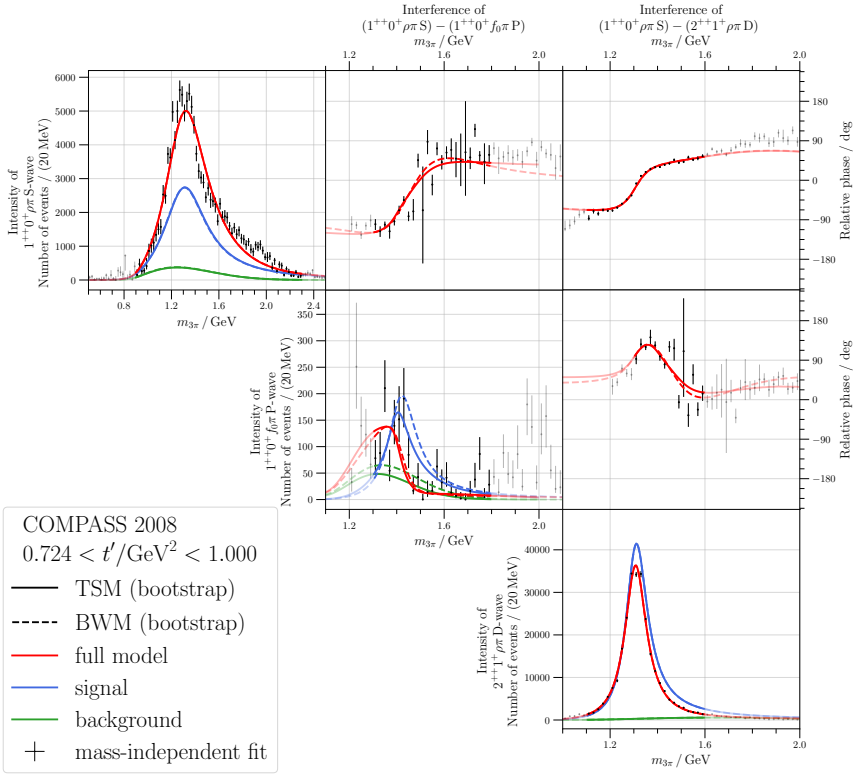
Interference of
$(1^{++}0^+\rho\pi\,\mathrm{S}) - (1^{++}0^+f_0\pi\,\mathrm{P})$
$m_{3\pi}$ / GeV
Interference of
$(1^{++}0^+\rho\pi\,\mathrm{S}) - (2^{++}1^+\rho\pi\,\mathrm{D})$
$m_{3\pi}$ / GeV
Intensity of
$1^{++}0^+\rho\pi$ S-wave
Number of events / (20 MeV)
Intensity of
$1^{++}0^+f_0\pi$ P-wave
Number of events / (20 MeV)
Intensity of
$2^{++}1^+\rho\pi$ D-wave
Number of events / (20 MeV)
Relative phase / deg
$m_{3\pi}$ / GeV
COMPASS 2008
$0.724 < t'/\mathrm{GeV}^2 < 1.000$
TSM (bootstrap)
BWM (bootstrap)
full model
signal
background
mass-independent fit

11)

APPENDIX D

Further Details of the $\pi^- K^0_S K^0_S$ Event Selection

D.1 $\pi^- K^0_S K^0_S$ with $K^0_S \to \pi^0\pi^0$

In order to obtain more events, one could think of trying to also include the neutral decay mode of $K^0_S \to \pi^0\pi^0$. However, as mentioned in section 5.1.3 this comes with some obstacles. Let us derive the relations that one would have to fulfill in order to obtain a K^0_S vector from four photon clusters. First, we define the known position of the photon clusters with respect to the PV by $\vec{r}_i$, where the index denotes one possible arrangement of the four photons. In the end one would have to try all three possible permutations to create two pairs out of four indices: $\{((1,2),(3,4)),((1,3),(2,4)),((1,4),(2,3))\}$. Also we denote the measured energy of the photons with E_i. The unknown quantity to extract is the position of the SV relative to the PV denoted by $\vec{R}$.

The 3-vector of the photons will be obtained by

$$\vec{p}_i = E_i \frac{\vec{r}_i - \vec{R}}{\left|\vec{r}_i - \vec{R}\right|} = E_i \frac{\vec{\delta}_i}{\delta_i} \qquad \text{with} \qquad \vec{\delta}_i := \vec{r}_i - \vec{R} \quad \text{and} \quad \delta_i := \left|\vec{r}_i - \vec{R}\right|,$$

where we already incorporated the mass condition $m_\gamma^2 = E_i^2 - \left|\vec{p}_i\right|^2 = 0$. The Minkowski product of the photon 4-vectors yields

$$p_1 \cdot p_2 = E_1 E_2 \left[1 - \frac{\vec{\delta}_1 \cdot \vec{\delta}_2}{\delta_1 \delta_2}\right] = E_1 E_2 (1 - \cos\theta_{12}), \qquad \cos\theta_{12} := \frac{\vec{\delta}_1 \cdot \vec{\delta}_2}{\delta_1 \delta_2} \tag{D.1}$$

with θ_{12} being the opening angle between the photon pair. Requiring the photon pair to come from a π^0, meaning $(p_1 + p_2)^2 \stackrel{!}{=} m^2_{\pi^0}$, completely constrains the opening angle to

$$\cos\theta_{12} = 1 - \frac{m^2_{\pi^0}}{2E_1 E_2}. \tag{D.2}$$

Now, we take two photon pairs fulfilling this constraint and combine them to a K_S^0:

$$\begin{aligned} m_{K_S^0}^2 &= \left(p_{\pi^0}^{(1)} + p_{\pi^0}^{(2)}\right)^2 = 2m_{\pi^0}^2 + 2p_{\pi^0}^{(1)} \cdot p_{\pi^0}^{(2)} \\ &= 2m_{\pi^0}^2 + 2(p_1 + p_2) \cdot (p_3 + p_4) = 2m_{\pi^0}^2 + 2\sum_{(i,j)} p_i \cdot p_j, \end{aligned}$$

where the sum goes over the index pairs $\{(1,3),(1,4),(2,3),(2,4)\}$. We can write the first summand with equation (D.1) as

$$\begin{aligned} p_1 \cdot p_3 &= E_1 E_3 \left[1 - \frac{\vec{\delta}_1 \cdot (\vec{\delta}_2 + \vec{\delta}_3 - \vec{\delta}_2)}{\delta_1 \delta_3}\right] \\ &= E_1 E_3 \left[1 - \frac{\delta_2}{\delta_3}\cos\theta_{12} - \frac{\vec{\delta}_1}{\delta_1} \cdot \frac{\vec{r}_3 - \vec{r}_2}{\delta_3}\right]. \end{aligned}$$

Since most of the photons are measured inside the second electromagnetic calorimeter ECAL2, we can make some simplifications by assuming that all of them are measured there. The geometrical dimension of ECAL2 is 2.44 m × 1.83 m [11]. Therefore, to be able to detect a pair of photons, the transverse distance of the cluster to the SV (situated approximately in the middle of the two photons) is maximally half of this, meaning $x_i - X < 1.22\,\text{m}$ and $y_i - Y < 0.92\,\text{m}$. For the longitudinal distance we can look at the expected maximal flight distance of a K_S^0. As discussed in section 5.1.3, most of them will decay already within 10 m, however, ECAL2 is located roughly 34 m behind the target, giving us a lower limit of $z - Z > 24\,\text{m}$. Therefore, the magnitudes δ_i can be approximated by only taking the z directions:

$$\delta_i = \sqrt{(x_i - X)^2 + (y_i - Y)^2 + (z_i - Z)^2} \approx (z_i - Z) \equiv (z - Z) \qquad \text{with} \quad \vec{r}_i := \begin{pmatrix} x_i \\ y_i \\ z_i \end{pmatrix} \quad \text{and} \quad \vec{R} := \begin{pmatrix} X \\ Y \\ Z \end{pmatrix},$$

where, in the last step, we use the fact that all photons are measured inside ECAL2, resulting in equal z_i – the distance to the PV – for all of them. Using the limiting values from above, we get a relative difference of only 2 ‰.

This simplifies the products of 4-momenta:

$$\begin{aligned} p_1 \cdot p_3 &\approx E_1 E_3 \left[1 - \cos\theta_{12} - \frac{\vec{\delta}_1 \cdot (\vec{r}_3 - \vec{r}_2)}{(z - Z)^2}\right] \\ &= \frac{E_3}{2E_2} m_{\pi^0}^2 - E_1 E_3 \frac{(x_1 - X)(x_3 - x_2) + (y_1 - Y)(y_3 - y_2)}{(z - Z)^2}. \end{aligned}$$

Here, we use equation (D.2) and the fact that the z component of $\vec{r}_3 - \vec{r}_2$ vanishes if all photon clusters are located in ECAL2.

We can obtain the corresponding equations for $p_2 \cdot p_3$, $p_1 \cdot p_4$ and $p_2 \cdot p_4$ by replacing the indices

$1 \leftrightarrow 2$ and $3 \leftrightarrow 4$ as needed. Collecting all terms yields

$$m_{K_S^0}^2 = m_{\pi^0}^2 \left(2 + \frac{E_3}{E_2} + \frac{E_3}{E_1} + \frac{E_4}{E_2} + \frac{E_4}{E_1}\right) - \frac{f(X,Y)}{(z-Z)^2}, \tag{D.3}$$

where $f(X,Y)$ is a long, but well-defined function of the transversal SV position. We can also apply the simplifications to the constraint from the π^0 mass, meaning equations (D.1) and (D.2):

$$1 - \frac{m_{\pi^0}^2}{2E_1E_2} = \frac{\vec{\delta}_1 \cdot (\vec{\delta}_1 + \vec{\delta}_2 - \vec{\delta}_1)}{\delta_1\delta_2} = \frac{\delta_1}{\delta_2} + \frac{\vec{\delta}_1 \cdot (\vec{r}_2 - \vec{r}_1)}{\delta_1\delta_2} \approx 1 + \frac{(x_1 - X)(x_2 - x_1) + (y_1 - Y)(y_2 - y_1)}{(z-Z)^2}.$$

The numerator on the right-hand side is always negative, because X and Y have to lie between the x_i and y_i, respectively. Therefore, always one of the two brackets is negative.

$$\frac{m_{\pi^0}^2}{2E_1E_2} = \frac{(x_1 - X)(x_1 - x_2) + (y_1 - Y)(y_1 - y_2)}{(z-Z)^2} \qquad \text{and with indices} \quad (1,2) \to (3,4) \tag{D.4}$$

With equations (D.3) and (D.4), now we have three constraints which in principle allow us to determine X, Y and Z. The problem is that this will work for all three possible permutations as mentioned at the beginning, yielding three candidates for a SV.

To solve this dilemma, one can use the collinearity angle as discussed in section 5.2.3, which is enclosed by the line that connects the SV with the PV and the momentum direction of the reconstructed K_S^0. In the case of the charged decay mode, this angle was very small, however, here one would expect some distribution and would have to determine a cut-off value with a significance study.

Although technically possible, this final state is not very useful to consider. Reasons beside the difficulty are given in the main text at the end of section 5.1.3.

D.2 Event Selection with $N_{\text{out}}^{\text{BPV}} \leq 5$

The plots in Figure D.1 were obtained at the end of the fine selection with an earlier development stage of the event selection on `Slot4` data, where the cut on $N_{\text{out}}^{\text{BPV}} \leq 2$ was not performed during the preselection. Also, no vertex separation was required for the SVs. One can see in Figure D.1(a) that the distributions of the resonance mass for $N_{\text{out}}^{\text{BPV}} \geq 3$ develop a peak at higher masses hinting towards a less homogeneous detector acceptance, or simply a stronger background from a different reaction. Figure D.1(b) shows the number of selected events for each $N_{\text{out}}^{\text{BPV}}$ class. All together the number of selected events for $N_{\text{out}}^{\text{BPV}} \geq 3$ only amounts to roughly 10 ‰, therefore, including them would rather increase the background than actually being beneficial.

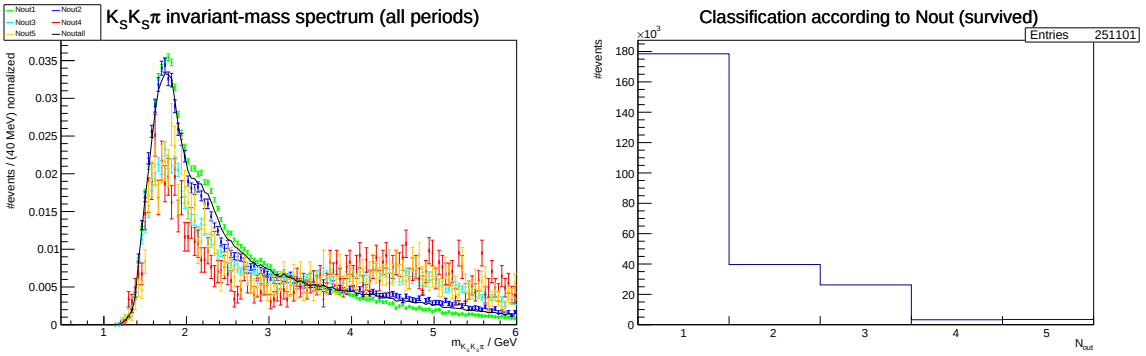

(a) Resonance mass

(b) Number of selected events

Figure D.1: In the left plot, the resonance-mass distribution after the fine selection of `Slot4` data is shown for different values of $N_{\text{out}}^{\text{BPV}}$ as indicated by the legend. The distribution is normalized to an integral of 1 for easier comparison. The right plot shows the amount of selected "good" events at the end of the selection.

D.3 Kinematic Fit

As mentioned in section 5.2.3, the kinematic fit is a special case of constraint fitting described in [67]. It was implemented for COMPASS by Tobias Schlüter [93] in order to fit two photon clusters to the mass of a π^0 coming from the BPV. Since photons are massless, some adjustments to the minimization condition have to be made for fitting of K_S^0 decaying to two charged pions. Also, the way how we obtain the detector uncertainty for the daughter tracks is different, since here, we are dealing with charged tracks. We will start with a short summary of the general procedure and follow up with the changes for K_S^0-fitting compared to π^0-fitting. We conclude with a simple estimation of the success rate of the algorithm.

D.3.1 General Procedure

Since the Gaussian width of $\sim 5\,\text{MeV}$ of the K_S^0 that we observe during the event selection (cf. Figure 5.14) is coming only from detector uncertainties, we can "correct" the K_S^0 momentum with the constraint that it has to have the nominal K_S^0 mass as given by the PDG. The constraint reads as

$$F(v) = (p_1 + p_2)^2 - m^2_{K_S^0} = 0, \quad \text{with } v = \left(\frac{p_{1x}}{|\vec{p}_1|}, \frac{p_{1y}}{|\vec{p}_1|}, E_1, \frac{p_{2x}}{|\vec{p}_2|}, \frac{p_{2y}}{|\vec{p}_2|}, E_2 \right). \tag{D.5}$$

With this we can numerically minimize $\chi^2 := \epsilon^T C^{-1} \epsilon$ with the condition $F(v + \epsilon) = 0$ defining the ϵ-vector, and C being the covariance matrix of v.

The program of Tobias Schlüter described in [93] uses the following three variables per particle for the minimization

$$E, \quad x := \frac{p_x}{|\vec{p}|}, \quad y := \frac{p_y}{|\vec{p}|}, \qquad \text{with } z := \frac{p_z}{|\vec{p}|} = \sqrt{1 - x^2 - y^2}.$$

Since the program was created to specifically fit neutral mesons decaying into photon pairs (e.g. π^0 and η), some adjustments have to be made.

D.3.2 Adjustments for K_S^0-Fitting

One can use the code from [93] as a base and has to adjust some of the functions as described in the following. The C++ function `massdiff`, corresponding to $F(v)$ from equation (D.5) to calculate the difference between the actual and the required mass, changes from

$$\texttt{massdiff} = 2 \cdot E_1 \cdot E_2 \cdot (1 - x_1 \cdot x_2 - y_1 \cdot y_2 - z_1 \cdot z_2) - m_{\pi^0}^2$$

to

$$d := \texttt{massdiff} = 2 \cdot \left(E_1 \cdot E_2 - \left|\vec{p}_1\right| \cdot \left|\vec{p}_2\right| \cdot (x_1 \cdot x_2 + y_1 \cdot y_2 + z_1 \cdot z_2) \right) + m_\pi^2 + m_\pi^2 - m_{K_S^0}^2 \quad \text{(D.6)}$$

with $|\vec{p}_i| = \sqrt{E_i^2 - m_i^2}$, because now we have non-vanishing rest masses of the daughters as well as a non-zero difference between E and $|\vec{p}|$.

Also derivatives in `dmassdiff` have to be changed accordingly

$$\texttt{dmassdiff} = \vec{\text{grad}}(d) = \begin{pmatrix} \frac{\partial d}{\partial x_1} \\ \frac{\partial d}{\partial y_1} \\ \frac{\partial d}{\partial E_1} \\ \frac{\partial d}{\partial x_2} \\ \frac{\partial d}{\partial y_2} \\ \frac{\partial d}{\partial E_2} \end{pmatrix} = \begin{pmatrix} 2\left|\vec{p}_1\right|\left|\vec{p}_2\right|(-x_2 + z_2 \frac{x_1}{z_1}) \\ 2\left|\vec{p}_1\right|\left|\vec{p}_2\right|(-y_2 + z_2 \frac{y_1}{z_1}) \\ 2\left(E_2 - \left|\vec{p}_2\right| \frac{E_1}{|\vec{p}_1|}(x_1x_2 + y_1y_2 + z_1z_2)\right) \\ 2\left|\vec{p}_1\right|\left|\vec{p}_2\right|(-x_1 + z_1 \frac{x_2}{z_2}) \\ 2\left|\vec{p}_1\right|\left|\vec{p}_2\right|(-y_1 + z_1 \frac{y_2}{z_2}) \\ 2\left(E_1 - \left|\vec{p}_1\right| \frac{E_2}{|\vec{p}_2|}(x_1x_2 + y_1y_2 + z_1z_2)\right) \end{pmatrix}. \quad \text{(D.7)}$$

Before, the inputs to the equations (D.6) and (D.7) were the $\vec{p}_\gamma$ directions obtained from $\vec{r}_{\text{Cluster}} - \vec{r}_{\text{BPV}}$, and the photon energy as determined by the `ECAL`s. Now, we can simply use the $\vec{p}_\pi$ directions and calculate the energy E_i from their measured momentum while making a pion-mass hypothesis $m_i = m_\pi$.

We also need a covariance matrix of the input variables for the minimization procedure. For the old code the uncertainties were taken from the covariance matrix of the calorimeter cluster `PaCaloClus cl` as provided by PHAST. For the K_S^0-fitting, we can use the uncertainties from the covariance matrix of the tracks of the daughter pions (`PaTPar`), but there is no direct access to the momentum vector $\vec{p}$.

In PHAST a track is defined by the "helix" parameters at a given z position: (`xpos`, `ypos`, `dx/dz`, `dy/dz`, `q/|p|`). We can obtain the momentum ratios from `dx/dz` and `dy/dz` and redefine

$$a := \frac{p_x}{p_z} = \texttt{dx/dz}, \quad b := \frac{p_y}{p_z} = \texttt{dy/dz}, \quad c := \frac{1}{|\vec{p}|} = \texttt{q/|p|} \quad \text{(D.8)}$$

Note that for neutral particle the last helix component is always set positive with `q` = 1 in PHAST. We

can obtain the needed covariance matrix with the following basis transformation:

$$\begin{pmatrix} \texttt{xpos} \\ \texttt{ypos} \\ a \\ b \\ c \end{pmatrix} \rightarrow \begin{pmatrix} p_x = a \cdot p_z \\ p_y = b \cdot p_z \\ p_z = 1 \Big/ \left(c\sqrt{a^2 + b^2 + 1}\right) \\ E = \sqrt{m^2 + 1/c^2} \end{pmatrix},$$

where one can calculate p_z first and, then, p_x and p_y using p_z.
Taking its Jacobian

$$B = \begin{pmatrix} 0 & 0 & \frac{\mathrm{d}p_x}{\mathrm{d}a} & \frac{\mathrm{d}p_x}{\mathrm{d}b} & \frac{\mathrm{d}p_x}{\mathrm{d}c} \\ 0 & 0 & \frac{\mathrm{d}p_y}{\mathrm{d}a} & \frac{\mathrm{d}p_y}{\mathrm{d}b} & \frac{\mathrm{d}p_y}{\mathrm{d}c} \\ 0 & 0 & \frac{\mathrm{d}p_z}{\mathrm{d}a} & \frac{\mathrm{d}p_z}{\mathrm{d}b} & \frac{\mathrm{d}p_z}{\mathrm{d}c} \\ 0 & 0 & \frac{\mathrm{d}E}{\mathrm{d}a} & \frac{\mathrm{d}E}{\mathrm{d}b} & \frac{\mathrm{d}E}{\mathrm{d}c} \end{pmatrix} = \begin{pmatrix} 0 & 0 & p_z + a \cdot \frac{\mathrm{d}p_z}{\mathrm{d}a} & a \cdot \frac{\mathrm{d}p_z}{\mathrm{d}b} & a \cdot \frac{\mathrm{d}p_z}{\mathrm{d}c} \\ 0 & 0 & a \cdot \frac{\mathrm{d}p_z}{\mathrm{d}a} & p_z + b \cdot \frac{\mathrm{d}p_z}{\mathrm{d}b} & b \cdot \frac{\mathrm{d}p_z}{\mathrm{d}c} \\ 0 & 0 & -a \cdot c^2 \cdot p_z^3 & -b \cdot c^2 \cdot p_z^3 & \frac{-p_z}{c} \\ 0 & 0 & 0 & 0 & \frac{1}{E} \sum\limits_{i \in \{x,y,z\}} p_i \frac{\mathrm{d}p_i}{\mathrm{d}c} \end{pmatrix} \tag{D.9}$$

we can calculate the transformed covariance matrix via:

$$C_{\vec{p},E} = B \cdot C_{\text{helix}} \cdot B^{\mathrm{T}}. \tag{D.10}$$

At first, one should calculate the third row of the matrix, then, the first and second row, and finally, the last row, always using the already determined entries.

In the C++ code, the first argument of the function `cov_mat` has to be changed from type `const PaCaloClus &cl` to `const PaTPar &pars` and set the values for `x`, `y` and `z` to `pars.Px()`, `pars.Py()` and `pars.Pz()`, respectively. The correct normalization will be performed later.

After creating the transformation matrix `A`

$$\texttt{A} = \begin{pmatrix} \frac{p_y^2 + p_z^2}{|\vec{p}|^3} & -\frac{p_x p_y}{|\vec{p}|^3} & -\frac{p_x p_z}{|\vec{p}|^3} & 0 \\ -\frac{p_x p_y}{|\vec{p}|^3} & \frac{p_x^2 + p_z^2}{|\vec{p}|^3} & -\frac{p_y p_z}{|\vec{p}|^3} & 0 \\ 0 & 0 & 0 & 1 \end{pmatrix},$$

which deals with the change from (p_x, p_y, p_z, E) to (x, y, E), one has to obtain the matrix B according to equation (D.9). Then, one applies the similarity equation (D.10) with the transformation matrix B on C_{helix} first and on the result $C_{\vec{p},E}$ the same relation with A instead of B to obtain $C_{x,y,E}$. The full covariance matrix for the fitter can be built using the $C_{x,y,E}$ of each daughter particle as sub-matrices in the full 6×6 matrix for the input vector v, assuming independence of the two particles in their tracking and momentum reconstruction (i.e. by setting the remaining off-diagonal entries to 0).

The `PaTPar pars` for each daughter track are obtained after extrapolating the track to the corresponding SV position.

Providing all the necessary information to the function `kinfit`, which are the input vector $v = (x_1, y_1, E_1, x_2, y_2, E_2)$, the correctly transformed covariance matrix according to the above recipe, the minimizer function `massdiff` and its gradient `dmassdiff`, it will start the fitting procedure. During this procedure it will iteratively determine the small adjustments Δv to the input vector, such that $v_{\text{new}} = v + \Delta v$ results in a smaller `massdiff`. Therefore, the fit has 6 parameters that it can tune, one so-called `pull` per input parameter.

The fitting procedure is stopped successfully if the value obtained from `massdiff` in equation (D.6) divided by the squared mother mass is smaller than the chosen precision goal $\epsilon = 10^{-10}$:

$$\left| \frac{d}{m^2_{K^0_S}} \right| < \epsilon.$$

It fails if a negative squared momentum ($|\vec{p}|^2 = E^2 - m^2$) is obtained for the daughters during the fitting procedure or if the number of maximal iterations (by default 10) is reached.

The function `kinfit` provides the resulting `pulls` that are needed to calculate the new parameters by adding them to the old ones. Here, one has to calculate the new $|\vec{p}|$ from the new energy first and one has to make sure that one scales the obtained new x and y with this new momentum instead of the new energy, as it was done for the di-photon decays.

D.3.3 Success Rate of the Algorithm

To summarize, it could be confirmed by looking at the kinematically-fitted invariant mass of the K^0_S particles that the procedure works: it shifts all K^0_S to the nominal mass resulting in a δ-distribution. Both K^0_S of all events that surpass the "2 K^0_S" cut (see Figure 5.25) enter the kinematic fit. From these, we can estimate the failure rate of the fit by dividing the amount of failed fits by the total amount of performed fits. This results in a failure rate of only 0.0079 % for "far" K^0_S and a slightly higher one of 0.0211 % for "shared" K^0_S. The event is discarded if at least one of the two K^0_S-fits fails.

D.4 Planarity Angle

To summarize the following calculation in one sentence, the planarity angle ϕ_{recoil} is defined as the angle between the transverse[1] momentum components of the resonance X and the recoil proton.

Therefore, we need a way to calculate the transverse momentum with respect to the beam direction. Let us start with the longitudinal component $\vec{p}^{\,\parallel}$, since it is easier to calculate. If we draw the corresponding right-angled triangle, we see that the magnitude of this parallel momentum component, $p^{\parallel} := |\vec{p}^{\,\parallel}|$, can be obtained from the scattering angle θ via

$$p^{\parallel} = p \cdot \cos\theta = p \cdot \frac{(\vec{p} \cdot \vec{p}_{\text{beam}})}{p \cdot p_{\text{beam}}} = \vec{p} \cdot \hat{\vec{p}}_{\text{beam}},$$

[1] transverse relative to the beam axis

where the second equality is just the mathematical relation between the cosine of the angle between two vectors and their scalar product, and the "hat" in the final expression denotes the corresponding unit vector. With this, we have a simple way to calculate the magnitude of the parallel component. On the other hand, the direction is – by definition – the same as the beam direction. Therefore, we obtain the parallel momentum component with

$$\vec{p}^{\,\parallel} = (\vec{p} \cdot \hat{\vec{p}}_{\text{beam}})\hat{\vec{p}}_{\text{beam}}.$$

The transverse component is the remainder after subtracting the parallel component from the full momentum

$$\vec{p}^{\,\perp} = \vec{p} - \vec{p}^{\,\parallel} = \vec{p} - (\vec{p} \cdot \hat{\vec{p}}_{\text{beam}})\hat{\vec{p}}_{\text{beam}}.$$

With this, we can calculate the recoil and resonance momentum components transverse to the direction of the beam, and construct the normal vector to the plane spanned by these two transverse momenta

$$\begin{aligned}
\vec{p}^{\,\perp}_{\text{recoil}} &= \vec{p}_{\text{recoil}} - (\vec{p}_{\text{recoil}} \cdot \hat{\vec{p}}_{\text{beam}})\hat{\vec{p}}_{\text{beam}} \\
\vec{p}^{\,\perp}_{\text{X}} &= \vec{p}_{\text{X}} - (\vec{p}_{\text{X}} \cdot \hat{\vec{p}}_{\text{beam}})\hat{\vec{p}}_{\text{beam}} \\
\vec{n} &= \vec{p}^{\,\perp}_{\text{X}} \times \vec{p}^{\,\perp}_{\text{recoil}}, \qquad \text{(scale } \vec{n} \text{ by } -1 \text{ if } n_z > 0\text{)},
\end{aligned}$$

where $\vec{p}_X$ denotes the $\pi^- K_S^0 K_S^0$ momentum (after the kinematic fitting of the K_S^0). With this we can finally calculate the planarity angle:

$$\begin{aligned}
x &= \cos\phi_{\text{recoil}} = \hat{\vec{p}}^{\,\perp}_{\text{X}} \cdot \hat{\vec{p}}^{\,\perp}_{\text{recoil}} \\
y &= \sin\phi_{\text{recoil}} = \frac{(\vec{n} \times \vec{p}^{\,\perp}_{\text{X}})}{\left|(\vec{n} \times \vec{p}^{\,\perp}_{\text{X}})\right|} \cdot \hat{\vec{p}}^{\,\perp}_{\text{recoil}} \\
\phi_{\text{recoil}} &= \texttt{atan2}(y, x) \qquad \text{shift } \phi_{\text{recoil}} \text{ by } 360^\circ \text{ if } \phi_{\text{recoil}} < 0.
\end{aligned}$$

D.5 Beam Energy

Let us use the indices b for beam, t for target, r for recoil and X for the combined final-state particles. On one hand, we obtain

$$t = (p_t - p_r)^2 = m_t^2 + m_r^2 - 2E_t E_r = 2m_p^2 - 2m_p(E_b + m_p - E_X) = -2m_p(E_b - E_X),$$

where we use the fact that the target is at rest and the same particle as the recoil, resulting in $E_t = m_t = m_r = m_p$ and $\vec{p}_t = 0$, as well as energy conservation $E_r = E_b + E_t - E_X$.

On the other hand, we get

$$t = (p_b - p_X)^2 = m_b^2 + m_X^2 - 2E_b E_X + 2\left|\vec{p}_b\right|\left|\vec{p}_X\right|\cos\theta_{bX}.$$

Combining both equations for t, we can solve for $E_b = \sqrt{\left|\vec{p}_b\right|^2 + m_b^2}$, square the equation and get a quadratic equation in $\left|\vec{p}_b\right|$:

$$2(E_X - m_p)E_b = m_b^2 + m_X^2 - 2m_p E_X + 2\left|\vec{p}_b\right|\left|\vec{p}_X\right|\cos\theta_{bX} \quad \rightsquigarrow \quad 0 = a\left|\vec{p}_b\right|^2 + b\left|\vec{p}_b\right| + c,$$

with

$$\begin{aligned} a &= 4\left|\vec{p}_X\right|^2 \cos\theta_{bX} - 4(E_x - m_p)^2 \\ b &= 4(m_b^2 + m_X^2 - 2m_p E_X)\left|\vec{p}_X\right| \cos\theta_{bX} \\ c &= (m_b^2 + m_X^2 - 2m_p E_X)^2 - 4m_b^2(E_x - m_p)^2. \end{aligned}$$

Solving the quadratic equation we can obtain $\left|\vec{p}_b\right|$ and from it finally E_b:

$$\left|\vec{p}_b\right| = \frac{-b + \sqrt{b^2 - 4ac}}{2a}, \qquad E_b = \sqrt{\left|\vec{p}_b\right|^2 + m_b^2}.$$

D.6 Simple Phase-Space Monte Carlo

In order to have an idea what to expect for the final-state momentum distributions, we perform a very simple phase-space MC. For this, we give all the 190 GeV beam energy to the resonance X and let it also fly in z-direction[2]. Then, we use the ROOT function `TGenPhaseSpace` to generate a three-dimensional phase space with X as the mother particle of uniformly distributed mass within 1.2 GeV and 3.5 GeV, and $\pi^- K_S^0 K_S^0$ as daughter particles. Like this we generate 1×10^6 MC-events and fill the corresponding momentum histograms and invariant-mass distributions of the possible two-body subsystems. The result can be found in Figure D.2, where we clearly see a peak at ~ 20 GeV for the π^-_{prim} momentum and a broader peak at ~ 70 GeV for the K_S^0 momenta. The invariant-mass distributions of the two-body subsystems show a rapid drop.

This simulation can explain the low-momentum peak of the π^-_{prim} and the broad shoulder of the K_S^0 in the event selection (see Figure 5.38), but it cannot explain the high-momentum peak of the π^-_{prim} and the low-momentum peak of the K_S^0.

One could suspect these to come from specific intermediate two-body resonances that result in an enhancement in specific momentum ranges. For this, we perform a second MC simulation, where we look at two subsequent two-body decays $X \to K^*(892) + K_S^0$ and $K^*(892) \to \pi + K_S^0$, fixing the invariant mass of the $K^*(892)$ to its nominal PDG value. The lower limit for the X-mass is increased to 1.4 GeV. The result in Figure D.3 shows a small shift to lower values of the momentum distributions compared to Figure D.2, however, it does not create a low-momentum peak for the K_S^0 and definitely not a high-momentum peak fo the π^-_{prim}. Also, the spectra look a lot less smooth compared to the real three-body phase-space MC in Figure D.2, especially in the invariant-mass spectra of the two-body subsystems, which makes sense since two-body decays are a lot more restricted in their available kinematics. The momentum in the CMS is fixed and can only be shifted by the boost into the LAB, and in addition the momentum of the resonance is fixed to 190 GeV making the boost only dependent on the decay angle in the CMS and the uniformly-distributed resonance mass.

Doing the same, but with an $f_2(1270)$ in the $K_S^0 K_S^0$ subsystem and a lower limit of 1.6 GeV for the X-mass yields a similar effect, as can be seen in Figure D.4. The K_S^0-momentum peak moves to 40 GeV and the π^-_{prim}-momentum peak moves to 70 GeV.

[2] If we only want to extract the magnitudes of the involved momenta, the direction of the resonance is not important. It would be important if we would want to extract the direction of the daughter particles to see if they hit active detector material or end up outside of the detector acceptance.

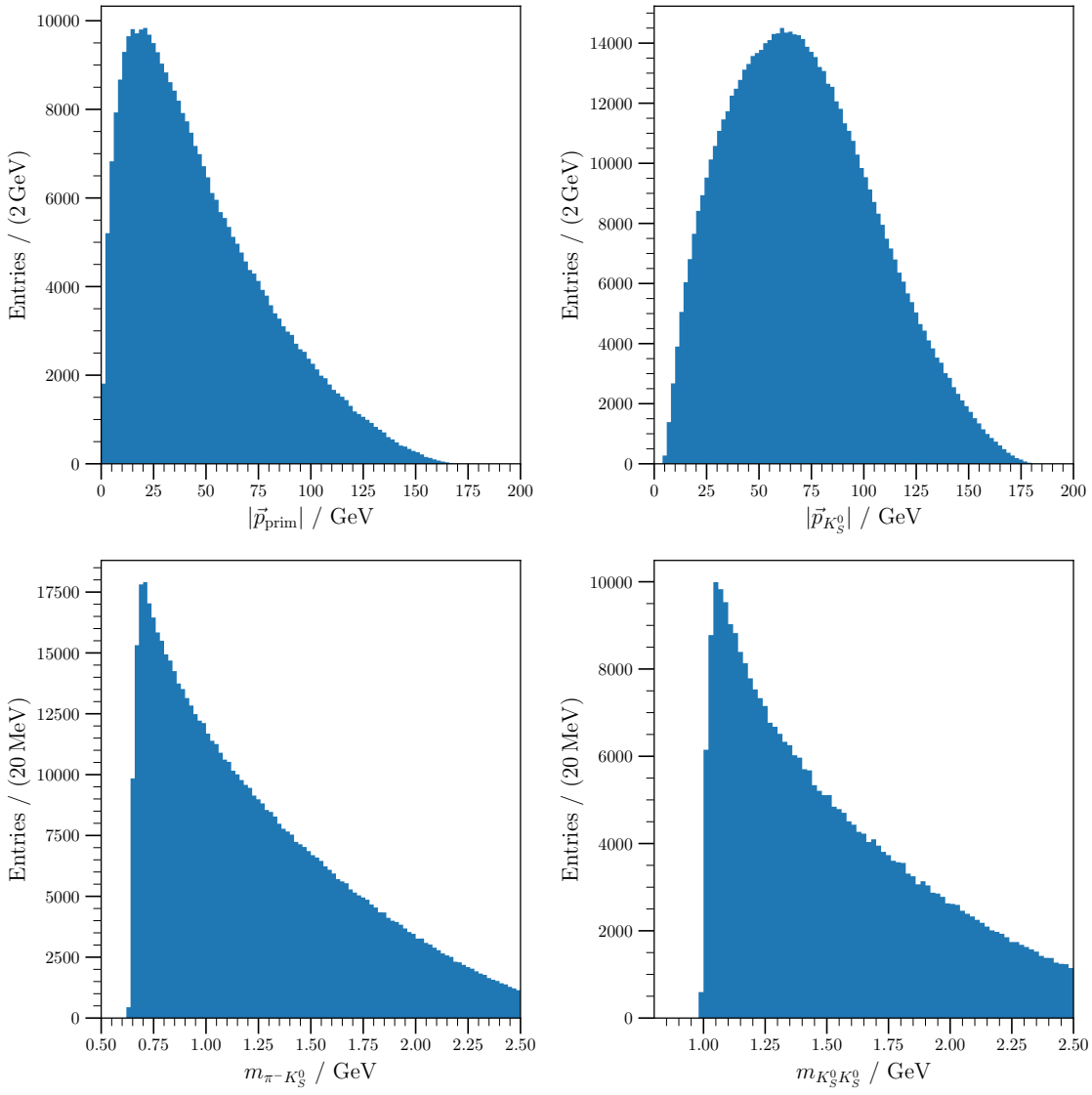

Figure D.2: Momentum distribution for the π^-_{prim} (top left) and the K_S^0 (top right, two entries per event) for a simple phase-space MC production with uniformly distributed resonance mass between 1.2 GeV and 3.5 GeV. In the second row, the invariant-mass distributions of the $\pi^- K_S^0$ (bottom left, two entries per event) and $K_S^0 K_S^0$ (bottom right) are shown.

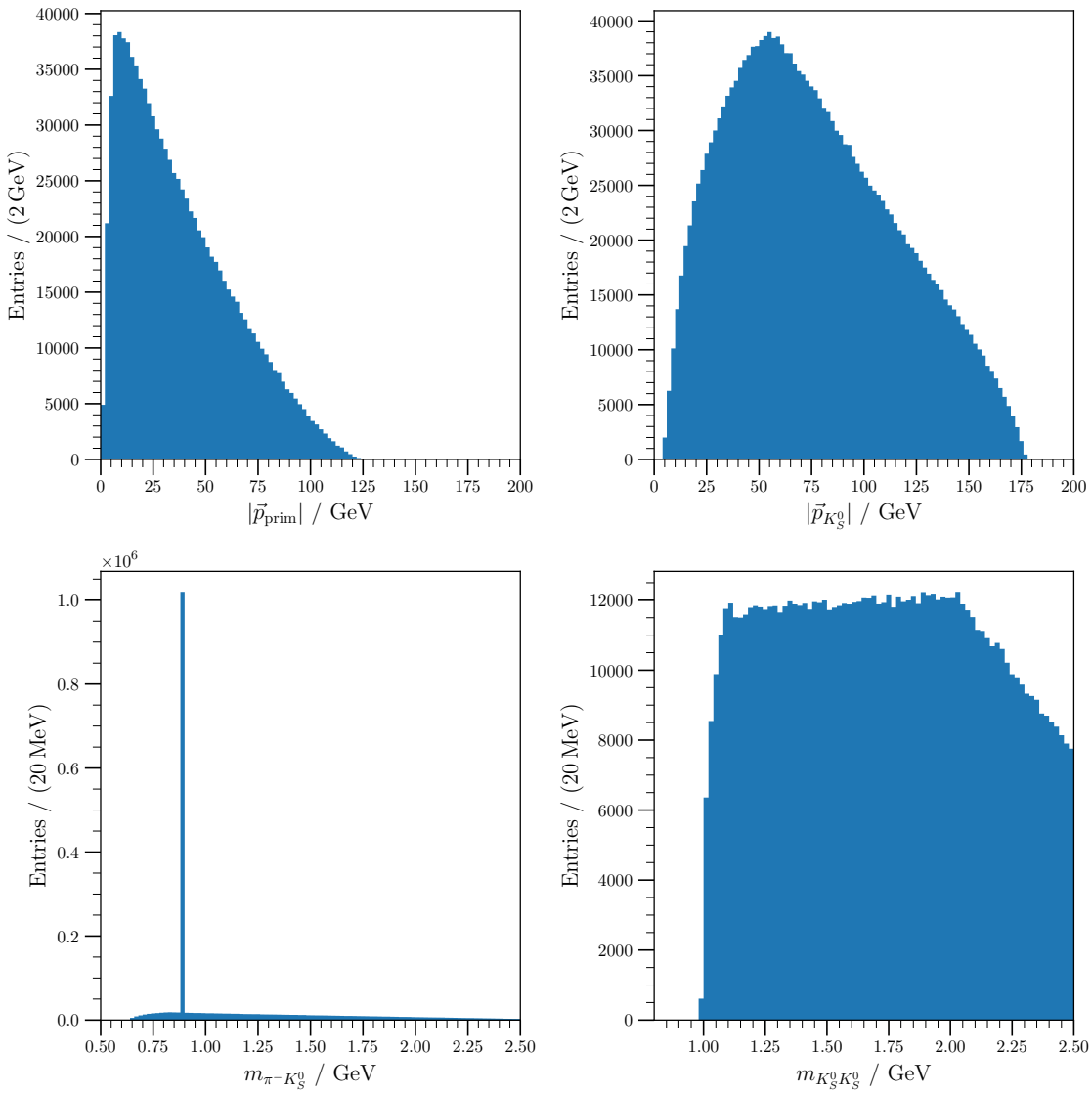

Figure D.3: Momentum distribution for the π^-_{prim} (top left) and the K^0_S (top right, two entries per event) for a simple phase-space MC production with uniformly distributed resonance mass between 1.4 GeV and 3.5 GeV, **and $\pi^- K^0_S$ fixed to the mass of a $K^*(892)$**. In the second row, the invariant-mass distributions of the $\pi^- K^0_S$ (bottom left, two entries per event) and $K^0_S K^0_S$ (bottom right) are shown.

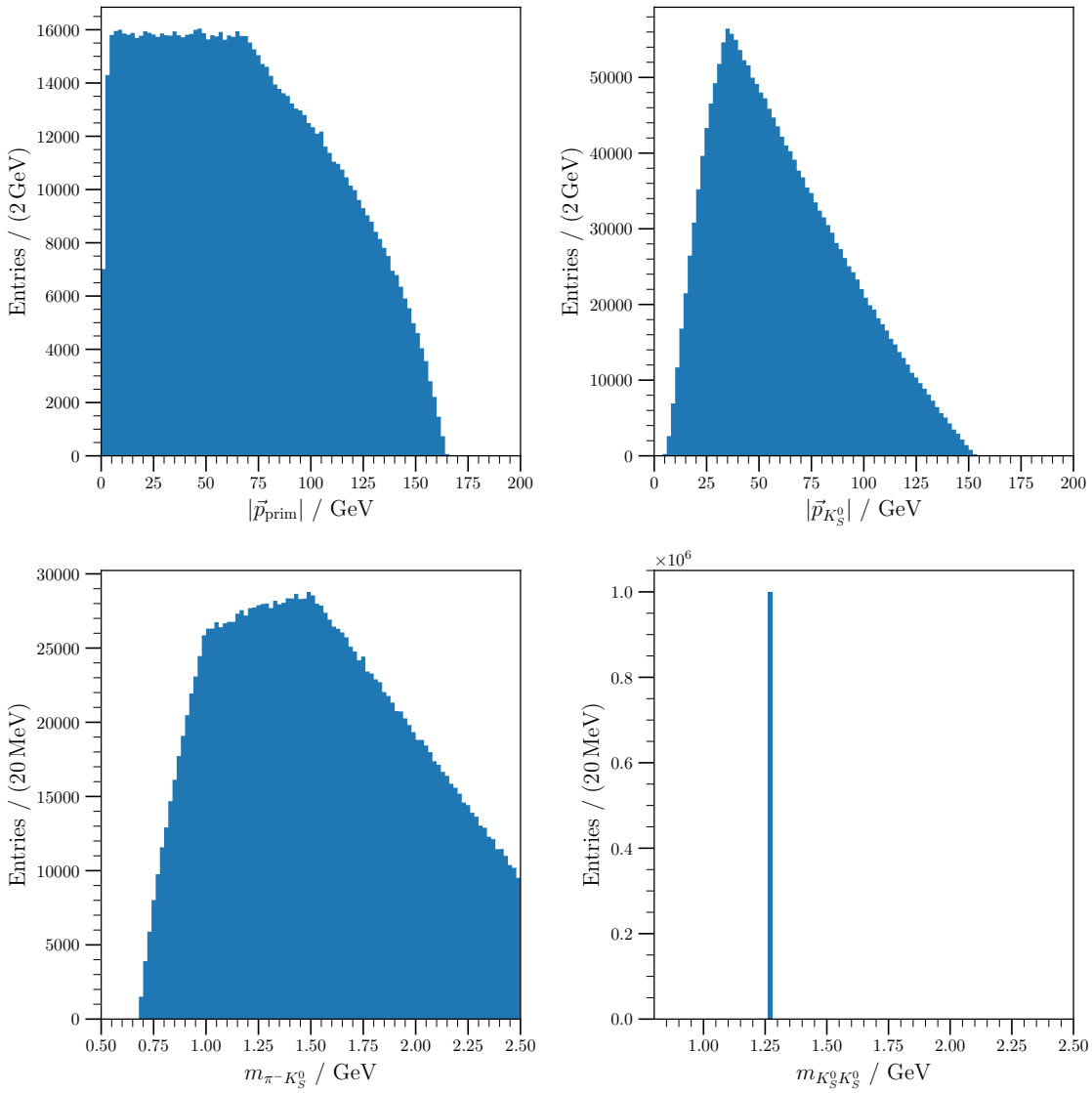

Figure D.4: Momentum distribution for the π^-_{prim} (top left) and the K_S^0 (top right, two entries per event) for a simple phase-space MC production with uniformly distributed resonance mass between 1.6 GeV and 3.5 GeV, **and $K_S^0 K_S^0$ fixed to the mass of a $f_2(1270)$**. In the second row, the invariant-mass distributions of the $\pi^- K_S^0$ (bottom left, two entries per event) and $K_S^0 K_S^0$ (bottom right) are shown.

This leads to the conclusion that this specific momentum configuration, i.e. high-momentum ("fast") π^-_{prim} together with low-momentum ("slow") K^0_S, has to come from a different kind of physics process other than a diffractive resonance production. A fast π^-_{prim} hints towards a t-channel scattering at the PV, instead of being the decay product of a produced resonance. This means the K^0_S pair has to be centrally produced and we have a double Pomeron or more general a double Reggeon exchange as depicted in Figure 5.39.

APPENDIX E

Bonn Event Selection Tool

Event selections at COMPASS are usually performed with PHAST. The tool Antok is used at TUM in order to facilitate these selections and the creation of corresponding plots. In order to perform independent crosschecks of such selections, the idea to create a similar tool for Bonn, the Bonn Event Selection Tool (BEST), came up. However, since the currently ongoing event selections used a very different style, each of them created their own "BEST"-version. The one created in the course of this work will be described in the following. This description should explain the implementation principle and can also serve as a guideline on how to use it.

Its implementation and structure is intended to be used in order to transform a classical implementation of a Waterfall-Style event selection into a BEST-Style event selection, without having to severely modify the basic structure of the code. For the first time, it was used for the crosscheck of the $\pi^- + p \rightarrow K_S^0\pi^- + p$, $K^- + p \rightarrow K_S^0 K^- + p$ and $K^- + p \rightarrow \Lambda\bar{p} + p$ event selections performed with Antok and described in [59]. Now, it is also used for the $\pi^- + p \rightarrow \pi^- K_S^0 K_S^0 + p$ event selection described in section 5.2 and in the release note [61], where the successful independent crosscheck was performed by Julien Beckers using Antok.

In principle one can divide it into four sections, the preamble, the initialization stage, the definition of histograms, and the event loop.

E.1 Preamble

The only prerequisites to use BEST are the presence of the `best.h` and `best.cc` files (or symbolic links to them) in the PHAST `user` folder, where all the `UserEvent`s are created. And one has to include the header file with

```
#include "best.h"
```

at the top of the file that contains your `UserEvent`.

At the beginning of the `UserEvent` function one should define an enumerator:

```
enum Cuts : int {
  cNONE = -1,
  cAll,
  cDT0,
```

```
    cBeamTime,
    cTargetR,
    ...,
    cCOUNT
  };
  static vector<std::string> cutlabels = {
    "All",
    "Is DT0",
    "-7 < Beam Time / ns < 7",
    "0 < r_{Target} / cm < 1.55",
    ...
  };
```

Here, you can give the cuts meaningful names, where it is recommended to start with a small "c" and to use camel style for the cut description as a convention. The enumerator should start with `cNONE = -1` which can be used as an error bit, directly followed by `cAll` filling the index `0`. The final entry should be `cCOUNT`, since it will automatically contain the number of cuts that are defined. The advantage of using an enumerator instead of a simple counting integer is, that we can directly understand which cut we are dealing with, and it is easy to change the order of cuts for the Waterfall-Style plots. One simply has to change the order of the corresponding elements in the two lists above. Having said that, it is still possible to use such a counter, since internally `BEST` uses simple `int`s to differentiate cuts.

In order to have access to all the functionality that `BEST` provides, one needs the line:

```
BEST &b = BEST::Ref();
```

E.2 Initialization

Although `BEST` will check if it was already initialized and will skip the following functions, it still makes sense to pack it inside a "static-first" block

```
static bool first = true;
if (first) {
  first = false;
  // do the initialization things
}
```

since one saves on several unnecessary function calls during the execution of the `UserEvent` and one can make sure that these things are only called once. Inside this initialization block one should call the function

```
b.Initialize(cCOUNT, Phast::Ref().h_file);
```

which has two mandatory arguments, the number of cuts `cCOUNT` and the `TFile*` pointer to the root file that should contain the outputs. Using the implementation as given above will save them to the normal histogram-output file as defined by the PHAST flag `-h` during the execution of the program. If a string different from the empty string `""` is provided as a third argument, it will ignore the `TFile*` pointer (so you can use the `nullptr`). Instead, it will create a new root file using the provided string as the file name and it will write all histograms to this file, but only if you have defined the function

```
void UserJobEndXXX(){
  BEST &b = BEST::Ref();
  b.SaveAllHistograms();
  // maybe some other code as well
}
```

below your `UserEvent`, where `XXX` stands for the same number as it appears in your actual `UserEvent` function in `void UserEventXXX(PaEvent &e)`. `BEST` will warn you during execution that you have to call `SaveAllHistograms` to make you aware of it, in case you are wondering where your output files ended up. However, if you forget this function call, the histograms still should be booked in the histogram file of PHAST due to "ROOT magic". In order to have a consistent result as expected, one should try to avoid this though and directly provide the reference to the phast file as in the example above. The forth optional argument is an unsigned integer (`uint`) that gives the approximate number of events processed by the function. This will reserve the respective memory for all internally used vectors such that they do not have to be reallocated so often. However, this only makes sense if one also calls

```
b.DeactivateImmediateFillHistograms();
```

since otherwise every event will be filled directly at the end of the `UserEvent`. Deactivating this immediate filling can be useful in case one wants to fill several times per actual PHAST event and to only decide which of these fills should actually be used afterwards. For example, this was used in the crosscheck of the $K_S^0\pi^-$, $K_S^0K^-$ and $\Lambda\bar{p}$ event selections since each SV was treated as its separate event and only after all SVs were processed, the event was discarded if more than one fulfilled all required cuts. To fill all events in the current buffer, one has to actively call

```
b.FillAllHistograms();
```

If the immediate filling is kept active, the filling will be automatically performed during the `EndEvent` call, but more on that later.

Next in the initialization stage is the call of

```
b.SetCutLabels("Waterfall Title", cutlabels);
```

where the first argument is the title of the created waterfall plot that displays how many events survived all up to a respective cut, and the second one is a vector of strings with the labels for the cuts, as defined in the preamble, section E.1. If too many labels are provided, the overflow will be discarded, and if too few are given, they will be filled up with the corresponding cut numbers. `BEST` will print a warning during execution if this happens.

Although the next part about defining histograms is still part of the initialization, it has to be done outside of the "static-first" block, since the declared variables are needed during the `UserEvent`.

E.3 Definition of Histograms

There are two ways to define a histogram with `BEST`. If possible, we will apply all following examples to the one of the preamble, section E.1, with two additional unspecified cuts in the `enum Cuts`. One can define a single histogram that can be saved in a simple `static uint` variable, or one can create a

whole group of histograms by providing a `static std::vector<uint>`. The former one was only used at the beginning, so it cannot be guaranteed that it is still compatible with other features that were developed later. Therefore, the latter is the recommended way, since it can more easily be adapted to create more or less histograms of the requested type and we will focus on it in this section. One can define a one-dimensional or two-dimensional histogram in the following way:

```
static std::vector<uint> hBeamTime; // 1d histogram
b.DefineHistogram(hBeamTime,
                  {b.CreateDefaultMask(cBeamTime, true),
                   b.CreateDefaultMask(cBeamTime, false)},
                  "BeamTime",
                  "Beam time;t_{Beam} / ns;#events / (0.1 ns)",
                  400, -20, 20
                 );
static std::vector<uint> hTargetXY; // 2d histogram
b.DefineHistogram(hTargetXY,
                  {b.CreateDefaultMask(cTargetR, true),
                   b.CreateDefaultMask(cTargetR, false)},
                  "TargetXY",
                  "xy-position of BPV;x_{BPV} / cm;y_{BPV} / cm;
                                                  #events / (0.1 cm)",
                  100, -5, 5, 100, -5, 5
                 );
```

As just mentioned, the `uint`-vectors will be used to reference these histograms in the future. It is very important that they are made `static`, otherwise every new event will create a new (empty!) vector of indices and the previously defined histograms are lost. However, the `DefineHistogram` function calls will only be executed for the first event. If the provided vector is not empty (e.g. because something went wrong during the first event or the event was not properly closed, more on that later), `BEST` will give a warning during execution.

The second argument to the `DefineHistogram` function is a list of strings, namely the bit mask of the histograms. This bit mask has the form of e.g. `"101011"` where each digit corresponds to a cut as defined by the `enum Cuts` in the preamble, starting from the right. The first digit on the right corresponds to the `cAll` cut, which will always be fulfilled. A `1` means that we require the cut to be fulfilled and a `0` means that we do not care about this cut (it can still be, but does not have to be fulfilled). Since this type of defining a bit mask is very tedious, error prone, and not very flexible in case the order of cuts changes, `BEST` provides the function `CreateDefaultMask`. One can provide it with the corresponding integer of a cut (i.e. `cBeamTime` in the example above) and a boolean. If the boolean is true, it will put in a `1` for all cuts except the provided one (e.g. `"111011"`). If the boolean is false, it will put in a `1` for all cuts before the provided one (e.g. `"000011"`). These two cases are the most common cases for an event selection, `BEST`-Style and the Waterfall-Style, respectively.

All following arguments to `DefineHistogram` are the constructor arguments of a `TH1D` or `TH2D` of ROOT, namely the identifier of the histogram, the title (with x-label and y-label separated by a "`;`"), the number of bins, the minimal value and the maximal value. `BEST` will decide on the dimension of the defined histogram depending on the amount of provided arguments. For a two-dimensional histogram, the last three arguments have to be repeated for the second axis.

BEST will always create a histogram with no cuts required ("000000" which is equivalent to "000001", since the last digit corresponds to cAll) and with all cuts required ("111111"). If this is not wanted, one can provide DefineHistogram with an additional boolean false as a final argument. If more than one cut is under investigation, for example if one is interested in the beam time of the event without restricting the allowed radial distance r of the PV from the beam line, one can provide CreateDefaultMask with a vector of Cuts, i.e. uints:

```
static std::vector<uint> hBeamTimeNoTargetR;
b.DefineHistogram(hBeamTimeNoTargetR,
                  {CreateDefaultMask({cBeamTime, cTargetR})},
                  ...
                 );
```

Here, always the corresponding BEST-Style histogram will be defined ("110011"), so no additional boolean is possible to change it to Waterfall-Style. Since the general histogram definition most likely will not change (labels, variables to be filled with), one can also simply add this additional bit mask to the list provided in the example before. This reduces the need for repetition of axes labels and so on, and one can also not forget to fill both uint-vectors with the beam time of the event.

Sometimes one has a list of integers on the x-axis of a histogram that should represent something different than the respective integer, e.g. a list of possible particle identities or a simple "yes" or "no" in case of a boolean. For the labels to reflect this, the function SetHistogramLabels1D can be used:

```
static vector<uint> hDT0;
b.DefineHistogram(hDT0,
                  {b.CreateDefaultMask(cDT0, true),
                   b.CreateDefaultMask(cDT0, false)},
                  "DT0", "Is DT0 event;;#events", 2, -0.5, 1.5
                 );
b.SetHistogramLabels1D(hDT0, {"no", "yes"});
```

If this is not enough and more detailed changes to the defined histograms are required, one can obtain the pointer to the underlying TH1D with the function Get1DHist. However, this function is not very refined, yet. It requests the index of a single histogram, which means one would have to manually call it in a loop over the histogram-index vector. BEST does not (and it actually cannot) check if the provided index comes from a one-dimensional histogram, so this functionality should be used with special care from the user.

If one does not like the calls of DefineHistogram to happen outside of the "static-first" block, one can move all vector declarations above the block and the corresponding histogram definitions inside of it. While improving the runtime very slightly, this will make things a bit more complicated since removal or addition of new histograms has to be done always at two different places, then.

Such a "static-first" block can also be created by using the BEST function IsFirstEvent. It will return true until the EndEvent or EmergencyEndEvent function was called for the first time. More details on that follow in the next sections.

E.4 Event Loop

The event loop should always start with these following two lines:

```
b.InitializeNextEvent(e);
b.SetCut(cAll, false);
```

The first function call is crucial, since it prepares the event for the filling of the histograms and many more things. The argument, the current `PaEvent e`, is optional and only needed if one wants to save the event numbers for event-by-event comparisons, see section E.6. The second function call is needed in order to be able to count all analyzed events, the first entry in the cut-flow diagram. This is also the function that one has to call for every following cut. It takes the cut index as first argument and a boolean `false` if the cut is fulfilled by the event and `true` if not. This might seem counter-intuitive at first, but it follows the classic event selection style where one asks

```
if(!<cut fulfilled>)
  return;
```

Another example to clarify this is

```
b.SetCut(cDT0, !isDT0);
b.FillHistogram(hDT0, (double)isDT0);
```

provided that the boolean `isDT0` is only `true` if the `DT0` trigger bit is set. Here, we specifically show how to fill a histogram with a boolean. One has to explicitly perform a type cast into a `double` giving `1` for `true` and `0` for `false`. A slightly more involved cut would be

```
double rBPV = sqrt(pow(BPV.X(), 2) + pow(BPV.Y(), 2));
b.FillHistogram(hTargetXY, BPV.X(), BPV.Y());
b.SetCut(cTargetR, rBPV >= 1.55);
```

where we cut the event if $r \geq 1.55\,\text{cm}$ and accept it for $r < 1.55\,\text{cm}$. Here we also see how the filling of a two-dimensional histogram works, we simply provide both values after the histogram vector. It also demonstrates that the order of function calls does not matter, since the actual filling of the histogram as well as the performance of the cut will only happen at the very end of the event loop (see section E.8 for more details). It is also possible to fill the same histogram vector several times with different values, for example when histogramming the momentum of all final state particles. One simply calls `FillHistogram` for each of the values successively.

The final line of the event loop should be

```
b.EndEvent(e);
```

It will call `e.TagToSave()` if all cuts were fulfilled and it will call `BEST`s `FillAllHistograms` function. It also saves some additional info, but more on that in section E.6. Finally, it will set the internal `_first_event` boolean of `BEST` to `false`, which disables all future calls of `DefineHistogram` and other initialization functions. From now on, the `BEST` function `IsFirstEvent` will return `false` as well.

Note that `BEST` will keep track of which cuts were performed and will warn you during the call of `EndEvent` if not all defined cuts were actually performed. By default, all cuts are set to `true`, therefore, the user should make sure that all `SetCut` calls happen. It is also the responsibility of the user to make sure that each cut is only performed once. `BEST` will not prevent from performing the same cut twice, but this will result in unexpected and most likely wrong results (it will not warn you).

E.5 Discard Events Earlier

As just mentioned, the `_first_event` boolean will only be set to `false` inside the `EndEvent` function. This means that one should not have a `return` statement during the `UserEvent`, since this could result in a redefinition of all histograms besides of other additional problems. However, if one has a cut that needs to be fulfilled for the rest of the `UserEvent` to work, e.g. in the case of the $\pi^- K_S^0 K_S^0$ final state the existence of exactly two K_S^0, `BEST` provides the function `EmergencyEndEvent`. It sets `_first_event = false`, all cuts to "failed" (except for `cAll`), and calls `FillAllHistograms` (if intermediate filling is not disabled) to fill the histograms with no requirements on fulfilled cuts (`"000000"`). If one does not wish the histograms to be filled with possibly already provided entries, one can empty the buffer with a call of `ResetHistogramsOfCurrentEvent`, however, it can also be useful to create a specific histogram for these exit cases that has a bit mask full of zeros. An example of such an emergency is

```
if(emergency_condition){
  b.ResetHistogramsOfCurrentEvent();
  // maybe fill some "000000" histograms with info on the emergency
  b.EmergencyEndEvent();
  return;
}
```

E.6 Save Additional Information

`BEST` provides several options on additional information that should be saved.

Save Event Numbers

One can save a unique event identifier in form of three integers, the run number, the spill number, and the event-in-spill number. The activation of such a saving can be done during the initialization stage of the `UserEvent`, somewhere between `Initialize` and `InitializeNextEvent`. If one only wants to know all events that were processed, one can use

```
b.ActivateSaveEventNumbersStart();
```

which will create a `TTree` with name "EventNumbersStart" containing the branches "RunNumber", "SpillNumber", and "EvInSpill". This tree will be filled during `InitializeNextEvent` if one calls it with the current `PaEvent e` as an argument.

If a bit more information is needed, one can instead use

```
b.ActivateSaveEventNumbersEnd();
```

which will create the `TTree` "EventNumbersEnd" that additionally contains a branch "Bitmask" that encodes which cuts were fulfilled for the event and which of them were not. This tree will be filled during `EndEvent` if the `PaEvent e` is given as an argument. Note that any intermediate return (hopefully in combination with `EmergencyEndEvent`) will result in the event being missing from the tree. However, they would be included in "EventNumbersStart".

If one is only interested in the event number of events that passed the full selection, one can give an optional boolean

```
b.ActivateSaveEventNumbersEnd(false);
```

The function `ActivateSaveEventNumbersAll` will simply activate both savings and one can pass a boolean to change the behavior of `ActivateSaveEventNumbersEnd` as just discussed.

Save Lorentz Vectors

Usually, one performs an event selection in order to extract the Lorentz vectors of the final-state particles. This can also be done with `BEST` by using

```
b.ActivateSaveLV({"beam", "recoil", "pion", "Kshort1", "Kshort2"});
```

Two optional arguments are the ROOT identifying name for the resulting `TTree` (default is "TreeParticles") and the title of the tree (default is the same as the previous argument). Each provided string in the list will result in a branch for a `TLorentzVector` of the respective string and an additional branch for an integer with the added suffix "`_flag`" that allows for an optional differentiation. For the $\pi^- K_S^0 K_S^0$ event selection this was used to differentiate "far" K_S^0 from "shared" K_S^0.

During the event loop one has to set the corresponding Lorentz vectors by using their position in the provided vector of strings. Therefore, it is recommended to create another enumerator

```
enum FinalStateParticles : int {
  pBeam, pRecoil, pPion, pKshort1, pKshort2,
};
```

Then, the actual saving will be done with

```
TLorentzVector lPion = ...;
int pion_flag = ...;
b.SaveParticleLV(pPion, lPion, pion_flag);
...
```

where a third optional argument (default is 0) can be provided to set the flag of the respective particle.

The actual filling of the `TTree` will happen during `EndEvent`, but only if one provides the `PaEvent e` as an argument. `BEST` will print a warning if the amount of `SaveParticleLV` calls is not equal to the expected number of `TLorentzVectors` from the initialization.

Save MC Truth

The saving of the MC truth (MCt) information works in a similar way as for the final-state particles in the previous section. One can activate it during the initialization stage with

```
b.SaveMCTruth({"MCbeam", "MCrecoil", "MCpion", "MCKshort1", "MCKshort2"});
```

coming with two optional strings as arguments exactly as before (default is this time "MCTreeParticles"). It will prepare a `TTree` with one `TLorentzVector` branch per string in the provided vector, always using the string for the branch name. The size of the provided vector has to match the amount of MC particles coming from the first MC-PV, `MCPV.NMCtrack()`, that `BEST` can find. It extracts them in order of how they were saved during the MC production. The user has to make sure that their order in the `UserEvent` is the same.

As before, the filling of the `TTree` will happen during `EndEvent` if one provides the `PaEvent e` as an argument. This also means that the MCt information will not be saved in case of an intermediate `return`.

E.7 Classification

A versatile feature of BEST is the possibility to create classifications of events. For example, this can be done with the number of outgoing particles from the BPV as presented in section 5.2.3 on the K_S^0 selection procedure. It can be activated in the initialization stage with

```
b.ActivateClassification("Nout", {"1", "2", "3", "4", "5"});
```

where the first argument is the common label of all classifications, and the second argument is a vector of labels for each separate class that will be concatenated with the common label to form the class label, i.e. `"Nout1"`, `"Nout2"` and so on. Let us call the amount of created classes determined by the length of the provided vector `Nclasses`, then, BEST will create each histogram in `Nclasses+1` variants, one for each class and one with all of them combined, called `"Noutall"` (the common label plus `"all"`). For a better overview, they will be stored in separate folders (labeled with the corresponding class label) inside the histogram file.

The stage for the definition and the filling of histograms will not change and one only has to set the class for the current event in the event loop (at an arbitrary point between `InitializeNextEvent` and `EndEvent`):

```
b.SetClassForEvent(NoutBPV - 1);
```

Note that the class indices start at zero. For more complicated cases than this example it might be better to use an enumerator as for the cuts and the final-state particles. Make sure that this function is called at least once per event and that the provided index is smaller than `Nclasses`, otherwise the first class (index `0`) will be assigned and in the latter case a warning will be printed.

This gives the opportunity though to create an additional "garbage collector" class `">5"` at the first position and to use

```
if (NoutBPV <= 5)
  b.SetClassForEvent(NoutBPV);
```

instead[1], however, in our case we already restrict ourselves to ≤ 5 outgoing particles from the BPV during the skimming (see section 5.2.1) making it irrelevant for this specific case, but maybe a useful tool for other selections.

For the user, there are no further changes, however, during the call of `FillAllHistograms` (or inside of `b.EndEvent(e)`) BEST will also fill two classification-specific additional histograms (stored outside the classification folder in the histogram file). One filled with the classifications of all events and one filled with the classifications of accepted events that fulfill all cuts.

E.8 The Inner Workings of BEST

In order to operate BEST, the previously discussed information should be sufficient. However, if one wishes to implement a new feature, a deeper understanding of the inner workings of BEST might be necessary. Therefore, this section will dive a bit deeper and explain what happens inside of BEST.

[1] Simply always filling it with `NoutBPV` is not advised, since a hypothetical value ≥ 5 would always result in a printed warning.

The Header File and the Event Buffer

Since BEST can work with a buffer for several events, most quantities are actually saved in vectors that are resized to zero at each call of FillAllHistograms. Inside of best.h a comment explains after each vector how big it is expected to be, also indicating what will actually be stored. For example the line

```
std::vector<std::vector<TH1D*>> _h1d; // <Nclasses+1<Nh1d>>
```

means that one will have one vector for each of the classes that contains the Nh1d defined one-dimensional histograms. The previously mentioned event buffer is indicated by Nevents as in the case of

```
std::vector<std::vector<std::vector<double>>>
    _h1dvalues; // <Nevents<Nh1d<NentriesInEvent>>>
```

where for each of the Nevents in the buffer, we have a vector for each of the Nh1d one-dimensional histograms that contains a vector of all values to be filled into the respective histogram. This outer vector will be emptied at the end of FillAllHistograms and a new element (std::vector<std::vector<double») of size Nh1d will be "emplaced" back[2] during InitializeNextEvent. The same is true for the two-dimensional histograms that are handled exactly the same, and in a simplified version also for the _classification vector and the _mask vector which contains the bit masks for each event as discussed in the next segment.

Bit Mask

The fulfilled cuts (or rather the not-fulfilled cuts) of each event are saved in a (bit) mask similar to the one discussed for histograms in section E.3. But since a handling of strings would be quite slow on an event-by-event basis (and not only once during the definition of a histogram), this will be done with the separate bits of an integer. For this, the type bits is defined. It is nothing more than an unsigned long long giving space for (at least[3]) a maximum of 64 cuts, since each actual bit (the digit in the binary representation of the decimal number) will tell us if the corresponding cut will actually "cut" the event, represented by a 1 in the binary representation of the mask at the position of the cut, or it will let it through, corresponding to a 0. This means that an event has fulfilled all cut criteria only if its mask is exactly 0.

During the function call of SetCut, this mask is modified by simply adding (bits)1 << iCut if the event does not fulfill the cut requirement. Here, iCut denotes the index of the corresponding cut from the Cuts enumerator and the operator << shifts the bits of the number on the left of it by the number on the right of it to the left, effectively multiplying the number by $2^{\texttt{iCut}}$. For example, taking iCut=3 will shift the binary number 000001 (1) to 001000 ($2^3 = 8$). This is the reason why calling

[2] This means that the constructor is called with the argument Nh1d, resulting in a vector of size Nh1d where the default constructor will be called for each element, in this specific case an empty std::vector<double>.

[3] It depends on the used computer architecture, how many bits are used for an unsigned long long. According to [94], in C++ it is guaranteed to have at least 64 bits. While an unsigned long would also usually have 64 bits on a 64-bit Unix-like machine, it only guarantees 32 bits of length. This is actually the case for 32-bit systems (and 64-bit Windows), thus, we directly use unsigned long long to make it a bit more system-independent. In hindsight, the usage of the C++ class std::bitset would have been a better option.

`SetCut` for the same `iCut` twice (and trying to cut the event both times) will result in a wrong outcome, because instead of performing the actual cut one performs the next cut (`001000` + `001000` = `010000`). If `SetCut` is called with the boolean `false`, nothing will be added to the `mask`, since all cut criteria are initially assumed to be fulfilled.

Filling of Histograms

After the event was processed and the function `FillAllHistograms` was called (e.g. inside of `EndEvent`), `BEST` will loop over all histograms and try to fill the saved values for each of them. Here, it will compare the bit mask of the event with each of the bit masks of the histogram using the "bit-wise and" operator "`&`".

In order to visualize this, we will use the example of the following histogram bit mask `011011`, which requires the first, third and forth cut to be fulfilled (remember that the digit on the very right corresponds to `cAll` and its "cut" is always fulfilled). If the event fulfills exactly and only the required cuts, its bit mask will be `100100`. Therefore, the "bit-wise and" will result in `000000`, even if one or both of the remaining two cuts would also be fulfilled. However, if a single cut of the required ones would not be fulfilled, e.g. `101100`, we would get `001000`. Therefore, we simply fill the value into a specific histogram if the "bit-wise and" between the bit mask of the histogram and the one of the event yields exactly `0`.

In case classification is activated (see section E.7), we will only fill the histogram at the current class index defined by the call to `SetClassForEvent` during the event loop, as well as the histogram of the `XXXall` class at index `Nclasses`.

If `ResetHistogramsOfCurrentEvent` was called, the classification of this specific event was set to `UINT_MAX` and it will be skipped during the filling.

This concludes the segment on the implementation of `BEST`. Although it provides a rudimentary plotting of histograms, they were read in afterwards and beautified with a python script to create the plots in chapter 5.

APPENDIX F

Further Results of the $\pi^- K^0_S K^0_S$ PWD

F.1 Rank Study

As mentioned in section 6.3, we use the final set of partial waves of Table 6.2 and perform a PWD fit with different ranks. The results for the flat wave are displayed in F.1, where we see a decrease in relative intensity and an increase in its threshold. On the other hand, the overview plot, where contributions from partial waves with equal isobars are added coherently, shows no major differences, see Figure F.2.

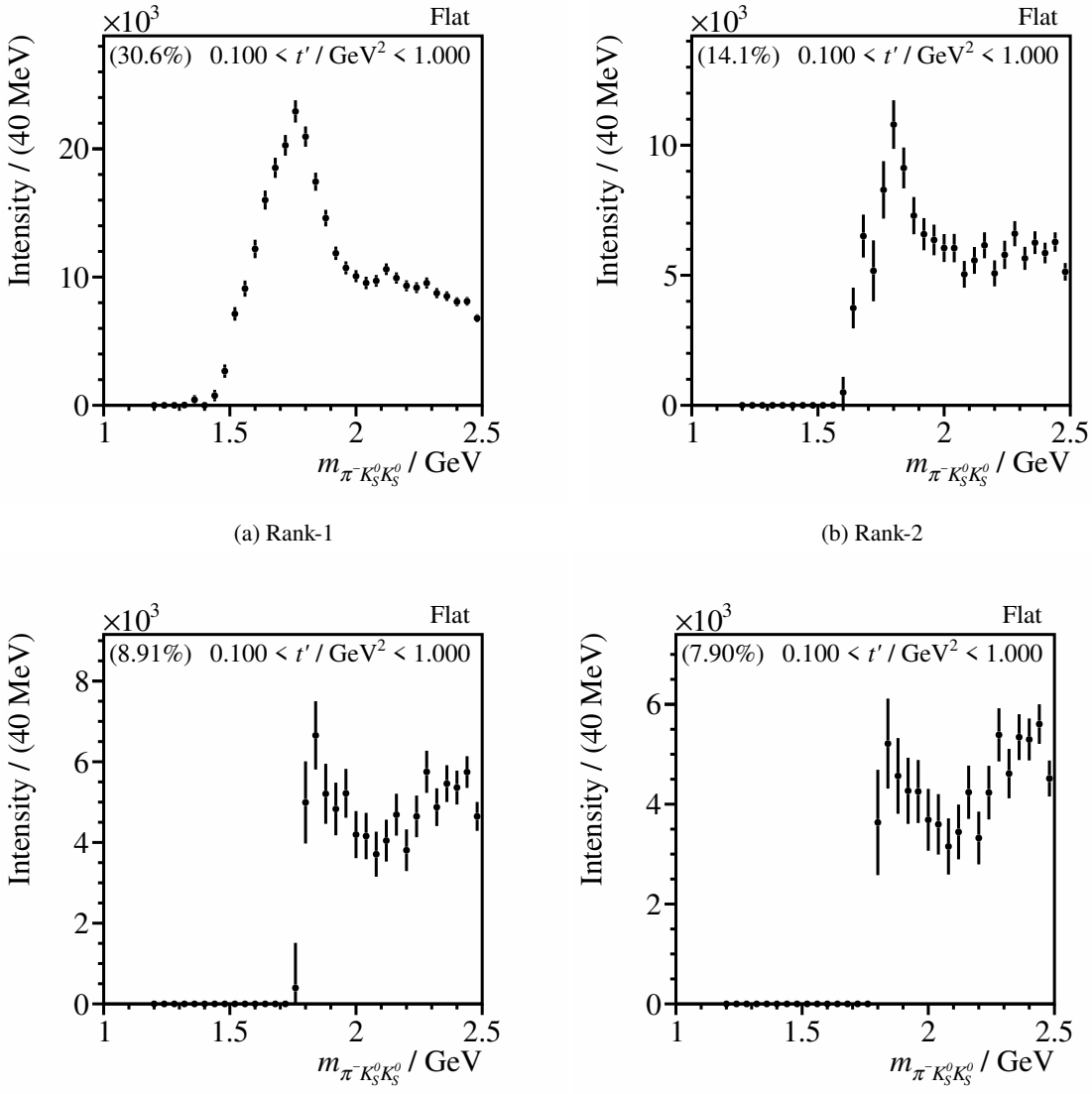

(a) Rank-1

(b) Rank-2

(c) Rank-3

(d) Rank-4

Figure F.1: Comparison of the Flat wave as extracted by a fit with the main wave set as presented in Table 6.2 for different rank as indicated by the individual captions.

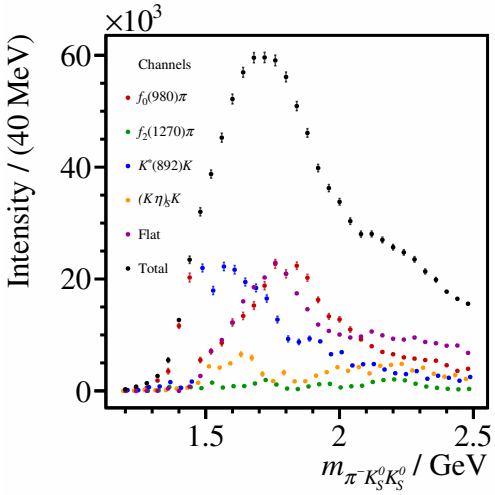

(a) Rank-1

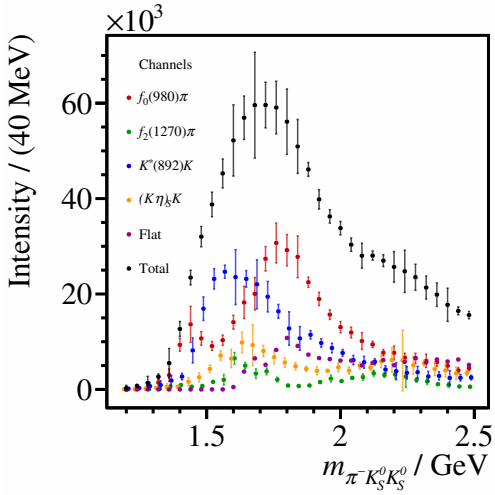

(b) Rank-2

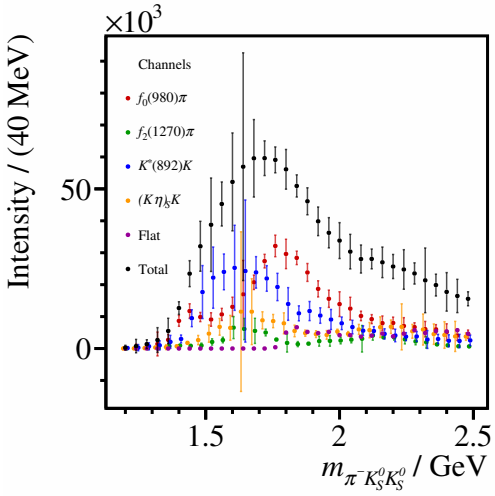

(c) Rank-3

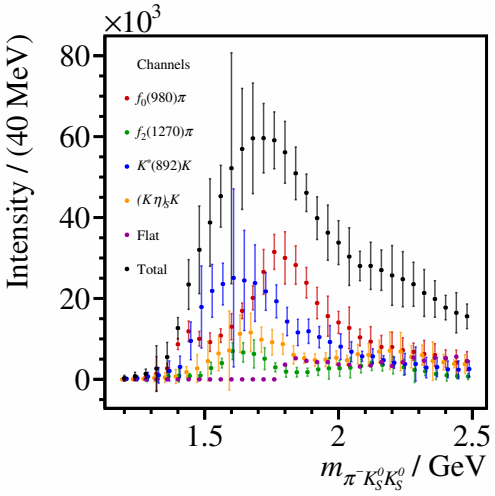

(d) Rank-4

Figure F.2: Coherent sum of the contributions from decay channels involving a certain isobar as indicated by the legends. The results are obtained by a fit with the main wave set as presented in Table 6.2 for different rank as indicated by the individual captions. The colored data points are slightly shifted sideways in order to make the error bars visible. All colored points actually lie where the corresponding black dot is located. Note that some uncertainty bands extend below zero. This is unphysical and shows that the used Gaussian approximation to propagate the uncertainties from the fit parameters to the intensities is not completely valid.

F.2 $a_1(1420)$ in Spin Projection $M = 1$

Only replacing the $f_0\pi\,\mathrm{P}_{a_1}$ by its corresponding $M = 1$ wave, $f_0\pi\,\mathrm{P}^1_{a_1}$, we also see phase motion at 1.4 GeV in the corresponding relative phases to the other two waves, see Figure F.3 and for the finer binning Figure F.8.

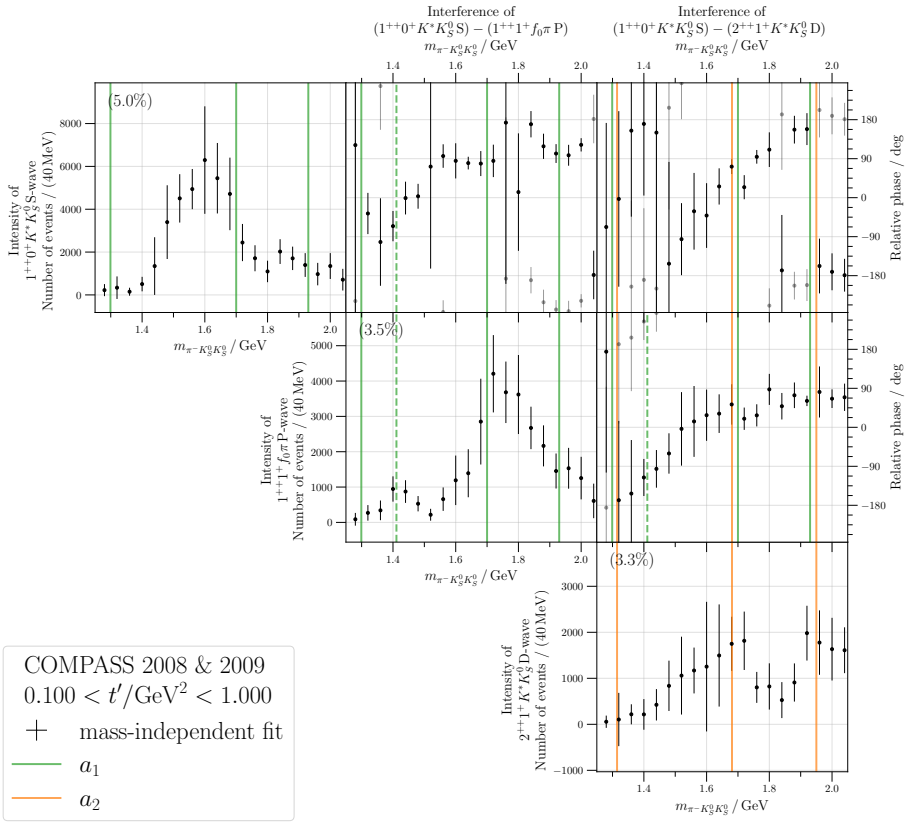

Figure F.3: Result of the $\pi^- K_S^0 K_S^0$ PWD presented as described in the main text in section 6.3. Displayed are the partial waves $K^* K_S^0\,\mathrm{S}_{a_1}$ (first row/column), $f_0\pi\,\mathrm{P}^1_{a_1}$ (second row/column) and $K^* K_S^0\,\mathrm{D}_{a_2}$ (third row/column). The same result for the fit with finer mass binning can be found in Figure F.8.

F.3 Remaining Partial Waves

The resulting spectra for 2^{-+} and 3^{++} have large uncertainties. We also did not take special care of these waves when performing the wave selection, therefore, we omitted them from the main part of the thesis. However, there is clear evidence for the $\pi_2(1670)$ in form of a peak in the intensity and phase motion in the relative phases to $f_0\pi\,\mathrm{S}_\pi$, see Figure F.5. The $\pi_2(1880)$ appeared as a dip in $\pi^-\pi^+\pi^-$ and it seems to be the case here, too.

For the $a_3(1875)$, there is no direct visible evidence in Figure F.4.

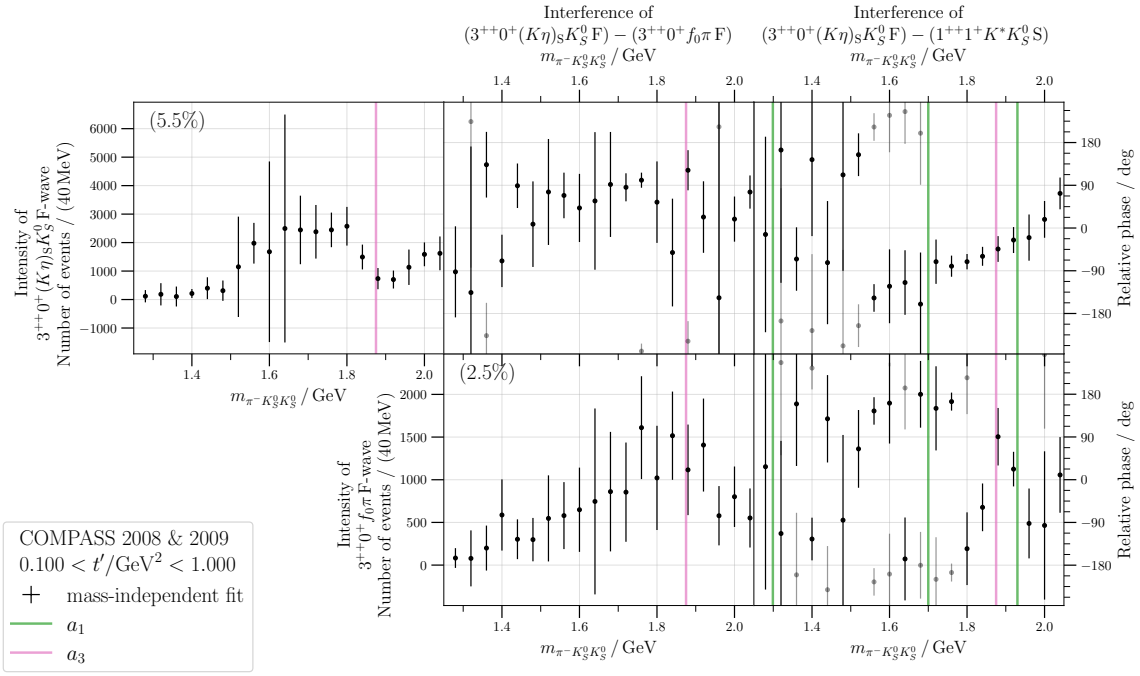

Figure F.4: Result of the $\pi^- K_S^0 K_S^0$ PWD presented as described in the main text in section 6.3. Displayed are the partial waves $(K\eta)_S K_S^0\,\mathrm{F}_{a_3}$ (first row/column), $f_0\pi\,\mathrm{F}_{a_3}$ (second row/column) and $K^* K_S^0\,\mathrm{S}_{a_1}$ (third column, intensity omitted). The same result for the fit with finer mass binning can be found in Figure F.11.

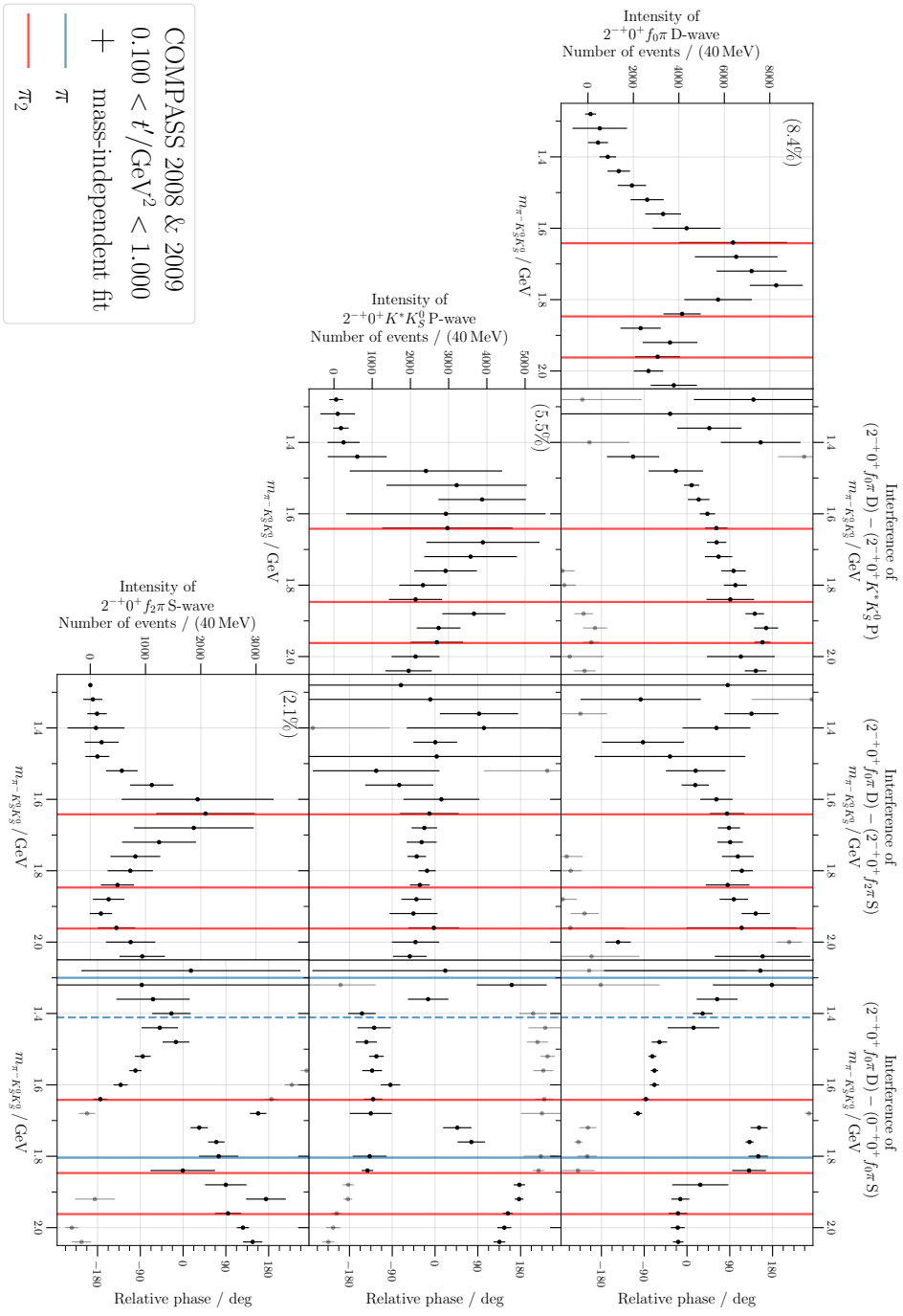

Figure F.5: Result of the $\pi^- K_S^0 K_S^0$ PWD presented as described in the main text in section 6.3. Displayed are the partial waves $f_0\pi\,\mathrm{D}^1_{\pi_2}$ (first row/column), $K^* K_S^0\,\mathrm{P}_{\pi_2}$ (second row/column), $f_2\pi\,\mathrm{S}_{\pi_2}$ (third row/column) and $f_0\pi\,\mathrm{S}_{\pi}$ (forth column, intensity omitted). Note that the figure is rotated by 90°. The same result for the fit with finer mass binning can be found in Figure F.12.

F.4 Results with Finer Mass Binning

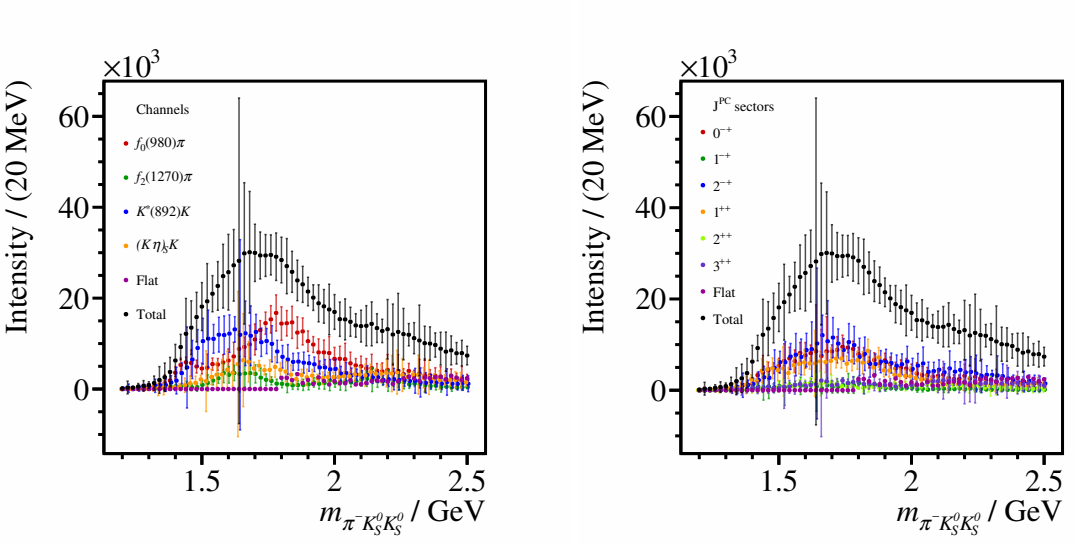

(a) (b)

Figure F.6: Overview of which decay channels (left) and which J^{PC} sectors (right) contribute during the main fit. Displayed is the coherent sum of all partial waves that belong to the sectors as indicated by the legend. The same result for the fit with 40 MeV mass bins can be found in Figure 6.15. The colored data points are slightly shifted sideways in order to make the error bars visible. All colored points actually lie where the corresponding black dot is located. Note that some uncertainty bands extend below zero. This is unphysical and shows that the used Gaussian approximation to propagate the uncertainties from the fit parameters to the intensities is not completely valid.

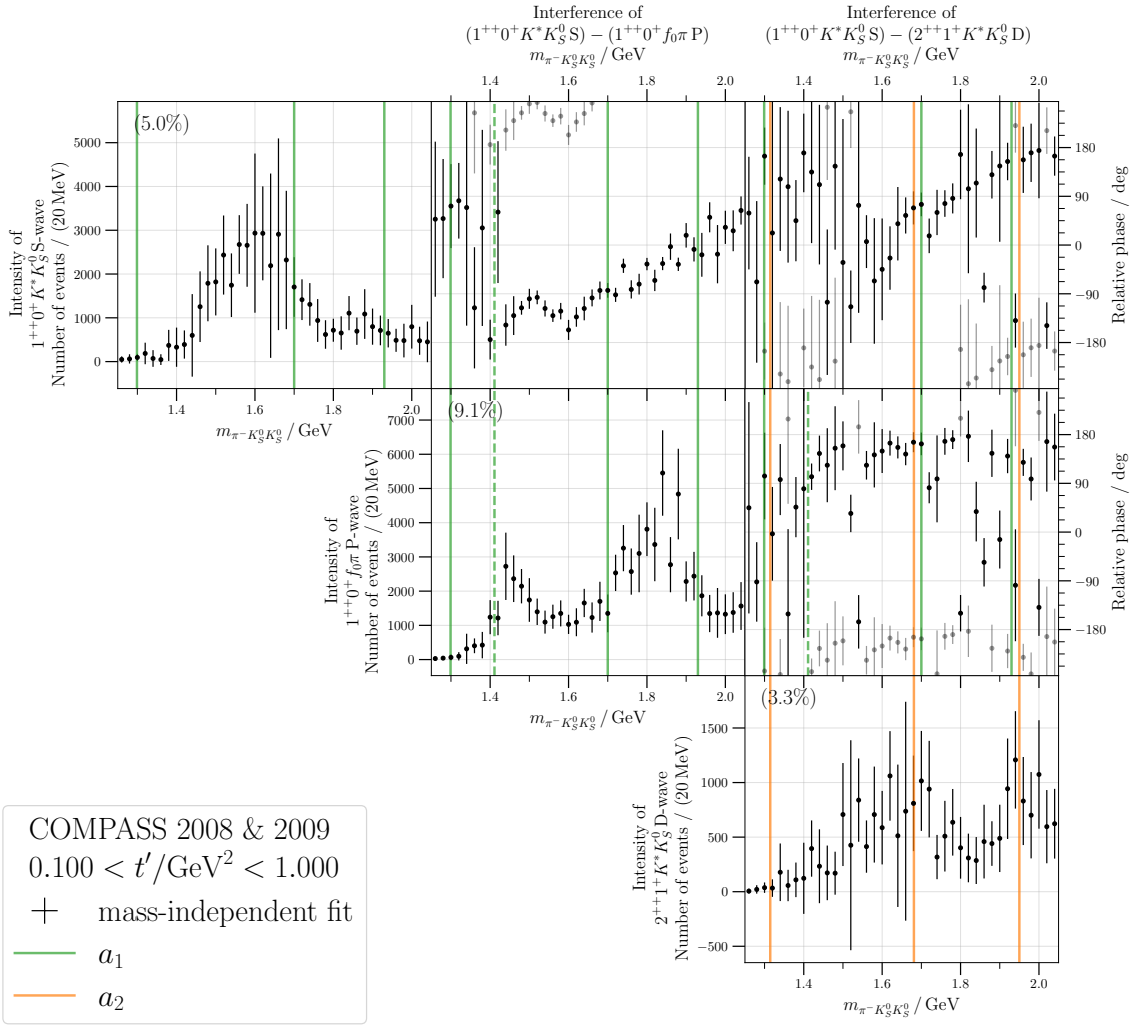

Figure F.7: Result of the $\pi^- K_S^0 K_S^0$ PWD presented as described in the main text. Displayed are the partial waves $K^* K_S^0\,\mathrm{S}_{a_1}$ (first row/column), $f_0\pi\,\mathrm{P}_{a_1}$ (second row/column) and $K^* K_S^0\,\mathrm{D}_{a_2}$ (third row/column). The same result for the fit with 40 MeV mass bins can be found in Figure 6.16.

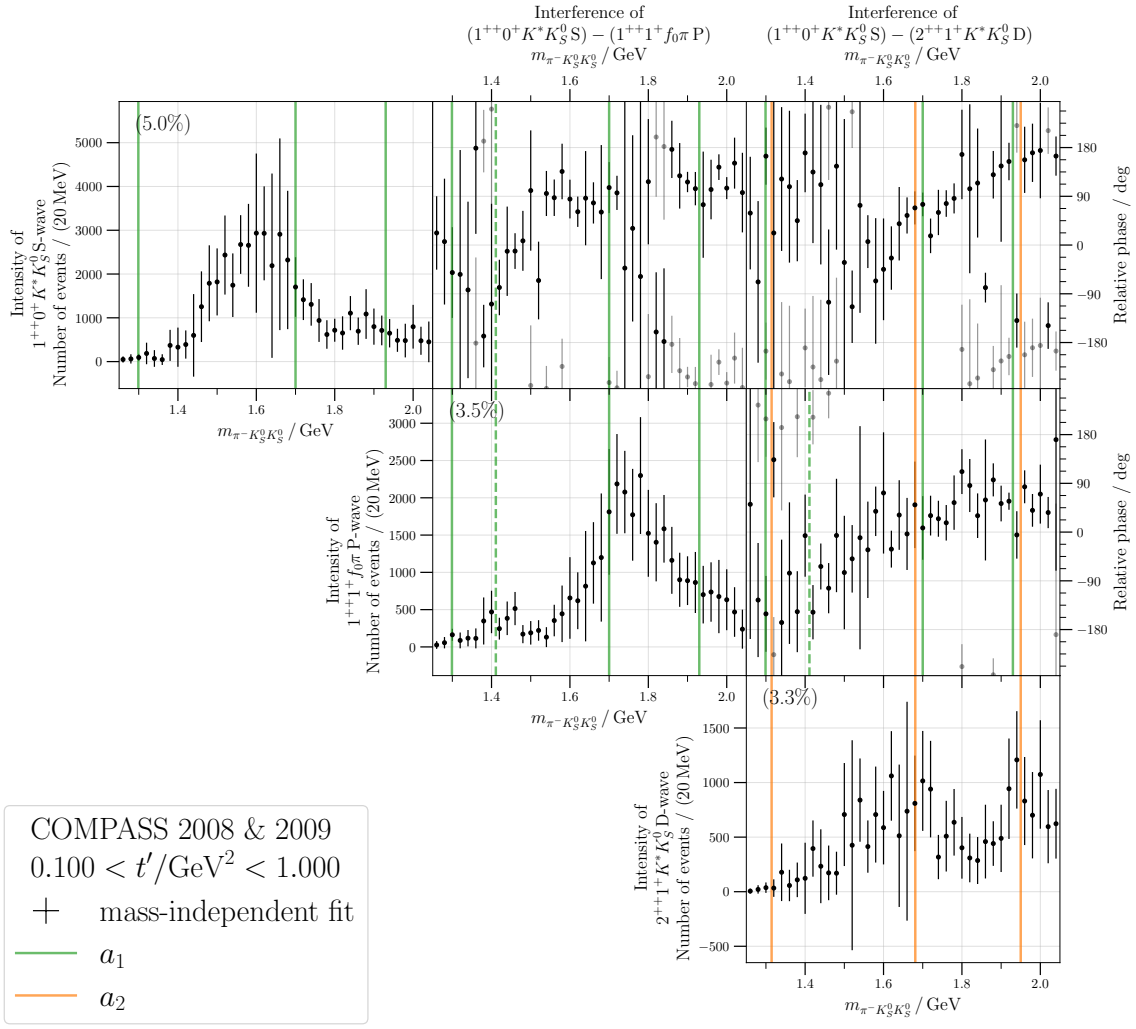

Figure F.8: Result of the $\pi^- K_S^0 K_S^0$ PWD presented as described in the main text in section 6.3. Displayed are the partial waves $K^* K_S^0\,\mathrm{S}_{a_1}$ (first row/column), $f_0\pi\,\mathrm{P}^1_{a_1}$ (second row/column) and $K^* K_S^0\,\mathrm{D}_{a_2}$ (third row/column). The same result for the fit with 40 MeV mass bins can be found in Figure F.3.

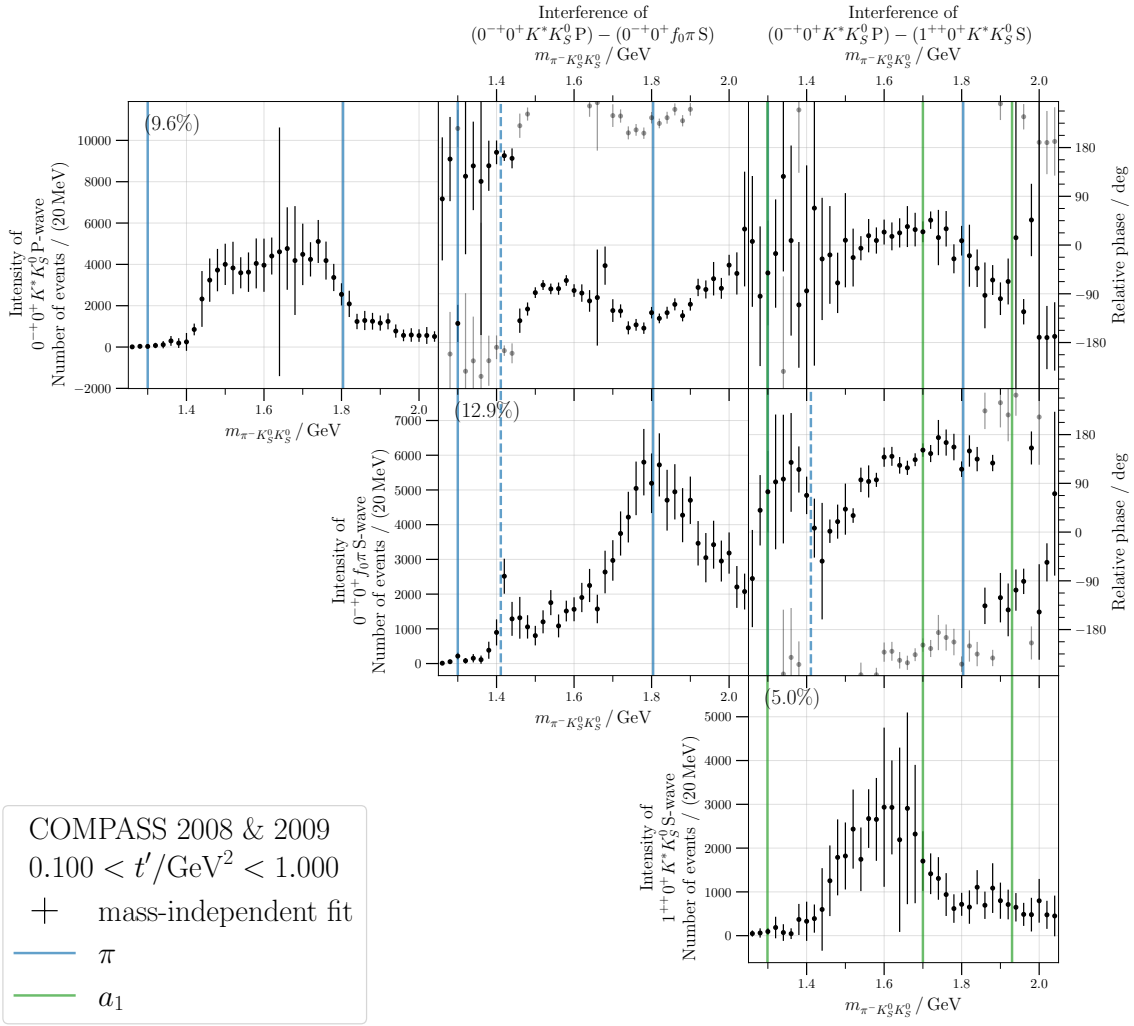

Figure F.9: Result of the $\pi^- K_S^0 K_S^0$ PWD presented as described in the main text. Displayed are the partial waves $K^* K_S^0\,\mathrm{P}_\pi$ (first row/column), $f_0\pi\,\mathrm{S}_\pi$ (second row/column) and $K^* K_S^0\,\mathrm{D}_{a_1}$ (third row/column). The same result for the fit with 40 MeV mass bins can be found in Figure 6.17.

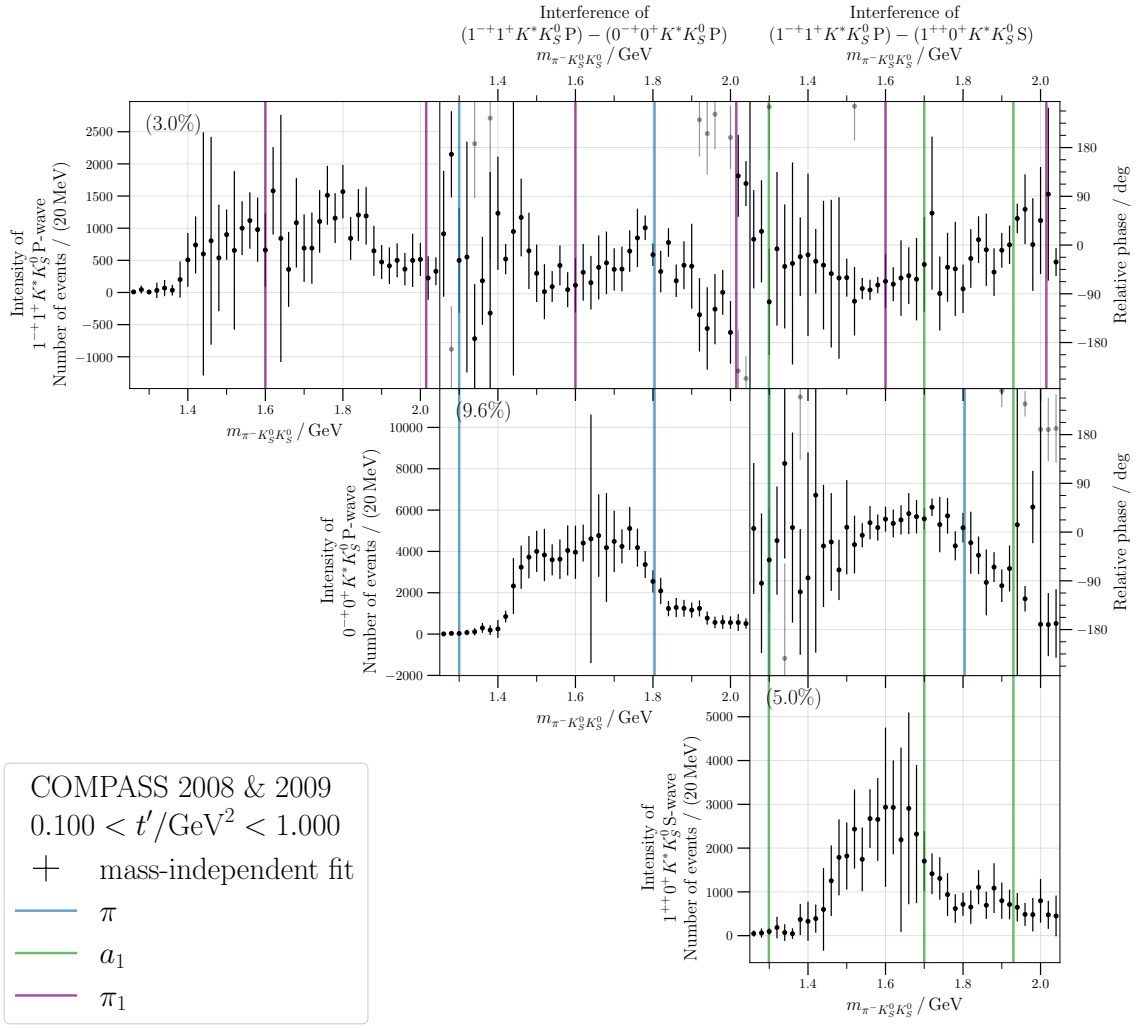

Figure F.10: Result of the $\pi^- K_S^0 K_S^0$ PWD presented as described in the main text. Displayed are the partial waves $K^* K_S^0\,\mathrm{P}_\pi$ (first row/column), $K^* K_S^0\,\mathrm{P}_\pi$ (second row/column) and $K^* K_S^0\,\mathrm{D}_{a_1}$ (third row/column). The same result for the fit with 40 MeV mass bins can be found in Figure 6.18.

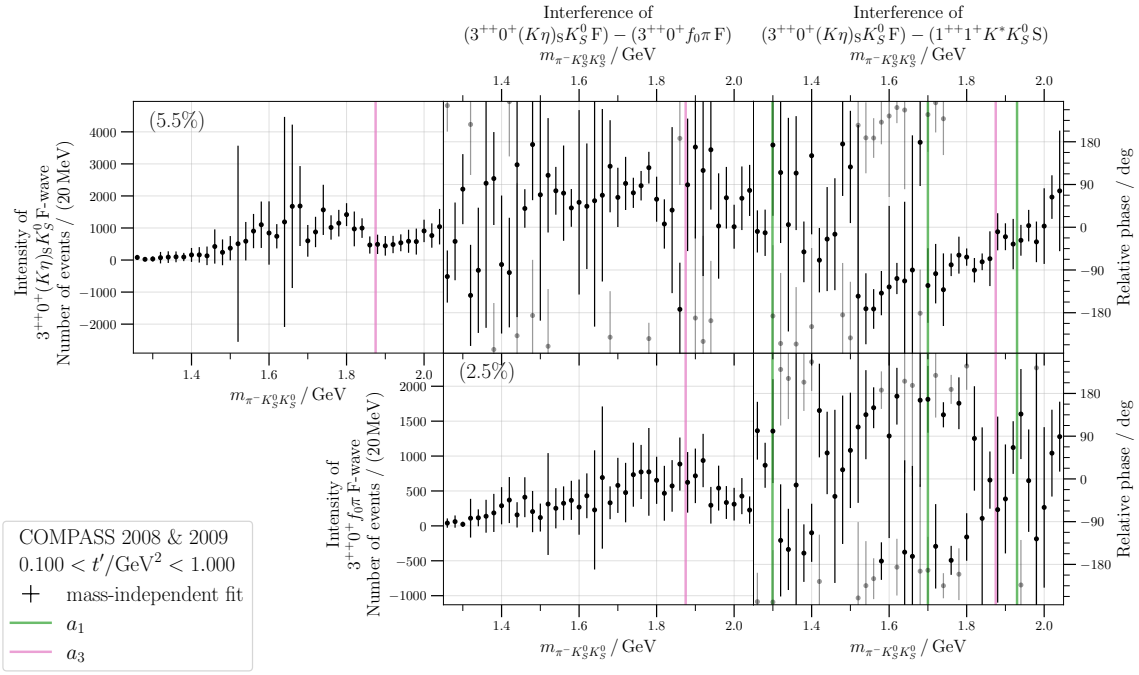

Figure F.11: Result of the $\pi^- K_S^0 K_S^0$ PWD presented as described in the main text in section 6.3. Displayed are the partial waves $(K\eta)_S K_S^0\,\mathrm{F}_{a_3}$ (first row/column), $f_0\pi\,\mathrm{F}_{a_3}$ (second row/column) and $K^* K_S^0\,\mathrm{S}_{a_1}$ (third column, intensity omitted). The same result for the fit with 40 MeV mass bins can be found in Figure F.4.

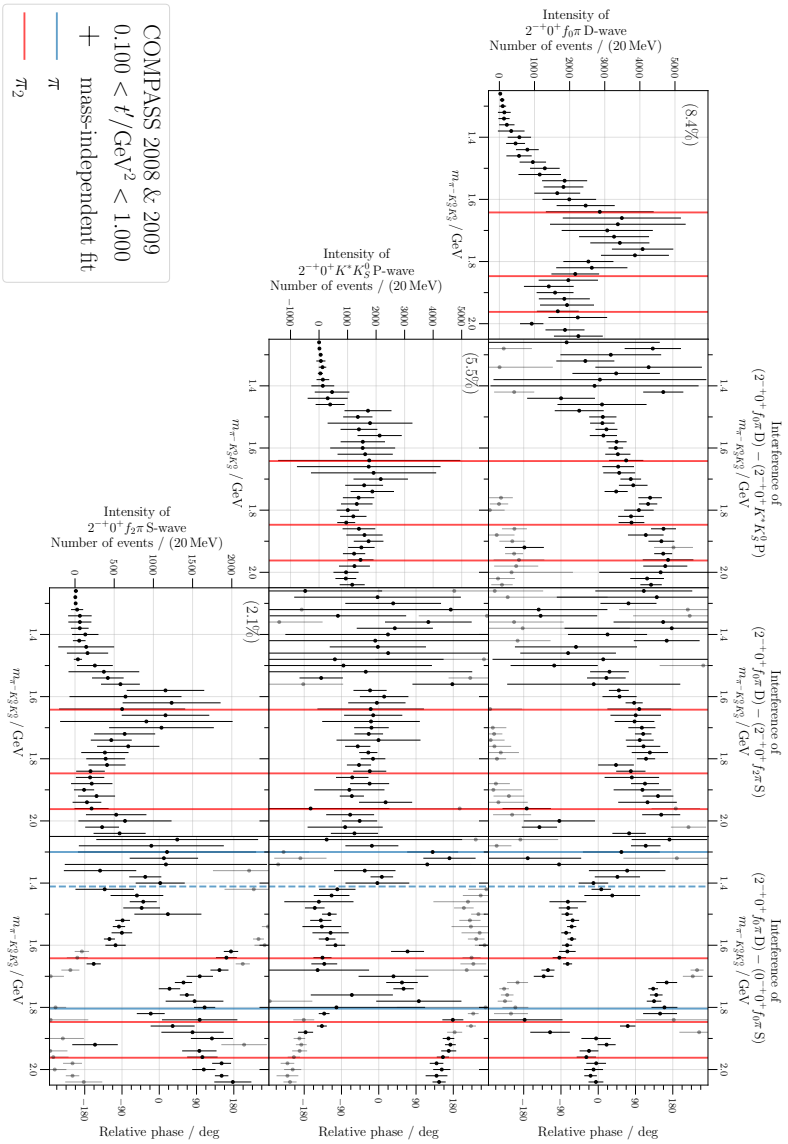

Figure F.12: Result of the $\pi^- K_S^0 K_S^0$ PWD presented as described in the main text in section 6.3. Displayed are the partial waves $f_0\pi\,\mathrm{D}^1_{\pi_2}$ (first row/column), $K^*K_S^0\,\mathrm{P}_{\pi_2}$ (second row/column), $f_2\pi\,\mathrm{S}_{\pi_2}$ (third row/column) and $f_0\pi\,\mathrm{S}_\pi$ (forth column, intensity omitted). Note that the figure is rotated by 90°. The same result for the fit with 40 MeV mass bins can be found in Figure F.5.

F.5 Full Plot of all Partial Waves

The following plots are intended for the digital version of this thesis, where one can zoom.

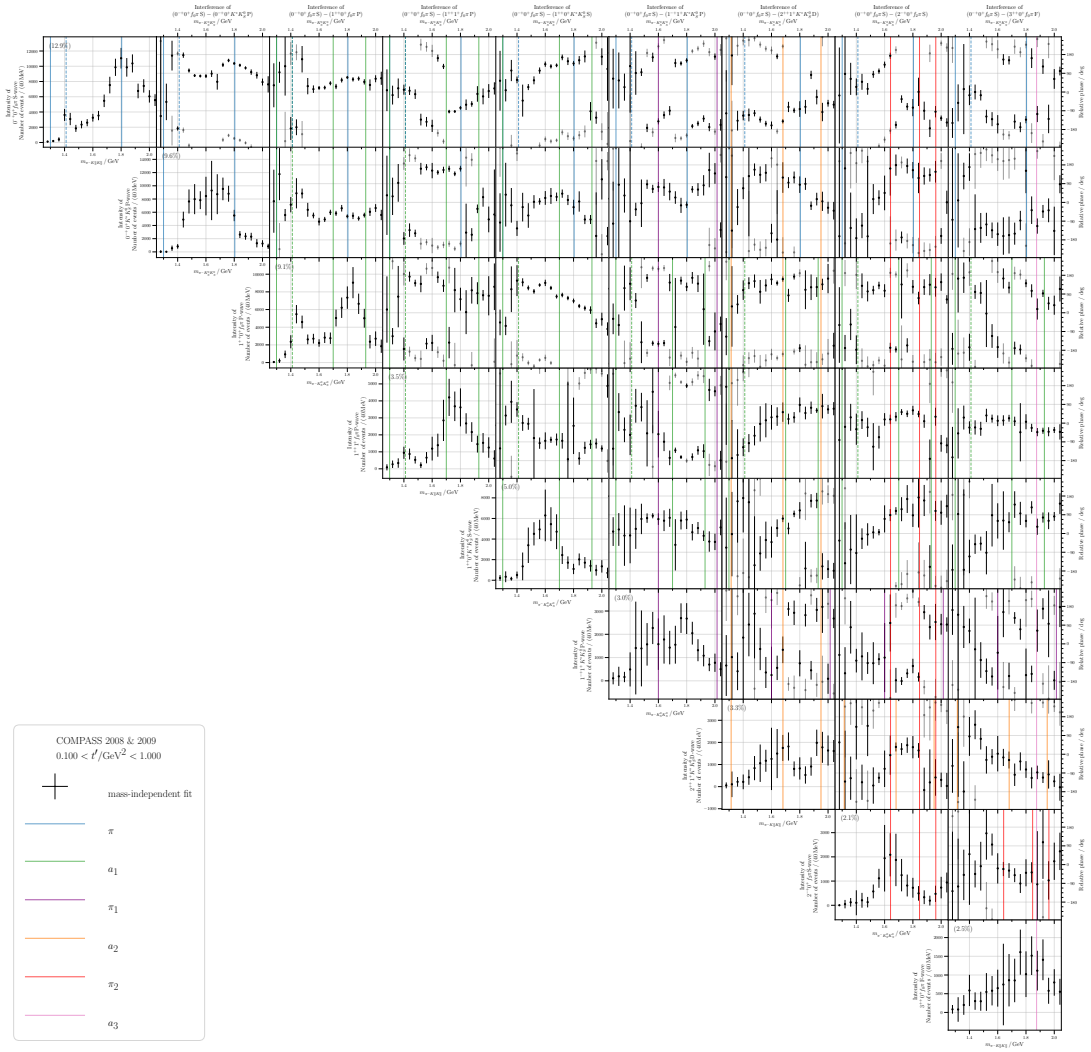

Figure F.13: Full plot with all discussed partial waves in the main text and some additional waves from the appendix. Plot intended for the digital version of this thesis.

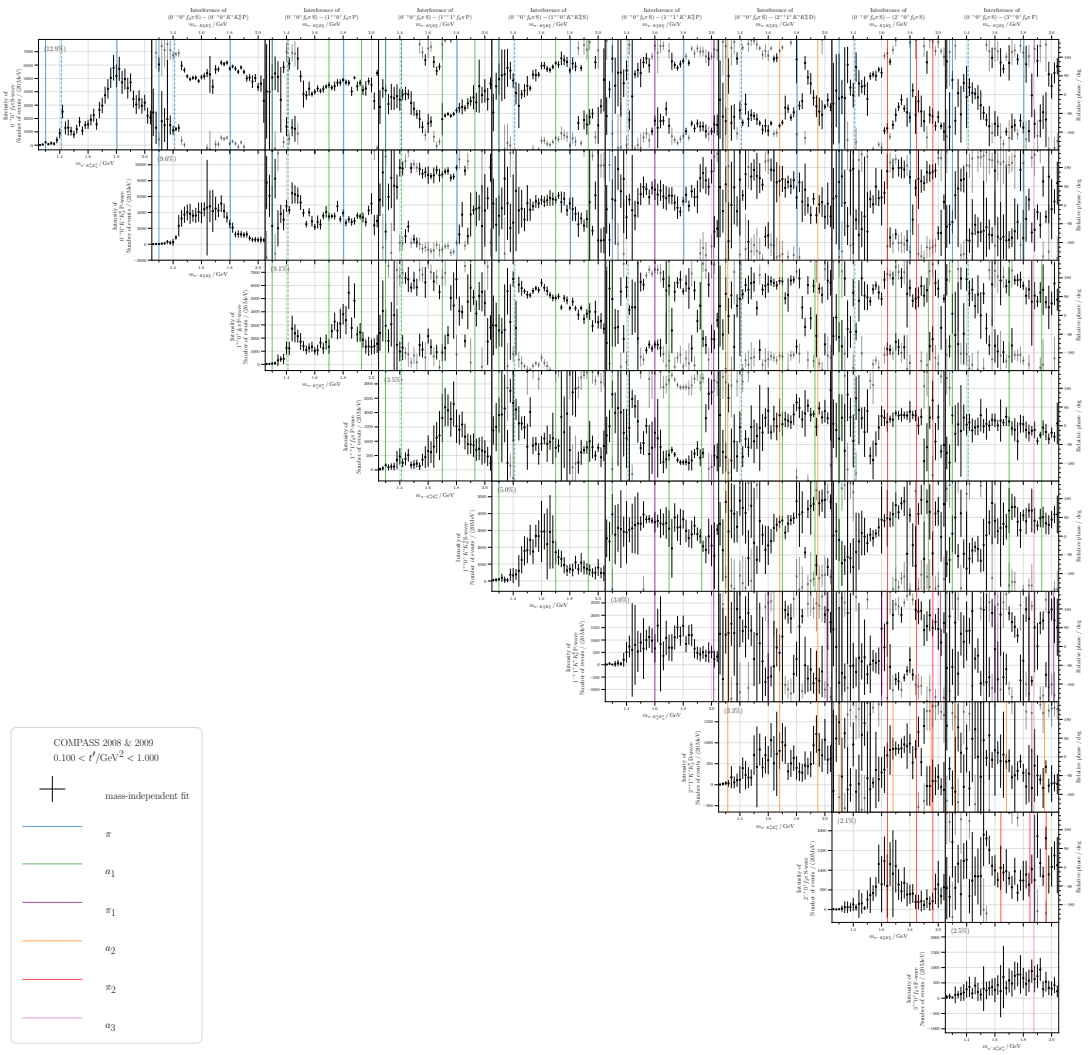

Figure F.14: Full plot with all discussed partial waves in the main text and some additional waves from the appendix. Fit with finer resonance mass binning. Plot intended for the digital version of this thesis.

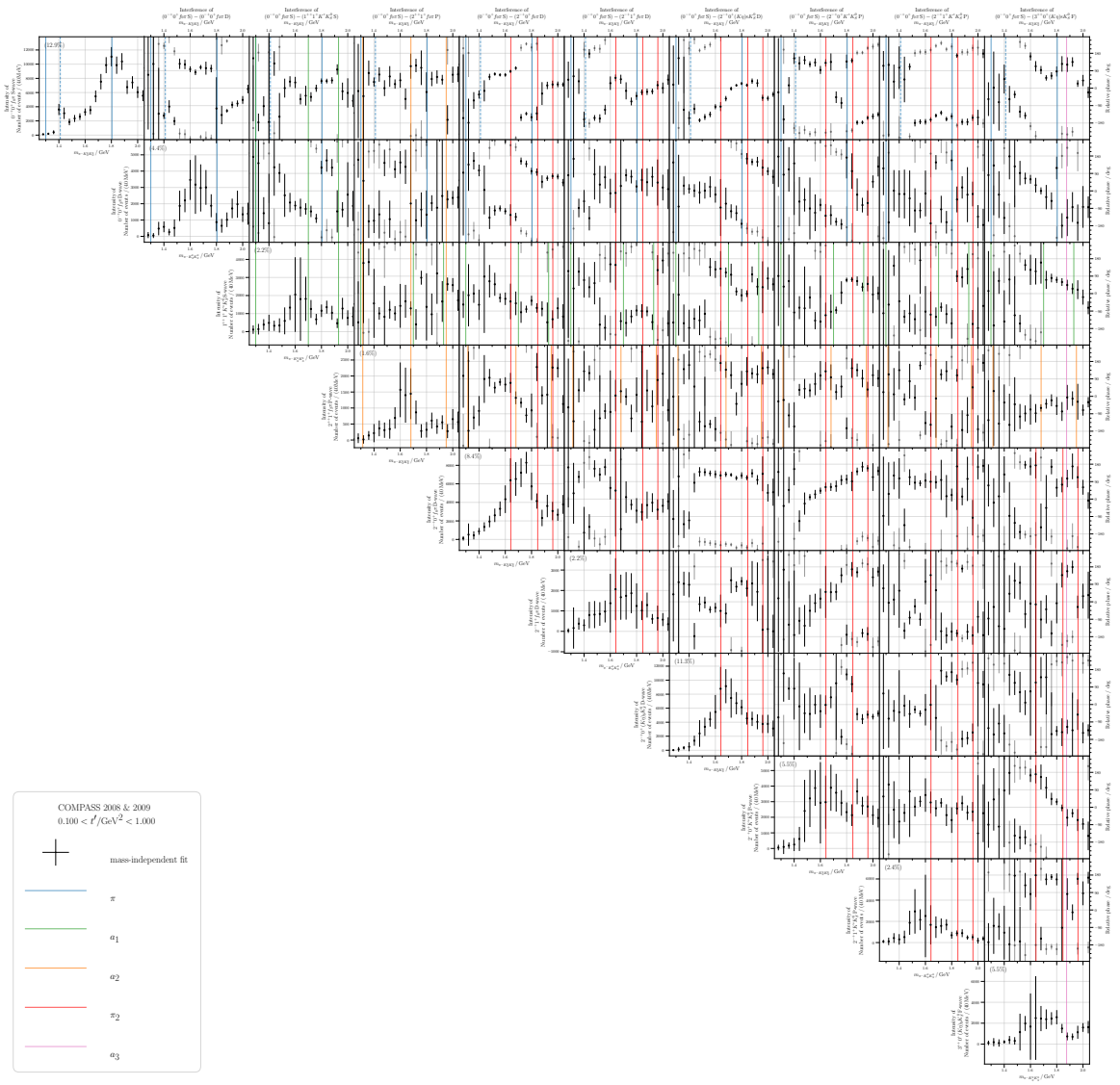

Figure F.15: The reference wave $0^{-+}0^+ f_0(980)\pi$ S together with all remaining waves not included in Figure F.13. Plot intended for the digital version of this thesis.

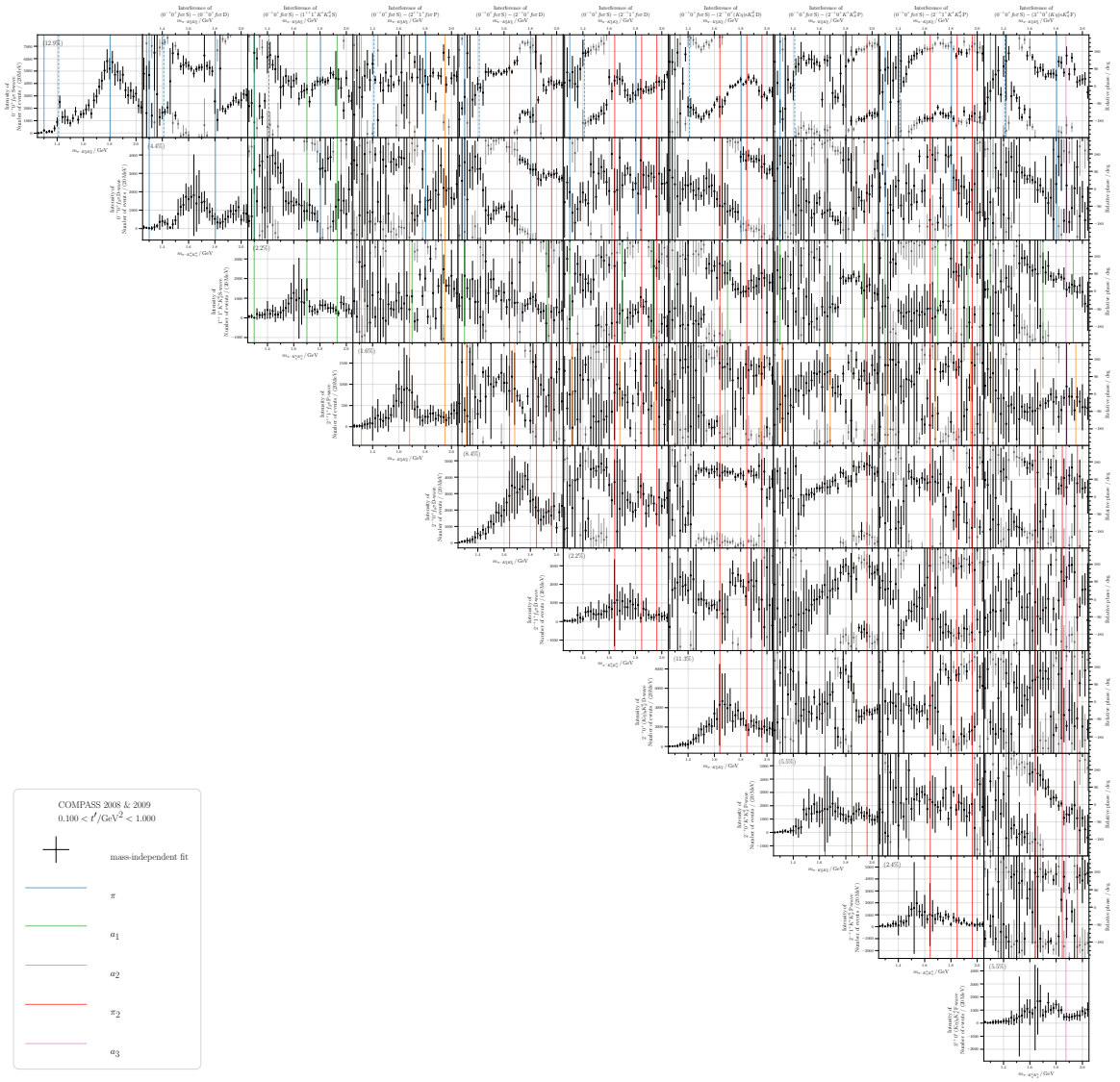

Figure F.16: The reference wave $0^{-+}0^{+}$ $f_0(980)\pi$ S together with all remaining waves not included in Figure F.14. Fit with finer resonance mass binning. Plot intended for the digital version of this thesis.

List of Figures

List of Tables

Glossary

K_S^0-candidate A SV where the two daughters, with assigned pion-mass hypothesis, have an invariant mass within ±50 MeV of the nominal K_S^0 mass. 119–121, 127, 128, 155, 191, 293

BEST-Style Plots created with `BEST`, where all cuts of the event selection are applied except the one on the discussed spectrum. 114–121, 129, 131, 135, 137, 138, 257, 260, 261

"ROOT magic" Obviously there is no magic involved, but sometimes root can create interesting or unexpected results due to its global pointers, object ownerships and clean-up functionalities, which will be referred to as "ROOT magic". 259, 293

"close" K_S^0 SV with both daughter particles also coming from the BPV. 121–125

"far" K_S^0 SV with none of the two daughter particles coming from the BPV. 122–128, 264, 293

"healthy" BPV A BPV is considered "healthy" if the event contains exactly five distinct charged tracks, two from each "true" K_S^0 and one negatively charged track from the BPV. In the case of $N_{\text{out}}^{\text{BPV}} = 2$ the one outgoing track of the BPV that is not part of the "shared" K_S^0, has negative charge. 128, 137

"shared" K_S^0 SV with one of the two daughter particles also coming from the BPV. 122–128, 159, 163, 175, 187, 264, 293

"true" K_S^0 A K_S^0-candidate with stronger invariant-mass requirement, see equation (5.6) and sufficiently large vertex separation, see equation (5.7) according to its classification as "far" K_S^0 or "shared" K_S^0. 128, 130–134, 293, 297

"true" PV The BPV or a different PV that has at least one track that is not part of the final state. 137, 138

GJ frame A specific CMS of the resonance, where the z-axis points in the direction of the boosted beam $\hat{z}_{\text{GJ}} = \hat{p}_{\text{beam}}$ and the y-axis is given by $\hat{y}_{\text{GJ}} \parallel \vec{p}_{\text{target}} \times \vec{p}_{\text{beam}}$, cf. section 3.4.4 and Figure 3.11 on the left. 41–44, 50, 153, 212

`Mathematica` convention Complex numbers are defined in polar coordinates using the range $\varphi \in (-\pi, \pi]$ for the polar angle. This is the convention used by `Mathematica` and it corresponds to `sqrt`$(z; 0)$ of equation (3.24). 16, 17, 19–24, 29, 32, 33, 221–224

acceptance Probability to detect a specific final state with an experimental setup for a given set of kinematic variables. 9, 10, 47, 48, 56, 99, 105, 111, 112, 115, 138, 155, 157–161, 169, 171, 173, 179, 189, 191, 193, 211, 245, 251

Antok Tool developed at TUM to perform event selections on COMPASS data and inspiration of BEST. 114, 257

Argand diagram For a three-body decay, the number of events (usually in a small window of the three-body invariant mass) is plotted against two squared invariant masses of the three possible two-body subsystems. See section 3.5.1 for more details. 26, 81, 82, 164–168, 220

bachelor The third particle in a three-body decay that is not part of the intermediate two-body resonance, the isobar. 36, 43, 83

BPV The PV with the smallest χ^2 during the vertex fitting. 113

break-up momentum Momentum of the daughter particles in a two-body decay of a resonance in its rest frame, which can be calculated via equation (A.2). 28, 30, 34, 87, 208, 209

camel style Style for naming variables in a coding language, where every new word for a variable or function name starts with a capital letter. 258

Chew-Mandelstam Function as defined by equation (3.38) that can be used instead of a two-body phase space, cf. equation (3.40). Its complex structure is discussed in section 3.3.3. 31–33

Chew-Mandelstam BW BW with an energy-dependent width as of equations (3.35) and (3.34), where we perform the replacement specified in equation (3.40). 31, 33, 60, 74, 77, 78, 83, 221, 222, 224

collinearity Angle between the reconstructed momentum direction of a K_S^0 and the connecting line between the BPV and its SV, see equation (5.1). 124, 125, 127, 245

COMGEANT Previous MC generator of the COMPASS collaboration based on GEANT3. 10

cyclic indices A set of indices $(ijk) \in \{(123), (231), (312)\}$, usually occurring when the indices of an expression stays valid via replacements $1 \to 2 \to 3 \to 1$ and $1 \to 3 \to 2 \to 1$. 42, 43, 59, 212

Dalitz plot For a three-body decay, the number of events (usually in a small window of the three-body invariant mass) is plotted against two squared invariant masses of the three possible two-body subsystems. See section 3.5.1 for more details. 5, 36, 40, 48, 49, 51, 54–57, 59, 108, 142, 146–151, 155, 161, 188–191, 193, 194, 216

diffractive A beam particle is excited via Pomeron exchange with the target and decays "diffractively" while keeping the target particle in tact. A depiction of such a process can be found in Figure 3.10(a). 5, 7, 9, 37, 41, 46, 48, 102, 103, 105, 110, 112, 155, 191, 194, 255

diquark A $[qq']$ pair is called a diquark, similarly a $[\overline{qq}']$ is called the corresponding antidiquark. They can appear in two forms, as spin-0 diquark in form of color-antitriplets and as spin-1 diquarks in form of color-sextuplets. In both cases they are flavor-antitriplets. Due to the antisymmetric flavor wave function, the quarks in a diquark cannot be equal. More details can be found in appendix C.2 and [42]. 68

dispersion relation A method to recover the full amplitude from its discontinuity or its imaginary part, for more details see equation (3.21). 17, 18, 73, 296

downstream With this, one means "in the direction of the beam". 115

Flatté Parametrization of an energy-depending width in the case of two possible decay channels, see equation (3.37). 30, 98, 164, 165

helicity frame A specific CMS of the isobar, without loss of generality in the (23) system, where the z-axis points in the opposite direction of the boosted particle 1, $\hat{z}_H = -\hat{p}_1$ and the y-axis is given by $\hat{y}_H \parallel \vec{p}_1 \times \vec{p}_{\text{beam}}$, cf. section 3.4.4 and Figure 3.11 on the right. 41–44, 50, 110, 210, 217–219

isobar Intermediate resonance in one of the two-body subsystems of a three-body decay. 36, 37, 40–43, 48, 50–52, 54, 55, 57, 59–62, 70, 74, 76, 82–84, 144, 145, 150, 151, 155, 159, 163–168, 170, 172, 174–176, 179, 188, 189, 192, 193, 195, 212, 220, 294, 295

isobar model Model for a three-body decay, which assumes a cascade of two two-body decays with an intermediate isobar resonance in one of the two-body subsystems, e.g. $X \to \xi\zeta_1$, $\xi \to \zeta_2\zeta_3$. Shortcomings of this model are the neglect of direct three-body decays without intermediate resonances like e.g. $\omega \to 3\pi$, as well as the omission of final-state interactions e.g. the rescattering process discussed as the origin of the $a_1(1420)$ signal. 36, 39–41, 43, 85, 210

naturality It is +1 for scalars $J^P = 0^+$, vectors $J^P = 1^-$, tensors $J^P = 2^+$ and so on, and −1 for pseudoscalars $J^P = 0^-$, pseudo-vectors $J^P = 1^+$, pseudo-tensors $J^P = 2^-$, therefore, it can be calculated via $P(-1)^J$. 36, 48, 295

physics convention Complex numbers are defined in polar coordinates using the range $\varphi \in [0, 2\pi)$ for the polar angle. The square-root function in `Mathematica` corresponds to $\texttt{sqrt}(z; \pi - \varepsilon)$ of equation (3.24). The ε is only necessary when one wants to evaluate the function exactly on the positive real axis. 16, 19, 20, 22–24, 29, 32, 33, 35, 221–224

Pomeron Hypothetical t-channel exchange particle – dominant in scattering with high beam energies – that can be interpreted as a gluon ladder, in first order approximation by a double-gluon exchange. 37, 40, 41, 48, 87, 105, 106, 151, 255, 294

PV A crossing of the beam track with an arbitrary number of tracks measured by the spectrometer downstream of the target. 111

reflectivity corresponds to the eigenvalue of the decay amplitude under reflection on the production plane and in the high-energy limit it is equal to the naturality of the exchange particle $\epsilon = P_{I\!R}(-1)^{J_{I\!R}}$. 36, 43, 45, 48, 55, 213–215

Reggeon General t-channel exchange particle, mostly dominated by pions. 36, 151, 255

Riemann sheet Branch cuts, e.g. from functions like the square root and the logarithm, open up gates to different sheets of the complex plane where we obtain different versions of these functions. Examples can be found in section 3.2 . 15, 16, 19–21, 24, 27–29, 31, 83, 222, 223

ROOT Object-oriented library developed at CERN and designed for data analysis in particle physics. It is not an acronym, but could be interpreted as "Rapid Object-Oriented Technology". 9, 251, 260, 264

Schwarz Reflection Principle A function fulfills $f^*(z) = f(z^*)$, for more details see section 3.2.1. 15–17, 20, 21, 24, 35

significance Quantity that allows for an optimization of certain cut criteria. It provides a reasonable compromise between quality and quantity and is defined in equation (5.2). 124–127

subtraction Method needed to obtain a dispersion relation for a function that does not vanish at complex infinity, see equation (3.22). 18, 60

SV A crossing of a positively and a negatively charged track. 106

TGEANT Current MC generator of the COMPASS collaboration based on GEANT4. 9, 10, 48, 157

upstream With this, one means "in the opposite direction of the beam". 114

Waterfall-Style The event selection follows the given cut flow as defined in the corresponding "cut-flow diagram" and only cuts before the discussed spectrum are applied. 114–120, 129, 135, 137, 138, 257, 258, 260, 261

Acronyms

ℓH2 liquid-hydrogen target. 7, 37, 157

μDST micro DST. 10

π^-_{prim} Negatively charged outgoing track from the BPV that is not part of any "true" K^0_S of the final state. The mass of a pion is assigned to this track. 128, 130, 131, 137, 151–155, 163, 251–255

$\pi^\pm_{\text{sec}}$ Daughter tracks from the "true" K^0_S. The mass of a pion is assigned to these tracks. 128, 130, 131, 137, 162

BEST Bonn Event Selection Tool described in appendix E. 114, 257–267, 293, 294, *Glossary:* BEST-Style

DT0 Diffractive Trigger. 7, 115, 262

ℓQCD lattice-QCD. 4, 5, 28, 175, 195

BC Beam Counter. 115

BK Beam Killer. 115

BMS Beam Momentum Station. 7

CEDAR ChErenkov Detector with Achromatic Ring focus. 7, 116, 117, 121, 158

DC Drift Chamber. 8, 124

ECAL Electromagnetic CALorimeter. 8, 9, 56, 111, 112, 137, 244, 247

GEM Gas Electron Multiplier. 8, 9, 110

HCAL Hadronic CALorimeter. 8, 9, 111, 112

LAS Large-Angle Spectrometer. 8, 9

LAT Large-Area Tracker. 8, 9

MWPC Multi-Wire Proportional Chamber. 8, 110

MW Muon Wall. 9

MicroMEGAS Micro MEsh GAseous Structures. 8, 124

NaN "not a number". 89

PMT Photo-Multiplier Tube. 119

PixelGEM Pixel Gas Electron Multiplier. 8, 9

RICH Ring-Imaging CHerenkov detector. 8, 105, 106, 112, 116, 117, 129–132, 137, 155, 158, 175, 189

RPD Recoil-Proton Detector. 7, 113, 115, 118–120, 134, 135, 155

SAS Small-Angle Spectrometer. 8, 9

SAT Small-Area Tracker. 8

SM1 Spectrometer Magnet 1. 8

SM2 Spectrometer Magnet 2. 8, 115

SciFi Scintillating Fiber. 7, 115

Silicon Silicon microstrip detector. 7–9, 123

Straws Straw Tube Trackers. 8

W45 Wire chambers. 8

WASP Wave Analysis Software Tool [72]. 163

aBT alternative Beam Trigger. 7, 115

AMBER Apparatus for Meson and Baryon Experimental Research. 9, 189, 192, 194

aMC accepted MC. 10, 48, 158–160, 187

BPV Best Primary Vertex. 113, 114, 118, 119, 121–124, 127–129, 137, 152, 160, 162, 175, 246, 265, 293, 294, 297, *Glossary:* BPV

BW Breit-Wigner. 24–27, 29–31, 33, 34, 60, 70, 72, 74, 77, 78, 83, 87, 88, 98, 164, 186, 221–224, 294

BWM Breit-Wigner Model. 25–27, 31, 33, 34, 43, 54, 63, 64, 74, 78, 81–83, 87, 88, 90–99, 101–104, 164–168, 178–180, 191, 192, 195, 220

c.c. complex conjugate. 68, 69

CDF Cumulative Distribution Function. 110

CERN European Council for Nuclear Research. 7, 296

CMS Center-of-Momentum System. 34, 38, 42, 207–209, 216, 217, 251, 293, 295

COMPASS COmmon Muon Proton Apparatus for Structure and Spectroscopy. 7–10, 37, 40, 47, 48, 54, 56, 63, 69, 85, 99, 100, 103, 105, 106, 110, 112, 113, 115, 129, 134, 138, 143, 144, 151, 155, 157, 158, 163, 176, 179, 189–194, 246, 294, 296

CORAL COmpass Reconstruction ALgorithm. 9, 10, 48, 158

CQM Constituent-Quark Model. 63, 64, 67

DAQ Data AcQuisition. 9

DST Data Storage Trees. 9, 10, 297, 299

em electromagnetic. 1, 2, 105

GEANT GEometry ANd Tracking. 10, 157, 158, 160, 294, 296

GJ Gottfried-Jackson. 41–44, 50, 153, 212, 293

gMC generated MC. 10, 157–161

LAB LAB System. 159, 207, 251

LED Light-Emitting Diode. 118

MC Monte-Carlo. 10, 44, 47, 48, 99, 111, 112, 118, 138, 151, 153–155, 157–163, 169, 173, 175, 187–189, 191, 193, 195, 210, 211, 251–254, 264, 294, 296, 298–300

MCt MC truth. 264

mDST mini DSTs. 9

PDG Particle Data Group [29]. 28, 59, 66, 80, 88, 98, 104, 108–111, 114, 120, 133, 142, 143, 146, 147, 164, 179, 186, 246, 251

PHAST PHysics Analysis Software Tools. 9, 10, 48, 113, 116, 122, 137, 247, 257–259

PID Particle IDentification. 117, 120, 121, 129, 130, 155, 189

PV Primary Vertex. 111–113, 116, 119, 128, 137, 138, 159, 189, 255, 261, 264, 293, 294, *Glossary:* PV

PWD Partial-Wave Decomposition. 10, 34, 40, 46, 54, 59, 64, 70, 74, 85, 86, 89, 91, 98–101, 103, 142–144, 150, 151, 154, 155, 157, 158, 163, 164, 166, 170, 171, 173–177, 179, 181, 183, 184, 186–195, 211, 269, 272–274, 276–281

QCD Quantum Chromo Dynamics. 4, 225, 226, 297

QED Quantum Electro Dynamics. 106

QN Quantum Number. 3–5, 10, 34, 36, 37, 39–43, 45, 48, 50, 55, 59, 63, 65–69, 74, 98, 102, 106, 107, 110, 143, 172, 176, 179, 185, 192, 213, 226

RD Real Data. 10, 48, 153, 157–163, 179, 187–189

rMC reconstructed MC. 10, 158

RMS Root Mean Square, i.e. the square root of the arithmetic mean of the squares. 99, 104, 192

SDM Spin-Density Matrix. 45, 46, 86

SPS Super Proton Synchrotron. 7, 112

SV Secondary Vertex. 106, 110, 111, 113, 114, 119–124, 128, 137, 159, 160, 162, 175, 189, 245, 259, 293, 294, *Glossary:* SV

TS Triangle Singularity. 69, 71, 72

TSM Triangle-Singularity Model. 88, 90–99, 101–104, 178, 191, 192, 194

TUM Technical University of Munich. 114, 257, 294

Danksagungen / Acknowledgements / Agradecimientos

An dieser Stelle möchte ich mich bei meinen Kollegen, meinen Freunden und meiner Familie bedanken. Allen voran geht mein größter Dank an meinen Doktorvater, Prof. Dr. Bernhard Ketzer. Vielen Dank, dass du mir den Weg in die Wissenschaft eröffnet hast. Ich habe durch dich immer wieder die Gelegenheit bekommen um über mich hinaus zu wachsen. Sei es die Fähigkeit, durch die vielen ermöglichten Konferenzen und Workshops, ohne Angst vor einem großen Publikum einen Vortrag über meine Ergebnisse zu halten. Oder die anvertrauten Aufgaben in der IT unserer Arbeitsgruppe inklusive erster Erfahrungen in Web-Design. Ich hatte sogar die Möglichkeit als Vorlesungsassistent zu fungieren und 300 Studierende zu bändigen, sowie selbstständig ein paar Vorlesungen zu halten. Durch dich und deine Unterstützung ist aus mir, glaube ich, ein ganz akzeptabler Physiker und Programmierer geworden.

Mein nächster Dank geht an Prof. Dr. Hartmut Schmieden. Vielen Dank für das Interesse an meiner Arbeit und die Bereitschaft mein zweiter Gutachter zu sein. Des Weiteren möchte ich mich bei den anderen beiden Mitgliedern meiner Prüfungskommission bedanken, Priv.-Doz. Dr. Bastian Kubis und meinem ehemaligen Mathematik-Professor Prof. Dr. Carl-Friedrich Bödigheimer, der mir die die Welt der komplexen Analysis eröffnet hat.

A big thanks goes to my colleagues at the COMPASS and the AMBER collaborations. Especially during my first visit on-site, but also later, there was always somebody in the building – very often the technical coordinators, no matter the time – that could help in case of problems with the experiment. During my many night shifts, I also had a lot of interesting conversations and discussions with my fellow shifters.

I do not want to miss mentioning the hadron-subgroup coordinators Dr. Boris Grube, Dr. Stephan Wallner and Prof. Dr. Mikhail Mikhasenko. During countless hadron-subgroup meetings I got valuable advices to be able to continue my work. Also to our colleagues in Munich goes a big thank you for the many informative discussions during these meetings. Here, a special thanks goes to Julien Beckers. We were a good team when working on each others crosschecks!

Nun zu meinen Arbeitskollegen in Bonn. First of all, I want to thank Prof. Dr. Mikhail Mikhasenko. Even now, long after you left the group, you are still always available for discussions about physics, providing helpful advice and guidance.

Ein riesen Dank geht an Henri Pekeler. Ohne dich und deine großartige Arbeit beim Beschleunigen von TGEANT würde ich wohl immer noch auf meine MC Daten warten. Und auch beim PWA-Programm hast du parallelisiert und optimiert wo es nur ging, obwohl dein Final State eh nur ne Minute braucht. Hier ist auch der Cluster-Support deinerseits zu erwähnen. Man muss quasi nur noch auf einen Knopf drücken und die Maschinerie läuft. Vielen Dank auch dafür, dass du dich die letzten

Monate vor Abgabe meiner Doktorarbeit quasi alleine um die IT-Aufgaben der Gruppe gekümmert hast!

Bei David Spülbeck möchte ich mich für die super Vorarbeit bei unserem PWD-Programm bedanken, unter anderem in Hinsicht auf die Umsetzung des Isobarenmodells und den dazugehörigen Parametrisierungen. Dadurch war die erste Implementierung meines Final States ein Klacks. Aber auch danach waren wir zusammen mit Henri ein gutes Team um unser WASP zu korrigieren, zu erweitern und zu optimieren.

Dr. Philip Hauer danke ich für seine ausführliche Dokumentation des Prozederes zur Abgabe der Doktorarbeit und dem Bereitstellen von Beispielen für Lebenslauf und Co. an denen man sich orientieren kann. Weiterhin vielen Dank, dass du dich Anfang des Semesters quasi alleine um die Physik-I Vorlesung gekümmert hast und mir damit einiges an Arbeit während des Abgabestresses abgenommen hast. Und danke für das finale Überprüfen der Formatierungen meiner Arbeit, sowie dass ich bei deiner eigenen Verteidigung dabei sein durfte, um einen Einblick in das Verfahren zu bekommen.

Meinen beiden Kollegen Martin Hoffmann und Michael Hösgen danke ich für hilfreiche Anmerkungen und Kommentare in unseren Gruppenmeetings und unsere sonstigen Gespräche im Büro oder Flur über dies und das.

Des Weiteren möchte ich auch meine anderen Doktorandenkollegen dankend erwähnen: Dr. Dmitri Schaab als mein erster Kontakt zur Gruppe im Particle-Physics-Tutorium zu meiner ersten Vorlesung mit Bernhard, Karl Flöthner und Fabian Metzger für eure Unterstützung am CERN, und die Mensa-Gang Jan Paschek und Ankur Yadav, aber auch meine inzwischen ehemaligen Kollegen Philipp Bielefeldt, Stephan Kürten (nochmals danke für den "Tritt", du weißt schon) und Elizaveta Fotina.

Bei meinen Schützlingen Waldemar Renz, Lukas Bayer und Jonas Aufdermauer bedanke ich mich für eure großartige Arbeit während eurer Bachelor- und Masterarbeiten.

Viele Teile meiner Arbeit wurden vorab von meinen Kollegen gelesen. An dieser Stelle möchte ich daher nochmal speziell in (alphabetischer Reihenfolge) Martin Hoffmann, Prof. Dr. Bernhard Ketzer, Prof. Dr. Mikhail Mikhasenko, Henri Pekeler und David Spülbeck danken. Meinem Schulfreund Marc Pause danke ich, dass du dich durch den ganzen physikalischen Kauderwelsch gequält hast für wohl tausende fehlende Kommata, falsch platzierte Zeitwörter und Präpositionen, sowie für allgemeinen Ausdruck.

Abseits meiner Arbeitsgruppe möchte ich mich noch bei Prof. Dr. Ian Brock für die Erstellung und Bereitstellung des LaTeX-Templates für diese Doktorarbeit bedanken. Ein weiterer persönlicher Dank geht an den IT-Support vom HISKP, Dr. Michael Lang, und vom PI, Dr. Andreas Wißkirchen und Dr. Oliver Freyermuth, für eure Hilfe bei allgemeinen IT-Problemen in unserer Arbeitsgruppe. Insbesondere dir Oliver möchte ich auch für deine großartige Arbeit beim Cluster-Support danken, denn es ist nicht nur einmal vorgekommen, dass man sogar am Wochenende eine Nachricht bekommen hat, dass mal wieder ein Job am Cluster hängt und Probleme macht.

I want to thank Prof. Dr. Volker Metag and Dr. Thomas Jude for your interest in my triangles and for giving me the chance to participate in your research.

Und last but not least möchte ich mich bei meiner Familie und meinen Freunden bedanken für die allgemeine Unterstützung und das Verständnis für meine Abwesenheit bei einigen Festivitäten, insbesondere im (etwas länger ausgefallenen) Entspurt meiner Arbeit. Aber nicht nur meiner Familie

in Deutschland, sondern auch meiner neugewonnen Familie in Mexiko, möchte ich danken. Muchas gracias por aceptarme como soy y por sus muchos buenos deseos y apoyo emocional. Les agradezco también por preparar una oficina en su casa para que pudiera seguir trabajando en mi tesis durante nuestra visita.

Por último, y aún más importante, quiero dar las gracias a mi esposa, que ha permanecido despierta conmigo durante los muchos turnos de noche, ayudándome en lo que ha podido, leyendo, revisando, escuchando y buscando documentos y artículos. También gracias por hacerme tomar descansos, dormir y salir a pasear al aire libre y por tu cuidado general de mi salud cuando yo no podía.

Contributions

Publications

Papers

- G. D. Alexeev et al., COMPASS, *Triangle Singularity as the Origin of the $a_1(1420)$*, **Phys. Rev. Lett. 127**, 082501 (Aug 2021)
  Own contributions: Perform the theoretical calculations, the fit to the data, and the systematic studies. Strong involvement in writing the text.

- V. Metag et al., CBELSA/TAPS, *Observation of a structure in the $M_{p\eta}$ invariant mass distribution near* $1\,700\,\mathrm{GeV}/c^2$ *in the $\gamma p \to p\pi^0$ reaction*, **Eur. Phys. J. A 57** (2021) 12, 325 (Dec 2021)
  Own contributions: Provide theory calculations of the rescattering (Fig. 17).

Internal COMPASS Release Notes

- M. Wagner et al., *Mass-dependent fit of the $a_1(1420)$ via the "Triangle Singularity"* (Oct 2017),
  URL: http://wwwcompass.cern.ch/compass/results/2017/september_triangular_a1_1420/release_note.pdf

- M. Wagner et al., *Update on the mass-dependent fit of the $a_1(1420)$ via the "Triangle Singularity"* (Oct 2019),
  URL: http://wwwcompass.cern.ch/compass/results/2019/october_a1_1420_triangle_sys/Release_note_a1_1420_triangle_sys.pdf

- J. Beckers et al., *Event Selection of the Reactions $\pi^- + p \to K^0_S K^- + p$, $K^- + p \to K^0_S \pi^- + p$, and $K^- + p \to \Lambda\bar{p} + p$* (Mar 2022),
  URL: http://wwwcompass.cern.ch/compass/results/2022/january_KsPi/KsPi_Event_Selection_COMPASS_release_note.pdf
  Own contributions: Perform cross check of the three event selections.

- M. Wagner et al., *Event Selection of $K^0_S K^0_S \pi^-$* (Mar 2023),
  URL: http://wwwcompass.cern.ch/compass/results/2023/march_KsKsPi_final_state/ReleaseNote_KsKspi_020323.pdf

Conference Talks

- M. Wagner, *"Dispersive approach to the triangle diagram in the decay of the $a_1(1260)$ resonance"*, **DPG spring meeting**, Münster (Mar 29, 2017)

- M. Wagner, *"The axial-vector $a_1(1420)$ as a triangle singularity"*, **DPG spring meeting**, Bochum (Feb 28, 2018)
- M. Wagner, *"Incorporating Spin into Rescattering Effects via Partial-Wave Projections – The $a_1(1420)$"*, **DPG spring meeting**, Munich (Mar 22, 2019)
- M. Wagner, *"From Pions to Kaons – Hadron Spectroscopy from COMPASS to AMBER"*, on behalf of COMPASS at **IWHSS**, Aveiro (Jun 25, 2019)
- M. Wagner, *"Fit of the $a_1(1420)$ as a Triangle Singularity"*, **Arbeitstreffen Kernphysik**, Schleching (Mar 3, 2020)
- M. Wagner, *"A Triangle Singularity as the Origin of the $a_1(1420)$"*, **HADRON**, Mexico City (Jul 30, 2021)
- M. Wagner, *"Fit of the $a_1(1420)$ as a Triangle Singularity"*, **DPG meeting**, virtual (Sep 3, 2021)
- M. Wagner, *"Fit of the $a_1(1420)$ as a Triangle Singularity"*, **Workshop "e^+e^- Collisions from Phi to Psi"**, Shanghai (Aug 19, 2022)
- M. Wagner, *"Diffractive resonance production in the reaction $\pi^- + p \to K^0_S K^0_S \pi^- + p$ at 190 GeV/c from COMPASS"*, **DPG spring meeting**, Dresden (Mar 22, 2023)

Additional Visited Workshops

- International Summer Workshop on Reaction Theory, Bloomington 2017
- TRR110 Workshop - Amplitudes for Three-Body Final States, Munich 2018
- Frontiers in Nuclear and Hadronic Physics, Florence 2019
- School on Efficient Scientific Computing, Bertinoro 2019

Supervised Theses

Master

- Waldemar Renz – *Partial-Wave Analysis of the $(\eta\pi)$-state with Bayesian LASSO at the COMPASS experiment* (2021)
- Lukas Bayer – *Selection and first analysis of the $\omega\pi\pi$ final state at COMPASS* (2022)

Bachelor

- Waldemar Renz – *Akzeptanzbestimmung mit einer Monte Carlo Simulation für den $\pi^- p \to \pi^- p \eta(\pi^+\pi^-\pi^0(\gamma\gamma))$-Zustand* (2018)
- Jonas Aufdermauer – *Monte-Carlo-Studien über den Rückstoßprotonendetektor des COMPASS-Experiments* (2019)

Miscellaneous

Service Work for COMPASS/AMBER

- $\sim$ 120 days on site for expert on-call for GEM and PixelGEM detectors
- 65 shifts for the data taking of the experiments
- Perform time calibration for GEM and PixelGEM detectors for data taking in 2022

IT Duties for the AG Ketzer

- Setup of new computers, integration into HISKP network
- Create and integrate computing accounts for new group members
- IT support for installation of custom software for various purposes
- Implementation and maintenance of group webpage with Plone5 (together with H.) Pekeler
- Implementation of webpage with Plone5 for the new FTD (together with H. Pekeler)

Tutorials

WS13/14	Analysis I (during Mathematics Bachelor)
SS15	Mathematics für Physicists II: Analysis in higher dimensions (during Physics Bachelor)
WS16/17	Mathematics for Physicists III: Complex Analysis (during Physics Master)
WS17/18	Physics V: Nuclear and Particle Physics
SS18	Advances Laboratory Course, Bachelor: P4: scanning tunneling microscope, P5 : Mott scattering
WS18/19	Theoretical Physics II: Electromagnetism
SS19	Hadron Physics
WS19/20	Particle Physics
SS20	Hadron Physics
WS20/21	Physics I: Mechanics/Thermodynamics - Head tutor (online lecture)
SS21	Physics II: Electrodynamics - Head tutor (online lecture)
WS22/23	Physics of Particle Detectors
SS23	Hadron Physics
WS24	Physics I: Mechanics/Thermodynamics - Head tutor Substitute lecturer for 4 lectures of “Mathematische Ergänzungen zur Physik I”
total	10× tutorials, 2× lab course experiments, 3× head tutor, 1× lecturer